To the Graduate Council:

I am submitting herewith a dissertation written by Jose A. Lamas, entitled "Evaluation of the Thermal Design of a Liquid-Lens Cooling System for Projection Picture Tubes." I have examined the final copy of this dissertation for form and content and recommend that it be accepted in partial fulfillment of the requirements for the degree of Doctor of Philosophy, with a major in Mechanical Engineering.

Robert J. Krane, Major Professor

We have read this dissertation
and recommend its acceptance:

Accepted for the Council:

Vice Provost and Dean of
Graduate Studies

EVALUATION OF THE THERMAL DESIGN OF A LIQUID-LENS COOLING SYSTEM FOR PROJECTION PICTURE TUBES

A Dissertation
Presented for the
Doctor of Philosophy Degree
The University of Tennessee, Knoxville

Jose Angel Lamas

May 2002

Thesis
2002b
.L36

Copyright © Jose A. Lamas, 2002
All rights reserved

ACKNOWLEDGEMENTS

I would like to thank professors R. J. Krane and J. R. Parsons for inviting me to become part of the four-member student team which participated in the research project aimed at investigating thermal design practices for television receivers. Thanks are due to North American Philips Consumer Electronics Corporation (NAPCEC) for providing the funding for such project, which originated in the spring of 1987 and lasted through the spring of 1988, and to the members of its engineering staff, Mr. A. Korte, Mr. D. Remeta, Mr. H. Vodinh, Mr. S. Waddell, and Mr. Z. Salij for their interest and assistance. I would like to acknowledge the participation of Mr. B. Zandi of the above student team in the co-development of a numerical model used to generate numerical results for the above research project. I would like to thank the former Engineering Science and Mechanics Department at the University of Tennessee for their providing the computer facilities used during the NAPCEC research project. Thanks are also in order to the College of Engineering and to the former University of Tennessee Computer Center (UTCC) for facilitating computer resources at times during this project, and to the Mechanical and Aerospace Engineering Department for providing laboratory facilities.

I would like to thank my major professor, Dr. Krane for his commitment and availability to bounce ideas, help to keep focused, and for his comments on my dissertation. Thanks are also due to the other graduate committee members, Dr. Parsons, Dr. M. Parang, and Dr. V. Alexiades, for their participation and guidance. I would like to thank Dr. W. Lawkins for our early discussions regarding numerical methods. I would like to convey my appreciation for the invaluable assistance provided by Mr. Dennis Higdon at the Mechanical & Aerospace Engineering instrumentation shop throughout the course of my dissertation research in instrumenting the experimental apparatus, and other laboratory activities.

Finally, I would like to thank my wife Nury, for her supporting my decision and implications of moving to Knoxville in order to complete my dissertation, and also to members of both of our families and our friends for their words of encouragement.

ABSTRACT

The thermal design of a liquid-lens system for cooling picture tubes in projection television receivers is evaluated using an experimentally benchmarked numerical model. Because of the intense brightness in the visual image, excessive waste heat is generated as the by-product of light emission from the phosphor screen as the electron beam sweeps across the raster region at the back of the face panel. Projection tube specifications indicate a maximum allowable temperature at the face-panel center and a maximum allowable temperature differential between the center and perimeter points. To cool the tube's face, an optical liquid (liquid lens) fills the space between the face panel and a meniscus lens directly in front of it. A metallic enclosure frame serves as support for the meniscus lens and a container for the liquid. Heat is transferred by natural convection from the face panel to the enclosure frame and from there to the interior environment of the television cabinet by convection and radiation.

A boundary-fitted, finite-volume-based numerical model of the conjugate heat transfer and fluid flow processes within the liquid-lens system was developed and benchmarked with experimental data for nominal operation with the tube face oriented upward, making 30° with the horizontal. Results proved the thermal design adequate, with additional performance margin. Approximately 94% of the electrical input power is converted into heat at the phosphor screen (6% into visible light). Of that heat, 79% is transferred to the face-panel front by conduction, 19% to the tube interior by radiation, and 2% to the face panel sidewalls by conduction. Thermal performance is virtually unaffected by changes in the enclosure frame dimension, meniscus-lens design and position, or by variations in the tilt angle between 0° (face up) and 130°. Thermal performance is virtually insensitive to the meniscus lens thermal conductivity, but it can be enhanced using an optical liquid having higher thermal conductivity, density, specific heat, and volume expansivity or lower kinematic viscosity. If the need arises for enhancements in thermal performance; that is, lower temperatures or smaller temperature gradients on the tube face, forced convection cooling should be used instead of natural convection.

TABLE OF CONTENTS

CHAPTER *PAGE*

1. INTRODUCTION 1
1.1. Motivation for the Present Research 1
1.2. A Typical Projection Television Receiver 1
1.2.1. Description of Major Components 1
1.2.2. Components of a Monochrome Projector 2
1.2.3. Components of a Picture Tube 4
1.2.4. Image Reproduction Process 6
1.3. The Liquid-Lens System 6
1.4. Modes of Heat Transfer 8
1.5. Liquid-Lens Thermal Performance 9
1.6. Statement of the Problem 10
1.7. Chapter Contents 11
2. BACKGROUND, RELATED HEAT TRANSFER RESEARCH, AND DETAILED SOLUTION APPROACH 12
2.1. Introduction 12
2.2. Natural Convection in Enclosures 12
2.2.1. Fundamentals 12
2.2.2. Two-Dimensional Enclosures 16
2.2.3. Three-Dimensional Enclosures 26
2.2.4. Conjugate Natural Convection Flows: The Effect of Wall Conduction 27
2.3. Effect of Thermal Radiation 28
2.4. Summary of the Review and Discussion 28
2.5. Detailed Solution Approach 33
3. EXPERIMENTAL EVALUATION OF THE LIQUID-LENS SYSTEM 36
3.1. Experimental Apparatus 36
3.1.1. Description of the Liquid-Lens System 36
3.1.2. Instrumentation 39
3.1.3. Experimental Setup 44
3.2. Experimental Results 45
3.2.1. Transient Temperature Measurements 46
3.2.2. Extrapolation of Transient Temperatures to Steady-State 46
3.3. Steady-State Experimental Temperatures on the CRT Face Panel 47

4. REVIEW OF NUMERICAL METHODS IN HEAT TRANSFER AND FLUID FLOW 53
4.1. Introduction 53
4.2. Dependent and Independent Variables 53
4.3. Formulations for Solving the Navier-Stokes Equations 54
4.3.1. Vorticity/Stream-Function Formulation 54
4.3.2. Vorticity-Velocity Formulation 55
4.3.3. Vector-Scalar Potential Formulation 55
4.3.4. Vector-Potential/Vorticity Formulation 56
4.3.5. Primitive-Variable Formulation 56
4.3.6. Summary 57
4.4. Methods for Solving Differential Equations 57
4.4.1. The Finite-Difference Method 57
4.4.2. The Finite-Element Method 58
4.4.3. The Finite-Volume Method 58
4.5. Discretization of the Differential Equations in Domains with Curved Boundaries 59
4.5.1. Direct Integration with Step-Wise Approximation 59
4.5.2. Solution of the Partial Differential Equations in the Transformed Domain 60
4.5.3. Solution of the Partial Differential Equations with Conforming Boundaries in the Physical Domain 62
4.6. Space Discretization 62
4.7. Time Discretization 65
4.8. Flux Discretization 67
4.9. Grid/Variable Arrangement 71
4.10. Iteration Structure for an Initial-Value Problem 73
4.11. Derivation of the Pressure Equation and Solution of the System of Mass-Momentum Equations 74
4.11.1. Time-Explicit Methods 75
4.11.2. Time-Implicit Methods 76
4.12. Summary 86
5. THE MATHEMATICAL MODEL 89
5.1. Scope of the Model 89
5.2. Assumptions in the Derivation of the Numerical Model for the Heat Transfer and Fluid Flow within the Liquid-Lens System 91
5.3. Dependent and Independent Variables 91

5.4. Conservation Laws 92
5.4.1. Law of Conservation of Mass 92
5.4.2. Newton's Second Law of Motion 93
5.4.3. Law of Conservation of Energy 94
5.4.4. Conservative Forms of the Governing Equations 96
5.4.5. Using Temperature as the Dependent Variable 97
5.4.6. Governing Differential Equations 99
5.4.7. Coordinate System and Base Vectors 100
5.4.8. General Conservation Equation 101
5.4.9. Non-Dimensionalization of the Generalized Conservation Equation 103
5.4.10. Non-Dimensionalization of the Particular Governing Equations 107
5.5. Dimensionless Forms of the Governing Equations 111
5.6. Summary 112
6. DEVELOPMENT OF THE FINITE-VOLUME HEAT TRANSFER AND FLUID FLOW NUMERICAL MODEL 114
6.1. Introduction 114
6.2. Preliminary Models 114
6.3. The Finite-Volume Model 114
6.4. Integration and Discretization of the General Advection-Diffusion Equation 115
6.5. Grid Structure and Discretization of Surface Areas, Volumes, and Fluxes for Hexahedral Topology 119
6.5.1. Statement of the Discretized Equation Using A Hexahedral, Structured Grid 119
6.5.2. Face Area Discretization and Face-Node Positioning 121
6.5.3. Cell Volume Discretization and Cell-Node Positioning 122
6.6. Discretization of Cell-Facet Fluxes 123
6.6.1. Advection/Diffusion Cell-Facet Flux Discretization 124
6.6.2. General Conservation Equation in Algebraic Form 130
6.6.3. General Boundary Condition 133
6.7. Conservation Equations in Algebraic Forms 134
6.7.1. Boundary Conditions for the Momentum Conservation Equations 137
6.7.2. Boundary Conditions for the Energy Equation 138
6.7.3. Closure 139
6.8. Solution Method Requirements 140
6.9. System of Equations 141
6.10. Iteration Scheme 144

6.11. Pressure-Velocity Coupling Equations 146
6.11.1. Face-Based Momentum Equations and Velocity Vector 146
6.11.2. Cell-Facet Normal Velocity 150
6.11.3. Enforcement of Mass Conservation 153
6.11.4. Face-Node Pressure Equation 155
6.12. Balance of the Conservation-Quantity Fluxes 156
6.13. Solution Algorithm 158
6.14. Program Checks 159
7. NUMERICAL MODEL OF THE LIQUID-LENS SYSTEM 164
7.1. Introduction 164
7.2. CFD Model Geometry 164
7.3. Thermophysical Properties 171
7.4. Grid-Coordinate Parameterization 171
7.5. Computational Grid 174
7.6. Hydrostatic Check Run 179
7.7. Computational Run with Nominal Inputs 179
7.7.1. Boundary Conditions 180
7.7.2. Program Results 188
7.8. Optimization of the Boundary Conditions 199
7.8.1. Optimization Solution Approach 199
7.8.2. Process for Identifying Suspect Data Points 200
7.8.3. Optimization Methodology 202
7.8.4. Optimization Criteria 205
7.8.5. Optimization Process 205
7.8.6. Optimization Solution Implementation 206
7.8.7. Optimization Program Results 206
7.8.8. Selection of the Reference Case 209
7.9. Reference Case Final Run 209
7.9.2. Liquid-Lens Thermal Performance 212
7.9.3. Heat Flux Analysis 214
7.9.4. Comparison against Predictions Using Heat Transfer Correlations 217
7.9.5. Full-Enclosure Run 217
7.9.6. Overall Thermal Characterization 217
7.9.7. Summary 219
8. VISUALIZATION OF NUMERICAL RESULTS 220
8.1. Introduction 220

8.2. Isobars 220
8.3. Description of Flow Circulation 220
8.4. Isotherms 229
8.5. Thermal Isoflux Lines 231
8.6. Thermal Isograds 231
8.7. Heatlines 237
9. DIMENSIONLESS PARAMETERS AND SIMPLIFICATION OF BOUNDARY CONDITIONS 241
9.1. Introduction 241
9.2. Reference Scales and Dimensionless Variables 241
9.2.1. Nondimensionalization of the Variables Used in the Benchmark Model 245
9.3. Simplification of Boundary Conditions 251
9.3.1. Case 1 -- Effect of Insulating Face Panel Side Surfaces 252
9.3.2. Case 2 -- Effect of Having an Isothermal Enclosure Frame 254
9.3.3. Case 3 -- Effect of Having an Isothermal Meniscus lens Exterior 254
9.3.4. Case 4 -- Effect of Insulating the Face Panel Back Surface 255
9.3.5. Case 5 -- Combined Effects 255
9.3.6. Case 6 -- Effect of Applying Heat Generation to the Entire Face Panel Back 255
9.4. Selection of Simplified Boundary Conditions to be Used in the Performance Study 256
10. A PERFORMANCE STUDY OF THE LIQUID-LENS SYSTEM 257
10.1. Introduction 257
10.2. Variation in Thermophysical Properties and Boundary Conditions 257
10.2.1. Variation in the Prandtl Number 257
10.2.2. Effect of Variation in the Modified Rayleigh Number 259
10.2.3. Effects of Variations in the Face-Panel Conductivity Ratio 261
10.2.4. Effects of Variations in the Meniscus Lens Conductivity Ratio 263
10.2.5. Discussion 265
10.2.6. Conclusion 268
10.3. Uncertainty in the Raster Region Dimensions 268
10.3.1. Effects of the Heated-Region Width Uncertainty 268
10.3.2. Effects of the Heated-Region Height Uncertainty 270
10.3.3. Summary 272
10.4. Variation in the Tilt Angle 272
10.5. The Effects of Varying Geometry on Thermal Performance 275
10.5.1. Effect of Variation in the Enclosure Frame Width 275

10.5.2. Effect of Variation in the Enclosure Height 277
10.5.3. Effect of Variation in the Enclosure Depth 277
10.5.4. Effect of Replacing the Meniscus Wall with a Circular Plate 279
10.6. Summary 280
11. ALTERNATIVE COOLING METHODS 284
11.1. Introduction 284
11.2. Enhancement of Internal Heat Transfer 284
11.3. Enhancement of External Heat Transfer 288
12. CONCLUSIONS AND RECOMMENDATIONS 291
12.1. Summary 291
12.2. Effects of Design Changes on Thermal Performance 292
12.3. Effects of Orientation Changes on Thermal Performance 293
12.4. Effects of Variation in Material Properties on Thermal Performance 293
12.5. Effects of the Uncertainty Raster Area Dimensions on Thermal Performance 293
12.6. Recommendations for Thermal Design Improvements 294
LIST OF REFERENCES 295
APPENDIX 307
APPENDIX A. EXPERIMENTAL APPARATUS 308
A.1. Equipment Description 308
A.1.1. Monochrome Projectors 308
A.1.2. Liquid Coolant Characteristics 318
A.2. Instrumentation Procedure 318
APPENDIX B. DATA COLLECTION 323
B.1. Preparation 323
B.2. Procedure 323
B.3. Experimental Measurements 324
B.4. Steady-State Limit 328
B.5. Uncertainty Analysis 332
B.6. Lumped-Parameter Model 332
APPENDIX C. THERMOPHYSICAL PROPERTIES 337
C.1. Fluid Thermophysical Properties 337
C.1.1. Reference Fluid Thermophysical Properties 337
C.1.2. Measurement of Fluid Mass Density 338

C.1.3. Calculation of Mass Density, Specific Heat, and Volume Expansivity 339
C.1.4. Calculation of Thermal Conductivity 340
C.1.5. Measurement of Fluid Kinematic Viscosity 342
C.1.6. Measurement of Fluid Dynamic Viscosity 345
C.1.7. Summary of Fluid Properties 347
C.2. Solid Thermophysical Properties 347
APPENDIX D. NUMERICAL MODEL BENCHMARK CASES 353
D.1. Heat Conduction in a Cubical Domain 353
D.2. Convection Boundary Condition 356
D.3. Self-Consistency between Curvilinear and Rectilinear Grids 357
D.4. Calculation Checks on Natural Convection in Tilted Rectangular Enclosures 362
D.5. Hydrostatic Check Run 364
D.5.1. Boundary and Operating Conditions 364
D.5.2. Program Run 368
D.5.3. Program Results 370
D.5.4. Summary of Results for the Hydrostatic Check Case 374
APPENDIX E. APPROXIMATION OF EXPERIMENTAL BOUNDARY CONDITIONS AS INPUTS TO THE NUMERICAL MODEL 375
E.1. CRT Face Panel Light Conversion Efficiency 375
E.2. Radiation Heat Transfer through the CRT Face Panel Glass 378
E.3. Effective Heat Transfer Coefficient for the CRT Face Panel Back 381
E.4. Base Plate Side Boundary Conditions 386
E.5. Effective Heat Transfer Coefficient for the Meniscus-Wall Front Surface 386
APPENDIX F. COMPUTER SETUP 388
APPENDIX G. CALCULATIONS FOR THE NUMERICAL MODEL OF THE EXPERIMENTAL RUN 389
G.1. Optimization of Boundary Conditions 389
G.2. Experimental Reference Case 398
G.2.1. Thermal Network Model 398
APPENDIX H. MATHEMATICAL BACKGROUND 403
H.1. Material Time Derivative Operator 403
H.2. Vector Operations 403
H.2.1. Gradient of a scalar function 403
H.2.2. Scalar (Dot) Product of Two Vectors 404

H.3. Matrix Operations 404
H.3.1. Unit Matrix 404
H.3.2. Transpose Operator. 404
H.3.3. Velocity Vector Gradient 405
H.3.4. Transposed Velocity Vector Gradient 405
H.3.5. Divergence of the Velocity Vector Gradient 405
H.3.6. Divergence of the Transposed Velocity Vector Gradient 406
APPENDIX I. Preliminary Numerical Models 407
I.1. Preliminary Cartesian Model 407
I.2. Preliminary Advection-Diffusion Interpolation Schemes 407
I.3. Preliminary Advection-Diffusion Interpolation Schemes 409
I.4. Summary 418
APPENDIX J. COORDINATE TRANSFORMATION 420
J.1. Base Vectors 420
J.2. Length, Area, and Volume Elements 421
J.3. Area Element Relationships 421
J.4. Transformation of the General Advection/Diffusion Equation 423
VITA 429

LIST OF TABLES

TABLE *PAGE*

Table 3-1. Thermocouple Locations 40

Table 3-2. CRT Face Panel Thermocouple Junction Coordinates and Channel Number 43

Table 3-3. Variables Related to Electron-Beam Input Power 46

Table 3-4. Steady-State Experimental Temperatures 51

Table 3-5. Experimental Values of the CRT Face Panel Steady-State Temperatures 52

Table 4-1. Summary of Common Implicit Prediction-Correction Pressure-Velocity Solution Algorithms 86

Table 5-1. Equivalence between Variables in the Generalized Conservation Equation and Variables in the Particular Conservation Equations 103

Table 5-2. Reference Quantities in the Generalized Conservation Equation 104

Table 5-3. Dimensionless Variables in the Particular Conservation Equations 112

Table 6-1. Set of Variables in the System of Equations 143

Table 6-2. Set of Independent Equations 143

Table 7-1. Computational Domain Dimensions 168

Table 7-2. Liquid-Lens System Domain Boundaries 169

Table 7-3. Thermophysical Properties Used in the Calculations 171

Table 7-4. Domain Cell Distribution within Parametric Space 176

Table 7-5. Sub-Domain Cell Distribution within Parametric Space 176

Table 7-6. Comparison of CFD-Grid and Exact Material Sub-Domain Volumes 179

Table 7-7. Sensitivity of the CRT Face-Panel Back-Surface Net Heat Transfer Coefficient to Back-Surface Temperature 184

Table 7-8. Base-Plate Side Surface Net Heat Transfer Coefficients 186

Table 7-9. Boundary Conditions for the Liquid-Lens Nominal Case 190

Table 7-10. Energy and Momentum Balance -- Nominal Case 191

Table 7-11. Nominal Case Numerical and Experimental Temperature Comparison at Face Panel Grid Locations 191

Table 7-12. Nominal-Case Statistics 195

Table 7-13. Parameter Fractions for the Optimization Grid 204
Table 7-14. Optimization Results' Summary 208
Table 7-15. Reference Case Heat Flux and Raster Dimensions 211
Table 7-16. Reference Case Numerical and Experimental Temperature Comparison at CRT Face Panel Grid Locations 212
Table 7-17. Reference Case Statistics 213
Table 7-18. Flux Balance – Experimental Reference Case 213
Table 7-19. Face Panel Thermal Compliance 214
Table 7-20. Reference Case CFD-Domain Thermal Boundary Fluxes and Mean Temperatures 215
Table 7-21. Heat Dissipation Distribution 218
Table 8-1. Maximum Values on the Base-Plate Back and Front Surfaces – Reference Case 239
Table 8-2. Minimum Values on the Base-Plate Back and Front Surfaces – Reference Case 240
Table 9-1. Independent Variables: Computational Domain Dimensions 242
Table 9-2. Independent Variables: Thermophysical Properties 242
Table 9-3. Independent Variables: Environmental Properties 242
Table 9-4. Independent Variables: Boundary Conditions 243
Table 9-5. Independent Reference Scales and Properties 246
Table 9-6. Dimensionless Parameters for Geometry Specification 246
Table 9-7. Property-Related Dimensionless Parameters 246
Table 9-8. Boundary-Condition Dimensionless Parameters 247
Table 9-9. Derived Reference Scales 247
Table 9-10. Dimensionless Results 248
Table 9-11. Performance Summary for Variations from the Reference Configuration 253
Table 10-1. Effect of Enclosure Frame Width Variations on Thermal Performance 276
Table 10-2. Effect of Enclosure Height Variations on Thermal Performance 278
Table 10-3. Effect of Enclosure Depth Variations on the Thermal Performance Parameters 281
Table 10-4. Maxima on the Base-Plate Back and Front Surfaces 283
Table 11-1. Effect of Forced Convection on Thermal Performance 286
Table A-1. Components of the Projection Monitor 310

Table A-2. Projection Assembly Parts 311
Table A-3. Picture Tube Mechanical Data 312
Table A-4. Picture Tube Performance Ratings 313
Table A-5. Relative Spectral Power Distribution Data for the Green CRT 315
Table A-6. Data Acquisition and Instrumentation Items 319
Table B-1. Rate of Change in the Mean Temperature at the End of the Experiment 325
Table B-2. Thermocouple Temperatures: Channels #00 - #09 326
Table B-3. Thermocouple Temperatures: Channels #10 - #19 327
Table B-4. Optimization-Variable Definitions 331
Table B-5. Calculation of Constants in the Curve-Fitting Equation (Equation of Motion) 331
Table B-6. Summary of Curve-Fitting Results – Channels 0 thru 9 333
Table B-7. Summary of Curve-Fitting Results – Channels 10 thru 19 334
Table B-8. Power-Measurement Related Values and Uncertainty 334
Table C-1. Reference Properties for Ethylene Glycol 337
Table C-2. Reference Properties for Glycerin 338
Table C-3. Correction Ratios for Density and Specific Heat 339
Table C-4. Fluid Properties Resulting from the Mixture Model 340
Table C-5. Conduction Model Results at the Reference Temperatures 342
Table C-6. Equipment for Kinematic Viscosity Measurements 343
Table C-7. Kinematic Viscosity Laboratory Data 344
Table C-8. Equipment for Thermal Conductivity Measurements 346
Table C-9. Dynamic Viscosity Laboratory Data and Comparison with Kinematic Viscosity Measurements 346
Table C-10. Fluid Property Functions 348
Table C-11. Fluid Properties Used for Interpolation 348
Table C-12. Equipment for Thermal Conductivity Measurements 349
Table C-13. EMF Transient Values for Ebonite, Glass 7740, and Quartz 350
Table C-14. Steady-State EMF Calibration Values for Ebonite, Glass 7740, and Quartz 351
Table C-15. EMF Transient Values for the CRT Face Panel Glass and the Meniscus Lens Glass 351

Table C-16. Experimentally Determined Thermal Conductivity Values for the CRT Face-Panel Glass and the Meniscus-Lens Glass 352
Table D-1. Heat transfer in Differentially Heated Cubical Domain with Isothermal Lower and Upper Surfaces 354
Table D-2. Solutions for Imposed Heat Flux and Isothermal Walls 355
Table D-3. Rayleigh Number, Prandtl Number, and Aspect Ratio for Cases of Natural Convection in Tilted Enclosure 363
Table D-3. Exact Solution for the Hydrostatic Check Case 368
Table D-4. Iteration Control: Exit Tolerances and Limits on the Number of Iterations 369
Table D-5. Inputs Used in the Calculation of the Net Body Force 370
Table D-6. Calculation of the Net Body-Force in Each Coordinate Direction 371
Table D-7. Hydrostatic Problem: Flux Balance and Body-Force 372
Table D-8. Pressure Comparison against the Exact Solution 372
Table E-1. Black-body Emissive Power and Glass Transmittance Used to Estimate Heat Radiation through the Face-Panel Glass 380
Table E-2. Calculations of the Linearized Heat Transfer Coefficient for Heat Transfer from the Face Panel Back to the Environment 387
Table G-1. Exponent of the Parametric Variables in the Cross-Run Interpolation Function 390
Table I-1. Surface/Volume-Discretization Metrics for Various Grid Options ... 411
Table I-2. Flux-Discretization Node-Cluster Coordinate Orthogonality for Various Grid Options 412

LIST OF FIGURES

FIGURE *PAGE*

Figure 1-1. Schematic Views of a Typical Projection Television Receiver 2
Figure 1-2. Monochrome Projector Plan Views 3
Figure 1-3. Monochrome Projector Cut-Away-View 4
Figure 1-4. Major Components of a Picture Tube 5
Figure 1-5. Liquid-Lens Concept and System Definition 7
Figure 1-6. Modes of Heat Transfer in the Liquid-Lens System 9
Figure 1-7. CRT Face Panel Thermal Performance Requirements 10
Figure 2-1. Geometry Configurations for Natural Convection in Rectangular Enclosures 14
Figure 2-2. Isotherms and Flow Structure in Natural Convection Enclosure Flows 18
Figure 2-3. Tilted Enclosure Typical Flow Configurations 21
Figure 2-4. Typical Nusselt Number Dependency on Enclosure Tilt Angle and Aspect Ratio 23
Figure 2-5. Natural Convection in Finite Rectangular Enclosures Heated From Below and Cooled on the Side 24
Figure 2-6. Natural Convection in a Vertical Enclosures with the Upper Wall Shaped as a Sine-Wave 25
Figure 2-7. Base Flow and Instability Contributions from Decomposition of Boundary Condition Types 31
Figure 2-8. Anticipated Three-Dimensional Base Flow Circulation 32
Figure 3-1. Cut-Away Views of the Experimental Liquid-Lens System 37
Figure 3-2. Liquid-Lens Configuration During the Experiment 38
Figure 3-3. Thermocouple Locations on the Enclosure Frame and Meniscus Lens 41
Figure 3-4. Location of Thermocouple Junctions: CRT Face Panel 42
Figure 3-5. Location of Thermocouple Junctions: Focusing Lens Array 43
Figure 3-6. Voltage Measurement Circuit Diagram 44
Figure 3-7. Instrumentation Setup 45
Figure 3-8. Temperature Curve Fits: Meniscus Lens 48
Figure 3-9. Temperature Curve Fits: Enclosure Frame 48
Figure 3-10. Temperature Curve Fits: CRT Face Panel Edge 49

Figure 3-11. Temperature Curve Fits: CRT Face Panel Grid 49
Figure 3-12. Temperature Curve Fits: Focusing Lens Interior 50
Figure 3-13. Steady-State Experimental Temperatures on the Face Panel 52
Figure 4-1. Coordinate Transformation Problem 64
Figure 4-2. Mass-Conservation/Energy-Conservation Control Volume and Velocity-Node Locations for the Colocated-Grid Arrangement 72
Figure 4-3. Time- and Iteration-Stepping Terminology for an Initial-Value Problem 74
Figure 4-4. Calculation Sequence for a Basic Implicit Prediction-Correction Method 79
Figure 4-5. Calculation Sequence for Common Implicit Prediction-Correction Methods 85
Figure 5-1. Liquid-Lens System Domain Outline and Generic Boundary Conditions 90
Figure 5-2. Elemental System 92
Figure 5-3. The Concept of the Hydrostatic Reference Field 99
Figure 6-1. Finite Volume Used for Integration 116
Figure 6-2. Variables Defining the Control-Volume Face Geometry 119
Figure 6-3. Identification of Face-Node Variables for a Structured-Grid Hexahedral Control Volume 120
Figure 6-4. Geometry Elements Involved in the Facet-Based Flux Discretization 125
Figure 6-5. Top-Level Solution Scheme 160
Figure 6-6. Equation-Variable Flowchart for the Outer Loop 161
Figure 6-7. Equation-Variable Flowchart for the Inner Loops 162
Figure 7-1. Computational Model Geometry 166
Figure 7-2. Computational Model Dimensions -- Orthogonal Projections 167
Figure 7-3. Schematic View of the Computational Model Boundaries 168
Figure 7-4. Schematic View of the Computational Model Boundaries 172
Figure 7-5. Parametric Space Coordinate Markers 175
Figure 7-6. Computational Grid Perspective and Exploded Views 177
Figure 7-7. Computational Grid Orthogonal Projection Views on Cartesian Planes and Geometry Model Overlays 178
Figure 7-8. Energy Conversion Model within the Phosphor Layer 181
Figure 7-9. Phosphor-Layer Energy Flow Breakdown 182

Figure 7-10. Network Model for Heat Transfer from the Face Panel Back to the Environment 184
Figure 7-11. Base-Plate Side Boundary Heat Transfer Coefficients 186
Figure 7-12. Summary of Boundary Conditions 189
Figure 7-13. Comparison between Numerical and Experimental Temperatures on the CRT Face Panel Grid – Nominal Case 193
Figure 7-14. Effect of Removing Individual Data Points from the Calculation of the Correlation Coefficient 195
Figure 7-15. Sequential Solution Optimization Search 201
Figure 7-16. Pre-Calculated-Solution Optimization Search 201
Figure 7-17. Gridded-Solution Optimization Search 203
Figure 7-18. Distribution of the Correlation Error Function and the Correlation Coefficient Over the Configuration Space 207
Figure 7-19. Comparison of Optimization Results 210
Figure 7-20. Comparison of Numerical and Experimental Temperatures on the CRT Face Panel 211
Figure 7-21. Reference Model Boundary Energy Fluxes 216
Figure 8-1. Isobars on Coordinate Planes 221
Figure 8-2. Pathlines Starting at Points 2 mm from the Base Plate and Isobar Overlay 222
Figure 8-3. Pathlines Starting at Points on the X_2=0 Plane 223
Figure 8-4. Pathlines Starting at Points on the X_1=0 Plane (Symmetry Plane) 224
Figure 8-5. Pathlines Starting at Points on Various Vertical Planes (at Constant X_1 Coordinates) 225
Figure 8-6. Domain Perspective View with Pathlines Departing from Selected Surfaces: Set I – Reference Case 226
Figure 8-7. Domain Perspective View with Pathlines Departing from Selected Surfaces: Set II – Reference Case 227
Figure 8-8. Isotherms on the Base Plate Back and Front Surfaces 230
Figure 8-9. Isotherms on Coordinate Planes 232
Figure 8-10. Isotherms on the Meniscus Wall 233
Figure 8-11. Thermal Isoflux Lines on the Base Plate Back and Front Surfaces 234
Figure 8-12. Domain-Outward Thermal Isoflux Lines on Cooled Surfaces 235

Figure 8-13. Lines of Thermal Isograds on the Base Plate Back and Front Surfaces 236
Figure 8-14. Heatlines and Isotherms on the Vertical Symmetry Plane 238
Figure 8-15. Heatlines Departing from the Baseplate Back Surface 239
Figure 10-1. Effect of Variation in the Prandtl Number with Heat Generation Applied to the Reference Area 258
Figure 10-2. Effect of Variation in the Modified Rayleigh Number with Heat Generation Applied to the Reference Area 260
Figure 10-3. Effect of Variation in the Face panel Conductivity ratio with Heat Generation Applied to the Reference Area 262
Figure 10-4. Effect of Variation in the Meniscus lens Conductivity Ratio with Heat Generation Applied to the Reference Area 264
Figure 10-5. Effect of Variation in the Heated-Region Width Fraction at the Reference Height Fraction 269
Figure 10-6. Effect of Variation in the Heated-Region Height Fraction at the Reference Width Fraction 271
Figure 10-7. Effect of Variation in the Tilt Angle with Heat Generation Applied to the Reference Area 274
Figure 10-8. Variations Limits for the Dimensions of the Enclosure-Frame Depth 279
Figure 10-9. Computational Model Geometry 282
Figure 11-1. Internal Forced-Convection Concept 285
Figure 11-2. Improved Cooling by Enhancements of Internal Heat Transfer 289
Figure 11-3. Improved Cooling by Enhancing External Heat Transfer 290
Figure A-1. Schematic of the 46-inch Color Projection Television Receiver Used for Laboratory Measurements 309
Figure A-2. Projection Picture Tube Dimensions 314
Figure A-3. Relative Spectral Power Distribution for the Green CRT 314
Figure A-4. Enclosure Frame Dimensions 316
Figure A-5. Meniscus Lens Dimensions 317
Figure A-6. Focusing Lens Dimensions 317
Figure A-7. Schematic of the CRT Face Panel Thermocouple Wire Routing 321
Figure B-1. Lumped-Parameter Model Used to Predict the Face-Panel Exterior Mean Temperature 335
Figure C-1. Conduction Models 341

Figure C-2. Fisher/Tag Saybolt Viscosimeter Used for Kinematic Viscosity Measurements 343
Figure C-3. Kinematic Viscosity Temperature Dependency 344
Figure C-4. Fisher MacMichael Viscosimeter Used for Dynamic Viscosity Measurements 345
Figure C-5. Dynamic Viscosity and Fluid Strain Rate 347
Figure C-6. Thermal Conductivity Measurement Instrument 349
Figure C-7. Thermal Conductivity Calibration Curve 351
Figure C-8. EMF Transient Values for all Materials 352
Figure D-1. Exterior-Surface-Grid for Conduction in a Cube 354
Figure D-2. Domain and Boundary Conditions for Checking the Solution with Convection Boundary Condition 356
Figure D-3. Equivalent Resistor Network 357
Figure D-4. Natural Convection Square Domain Enclosure with Superimposed 10x10 Rectilinear and Curvilinear Grids 358
Figure D-5. Comparison of the Horizontal and Vertical Centerline Maximum Velocities for Solutions using Rectilinear and Curvilinear Grids ..359
Figure D-6. Comparison of the Nusselt Number at the Heated-Wall from Rectilinear and Curvilinear Grid Solutions 360
Figure D-7. Geometry and Boundary Conditions for the Case of Natural Convection in Tilted Rectangular enclosures 362
Figure D-8. Comparison between Present Numerical Results and Experimental Data in the Literature for Natural Convection in a Tilted Differentially Heated Rectangular enclosure of Aspect Ratio 3 and for Various Rayleigh and Prandtl Number Sets 363
Figure D-9. Comparison between Present Numerical Results and Experimental Data in the Literature for Natural Convection in a Tilted Differentially Heated Rectangular enclosure of Aspect Ratio 4, and for Various Rayleigh and Prandtl Number Sets 364
Figure D-10. Computational Model Orientation, Initial, and Boundary Conditions 365
Figure D-12. Natural-Convection Upper-Bound-Velocity Scaling Model 366
Figure D-13. Isobars on the Vertical Symmetry Plane 373
Figure D-14. Pressure Profiles along the Base Plate Slope 374
Figure E-1. Spectral Power Distribution 377
Figure E-2. Network Model for Heat Transfer from the Face Panel Back to the Environment 382

Figure G-1. Network Model for Lumped-System Analysis 399
Figure G-2. Network Model for the Experimental Reference Case 402
Figure I-1. Options for Grid Coordinate Parameterization 410
Figure I-2. Pressure Node Cluster for the Dual Grid Arrangement 415
Figure J-1. Schematic of Curvilinear Coordinates and Base Vectors in Cartesian Space 420

LIST OF SYMBOLS

Abbreviations/Acronyms

CDS	Central Differencing Scheme
CFD	Computational Fluid Dynamics
CRT	Cathode Ray Tube
CTS	Consistent Time Step
DAQ	Data Acquisition
EDS	Exponential Differencing Scheme
EMF	Electro-Motive Force
HDS	Hybrid Differencing Scheme
LOADS	Locally Analytic Differencing Scheme
N/A	Not Available
PISO	Pressure-Implicit with Splitting of Operators
PLDS	Power-Law Differencing Scheme
QUDS	Quadratic-Upwind Differencing Scheme
QUICK	Quadratic Interpolation for Convective Kinematics
SIMPLE	Semi-Implicit Method for Pressure-Linked Equations
SIMPLEC	SIMPLE, Consistent
SIMPLER	SIMPLE, Revised
SIVA	Simultaneous Variable Adjustments
SUDS	Skew-Upwind Differencing Scheme
TV	Television
UDS	Upwind-Differencing Scheme
VDC	Direct-Current Voltage
WQUDS	Weighed, Quadratic-Upwind Differencing Scheme

Variables

Order of Precedence: Uppercase, Lowercase, Subscript, Superscript

Variable	*Description* [Units][1]
A^j	General face area in parametric direction j (j=1,2,3)
A_{f}^j	j-Facet Area (j=1,2,3)
A_i^j	j-Facet Area projection on i-Cartesian coordinate plane (i,j=1,2,3)
A_R	Raster surface area [m^2]
Ar	Aspect ratio [-]
A_b	Baseplate face surface area [m^2]
$\bar{a}_j$	Covariant base vector in parametric direction j (j=1,2,3) [-]
$\bar{a}^j$	Contravariant base vector in parametric direction j (j=1,2,3) [-]
a_{c}^p	Coefficient of the pressure-equation cell-node pressure [-]
a_{c}^t	Coefficient of the temperature-equation cell-node temperature [-]
a_{c}^u	Coefficient of the velocity-equation cell-node velocity [-]
$a_{\mathrm{f}_j^-}^p$	Coefficient of the cell's negative-side face pressure in parametric direction j (j=1,2,3) [-]
$a_{\mathrm{f}_j^+}^p$	Coefficient of the cell's positive-side face pressure in parametric direction j (j=1,2,3) [-]
$a_{\mathrm{f}_j^-}^t$	Coefficient of the cell's negative-side face temperature in parametric direction j (j=1,2,3) [-]
$a_{\mathrm{f}_j^+}^t$	Coefficient of the cell's positive-side face temperature in parametric direction j (j=1,2,3) [-]

[1] Vector and tensor units are for the individual components

$a^{u}_{f_j^-}$	Coefficient of the cell's negative-side face velocity in parametric direction j (j=1,2,3) [-]
$a^{u}_{f_j^+}$	Coefficient of the cell's positive-side face velocity in parametric direction j (j=1,2,3) [-]
a^{t}_{o}	Coefficient of the previous-time-step temperature [-]
a^{u}_{o}	Coefficient of the previous-time-step velocity [-]
b^{p}_{c}	Constant term in the pressure algebraic equation [-]
b^{t}_{c}	Constant term in the energy conservation algebraic equation [-]
$b^{u_i}_{c}$	Constant term in the i-momentum conservation algebraic equation (i=1,2,3) [-]
c	Capacitance [-]
c_D	Dimensioning scale for the thermal capacity density [J/m^3-K]
c_m	Thermal capacity per unit volume [J/m^3-K]
c_p	Constant-pressure specific heat [J/kg-K]
$c_{p,D}$	Dimensioning scale for the constant-pressure specific heat [J/kg-K]
c_v	Constant-volume specific heat [J/kg-K]
δ^i_j	Kroenecker delta: $\delta^i_j = 1$ for $i = j$; $\delta^i_j = 0$ for $i \neq j$
$\vec{f}_b$	Body force vector per unit volume [N/m^3]
$\vec{f}_s$	Surface force vector per unit volume [N/m^3]
G	Correlation error function
G^u_c	Cell-node pressure-gradient factor
G^u_f	Face-node pressure-gradient factor
g_i	Cartesian component of the gravitational acceleration vector in direction i (i=1,2,3) [m/s^2]
$\vec{g}$	Gravitational acceleration vector [m/s^2]
H	General surface flux generation ***or*** Heated-region height [m]
h	Convection coefficient [W/m^2-K] ***or*** General surface flux-density generation
I_k	Anode current [mA]
I_v	Luminous intensity [cd]

$\mathbb{I}$	Unit tensor [-]
J	Jacobian of the coordinate transformation [-]
J_i^l	l-i area equivalence factor (projection of the l-direction contravariant base vector in the i-direction Cartesian coordinate; i,l=1,2,3) [-]
k	Thermal conductivity [W/m-K], also fluid thermal conductivity [W/m-K]
k_1	Baseplate thermal conductivity [W/m-K]
k_2	Meniscus wall thermal conductivity [W/m-K]
k_D	Dimensioning scale for the thermal conductivity [W/m-K]
k_e	Baseplate effective thermal conductivity [W/m-K]
k_m	Thermal conductivity for material m [W/m-K]
$\hat{k}_m$	Dimensionless thermal conductivity for material m [-]
L_v	Radiance [ft-L]
m	Current iteration step (outer loop) [-]
Nu	Nusselt number [-]
Nu^*	Modified Nusselt number [-]
Nu_1	Nusselt number contribution from heat transfer to the meniscus wall [-]
Nu_2	Nusselt number contribution from heat transfer to the enclosure [-]
n	Previous time step (transient loop) [-]
P	Piezometric pressure (difference between the local static pressure, P_s, and the reference-field hydrostatic pressure, P_{hs}, at the same gravitational potential plane, $P = P_s - P_{hs}$) [Pa]
P_{hs}	Reference-field hydrostatic pressure at the reference temperature (T_0) [Pa]
Pr	Prandtl number [-]
P_s	Static pressure [Pa]
P_v	Luminous flux [lm] ***or*** Velocity pressure [Pa]
P_λ	Spectral power [W/nm]
p	Dimensionless piezometric pressure [-]
p_c	Pressure evaluated at the cell node [-]
Δp_c	Pressure increment from cell node to cell auxiliary node [-]
p_f	Pressure evaluated at the face node [-]
p'	Pressure corrector [-]

Q_{f}^{j}	j-Face volumetric flow rate (j=1,2,3)
$\hat{Q}_{\mathrm{f}}^{j}$	j-Face pseudo-volumetric flow rate (j=1,2,3)
$\hat{\hat{Q}}_{\mathrm{f}}^{j}$	j-Face gross pseudo-volumetric flow rate (j=1,2,3)
Ra	Rayleigh number [-]
Ra_{m}	Rayleigh number based on the baseplate front mean temperature [-]
Ra^{*}	Modified Rayleigh number [-]
R_{λ}	Relative spectral power [1/nm]
T	Static temperature [°C, K]
T_{j}^{E}	Experimental temperature at point j
T_{j}^{N}	Numerical temperature at point j
T_{o}	Reference temperature [°C, K]
S^{u_i}	Momentum source in the i-direction, i=1,2,3
$\mathbb{T}$	Stress tensor [Pa]
$\mathbb{T}_{str}$	Strain-induced stress tensor [Pa]
t	Dimensionless temperature [-]
t_{c}	Cell-node temperature [-]
t_{c}^{m}	Cell-node temperature at the end of the current (outer loop) iteration step [-]
t_{c}^{m*}	Cell-node intermediate-step (inner loop) temperature [-]
$t_{\hat{\mathrm{c}}}$	Temperature evaluated at the auxiliary cell node
Δt_{c}	Temperature increment from cell node to auxiliary cell node [-]
t_{f}	Face-node temperature [-]
t_{f}^{m}	Face-node temperature at the end of the current (outer loop) iteration step [-]
t_{f}^{m*}	Face-node intermediate-step (inner loop) temperature [-]
t_{m}	Dimensionless mean temperature [-]
t_{o}	Previous time-step-level cell-node temperature [-]
U_{D}	Reference velocity scale [m/s]
U_{i}	Cartesian velocity component in direction i (i=1,2,3) [m/s]

$\vec{U}$	Velocity vector [m/s]
u_i	Dimensionless Cartesian velocity component in direction i (i=1,2,3) [m/s]
u'	Velocity corrector [-]
$\vec{u}$	Dimensionless Cartesian velocity vector, $\vec{u} = \sum_{i=1}^{3} u_i \vec{\varepsilon}_i$ [-]
$\vec{u}_c$	Cell-node Cartesian velocity vector [-]
$\vec{\hat{u}}_c$	Cell-node Cartesian pseudo-velocity vector [-]
$\vec{u}_f$	Cartesian velocity vector evaluated at the face node [-]
$\vec{\hat{u}}_f$	Face-node Cartesian pseudo-velocity vector [-]
$u_{i,c}$	Cell-node Cartesian velocity in i-direction (i=1,2,3) [-]
$u_{i,c}^{m}$	Cell-node Cartesian velocity in i-direction (i=1,2,3) at the end of the current (outer loop) iteration step [-]
$u_{i,c}^{m*}$	Cell-node intermediate-step (inner loop) Cartesian velocity in i-direction (i=1,2,3) [-]
$u_{i,f}$	Face-node Cartesian velocity in i-direction (i=1,2,3) [-]
$u_{i,f}^{m}$	Face-node Cartesian velocity in i-direction (i=1,2,3) at the end of the current (outer loop) iteration step [-]
$u_{i,f}^{m*}$	Face-node intermediate-step (inner loop) Cartesian velocity [-]
$\hat{u}_{i,c}$	Cell-node Cartesian pseudo-velocity in i-direction (i=1,2,3) [-]
$\Delta u_{i,c}$	i-Cartesian-velocity increment from cell node to auxiliary cell node (i=1,2,3) [-]
$u_{i,o}$	Previous time-step-level cell-node Cartesian velocity in i-direction (i=1,2,3) [-]
$\vec{u}$	Dimensionless velocity vector [-]
u_i^{m*}	Intermediate-step (inner-loop) velocity component in i-direction (i=1,2,3) [-]
u_i'	Velocity-correction component in direction i (i=1,2,3) [-]
$\hat{u}_i'$	Pseudo-velocity-correction component in direction i (i=1,2,3) [-]
$V(\lambda)$	Spectral luminous efficiency [-]

$\mathcal{V}_c$	Cell volume [-]
v_f	Face-normal velocity [-]
v_f^j	j-Face normal velocity (j=1,2,3) [-]
$\hat{v}_f$	Face-normal pseudo-velocity [-]
$\hat{v}_f^j$	j-Face normal pseudo-velocity (j=1,2,3) [-]
$\hat{\hat{v}}_f^j$	j-Face normal gross pseudo-velocity (j=1,2,3) [-]
W	Heated-region width [m]
X_D	Dimensioning length scale [m]
X_i	Cartesian coordinate in direction i, i=1,2,3 [m]
$\vec{X}$	Position vector [m]
x_i	Dimensionless Cartesian coordinate in direction i, i=1,2,3 [-]
$\vec{x}$	Dimensionless position vector, $\vec{x} = \sum_{i=1}^{3} x_i \vec{\varepsilon}_i$ [-]
y^j	Curvilinear coordinate in parametric direction j (j=1,2,3) [-]
z^j	Local j-face normal coordinate in parametric direction j (j=1,2,3) [-]
$\Delta z_{\pm}^j$	Distance between the face node and the cell auxiliary node on the negative (-) or positive (+) parametric side of the face (j=1,2,3) [-]

Variables Beginning with Greek Letters

Variable	*Description* [Units][1]
α	Thermal diffusivity [m²/s]
β	Volume expansivity (thermodynamic definition) (also coefficient of constant-pressure thermal volumetric expansion, also thermal expansivity) [1/K]
β_o	Reference volume expansivity [1/K]
γ	Diffusivity [-]
$\vec{\varepsilon}_i$	Cartesian unit vector in direction i (i=1,2,3) [-]
ζ_1	Baseplate width fraction (X_1/L_1) [-]
ζ_2	Baseplate height fraction (X_2/L_2) [-]

[1] Vector and tensor units are for the individual components

η Correlation deviation [-]

η_i^j Projection of the j-direction face-normal unit vector in the Cartesian direction i (i, j=1,2,3) [-]

$\vec{\eta}^j$ Face-normal unit vector consistent with the parametric j-direction (j=1,2,3), $\vec{\eta}^j = \sum_{i=1}^{3} \eta_i^j \vec{\varepsilon}_i$ [-]

$\vec{\eta}_o^{\,j}$ j-Face normal, outward unit vector with respect to the control volume (j=1,2,3) [-]

κ_1 Baseplate conductivity ratio (k_1/k) [-]

κ_2 Meniscus lens conductivity ratio (k_2/k) [-]

λ Wave length [nm] ***or*** Coefficient of bulk viscosity [Pa-s]

μ Coefficient of viscosity (dynamic viscosity) [Pa-s]

μ_D Reference scale for viscosity [Pa-s]

μ_o Reference coefficient of viscosity [Pa-s]

$\hat{\mu}$ Dimensionless coefficient of viscosity [-]

ν Kinematic viscosity [m^2/s]

ρ Mass density [kg/m^3]

ρ_D Reference scale for mass density [kg/m^3]

ρ_o Reference mass density [kg/m^3]

$\hat{\rho}$ Dimensionless mass density [-]

σ Standard deviation ***or*** Transformed-space surface area [m^2, -]

σ_1 Heated-region width fraction (W/L_1) [-]

σ_2 Heated-region height fraction (H/L_2) [-]

$\delta\sigma$ Transformed-space surface element [-]

$\tilde{\tau}$ Time [s]

τ Dimensionless time [-]

$\tilde{\tau}_D$ Reference time scale [s]

ψ Enclosure tilt angle [degrees]

Ω Transformed-space volume [m^3, -]

$\delta\Omega$ Transformed-space volume element [m^3, -]

Operators

Symbol	*Description*
∇	Gradient operator, e.g. $\sum_{i=1}^{3} \bar{\varepsilon}_i \frac{\partial(\ )}{\partial x_i}$
$(\ )_x$	Partial derivative of ( ) with respect to x: $\frac{\partial(\ )}{\partial x}$, where x is an independent variable
$\frac{\delta(\ )}{\delta x}$	Difference operator for the first derivative with respect to x, where x is an independent variable
$\frac{\mathrm{D}(\ )}{\mathrm{D}\tilde{\tau}}$	Material (substantial) time derivative
$(\ )^{\mathrm{T}}$	Matrix-transpose operator

Special Symbols

Symbol	*Description*
c	Cell node
$\hat{\mathrm{c}}$	Auxiliary cell node
f	Face node
$nb(i)$	Set of neighbor nodes associated to node i
$(\ )_{\mathrm{c}_j^{\pm}}$	Indicates that ( ) is evaluated at the cell-node location on the negative (-) or positive (+) side of the j-face based on the j-parametric coordinate direction (j=1,2,3)
$(\ )_{\mathrm{f}_{\pm}}$	Indicates that ( ) is referenced to the parametric-coordinate negative (-) or positive (+) side of the face
$(\ )_{\mathrm{f}_j^{\pm}}$	Denotes evaluation of ( ) is made at the control volume's negative (-) or positive (+) direction cell-facet-side in the parametric direction j (j=1,2,3)

Units	*Description*	*Quantity*
A	Ampere	Electric Current
BTU	British Thermal Unit	Energy
°C	Degrees Celsius	Temperature
°F	Degrees Fahrenheit	Temperature
cd	Candela	Luminous Intensity
cm	Centi-Meter	Length
cs	Centi-Stoke	Viscosity
ft-L	Foot-Lambert	Radiance
GHz	Giga-Hertz	Frequency
h	Hour	Time
in.	Inch	Length
kV	kilo-Volt	Electric Potential
K	Kelvin	Temperature
lbm	Pound mass	Mass
lm	Lumens	Luminous Flux
MB	Mega-Byte (1024 bytes)	Computer Memory
m	Meter	Length
mA	Milli-Ampere	Electric Current
mm	Milli-Meter	Length
mmHg	Milli-Meters of Mercury	Pressure
mN	Milli-Newton	Force
nm	Nano-Meter	Length
Pa	Pascal	Pressure
s	Second	Time
V	Volt	Electric Potential
W	Watt	Power
μA	Micro-Ampere	Electric Current

1. INTRODUCTION

1.1. Motivation for the Present Research

This research was motivated by the need of North American Philips Consumer Electronics Corporation (NAPCEC) to investigate the thermal design of a so-called *liquid-lens* system used in their commercial projection television receivers. This system plays the dual role of serving as an active element in the optical system, while cooling the picture tube. The lack of directly applicable heat transfer research in the open literature prompted the need for the use of both experimental and numerical techniques to evaluate the adequacy of the thermal design of the liquid-lens system.

1.2. A Typical Projection Television Receiver

Projection television receivers use the same principle for image reproduction as standard direct-view television receivers, that is, a visual image is reproduced on the picture tube screen, but utilize projection techniques to project such image on a viewing screen. In this manner, the viewing image can be on a screen much larger than the original image reproduced on the picture tube screen.

1.2.1. Description of Major Components

Figure 1-1 shows front and lateral views of a typical projection television receiver. The main components are the cabinet, the monochrome projectors, the back mirror, the viewing screen, and the power supply and electronics. The cabinet is a frame of wood and metal construction that houses all of the components in the receiver. The viewing screen and the control panel are on the front side of the cabinet. The power cable and other input-output sockets are on the back of the cabinet. There are three monochrome projectors: one for red, one for green, and one for blue images. The monochrome projectors are subassemblies in projection TV receivers; each composed of a monochrome picture tube and an optical system,

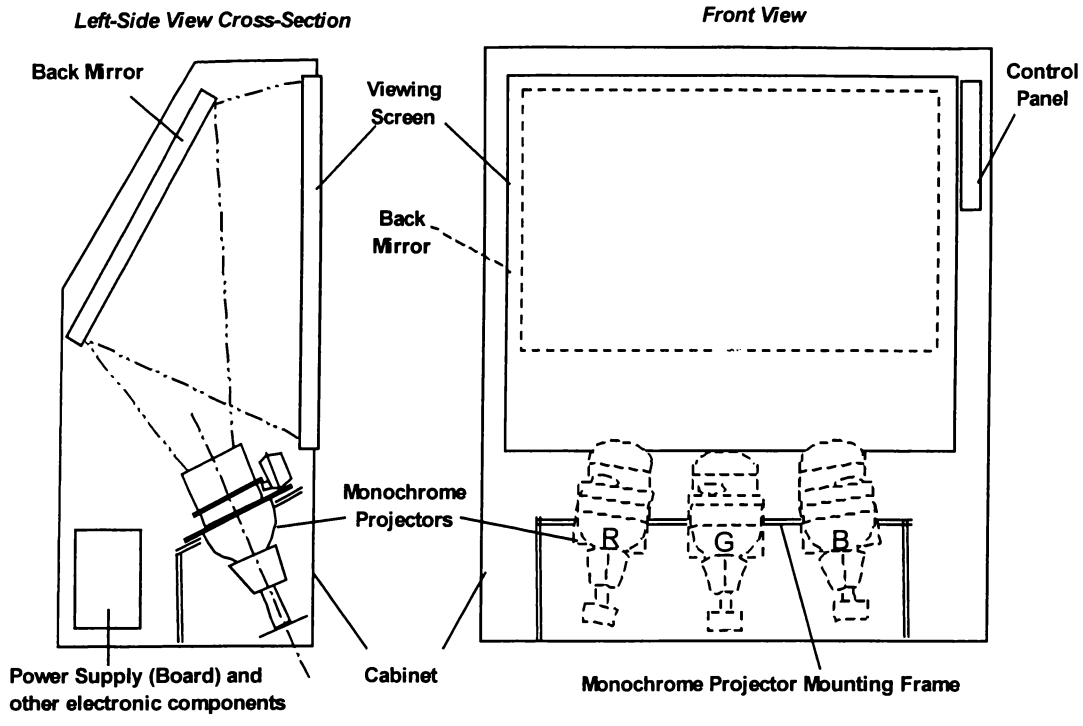

Figure 1-1. Schematic Views of a Typical Projection Television Receiver

whose function is to convert the video signals into visible images and to project the image into a viewing screen. The projection TV receiver used in the present research had the three monochrome projectors mounted on a frame near the bottom of the cabinet and oriented toward a rectangular mirror located in the rear-upper corner of the cabinet. These optical axes were tilted at 60° above the horizontal. Most of the electronic components are mounted on the bottom half of the cabinet.

1.2.2. Components of a Monochrome Projector

Figure 1-2 shows plan views of the green (central) monochrome projectors, and *Figure 1-3* shows a cut-away view of the assembly. Each monochrome projector consists of a projection picture tube (cathode-ray tube or CRT), an enclosure frame, an expansion chamber, a meniscus lens, a focusing lens, optical liquid, and supporting assembly hardware. The enclosure frame is mounted against the picture-tube face panel and serves as a support for the meniscus lens and a container for the optical liquid. A rubber gasket is positioned between the face panel

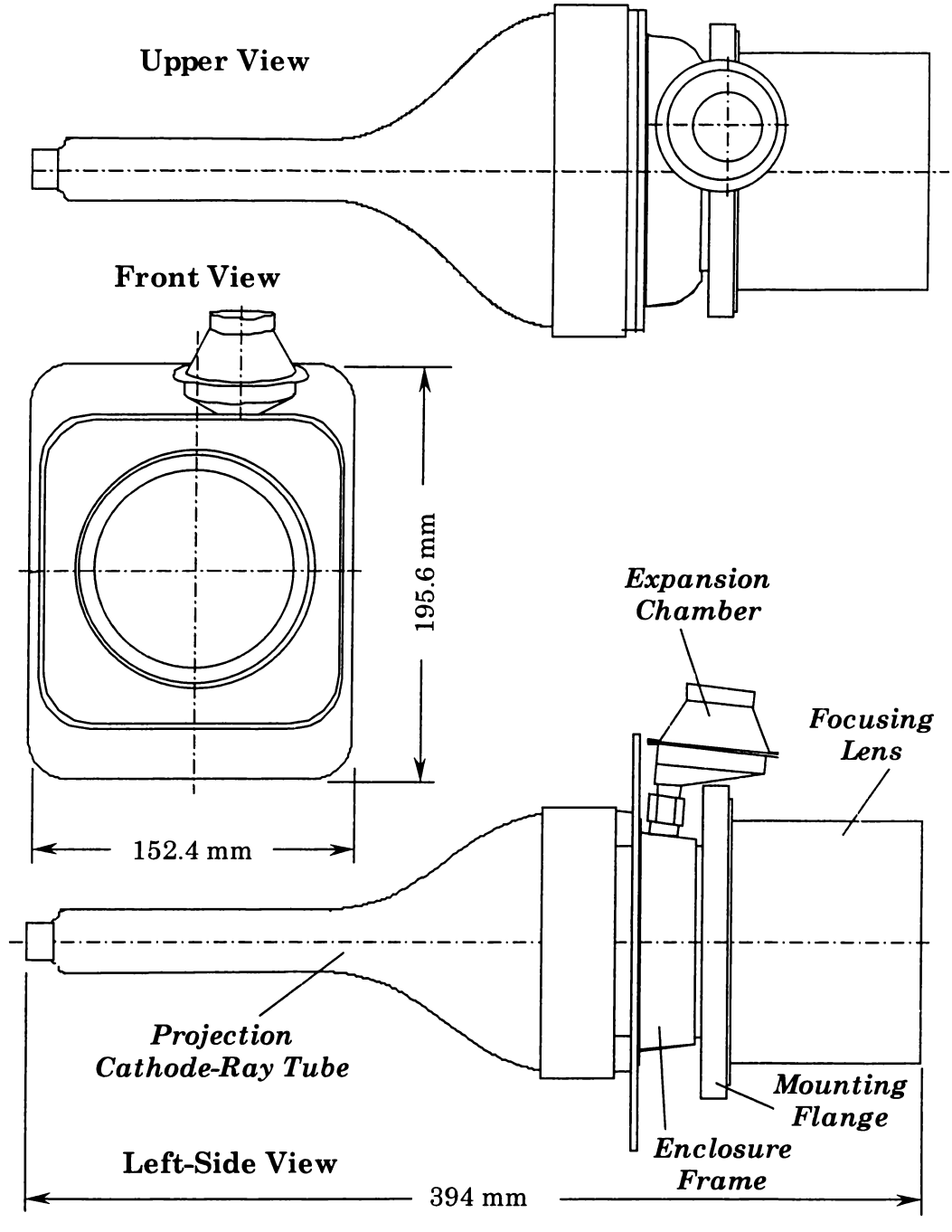

Figure 1-2. Monochrome Projector Plan Views

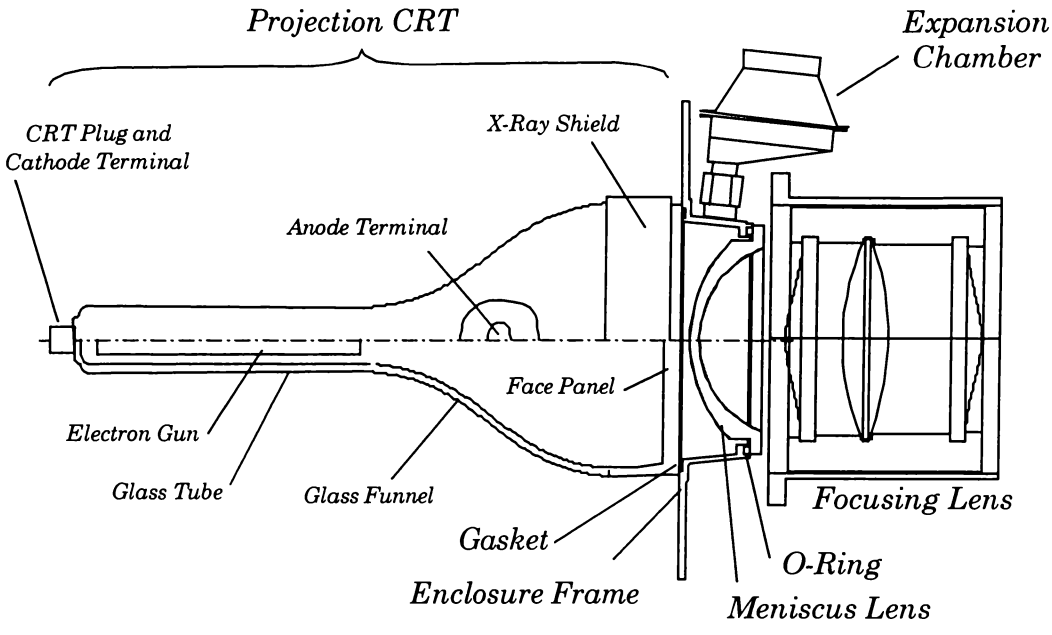

Figure 1-3. Monochrome Projector Cut-Away-View

and the enclosure frame to prevent fluid leakage (see *Figure 1-3*). The meniscus lens is mounted with the convex side toward the face panel. An O-ring is mounted between the enclosure frame and the meniscus lens to prevent leakage (see *Figure 1-3*). A mounting flange holds the meniscus lens in place by the use of screws (not shown) extending from the mounting flange to the enclosure frame. The focusing lens is an assembly of lenses capable of sliding within a cylindrical housing, which is bolted to the mounting flange.

1.2.3. Components of a Picture Tube

The picture tube consists of three basic components: a glass bulb with a face panel, an electron gun, and a focus/deflection coil, as shown in *Figure 1-4*. The glass bulb and the face panel form a sealed container, which is evacuated upon assembly. The glass bulb has a cylindrical extension (neck), which houses the electron gun. The electron gun consists of a series of annular electrodes aligned along the tube's neck longitudinal axis. The first electrode is the cathode. Here, electrons are released at ground potential (zero VDC). All other electrodes are anodes with

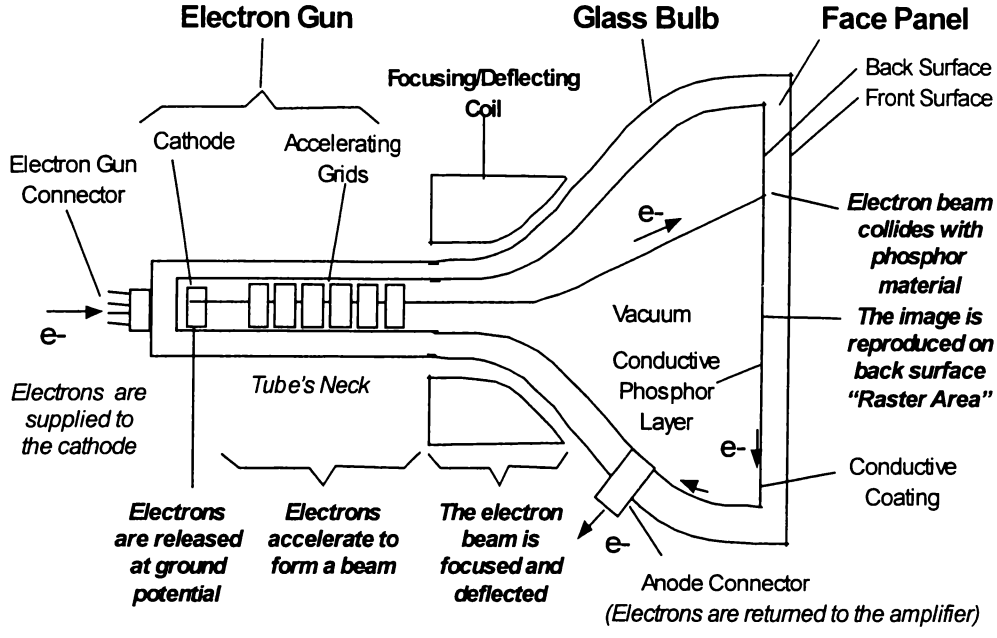

Figure 1-4. Major Components of a Picture Tube

positive electric potential. In projection applications, these anodes are maintained at an electric potential typically around 25 kV, but it can be as high as 50 kV in special picture tubes [21][1]. The electron beam current in projection applications is typically 500 μm [21]. The focus/deflection coil deflects the beam and focuses it on the face-panel phosphor screen. Focusing and directional control is usually achieved by applying a magnetic field generated by external coil, although this can also be achieved by electrostatic means. The face panel has a thin electrically conducting phosphor layer on the back surface (interior), which emits light upon electron beam collision. The thickness of the phosphor layer is determined in order to maximize the light output. A typical thickness is 16 μm [144]. As electrons hit the atoms in the phosphor layer, light is emitted carrying a fraction of the kinetic energy in the electron beam. Light is emitted in all directions, and therefore nearly half is emitted backward into the CRT interior. To reduce light losses from the back of the face panel, a thin aluminum coating of typically 0.10 to 0.14 μm in thickness [25] is

[1] Numbers enclosed in brackets [ ] indicate references listed in the "List of References" section.

applied on top of the phosphor screen. This coating is effectively a mirror, reflecting the light that otherwise would be emitted into the CRT interior into the forward direction. The aluminized phosphor layer is also the final anode of the tube, which in projection applications is subject to an electrical potential typically no less than 25 kV. The frequency in which the electron beam sweeps the phosphor screen is such that the image appears as "continuous" to the eye. This effect is due to light "persistance" in the phosphor screen -- a property that allows for some light output even after the electron beam excitation has been stopped. A typical persistance is 5 ms [25].

1.2.4. Image Reproduction Process

Electronic image signals are processed, amplified, and fed into the picture tube. Electrons are released from the cathode, and then they are accelerated by the anode grids, and focused into a beam. This beam is forced to sweep the phosphor screen in a line-by-line pattern by the action of the magnetic field created by the focus/deflection coil. The image is formed as light is emitted from every spot in the phosphor screen on which the electron beam has made contact. Light rays from the phosphor screen travel directly to the meniscus-lens/air interface. Light is refracted at such interface and redirected into the focusing lens array. A series of lenses in the focusing lens array realign light rays so they are ready for projection. Light leaving the lens array of each of the monochrome projectors is directed toward the rectangular mirror, to be reflected forward onto the viewing screen. Once in focus, the three monochromatic images are combined into the viewing color image on the viewing screen.

1.3. The Liquid-Lens System

Figure 1-5 shows a schematic of the liquid-lens concept. The liquid lens system is composed of the picture tube face panel, the meniscus lens, the optical liquid, and its enclosure. The name "liquid lens" refers to the fluid serving as an optical lens, with a shape conforming to the face panel on one side and the meniscus lens on the other. The idea behind the liquid lens concept is to form an optical

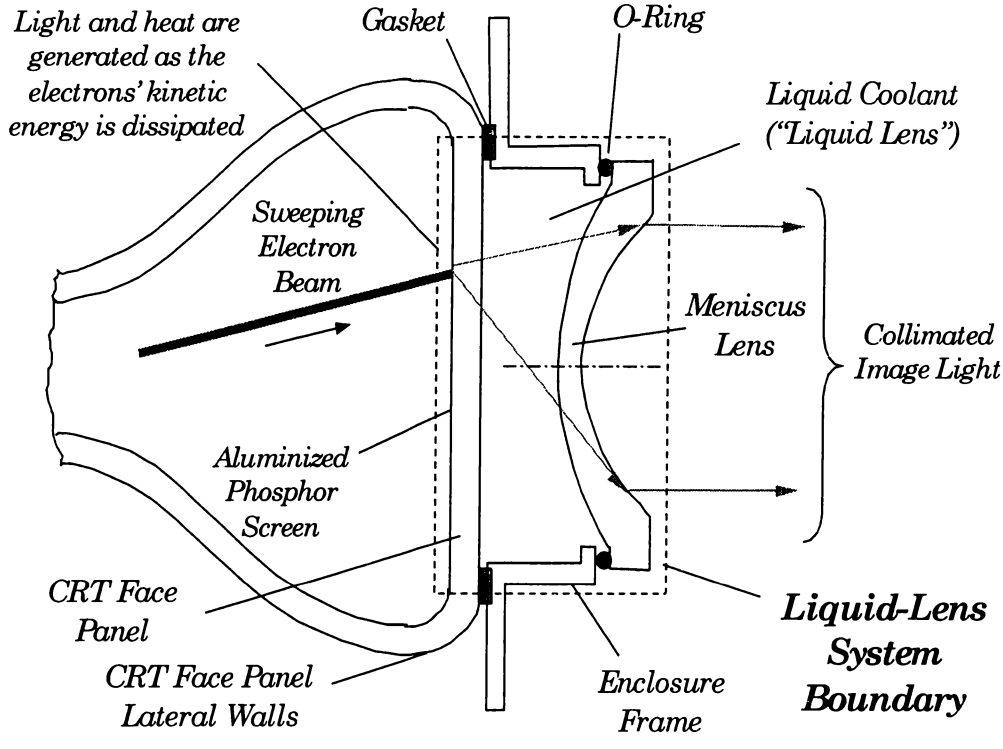

Figure 1-5. Liquid-Lens Concept and System Definition

system that "appears" as a single lens to the visible light. The concept is derived from the fact that light passing across an interface between materials of identical index of refraction does not diffract. Therefore, if the picture-tube face panel, the optical liquid, and the meniscus lens have identical indices of refraction, the assembly of these components would appear as a single lens to light. Light leaves the meniscus lens exterior surface as a collimated beam ready for focusing and projection.

Besides having an index of refraction that closely matches that of the face panel and meniscus lens, an important factor in the selection of the liquid coolant is corrosion. Low corrosion liquids are desirable. Following several tests with various liquid mixtures [132], NAPCEC selected for production an optical liquid resulting from a mixture of 69% ethylene glycol, 30 % glycerin, and 1 % stabilizing ingredients, manufactured by Dow Chemical [86], and designated "Developmental Heat Transfer Fluid." The optical liquid serves also the important role of cooling the picture tube face panel. Without adequate cooling, the face panel could be subject to

overheating and/or uneven heating, which could ultimately lead to picture tube failure. Overheating could lead to the deterioration of the phosphor-screen material, while uneven heating could lead to temperature gradients, in turn, resulting in stress-related fracture of the face-panel glass.

1.4. Modes of Heat Transfer

Figure 1-6 summarizes the various modes of heat transfer involved within the liquid-lens system. As the electron beam sweeps the CRT face panel back, electrons in the beam are absorbed as kinetic energy is converted into electromagnetic emissions and internal energy of the phosphor material. Most of the electromagnetic emission is in the form of visible light, and a small amount is in the form of X-rays. A greater fraction is converted into internal energy of the phosphor material producing a temperature rise. This rise in temperature results in infrared thermal radiation and conduction heat transfer. Most of the infrared thermal radiation is directed backwards towards the CRT interior surfaces. A negligible amount of the thermal radiation is directed forward into the face-panel glass material, as glass can be regarded as opaque to infrared radiation. The rise in temperature also results in heat conduction within the face panel material.

A fraction of the heat within the CRT face panel goes directly to the face panel lateral (perimeter) surfaces by conduction and the rest goes to the face-panel front surface. Heat from the face-panel front surface is transferred by convection to the liquid. Then natural convection in the liquid carries the heat to the enclosure and meniscus lens walls. Heat is again transferred by conduction through the enclosure and meniscus-lens walls, and finally transferred by convection and radiation from the outer surfaces to the environment.

As mentioned earlier, visible light from the phosphor screen is emitted in all directions. Therefore, a fraction of this light does not reach the meniscus lens exterior (concave) surface. Instead, this light hits the enclosure walls and lateral walls along the perimeter of the face panel. As these surfaces have a black coating, most of the light is absorbed, and the energy converted directly into internal energy. The remainder of the light leaves the system through the meniscus lens, except for a

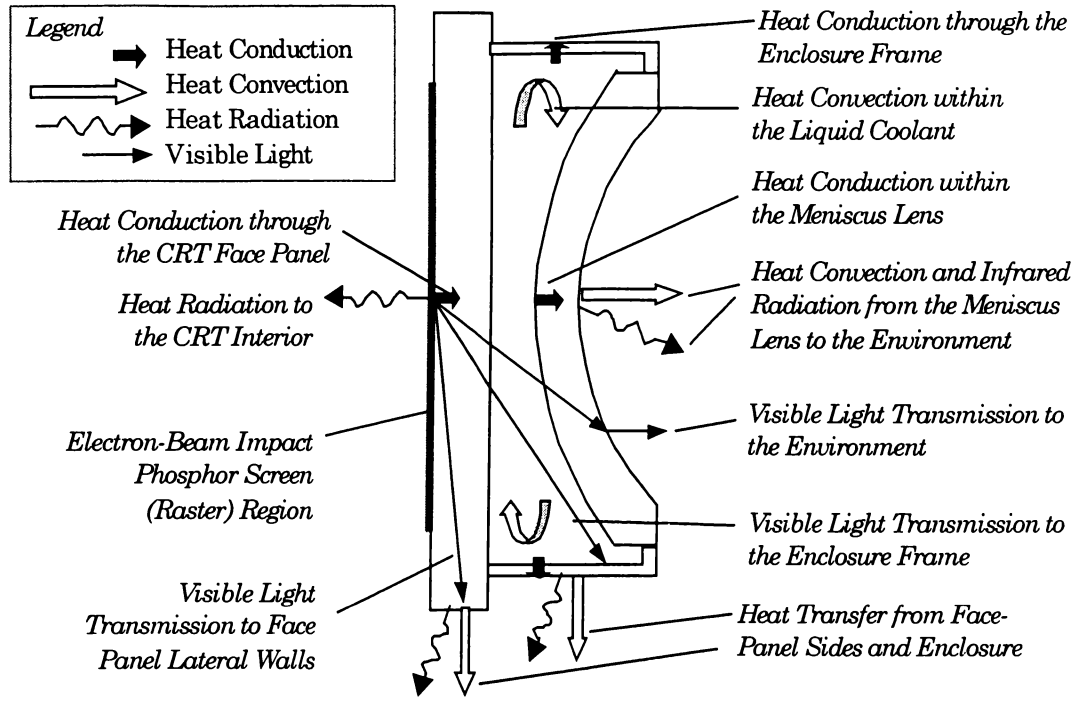

Figure 1-6. Modes of Heat Transfer in the Liquid-Lens System

small fraction lost in the transmission process through the solid and liquid media, and the interfaces between them. This fraction is converted into internal energy.

1.5. Liquid-Lens Thermal Performance

Thermal performance is ultimately dictated by the maximum temperature of the phosphor layer and the maximum temperature gradients across the CRT face panel material (glass) in steady-state operation. However, performance must be measurable by the use of practical, feasible non-intrusive means. Measuring the temperature directly on the phosphor screen, therefore, is avoided. Instead, picture-tube manufacturers base their specifications on externally measured temperatures. Hitachi, the manufacturer of the projection CRT used in the present research, requires that the exterior temperature on the face-panel center does not exceed 90 °C, and that the temperature difference between this point and points near the periphery along the major (horizontal) and minor (vertical) axes does not exceed 21 °C [15]. *Figure 1-7* shows the thermal performance requirements for the face panel of the Hitachi CRT used in this research.

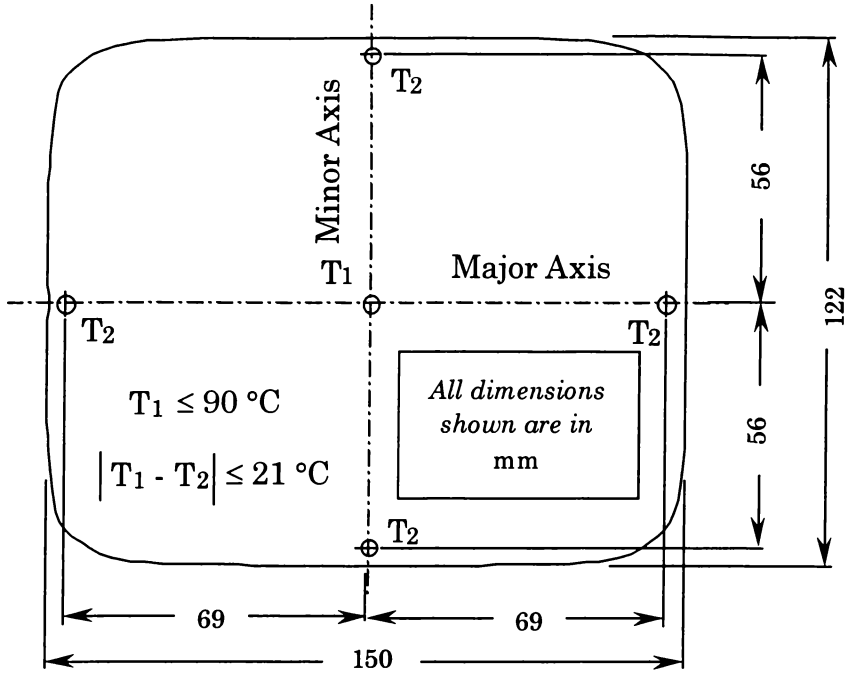

Figure 1-7. CRT Face Panel Thermal Performance Requirements

1.6. Statement of the Problem

The objectives of this research were to evaluate the adequacy of the thermal design of a typical liquid-lens cooling system as part of a projection television receiver, and to provide insight into the heat transfer mechanisms to enable improvements in the thermal design. The general approach to achieve the above goals consists of completing the following tasks:

(1) Review related heat transfer work to gain insight into the problem and to clearly shape the method of solution.

(2) Conduct experimental measurements using a typical liquid-lens system for cooling projection picture tubes,

(3) Construct a numerical model to simulate the three-dimensional heat transfer and fluid flow processes in the liquid-lens system,

(4) Benchmark the numerical model with experimental data,

(5) Use the numerical model in conjunction with experimental data to evaluate the thermal design of the liquid-lens system,

(6) Conduct sensitivity studies of the major performance parameters, and

(7) Provide guidelines for the improvement of the thermal design.

The experimental measurements were made using the liquid-lens system in a 1987-model, 46-inch Magnavox projection monitor, provided by NAPCEC [89]. The numerical model was based on a boundary-conforming finite-volume approach.

1.7. Chapter Contents

Chapter 2 reviews the related published research on conjugate natural convection flows (flows that are coupled with wall conduction and/or radiation within the fluid) in enclosures. *Chapter* 3 discusses the laboratory measurements of the liquid-lens experimental apparatus. *Chapter* 4 reviews the various techniques available for use in the numerical model. *Chapter* 5 contains the assumptions used and the derivation of the mathematical model governing equations for the liquid-lens system. *Chapter* 6 contains the derivation of the boundary-conforming, finite-volume numerical model. *Chapter* 7 contains the steps for benchmarking the numerical model of the liquid-lens with experimental data and the evaluation of the adequacy of the thermal design. *Chapter* 8 presents field visualization for the benchmark results in *Chapter* 7. *Chapter* 9 examines the effects of geometry variations better understand the basic flow structure and heat transfer mechanisms. *Chapter* 10 presents alternative cooling methods for enhancing thermal performance. *Chapter* 11 examines the effects of varying basic parameters related to properties, boundary conditions, as well as the orientation of the system. *Chapter* 12 contains the conclusions of the evaluation and recommendations for thermal design improvements.

2. BACKGROUND, RELATED HEAT TRANSFER RESEARCH, AND DETAILED SOLUTION APPROACH

2.1. Introduction

The liquid-lens system is composed of a liquid contained in a tilted enclosure with a conductive plate (face-panel glass) on one side and a curved, conducting wall (meniscus lens) on the opposite side. The system is heated by applying a heat flux below the conductive plate, and cooled on the other walls. An initial search did not report enclosure systems with similar characteristics, therefore, and alternative approach was needed. The approach was to review the effects due to contributions from the individual features involved and then to assemble a composite picture of the processes. Therefore, the review focused first on natural convection in two- and three-dimensional rectangular enclosures of finite aspect ratio, and then on enclosures with geometries or boundary conditions similar to those in the liquid-lens system. Furthermore, the review was limited to laminar natural convection, as this was the regime suggested by preliminary estimates. Conjugate natural convection was also reviewed to gain insight into the effect of wall conduction. Finally, thermal radiation was reviewed regarding media participation.

2.2. Natural Convection in Enclosures

Fundamentals of natural convection in enclosures will be reviewed, followed by natural convection in enclosures. Research on so-called conjugate problems involving coupled natural convection and wall conduction will also be discussed.

2.2.1. Fundamentals

Natural convection occurs as a result of buoyancy forces caused by non-uniform density distributions resulting from temperature gradients in the fluid. Usually an increase in temperature produces a decrease in density, resulting in a lighter, more buoyant fluid. In an enclosure, the fluid is heated either by contact

with an enclosure wall and/or by volumetric heating. As the fluid is heated, it tends to rises, while the cooler fluid tends to sink. Eventually the fluid reaches the vicinity of a wall at a lower temperature, where it is cooled. As the fluid is cooled, it becomes heavier, which causes it to sink, giving rise to a recirculation pattern.

The most frequently studied natural convection flows are those in rectangular enclosures. Rectangular enclosures can be classified as up-right and tilted enclosures. Up-right enclosures can be heated and cooled either on the vertical walls or on the horizontal walls. The relevant parameters describing the geometry for natural convection in two-dimensional rectangular enclosures is shown in *Figure 2-1.*

The aspect ratio (*Ar)* is usually defined in terms of the principal heat-transfer direction. Therefore, for vertical enclosures heated and cooled on the sides, the aspect ratio is defined as the height-to-width ratio, $Ar = H/W$, where H is the enclosure height, and W is the enclosure width and also the principal heat-transfer direction. A formal definition has not been established, but vertical enclosures usually refer to up-right enclosures having an aspect ratio equal or greater than one, while horizontal enclosures refer to up-right enclosures having an aspect ratio less than one. Unless otherwise indicated, the temperatures are specified on the two vertical walls. In tilted enclosures, the angle of inclination usually refers to the angle between the horizontal and the heated or cooled wall. The base-flow circulation indicates the tendency for fluid movement in stable conditions: the heated (lower-density) fluid should rise near the hot wall, and the cooled (higher-density) fluid should sink near the cold wall.

The heat transfer rate in the enclosures above can be calculated as

$$\dot{q} = hA\left(T_h - T_c\right), \tag{2.1}$$

where h is the heat transfer coefficient and A is the area of the heated wall. The heat transfer coefficient can be calculated once the Nusselt number is known. The Nusselt number is defined in terms of the heat transfer coefficient, h, the characteristic length, L, and the fluid thermal conductivity, k, as

Up-Right Enclosures

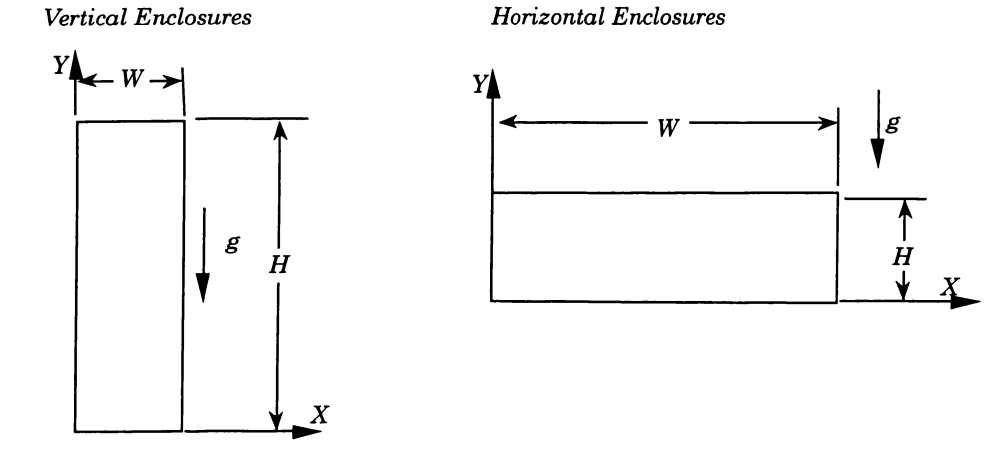

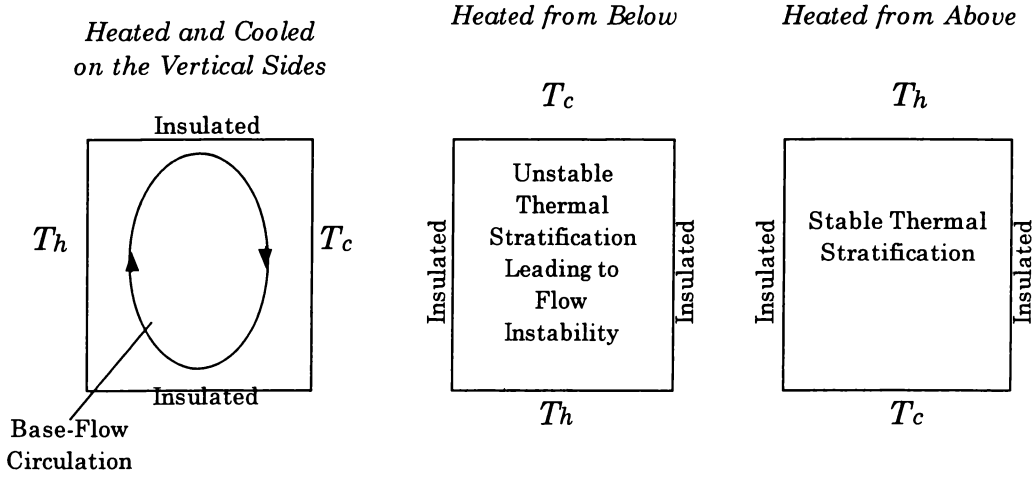

Tilted Enclosures

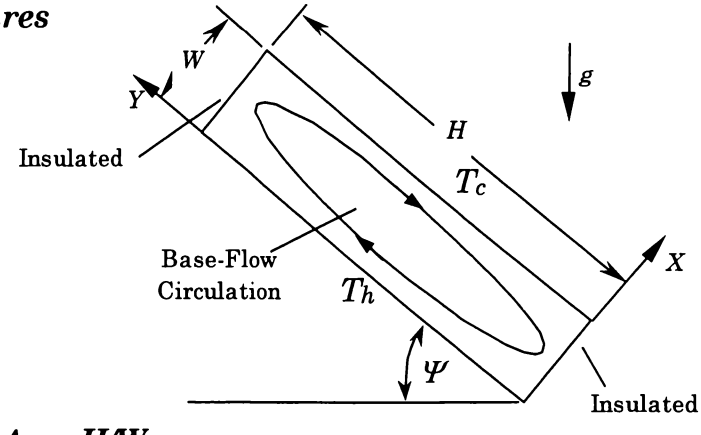

Aspect Ratio = *Ar* = *H/W*

Figure 2-1. Geometry Configurations for Natural Convection in Rectangular Enclosures

$$Nu_L = \frac{h}{k/L}. \tag{2.2}$$

The Nusselt number is the ratio of heat transfer by convection to heat transfer by conduction in the hypothetical situation in which the fluid is motionless, and provides an indication of the rate of heat transfer. The Nusselt number is a function of the Rayleigh number, Ra_L, the Prandtl number, Pr, and the aspect ratio:

$$Nu_L = \frac{h}{k/L} = \mathrm{f}\left(Ra_L, Pr, Ar\right) \tag{2.3}$$

where L denotes an appropriate characteristic length. The Rayleigh number, in turn is the product of the Grashof number and the Prandtl Number:

$$Ra_L = Gr_L\, Pr. \tag{2.4}$$

The Grashof number is the ratio of buoyancy forces and viscous forces, and is expressed as:

$$Gr_L = \frac{g\,\beta\left(T_h - T_c\right)L^3}{\nu^2}, \tag{2.5}$$

and the Prandtl number is the ratio of momentum diffusivity and thermal diffusivity, given as:

$$Pr = \frac{\nu}{\alpha}, \tag{2.6}$$

where ν is the kinematic viscosity and α is the thermal diffusivity. Substituting Eqs. (2.5) and (2.6) in (2.4) yields an alternative expression for the Rayleigh number:

$$Ra_L = \frac{g\,\beta\left(T_h - T_c\right)L^3}{\nu\,\alpha}. \tag{2.7}$$

In the situations where heat flux is specified, a scale for temperature must be found to replace the temperature differential in the above equations. A scale for temperature can be obtained using Fourier law and assuming that one-dimensional heat conduction takes place across the fluid layer of width L from the hot wall to the cold wall:

$$\left(T_h - T_c\right) = \frac{\dot{q}'' L}{k}, \tag{2.8}$$

where $\dot{q}''$ is the heat rate per unit area and k is the fluid thermal conductivity. Substitution of the above equation for temperature scale into Eq. (2.7) yields an expression for a *modified* Rayleigh number based on heat flux:

$$Ra_L = \frac{g\,\beta\,\dot{q}''\,L^4}{\nu\,\alpha\,k}. \tag{2.9}$$

2.2.2. Two-Dimensional Enclosures

Extensive effort has been devoted to the study of natural convection in vertical, horizontal, and tilted rectangular enclosures. Two-dimensional laminar natural convection flows have received most of the attention [55], because they are easier to analyze and are more suitable for experimental measurements, as compared to flows in three-dimensional enclosures. Heat transfer correlations are available for a wide range of Rayleigh number, Prandtl number, and aspect ratio, and they can be found in standard heat-transfer books (see Refs. [35],[48],[62]). It must be noted that although the intention of these studies is aimed at two-dimensional flows, experiments are always carried-out in three-dimensional, prismatic cavities. In order to minimize end-wall effects, the dimension along the third direction is made significantly larger than the other two dimensions defining the enclosure height and width, and measurements are made as far away as possible from the end walls. Despite of these measures, three-dimensional effects are always present, not necessarily because the finite length in the transverse direction, but also because physical instabilities inducing flow in the transverse direction.

Differentially Heated Up-Right Enclosures Heated and Cooled from the Sides

Extensive research has been done on natural convection flows in vertical enclosures. The general flow depends on the Rayleigh number, Prandtl number, and aspect ratio. For large aspect ratios, heat transfer is dictated by conduction in the

transverse direction, as there is little cross-flow, and therefore, advection between the vertical walls, except in the regions near the upper and lower ends. For aspect ratios of order of magnitude one, both the heat transfer and the flow structure are closely tied to the Rayleigh number. *Figure 2-2* shows the major natural-convection-flow regimes for vertical enclosure flows. The base (primary) flow is unicellular with the fluid rising near the heated wall, and falling near the cooled wall. Low Rayleigh numbers (typically $Ra < 10^3$) produce a unicellular circulation with a well-behaved, elliptic-like flow pattern, and nearly vertical isotherms. Between Rayleigh numbers of 10^3 and 10^5 the flow enters into a transition regime, where heat advection begins to dominate conduction. As the Rayleigh number increases past $Ra \sim 10^5$, a boundary-layer type flow develops, resulting in nearly horizontal isotherms in the central core flow in the enclosure. This is accompanied by the appearance of secondary cells. Aspect ratios larger than one may result in the appearance of multiple cells, as the boundary layer is formed and is detached at regular intervals along the vertical walls. Aspect ratios smaller than one may result in multiple cells with alternating rotation direction.

Differentially Heated Tilted Enclosures

A wide range of the parameter base for tilted enclosures has been studied and correlated. Natural convection research in inclined boxes and layers has been carried-out by Liang and Acrivos [78], Hart [41], Unny [129], and Hollands and Konicek [44] (among others) to study flow instabilities leading to the formation of transverse and longitudinal rolls. Catton, Ayyaswamy, and Clever [18] studied the natural convection flow in rectangular slots tilted at angles $60° \leq \psi \leq 165°$, Rayleigh numbers up to 2×10^6, and aspect ratios from 0.1 to 20. They reported flow distributions, temperature profiles, and heat transfer rates. Ozoe, Sayama, and Churchill [92] studied the natural convection heat transfer in square channels for tilt angles between 0° and 90°. They conducted two-dimensional numerical runs and experimental measurements in a long square channel, and reported Nusselt number dependency and the type of secondary rolls involved. Ozoe, et al. [96] extended the previous study into rectangular enclosures. They conducted two-dimensional

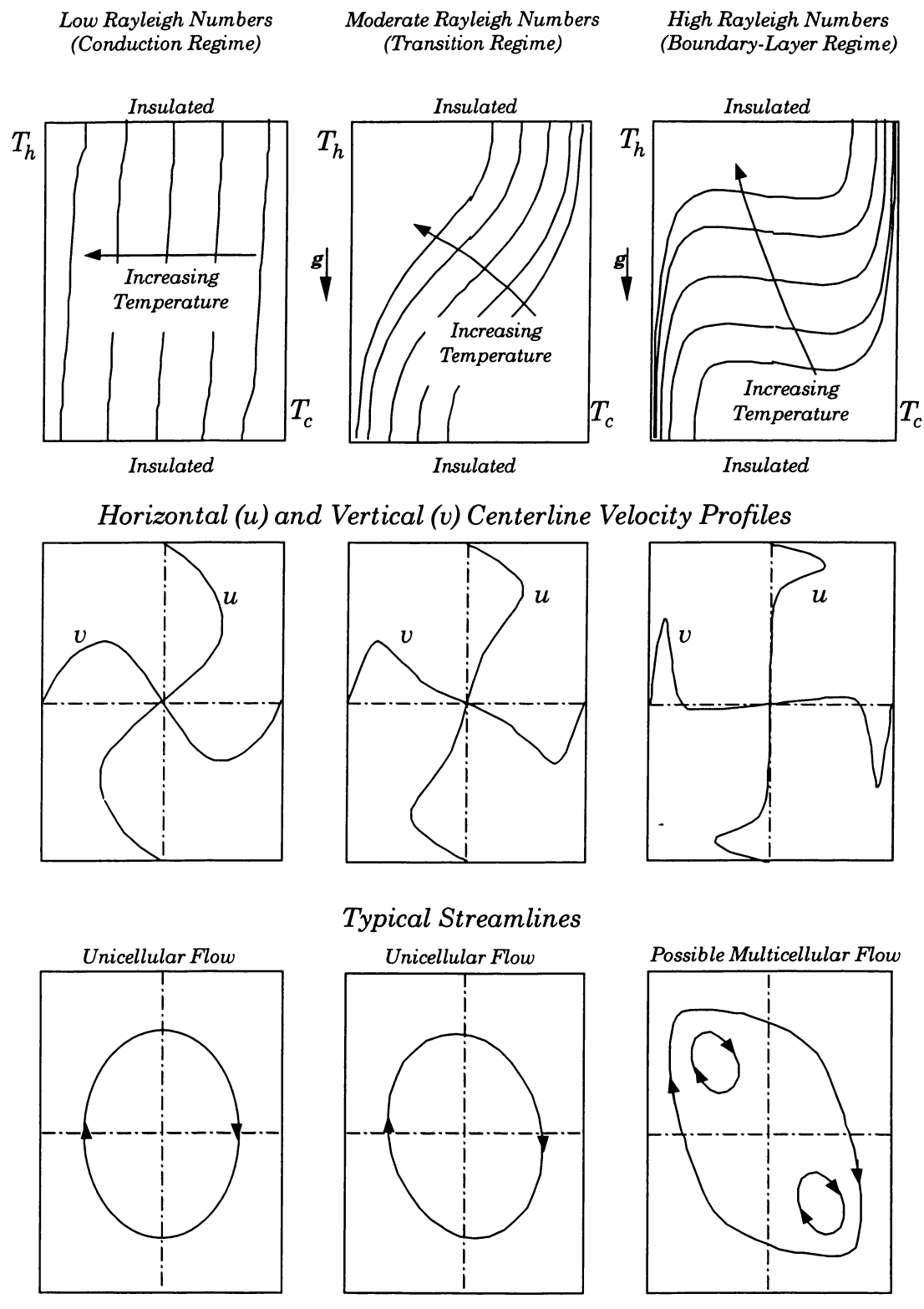

Figure 2-2. Isotherms and Flow Structure in Natural Convection Enclosure Flows

numerical runs with aspect ratios of 1, 2, 3, 4, and ∞, Rayleigh numbers of 2000, 4000, and 8000, and tilt angles from 0° to 180°. They compared results against experimental data and reported preferred circulation, and Nusselt number dependency. Ozoe, Sayama, and Churchill [93] complemented the preceding study with experimental measurements in rectangular channels of aspect ratios from 1 to 15.5, Rayleigh numbers from 3×10^3 to 10^5, and the same tilt-angle range. Arnold, Catton, and Edwards [3] conducted experiments to study the natural convection in rectangular channel of aspect ratios from 1 to 12, and Rayleigh numbers between 10^3 and 10^6, and made comparisons with previous theoretical work. They reported correlations for the Nusselt number. Hollands et al [45] conducted experimental measurements of air in rectangular enclosures of high aspect ratios, Rayleigh numbers up to 10^5, and for tilt angles between 0° and 70°. They reported Nusselt number correlations. Ozoe, Sayama, and Churchill conducted experimental measurements and photography [94], and three-dimensional numerical runs [95] to study the natural convection patterns in an inclined rectangular channel of aspect ratio of 2. They reported oblique cells for tilt angles less than ~7° and longitudinal roll cells for angles greater than ~7°. Linthorst, Schinkel, and Hoogendoorn [79] conducted experiments to study the flow structure in air-filled rectangular channels of aspect ratio $0.25 \leq \psi \leq 7$, tilt angles from 0° to 90°, and Rayleigh numbers from 5×10^3 to 2.5×10^5. They reported conditions for the transitions between steady and unsteady flows, as well as from two-dimensional to three-dimensional rolls. Wirtz, Righi, and Zirilli conducted experiments to study the three-dimensional natural convection of water in boxes of aspect ratios of 0.1 and 0.2 with the enclosure depth comparable to its height. The Rayleigh number ranged from 10^5 to 4×10^7, and the tilt angle was varied from 0° to 90°. Nusselt number correlations were reported. Symons and Peck [125] conducted experimental measurements and flow visualization to study the natural convection in rectangular enclosures of large aspect ratios and small depth aspect ratio, and small aspect ratio and large depth aspect ratio. Flow circulation and Nusselt number dependency were reported.

The heat transfer rates in tilted enclosures is very much related to the structure of the flow. This is why it is important to have a basic insight into the flow

structure. The flow in tilted enclosures can be understood in terms of a base flow describing the gross circulation and instability flows leading to rolls with axes not necessarily aligned with the base-flow circulation axis. Two limiting enclosure orientations do not have an inherent base flow. They are the heated-from-above orientation ($\psi = 180°$), and the heated-from-below orientation ($\psi = 0°$). The heated-from-above orientation, where lighter fluid stays at the top, and heavier fluid stays at the bottom of the enclosure, results in a motionless flow field and heat is transferred by conduction. The heated-from-below orientation results in an inherently unstable thermally stratified field. As the fluid in the layers near the bottom wall is heated, its density drops, and it becomes lighter than the fluid in upper layers, giving rise to a potentially unstable situation. At that point, the fluid is motionless, but thermally unstable. As the Nusselt number is increased above certain critical value, thermal instability causes the breakdown of the unstably stratified layer, as the lighter fluid finds its way upward, and the heavier fluid above finds its way downward. Then, a flow pattern is established with counter-rotating rolls, each of them occupying the entire vertical dimension and with their axes in the horizontal direction and parallel to the shorter dimension of the enclosure. The fluid is then subject to cyclical heating and cooling within every single roll. In the case of rectangular channels (with relatively large depths), the shorter horizontal direction is that in the direction between the insulated sidewalls. Such rolls are also called longitudinal rolls.

Flow patterns in tilt angle other than those discussed above are significantly more complex. *Figure 2-3* shows typical flow configurations for various tilt angles. As the enclosure is tilted away from the heated-from-below orientation, a new flow instability develops, responsible for the unicellular base flow similar to that in differentially heated vertical enclosures, as well as secondary transverse rolls. The lighter fluid near the bottom wall tends to rise along the slope of the hot surface, and the heavier fluid near the top wall tends to sink along the slope of the cold surface. The fluid ultimately detaches from these walls by the action of the prevailing longitudinal rolls, giving rise to the so-called oblique rolls. As the enclosure tilt angle is increased, hydrodynamic instability responsible the base-flow type of

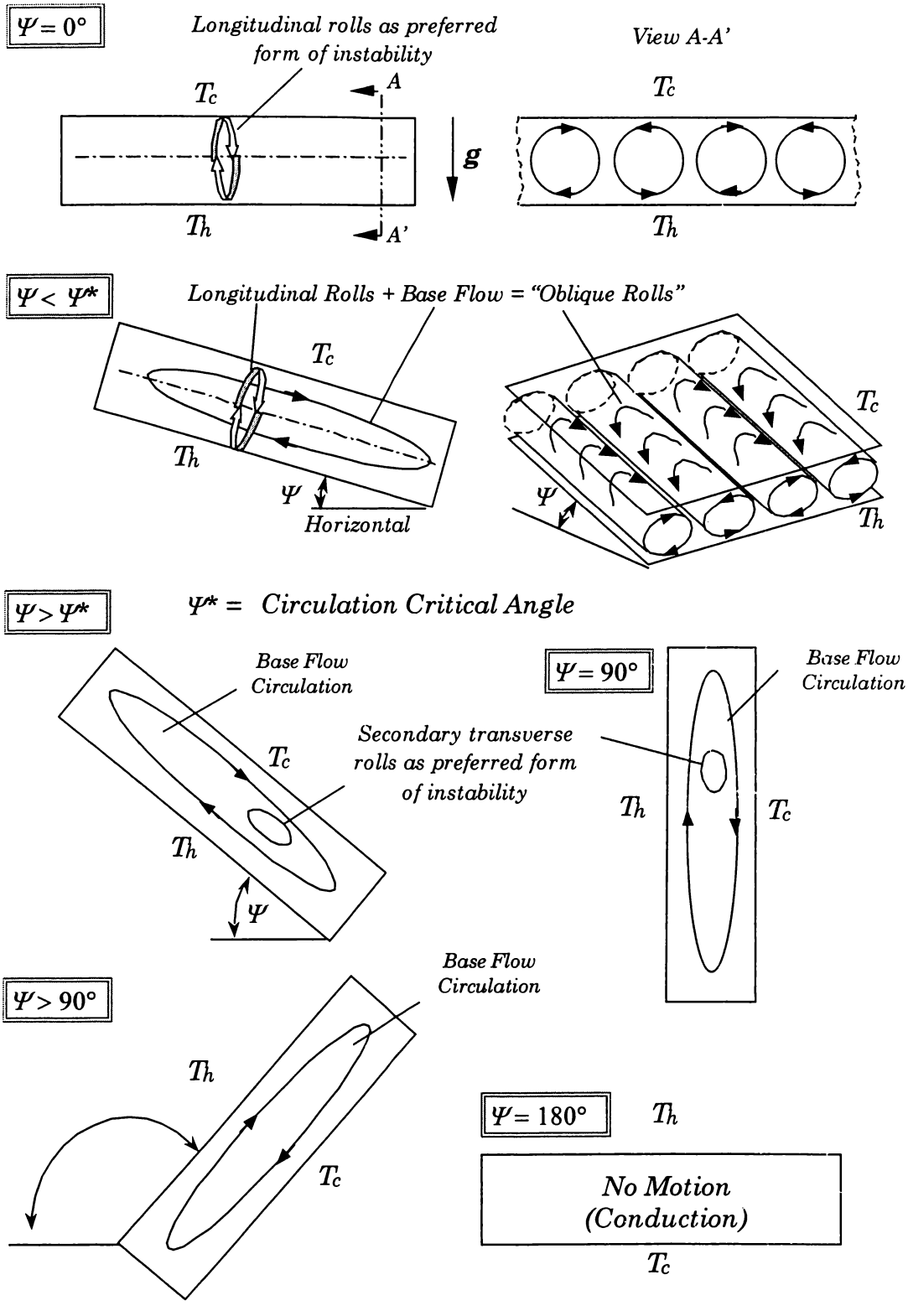

Figure 2-3. Tilted Enclosure Typical Flow Configurations

circulation begins to overcome the thermal instability responsible for the longitudinal rolls. At certain critical tilt angle ($\psi = \psi^*$) longitudinal rolls are no longer the preferred mode of circulation, and a base-flow type of circulation becomes the preferred mode. Depending on parameters such as the aspect ratio, the Prandtl number, and the Rayleigh number, transverse roll instability may emerge, leading to multiple secondary transverse rolls with axes oriented in the horizontal direction (into the channel). Hydrodynamic instabilities leading to transverse rolls tend to decay with increasing tilt angle. Eventually, as the tilt angle approaches $\psi = 180°$, thermal and hydrodynamic instabilities vanish, resulting in the motionless, thermally stable stratified field of the heated-from-above orientation.

Figure 2-4 illustrates the dependency of Nusselt number on the enclosure tilt angle. The minimum Nusselt number (Nu = 1) occurs when the enclosure is heated from above ($\psi = 180°$), as the stable thermal stratification results in heat transfer by conduction. (Exceptions are cases in which the fluid contracts with increasing temperature, such as water near the freezing point.) As the enclosure is tilted away from this orientation, the flow begins to rise along the heated wall as it begins to fall along the cooled wall, giving rise to the base flow structure. As this occurs, the Nusselt number begins to increase due to advection. A local maximum occurs at certain angle ($\psi_{c,max}$), which depends strongly on the enclosure aspect ratio and weakly on the Rayleigh number. At large aspect ratios ($Ar > 12$) the critical tilt angle for the local maximum in the heat transfer approaches 90°. At large aspect ratios, further decrease in the tilt angle results in Nusselt number increases until an absolute maximum is reached at $\psi = 0°$ (heated-from-below orientation). At moderate aspect ratios ($1<Ar<12$), the critical tilt angle for the local maximum in the heat transfer is less than 90°. Further decreases in the tilt angle results in Nusselt number decreases until a local minimum is reached at certain critical tilt angle for minimum heat transfer ($\psi_{c,min}$). Both the critical angle for heat transfer local maximum ($\psi_{c,max}$), and local minimum ($\psi_{c,min}$) decrease with decreasing aspect ratio. As the tilt angle is further reduced past the angle for the heat transfer rate local minimum, the Nusselt number begins to increase until a second maximum is reached in the heated-from-below orientation ($\psi = 0°$). It is presumed that for

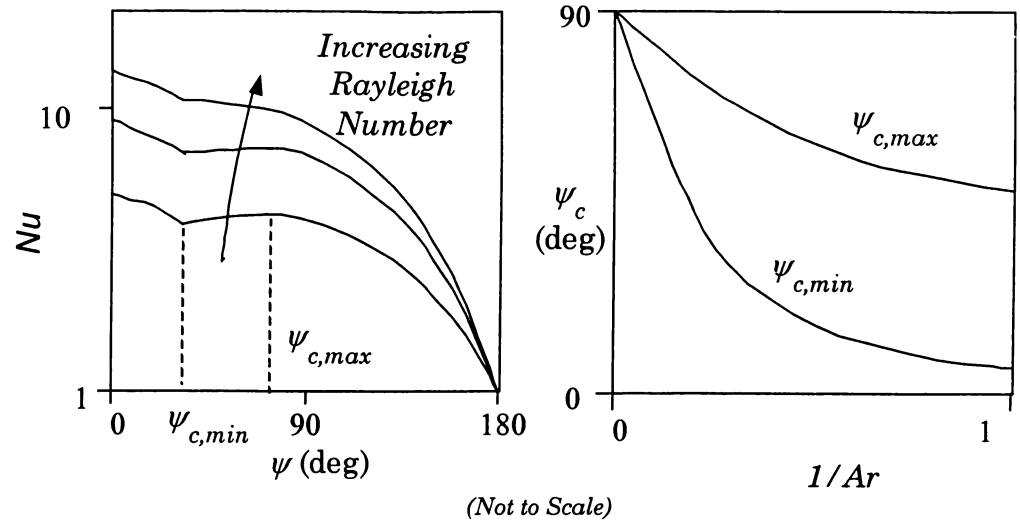

Figure 2-4. Typical Nusselt Number Dependency on Enclosure Tilt Angle and Aspect Ratio

moderate to high aspect ratios the local minimum in the heat transfer rate is caused by a change in the flow instability preferred direction from transverse rolls to longitudinal rolls [3]. This, however, is not the case for small aspect ratios ($Ar << 1$), where the flow transition occurs at intermediate Nusselt numbers [135]. For small aspect ratios and for tilt angles less than 90°, the Nusselt number is a weak function of tilt angle. For such aspect ratios, and in contrast to trends for moderate-to-high aspect ratios, the Nusselt number decreases as the tilt angle approaches 0° (heated-from-below orientation).

Rectangular Enclosures Heated from Below with Side-Wall Cooling

November and Nansteel [91] conducted numerical studies of the two-dimensional natural-convection of water in a square enclosure heated from below and cooled on one side, as shown in *Figure 2-5*(a). Both the heated and the cooled surfaces were kept isothermal. Results were obtained for the range of $0 \leq Ra \leq 10^6$. They calculated the Nusselt number as the ratio of the rate of heat transfer by convection to the rate of heat transfer obtained by forcing the fluid to remain motionless. Their calculations showed a unicellular base flow structure such that

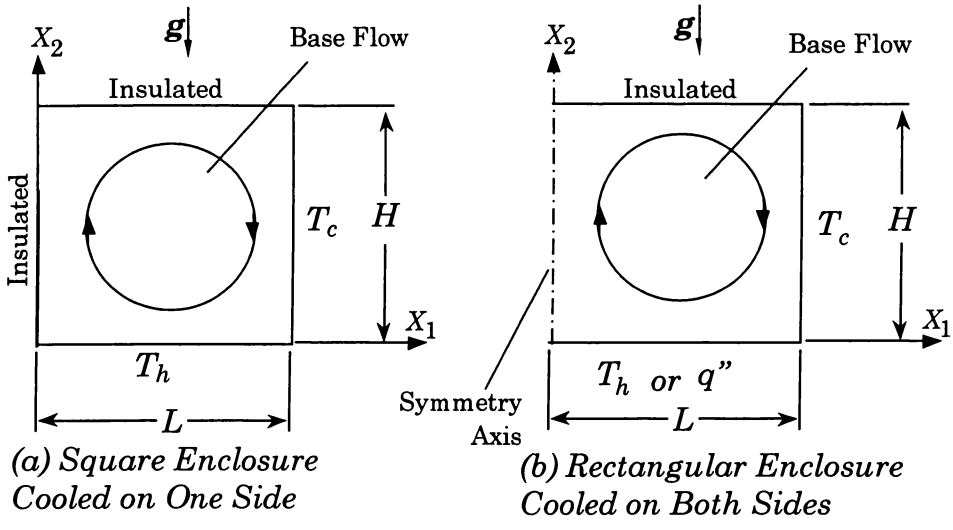

Figure 2-5. Natural Convection in Finite Rectangular Enclosures Heated From Below and Cooled on the Side

fluid near the cooled sidewall falls and the fluid near the opposite (insulated) wall rises.

Ganzarolli and Milanez [33] conducted numerical studies of the two-dimensional natural-convection in rectangular enclosures with isothermal sidewalls, an insulated top wall, and a heated bottom wall subject to either uniform temperature or uniform heat flux, as shown in *Figure 2-5*(b). The enclosure aspect ratios studied ranged between 1/2 and 1/9. The Rayleigh number based on the enclosure height was varied from 10^3 to 10^7, and the Prandtl number from 0.7 to 7. They assumed a symmetric flow about the vertical centerline to simplify calculations. The base flow consisted on two counter-rotating cells (one on each side of the vertical centerline), with flow circulating such that the fluid in the central region rises, and the fluid near the cooled walls falls. The enclosure of aspect ratio of 1/2 did not show secondary rolls. However, for smaller aspect ratios, secondary cells appeared as the Rayleigh number was increased.

Differentially Heated Enclosures with Cross-Sections Similar to that of the Liquid Lens

Besides rectangular enclosures, research has been carried-out in other enclosure geometries, such as triangular and cylindrical enclosures among others, which do not provide significant additional insight into the present problem. Exceptions were the numerical investigations by Lee and Lee [72], Karyakin [59], and Martyneko et al. [83] who studied differentially heated vertical enclosures with the upper wall shaped as a sine wave, as shown in *Figure 2-6.*

Lee and Lee [72] conducted numerical studies for height aspect ratios $1.25 \leq H_c/H_h \leq 2$ and $H_h/L = 1$ for air ($Pr = 0.71$) and $10^4 \leq Ra \leq 10^6$ and calculated streamlines and Nusselt numbers. They concluded that the "S" shaped enclosure had slightly lower Nusselt numbers than an enclosure of similar dimensions, but with a straight, tilted upper wall. Karyakin model a similar geometry numerically $H_h/L = 1/2$ and $H_c/L = 1$ for $Pr = 0.7$ and $10^2 \leq Gr \leq 10^6$. He reported that isotherms changed from nearly vertical for the smaller Grashof number to nearly horizontal in the central region for the larger Grashof number, which indicates the presence of thermal stratification. His results showed a unicellular circulation with the circulation center moving upwards as the Grashof number was increased. Martyneko et al. [83] solved a similar problem. The cross-sectional shape of this

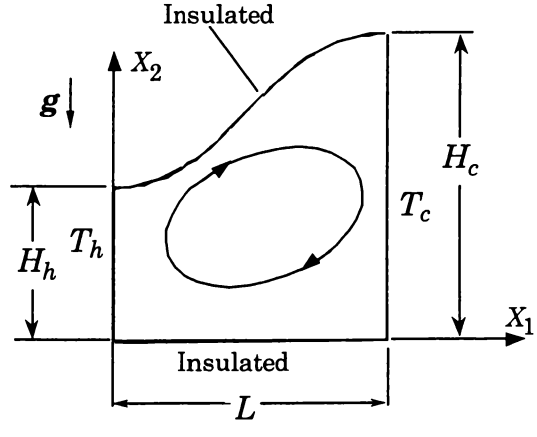

Figure 2-6. Natural Convection in a Vertical Enclosures with the Upper Wall Shaped as a Sine-Wave

enclosure is similar to the cross-section of the liquid lens along the major axis with the symmetric half-side removed. However, boundary conditions are incompatible to the extent that further analogies between the two problems should not be pursued.

2.2.3. Three-Dimensional Enclosures

Experimental and numerical studies on natural convection in three-dimensional enclosures are not as abundant as those intended for two-dimensional natural enclosures. Non-invasive field measurement, as the Mach-Zender interferometry cannot be used and flow visualization becomes difficult to carry out, and theoretical analyses are limited to perturbation methods [55]. This leaves numerical analysis as the best alternative. Even so, little published research was found regarding numerical studies on natural convection in three-dimensional enclosures. Studies of flows in very simple enclosure geometries, such as vertical boxes are available. A new parameter, the depth aspect ratio (A_d), is introduced when dealing with vertical boxes, defined as the ratio between the depth of the enclosure (in the third dimension) and the enclosure with, as defined previously for two-dimensional enclosures. Ozoe et al. [97] conducted numerical studies on the three-dimensional natural convection flow in box-like enclosures heated from below. The numerical solution was based on the vector-potential/vorticity formulation [136]. They reported that solutions for a cubical cavity depended on the initial condition. Comparisons were made with prior theoretical results, showing good agreement.

Mallinson and de Vahl Davis [82] conducted numerical studies on the three-dimensional natural convection flow in differentially heated, vertical boxes of square cross-sections with aspect ratios $Ar \geq 1$. Their numerical solutions were based on the vector-potential/vorticity formulation. Studies on a square cross-section and depth aspect ratio $A_d = 2$ indicated the presence of a single roll for $Ra \leq 6 \times 10^4$ and $0.1 \leq Pr \leq 100$. They indicated that the general flow resulted from the superposition of axial flow (moving away from the insulated vertical walls in the third dimension) and the two-dimensional enclosure flow. For higher Rayleigh numbers, they reported two secondary rolls (equivalent to those found in two-dimensional flows),

resulting in a more complex flow pattern. They reported Nusselt numbers slightly lower than predicted by two-dimensional models.

Chao, Ozoe, and Churchill [19] conducted numerical studies of the effect of having a non-uniform surface temperature on the natural convection in a box. They reported that circulation patterns were not significantly affected by surface temperature distributions, and that the Nusselt number magnitude increased with temperature non-uniformity, especially in heated-from-below orientations.

Other three-dimensional studies involve the flow in cylindrical cavities [10], hemispherical enclosures [118], the region between concentric spheres [16], and between bodies and their spherical enclosure [107].

2.2.4. Conjugate Natural Convection Flows: The Effect of Wall Conduction

The effect of wall conduction on natural convection in enclosures has received little attention. Kim and Viskanta [63] conducted analytical and experimental studies on the effect of wall conduction on the transient, natural convection flow. The study focused on a 2-dimensional square enclosure with two thick horizontal walls, insulated on their outer surfaces, and two thick vertical walls kept at different, but uniform and constant temperature. They indicated that wall conduction increased flow stability and reduced temperature differences across the enclosure, thereby, reducing convection heat transfer.

Kaminski and Prakash [56] conducted a numerical study on the natural-convection heat transfer in an air-filled differentially heated vertical square cavity with a thick conductive wall between the heated surface and the fluid. They concluded that the temperature distribution within the conductive wall became two-dimensional for Grashof numbers greater than 10^5. The two-dimensional temperature distribution resulted in a non-uniform wall temperature, which, in turn produced asymmetrical flow with respect to the fluid cavity center. They also pointed-out that nearly the same result for the overall heat transfer could be obtained using a lumped model, a one-dimensional, or a two-dimensional heat transfer model.

2.3. Effect of Thermal Radiation

Thermal radiation in non-participating media has the general effect of reducing the magnitude of temperature differentials throughout the region. The less "transparent" the media (the more opaque to thermal radiation), the larger the temperature differential across the region. Most materials transparent to visible light are opaque to infrared thermal radiation. This applies to solids and liquids. In the visible range, these materials have high transmittance; that is, they behave as non-participating media in this range.

Infrared thermal radiation in solids and liquids, however, is usually neglected; that is, they are assumed opaque to thermal radiation. The spectral transmittance for a fused-quartz plate of 6 mm in thickness drops from approximately 0.9 at $\lambda \approx 3$ μm to zero at $\lambda \approx 5$ μm, and remains zero thereafter [48]. This means that such plate of glass should absorb most of the thermal radiation in the near-infrared range and beyond. Other types of glass, such as the type used in the face panel and meniscus lens should exhibit a similar behavior. Radiative properties of particular liquids are seldom available, as it was the case for the liquid coolant used in the liquid lens system. Spectral transmittance for individual components of the optical liquid, Ethylene Glycol and Glycerin, were not found in the literature reviewed. It is evident that these two liquids and the resulting mixture are transparent to visible light, however, as in the case of most liquids, they should be opaque to thermal radiation in the infrared range. For instance, water, is essentially transparent to thermal radiation in the visible range ($0.4\ \mu m < \lambda < 0.7\ \mu m$); however, at wavelengths of $\lambda \approx 1$ μm, the absorption coefficient begins to increase, and becomes larger for larger wavelengths [121]. Therefore, water may be considered opaque for wavelengths greater than 1 μm (the near infrared range and beyond).

2.4. Summary of the Review and Discussion

A review of the open literature was made to gain insight into the problem and to establish the best solution approach. The review covered the fundamentals of

natural convection, studies of natural convection in two- and three-dimensional enclosures of similar geometries, conjugate heat transfer including the effect of wall conduction and thermal radiation, and the basic experimental and analysis techniques. The review led to the following conclusions:

(1) Studies on three-dimensional natural convection in enclosures with shapes similar to that of a liquid-lens system were not found in the open literature.

(2) Studies of two-dimensional natural convection in an enclosure with geometry similar to that of the liquid-lens geometry were found. The enclosure, however, had a different set of boundary conditions, and therefore, results were not directly applicable.

(3) General heat transfer correlations are available for two-dimensional enclosures. No correlations exist for the liquid-lens configuration or for similar three-dimensional enclosures.

(4) Wall conduction tends to reduce temperature differences within the fluid domain, and to add stability to the flow.

(5) The glass in the face panel and meniscus lens and the optical liquid can be assumed transparent for the radiation visible range. All of the materials, however, may be assumed opaque to infrared thermal radiation.

(6) Three-dimensional, non-invasive field characterization is difficult to achieve experimentally, and the use of perturbation methods has limited theoretical applicability. This leaves numerical analysis as the best viable alternative.

In spite of the lack of studies on enclosures with geometries and boundary conditions similar to those in the liquid-lens system, the principle of superposition can be used to attempt to anticipate the three-dimensional base-flow circulation in the liquid lens. It is reasonable to expect that the three-dimensional base flow pattern should involve the superposition of the two-dimensional base flows acting on the three perpendicular planes. A basic idea of the base flow patterns in each of these planes can be derived from boundary conditions and the direction of the gravitational

acceleration. The first plane to be considered is the vertical-plane cross-section of the liquid-lens system perpendicular to the CRT face panel, as shown in *Figure 2-7*. Since the geometry and boundary conditions for this configuration are not readily available in the open literature, some simplifications must be made. First, the CRT face panel and the meniscus lens are removed, and isothermal walls are assumed. Furthermore, boundary conditions are decomposed into two sets applied to enclosure problems, for which base flow patterns can be anticipated. The first problem is that of natural convection in a differentially heated vertical enclosure, and the second problem is the natural convection in a horizontal enclosure heated from below and cooled on the sides. If the velocity fields for these two enclosure flows was known, the principle of superposition could be applied to obtain a "first-cut" approximation of the base flow for the actual problem. The resultant base flow may be composed of two counter-rotating cells, as shown in the figure, or a single cell (not shown), depending on the enclosure tilt angle. It will be assumed, for the moment, that the tilt angle is small enough so that the base flow for the plane being considered is composed of two counter-rotating cells, as shown. Flow instabilities may result in longitudinal and/or transverse secondary rolls. A similar thought process can be followed for the remaining two planes to arrive at their respective base-flow patterns.

Figure 2-8 summarizes the anticipated base-flow circulation patterns for the three system cross-sections under the above assumptions, and assuming that the flow is symmetric with respect to the vertical midplane. Four base-flow circulation cells are shown. Two of these cells are counter-rotating, with rotation axes in the horizontal direction and parallel to the face panel. A third base-flow cell rotates about an axis along the slope of the CRT face panel with the heated fluid rising in the face-panel central region, and with the cooled fluid moving downward near the enclosure lateral wall. A fourth base-flow cell rotates about an axis perpendicular to the CRT face panel, with the flow rising in the face-panel central region and moving downward near the enclosure lateral wall.

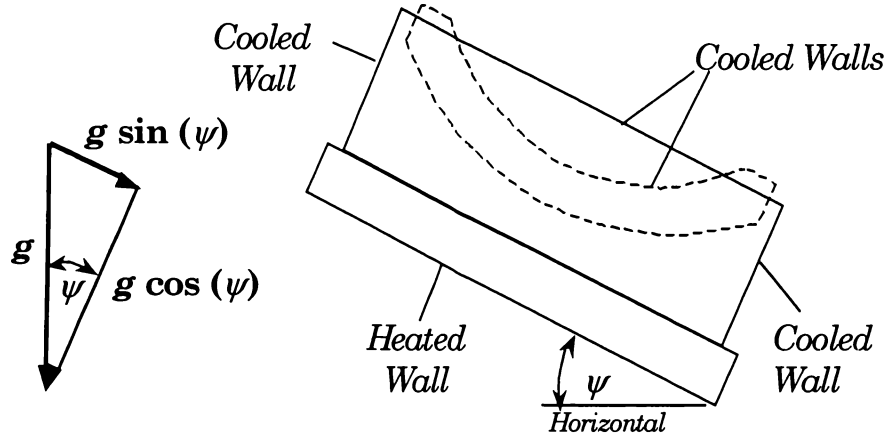

Base Flow Components

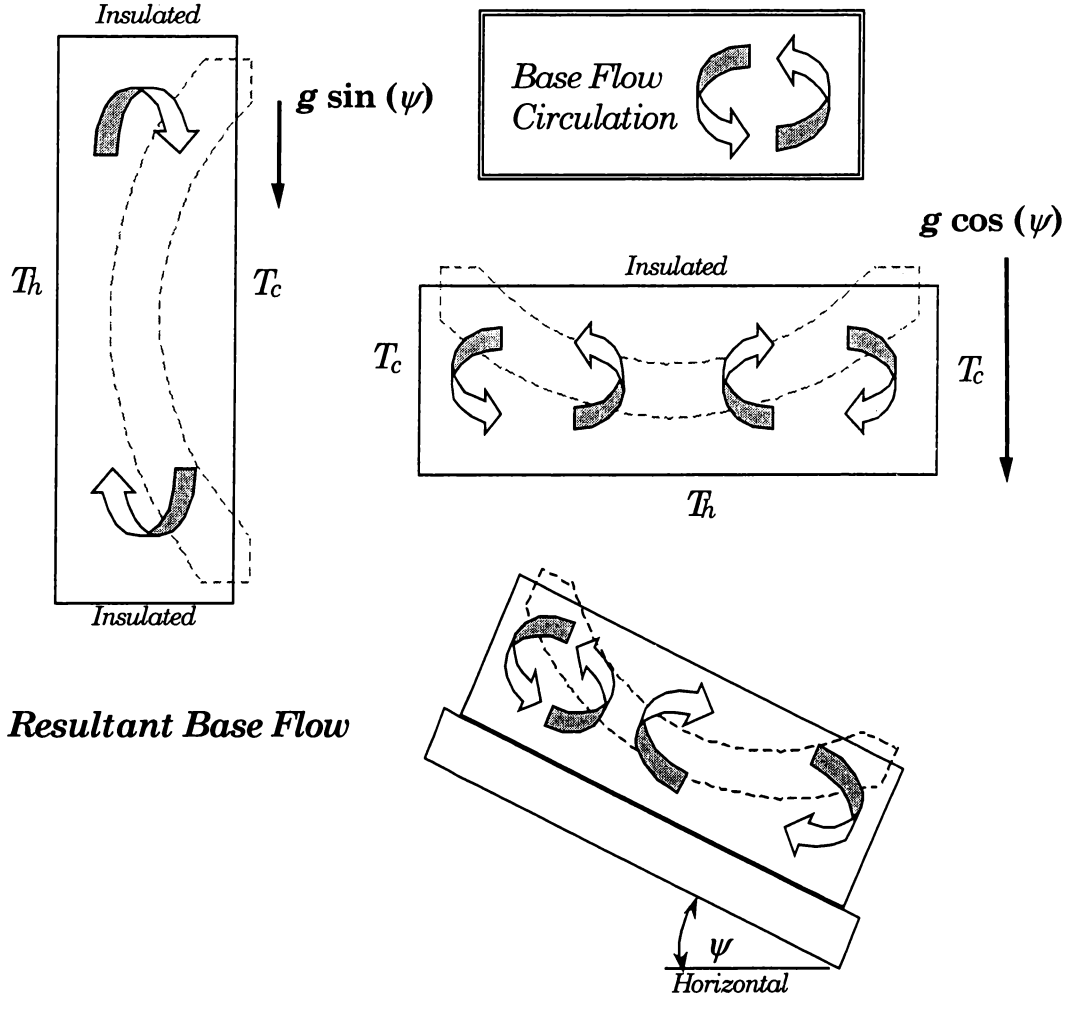

Resultant Base Flow

Figure 2-7. Base Flow and Instability Contributions from Decomposition of Boundary Condition Types

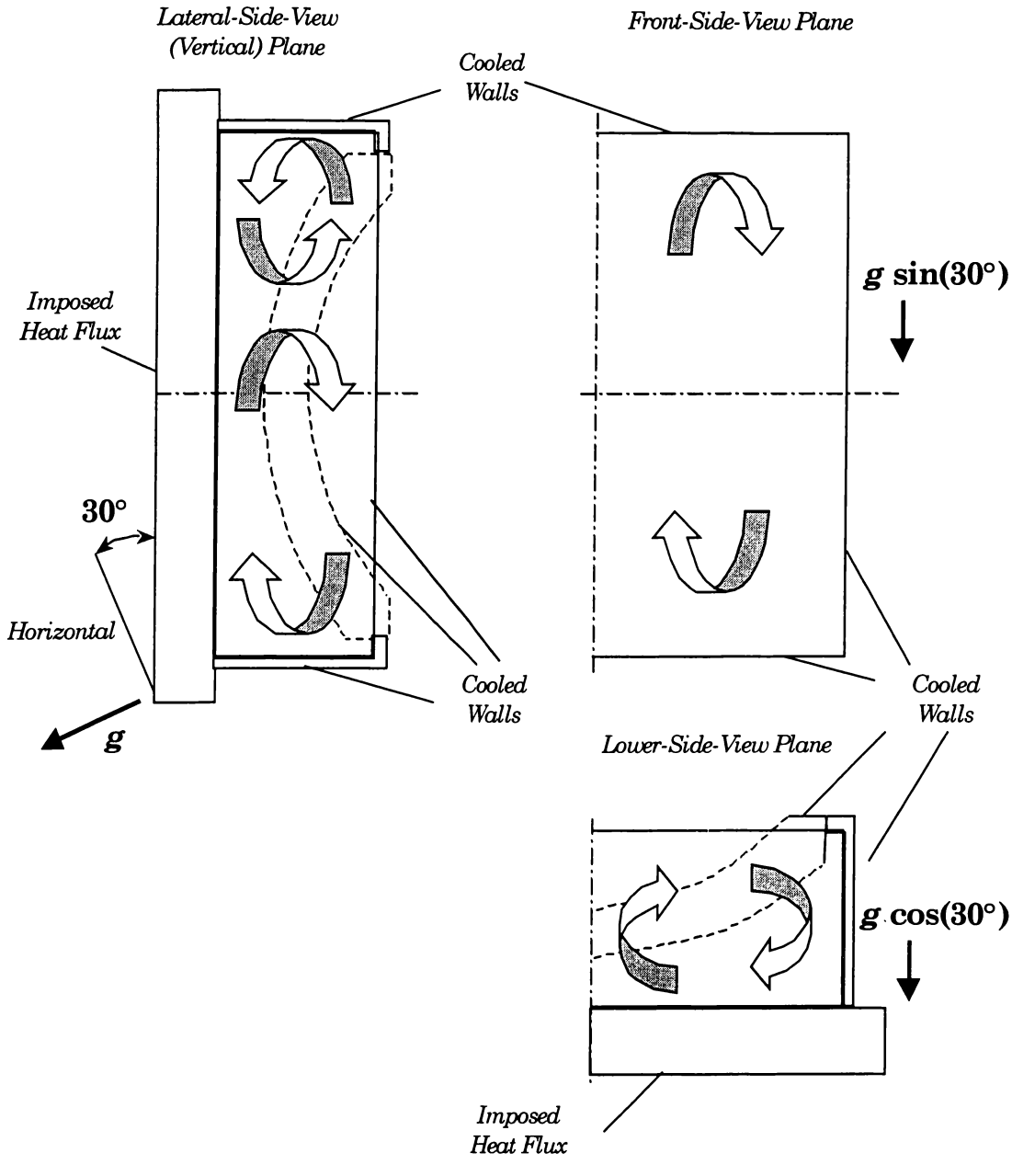

Figure 2-8. Anticipated Three-Dimensional Base Flow Circulation

As in the case of the natural convection flows in rectangular slots, flow instabilities have the potential to induce secondary rolls. Based on preliminary calculations, longitudinal rolls are more likely than transverse rolls, as the enclosure critical angle is greater than the actual tilt angle. The calculations assumed natural convection in a rectangular channel heated from below, with an aspect ratio of 3.82 (based on enclosure dimensions), for which the critical angle is approximately 60° [3]. The potential, however, still exists for secondary rolls in all of the three directions because of the complexity in geometry and boundary conditions.

Due to the lack of heat transfer correlations directly applicable to the liquid-lens system, only a "first-cut" estimate of the face panel temperature can be made using correlations intended for natural convection in rectangular enclosures of infinite depth. The calculation procedure, however, must be modified because of the differences in boundary conditions, the presence of the meniscus lens, and the finite enclosure depth. For more accurate results, experimental or numerical models should be used.

The mathematical model for heat transfer within the liquid lens may be simplified if the liquid and the glass in the face-panel and meniscus lens are assumed opaque to infrared thermal radiation. Visible light, can be assumed to travel without being absorbed, diffracted, or reflected through the glass and liquid. Only that fraction of the light emitted at the phosphor screen and directed to the enclosure and face panel sidewalls is assumed absorbed right at these surfaces. This implies that some amount of heat will be generated by the conversion of electromagnetic energy in the light into internal energy in the surface material, although this amount is believe to be small.

2.5. Detailed Solution Approach

As stated earlier, no studies were found on problems with geometries and boundary conditions like those of the liquid-lens system. Therefore, experimental and numerical models are needed to provide sufficient knowledge that will enable the evaluation of the thermal design. The approach is to use experimental data to benchmark the numerical model, and to use the numerical model as the analysis

tool. For the lack of better data, preliminary estimates of the mean temperature of the CRT face panel front and back surfaces can be obtained using Nusselt number correlations for differentially heated tilted enclosures. This can be achieved by constructing a lumped-parameter heat transfer model, as will be described in the next chapter. These results will be used as reference for experimental and numerical results.

Experimental measurements are necessary to gather enough data to validate the numerical model. Such measurements were conducted on a liquid-lens system as part of a projection TV receiver. Due to the limited amount of time, only one experimental run was made, so only one set of steady-state data was available to validate the numerical model. The numerical model should involve the solution in three-dimensional space of the equations for conservation of mass, momentum, and energy within the CRT face panel, the meniscus lens, and the enclosed liquid. The equations involved are elliptic. Therefore, the results within the solution domain require the specification of boundary conditions on all of the domain boundaries. The numerical model is benchmarked with experimentally measured temperatures and heat transfer data under steady-state conditions. Input model data consists of external temperatures and heat flux data. The model should recover experimental temperatures at points internal to the solution domain. If the numerical model captures all the physics involved, and it reproduces the experimental results, then this model can be used to provide a complete parametric analysis for the conditions observed during the experiment. Furthermore, the model can be used as a prediction tool for other flow conditions (as long as they do not depart drastically from those used to validate the original solution).

The task was to design an experiment from which boundary conditions could be measured to fulfill the above objective. Exterior system temperatures can be measured without much difficulty. The challenge was to measure the amount of heat generated at the phosphor screen, and the dimensions of the area where heat is generated. Heat transfer applied to the back of the face panel is not measurable by direct means, but it may be calculated indirectly from input electrical power. The remaining source of uncertainty is the size of the raster area where the heat is

generated. It was decided that internal temperatures to be used to benchmark the numerical model were measured on the face-panel front surface at pre-established locations. This decision was made (1) because previous practices by the tube's manufacturer involved measuring temperatures on the face panel exterior [90], and (2) because quantification of thermal performance involves the knowledge of temperatures on this surface. Temperature measurement on the face panel back was not pursued, because it would disrupt the equipment operation and temperature and velocity measurement within the fluid was avoided to prevent disturbing the delicate natural convection flow. Neither of these options was acceptable.

Once the numerical model has been benchmarked, a series of runs are conducted to determine the effects of modifying the system's thermal design without affecting the optical design. This requires that the geometry of the CRT face panel and the meniscus lens be left intact, which leaves only the enclosure width, height, and depth as candidates for modification. In addition, boundary conditions applied to the enclosure will be modified to examine the effects on thermal performance. In particular, the use of forced convection will be examined, which can be implemented by feeding flow from the enclosure lower wall and removing it from the upper wall. The meniscus lens design will be modified to check thermal performance sensitivity to the optical design. Finally, a series of runs is aimed at examining the effects of variation in the input heat, thermophysical properties of the CRT face panel, meniscus lens, and optical fluid, system tilt angle, and heated region dimensions.

3. EXPERIMENTAL EVALUATION OF THE LIQUID-LENS SYSTEM

3.1. Experimental Apparatus

Experimental measurements were made using the liquid-lens system in a production-model projection TV monitor provided by North American Philips Consumer Electronic Corporation (NAPCEC). The following description will concentrate on the liquid-lens system, and pertinent equipment. Details regarding the projection monitor and hardware specifications are in APPENDIX A.

3.1.1. Description of the Liquid-Lens System

The liquid-lens system is composed of the face-panel of a projection picture tube and a meniscus lens mounted in an aluminum frame (enclosure), as shown in *Figure 3-1*. A liquid coolant fills the enclosed space between the tube and the lens, leaving a small air volume to allow for thermal expansion.

The face panel is a uniform thickness semi-rectangular glass piece with flat front (exterior) and back (interior) surfaces that are parallel to each other. The projection tube face panel thickness was measured as 7.1 mm (following the experiment). The face panel outer-envelope dimensions were 154.0 mm (width) by 136.0 mm (height). The actual dimensions of the glass material were measured at 150.0 mm (width) by 122.0 mm (height).

The enclosure frame was made of cast aluminum with inner base dimensions measured at 122.4 mm (width) by 97.4 mm (height). The interior depth (base-to-front wall) was measured at 25.3 mm. The overall thickness was 3.18 mm. A "d-shape" cross-section ring is placed along the perimeter at the enclosure base to seal against the face panel surface, with an installed thickness of 0.2 mm. This added thickness results in a distance of 25.5 mm, measured from the face panel exterior to the enclosure-frame front wall (interior side). The meniscus lens is a glass piece with two surfaces of spherical cross-section of radii 39.5 mm on the concave side and

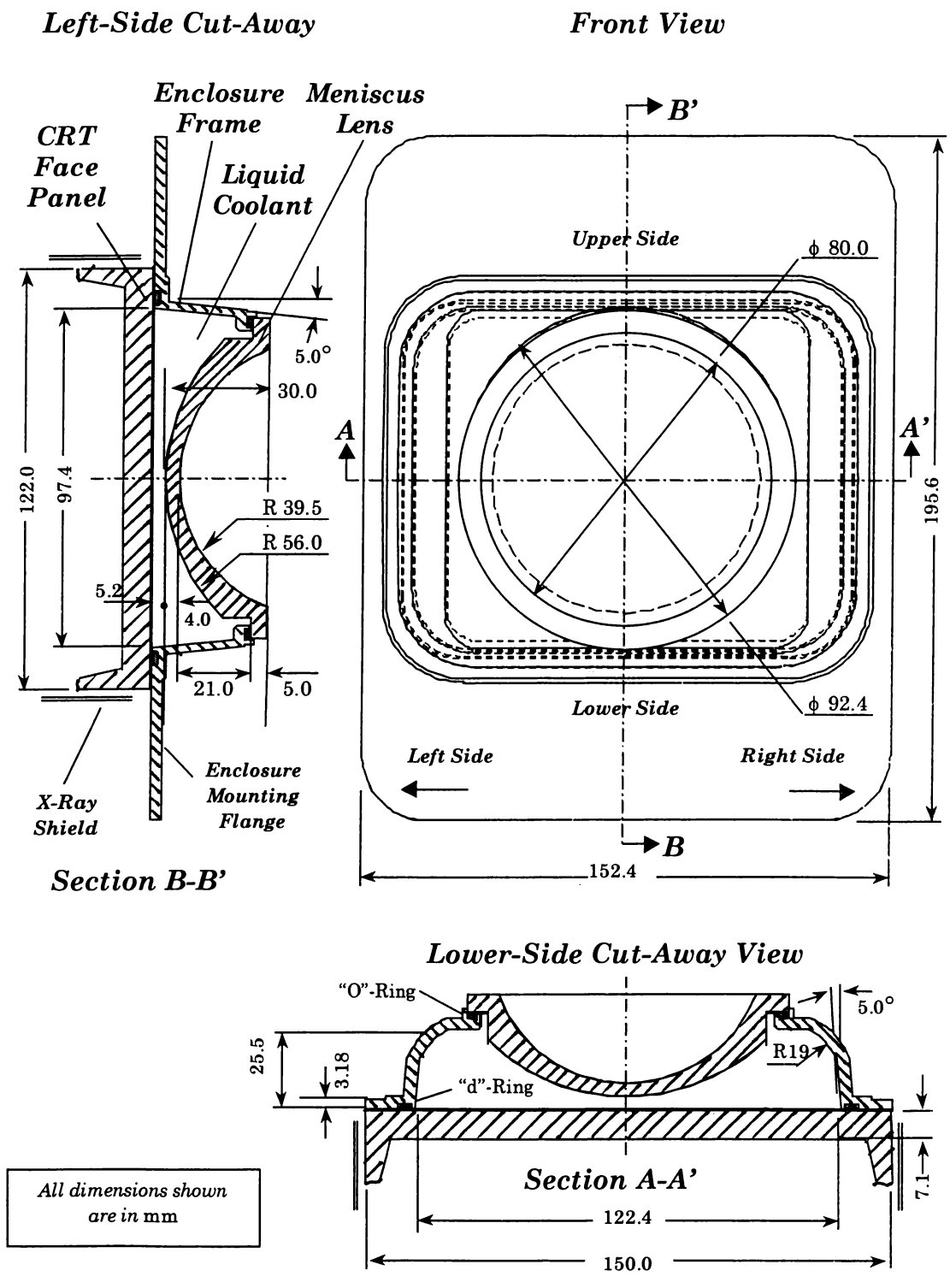

Figure 3-1. Cut-Away Views of the Experimental Liquid-Lens System

56.0 mm on the convex side. The thickness along the symmetry axis is 4.0 mm. The meniscus lens is installed such that the convex side faces the face panel. The meniscus lens rests against O-rings inserted along circular slots on the enclosure-frame front. A mating flange (not shown) presses against the meniscus rim on the front side to ensure sealing against the O-rings. When installed, the meniscus lens is positioned with the center point of the convex side 5.2 mm away from the face panel surface at the center.

A side view showing the hardware as installed during the experiment is shown in *Figure 3-2.* The liquid-lens system sits at an angle such that the face-panel minor axis makes a 30°-angle with the horizontal. The major axis is horizontal. An air volume was left inside the enclosure forming a free surface intersecting the meniscus-lens convex surface, as shown. An expansion chamber and a focusing lens were part of the original equipment and were left in place. The expansion chamber serves as a pressure-relief space as the liquid-coolant volume increases during heating. The focusing lens is mounted against the mating flange

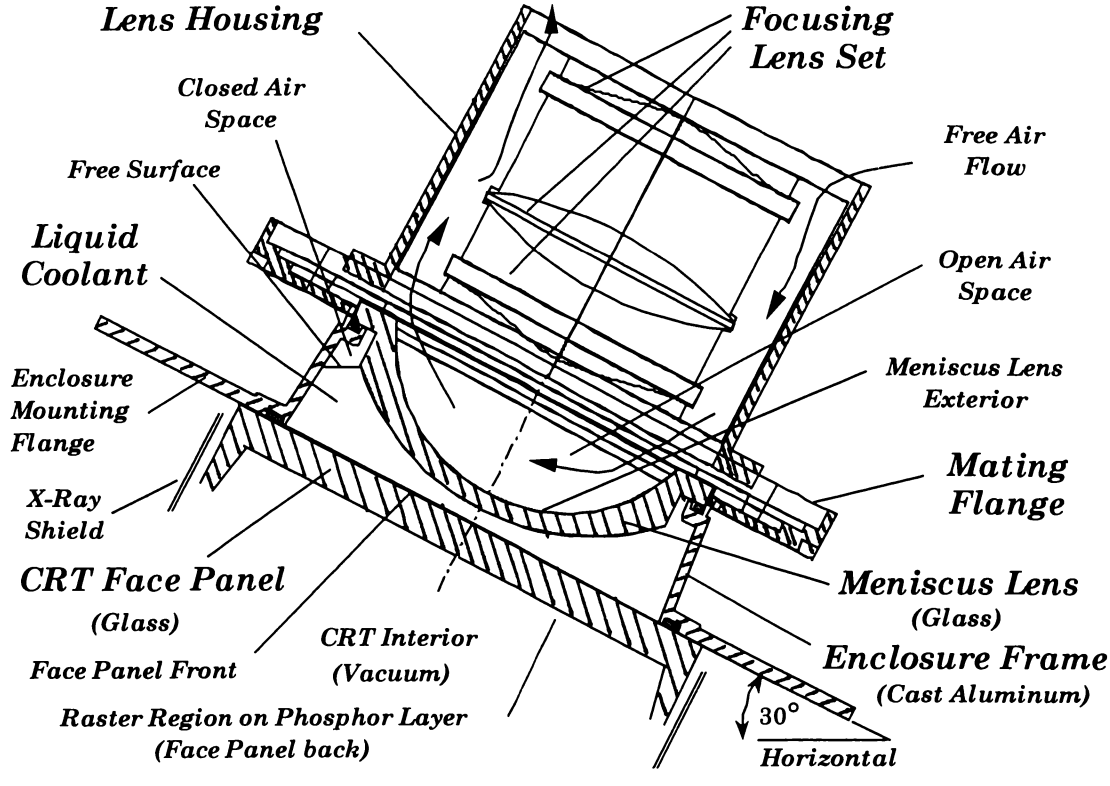

Figure 3-2. Liquid-Lens Configuration During the Experiment

holding the meniscus lens in place. There are gaps between the focusing lens moving piece (set of lenses) and the housing, allowing air to move in and out of the space adjacent to the meniscus lens.

3.1.2. Instrumentation

The experimental apparatus was instrumented for temperature and voltage measurement. Temperatures were measured using copper-constantan thermocouples and thermometers. Voltage measurements were made using a digital multi-meter, in order to calculate the input electrical power to the electron beam.

Instrumentation for Temperature Measurement

Thermocouple junctions were affixed to the CRT face panel exterior, the enclosure frame exterior, the meniscus lens, and the focusing lens array. In total, 20 thermocouples were used in the experiment. Their description is shown in Table 3-1. For reference, it is assumed that the projector assembly is viewed in the direction from the front to back (the electron gun points away from the observer). One thermocouple (Channel #0) was used to establish the ice-point reference temperature. One thermocouple (Channel #1) was used to measure the air temperature inside the cabinet, 1 cm from the bottom, below the green CRT. *Figure 3-3* shows thermocouple locations on the meniscus lens and enclosure frame. Two thermocouples were used to measure meniscus surface temperature: one on the convex side (Channel #2) and one on the concave side (Channel #3). Three thermocouples were used to measure enclosure frame temperatures. One was placed at the center of the upper horizontal surface (Channel #4), one at the center the lateral vertical surface (Channel #5), and one at the center of the lower horizontal surface (Channel #6). Twelve thermocouples were used to measure face panel temperatures, as shown in *Figure 3-4*. Three thermocouples (Channels #7, #8, and #9) were placed at edge locations, and nine (Channels #10 through #18) were arranged in the form of a 3x3 grid. From the three edge thermocouples, two were positioned along the vertical centerline, 56 mm above and below the face panel center, and one along the horizontal centerline, 69 mm to the right side of the

Table 3-1. Thermocouple Locations

Channel #	*Location*
0	Ice/Water Bath Thermometer Bulb
1	PTV Interior Environment (below CRT, 1 cm above cabinet bottom)
2	Meniscus Lens Interior (Convex Side), Center
3	Meniscus Lens Exterior (Concave Side), Center
4	Enclosure Frame Exterior Upper Surface
5	Enclosure Frame Exterior Lateral Surface
6	Enclosure Frame Exterior Lower Surface
7	Face Panel at (0, -56) mm
8	Face Panel at (69, 0) mm
9	Face Panel at (0, +56) mm
10	Face Panel at (50, -35) mm
11	Face Panel at (25, -35) mm
12	Face Panel at (0, -35) mm
13	Face Panel at (50, 0) mm
14	Face Panel at (25, 0) mm
15	Face Panel at (0, 0) mm
16	Face Panel at (50, +35) mm
17	Face Panel at (25, +35) mm
18	Face Panel at (0, +35) mm
19	Focusing Lens Closest to Meniscus Lens, Center

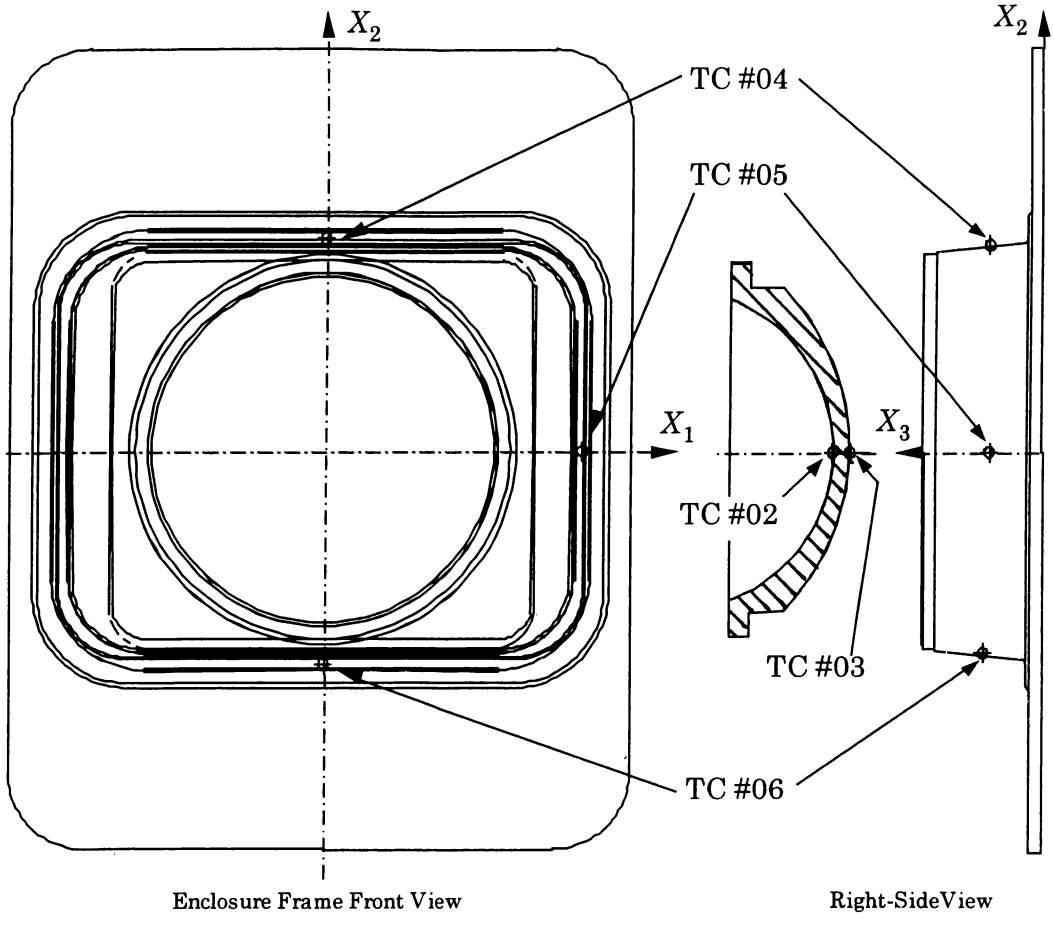

Figure 3-3. Thermocouple Locations on the Enclosure Frame and Meniscus Lens

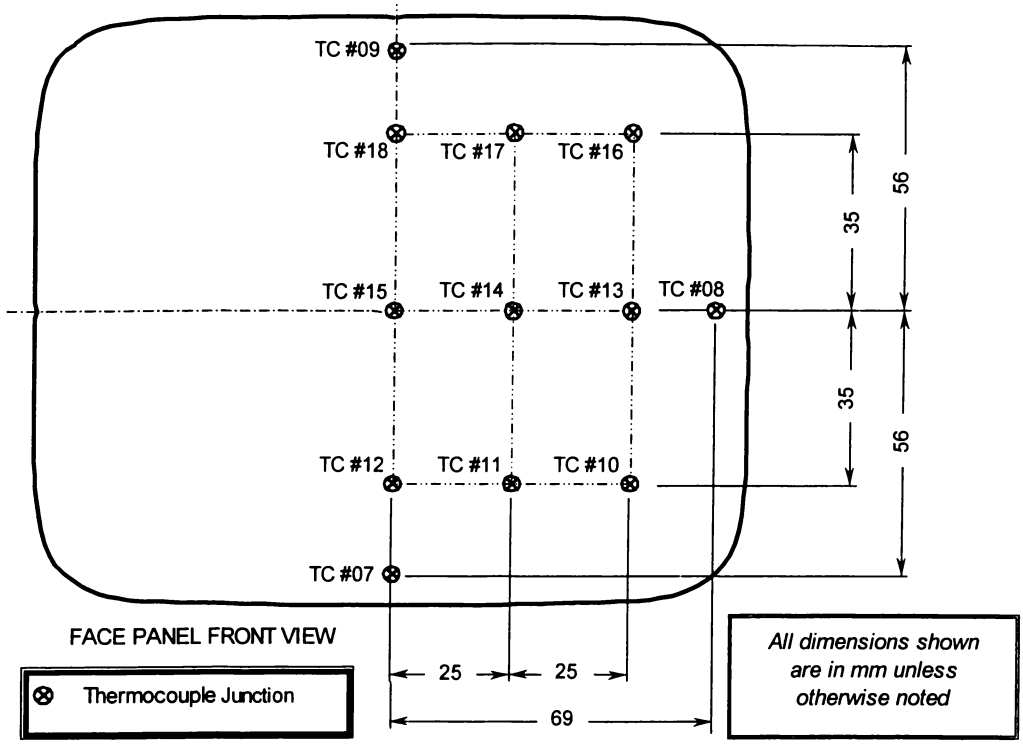

Figure 3-4. Location of Thermocouple Junctions: CRT Face Panel

face panel center (Channel #9). The 3x3 grid was constructed by placing the thermocouple junctions at intersections between horizontal and vertical lines (parallel to the major and minor axes, respectively). The horizontal gridlines were the horizontal centerline, and two lines parallel to it, one 35 mm above, and one 35 mm below. The vertical gridlines were the vertical centerline and two lines parallel to it, one at 25 mm and another at 50 mm to the right. Coordinate locations for the above thermocouples on the face panel are shown in Table 3-2. Finally, one thermocouple junction (Channel #19) was attached to the center of the most interior lens of the focusing lens array, as shown in *Figure 3-5*.

Instrumentation for Voltage Measurement

Input power was obtained indirectly by measuring voltages. To measure the input electrical power to the electron beam, the beam electrical current and the anode voltage are required. *Figure 3-6* shows a circuit diagram with the elements involved in voltage and current measurement. To measure the beam electrical

Table 3-2. CRT Face Panel Thermocouple Junction Coordinates and Channel Number

X_2 (mm)	X_1 = 0 mm	X_1 = 25 mm	X_1 = 50 mm	X_1 = 69 mm
56	(0,+56) #09	---	---	---
35	(0,+35) #18	(25,+35) #17	(50,+35) #16	---
0	(0, 0) #15	(25, 0) #14	(50, 0) #13	(69, 0) #08
-35	(0,-35) #12	(25,-35) #11	(50,-35) #10	---
-56	(0,-56) #07	---	---	---

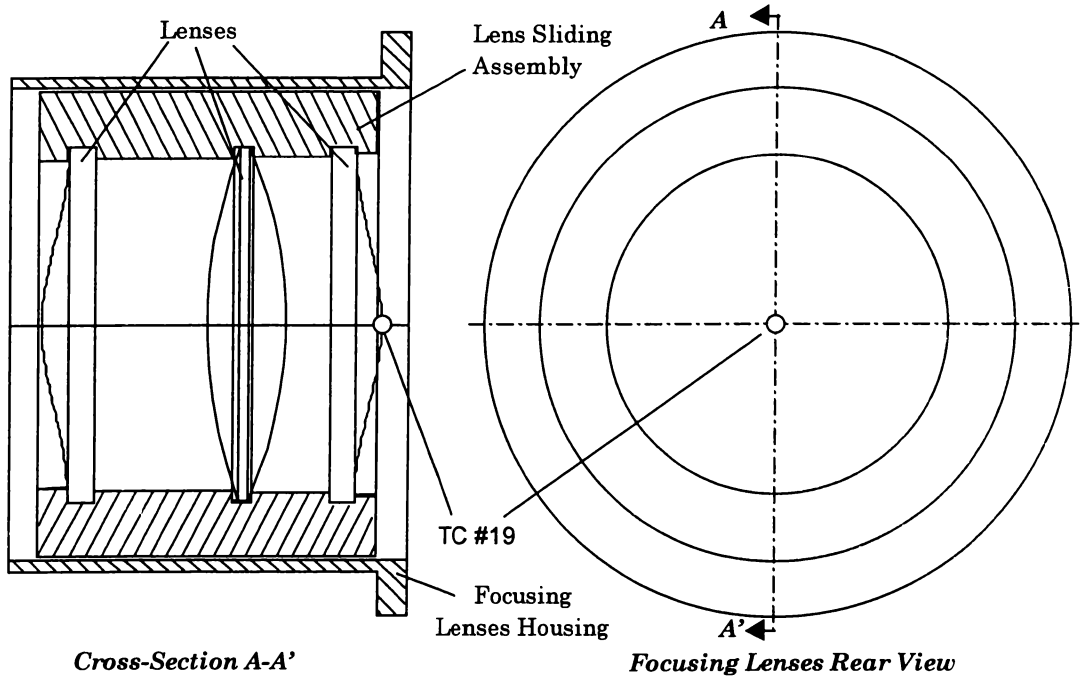

Figure 3-5. Location of Thermocouple Junctions: Focusing Lens Array

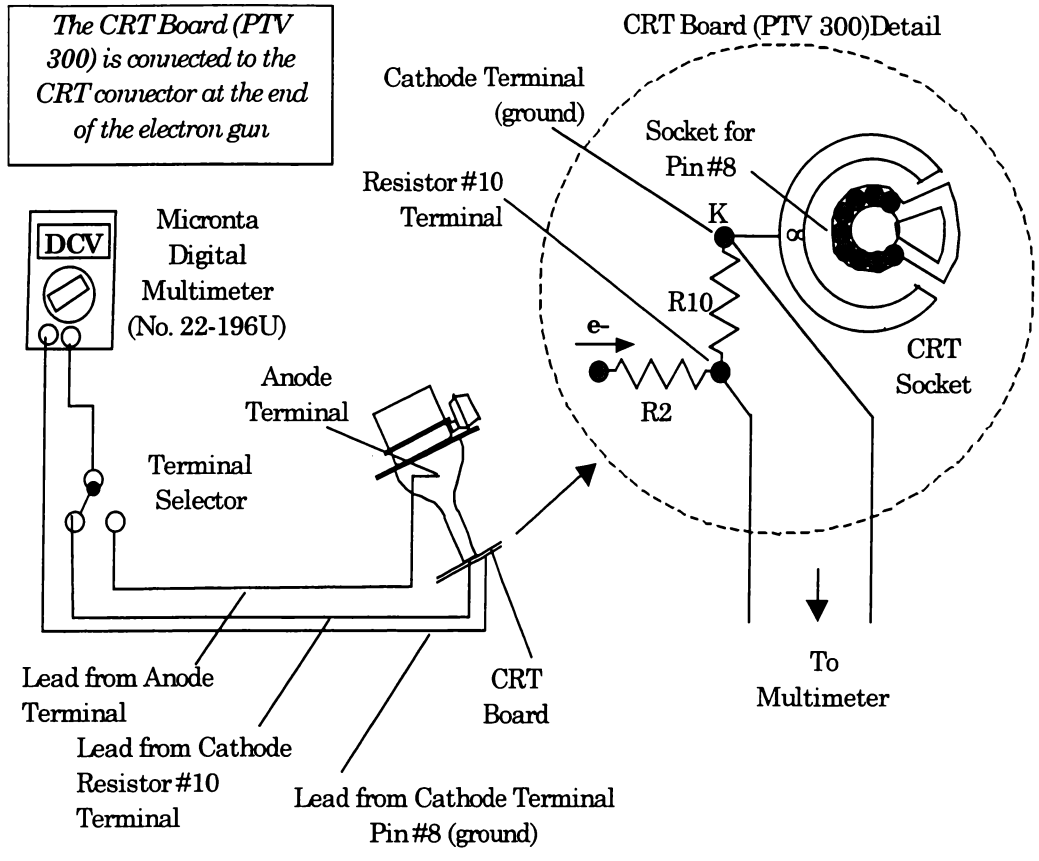

Figure 3-6. Voltage Measurement Circuit Diagram

current, a voltmeter was used to read the voltage across resistor R10 on the circuit board that connects to the CRT. Resistor R10 has a resistance of 954 Ω, and has one of its terminals connected to pin #8. This pin connects directly to the CRT cathode. The anode voltage was taken from the anode electrode on the CRT-funnel side and measured with respect the ground voltage at the cathode terminal (pin #8). The voltages were measured with a digital voltmeter.

3.1.3. Experimental Setup

The major components of the experimental apparatus and data acquisition system are shown in *Figure 3-7.* Temperature was measured using copper-constantan thermocouples and two thermometers. Voltage measurements were taken using a Micronta Digital Multi-meter Model No. 22-196U. The data acquisition system consisted of a Hewlett-Packard Data Acquisition and Control

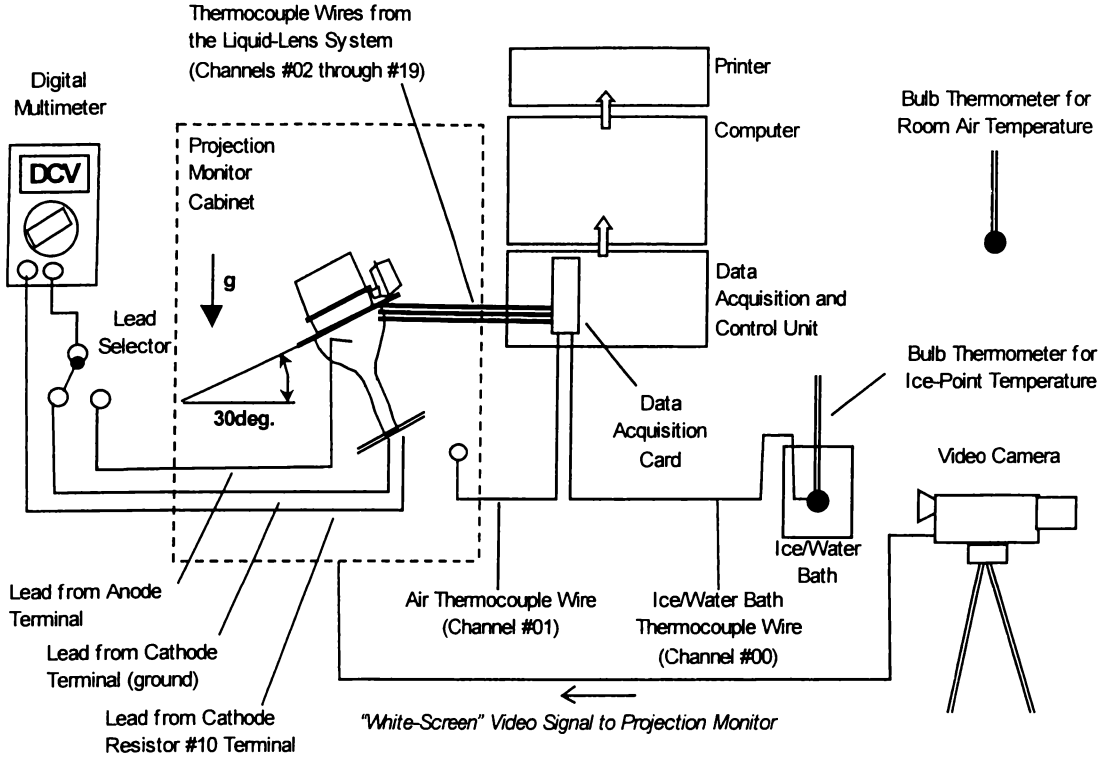

Figure 3-7. Instrumentation Setup

Unit Model HP 3497A, a computer model HP9826, and a printer model HP2671G. The video signal used during testing was provided by a standard video camera.

3.2. Experimental Results

The room air temperature at the end of data collection was 21.7 °C ± 0.1 °C. The variables involved in the calculation of electron-beam power are shown in Table 3-3. The average anode voltage was 27.8 kV, and the average voltage drop across resistor R10 was 0.487 V. Averages were from two readings. The resistance of resistor R10 was measured at 0.954 Ω immediately following data collection, when the material was still warm. The cathode current was calculated from steady-state values of voltage across resistor R10 and its resistance. The value was calculated as 510 μA. The input electrical power was calculated as the product of the anode voltage and resistor R10 current. The result was 14.2 W. Uncertainties are shown in the table.

Table 3-3. Variables Related to Electron-Beam Input Power

Variable		*Units*	*Value*	*Uncertainty*
Anode Voltage	(measured)	kV	27.8	±0.55
Resistor R10 Voltage	(measured)	V	0.487	±0.005
Resistor R10 Resistance	(measured)	Ω	954	±40
Cathode Current	(calculated)	μA	510	±27
Electrical Input Power	(calculated)	W	14.2	±0.7

3.2.1. Transient Temperature Measurements

Temperature data was collected from the 20 channels every 10 minutes, at the end of which 10 samples were collected and averaged per channel, spaced at 0.05 s from each other. Raw temperature data is in APPENDIX B. At the end of the data collection period, the internal cabinet environment temperature was rising at the rate of 0.2 to 0.3 °C per hour. This rate of increase may be considered small enough when compared to the rates of increase at the start of the experiment. In view of this, condition at the end of the experiment can be deemed "steady state." The temperatures at the end of the experiment kept fluctuating slightly between data acquisition events; therefore, averaging data points to get steady-state temperatures was avoided since the result depended on an arbitrary number of data points used. To get steady-state temperatures, a curve-fit function was used to extrapolate the data to steady state.

3.2.2. Extrapolation of Transient Temperatures to Steady-State

To be able to arrive at a set of uniform and consistent data, and to be able to extrapolate to steady state, curve-fitting functions were used. Standard exponential functions, resulting from lumped-parameter heat-transfer models did not work satisfactorily, as they only fitted part of the data. The reasoning was that these models do not take into account the "inertia" or "impedance" of the system. These models are analog to a spring-damper system (no mass). The data can be curve-fitted surprisingly well by adding the "mass" to the spring-damper system. Details

about the derivation of the curve-fitting equations are in APPENDIX B. Curve fits were obtained using an n optimization process that resulted in a *damping ratio* of unity (critically damped motion) or slightly below unity (under-damped motion) for all data channels. The resulting curve fits depict the experimental data quite well throughout the entire data-collection period, as shown in *Figures 3-8* through *3-12*.

3.3. Steady-State Experimental Temperatures on the CRT Face Panel

Once the curve-fitting functions were obtained, extrapolation to steady state was trivial. Steady-state temperatures obtained from curve-fitting functions for all channels at infinite time are shown in Table 3-4. Table 3-5 shows the steady-state temperatures on the face panel locations. These results are illustrated in *Figure 3-13* as temperature profiles at constant X_1-coordinate locations. Notice that dashed lines in these profiles were used to indicate that they do not necessarily represent the actual values between data points, and are used for visual convenience. A preliminary lumped-parameter model, using a convection coefficient derived from two-dimensional enclosure natural convection was used to check temperature levels. The model used is shown schematically in *Figure B-1*. The lumped-parameter model predicts a face-area-weighed mean temperature of 60.3 °C for the face panel exterior, which is within the range of experimental data (50.4 °C to 64.9 °).

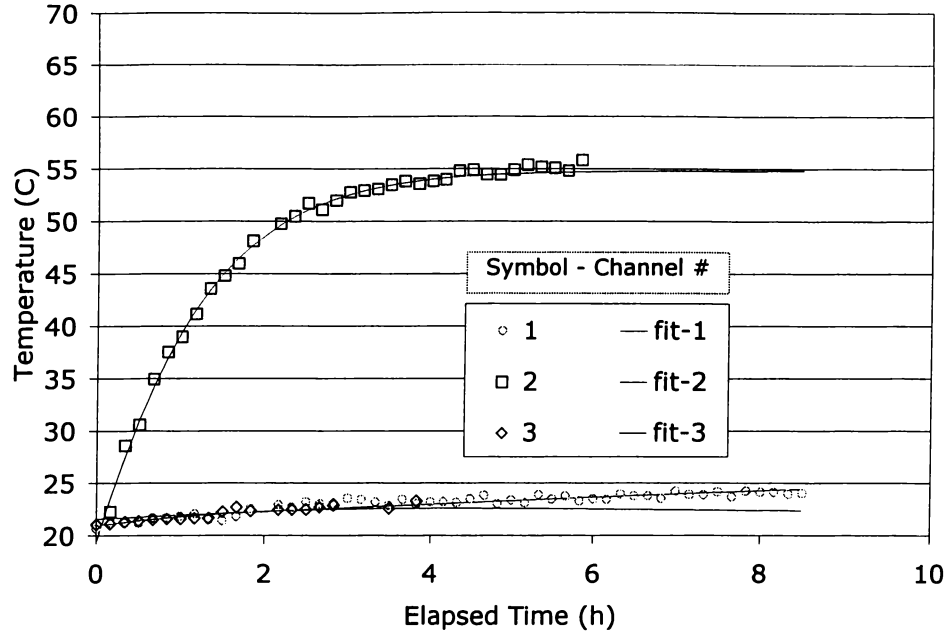

Figure 3-8. Temperature Curve Fits: Meniscus Lens

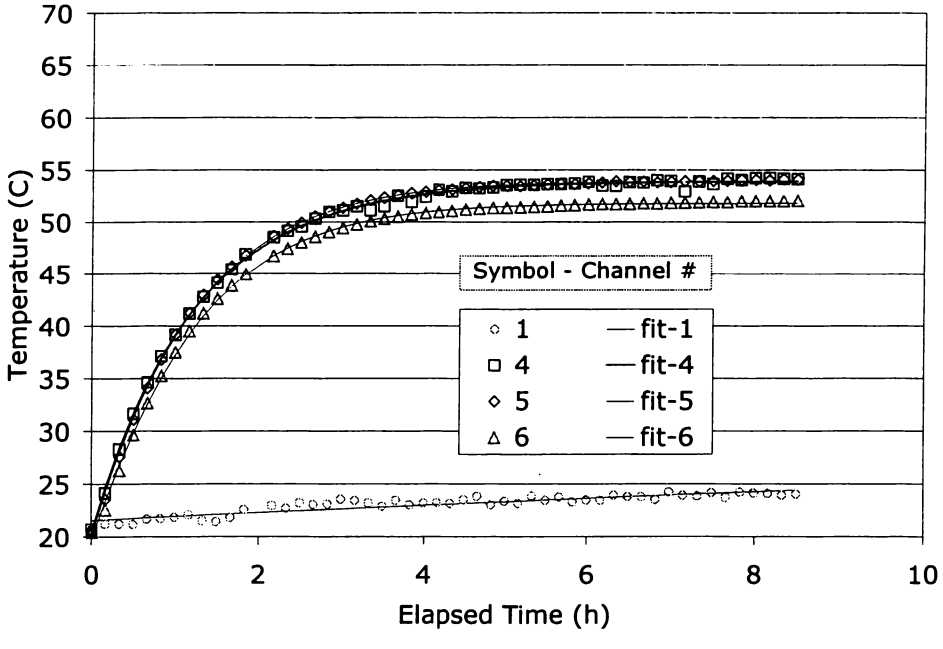

Figure 3-9. Temperature Curve Fits: Enclosure Frame

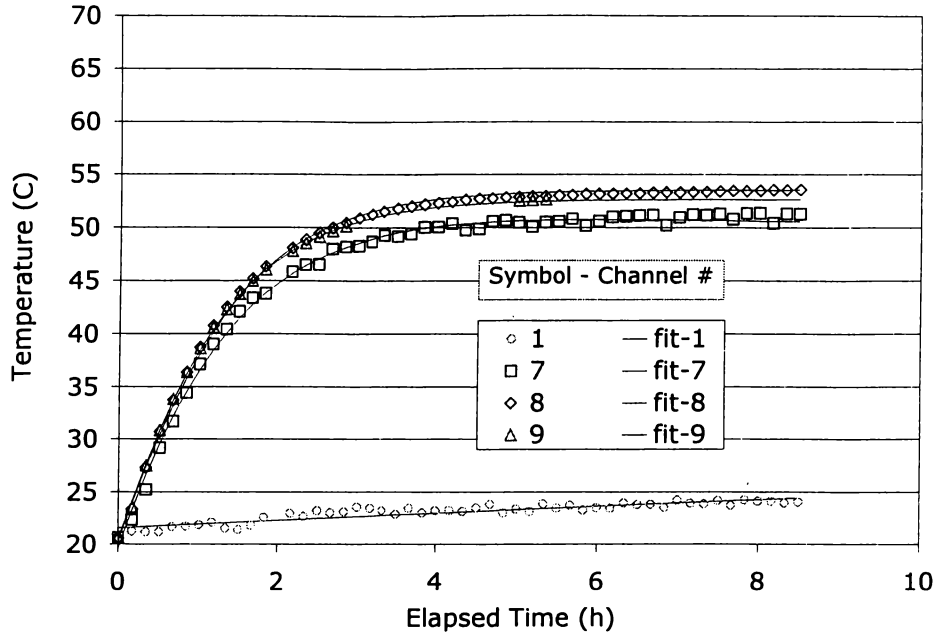

Figure 3-10. Temperature Curve Fits: CRT Face Panel Edge

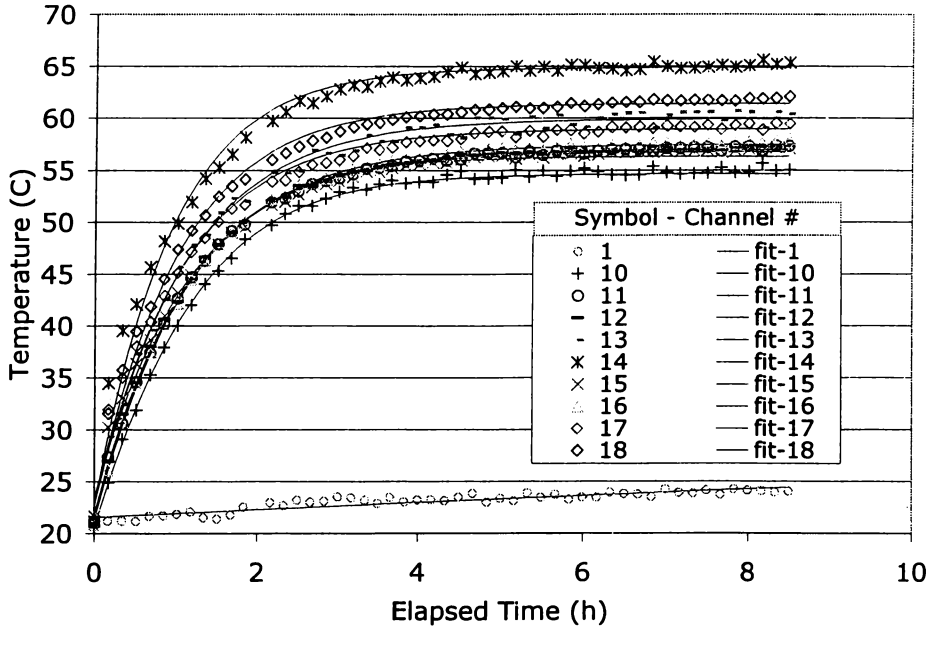

Figure 3-11. Temperature Curve Fits: CRT Face Panel Grid

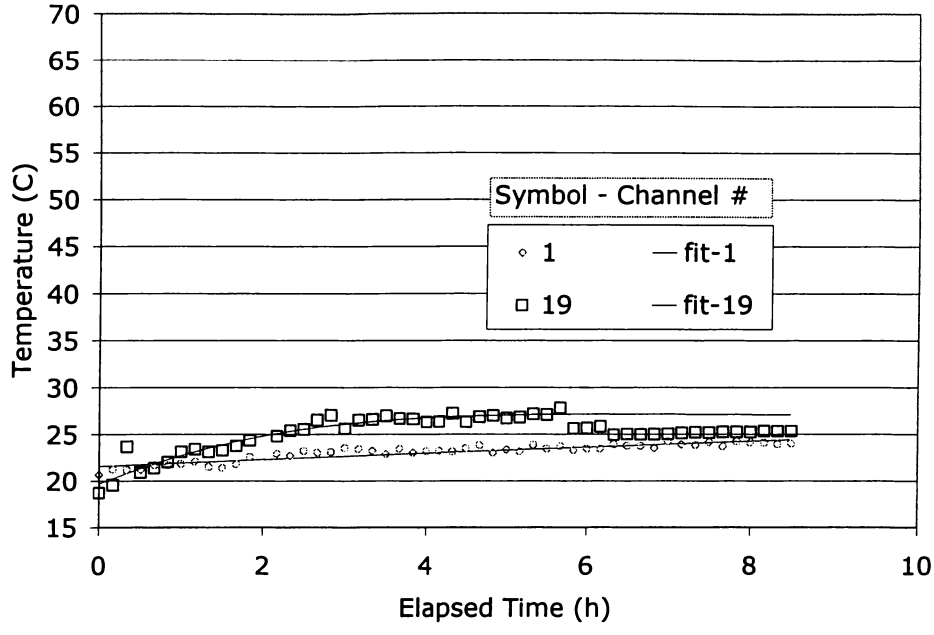

Figure 3-12. Temperature Curve Fits: Focusing Lens Interior

Table 3-4. Steady-State Experimental Temperatures

Calibration Uncertainty ±0.1 °C

Channel #	*Location*	*Temperature °C*
1	PTV Interior Environment (below CRT, 1 cm above cabinet bottom)	23.9
2	Meniscus Lens Interior (Convex Side), Center	54.8
3	Meniscus Lens Exterior (Concave Side), Center	----
4	Enclosure Frame Exterior Upper Surface	53.9
5	Enclosure Frame Exterior Lateral Surface	53.9
6	Enclosure Frame Exterior Lower Surface	51.8
7	Face Panel at (0, -56) mm	50.4
8	Face Panel at (69, 0) mm	53.5
9	Face Panel at (0, +56) mm	52.7
10	Face Panel at (50, -35) mm	54.7
11	Face Panel at (25, -35) mm	56.3
12	Face Panel at (0, -35) mm	57.0
13	Face Panel at (50, 0) mm	59.9
14	Face Panel at (25, 0) mm	64.9
15	Face Panel at (0, 0) mm	56.8
16	Face Panel at (50, +35) mm	57.5
17	Face Panel at (25, +35) mm	59.0
18	Face Panel at (0, +35) mm	61.4
19	Focusing Lens Closest to Meniscus Lens, Center	27.5

Steady-state temperatures were calculated using curve-fit functions and extrapolating to infinite time (see Appendix B).

Table 3-5. Experimental Values of the CRT Face Panel Steady-State Temperatures

X_1 (mm) →	0	25	50	69
X_2 (mm)	*Temperature* (°C)			
56	52.7	---	---	---
35	61.4	59.0	57.5	---
0	56.8	64.9	59.9	53.5
-35	57.0	56.3	54.7	---
-56	50.4	---	---	---

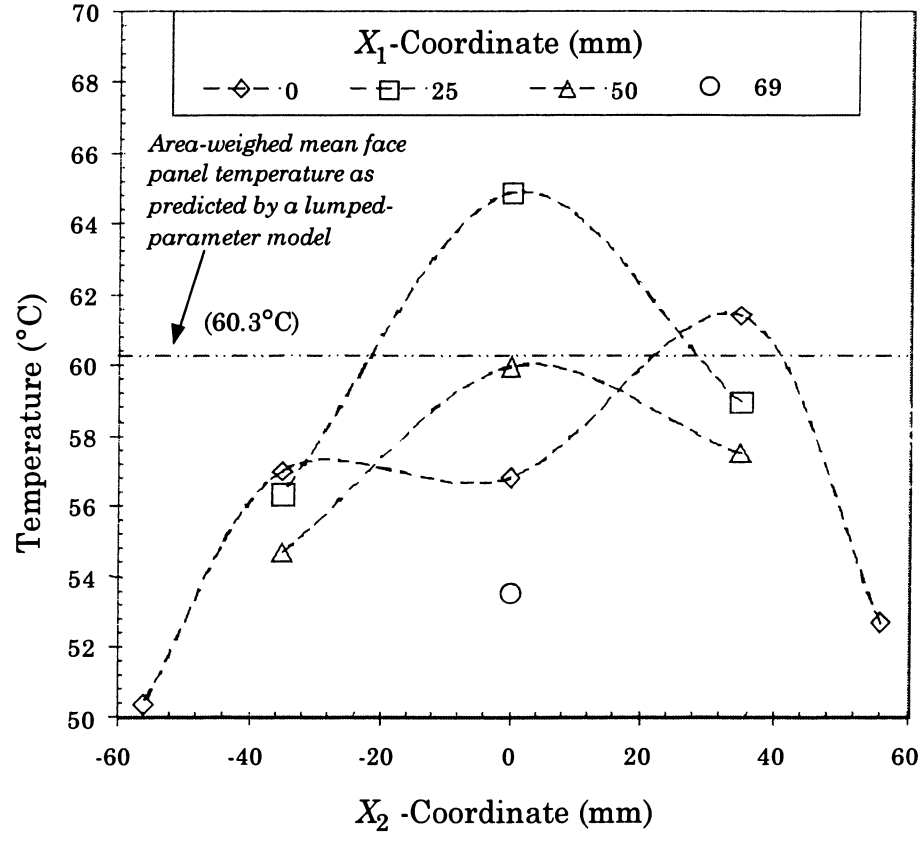

Figure 3-13. Steady-State Experimental Temperatures on the Face Panel

4. REVIEW OF NUMERICAL METHODS IN HEAT TRANSFER AND FLUID FLOW

4.1. Introduction

A numerical technique is required to resolve the natural convection flow in the liquid lens system. The equations to be solved are the differential equations for mass, momentum, and energy within the solid and fluid domains. The steps for solving the conservation equations of mass, momentum, and energy are as follows. First, a formulation of the mathematical model in differential form is developed; second, the set of differential equations is transformed into a set of algebraic equations; and third, the set of algebraic equations is solved numerically.

In natural convection flows, the differential equations for momentum and energy are coupled, as temperature appears in the body-force term of the momentum equations. Therefore, the momentum differential equations cannot be solved independently from the energy differential equation. These equations are solved in an iteration process, as direct methods may prove very costly. The solution of the energy equation becomes immediately available once the flow field is known. On the other hand, the flow field is dictated by the momentum equations, which include the temperature as an independent variable. The momentum equations must be combined with the mass conservation equation to resolve the pressure and velocity fields. In an iterative process, these equations are solved systematically with the solution being updated throughout the process until conservation is satisfied.

4.2. Dependent and Independent Variables

The conservation equations are usually available in terms of primitive variables, where temperature, velocity, and pressure are the dependent variables, and time and position-vector are the independent variables. There are methods for solving the energy equation, in which internal energy or enthalpy are used instead of temperature. Once the internal energy or enthalpy field is solved, temperature

becomes readily available by a functional relation. Other methods for solving the mass and momentum equations use a scalar potential, a vector potential, and the vorticity as the dependent variables, the velocities and pressure becoming available as a post-solution calculation. The flow field in the problem at hand belongs to the class of Newtonian flows. Thus, the attention will be focused to the solution of the Navier-Stokes equations. A review of the most common types of formulations for solving the Navier-Stokes equations is presented next.

4.3. Formulations for Solving the Navier-Stokes Equations

There are various ways to approach the solution of the Navier-Stokes equations, with each approach yielding a mathematical statement of the problem in differential form as a set of partial differential equations along with boundary and initial conditions. The most widely known formulation types are (1) the vorticity/stream-function formulation, (2) the vorticity-velocity formulation, (3) vector/scalar-potential formulation, (4) the vector-potential/vorticity formulation, and (5) the primitive-variable formulation.

4.3.1. Vorticity/Stream-Function Formulation

In the vorticity/stream-function formulation, the vorticity and the stream function are defined in terms of the velocities and introduced as new dependent variables to replace the pressure and the velocities. The result is the transformation of a set of three differential equations in three dependent variables (the pressure and two velocities) into a set of two differential equations in two dependent variables. The advantage of this formulation is that continuity is satisfied automatically. The disadvantages of using the vorticity/stream-function formulation are that (1) the solution cannot be applied to three-dimensional flows, and (2) that the method has limitations when solving multiply connected regions Farouk and Gouceri [29].

4.3.2. Vorticity-Velocity Formulation

The vorticity-velocity formulation uses the vorticity as a new variable, and the momentum equations are written in the vorticity transport form. This leads to the elimination of the pressure from the problem statement. In two dimensions, one vorticity component exists --the one normal to the plane of the solution-- which results in one vorticity transport equation and two Poisson equations for obtaining the velocity components. The two Poisson equations result from taking derivatives of the equation defining the vorticity and combining with the continuity equation. The advantage is that the formulation applies to three-dimensional flows. The disadvantage is that in three-dimensional cases, the formulation requires six dependent variables to just solve the Navier-Stokes equations: three velocity components and three vorticity components. This results in three vorticity transport equations and three Poisson equations to compute the velocities. Fusegi and Farouk [32] report that the vorticity-velocity formulation produces stable results for high Reynolds and Grashof numbers.

4.3.3. Vector-Scalar Potential Formulation

The vector-scalar potential formulation uses a scalar potential function, a vector potential function, and a vorticity vector function as the flow dependent variables. The velocity vector is obtained in terms of the gradient of a scalar potential field plus the curl of a vector potential function. The equation for the scalar potential is obtained by substituting the resulting expression for the velocity vector into the continuity equation, and assuming a solenoidal vector potential field. The vorticity vector equation is obtained by taking the curl of the momentum equations. An equation relating the vorticity and the vector potential is obtained by taking the curl of the velocity as defined above. Boundary conditions must be determined for the scalar potential, the vector potential components, and the vorticity vector components, which is usually difficult to accomplish. The advantage of this formulation is that it can treat three-dimensional flows. Among the disadvantages is the increased number of equations to solve. Another disadvantage is that boundary-condition discontinuities in the scalar potential may lead to

spurious solutions as noted by Tutty [128], who also suggests that the alternative vector-potential/vorticity formulation should eliminate this problem.

4.3.4. Vector-Potential/Vorticity Formulation

The vector-potential/vorticity formulation uses the vorticity vector and the vector-potential as dependent variables, yielding two vector equations. An equation for the vorticity vector is obtained by taking the curl of the momentum equations, thus eliminating the pressure. The velocity vector is expressed as a function of the curl of a vector potential function plus a complement vector field. The type of such vector field depends on the problem. Wong and Reizes [136] require in their formulation that the added vector field be both solenoidal and irrotational. Tutty [128] states this to be an over-requirement, and suggests that the vector field be required only to be solenoidal. A relationship between the vorticity vector and the vector potential is obtained by taking the curl of the velocity vector as defined above. Boundary conditions must be determined for the vorticity vector components and for the vector potential components. The advantage of this formulation is the ability to solve three-dimensional problems in simply or multiply connected regions, as reported by Wong and Reizes [137]. The major disadvantage is the difficulty in the determination of the boundary condition for the vector potential, and having to find an appropriate complement vector field.

4.3.5. Primitive-Variable Formulation

In the primitive-variable formulation, a solution of the Navier-Stokes equations is sought in terms of the primitive variables of the problem, that is, the pressure and the velocity components. The energy equation is solved in terms of the temperature, enthalpy, or internal energy. The advantage of this formulation is that it can be applied to two- or three-dimensional flows. The disadvantage of this method is that an additional equation for pressure must be derived by combining the continuity and the momentum equations.

4.3.6. Summary

All of the above formulations lead to a set of differential equations and initial and boundary conditions, and with the exception of the vorticity/stream-line formulation, all of the formulation types can treat three-dimensional problems. However, all with the exemption of the primitive variable formulation require the introduction of additional variables, which in turn require the restatement of the differential equations and their initial and boundary conditions. The drawback is increasing the chances for mistakes and the difficulty associated with the restatement of boundary conditions, which in some cases may not be feasible, especially in three-dimensional situations. The primitive-variable formulation, on the other hand, keeps the original forms of the equations without introducing additional variables and boundary conditions. As will be shown in subsequent sections, there are methods available for solving the set of equations formulated in terms of primitive variables, which prove to be more generally applicable to various types of domain geometry and boundary conditions. Based on the above considerations, it was decided to use the primitive-variable formulation.

4.4. Methods for Solving Differential Equations

The first step toward the numerical solution of the partial differential equations is to use a discretization method to transform the set of differential equations along with their initial and boundary conditions into a set of algebraic equations. This involves the discretization of space, time, and fluxes, leading to the solution of the dependent variable on a finite set of points throughout the solution domain. There are three major methods used to discretize differential equations: (1) the finite-difference method, (2) the finite-element method, and (3) the finite volume method.

4.4.1. The Finite-Difference Method

The finite-difference method is based on the direct application of Taylor series expansion to the derivatives in the differential equation. Approximations of

these derivatives are then written as linear combinations of truncated Taylor series in terms of the dependent variable (or variables) (See Refs. [52] and [1]). The resulting equation is of algebraic form, and then can be solved numerically. The main advantage of the finite difference method is its ease of implementation. The major disadvantage is that satisfaction of conservation laws cannot be guaranteed. The second disadvantage is that domains with curved boundaries cannot be easily modeled. Implementation of this method is straight forward in regions where the physical boundaries match coordinate boundaries. However, application of this method to regions with non-conforming coordinate surfaces requires special treatment at the boundary nodes. The accuracy, however, is poor because of the rough approximation of the boundary contour. Results are improved if the number of nodes is increased, or if curvilinear coordinates are substituted to obtain a new set of partial-differential equations such that coordinate surfaces conform to domain boundaries.

4.4.2. The Finite-Element Method

In contrast with the finite-difference method, which provides point-wise approximations to the differential equations, finite-element methods provides regional approximations to the differential equations (See Refs. [52] and [6]). Unlike finite differences, finite elements can be used directly in regions with curved boundaries, but the resulting set of equations to be solved becomes much more complex even in two-dimensional fields.

4.4.3. The Finite-Volume Method

In the finite-volume method, the solution domain is partitioned into "control volumes" or *cells* where the differential equations are integrated. Each cell is assigned a node, usually at the volume centroid, where the dependent variable is evaluated. The governing differential equations are integrated over the volume of each cell. To ensure global conservation, that is conservation through the whole domain, volume integrals of "fluxed" quantities in these equations are converted into surface integrals. Examples of these are advection and diffusion terms. Expressions

for the fluxes are set in terms of the cell-node dependent variable by the use of appropriate interpolation schemes. A set of one equation per cell results, which is solved iteratively. Theoretically, this method can be used to integrate the partial differential equations directly within physical space. This requires that the space is discretized such that boundary faces are conforming to domain boundaries. Alternatively, this method can be applied to integrate the equations following a coordinate transformation, involving the transformation of partial differential equations by substituting curvilinear coordinates that ensure that domain boundaries conform to grid boundary faces. Either approach provides the same solution.

4.5. Discretization of the Differential Equations in Domains with Curved Boundaries

Integration and discretization of differential equations is relatively straight forward, when domain boundaries conform to coordinate surfaces, as boundary conditions can be applied directly to boundary discretization nodes. When domain boundaries do not conform to coordinate surfaces, special treatment must be applied to boundary conditions.

The partial differential equations can be discretized using any of the following methods:

(1) Direct integration in physical space based on the coordinate system available and the use of step-wise approximation of boundaries,

(2) Use of coordinate transformation to transform both the solution domain and the set of equations to a transformed space, where the equations are integrated and discretized, and

(3) Direct integration in physical space based on control-volume space discretization.

4.5.1. Direct Integration with Step-Wise Approximation

This approach seems the easiest, but significant errors are introduced by the step-wise approximation of boundaries. Step-wise approximation of boundaries

results in excessive surface area at boundary cells, which somehow must have to be adjusted to properly account for boundary fluxes, or else, boundary fluxes must be adjusted to math the total flux.

4.5.2. Solution of the Partial Differential Equations in the Transformed Domain

If a curvilinear coordinate system can be implemented such that the walls of the physical domain overlap curvilinear coordinate planes, the physical space can be mapped into the transformed space. Once the differential equations are rewritten in terms of the curvilinear coordinates, integration and discretization are conducted in transformed space of rectangular shape (Refs. [2], [28], [126], [127]). Integration is achieved by any of the methods readily available, for instance, finite-difference. A drawback of solving the equations in transformed space is that the resulting set of equations may be quite involved, especially if the curvilinear coordinates are non-orthogonal. Vector quantities can be stated in terms of Cartesian, covariant or contravariant base vectors. Covariant base vectors are defined as partial derivatives of Cartesian coordinates with respect to each of the curvilinear coordinates. Contravariant base vectors are defined as the gradient of the curvilinear coordinates. Thus, three covariant- and three contravariant- base vectors exist at every point. Expression of the Cartesian velocity components in the momentum equations in terms of Cartesian base vectors is preferred as no "curvature terms" are involved towards satisfaction of these equations. Advection velocities are usually written as contravariant velocities. Enforcement of mass conservation is best achieved using contravariant velocities.

Once the differential equations are stated in transformed space. Integration and discretization may be done by any of the methods available, i.e. finite difference, finite element, or finite volume methods. Most of the research has been devoted to two-dimensional problems. Methods involving non-orthogonal two-dimensional domains have been proposed by various investigators such as Faghri et al. [30], Shyy et al. [120], Hadjisophocleous et al. [38], Karki and Patankar [58] and others. Methods involving orthogonal two-dimensional domains have been proposed by

Raithby et al. [110]. Most of these procedures use variations of the SIMPLE method for coupling mass and momentum equations.

Very few references were found treating three-dimensional domains. Among these are publications by Peric [105], and Braaten and Shyy [11]. Peric presented a thorough and detailed solution procedure for three-dimensional flows, and uses a hexahedral, co-located (non-staggered) variable/grid arrangement and non-orthogonal curvilinear a coordinates to transform the differential equations. The grid is completely defined in terms of the eight vertices of hexahedral cells. Peric starts by writing the original conservation equations in terms of primitive variables and in a *strong conservation form.* (The strong conservation form refers to the form of the momentum equations in which each term is expressed as the divergence of a vector or tensor [31].) Cartesian velocity components are calculated at cell nodes and contravariant velocity components are used at face nodes. Integration is carried-out in the transformed domain using a finite-volume approach. Coordinate transformation metrics in the algebraic equations are discretized such that surface areas and volumes recover their values in physical space. One observation regarding Peric's work is that integration of the pressure terms in the momentum equations is done in terms of volume integrals of the pressure gradient. Therefore, global conservation is not necessarily enforced for momentum. The work by Braaten and Shyy dealt with three-dimensional nonorthogonal coordinate transformation using hexahedral grid structure applied to duct-type flows, but was more oriented toward the study of pressure-correction methods.

As emphasized by Peric, in getting the discretized equations, care must be exercised such that volumes, areas, and fluxes are consistent with those in the physical space. In other words, finite volume equations in the physical space must be recovered for the solution to be physically realistic. It would seem that having to introduce additional coordinates to transform the differential equations, and at the end having to recover their forms in physical space creates an unnecessary "loop" conducive to additional sources of error. It also seems logical that this loop of could be avoided altogether if integration of the differential equations is conducted directly within the physical space domain, as will be seen next.

4.5.3. Solution of the Partial Differential Equations with Conforming Boundaries in the Physical Domain

This approach requires that the physical space be subdivided into control volumes. Domain boundaries then must overlap boundaries of some of the control volumes. Solution of the partial differential equations requires that volume integrals of flux terms be converted into surface integrals. This can be achieved using Gauss' divergence theorem. This method is very attractive as compared to the previous one, because all of the calculations are done in physical space without the need to introduce additional space transformation metrics.

There are several advantages in using this approach. One of them is that equations stay as they were initially derived, as no additional coordinates are introduced. Another advantage is that vector directions can be visualized in physical space, making it easier to follow directions in the three-dimensional space. Vector visualization may be difficult, or even impossible when vector components are expressed in terms of covariant or contravariant base vectors for curvilinear coordinates.

The strategy for implementing this method is diverse. One way of implementing this method is based on the so-called "control-volume-based finite element method," in which control volumes are assembled from parts of triangular or quadrilateral elements. The method was implemented with triangular elements by Baliga and Patankar [8] and Masson et al. [85]. Schneider and Raw [115] used quadrilateral elements. The above strategies may prove cumbersome when extending them to three-dimensional geometries. A more general strategy is that in which control-volumes are not assembled, but directly created in terms of the associated cell faces. This is the strategy to be used in the present research.

4.6. Space Discretization

Discretization of the spatial domain involves partitioning the domain into control volumes such that those control volumes adjacent to domain boundaries have faces that conform to the boundaries of the solution domain. In principle, only a boundary-conforming grid is required. This allows for both *structured* and

unstructured grids. Structured grids refer to those that use a coordinate direction to establish a geometrical order. This is convenient mainly for identifying which control volumes are associated with any particular control volume in terms of a coordinate system. The major disadvantage of structured grids is that computer space may be wasted if array locations are not assigned to "active" cells. Unstructured grids, on the other hand, have no coordinate associated for the organization of the grid, and they are best suited for highly irregular geometries. No computer storage space is wasted, since the array containing cell information is now one-dimensional. Only information as to which faces and which neighboring control volumes are associated to the current control volume is needed. Solution of the algebraic equations requires some form of search or look-up table specifying the grid connectivity. Structured grids, on the other hand, have a coordinate direction implicit in them, making it easier locating neighboring control volumes or faces. Structured grids can be generated by the use of any of the grid generation systems shown next.

Boundary-conforming grid generation is used to create a structured grid in domains whose boundaries do not conform to the coordinate system in which the governing partial differential equations are based. Grid generation in this manner should provide not only a grid in which coordinate surfaces conform to the domain boundaries, but also an ordered, structured grid. This grid structure is very useful when solving the system of equations when trying to locate neighboring nodes. The grid structure is provided by a curvilinear coordinate system based on the transformed domain. The problem is to obtain the physical-space coordinates in such a domain by specifying the physical-space coordinates on the boundaries of the transformed domain. *Figure 4-1* serves to illustrate the case where a Cartesian coordinate system is used to describe position (X_1, X_2) within the physical space. If Y^1 and Y^2 are the curvilinear coordinates, the problem becomes finding the functions

$$X_1 = X_1(Y^1, Y^2), \tag{4.1.a}$$

$$X_2 = X_2(Y^1, Y^2). \tag{4.1.b}$$

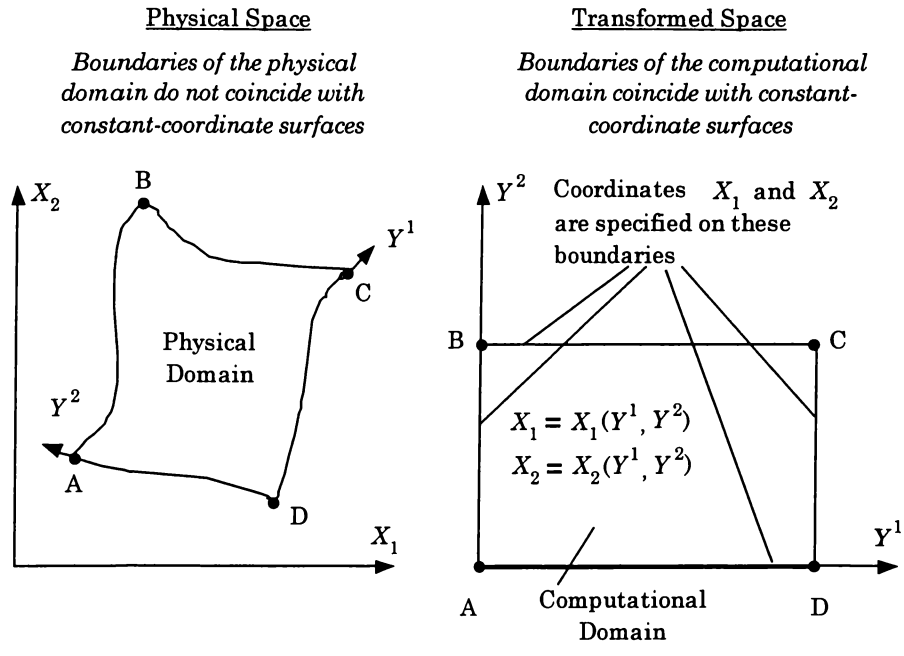

Figure 4-1. Coordinate Transformation Problem

There are various boundary-conforming grid-generation techniques. They are second-order-differential-type systems, algebraic systems, orthogonal systems, conformal mapping systems, and adaptive systems ([128],[127],[126]). Each of these grid generation systems is briefly described next. For additional details about these grid-generation techniques, the reader may consult the reference by Thompson, et al. [127].

Grid generation by second-order-differential-type systems can be sub-classified into elliptic-, parabolic-, and hyperbolic-type systems. These systems consist of second-order linear partial differential equations of elliptic, parabolic, or hyperbolic types [34] written with the physical-space coordinates as dependent variables, and the curvilinear coordinates as independent variables. One partial differential equation must be solved for each physical-space coordinate. The equations are stated as boundary-value problems, or a combination of boundary-value and free-boundary problem, depending on the type of equation, with the value of the Cartesian coordinate is specified on the boundary. The mean value theorem

ensures that the solution within the domain will not have extrema exceeding boundary values. In other words, solution values for the physical-space coordinates are guaranteed to be unique for every point. Elliptic systems are used when points are specified along all of the domain boundaries. Parabolic and hyperbolic systems can generate grids when points are specified along part of the boundary. Hyperbolic systems are used when points are specified along one boundary only.

Algebraic systems involve the use of algebraic functions to express dependency on curvilinear coordinates. The value of the physical-space coordinate is determined by uni-directional or multi-directional interpolation, depending whether the dependency is on one or more curvilinear coordinates.

Orthogonal grid-generation systems ensure that grid lines intersect at right angles in the physical domain. There are two basic types, the one in which orthogonal trajectories are constructed based on non-orthogonal systems, and the one based on the solution of partial differential equations.

Conformal mapping systems use complex variable transformations [14] to generate the grid. The disadvantage is that this system can not be used to generate the grid in three dimensions, except for trivial cases.

Adaptive systems allow the grid to re-adjust itself during the solution process of the governing equations such that grid lines become closer to each other in regions where the dependent variables show large spatial variations.

From the above grid-generation systems, algebraic systems are the easiest to implement if the Cartesian coordinates of the domain boundaries can be expressed as a function of curvilinear coordinates. The algebraic grid-generation system was selected for the present problem, since the domain boundaries can be made to comply with the above condition.

4.7. Time Discretization

The transient solution of the governing partial-differential equations consists of solving an initial-value problem of a parabolic-type partial-differential equation in time. This problem is well posed, as time is specified at the initial-time boundary.

Numerical solutions methods for well-posed initial boundary-value problems can be classified as either explicit or implicit formulation methods [130].

Explicit formulation methods assume that the dependent variables appearing in non-time-derivative terms are evaluated at the "previous" time level. Thus, the dependent variable appearing in the time-derivative term is expressed in terms of "previous" values of the dependent variable. This method can be unstable if the discretization time interval is too large. A stability criterion can be derived by expressing the dependent variable in terms of a Fourier series, and substituting it into the discretized equation. This stability criterion results in a maximum time interval for stability of

$$\Delta t < \frac{\Delta x}{2\gamma}, \tag{4.2}$$

where Δx is the characteristic grid spacing, and γ is the diffusivity, which depends on the type of conservation equation:

$$\gamma = \begin{cases} \dfrac{k}{\rho c_p} \text{ (energy equation)} \\ \dfrac{\mu}{\rho} \text{ (momentum equations).} \end{cases} \tag{4.3}$$

Implicit formulation methods remove the restriction of having to evaluate the dependent variables appearing in terms not containing time derivatives at the "previous" time level. Some of the established implicit formulation methods are the backward-differencing method, the Crank-Nicolson method, and the Dufort-Frankel method. The Backward-differencing (fully implicit) method assumes that the dependent variable appearing in the terms not containing time derivatives are evaluated at the "new" time level. This method is unconditionally stable, providing a solution for any discretization time-interval size. The Crank-Nicolson method uses values of the dependent variable at both "previous" and "new" time levels. The Dufort-Frankel method uses values of the dependent variable from three time levels: the "new" time level, the "previous" time level, and the "before-previous" time level.

Other time-discretization formulation methods have been developed, but they will not be mentioned here. For further details, the reader may consult Ref. [130] by Vemuri and Karplus, or any book in numerical solutions of differential equations. Due to its simplicity, and good stability characteristics, the fully implicit, backward-differencing formulation method will be used for time discretization in the present numerical model.

4.8. Flux Discretization

The finite-volume method yields a set of conservation equations with fluxes crossing cell faces expressed in terms of the dependent variable and its derivatives. Since the dependent variable is evaluated at cell nodes, some interpolation scheme must be used to express the value of the dependent variable and its derivatives in terms of the dependent variable at cell nodes. In selecting interpolation schemes for advection and diffusion fluxes, three characteristics are important. First, the scheme must be stable and provide a physically realistic solution; that is, it must provide a bounded solution (in the absence of sources) for cell-node variables. Second, it must provide adequate, if not minimal *false diffusion*. False diffusion is a deficiency in a numerical method resulting from the approximation of fluxes, producing an *artificial* "spread" of the physical quantity at a rate above theoretical levels. The effect is similar to that produced by an *increased* diffusivity. Third, the discretization scheme must use the minimum possible number of interpolating nodes and variables, so its implementation into computer coding becomes as simple as possible, requiring minimal storage.

Some of the most common interpolation schemes are the central-differencing scheme (CDS), the upwind-differencing scheme (UDS), the quadratic-upwind-differencing scheme (QUDS), the skew-upwind-differencing scheme (SUDS), the exponential-differencing scheme (EDS), the power-law-differencing scheme (PLDS), and the locally-analytic-differencing scheme (LOADS).

The central differencing scheme (CDS) is one of the simplest interpolation schemes for face fluxes. This scheme requires that the dependent variable be available at two adjacent cell nodes. A linear interpolation provides the value of the

dependent variable and its derivative at the face-node location. False diffusion occurs in flows, where the "cell" *Peclet* number representing the face flow is different from zero. The cell Peclet number, (also "Peclet" number), is defined as the ratio of advection to diffusion of a given physical conservation quantity (momentum or energy) within a characteristic grid size, L:

$$P_e = \frac{uL}{\gamma}, \tag{4.4}$$

where u is the fluid velocity and γ is the diffusivity.

A stability criterion for uniform grids results in a limiting Peclet number of two. When the Peclet number reaches that limit, the dependent variable at the face node reaches the value at one of its cell-node neighbors. For Peclet numbers greater than two, the interpolated variable at the face-node location exceeds the values at its neighboring cell nodes. This may lead to instability in the numerical convergence process in high-velocity, or more precisely, high cell Peclet-number flows [52, p.82]. Therefore, CDS should be used only for low Peclet-number flows.

The simplest way to eliminate the unboundedness of CDS is to calculate the advection flux by setting the value of the dependent variable at the face-node equal to the upstream cell node. This scheme is known as the *upwind* differencing scheme (UDS). The diffusion flux could still be calculated via CDS. The UDS resolves the stability problem found in CDS, since the interpolated variable is guaranteed to fall within the range of cell-node values. This is, however, at the cost of additional false diffusion in low-velocity flows.

To take advantage of the stability of UDS at high flow velocities, and the lower amount of false diffusion of CDS at low flow velocities, a hybrid scheme can be devised based on these two schemes. The hybrid-differencing scheme (HDS) uses velocity-dependent weighing factors that favor CDS when advective rates are low and UDS when advective rates are high. There are various versions of HDS, depending on the type of functional velocity dependency of the weighting factors. The unweighted version of this scheme uses CDS for $Pe < 2$ and UDS for $Pe \geq 2$.

The quadratic upwind differencing scheme (QUDS, also known as QUICK [74]) is a second-order differencing scheme that, in one-dimensional applications,

uses one nodal point downstream, and two nodal points upstream of the desired interpolation location. Therefore, five points are used per control volume in one-dimension. In two-dimensional problems using quadrilaterals, nine points are used, and in three-dimensional problems using hexahedra, 13 points are used. A two-dimensional version of the scheme uses 12 points instead of five for two-dimensional problems. The extra points are added to the corners of the quadrilateral cell. A three-dimensional version uses 35 interpolation points instead of the 13 used in the one-dimensional version, with the extra 12 points added along the edges of the hexahedra. QUDS has been shown to have a lower amount of false diffusion as compared to first-order schemes, such as the CDS. However, as with any other polynomial schemes, QUDS may yield unrealistic solutions if the advective flux becomes large [138]. In one-dimensional flows, the scheme becomes unstable when the cell Peclet number exceeds two, as was tested by the author, and to avoid this problem additional cells must be added until the cell Peclet number drops below two.

The skew-upwind differencing scheme (SUDS) is similar to the UDS in that upstream values are used as face-node values. The difference is that the upstream point is aligned along the flow direction. The dependent variable is interpolated at this point, and its value assigned to the face node location.

The above interpolation schemes are based on polynomial functions. A second class of differencing schemes can be derived based on the solution of partial differential equation of the general advection/diffusion equation. The simplest of them is the exponential differencing scheme. The exponential differencing scheme (EDS) is a two-point interpolation scheme, based on the exact solution of the one-dimensional advection/diffusion partial-differential equation, with no sources. It provides the value of the dependent variable and its derivatives at any location within the integration interval. With known values of the independent variable at cell-node locations, and a known face-node velocity, EDS provides the value of the dependent variable and its derivative at the face-node location. EDS provides a smooth behavior as the flow velocity changes. EDS provides the exact solution for one-dimensional advection/diffusion with no sources. In the case of two- and three-dimensional flows, and flows with volumetric sources, this scheme may provide a

reasonable approximation for the dependent variable. This, however, is at the expense of added false diffusion.

The power-law-differencing scheme (PLDS) is a fifth-degree-polynomial approximation to the exponential differencing scheme [103].

The locally analytic differencing scheme (LOADS), proposed by Wong and Raithby [138] is based on an exponential scheme with a source added. The source takes into account cross-flow effects and other sources appearing in the differential equation.

The CDS, UDS, QUDS, and SUDS are insensitive to the strength of advection. That is, the "shape" of the interpolation function does not depend on flow velocity, but on the dependent variable at cell nodes. This is a deficiency, and a potential source of instability, which could lead to physically unrealistic solutions and even divergence.

Leschhziner [77] (1980) compares the unweighed HDS, a hybrid CDS-SUDS (CSUDS), and a weighed variation of QUDS (WQUDS) against the UDS. Leschhziner reported that the UDS might result in severe solution errors in high velocity, skew-flow regions. CSUDS and WQUDS were found to produce better solutions, but they presented some unboundedness problems.

Huang et al. [47] (1985) compared the PLDS, QUDS, SUDS, and LOADS. The schemes were tested in six cases against analytical solutions or highly accurate numerical solutions. They reported that all of these schemes were more accurate than the upwind scheme and suggested avoiding PLDS, unless the grids were closely aligned. They indicated that LOADS might fail to converge because of the iterative nature of the scheme. SUDS was reported as accurate, in general, but in some cases it provided results no better than PLDS (exponential power law). QUDS was reported as the most accurate, but it required approximately 65% more computational time than PLDS using a similar mesh. It may be argued that QUDS may be made stable by adding more cells, as computer memory becomes larger and less expensive. However, this is at a cost of additional computational time. An additional problem is that as with most problems, the final flow solution is not known in advance and, therefore the velocity field. The implications are that

perhaps several trials could be needed until the grid is fine enough to produce stable results. One more disadvantage is that the implementation of adaptive grid procedure could not guarantee successful convergence, since the process involves the use of a coarse mesh at various stages along the process.

There is no restriction as to having to select the same scheme for both advection and diffusion fluxes. As in the case of the upwind differencing scheme, the dependent variable and its derivative may be calculated using two different functions. In the present research, QUDS was initially selected because of its attractive reduction of false diffusion, but later abandoned and replaced with the EDS because of stability concerns.

4.9. Grid/Variable Arrangement

In principle, the physical space could be discretized differently for each equation, as long as conservation holds for each of the discretized equations. However, this might be impractical, and it is best to establish an order to facilitate addressing variables from one equation to the next. The most basic types of grid arrangement for hexahedral topology are shown in *Figure 4-2*. These are (1) the co-located (non-staggered) grid arrangement, (2) the staggered grid arrangement, and (3) the dual grid arrangement.

In the co-located (non-staggered) grid arrangement, pressure, temperature, and velocity nodes are *co-located* at cell-node locations. The conservation laws associated with these variables are applied to a single control volume (cell) (*Figure 4-2.a*). Geometry specification for this arrangement is the simplest, as there is one set of control volumes in the whole domain. The staggered grid arrangement, evaluates pressure and temperature at main cell-node locations, while velocities are evaluated at face-node locations. In Cartesian coordinates, velocity components are staggered in the respective coordinate direction. This arrangement is the most complex from the geometry viewpoint, as one geometry set is required for each staggered direction, demanding additional computer storage and processing resources. In hexahedral topology, for instance, staggered grids have four cell geometry sets, one for the main control volume, and one for each staggered velocity

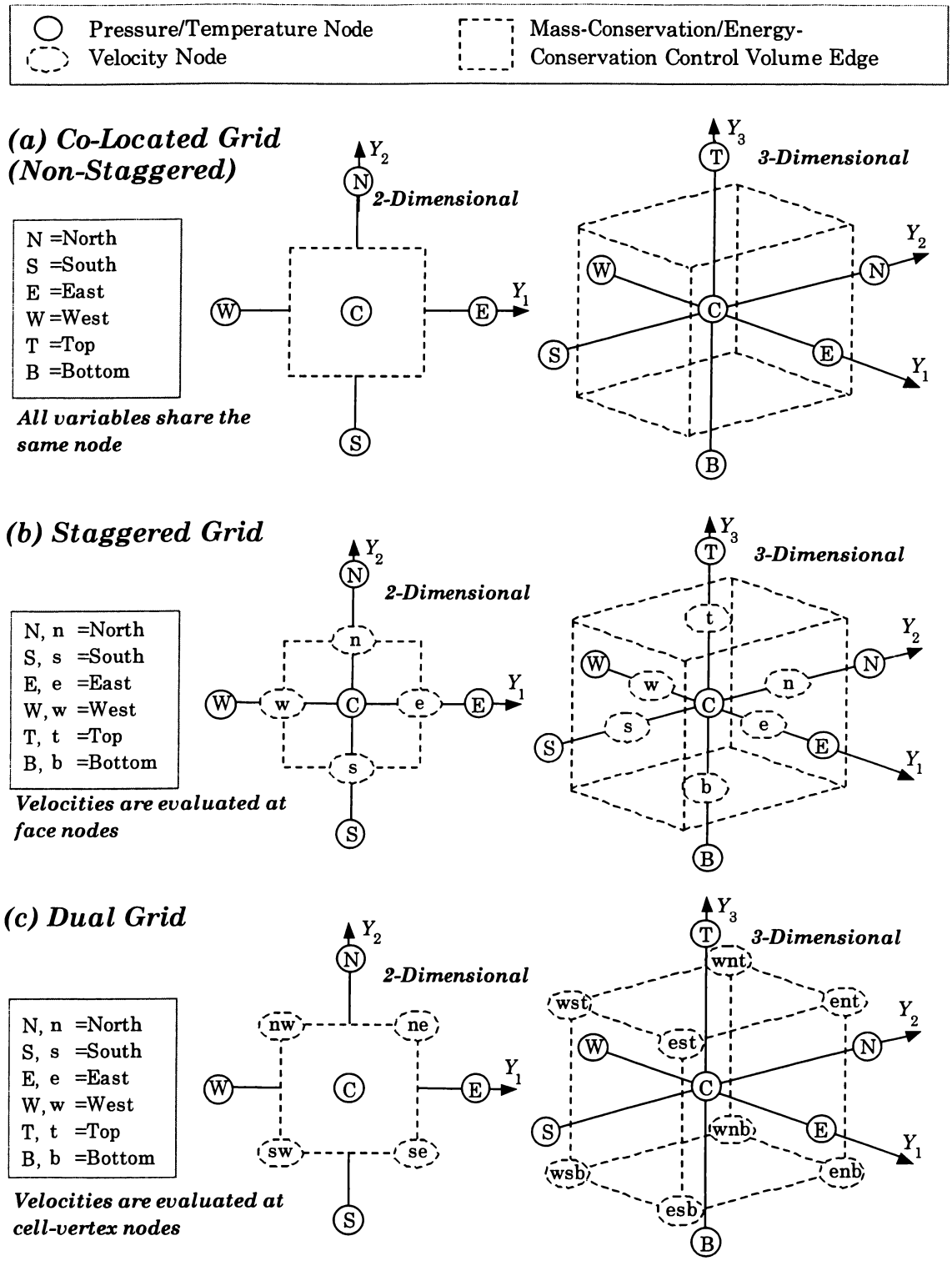

Figure 4-2. Mass-Conservation/Energy-Conservation Control Volume and Velocity-Node Locations for the Colocated-Grid Arrangement

control volume (*Figure 4-2.b*). The dual grid arrangement, in which the pressure and temperature are evaluated at cell nodes, while the velocities are evaluated at the cell-vertex nodes. Dual grids have two cell geometry sets, one for the main cells (for evaluation of pressure and temperature), and one for the velocity cells (*Figure 4-2.c*). This suggests that geometry-related bookkeeping should be easier to handle as compared to the staggered-grid arrangement.

The staggered grid arrangement introduced by Harlow and Welch [40], results in the simplest set of equations to solve, with the fewest variables. This grid arrangement is suitable for equations where the velocities are aligned with the coordinate lines, as in Cartesian, cylindrical, and polar coordinate systems. A version of the dual grid was used in two dimensions by Hirt, Amsden, and Cook [43]. This version had the boundaries of the velocity control volumes running along diagonal lines connecting pressure cell nodes. No published research was found using this approach for three-dimensional applications.

A very limited use of the co-located grid arrangement has been found in the past because of inconsistencies in the way the pressure equation was obtained. Peric [105] was successful in using the co-located grid arrangement for the general three-dimensional solution of the Navier-Stokes equations in non-orthogonal grids, producing satisfactory results for flows in pipe networks. The co-located grid is attractive because only one set of parameters is used to describe the geometry for the grid structure.

Shih, Tan, and Hwang [117] studied the accuracy of these and other grid arrangements in the solution of two-dimensional, Navier-Stokes-type flows, and concluded that the dual grid arrangement shown in *Figure 4-2.c*, was the best arrangement in terms of "overall performance", and that adequate solutions were obtained by the staggered-grid arrangement. They reported that the co-located arrangement provided high accuracy, using higher order interpolating functions.

4.10. Iteration Structure for an Initial-Value Problem

Solving an initial-value problem involves a procedure for advancing the solution along the time axis. A discretization scheme should provide the solution at

discrete locations along the axis. Depending whether an accurate transient solution is required, a "true" or "false" advancing scheme may be used -- the difference being whether the transient solution at the discrete steps is accurate. Within each time step, iterations may be needed to produce acceptable solutions. These iterations are called *outer iterations* and are made within an *outer loop*. Outer-loop iteration steps may involve sub-iterations to resolve the individual variables in what are called *inner-loop* iterations. A schematic of this process is shown in *Figure 4-3*.

4.11. Derivation of the Pressure Equation and Solution of the System of Mass-Momentum Equations

The most challenging problem in the solution of the system of equations is to solve the system of mass and momentum equations. When using primitive

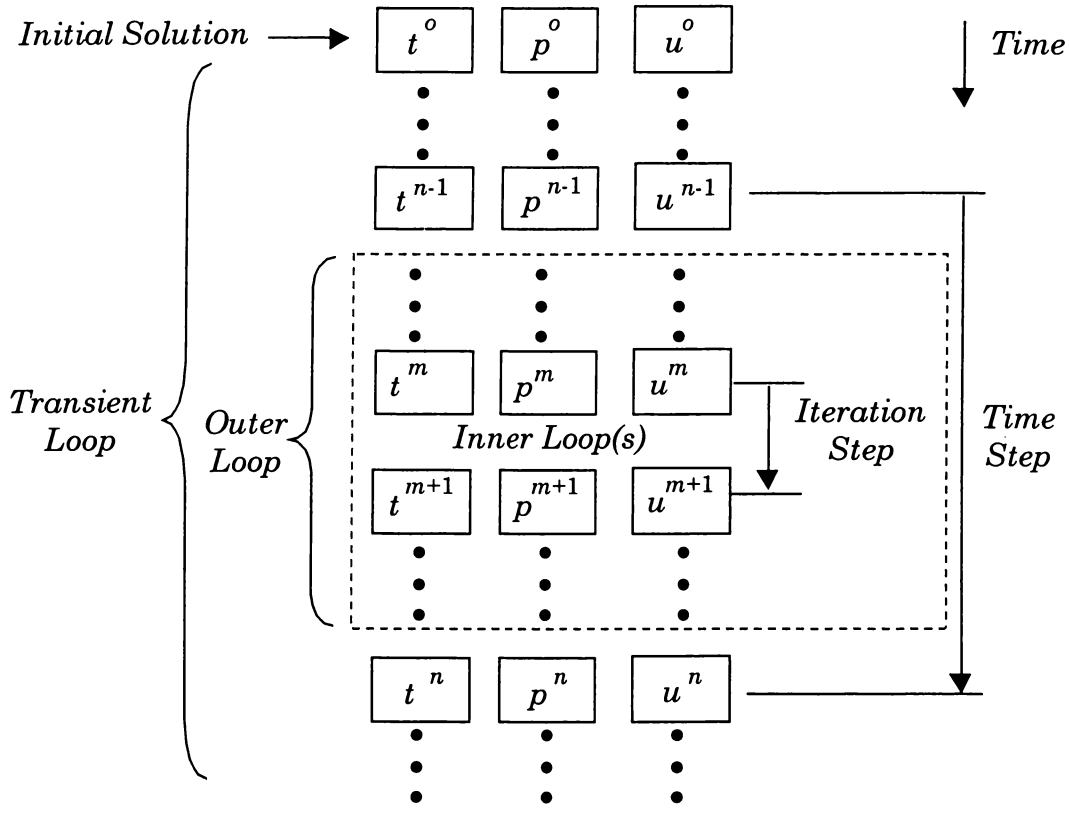

Figure 4-3. Time- and Iteration-Stepping Terminology for an Initial-Value Problem

variables, a pressure equation is obtained by combining the mass and momentum conservation equations. It can be initially obtained in differential form or in discretized form. To obtain a pressure equation in differential form, the divergence of the momentum equation in vector form is taken, which results in a Poisson equation for pressure. This equation is, then integrated and discretized to obtain an algebraic form of the pressure equation. To obtain a pressure equation initially in discretized form, the velocities in the algebraic forms of the momentum equations are substituted in the algebraic form of mass conservation, which results in an algebraic form of the pressure equation. In order for the two methods to produce the same result, discretization of the divergence operator in the mass-conservation equation, and the pressure-gradient operator appearing in the momentum equations must be done consistently for the two methods. If the divergence and/or gradient operators are discretized incorrectly, conservation of mass and/or momentum may not hold for the discretized space. To avoid this problem, it is best to construct the pressure equation from the algebraic forms of mass and momentum equations.

The system of mass and momentum conservation equations is an initial-value problem, and discretization algebraic equations may be solved using time-explicit or time-implicit methods. The discussion in the sections below assumes a rectangular, staggered-grid arrangement for the sake of simplicity, but without compromising generality to other types of grids. In this arrangement, pressure is evaluated at the mass-conservation cell node, and velocities are evaluated at staggered momentum cells, with cell nodes at the locations of mass-conservation face nodes.

4.11.1. Time-Explicit Methods

Most of the early effort in the development of time-explicit methods was done by researchers at Los Alamos Laboratory in the 1960's and 1970's. In a time-explicit method, the dependent variables at the new time level are calculated based on values at the previous time level. If n denotes the time-step level, the velocity at the new time-level is calculated as:

$$a_i^u\, u_i^{n+1} = \sum_{j=n\,b(i)} a_j^u\, u_{i,j}^n + b_{i-p}^u - \sum_{j=1}^{3}\left[A^j\, p^n\right]_{j^-}^{j^+},\ i=1,2,3, \tag{4.5}$$

where the most recent set of velocities must be corrected for mass conservation at the new time level:

$$\sum_{j=1}^{3}\left[u_j^{n+1} A_j\right]_{j^-}^{j^+} = 0 \tag{4.6}$$

Time-explicit methods advance the solution one time-step at a time without the need of iterations, but as discussed earlier, these methods require careful control of the time-step size, or divergence may occur. Many times an accurate transient solution is not needed; this is the case in steady-state problems, where the solution is desired at steady state, but it can be obtained using false-transient methods. In order to have a solution procedure applicable to both these types of situations, an implicit method is preferred.

4.11.2. Time-Implicit Methods

In fully implicit methods, the dependent variable is evaluated at the new time-step level. This applies to both mass and momentum equations. In the momentum equations, cell-node velocities are calculated in terms of the cell-neighbor velocities and pressure values at the new time level:

$$\sum_{j=1}^{3}\left[u_j^{n+1} A_j\right]_{j^-}^{j^+} = 0, \tag{4.7.a}$$

$$a_i^u\, u_i^{n+1} = \sum_{j=n\,b(i)} a_j^u\, u_{i,j}^{n+1} + b_{i-p}^u - \sum_{j=1}^{3}\left[A^j\, p^{n+1}\right]_{j^-}^{j^+},\ i=1,2,3, \tag{4.7.b}$$

where b_{i-p}^u is the constant term containing all of the remaining terms contributing to momentum, except terms involving pressure. Similarly to explicit methods, cell-

face velocities must be somehow adjusted to satisfy mass conservation at the new time-step level:

$$\sum_{j=1}^{3}\left[u_j^{n+1}A_j\right]_{j^-}^{j^+}=0 \tag{4.8}$$

In fully implicit iterations methods, iterations are usually made within one time step to obtain the mass- and momentum-conserving solutions.

For the derivations ahead, it is more convenient to drop the time–step index, n from the equations, and to rewrite above equations as:

$$\sum_{j=1}^{3}\left[u_j A_j\right]_{j^-}^{j^+}=0\,, \tag{4.9.a}$$

$$a_i^u\,u_i=\sum_{j=n\,b(i)}a_j^u\,u_{i,j}+b_{i-p}^u-\sum_{j=1}^{3}\left[A^j\;p\;\right]_{j^-}^{j^+},\ i=1,2,3\,. \tag{4.9.b}$$

Robustness of a Solution Procedure

An iterative solution is robust if at the end of each iteration step, both mass and momentum are satisfied. This is not so easily achieved, and most methods attempt to satisfy these equations at least individually once through the iteration step. Self-consistency is another factor affecting robustness. An algorithm in which both pressure and velocity are calculated self-consistently to produce the desired conservation equation is, in principle more robust than one in which velocities and pressure values are calculated without self consistency; however, converged solutions are still possible.

A Basic Solution Advancing Scheme

A simple solution advancing method [31] uses the properties of the existing velocity field to calculate a pressure field that is forced to satisfy mass conservation. The basic idea is to "split" the algebraic operators in the momentum equations along

the iteration axis such that the "corrected" velocities at the end of the current iteration are expressed in terms of intermediate velocities at the current iteration and the pressure at the end of the current iteration. This may be done as follows. The first step is to rewrite the momentum equation 4.9(b) in terms of the updated (intermediate) velocities and the previous-iteration pressure values as follows:

$$u_i^{m*} = \hat{u}_i^{m*} - \sum_{j=1}^{3} \left[G_i^j \; p^{m-1} \right]_{j^-}^{j^+}, \quad i = 1,2,3 \tag{4.10}$$

where $\hat{u}_i^{m*}$ is a "pseudo-velocity," expressed as:

$$\hat{u}_i^{m*} = \frac{1}{a_i^u} \left[\sum_{j=n\,b(i)} a_j^u \; u_{i,j}^{m*} + b_{i-p}^u \right] \tag{4.11}$$

and

$$G_i^j = \frac{A^j}{a_i^u}. \tag{4.12}$$

The second step is to "split" the velocity operators in Eq. (4.10) along the iteration axis (m), such that the velocities at the end of the iteration cycle is expressed in terms of intermediate velocities and pressure values at the end of the cycle. The new momentum equation becomes:

$$u_i^m = \hat{u}_i^{m*} - \sum_{j=1}^{3} \left[G^j \; p^m \right]_{j^-}^{j^+}, \quad i = 1,2,3. \tag{4.13}$$

If this new set of velocities are substituted into the equation for mass conservation, the resulting pressure field, p^m, must be consistent with mass conservation. Substituting Eq. (4.13) into Eq. (4.9.a) yields the equation for pressure at the new iteration level, m:

$$a_c^p \, p_c^m = \sum_{j=n\,b(c)} a_j^p \, p_j^m + b^p. \tag{4.14}$$

The resulting pressure can now be used to calculate the mass-conserving velocities using Eq. (4.13). The concept for this method is shown as a variable-equation flow chart in *Figure 4-4.*

In the above method, p^{m-1} and u^{m*} are self-consistent for momentum conservation, while p^{m} and u^{m} are self-consistent for mass conservation. Thus, at the end of the iteration step, only mass is satisfied self-consistently. Momentum was satisfied at the intermediate step.

Prediction-Correction Advancing Schemes

Most of the effort in the past to advance the pressure-velocity solution systematically has been focused on prediction-correction methods. In prediction-correction methods, the basic idea to predict a velocity field, and then, apply

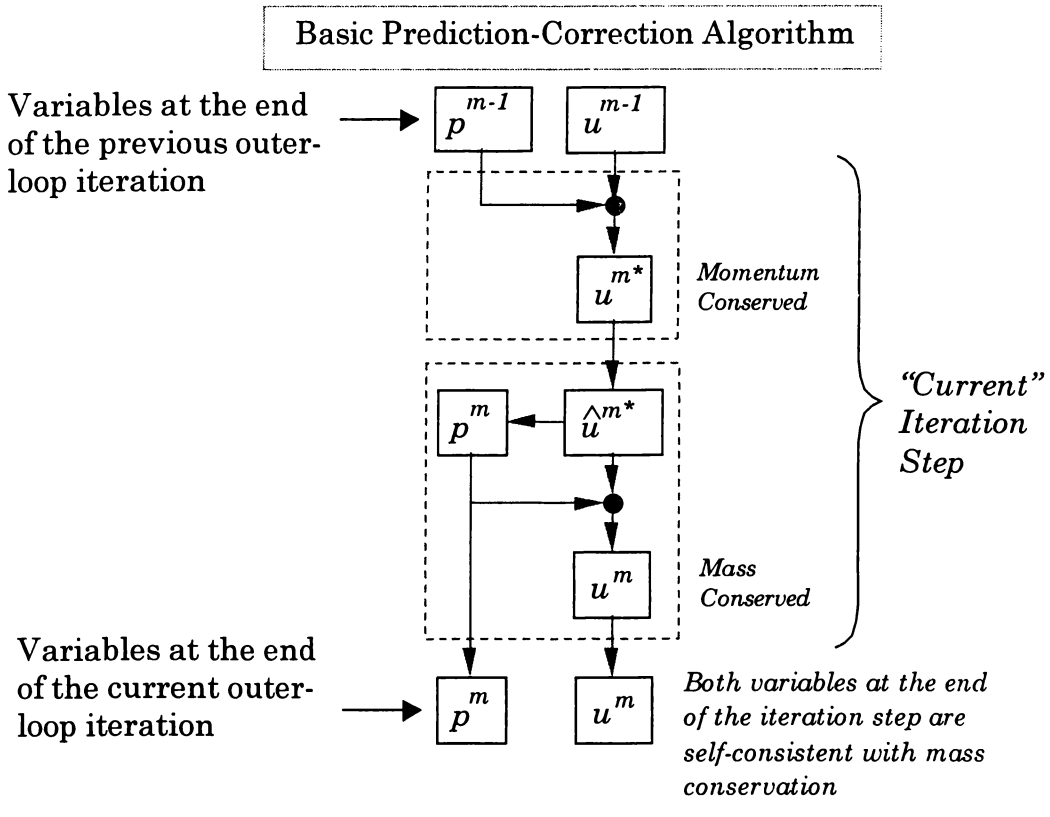

Figure 4-4. Calculation Sequence for a Basic Implicit Prediction-Correction Method

corrections to velocity and pressure to satisfy mass conservation at the end of the iteration step. These methods are based on the use of velocity and pressure correction quantities to modify the previous values for consistency with mass conservation at the end of the iteration cycle. The equations for the variables at the new iteration level can be written as:

$$u_i^m = u_i^{m*} + u_i' \tag{4.15.a}$$

$$p^m = p^{m-1} + p' \tag{4.15.b}$$

where u_i' is the velocity corrector and p' is the pressure corrector. If the momentum equations at the intermediate iteration level and the final iteration level are given as:

$$a_i^u \, u_i^{m*} = \sum_{j=n\,b(i)} a_j^u \, u_{i,j}^{m*} + b_{i-p}^u - \sum_{j=1}^{3} \Big[A^j \, p^{m-1} \Big]_{j^-}^{j^+}, \; i = 1,2,3 \tag{4.16}$$

and

$$a_i^u \, u_i^m = \sum_{j=n\,b(i)} a_j^u \, u_{i,j}^m + b_{i-p}^u - \sum_{j=1}^{3} \Big[A^j \, p^m \Big]_{j^-}^{j^+}, \; i = 1,2,3, \tag{4.17}$$

respectively, then subtracting Eq. (4.16) from Eq. (4.17), and substituting Eq. (4.15) yields an equation for the velocity corrector in terms of pressure correctors, as:

$$a_i^u \, u_i' = \sum_{j=n\,b(i)} a_j^u \, u_{i,j}' - \sum_{j=1}^{3} \Big[A^j \, p' \Big]_{j^-}^{j^+}, \; i = 1,2,3. \tag{4.18}$$

Dividing by a^u and redefining terms yields:

$$u_i' = \hat{u}_i' - \sum_{j=1}^{3} \Big[G_i^j \, p' \Big]_{j^-}^{j^+}, \; i = 1,2,3, \tag{4.19}$$

where $\hat{u}_i'$ is the pseudo-velocity-corrector, expressed as:

$$\hat{u}_i' = \frac{1}{a_i^u} \sum_{j=nb(i)} a_j^u u_{i,j}', \; i = 1,2,3, \tag{4.20}$$

and G^j is as defined in Eq. (4.12).

Substitution of Eq. (4.19.a) into Eq. (4.15) yields an equation for the velocity at the end of the iteration step based on the intermediate velocities, pseudo-velocity corrector, and pressure corrector:

$$u_i^m = u_i^{m*} + \hat{u}_i' - \sum_{j=1}^{3} \left[G_i^j \, p' \right]_{j^-}^{j^+}, \; i = 1,2,3. \tag{4.21}$$

The above equation can be used to obtain the corrected, mass-conserving velocities at the end of the iteration, once the pressure corrector is known. To do so, Eq. (4.21) is substituted into mass conservation, Eq. (4.19.a), which yields an equation for the pressure corrector as:

$$a_c^p p' = \sum_{j=nb(c)} a_j^p p_j' + b^p, \tag{4.22}$$

where b^p is a constant term containing intermediate velocities, u_i^{m*}, and pseudo-velocity-correctors, $\hat{u}'$.

At the start of the iteration process, the velocity corrector, u_i', is unknown, and so is the pseudo-velocity corrector, $\hat{u}_i'$, appearing in Eq. (4.21). In principle, these terms could be either approximated, or calculated as subsequent steps within the same iteration. Ultimately, velocities at the end of the iteration step, the process should result in the set of velocities, corrected for mass conservation, u_i^m, and the pressure, p^m.

There are a number of implicit methods using primitive variables and a prediction-correction approach, developed within the past four decades by various investigators. Some of the most commonly known algorithms are SIMPLE (by Caretto et al. [13]), SIMPLER (by Patankar [103]), SIMPLEC (by van Doormaal and Raithby [27]), and PISO (by Issa [51]). These algorithms were originally developed based on staggered velocity grids. Reviews of the first set of methods above have

been made by Jang et al.[53] (1986) and Ferziger and Peric [31] (1996). Other algorithms have been proposed in the past, many of which are variations of SIMPLE. Examples of other algorithms are in Refs. [12], [111], and [71].

The SIMPLE algorithm (Caretto et al. [13]), first predicts the intermediate velocity field, u_i^{m*}, from the previous-iteration pressure values, and calculates the pressure corrector by neglecting the pseudo-velocity-corrector, $\hat{u}_i'$, appearing in Eq. (4.21). This results in the following velocity-correction equation:

$$u_i^m = u_i^{m*} - \sum_{j=1}^{3} \left[G_i^j \; p' \right]_{j^-}^{j^+}, i = 1,2,3. \tag{4.23}$$

In this case, the constant term, $b^{p'}$, in Eq. (4.22) contains only intermediate velocities, u_i^{m*}. Substituting this equation in the discretized equation for mass conservation yields the pressure corrector equation, which is solved and the pressure-corrector field obtained is substituted back in the above equation to obtain correct the corrected velocities. The pressure is calculated by adding the pressure corrector to the previous-iteration pressure values.

The SIMPLER algorithm proposed (Patankar [103]) uses the same approach, predicting a velocity field using the previous-iteration velocity and pressure fields, and corrects the velocity field with the pressure corrector, neglecting the pseudo-velocity-corrector, $\hat{u}_i'$. The pressure, on the other hand, is not corrected, but instead obtained from the corrected velocities, u_i^m. This approach, however, creates an inconsistency, as the pressure itself is predicted from the combination of mass and momentum equations, but not corrected for mass conservation. Hence, the SIMPLER algorithm has one predictor step for velocity and one predictor step for the pressure, but correction is done only for velocity.

The SIMPLEC algorithm (van Doormaal and Raithby [27]) uses an approximation to lessen the impact of neglecting $\hat{u}_i'$. The method subtracts the term:

$$\sum_{j=n\,b(i)}^{3} a_j^u \, u_i' \tag{4.24}$$

from Eq. (4.18) , resulting in:

$$u_i' = \hat{u}_i' - \sum_{j=1}^{3} \left[G_i^j \; p' \right]_{j^-}^{j^+}, \; i = 1,2,3, \tag{4.25}$$

where the pseudo-velocities are now expressed as:

$$\hat{u}_i' = \frac{1}{a_i^u} \left(\sum_{j=nb(i)} a_j^u \; u_{i,j}' \right) - u_i', \; i = 1,2,3, \tag{4.26}$$

and the pressure factors are expressed as:

$$G_i^j = \frac{A^j}{a_i^u - \sum_{j=nb(i)} a_j^u \; u_{i,j}'}. \tag{4.27}$$

The newly defined pseudo-velocity corrector, $\hat{u}_i'$, is neglected, assuming the right-hand side of Eq. (4.26) is small, resulting in an equation similar to that in SIMPLE, but with the pressure factors modified, as shown in Eq. (4.27).

The PISO algorithm (Issa [51]) uses one prediction step for the velocity based on momentum conservation, and several correction steps for velocity and an equal number of prediction steps for pressure, both of these consistent with mass conservation. The velocity correction steps are based on the operator-splitting technique, in which the velocity is discretized explicitly in time and the pressure is discretized implicitly. The resulting velocities can be substituted into mass conservation and the resulting equations solved for the pressure, as the first predictor step. This pressure field is then substituted into the explicit equation just derived, to obtain the corrected velocities. This process, in theory, can be repeated any number of times, but Issa suggests that two times to be an acceptable minimum number. The end if the second correction stage, becomes then the end of a full iteration step. The main difference between PISO and the former algorithms is that the iteration step is actually a time step, and the solution after the correction steps is assumed available as the solution of the "next" time step. Therefore, care must be

exercised in determining the time-step size when trying to calculate time-accurate solutions, as the error in the solution depends on it, as indicated by Issa.

A summary of the calculation sequence for the above algorithms is shown in *Figure 4-5*. A summary of the number of prediction and correction steps, as well as consistency characteristics is shown in Table 4-1. All of the algorithms discussed have one prediction step for the velocity field based on the equation for conservation of momentum. SIMPLE, SIMPLER and SIMPLEC have one correction step for the velocity, whereas PISO allows for several velocity-correction steps. SIMPLE and SIMPLEC have one pressure correction step. SIMPLER has one pressure prediction step, but inconsistent with mass conservation, whereas PISO allows for various pressure prediction steps consistent with mass conservation. All of the algorithms, except SIMPLER enforce self-consistently between the pressure and velocity fields with mass conservation at the end of the iteration step. In the SIMPLER algorithm, only the iteration-final velocities are necessarily consistent with mass conservation. The pressure is calculated following the velocity correction, in an explicit manner. In other words, substituting these pressure values back into the velocity equations would not necessarily reproduce the same velocities. Therefore, the pressure field that results at the end of each iteration step is not necessarily consistent with mass conservation, unless a converged solution exists. There can be no assurance that a solution algorithm for the pressure-velocity-coupled solution will always converge. Depending on the type of boundary conditions and the magnitude of momentum sources, under-relaxation may be required to enable convergence, either by using weighing factors between previous and next solutions, and/or by decreasing the time step (adding "inertia").

In their review, Jang et al. [53] indicated that PISO demonstrated robust convergence in problems where the momentum equations was not coupled with other scalars, i.e. temperature, and that it required less computational effort than SIMPLER of SIMPLEC. However for strongly linked problems, SIMPLER and SIMPLEC exhibit better behavior. No clear superiority was established between SIMPLER and SIMPLEC, but SIMPLER was reported to have a rather inconsistent behavior in transient solutions.

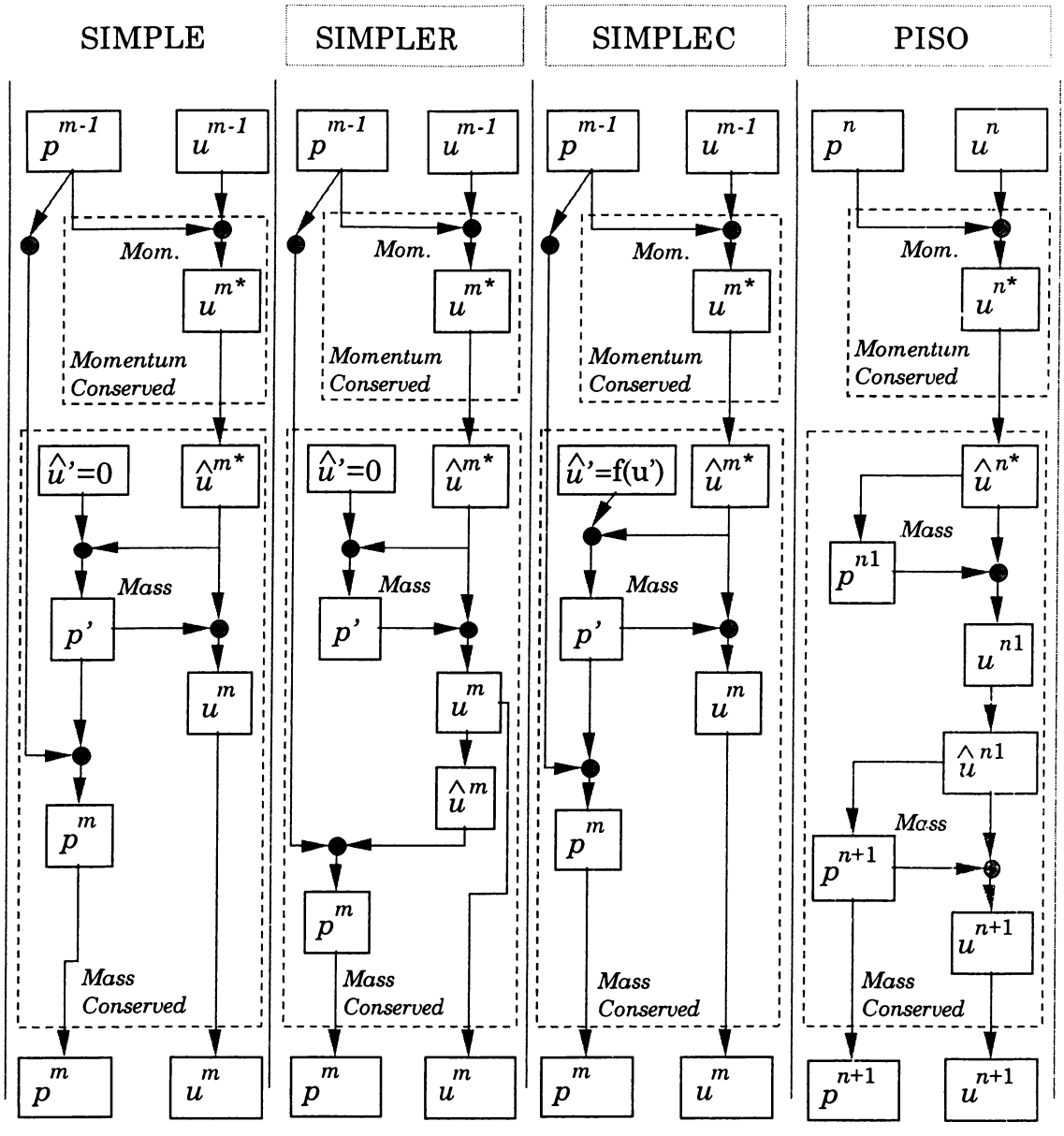

Figure 4-5. Calculation Sequence for Common Implicit Prediction-Correction Methods

Table 4-1. Summary of Common Implicit Prediction-Correction Pressure-Velocity Solution Algorithms

	SIMPLE	SIMPLER	SIMPLEC	PISO
Velocity Prediction Steps	1	1	1	1
Velocity Correction Steps	1	1	1	various
Pressure Correction Steps	1	0	1	0
Pressure Prediction Steps	0	1	0	various
The Pressure is Necessarily Self-Consistent with Mass Conservation	Yes	No	Yes	Yes
Variables Consistent with Mass Conservation	p^m AND u^m	u^m	p^m AND u^m	p^{n+1} AND u^{n+1}

In the above methods, the solution is advanced simultaneously for the whole field at every step through the iteration process. There are other methods, such as the SIVA solution procedure proposed by Caretto et al. [12] (1972), in which the solution is advanced on a cell-by-cell basis. That is, the cell pressure and face velocities are calculated simultaneously to satisfy mass conservation for one cell at a time. The calculation is repeated for every cell in the domain until convergence is achieved.

4.12. Summary

This chapter reviewed the methods available to approximate the governing differential equations and solve them numerically in a domain of arbitrary shape. The types of formulations were reviewed, namely the vorticity/stream-function formulation, the vorticity-velocity formulation, the vector/scalar-potential formulation, the vector-potential/vorticity formulation, and the primitive-variable formulation. The primitive-variable formulation was selected because it allows for the solution of the equations without the need for introducing additional variables, and because there are methods available for the solution of three-dimensional flows.

Then, the methods for solving the governing differential equations were reviewed, namely the finite-difference method, the finite-element method, and the finite-volume method. This was followed by a review of methods for discretizing the equations in domains with curved boundaries. The finite volume method with direct integration within physical space was selected because it may be used to solve the governing equations in domains of arbitrary shape, while allowing for the solution without the need to transform the differential equations. The various methods to discretize the space in domains with curved boundaries was reviewed, along with grid-generation systems, namely second-order-differential systems, algebraic systems, orthogonal systems, conformal mapping systems, and adaptive systems. Algebraic grid-generation systems were selected for the present problem geometry because of the simplicity in the implementation. Methods for time discretization were reviewed and the fully implicit method was selected because of its unconditional stability. Flux discretization schemes were reviewed, namely, the central-differencing scheme (CDS), the upwind-differencing scheme (UDS), the quadratic-upwind-differencing scheme (QUDS), the skew-upwind-differencing scheme (SUDS), the exponential-differencing scheme (EDS), the power-law-differencing scheme (PLDS), and the locally-analytic-differencing scheme (LOADS). The QUDS was attractive from the point of view of reduction in the false diffusion, but at a cost of unacceptable sources of instability in high Peclet number flows. This scheme was initially selected, but later replaced with the exponential-differencing scheme (EDS) to remove the stability problems at the expense of added false diffusion. It was also concluded that the levels of false diffusion could always be reduced, however, by refining the mesh.

The arrangement for placement of nodal points where variables are calculated in relation to the grid was reviewed. The basic types of arrangements are the co-located, staggered, and dual grid-variable arrangements. The co-located arrangement was selected because it requires only one set of geometrical data, allowing for all of the variables to share the same control volume and faces, thus minimizing bookkeeping.

The basic principles behind the iterative processes for solving the set of equations were reviewed. The terminology and the basic iteration loop structure applicable to both transient and steady-state problems was defined in terms of the outer loop and inner loops. The rationale for the derivation of the pressure equation was presented in terms of time-explicit and time-implicit methods. The concept of "robust" iteration procedure was introduced requiring that pressure and velocities were self-consistent with mass and momentum conservation at the end of an outer iteration cycle. The basic concept of iteration progress by splitting operators was reviewed, in which the velocity is predicted using the momentum equations, and then corrected by readjusting the pressure field to enforce mass conservation. This was followed by a review of common implicit iteration procedures, namely, the SIMPLE, SIMPLER, SIMPLEC, and PISO procedures. The first three procedures may involve multiple outer-loop iterations within a time step, while the later involves a single iteration. All of these procedures are based on the prediction-correction concept in which a velocity field is predicted based on satisfaction of the momentum equations, and then corrected based on the satisfaction of mass conservation. It was concluded that in the above procedures, pressure and velocities are self-consistent with mass conservation at the end of an outer-loop iteration cycle with the exception of SIMPLER, in which only the velocity is consistent with mass conservation. Based on the review on the iteration procedures, no significant advantages are shown by the predictor-correction implicit procedures over the basic "projection" procedure using splitting velocity operators. Selection of the final procedure seems a matter of preference. The SIMPLER algorithm was initially selected for this research, but as was demonstrated from tests by the author, its stability depended from the accurate solution of the pressure equation with sometimes, large over-relaxation. This algorithm was subsequently replaced by the basic "projection" procedure, which proved to be more robust and stable, producing solutions with minimal adjustment of relaxation parameters and without having to solve the pressure equation to a tight tolerance.

5. THE MATHEMATICAL MODEL

5.1. Scope of the Model

The mathematical model must portray all modes of heat transfer from the heat source to the surroundings (ultimate heat sink). For convenience, the physical domain is divided into two sub-domains having separate models: the inner domain, and the outer domain. The inner domain is defined as the liquid-lens system itself. It comprises (1) the CRT face panel, (2) the enclosure frame, (3) the meniscus lens and (4) the liquid coolant. The outer domain comprises that part of the system that is not included in the inner domain. It includes (1) the portion of the CRT that is not part of the face panel, (2) the enclosure frame extensions, (3) the mounting frame itself, (4) the focusing lens, and (5) the cabinet internal environment. The enclosure frame extensions are plates used to attach the enclosure frame to the mounting frame. The cabinet internal environment is the "ultimate" heat sink. It consists of the air (within the TV cabinet) and elements involved in thermal radiation exchange, such as the cabinet surrounding structure and electronics.

Figure 5-1 shows the liquid-lens system domain and boundary conditions. The boundary conditions can be modeled in terms of heat-flux type and a convective type boundary condition. Heat flux is applied to the raster region at the back of the face panel, and the convection-type boundary condition is applied to all of the liquid-lens system boundaries. The convective-type boundary condition is modeled in terms of a "local ambient" temperature associated with a local effective-heat-transfer coefficient, which may involve convection, conduction, and radiation. Values for the local ambient temperature and the local effective-heat-transfer coefficient are associated with each boundary and may vary depending on location. The mathematical model for the inner domain will involve a numerical solution using computational fluid dynamics and heat transfer model. Thermal models for the outer domain yield the boundary conditions applied to the inner computational domain.

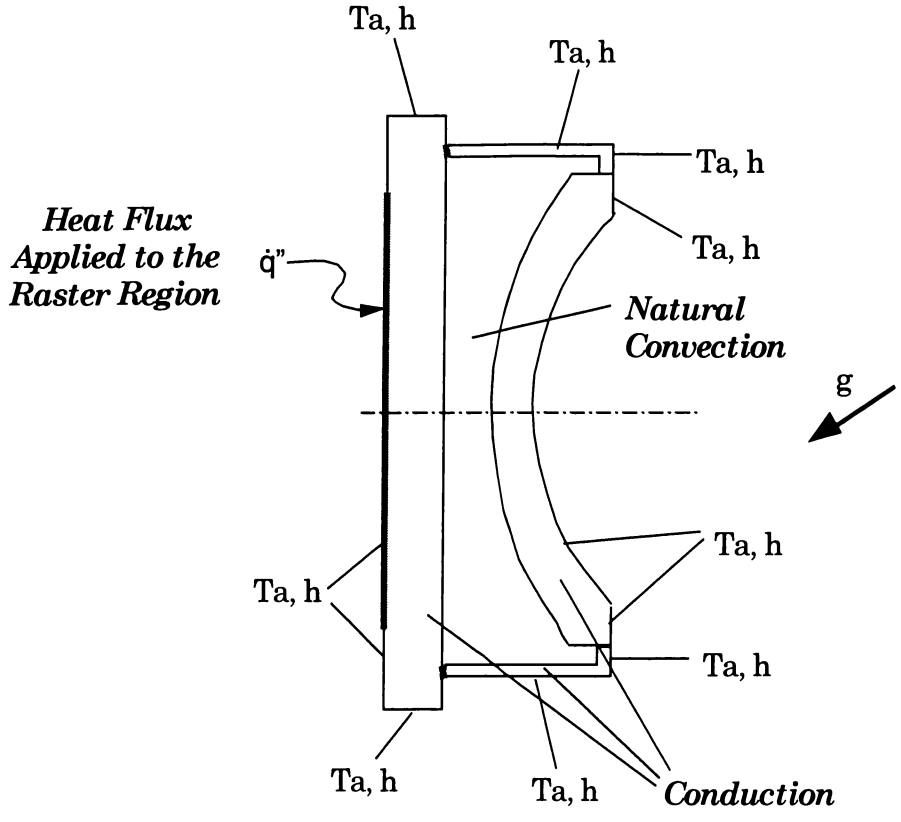

Mixed Convection/Radiation Applied as Boundary Conditions

$\dot{q}$" = Heat Flux
h = Effective Heat Transfer Coefficient
Ta = Environmental Temperature
g = Gravitational Acceleration

Note: Values of h and Ta depend on the particular location

Figure 5-1. Liquid-Lens System Domain Outline and Generic Boundary Conditions

5.2. Assumptions in the Derivation of the Numerical Model for the Heat Transfer and Fluid Flow within the Liquid-Lens System

The following are assumptions used in the derivation of the numerical model.

(1) Mass, momentum, and energy transfer occur in an inertial frame of reference.

(2) The liquid-lens system is composed of fluid and solid homogeneous phases.

(3) The fluid and solid phases are isotropic materials; that is, thermophysical properties are independent of direction.

(4) The fluid is incompressible and the solid is rigid.

(5) The fluid is Newtonian. That is, the shear stress tensor is linearly dependent on the rate of shearing strain and the coefficient of viscosity is independent of the rate of shearing strain.

(6) The only body forces acting on the system are gravitational forces.

(7) Both the fluid and solid phases have constant thermophysical properties, and the density in the body-force terms is dependent only on temperature. That is, the Boussinesq approximation is valid. The viscosity, thermal conductivity, and specific heat are constant.

(8) Conduction heat transfer obeys the Fourier-Biot law.

(9) Thermal radiation may be neglected.

(10) The effects of viscous dissipation in the natural convection flow in the liquid-lens coolant are negligibly small.

5.3. Dependent and Independent Variables

The governing equations shall be stated according to the *Eulerian* method of description, with the independent variables being the position vector, $\vec{X}$, and time, $\tilde{\tau}$. The dependent variables shall be the temperature, T, the velocity vector, $\vec{U}$, and the static pressure, P_s. These are functions of position and time:

$$T = T(\vec{X},\ \tilde{\tau}), \tag{5.1}$$

$$\vec{U} = \vec{U}(\vec{X}, \tilde{\tau}), \text{ and} \tag{5.2}$$

$$P_s = P_s(\vec{X}, \tilde{\tau}). \tag{5.3}$$

5.4. Conservation Laws

The conservation laws in differential form are applied to a differential *system* element (elemental system) of mass m and volume $\mathcal{V}$, moving and deforming through a three-dimensional space, as shown in *Figure 5-2.* The elemental system is subject to surface forces, body forces, and surface heat and work transfers.

5.4.1. Law of Conservation of Mass

The conservation equation for mass for an elemental system is written as [133]:

$$\frac{\mathrm{D}\rho}{\mathrm{D}\tilde{\tau}} + \rho\nabla\bullet\vec{U} = 0, \tag{5.4}$$

where the time derivative denotes total or material derivative, ρ is the mass density defined as:

$$\rho = \lim_{\mathcal{V}\to 0} \frac{\mathcal{M}}{\mathcal{V}}, \tag{5.5}$$

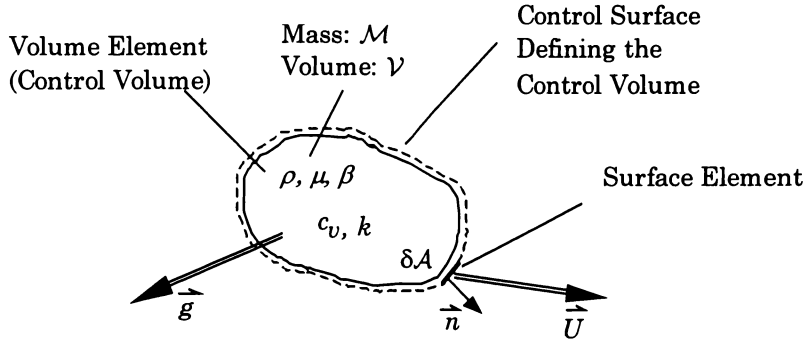

Figure 5-2. Elemental System

and $\vec{U}$ is the velocity vector. The equation for conservation of mass can alternatively be written for an elemental control volume as

$$\frac{\partial \rho}{\partial \tilde{\tau}} + \nabla \bullet \left(\rho \vec{U} \right) = 0 . \tag{5.6}$$

5.4.2. Newton's Second Law of Motion

Newton's second law of motion states that the mass of a particle (elemental system) times its acceleration is proportional to the summation of all external forces acting on it. This law can be stated as a conservation equation for lineat momentum on a per unit volume basis as [133]:

$$\rho \frac{\mathrm{D}\vec{U}}{\mathrm{D}\tilde{\tau}} = \vec{f}_s + \vec{f}_b , \tag{5.7}$$

where $\vec{f}_s$ is the surface force per unit volume, and $\vec{f}_b$ is the body force per unit volume. If the surface force is expressed in terms of the stress tensor and the body force in terms of the gravitational acceleration, the above equation can be rewritten as

$$\rho \frac{\mathrm{D}\vec{U}}{\mathrm{D}\tilde{\tau}} = \nabla \bullet \mathbb{T} + \rho \vec{g} , \tag{5.8}$$

where $\mathbb{T}$ is the stress tensor and $\vec{g}$ is the gravitational acceleration vector. It is convenient to decompose the stress tensor into a pressure component independent of fluid rate of strain and a component solely dependent on fluid rate of strain as:

$$\rho \frac{\mathrm{D}\vec{U}}{\mathrm{D}\tilde{\tau}} = \nabla \bullet \mathbb{T}_{str} - \nabla P_s + \rho \vec{g} , \tag{5.9}$$

where $\mathbb{T}_{str}$ is the strain-induced stress tensor containing the stresses produced by fluid strain alone, and P_s is the static pressure. A linear dependence of stress to strain yields the following equation form:

$$\rho \frac{\mathrm{D}\vec{U}}{\mathrm{D}\tilde{\tau}} = \nabla \bullet \left\{ \mu \left[\left(\nabla \vec{U} \right) + \left(\nabla \vec{U} \right)^{\mathbf{T}} \right] + \lambda \nabla \bullet \vec{U} \mathbb{I} \right\} - \nabla P_s + \rho \vec{g} , \tag{5.10}$$

where μ is the coefficient of viscosity, λ is the coefficient of bulk viscosity, $\mathbb{I}$ is the unit tensor, and $(\ )^{\mathrm{T}}$ denotes the matrix-transpose operator. For a constant-viscosity fluid, the above equation reduces to:

$$\rho\frac{\mathrm{D}\vec{U}}{\mathrm{D}\tilde{\tau}} = \mu\nabla^2\vec{U} + \mu\nabla^{\mathrm{T}}\left(\nabla\bullet\vec{U}\right) + \lambda\nabla\bullet\left(\nabla\bullet\vec{U}\right)\mathbb{I} - \nabla P_s + \rho\vec{g}\,. \tag{5.11}$$

For an incompressible flow, the above equation reduces to

$$\rho\frac{\mathrm{D}\vec{U}}{\mathrm{D}\tilde{\tau}} = \mu\nabla^2\vec{U} - \nabla P_s + \rho\vec{g}\,. \tag{5.12}$$

The above equation may be written for an elemental control volume by applying the total derivative operator on the left-hand side of the equation, which yields.

$$\rho\left(\frac{\partial\vec{U}}{\partial\tilde{\tau}} + \vec{U}\bullet\nabla\vec{U}\right) = \mu\nabla^2\vec{U} - \nabla P_s + \rho\vec{g}\,. \tag{5.13}$$

5.4.3. Law of Conservation of Energy

The basic form of the equation for energy conservation originates from the first law of thermodynamics, which states that energy can be neither created nor destroyed. This can be stated for a material particle (elemental system) on a per-unit mass basis as [133]:

$$\frac{\mathrm{D}e}{\mathrm{D}\tilde{\tau}} = -\frac{\mathrm{D}e_{out}}{\mathrm{D}\tilde{\tau}}, \tag{5.14}$$

where e is the total energy per unit mass, and e_{out} is the net *effluxed* energy per unit mass. The effluxed energy is composed of heat and work exerted by the material particle on its surroundings. The heat component accounts for conduction heat transfer out of the element. The work component accounts for advection of kinetic and potential energy, strain-related dissipation, and pressure boundary work. Substituting expressions for these components into Eq. (5.14) yields

$$\rho\frac{\mathrm{D}e}{\mathrm{D}\tilde{\tau}} = -\nabla\bullet\vec{q}'' + \rho\,\vec{U}\bullet\left(\frac{\mathrm{D}\vec{U}}{\mathrm{D}\tilde{\tau}} - \vec{g}\right) + \Phi - P_s\nabla\bullet\vec{U}. \tag{5.15}$$

where $\vec{q}''$ is the heat flux vector, and Φ is the *dissipation function*, which accounts for the transformation of kinetic energy into internal energy, because of fluid strain. The total energy in the elemental system, e, results from the addition of kinetic energy, e_k, potential energy, e_p, and internal energy, e_i. An expression for the total time derivative of the total energy in terms of these components become

$$\frac{\mathrm{D}e}{\mathrm{D}\tilde{\tau}} = \vec{U}\bullet\left(\frac{\mathrm{D}\vec{U}}{\mathrm{D}\tilde{\tau}} - \vec{g}\right) + \frac{\mathrm{D}e_i}{\mathrm{D}\tilde{\tau}}. \tag{5.16}$$

Substituting this result into the energy conservation equation, Eq. (5.15) yields

$$\rho\left(\vec{U}\bullet\left(\frac{\mathrm{D}\vec{U}}{\mathrm{D}\tilde{\tau}} - \vec{g}\right) + \frac{\mathrm{D}e_i}{\mathrm{D}\tilde{\tau}}\right) = -\nabla\bullet\vec{q}'' + \rho\,\vec{U}\bullet\left(\frac{\mathrm{D}\vec{U}}{\mathrm{D}\tilde{\tau}} - \vec{g}\right) + \Phi - P_s\nabla\bullet\vec{U}. \tag{5.17}$$

The kinetic and potential terms cancel, yielding the following equation for the conservation if internal energy

$$\rho\frac{\mathrm{D}e_i}{\mathrm{D}\tilde{\tau}} = -\nabla\bullet\vec{q}'' + \Phi - P_s\nabla\bullet\vec{U}. \tag{5.18}$$

For an incompressible flow, with negligible viscous dissipation, the above equation reduces to

$$\rho\frac{\mathrm{D}e_i}{\mathrm{D}\tilde{\tau}} = -\nabla\bullet\vec{q}''. \tag{5.19}$$

The preceding conservation equations may be written based on an elemental control volume by expanding the total time-derivative operator as

$$\frac{\partial\rho}{\partial\tilde{\tau}} + \nabla\bullet\left(\rho\vec{U}\right) = 0, \tag{5.20.a}$$

$$\rho\left(\frac{\partial\vec{U}}{\partial\tilde{\tau}} + \vec{U}\bullet\nabla\vec{U}\right) = \mu\nabla^2\vec{U} - \nabla P_s + \rho\vec{g}, \tag{5.20.b}$$

$$\rho\left(\frac{\partial e_i}{\partial\tilde{\tau}} + \vec{U}\bullet\nabla e_i\right) = -\nabla\bullet\vec{q}''. \tag{5.20.c}$$

5.4.4. Conservative Forms of the Governing Equations

When integrating the differential equations over a finite volume, it is convenient to have the equations written in *conservative* form so that fluxes written for each pair of control volumes separated by a common control surface are consistent. In this manner, the flow of the conserved quantity leaving one control volume is identical to the flow entering the neighbor control volume. This is necessary for having both local and global conservation. To achieve this, all of the terms involved in advection or diffusion of fluxes must be written as the divergence of the flux. The equation for mass conservation is already in conservative form. Conservative forms of the momentum conservation equation is obtained by rewriting the left-hand side of the equation as

$$\rho\left(\frac{\partial \vec{U}}{\partial \tilde{\tau}} + \vec{U}\bullet\nabla\vec{U}\right) = \frac{\partial \rho\vec{U}}{\partial \tilde{\tau}} + \nabla\bullet\left(\rho\vec{U}\vec{U}\right) - \vec{U}\left(\frac{\partial \rho}{\partial \tilde{\tau}} + \nabla\bullet\left(\rho\vec{U}\right)\right). \tag{5.21}$$

Substituting the above expression into Eq. (5.20.a) yields

$$\frac{\partial\left(\rho\vec{U}\right)}{\partial \tilde{\tau}} + \nabla\bullet\left(\rho\vec{U}\vec{U}\right) = \mu\nabla^2\vec{U} - \nabla P_s + \rho\vec{g} + \vec{U}\left(\frac{\partial \rho}{\partial \tilde{\tau}} + \nabla\bullet\left(\rho\vec{U}\right)\right), \tag{5.22}$$

Conservative forms of the internal energy conservation equation is obtained by rewriting the left-hand side of the equation as

$$\rho\left(\frac{\partial e_i}{\partial \tilde{\tau}} + \vec{U}\bullet\nabla e_i\right) = \frac{\partial \rho e_i}{\partial \tilde{\tau}} + \nabla\bullet\left(\rho\vec{U}e_i\right) - e_i\left(\frac{\partial \rho}{\partial \tilde{\tau}} + \nabla\bullet\left(\rho\vec{U}\right)\right) \tag{5.23}$$

substituting the above expression into Eq. (5.20.a) yields

$$\frac{\partial\left(\rho e_i\right)}{\partial \tilde{\tau}} + \nabla\bullet\left(\rho\vec{U}e_i\right) = -\nabla\bullet\vec{q}'' + e_i\left(\frac{\partial \rho}{\partial \tilde{\tau}} + \nabla\bullet\left(\rho\vec{U}\right)\right). \tag{5.24}$$

Notice that the term involving the mass source on the right-hand-side of the conservation equation was retained intentionally. This was done because this term must be discretized consistently with mass conservation. Neglecting this term will assume that mass is always conserved, which may not be necessarily true in intermediate iteration steps.

By assuming constant-density, the above conservation equations reduce to

$$\nabla\bullet(\rho\vec{U}) = 0\,, \tag{5.25.a}$$

$$\frac{\partial\left(\rho\vec{U}\right)}{\partial\tilde{\tau}} + \nabla\bullet\left(\rho\vec{U}\vec{U}\right) = \nabla\bullet\mu\nabla\vec{U} - \nabla P_s + \rho\vec{g} + \vec{U}\nabla\bullet\left(\rho\vec{U}\right), \tag{5.25.b}$$

$$\frac{\partial\left(\rho e_i\right)}{\partial\tilde{\tau}} + \nabla\bullet\left(\rho\vec{U}e_i\right) = -\nabla\bullet\vec{q}'' + e_i\nabla\bullet\left(\rho\vec{U}\right). \tag{5.25.c}$$

5.4.5. Using Temperature as the Dependent Variable

In order to have temperature written explicitly in the above equations, a functional dependency must be available for the internal energy and for the density in the momentum-equation body-force term.

Temperature Dependency for Internal Energy and Heat Conduction

It will be assumed that the internal energy is a linear function of temperature and that heat conduction obeys Fourier's law, as stated below.

$$e_i(T) = c_v\left(T - T_{ref}\right) + e_{i,ref}\,, \tag{5.26.a}$$

$$\vec{q}'' = -k\nabla T \tag{5.26.b}$$

where c_v is the constant-volume specific heat, T_{ref} is a reference temperature, $e_{i,ref}$ is a reference value for internal energy at the reference temperature, and k is the thermal conductivity. Substituting the above two expressions in the previous equation, and setting $e_{i,ref}$ to zero yields the following

$$\frac{\partial\left(\rho c_v T\right)}{\partial\tilde{\tau}} + \nabla\bullet\left(\rho\vec{U}c_v T\right) = \nabla\bullet k\nabla T + c_v\left(T - T_{ref}\right)\nabla\bullet\left(\rho\vec{U}\right). \tag{5.27}$$

For convenience, the above equation will be stated in terms of the constant-pressure specific heat. It can be shown that for a constant-density fluid, with both specific heats expressed as linear functions of temperature, the two specific heats must be identical. Therefore, the above equation may be written as

$$\frac{\partial\left(\rho c_p T\right)}{\partial\tilde{\tau}} + \nabla\bullet\left(\rho\vec{U}c_p T\right) = \nabla\bullet k\nabla T + c_p\left(T - T_{ref}\right)\nabla\bullet\left(\rho\vec{U}\right), \tag{5.28}$$

where c_p is the constant-pressure specific heat.

Temperature Dependency for the Density in the Body-Force Term

The flow in the present problem is driven by natural convection. Therefore, a small variation must be allowed for the density in the body-force term in the momentum equation, responding to changes in fluid temperature. It is convenient to express the density in the body-force term implicitly as a function of temperature. The simplest function originates from the so-called Boussinesq approximation, which uses the first two terms in a Taylor-series expansion of density to approximate its value as a linear function of temperature. If ρ_o is a density at a reference temperature, T_o, and the coefficient of thermal expansion is known, the density can be approximated as

$$\rho(T) = \rho_o (1 - \beta_o \Delta T) \tag{5.29}$$

where

$$\beta_o = \frac{1}{v}\left(\frac{\partial v}{\partial T}\right)_p\Bigg|_{T=T_o} = -\frac{1}{\rho}\left(\frac{\partial \rho}{\partial T}\right)_p\Bigg|_{T=T_o}, \tag{5.30}$$

and

$$\Delta T = T - T_o . \tag{5.31}$$

Substituting Eq. (5.29) in Eq. (5.22) yields

$$\frac{\partial\left(\rho\vec{U}\right)}{\partial\tilde{\tau}} + \nabla\bullet\left(\rho\vec{U}\vec{U}\right) = \nabla\bullet\mu\nabla\vec{U} - \nabla P_s + \rho_o(1-\beta_o\Delta T)\vec{g} + \vec{U}\nabla\bullet\left(\rho\vec{U}\right). \tag{5.32}$$

For convenience, the static pressure gradient and the constant term of the buoyancy force are combined by introducing the piezometric pressure. The piezometric pressure gradient is defined as

$$\nabla P = \nabla P_s - \rho_o\vec{g} \tag{5.33}$$

Thus, the piezometric pressure becomes the difference between the hydrostatic pressure within an isothermal field at the reference temperature and the static pressure at the local point:

$$P = P_s - P_{hs}. \tag{5.34}$$

The hydrostatic pressure, P_{hs}, is defined as

$$P_{hs} = \rho_o \vec{g} \bullet (\vec{X} - \vec{X}_o) \tag{5.35}$$

where $\vec{X}$ is the local fluid element position vector, and $\vec{X}_o$ is the position vector at a reference location, which may be chosen to be the same as that for the reference temperature. The relationship among the above variables is depicted in *Figure 5-3.* Substituting Eq. (5.33) in Eq. (5.32), and assigning the same value for the density in all terms, the following form of the momentum equation is obtained.

$$\frac{\partial(\rho_o \vec{U})}{\partial \tilde{\tau}} + \nabla \bullet (\rho_o \vec{U}\vec{U}) = \nabla \bullet \mu \nabla \vec{U} - \nabla P - \rho_o \vec{g} \beta_o \Delta T + \vec{U} \nabla \bullet (\rho_o \vec{U}). \tag{5.36}$$

5.4.6. Governing Differential Equations

The set of differential equations the conservation of mass, linear momentum,

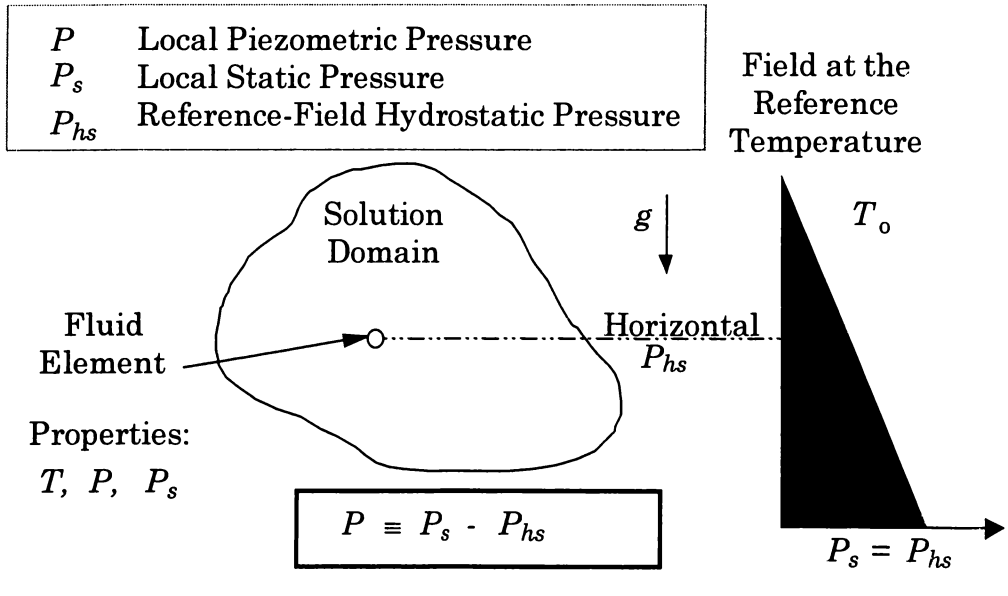

Figure 5-3. The Concept of the Hydrostatic Reference Field

and internal energy, for a constant-property system composed of a single incompressible fluid phase, and M rigid solid phases are as follows:

$$\nabla\bullet(\rho_o \vec{U}) = 0\,, \tag{5.37.a}$$

$$\frac{\partial\left(\rho_o \vec{U}\right)}{\partial \tilde{\tau}} + \nabla\bullet\left(\rho_o \vec{U}\vec{U}\right) = \nabla\bullet\left(\mu_o \nabla \vec{U}\right) - \nabla P - \rho_o \vec{g}\beta_o \Delta T + \vec{U}\nabla\bullet\left(\rho_o \vec{U}\right), \tag{5.37.b}$$

$$\frac{\partial\left(\rho_m c_{p,m} T\right)}{\partial \tilde{\tau}} + \nabla\bullet\left(\rho_m c_{p,m} \vec{U} T\right) = \nabla\bullet\left(k_m \nabla T\right) + \left(T - T_{ref}\right)\nabla\bullet\left(\rho_m c_{p,m} \vec{U}\right)\,, m = 1,2,\ldots,M \tag{5.37.c}$$

where

ρ_o is the fluid mass density,

μ_o is the fluid coefficient of viscosity,

β_o is the fluid volume expansivity,

ρ_m is the mass density of for material m,

$c_{p,m}$ is the constant-pressure specific heat for material m,

k_m is the thermal conductivity for material m, and

M is the number of materials.

5.4.7. Coordinate System and Base Vectors

Let $\vec{X}$ be described by the Cartesian coordinates X_1, X_2, X_3 using a right-handed convention system. Let the base vectors be the unit vectors in coordinate directions X_1, X_2, and X_3 be denoted as $\vec{\varepsilon}_1$, $\vec{\varepsilon}_2$, and $\vec{\varepsilon}_3$, respectively. The position vector, $\vec{X}$, can now be expressed in terms of the Cartesian coordinates and unit vectors as

$$\vec{X} = \sum_{i=1}^{3} X_i \vec{\varepsilon}_i\,, \tag{5.38}$$

$$\vec{U} = \sum_{i=1}^{3} U_i \vec{\varepsilon}_i\,, \tag{5.39}$$

and the gradient operators becomes:

$$\nabla = \sum_{i=1}^{3} \vec{\varepsilon}_i \frac{\partial}{\partial X_i}. \tag{5.40}$$

Substituting the above into Eqs. (5.37) yields the following set of partial differential equations based on Cartesian coordinates.

$$\sum_{j=1}^{3} \left(\rho_o U_j \right)_{X_j} = 0 \tag{5.41.a}$$

$$\begin{aligned} \left(\rho_o U_i \right)_{\tilde{\tau}} + \sum_{j=1}^{3} \left(\rho_o \, U_j U_i - \mu_o \left(U_i \right)_{X_j} + \delta_j^i P \right)_{X_j} = \\ = -\left(\rho_o \, g_i \, \beta_o \, \Delta T \right) + \rho_o \, U_i \sum_{j=1}^{3} \left(U_j \right)_{X_j} \end{aligned} \tag{5.41.b}$$

$$\left(c_m T \right)_{\tilde{\tau}} + \sum_{j=1}^{3} \left(c_m \, U_j T - k_m \left(T \right)_{X_j} \right)_{X_j} = c_m \, T \sum_{j=1}^{3} \left(U_j \right)_{X_j} \tag{5.41.c}$$

where

ρ_o is the mass density of the liquid phase;

μ_o is the coefficient of viscosity of the liquid phase;

β_o is the volume expansivity of the liquid phase;

δ_j^i is the Kroenecker delta, defined as

$$\delta_j^i = \begin{cases} 1, i = j \\ 0, i \neq j \end{cases}; \tag{5.42}$$

c_m is the *thermal capacity per unit volume* for material m, defined as

$$c_m = \rho_m c_{p,m}; \tag{5.43}$$

k_m is the thermal conductivity for material m, and

$( )_z$ denotes the partial derivative of $( )$ with respect to a generic variable, z.

5.4.8. General Conservation Equation

The above conservation equations for mass, momentum, and energy have the general form:

$$(C\Phi)_{\tilde{\tau}} + \sum_{j=1}^{3}\left(C\,U_j\,\Phi - \Gamma\,\Phi_{X_j} + H_j \right)_{X_j} = S + C\,\Phi \sum_{j=1}^{3}\left(U_j \right)_{X_j}, \tag{5.44}$$

or

$$(C\Phi)_{\tilde{\tau}} + \sum_{j=1}^{3}\left(F_j^{\Phi} \right)_{X_j} = S + C\,\Phi \sum_{j=1}^{3}\left(U_j \right)_{X_j}, \tag{5.45}$$

where F_j is the j-component of the flux of the transport quantity Φ,

$$F_j^{\Phi} = \left(C\,U_j\,\Phi - \Gamma\,\Phi_{X_j} + H_j \right), j = 1,2,3. \tag{5.46}$$

Alternatively, the general conservation equation above can be expressed in coordinate-independent form as

$$(C\Phi)_{\tilde{\tau}} + \nabla\bullet\vec{F}^{\Phi} = S + C\,\Phi\,\nabla\bullet\vec{U}, \tag{5.47}$$

where

$$\vec{F}^{\Phi} = C\,\vec{U}\,\Phi - \Gamma\,\nabla\Phi + \vec{H}. \tag{5.48}$$

is the general flux vector. The last term in the equation above may be expressed in terms of its components (previously defined) as:

$$\vec{H} = \sum_{j=1}^{3} H_j\,\vec{\varepsilon}_j. \tag{5.49}$$

The general flux vector may also be decomposed in terms of the advection/diffusion contribution and a vector field contribution as

$$\vec{F} = \vec{F}^{AD} + \vec{H}, \tag{5.50}$$

where

$$\vec{F}^{AD} = C\,\vec{U}\,\Phi - \Gamma\,\nabla\Phi. \tag{5.51}$$

The correspondence between the generalized variables in the above generalized conservation equation and the variables in the particular conservation equations is shown in Table 5-1.

Table 5-1. Equivalence between Variables in the Generalized Conservation Equation and Variables in the Particular Conservation Equations

		Particular Conservation Equation		
	Generic Variable	Mass	i-Momentum (i = 1,2,3)	Energy
Dependent Variable	Φ	1	U_i	T
Time	$\tilde{\tau}$	$\tilde{\tau}$	$\tilde{\tau}$	$\tilde{\tau}$
Capacitance	C	ρ_o	ρ_o	c_m
Diffusion Coefficient	Γ	0	μ_o	k_m
Boundary Source (j=1,2,3)	H_j	0	$\delta_j^i P$	0
Advecting Velocity (j=1,2,3)	U_j	U_j	U_j	U_j
Position (j=1,2,3)	X_j	X_j	X_j	X_j
Volumetric Source	S	0	$-\rho_o g_i \beta_o \Delta T$	0

5.4.9. Non-Dimensionalization of the Generalized Conservation Equation

The purpose of this section is to rewrite the governing equations in dimensionless form. To express the general conservation equation in dimensionless form, reference scales must be introduced. Dimensionless variables are then defined in terms of physical variables and reference quantities. It must be noted that the intention here is not to identify characteristic scales of the problem, but just any appropriate reference quantity that can be used to non-dimensionalize these equations. A list of reference quantities and their corresponding physical variables and dimensionless variables is shown in Table 5-2.

Table 5-2. Reference Quantities in the Generalized Conservation Equation

	Physical Variable	Dimensionless Variable	Reference Quantity
Dependent Variable	Φ	ϕ	Φ_D
Time	$\tilde{\tau}$	τ	$\tilde{\tau}_D$
Capacitance	C	c	C_D
Diffusion Coefficient	Γ	γ	Γ_D
Boundary Source Term	$H_j, j=1,2,3$	$h_j, j=1,2,3$	H_D
Velocity	$U_j, j=1,2,3$	$u_j, j=1,2,3$	U_D
Coordinate	$X_j, j=1,2,3$	$x_j, j=1,2,3$	X_D
Volumetric Source Term	S	s	S_D
Flux	$F_j^{\Phi}, j=1,2,3$	$f_j^{\phi}, j=1,2,3$	F_D

The dimensionless variables may be defined in terms of the physical variables and the reference quantities as:

$$\phi = \frac{\Phi}{\Phi_D}, \tag{5.52.a}$$

$$\tau = \frac{\tilde{\tau}}{\tilde{\tau}_D}, \tag{5.52.b}$$

$$c = \frac{C}{C_D}, \tag{5.52.c}$$

$$\gamma = \frac{\Gamma}{\Gamma_D}, \tag{5.52.d}$$

$$h_j = \frac{H_j}{H_D}, \quad j=1,2,3, \tag{5.52.e}$$

$$u_j = \frac{U_j}{U_D}, \quad j=1,2,3, \tag{5.52.f}$$

$$x_j = \frac{X_j}{X_D}, \quad j=1,2,3, \tag{5.52.g}$$

$$s = \frac{S}{S_D}, \text{ and} \tag{5.52.h}$$

$$f_j^{\phi} = \frac{F_j^{\Phi}}{F_D}, \quad j = 1,2,3. \tag{5.52.i}$$

The physical variables can now be expressed in terms of dimensionless variables as:

$$\Phi = \phi\, \Phi_D, \tag{5.53.a}$$

$$\tilde{\tau} = \tau\, \tilde{\tau}_D, \tag{5.53.b}$$

$$C = c\, C_D, \tag{5.53.c}$$

$$\Gamma = \gamma\, \Gamma_D, \tag{5.53.d}$$

$$H_j = h_j\, H_D, \quad j = 1,2,3, \tag{5.53.e}$$

$$U_j = u_j\, U_D, \quad j = 1,2,3, \tag{5.53.f}$$

$$X_j = x_j\, X_D, \quad j = 1,2,3, \tag{5.53.g}$$

$$S = s\, S_D, \text{ and} \tag{5.53.h}$$

$$F_j^{\Phi} = f_j^{\phi}\, F_D, \quad j = 1,2,3. \tag{5.53.i}$$

To obtain the general conservation equation in dimensionless form, the above physical variables are substituted in Eq. (5.45), resulting in the following equation,

$$\left(\frac{C_D \Phi_D}{\tilde{\tau}_D}\right)(c\phi)_{\tau} + \left(\frac{F_D}{X_D}\right)\sum_{j=1}^{3}\left(f_j\right)_{x_j} = \left(S_D\right)s + \left(\frac{C_D\, U_D \Phi_D}{X_D}\right)c\phi \sum_{j=1}^{3}\left(u_j\right)_{x_j}. \tag{5.54}$$

Multiplying both sides of the equation by $\left(\frac{X_D}{C_D U_D \Phi_D}\right)$ yields the following dimensionless form of the generalized conservation equation in terms of dimensionless groups:

$$\left(\frac{X_D}{\tilde{\tau}_D U_D}\right)(c\phi)_{\tau} + \left(\frac{F_D}{C_D U_D \Phi_D}\right)\sum_{j=1}^{3}\left(f_j\right)_{x_j} = \left(\frac{S_D X_D}{C_D U_D \Phi_D}\right)s + c\phi \sum_{j=1}^{3}\left(u_j\right)_{x_j}. \tag{5.55}$$

The dimensionless form of the flux is obtained by substituting the physical variables from Eqs. (5.53), into the flux equation, Eq. (5.46) resulting in the following equation:

$$(F_D) f_j = (C_D U_D \Phi_D)(c\, u_j\, \phi) - \left(\frac{\Gamma_D \Phi_D}{X_D}\right)(\gamma\, \phi_{x_j}) + (H_D) h_j,\ j = 1,2,3. \qquad (5.56)$$

Multiplying both sides of the equation by $\left(\frac{1}{C_D U_D \Phi_D}\right)$ yields the following dimensionless form of the flux equation:

$$\left(\frac{F_D}{C_D U_D \Phi_D}\right) f_j = (c\, u_j\, \phi) - \left(\frac{\Gamma_D}{C_D U_D X_D}\right)(\gamma\, \phi_{x_j}) + \left(\frac{H_D}{C_D U_D \Phi_D}\right) h_j . \qquad (5.57)$$

The above equations for generalized transport-property conservation contain five <u>independent</u> dimensionless groups, namely.

$$\frac{X_D}{\tilde{\tau}_D U_D}, \qquad (5.58.a)$$

$$\frac{F_D}{C_D U_D \Phi_D}, \qquad (5.58.b)$$

$$\frac{S_D X_D}{C_D\, U_D \Phi_D}, \qquad (5.58.c)$$

$$\frac{\Gamma_D}{C_D U_D X_D}, \text{ and} \qquad (5.58.d)$$

$$\frac{H_D}{C_D U_D \Phi_D}. \qquad (5.58.e)$$

Since these groups are independent, their value may arbitrarily be set to unity to obtain the final dimensionless form of the conservation equation and flux equation as:

$$(c\phi)_\tau + \sum_{j=1}^{3} \left(f_j^\phi\right)_{x_j} = s + c\phi \sum_{j=1}^{3} \left(u_j\right)_{x_j}, \qquad (5.59.a)$$

$$f_j^\phi = c\, u_j\, \phi - \gamma\, \phi_{x_j} + h_j,\ j = 1,2,3, \qquad (5.59.b)$$

or in coordinate-independent form,

$$(c\,\phi)_\tau + \nabla \bullet \vec{f}^{\,\phi} = s + c\,\phi \nabla \bullet \vec{u}, \qquad (5.60)$$

where

$$\vec{f}^{\phi} = c\,\vec{u}\,\phi - \gamma\nabla\phi + \vec{h} \tag{5.61}$$

is the dimensionless flux vector. The last term in the above equation may be expressed in terms of its components (previously defined) as:

$$\vec{h} = \sum_{j=1}^{3} h_j\,\vec{\varepsilon}_j\,. \tag{5.62}$$

There are nine reference quantities, as shown in the right column of Table 5-2, but only five independent equations, as shown in Eqs. (5.58). Therefore, four reference quantities must have assumed known values. Assume the values for the reference quantities X_D, C_D, U_D, and Φ_D are known. Then, it follows, from Eqs. (5.58), that the remaining reference quantities can be calculated as:

$$\tilde{\tau}_D = \frac{X_D}{U_D}, \tag{5.63.a}$$

$$F_D = C_D U_D \Phi_D, \tag{5.63.b}$$

$$S_D = \frac{C_D\,U_D\,\Phi_D}{X_D}, \tag{5.63.c}$$

$$\Gamma_D = C_D U_D X_D, \text{ and} \tag{5.63.d}$$

$$H_D = C_D U_D \Phi_D. \tag{5.63.e}$$

Next, the above definitions will be applied to each of the particular conservation equations to obtain the dimensionless forms.

5.4.10. Non-Dimensionalization of the Particular Governing Equations

Following the variable correspondence between particular and generic variables in Table 5-1, the reference quantities for the main dependent variables are $\Phi_D = 1$ in the mass-conservation equation, $\Phi_D = U_D$ in the momentum-conservation equation, and $\Phi_D = \Delta T_D$ in the energy-conservation equation. The reference length scale is defined as X_D for all conservation equations. The reference scale for advecting velocity is defined as U_D for all conservation equations. The reference quantities for capacitance for mass-, momentum-, and energy conservation equations are:

$C_D = \rho_o$ (mass conservation), (5.64.a)

$C_D^u = \rho_o$ (momentum conservation), (5.64.b)

$C_D^t = c_o$ (energy conservation). (5.64.c)

For convenience, let the reference density be the one for the fluid:

$$\rho_D = \rho_o \tag{5.65}$$

Define the reference velocity as:

$$U_D = \frac{\alpha_o}{X_D} \tag{5.66}$$

The reference time scale is obtained as:

$$\tilde{\tau}_D = \frac{X_D}{U_D} = \frac{{X_D}^2}{\alpha_o}. \tag{5.67}$$

The remaining reference quantities for mass conservation are:

$$F_D = C_D U_D \Phi_D = \rho_o \frac{\alpha_o}{X_D}, \text{ and} \tag{5.68}$$

$$S_D = \frac{C_D U_D \Phi_D}{X_D} = \frac{\rho_o \alpha_o}{{X_D}^2}. \tag{5.68}$$

(Γ_D and H_D are not applicable.) The remaining reference quantities for momentum conservation are:

$$F_D^u = C_D U_D \Phi_D = \rho_o \frac{{\alpha_o}^2}{{X_D}^2}, \tag{5.69}$$

$$S_D^u = \frac{C_D U_D \Phi_D}{X_D} = \frac{\rho_o {\alpha_o}^2}{{X_D}^3}, \tag{5.69}$$

$$\Gamma_D^u = C_D U_D X_D = \rho_o \alpha_o, \text{ and} \tag{5.69}$$

$$H_D^u = C_D U_D \Phi_D = \rho_o \frac{{\alpha_o}^2}{{X_D}^2}. \tag{5.69}$$

The remaining reference quantities for energy conservation are:

$$F_D^t = C_D U_D \Phi_D = c_o \frac{\alpha_o}{X_D} \Delta T_D, \tag{5.70.a}$$

$$S_D^t = \frac{C_D U_D \Phi_D}{X_D} = \frac{c_o \alpha_o \Delta T_D}{{X_D}^2}, \text{ and} \tag{5.70.b}$$

$$\Gamma_D^t = C_D U_D X_D = k_o, \tag{5.70.c}$$

(H_D^t is not applicable) where k_o is the fluid thermal conductivity

Next, expressions are obtained for each of the dimensionless variables appearing in the generalized equations for conservation and flux, Eqs. (5.59), in terms of dimensionless variables in the particular equations. The dimensionless dependent variables will be expressed in terms of physical variables and reference quantities for each conservation equation, by applying Eq. (5.52) to the conservation equations for mass, momentum (Newton's second law), and energy.

Dimensionless Variables for the Mass Conservation Equation

The physical variables are (see Table 5-1) $\Phi = 1$, $C = \rho_o$, $\Gamma = 0$, $H_j = 0\,(j = 1,2,3)$, and $S = 0$. Substituting these variables, and the reference quantities for mass conservation yields:

$$\phi = \frac{\Phi}{\Phi_D} \Rightarrow \phi = \frac{1}{1} = 1, \tag{5.71.a}$$

$$c = \frac{C}{C_D} = 1, \tag{5.71.b}$$

$$\gamma = \frac{\Gamma}{\Gamma_D} = 0, \tag{5.71.c}$$

$$h_j = \frac{H_j}{H_D} = 0,\ j = 1,2,3, \text{ and} \tag{5.71.d}$$

$$s = \frac{S}{S_D} = 0. \tag{5.71.e}$$

Dimensionless Variables for the Momentum Conservation Equation

The physical variables are $\Phi^u = U_i$, $C^u = \rho_o$, $\Gamma^u = \mu_o$, $H_j^u = \delta_j^i P$, and $S^u = -\rho_o g_i \beta_o \Delta T$ (see Table 5-1). Substituting these variables, and the reference quantities for momentum conservation yields:

$$\phi^u = \frac{\Phi^u}{\Phi_D^u} \Rightarrow u_i = \frac{U_i}{U_D}, \tag{5.72.a}$$

$$c^u = \frac{C^u}{C_D^u} = 1, \tag{5.72.b}$$

$$\gamma^u = \frac{\Gamma^u}{\Gamma_D^u} = Pr, \tag{5.72.c}$$

$$h_j^u = \frac{H_j^u}{H_D^u} = \frac{\delta_j^i P}{\rho_o \frac{\alpha_o^2}{X_D 2}} = \delta_j^i p, \quad j = 1,2,3, \text{ and} \tag{5.72.d}$$

$$s^u = \frac{S^u}{S_D^u} = -\frac{\rho_o g_i \beta_o \Delta T}{\frac{\rho_o \alpha_o^2}{X_D^3}} = -\hat{g}_i B_o t, \tag{5.72.e}$$

where $i = 1,2,3$, p is the dimensionless pressure, defined as:

$$p \equiv \frac{P}{\rho_D U_D^2} = \frac{P}{\rho_o \frac{\alpha_o^2}{X_D 2}}, \tag{5.73}$$

$\hat{g}_i$ is the dimensionless gravitational-acceleration component, defined as:

$$\hat{g}_i \equiv \frac{g_i}{g}, i = 1,2,3, \tag{5.74}$$

B_o is the Boussinesq number, defined as:

$$B_o = \frac{g \beta_o \Delta T_D X_D^3}{\alpha_o^2} \left(= Ra \cdot Pr\right), \tag{5.75}$$

and , t is the dimensionless temperature differential, defined as:

$$t \equiv \frac{T - T_o}{\Delta T_D}. \tag{5.76}$$

Dimensionless Variables for the Energy Conservation Equation

The physical variables are $\Phi^t = T - T_o$, $C^t = c_m$, $\Gamma^t = k_m$, $H_j^t = 0$, and $S^t = 0$ (see Table 5-1). Substituting these, and the reference quantities for momentum conservation yields:

$$\phi^t = \frac{\Phi^t}{\Phi_D^t} \Rightarrow t = \frac{T - T_o}{\Delta T_D}, \tag{5.77.a}$$

$$c^t = \frac{C^t}{C_D^t} = \hat{c}_m, \tag{5.77.b}$$

$$\gamma^t = \frac{\Gamma^t}{\Gamma_D^t} = \hat{k}_m, \tag{5.77.c}$$

$$h_j^t = \frac{H_j^t}{H_D^t} = 0,\ j = 1,2,3, \text{ and} \tag{5.77.d}$$

$$s^t = \frac{S^t}{S_D^t} = 0, \tag{5.77.e}$$

where $\hat{c}_m$ and $\hat{k}_m$ are the thermal capacity ratio, and the thermal conductivity ratio for material "m", defined as:

$$\hat{c}_m \equiv \frac{c_m}{c_o}, \text{ and} \tag{5.78.a}$$

$$\hat{k}_m \equiv \frac{k_m}{k_o}. \tag{5.78.b}$$

A list of the general and particular dimensionless variables is shown in Table 5-3.

5.5. Dimensionless Forms of the Governing Equations

The following conservation equation dimensionless forms for mass, momentum, and energy are obtained by substituting the results from Eqs. (5.71), (5.72), and (5.77) into Eqs. (5.59):

Table 5-3. Dimensionless Variables in the Particular Conservation Equations

	Generic Variable	Particular Conservation Equation		
		Mass	i-Momentum (i = 1,2,3)	Energy, Material m[1]
Dependent Variable	ϕ	1	u_i	t
Capacitance	${}_c\phi$	1	1	$\hat{c}_m$
Diffusion Coefficient	${}_\gamma\phi$	0	Pr	$\hat{k}_m$
Boundary Source (j=1,2,3)	h_j^ϕ	0	$\delta_j^i\, p$	0
Volumetric Source	${}_s\phi$	0	$-\hat{g}_i B_o \Delta t$	0

[1] m denotes any particular material

$$\sum_{j=1}^{3}\left(u_j\right)_{x_j} = 0, \tag{5.79.a}$$

$$\left(u_i\right)_\tau + \sum_{j=1}^{3}\left(u_j u_i - Pr\left(u_i\right)_{x_j} + \delta_j^i p\right)_{x_j} = -\left(\hat{g}_i B_o\, t\right) + u_i \sum_{j=1}^{3}\left(u_j\right)_{x_j} \tag{5.79.b}$$

$$\left(\hat{c}_m t\right)_\tau + \sum_{j=1}^{3}\left(\hat{c}_m\, u_j\, t - \hat{k}_m\left(t\right)_{x_j}\right)_{x_j} = \hat{c}_m\, t \sum_{j=1}^{3}\left(u_j\right)_{x_j} \tag{5.79.c}$$

where τ is the dimensionless time,

$$\tau = \tilde{\tau}\left(\frac{\alpha_o}{X_D{}^2}\right), \tag{5.80}$$

x_j is the dimensionless j-direction Cartesian coordinate,

$$x_j = \frac{X_j}{X_D},\ j = 1,2,3, \tag{5.81}$$

and m is the sub-domain material index for the fluid or a particular solid.

5.6. Summary

In this chapter, the assumptions used in the development of the mathematical model of the thermal and fluid transport in the liquid-lens system

were presented. Then, the governing partial-differential equations of mass, momentum, and energy were derived. Finally, these equations were non-dimensionalized. It now remains to solve these equations numerically, which will be presented in the next chapter.

6. DEVELOPMENT OF THE FINITE-VOLUME HEAT TRANSFER AND FLUID FLOW NUMERICAL MODEL

6.1. Introduction

This chapter deals with the numerical solution of the mathematical model. The basic idea is to transform the set of partial-differential governing equations into a set of algebraic equations to be solved on a digital computer. Preliminary effort will be briefly mentioned next, before going into the derivation of the finite-volume numerical model.

6.2. Preliminary Models

A Cartesian-grid model was built initially to serve as a "test bed" for various numerical concepts, as well as flux-discretization schemes. This model evolved into a body-fitted coordinate model in which the equations were transformed into curvilinear space before integration and discretization. This model was abandoned because of the presence of artificial flows, which produced velocities with order of magnitude comparable to that for the natural convection flow in the actual problem being solved. These artificial flows resulted from spurious momentum sources, believed due to improper approximations in the transformation metrics. A more detailed description of the preliminary effort is presented in APPENDIX I. To avoid having to introduce transformation metrics altogether, it was decided to integrate the differential equations directly in physical space. This is the subject of the remainder of this chapter.

6.3. The Finite-Volume Model

The lessons learned above helped in deciding what approach to take for the final model. It is imperative that the model should not produce residual velocities of the same or greater order of magnitude as the natural convection velocities. Transforming the differential equations into curvilinear space requires focusing

attention on the discretization process to ensure consistency with physical space. To ensure consistency and solution correctness, the transformed equations must recover the integrated and discretized forms of the equations in Cartesian space. To add to the level of complexity, vector quantities become harder to visualize in curvilinear space, eliminating any intuitive element of vector visualization from the process of locating errors and program debugging. Having to transform the equations into curvilinear space, and having to recover physical quantities for consistency seems to be adding an unnecessary step to the solution process. It is best to avoid this unnecessary step altogether, and complete the whole process within Cartesian space, without transforming the equations. This can be achieved by applying the Gauss' divergence theorem to convert the volume integrals of conservation fluxes into surface integrals. In principle, control-volumes of arbitrary shape can be treated. The sections remaining will apply this method to the conservation equations for mass, momentum, and energy in order to arrive at the algebraic set of equations for the numerical solution of the problem.

6.4. Integration and Discretization of the General Advection-Diffusion Equation

In a finite-volume method, the solution domain is discretized into a finite set of volume elements, and integration of the partial-differential conservation equations is conducted within each of these elements. This section presents the integration of these equations in space and time within a single volume element, and the discretization of integral quantities. For ease of presentation, integration will be done using the general advection-diffusion equation and later the results will be applied to the particular equations.

It is assumed that the solution space domain has been discretized into finite-volume elements, each of them being simply connected, that is, without "holes", and that the sum of the finite volumes equals the volume of the solution domain. The restriction about being simply connected only applies to the volume elements, not to the solution domain. A general finite volume for space integration is shown in *Figure 6-1*. The above subdivision of the solution space will result in a finite set of

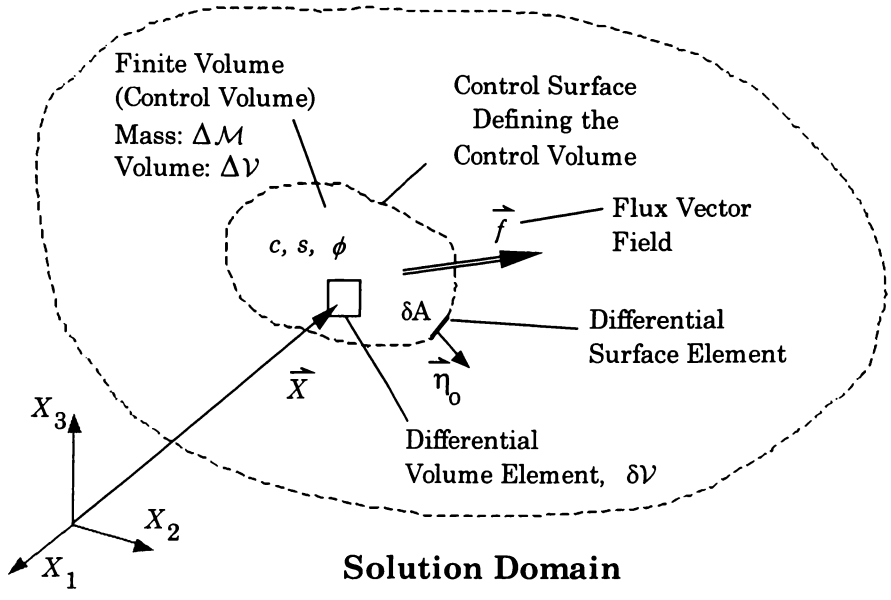

Figure 6-1. Finite Volume Used for Integration

boundary and internal interfaces. Volume elements adjacent to domain boundaries share these boundaries with the domain. *Internal boundaries* are shared between volume elements, unless a volume element is isolated.

Domain boundary conditions are directly applied to those volume elements sharing domain boundaries. Boundary conditions on internal boundaries are "shared" between the adjacent volume elements. These boundary conditions are imposed as sets of equations with an equal number of unknowns, which should be determined as part of the solution, as will be discussed under the flux discretization section. Time integration will be done through a time interval $\Delta\tau$, and space integration will be done through a finite volume $\Delta\mathcal{V}$ for the general volume element, subject to initial and boundary conditions.

The general conservation equation (as applied to momentum and energy) in vector form, Eq. (5.60), can be integrated within the space and time elements indicated above as:

$$\int_{\Delta\tau}\int_{\Delta\mathcal{V}} (c\,\phi)_\tau \, d\mathcal{V}\, d\tau + \int_{\Delta\tau}\int_{\Delta\mathcal{V}} \nabla\cdot\vec{f}^{\,\phi} \, d\mathcal{V}\, d\tau = \int_{\Delta\tau}\int_{\Delta\mathcal{V}} s \, d\mathcal{V}\, d\tau + \int_{\Delta\tau}\int_{\Delta\mathcal{V}} c\,\phi\,\nabla\cdot\vec{u}\, d\mathcal{V}\, d\tau \tag{6.1}$$

Notice that this equation is general for momentum and energy only; since the second term on the right-hand side of the equation is identically zero in the equation of mass conservation. Although this equation could be applied generally to all equations with the understanding that the above restriction must hold during particularization, it is preferred that integration of mass conservation is treated separately to avoid adding unnecessary confusion.

Time Discretization

A fully implicit differencing scheme will be used to discretize time, such that conservation is self-consistent at the end of the time interval. Thus, the equation above can be rewritten as:

$$\frac{1}{\Delta\tau}\int_{\Delta\mathcal{V}} c\left(\phi-\phi_o\right)\mathrm{d}\mathcal{V}+\int_{\Delta\mathcal{V}}\nabla\bullet\bar{f}^{\phi}\,\mathrm{d}\mathcal{V}=\int_{\Delta\mathcal{V}} s\,\mathrm{d}\mathcal{V}+\int_{\Delta\mathcal{V}} c\,\phi\,\nabla\bullet\bar{u}\,\mathrm{d}\mathcal{V}, \tag{6.2}$$

where all variables, except for ϕ_o are evaluated at the end of the integration time interval.

Space Discretization

In order to enforce global conservation, fluxes resulting from vector fields should be integrated over the area of the volume element. Not doing so may result in spurious fluxes resulting from discretization, which generally do not ensure conservation for the domain as a whole. The terms involving gradients above can be converted to surface integrals using the Gauss' divergence theorem, since the volume elements are simply connected. For vector field, $\bar{q}$, the divergence theorem states:

$$\int_{\Delta\mathcal{V}}\nabla\bullet\bar{q}\,\mathrm{d}\mathcal{V}=\int_{A}\bar{q}\bullet\bar{\eta}_o\,\mathrm{d}A, \tag{6.3}$$

where $\bar{\eta}_o$ is the control-volume outward unit-normal vector.
Applying the above to the second terms on the left- and right-hand sides of the integral in Eq. (6.2), and operating on volume integrals yields:

$$\frac{1}{\Delta\tau}\overline{c\left(\phi-\phi_o\right)}\,\Delta\mathcal{V}+\int_A \bar{f}^{\phi}\bullet\bar{\eta}_o\,\mathrm{d}A=\bar{s}\,\Delta\mathcal{V}+\overline{c\,\phi}\int_A \bar{u}\bullet\bar{\eta}_o\,\mathrm{d}A\,, \tag{6.4}$$

where the bars denote mean values over the volume element. The mean value for the dependent variable will be evaluated at the cell volume centroid. For convenience the bars will be dropped, with the understanding that these variables are taken as volumetric mean values. Furthermore, it is assumed that the mean value of a product can be approximated as the product of mean values. With these assumptions, the above equation can be rewritten as:

$$\left(\phi_{\mathrm{c}}-\phi_{\mathrm{o}}\right)\frac{c\,\Delta\mathcal{V}}{\Delta\tau}+\int_A \bar{f}^{\phi}\bullet\bar{\eta}_o\,\mathrm{d}A=s\,\Delta\mathcal{V}+c\,\phi_{\mathrm{c}}\int_A \bar{u}\bullet\bar{\eta}_o\,\mathrm{d}A\,, \tag{6.5}$$

The last task remaining is to discretize the area integrals. Since there is a finite set of internal "shared" and domain boundary interfaces, the area integrals may be discretized into a finite summation set as:

$$\frac{c\,\Delta\mathcal{V}}{\Delta\tau}\left(\phi_{\mathrm{c}}-\phi_{\mathrm{o}}\right)+\sum_{j=1}^{N}\overline{\bar{f}^{\phi}\bullet\bar{\eta}_o^{\,j}}\,\Delta A^j=s\,\Delta\mathcal{V}+c\,\phi_{\mathrm{c}}\sum_{j=1}^{N}\overline{\bar{u}\bullet\bar{\eta}_o^{\,j}}\,\Delta A^j\,, \tag{6.6}$$

where N is the number of interfaces associated with the particular volume element, and the bars denote representative mean values over the finite surfaces. Again, for the sake of clarity, the bars will be dropped, understanding that fluxes are to be evaluated as mean values over these surfaces:

$$\frac{c\,\Delta\mathcal{V}}{\Delta\tau}\left(\phi_{\mathrm{c}}-\phi_{\mathrm{o}}\right)+\sum_{j=1}^{N}\bar{f}^{\phi}\bullet\bar{\eta}_o^{\,j}\,\Delta A^j=s\,\Delta\mathcal{V}+c\,\phi_{\mathrm{c}}\sum_{j=1}^{N}\bar{u}\bullet\bar{\eta}_o^{\,j}\,\Delta A^j\,. \tag{6.7}$$

The above equation is the general advection-diffusion equation in discretized form. This equation, in principle could be applied to volume elements of any shape, but for this equation to be useful for the calculation of the dependent variable, it must be stated in algebraic form. This can be achieved by discretizing the flux vector as a function of the dependent variable evaluated at known physical locations. Deploying these nodes requires some ordering scheme to facilitate addressing them during the calculations. Therefore, a pre-defined grid structure is preferred along with a

coordinate system that can be used to locate grid points where variables are evaluated.

6.5. Grid Structure and Discretization of Surface Areas, Volumes, and Fluxes for Hexahedral Topology

A structured grid based on hexahedra will be used along with three parametric coordinates, as shown in *Figure 6-2*. The volume elements created will be referred to as cells, and the control surfaces (interfaces) will be referred to as faces. The grid structure is such that the geometry is fully defined once the coordinates of cell vertices have been specified. Faces are defined first in terms of these vertices; then cells are defined in terms of the already defined faces. For hexahedral topology, there are four vertices per face (eight per cell).

6.5.1. Statement of the Discretized Equation Using A Hexahedral, Structured Grid

For a hexahedral grid structure with cell-facet node notation as shown in *Figure 6-3*, the summation terms in Eq. (6.7) can be rewritten as:

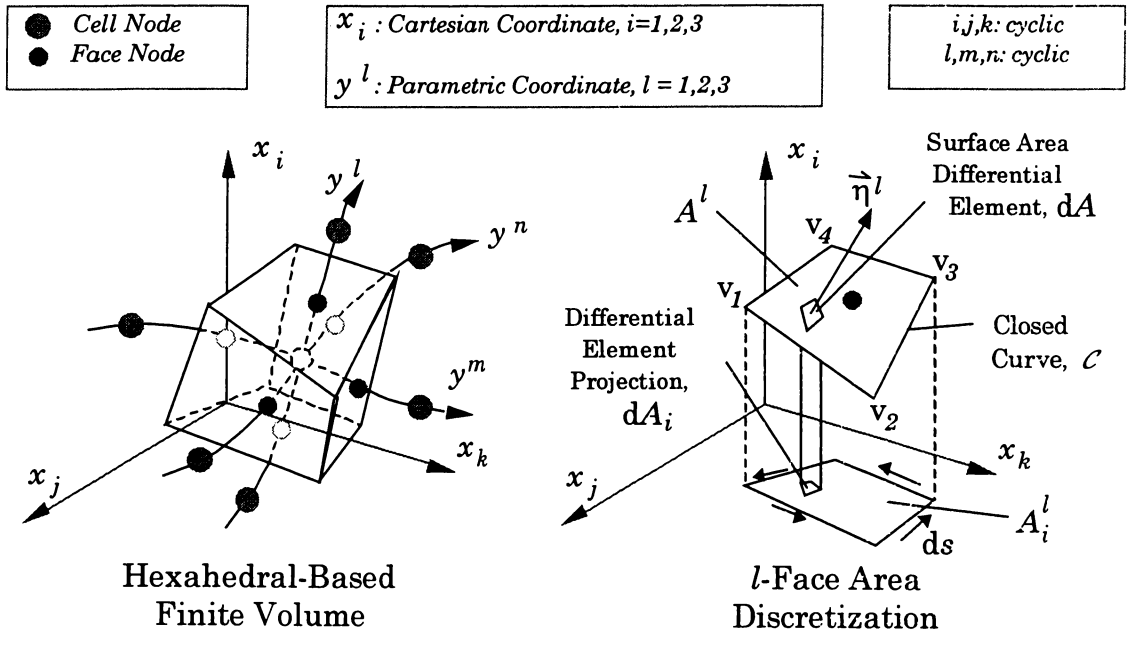

Figure 6-2. Variables Defining the Control-Volume Face Geometry

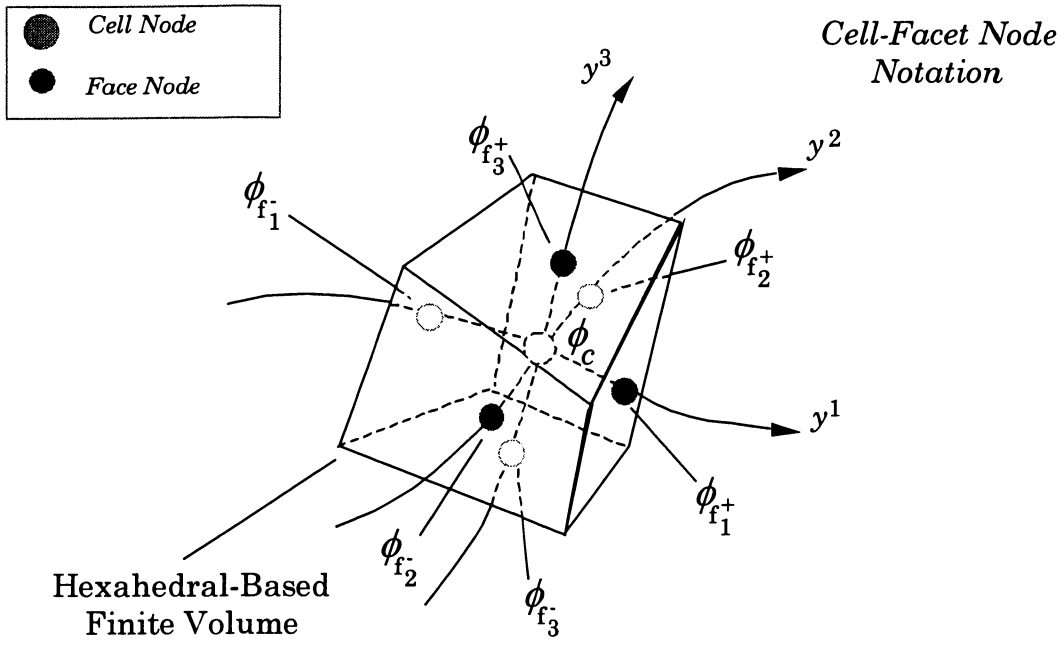

Figure 6-3. Identification of Face-Node Variables for a Structured-Grid Hexahedral Control Volume

$$\sum_{j=1}^{N} \vec{f}^{\phi} \bullet \vec{\eta}_o^j \, \Delta A^j = \sum_{j=1}^{3} \left[\vec{f}^{\phi} \bullet \vec{\eta}^j \, \Delta A^j \right]_{f_j^-}^{f_j^+}, \tag{6.8}$$

and

$$\sum_{j=1}^{N} \vec{u} \bullet \vec{\eta}_o^j \, \Delta A^j = \sum_{j=1}^{3} \left[\vec{u} \bullet \vec{\eta}^j \, \Delta A^j \right]_{f_j^-}^{f_j^+}, \tag{6.9}$$

where $\vec{\eta}^j$ is the face-normal unit vector consistent with the positive parametric direction, unlike $\vec{\eta}_o^j$, which was outward-oriented with respect to the control-volume surface. The equation for hexahedral, structure grid can be now obtained by substituting the above two equations in Eq. (6.7) as:

$$\frac{c \, \Delta \mathcal{V}}{\Delta \tau} \left(\phi_c - \phi_o \right) + \sum_{j=1}^{3} \left[\vec{f}^{\phi} \bullet \vec{\eta}^j \, \Delta A^j \right]_{f_j^-}^{f_j^+} = s \, \Delta \mathcal{V} + c \, \phi_c \sum_{j=1}^{3} \left[\vec{u} \bullet \vec{\eta}^j \, \Delta A^j \right]_{f_j^-}^{f_j^+}. \tag{6.10}$$

6.5.2. Face Area Discretization and Face-Node Positioning

The face area centroids are positioned at the average coordinates of these vertices; that is,

$$x_i^{\mathrm{f}} = \frac{1}{4}\sum_{\nu=1}^{4} x_{i,\nu}\,,\ i=1,2,3, \tag{6.11}$$

where ν is an index that denotes the face vertex. Face area components are calculated using Green's theorem, resulting in the following equation for the projected l-face area in direction i, with i, j, k cyclic:

$$A_i^l = \oint_C x_j \,\mathrm{d}s_k,\ (i,l)=1,2,3;\ (i,j,k)\ cyclic \tag{6.12}$$

where x_j is the j-coordinate $\mathrm{d}s_k$ is the projection of the arc element, ds in the k-direction. The above integral can be approximated as:

$$A_i^l = \sum_{\mu=1}^{4}\left[\bar{x}^j \Delta s_k\right]_{(\mu)},\ (i,l)=1,2,3;\ (i,j,k)\ cyclic \tag{6.13}$$

where $\bar{x}^j$ is the segment mid-point coordinate, Δs_k is the segment length, and μ is an index associated with the segment (face edge) connecting vertices.

The face area vector can now be determine by vector summation of its components:

$$\vec{A}^l = \sum_{i=1}^{3} A_i^l\ \vec{\varepsilon}_i\,,\ l=1,2,3\,. \tag{6.14}$$

The face area, then is calculated as:

$$A^l = \left(\sum_{i=1}^{3}\left[A_i^l\right]^2\right)^{1/2},\ l=1,2,3, \tag{6.15}$$

The face-normal unit vectors are expressed in terms of their components:

$$\vec{\eta}^j = \sum_{i=1}^{3}\eta_i^j\ \vec{\varepsilon}_i,\ j=1,2,3\,. \tag{6.16}$$

where the components are calculated based on area ratios above:

$$\eta_i^j = \frac{A_i^j}{A^j}, (i,j) = 1,2,3 \tag{6.17}$$

6.5.3. Cell Volume Discretization and Cell-Node Positioning

The cell node coordinates are calculated at the cell volume centroid, based on face geometry information. One method to calculate the coordinates of the volume centroid is to define a vector field a Cartesian unit vector:

$$\vec{F} = x_i \, \vec{\varepsilon}_i \, , \; i = 1 \text{ or } 2 \text{ or } 3 , \tag{6.18}$$

and integrating the field throughout the cell volume. The volume can be obtained, then by applying the Gauss' divergence theorem to express the volume integral in terms of area integrals, that is face areas and centroids:

$$\int_{\Delta \mathcal{V}} \nabla \bullet x_i \, \vec{\varepsilon}_i \, \mathrm{d}\, \mathcal{V} = \int_A x_i \, \vec{\varepsilon}_i \bullet \vec{\eta}_o \, \mathrm{d}\, A \, , \; i=1 \text{ or } 2 \text{ or } 3 \tag{6.19}$$

The resulting equation for the volume centroid is:

$$\Delta \mathcal{V} = \sum_{j=1}^{3} \left[x_i^{\mathrm{f}} A_i^j \right]_{\mathrm{f}_j^-}^{\mathrm{f}_j^-} \, , \; i = 1 \text{ or } 2 \text{ or } 3 \tag{6.20}$$

where x_i^{f} is the i-direction face area centroid, and A_i^j is the j-face-area component in the i-direction.

The coordinates of the cell volume centroid are calculated in a similar manner as the cell volume, but the vector field in the volume integral this time is defined as one-half of the square of the coordinate. To find the centroid coordinate in i-direction, the vector field is defined as:

$$\vec{F} = \frac{1}{2} x_i^2 \, \vec{\varepsilon}_i \, , \; i = 1 \, or \, 2 \, or \, 3 . \tag{6.21}$$

Application of the divergence theorem to the above vector field yields:

$$x_i^c \Delta\mathcal{V} = \int_{\Delta\mathcal{V}} \nabla\bullet\frac{1}{2}x_i^{\,2}\,\vec{\varepsilon}_i \,\mathrm{d}\,\mathcal{V} = \int_A \frac{1}{2}x_i^{\,2}\,\vec{\varepsilon}_i\bullet\vec{\eta}_o \,\mathrm{d}\,A\,, \tag{6.22}$$

which results in the following equation for the cell-volume centroid coordinate in the i-direction:

$$x_i^c = \frac{1}{2(\Delta\mathcal{V})}\sum_{j=1}^{3}\left[\left(x_i^f\right)^2 A_i^j\right]_{\mathrm{f}_j^-}^{\mathrm{f}_j^+}\,,\ i=1,2,3\,. \tag{6.23}$$

6.6. Discretization of Cell-Facet Fluxes

For convenience, cell-facet fluxes appearing in the discretized conservation equation will be decomposed into an advection/diffusion component, and a flux-generation component. This is done by rewriting the dimensionless flux vector in Eq. (5.61) as:

$$\vec{f}^{\,\phi} = \vec{f}^{\,\phi,AD} + \vec{h}\,, \tag{6.24}$$

where

$$\vec{f}^{\,\phi,AD} = c\,\vec{u}\,\phi - \gamma\nabla\phi \tag{6.25}$$

is the advection/diffusion contribution. Discretization of the two contributions types will be done separately. Substitution of Eq. (6.24) in Eq. (6.10) results in the following discretized form of the general conservation equation:

$$\frac{c\,\Delta\mathcal{V}}{\Delta\tau}\left(\phi-\phi_0\right) + \sum_{j=1}^{3}\left[\vec{f}^{\,\phi,AD}\bullet\vec{\eta}^{\,j}\,A^j\right]_{\mathrm{f}_j^-}^{\mathrm{f}_j^+} = \tilde{b}^{\phi} + c\,\phi\sum_{j=1}^{3}\left[\vec{u}\bullet\vec{\eta}^{\,j}\,A^j\right]_{\mathrm{f}_j^-}^{\mathrm{f}_j^+}\,, \tag{6.26}$$

where

$$\tilde{b}^{\phi} = s\,\Delta\mathcal{V} - \sum_{j=1}^{3}\left[\vec{h}\bullet\vec{\eta}^{\,j}\,A^j\right]_{\mathrm{f}_j^-}^{\mathrm{f}_j^+} = s\,\Delta\mathcal{V} - \sum_{j=1}^{3}\left[H^j\right]_{\mathrm{f}_j^-}^{\mathrm{f}_j^+}\,. \tag{6.27}$$

Eq. (6.26) may be rewritten as:

$$\frac{c\,\Delta\mathcal{V}}{\Delta\tau}\left(\phi_c-\phi_o\right)+\sum_{j=1}^{3}\left[\tilde{F}_j^{\phi,AD}\right]_{f_j^-}^{f_j^+}=\tilde{b}^{\phi}+c\,\phi_c\sum_{j=1}^{3}\left[Q^j\right]_{f_j^-}^{f_j^+}, \tag{6.28}$$

where

$$\tilde{F}_j^{\phi,AD}=\left(c\,\vec{u}\,\phi-\gamma\,\nabla\phi\right)\bullet\vec{\eta}^{\,j}\;A^j \tag{6.29}$$

is the net advection/diffusion flow crossing the j-face, and

$$Q^j=\vec{u}\bullet\vec{\eta}^{\,j}\;A^j \tag{6.30}$$

is the volumetric flow rate crossing the j-face. The discretization of the advection/diffusion contribution is presented next.

6.6.1. Advection/Diffusion Cell-Facet Flux Discretization

The task in this section is to obtain algebraic equations for the advection/diffusion fluxes, so they can be substituted in the discretized conservation equation. The advection/diffusion flow in Eq. (6.29) can be expressed in terms of the face-normal velocity and the partial derivative of the dependent variable in the face-normal direction as:

$$\tilde{F}_j^{\phi,AD}=\left(c\,v^j\,\phi-\gamma\,\phi_{z^j}\right)A^j, \tag{6.31}$$

where

$$v^j=\vec{u}\bullet\vec{\eta}^{\,j}, \tag{6.32}$$

$$\phi_{z^j}=\nabla\phi\bullet\vec{\eta}^{\,j}, \tag{6.33}$$

c is the general capacity per unit volume, and γ is the general diffysivity.

The volumetric flow rate can alternatively be expressed in terms of the j-face normal velocity and area as:

$$Q^j=v^jA^j. \tag{6.34}$$

The objective now is to find the net advection/diffusion flow in Eq. (6.31) in algebraic form. Since the primary objective at this point is to have a reliable

interpolation scheme, whose implementation presents the minimal amount of effort, an exponential scheme was selected for the discretization of advection-diffusion flux. It is understood that this scheme results in greater amounts of false when compared to other more sophisticated schemes. In the event that accuracy becomes an issue, false diffusion could be reduced by refining the grid. Optimization of the interpolation scheme will be left for further research, and is not within the scope of this research.

The face flux is discretized based on the cell-face node arrangement shown in *Figure 6-4.* The sketch is shown in two dimensions for clarity, but the actual locations of the cell nodes and the direction of the velocity vector do not have to lie necessarily on the plane shown. The central idea for flux discretization consists of calculating the flux across the face based on the normal velocity and the values of the dependent variable at auxiliary cell nodes. These nodes are located along lines orthogonal to the face, and passing through the face node.

The advection/diffusion flow defined in Eq. (6.31) can be rewritten as:

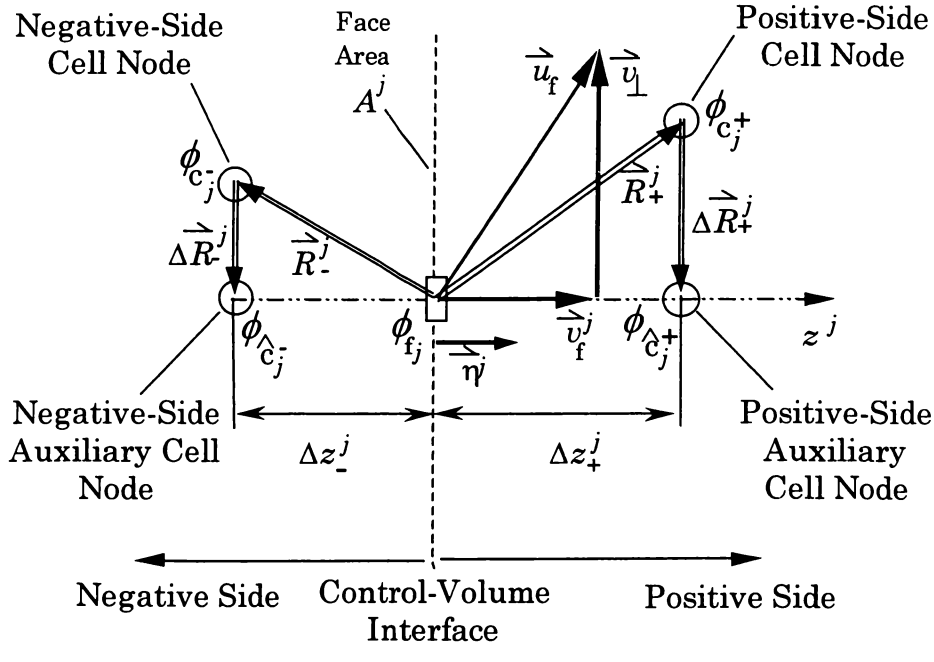

Figure 6-4. Geometry Elements Involved in the Facet-Based Flux Discretization

$$\tilde{F}_j^{\phi,AD} = \tilde{f}_{j_f}^{AD} A^j , \tag{6.35}$$

where

$$\tilde{f}_{j_f}^{AD} = \left[c\, v^j \phi - \gamma \phi_{z^j} \right]_{j_f} \tag{6.36}$$

is face-normal flux for a particular face "j", c is the general capacity per unit volume, $\bar{u}$ is the velocity vector, and γ is the general diffusivity. The normal component of the flux vector can be obtained by performing a scalar product with the face-normal unit vector. To evaluate the advection term, the assumption is made that no discontinuities exist in the dependent variable across the interface. It will also be assumed that only one homogeneous fluid phase exists within each fluid sub-domain, and that the fluid velocity is continuous. Therefore, the normal velocity approaching from the two sides of the interface reaches a unique value at the interface, and so does the dependent variable. For the diffusion term, discretization of the fluxes must be general enough to allow for different materials on both sides of an interface, as it may apply for the energy transfer between two solid materials.

The above flux equations can be discretized in terms of Peclet number and cell-node variables evaluated on the negative (-) and positive (+) of the face sides (where "+" indicates positive j-direction) using weighing functions of the Peclet number as:

$$\tilde{f}_{j_\pm}^{AD} = \pm \left(\frac{\gamma_\pm}{\Delta z_\pm^j} \right) \left[\mathcal{A}(\mp P_e^\pm)\, \phi_{f_j} - \mathcal{A}(\pm P_e^\pm)\, \phi_{\hat{c}_j^\pm} \right]_j \tag{6.37}$$

where the subscripts or superscripts (+) and (-) denote association with the positive (+) or negative (-) side of the particular face. Peclet numbers are evaluated at either side of face as:

$$P_e^\pm \Big|_j = \frac{c\, v^j\, \Delta z_\pm^j}{\gamma_\pm} , \tag{6.38}$$

f_j denotes the particular j-face,

$\hat{c}_j^-$ denotes the cell auxiliary node on the negative side of the j-face, and

$\hat{c}_j^+$ denotes the cell auxiliary node on the positive side of the j-face.

Advection/Diffusion Interpolation Scheme

The weighing factor, $\mathcal{A}(P_e)$, depends on the interpolation scheme(s) used to obtain the dependent variable and its derivative at the face-node location. As mentioned earlier, the exponential differencing scheme will be used to interpolate advection and diffusion fluxes at face locations. The interpolation function results from solving the one-dimensional advection/diffusion differential equation. To bypass the use of the exponential function in the limit of zero velocity and for large velocity values a piece-wise function is used as follows:

$$\mathcal{A}(P_e)=\begin{cases} 1-P_e, & |P_e|<P_{e\min} \\ -P_e, & P_e<-P_{e\max} \\ 0, & P_e>P_{e\max} \\ \dfrac{P_e}{\exp(P_e)-1}, & P_{e\min}\le|P_e|\le P_{e\max}, \end{cases} \tag{6.39}$$

where

$$P_{e\min}=1\times10^{-4}, \tag{6.40.a}$$

and

$$P_{e\max}=40. \tag{6.40.b}$$

The values for these constants were selected to provide an exponential function for a wide range on Peclet numbers, while avoiding the singularities and overflows in the limits of Pe = 0 and infinity. The function $\mathcal{A}(P_e)$ has the following property:

$$\mathcal{A}(-P_e)=P_e+\mathcal{A}(P_e). \tag{6.41}$$

This property will be used to rewrite the flux equations in Eq. (6.37) such that the Peclet number appearing in the function $\mathcal{A}(P_e)$ has a positive sign for the left-side flux equation, and a negative sign for the right-side flux equation:

$$\tilde{f}_{j_\pm}^{\phi,AD} = \left(\frac{\gamma_\pm}{\Delta z_\pm^j}\right)\left[\pm\mathcal{A}(\mp P_e^\pm)\,\phi_{f_j} \mp \mathcal{A}(\mp P_e^\pm)\,\phi_{\hat{c}_j^+} + P_e^\pm \phi_{\hat{c}_j^\pm}\right]_j \tag{6.42}$$

To obtain the net advection/diffusion face flux approaching from both sides of the face, the above equations are substituted in Eq. (6.35):

$$\tilde{F}_{j_\pm}^{\phi,AD} = \left(\frac{\gamma_\pm}{\Delta z_\pm^j}\right)\left[\pm\mathcal{A}(\mp P_e^\pm)\,\phi_{f_j} \mp \mathcal{A}(\mp P_e^\pm)\,\phi_{\hat{c}_j^\pm} + P_e^\pm \phi_{\hat{c}_j^\pm}\right]_j A^j, \tag{6.43}$$

where it is understood that all of the terms in the bracket are evaluated relative to, and have meaning only associated with face j. At this point, it is convenient to introduce the interface *conductance* coefficients, which will eventually become the coefficients of the discretization equation as:

$$a_{j_\pm}^\phi = \left(\frac{\gamma_\pm}{\Delta z_\pm^j}\right)\mathcal{A}(\mp P_e^\pm)A^j, \tag{6.44}$$

Two sets of coefficients are associated with each interface: one relates to the cell node on the positive side, and one relates to the cell node on the negative side. Substitution of the above definitions in Eq. (6.43) and using the definitions of the Peclet number in Eq. (6.38) yields the following general equations for the advection/diffusion flow crossing cell faces:

$$\tilde{F}_{j_\pm}^{\phi,AD} = \mp a_{j_\pm}^\phi \phi_{\hat{c}_j^\pm} \pm a_{j_\pm}^\phi \phi_{f_j} + Q^j \phi_{\hat{c}_j^\pm}, \tag{6.45}$$

where Q^j is the net volumetric flow rate crossing the j-cell-face.

Calculation of the Dependent Variable at Auxiliary Cell Nodes

The value of the dependent variable at the auxiliary cell-node locations can be obtained from cell nodes by adding the increment from the cell node to the auxiliary node. For the auxiliary cell nodes on the two sides of the interface, the dependent variable is calculated as:

$$\phi_{\hat{c}_j^\pm} = \phi_{c_j^\pm} + \Delta\phi_{c_j^\pm}, \tag{6.46}$$

where

c_j^- denotes the cell node on the negative side of the j-face, and

c_j^+ denotes the cell node on the positive side of the j-face.

The increment from the cell node to the auxiliary node can be determined if the gradient and the position vector of the auxiliary node relative to the cell node are known. The gradient of the dependent variable can be determined from face values by applying Gauss' divergence theorem as follows:

$$\int_{\mathcal{V}} \nabla \cdot \left(\phi \vec{\varepsilon}_i\right) \mathrm{d}\mathcal{V} = \int_{\mathcal{V}} \phi_{x_i} \mathrm{d}\mathcal{V} = \int_A \phi \vec{\varepsilon}_i \cdot \vec{\eta} \, \mathrm{d}A, \; i = 1,2,3 . \tag{6.47}$$

The above integral can approximate a men value for the gradient component:

$$\phi_{x_i} = \frac{1}{\mathcal{V}} \sum_{j=1}^{3} \left[\phi_{\mathrm{f}_j} \eta_i^j A_{\mathrm{f}}^j \right]_{\mathrm{f}_j^-}^{\mathrm{f}_j^+} , \tag{6.48}$$

where

$\mathcal{V}$ is the cell volume,

η_i^j is the dependent variable at the j-face,

ϕ_{f_j} is the i-Cartesian component of the j-face normal unit vector, always defined in the parametric-coordinate direction, and

A_{f}^j is the j-face area.

The dependent-variable increments from the cell-node to the auxiliary node can be expressed as:

$$\Delta\phi_{c_j^\pm} = \Delta\vec{R}\big|_{c_j^\pm} \cdot \nabla\phi\big|_{c_j^\pm} , \tag{6.49}$$

where $\pm$ indicates whether the cell node is on the negative or positive side of the face, and $\nabla\phi$ is the gradient of the dependent variable, which is readily available in terms of its components as:

$$\nabla\phi = \sum_{i=1}^{3} \phi_{x_i} \vec{\varepsilon}_i . \tag{6.50}$$

6.6.2. General Conservation Equation in Algebraic Form

In the preceding section, the advection/diffusion flow crossing any cell face was discretized in terms of the adjacent cell-node values of the dependent variable. This result can now be used to arrive at the discretized form of the general conservation equation. A change of notation is required to express quantities based on cell nodes as opposed to face nodes. The cell-facet arrangement and notation is shown for a hexahedral grid in *Figure 6-3.*

For a general parametric coordinate direction, the advection/diffusion flows for faces on the positive- and negative-sides relative to the cell node are given as:

$$\tilde{F}^{\phi,AD}_{\mathrm{f}_j^{\pm}} = \pm a^{\phi}_{\mathrm{f}_j^{\pm}} \, \phi_{\hat{\mathrm{c}}_{\mathrm{f}_j^{\pm}}} \mp a^{\phi}_{\mathrm{f}_j^{\pm}} \, \phi_{\mathrm{f}_j^{\pm}} + Q_{\mathrm{f}_j^{\pm}} \phi_{\hat{\mathrm{c}}_{\mathrm{f}_j^{\pm}}} , \tag{6.51}$$

where

f_j^{+} denotes the positive-side face node associated with the integration cell,

f_j^{-} denotes the negative-side face node associated with the integration cell,

$\phi_{\hat{\mathrm{c}}_{\mathrm{f}_j^{+}}}$ denotes the cell-auxiliary-node value associated with face f_j^{+},

$\phi_{\hat{\mathrm{c}}_{\mathrm{f}_j^{-}}}$ denotes the cell-auxiliary-node value associated with face f_j^{-},

and the a-coefficients are defined in terms of the negative-side cell-node with respect to the positive-side face, and the positive-side cell-node with respect to the negative - side face:

$$a^{\phi}_{\mathrm{f}_j^{\pm}} = a^{\phi}_{j_{\mp}} \Big|_{\mathrm{f}_j^{\pm}} , \tag{6.52}$$

To expressed the quantity-flow equations based on values of the dependent variable at cell-node locations, the definitions in Eq. (6.46) is applied to Eq. (6.51) resulting in the following quantity-flow equations:

$$\tilde{F}^{\phi,AD}_{\mathrm{f}_j^{\pm}} = \pm a^{\phi}_{\mathrm{f}_j^{\pm}} \left(\phi_{\mathrm{c}} + \Delta\phi_{\mathrm{c}_{\mathrm{f}_j^{\pm}}} \right) \mp a^{\phi}_{\mathrm{f}_j^{\pm}} \, \phi_{\mathrm{f}_j^{\pm}} + Q_{\mathrm{f}_j^{\pm}} \left(\phi_{\mathrm{c}} + \Delta\phi_{\mathrm{c}_{\mathrm{f}_j^{\pm}}} \right), \tag{6.53}$$

where

$\Delta\phi_{c_{f_j^{\pm}}}$ denotes the increment of the dependent variable from the cell node to the auxiliary node associated with face f_j^+ or face f_j^-.

Substitution of the above quantity-flow equations in the discretized form of the conservation equation, Eq. (6.28) yields:

$$\left.\begin{aligned}&\frac{c\,\Delta\mathcal{V}}{\Delta\tau}\left(\phi_c-\phi_o\right)+\sum_{j=1}^{3}\left[\left(+a^{\phi}_{f_j^+}\left(\phi_c+\Delta\phi_{c_{f_j^+}}\right)-a^{\phi}_{f_j^+}\,\phi_{f_j^+}+Q_{f_j^+}\left(\phi_c+\Delta\phi_{c_{f_j^+}}\right)\right)+\right.\\&\left.-\left(-a^{\phi}_{f_j^-}\left(\phi_c+\Delta\phi_{c_{f_j^-}}\right)+a^{\phi}_{f_j^-}\,\phi_{f_j^-}+Q_{f_j^-}\left(\phi_c+\Delta\phi_{c_{f_j^-}}\right)\right)\right]=\\&=\tilde{b}^{\phi}+c\,\phi_c\sum_{j=1}^{3}\left[Q_{f_j^+}-Q_{f_j^-}\right]\end{aligned}\right\}\quad(6.54)$$

Factoring-out the cell-node dependent variable, and separating summations containing face values and increment values yields:

$$\left.\begin{aligned}&\phi_c\left(\frac{c\,\Delta\mathcal{V}}{\Delta\tau}+\sum_{j=1}^{3}\left(a^{\phi}_{f_j^+}+a^{\phi}_{f_j^-}\right)+c\sum_{j=1}^{3}\left(Q_{f_j^+}-Q_{f_j^-}\right)\right)-\frac{c\,\Delta\mathcal{V}}{\Delta\tau}\phi_o+\\&-\sum_{j=1}^{3}\left(a^{\phi}_{f_j^+}\,\phi_{f_j^+}+a^{\phi}_{f_j^-}\phi_{f_j^-}\right)+\sum_{j=1}^{3}\left(\left(a^{\phi}_{f_j^+}+Q_{f_j^+}\right)\Delta\phi_{c_{f_j^+}}+\left(a^{\phi}_{f_j^-}-Q_{f_j^-}\right)\Delta\phi_{c_{f_j^-}}\right)\\&=\tilde{b}^{\phi}+c\,\phi_c\sum_{j=1}^{3}\left[Q_{f_j^+}-Q_{f_j^-}\right]\end{aligned}\right\}\quad(6.55)$$

Notice that the volumetric source on the right hand-side of the equation, which was retained in when converting from the Lagrangian to the Eulerian method of description cancels with an identical term on the left-hand side of the equation. Regrouping terms such that the cell-node dependent variable is left alone on the left-hand side yields:

$$\left.\begin{aligned}\phi_c\left(a_o^\phi+\sum_{j=1}^{3}\left(a_{f_j^+}^\phi+a_{f_j^-}^\phi\right)\right)&=\sum_{j=1}^{3}\left(a_{f_j^+}^\phi\,\phi_{f_j^+}+a_{f_j^-}^\phi\,\phi_{f_j^-}\right)+\tilde{b}^\phi+a_o^\phi\phi_o+\\-\sum_{j=1}^{3}&\left(\left(a_{f_j^+}^\phi+Q_{f_j^+}\right)\Delta\phi_{c_{f_j^+}}+\left(a_{f_j^-}^\phi-Q_{f_j^-}\right)\Delta\phi_{c_{f_j^-}}\right)\end{aligned}\right\}\tag{6.56}$$

where

$$a_o^\phi=\frac{c\,\Delta\mathcal{V}}{\Delta\tau}.\tag{6.57}$$

A final form of the general conservation algebraic equation is stated as:

$$a_c^\phi\,\phi_c=\sum_{j=1}^{3}\left(a_{f_j^+}^\phi\,\phi_{f_j^+}+a_{f_j^-}^\phi\,\phi_{f_j^-}\right)+b_c^\phi\tag{6.58}$$

where

$$a_c^\phi=a_o^\phi+\sum_{j=1}^{3}\left(a_{f_j^+}^\phi+a_{f_j^-}^\phi\right),\tag{6.59}$$

is the coefficient of the cell-node dependent variable, and

$$\left.\begin{aligned}b_c^\phi=s\,\Delta\mathcal{V}-\sum_{j=1}^{3}&\left[H_{f_j^+}^j-H_{f_j^-}^j\right]+a_o^\phi\,\phi_o+\\-\sum_{j=1}^{3}&\left[\left(a_{f_j^+}^\phi+Q_{f_j^+}\right)\Delta\phi_{c_{f_j^+}}+\left(a_{f_j^-}^\phi-Q_{f_j^-}\right)\Delta\phi_{c_{f_j^-}}\right]\end{aligned}\right\}\tag{6.60}$$

is the constant term involving volumetric sources, surface sources, the contribution from the previous-time-step value of the dependent variable, and the contributions from cell-node-to-auxiliary-node dependent-variable increments.

6.6.3. General Boundary Condition

An equation for the general boundary condition can be obtained by enforcing flux balance on the cell facet. Flux conservation across the cell facet can be stated as:

$$\tilde{F}^{\phi,AD}_{j_-} + S^{\phi}_{j} = \tilde{F}^{\phi,AD}_{j_+}, \tag{6.61}$$

where S^{φ}_{j} is the quantity-flow generated at the surface. Substituting Eq. (6.45) into the above equation yields:

$$+a^{\phi}_{j_-}\phi_{\hat{c}^-_j} - a^{\phi}_{j_-}\phi_{f_j} + Q^j\phi_{\hat{c}^-_j} + S^{\phi}_{j} = -a^{\phi}_{j_+}\phi_{\hat{c}^+_j} + a^{\phi}_{j_+}\phi_{f_j} + Q^j\phi_{\hat{c}^+_j}. \tag{6.62}$$

The resulting value of the dependent variable at the face node can be obtained from the above equation as:

$$\phi_{f_j} = \frac{\left(a^{\phi}_{j_-} + Q^j\right)\phi_{\hat{c}^-_j} + \left(a^{\phi}_{j_+} - Q^j\right)\phi_{\hat{c}^+_j} + S^{\phi}_{j}}{\left(a^{\phi}_{j_-} + a^{\phi}_{j_+}\right)}, \tag{6.63}$$

or in a more general form:

$$\phi_{f_j} = \frac{G^{\phi}_{j_-}\phi_{\hat{c}^-_j} + G^{\phi}_{j_+}\phi_{\hat{c}^+_j} + S^{\phi}_{j}}{\left(G^{\phi}_{j_-} + G^{\phi}_{j_+}\right)}, \tag{6.64}$$

where the G's are *conductances* analogous to those in a conductor network. For internal interfaces, the G's are calculated as

$$G^{\phi}_{j_\pm} = a^{\phi}_{j_\pm} \mp Q^j. \tag{6.65}$$

The above general boundary-condition equation for internal cell boundaries, Eq. (6.64) can be modified to handle convective-type boundary conditions on solution-domain (external) boundaries. For the general convective boundary condition imposed on a cell's "negative-side" face, the face-node value is calculated as:

$$\phi_{f_j} = \frac{G^{\phi}_{j_-} \phi^{e}_{f_j} + G^{\phi}_{j_+} \phi_{\hat{c}^{+}_j} + S^{\phi}_{j}}{\left(G^{\phi}_{j_-} + G^{\phi}_{j_+} \right)}, \tag{6.66}$$

where

$$G^{\phi}_{j_-} = h^{\phi}_{j} A^{j}, \tag{6.67.a}$$

$$G^{\phi}_{j_+} = a^{\phi}_{j_+}, \tag{6.67.b}$$

$\phi^{e}_{f_j}$ is the "environmental" value of ϕ associated with the face, and

h^{ϕ}_{j} is the effective conductance per unit area associated with the face.

For the general convective boundary condition imposed on a cell's "positive-side" face, the face-node value is calculated as:

$$\phi_{f_j} = \frac{G^{\phi}_{j_-} \phi_{\hat{c}^{-}_j} + G^{\phi}_{j_+} \phi^{e}_{f_j} + S^{\phi}_{j}}{\left(G^{\phi}_{j_-} + G^{\phi}_{j_+} \right)}, \tag{6.68}$$

where

$$G^{\phi}_{j_-} = a^{\phi}_{j_-}, \text{ and} \tag{6.69.a}$$

$$G^{\phi}_{j_+} = h^{\phi}_{j} A^{j}. \tag{6.69.b}$$

6.7. Conservation Equations in Algebraic Forms

Next, the above general algebraic conservation equation given above is applied to each of the conservation equations.

Mass Conservation. The algebraic equation for mass conservation can be obtained by direct integration of Eq. (5.79.a) over the cell volume and time interval:

$$\int_{\Delta\tau} \int_{\Delta\mathcal{V}} \hat{\rho} \nabla \cdot \vec{u} \, \mathrm{d}\mathcal{V} \, \mathrm{d}\tau = 0. \tag{6.70}$$

Time cancels from the equation as the fluxes are evaluated as representative values held constant for the time interval. The following equation is obtained, with the flux terms evaluated at the end of the time interval, for consistency with the time-implicit discretization of fluxes used in the general equation:

$$\int_{\Delta\mathcal{V}} \nabla\bullet\vec{u}\,\mathrm{d}\,\mathcal{V} = 0\,. \tag{6.71}$$

The volume integral can be transformed into a surface integral over the cell surface by applying Green's divergence theorem:

$$\int_{A} \vec{u}\bullet\vec{\eta}_o\,\mathrm{d}\,A\,. \tag{6.72}$$

Discretization of the above equation yields:

$$\sum_{j=1}^{3}\left(v_{\mathrm{f}}^{j}\,A_{\mathrm{f}}^{j}\right)_{\mathrm{f}_j^-}^{\mathrm{f}_j^+} = 0\,, \tag{6.73}$$

where

$$v_{\mathrm{f}}^{j} = v^{j}\Big|_{\mathrm{f}} = \vec{u}\bullet\vec{\eta}^{\,j}\Big|_{\mathrm{f}}\,, \tag{6.74}$$

is the j-face normal velocity, consistent with the parametric direction, and A_{f}^{j} is the cell-facet area.

Momentum Conservation. The algebraic equation for momentum conservation uses the following definitions.

$$\phi = u_i\,,\ a_{\mathrm{c}}^{\phi} = a_{\mathrm{c}}^{u}\,,\ a_j^{\phi} = a_j^{u}\,,\ s = S_i^{u}\,,\ H^j = A_i^j p\,. \tag{6.75}$$

Substitution of the above in Eq. (6.58) and setting $\mathcal{V}_{\mathrm{c}} = \Delta\mathcal{V}$ yields

$$a_{\mathrm{c}}^{u}\,u_{i,\mathrm{c}} = \sum_{j=1}^{3}\left(a_{\mathrm{f}_j^+}^{u}\,u_{i\,\mathrm{f}_j^+} + a_{\mathrm{f}_j^-}^{u}\,u_{i\,\mathrm{f}_j^-}\right) + b_{\mathrm{c}}^{u_i}\,,\ i = 1,2,3\,, \tag{6.76}$$

where

$$a^u_{\mathrm{f}^\pm_j} = a^u_{j_\mp}\Big|_{\mathrm{f}^\pm_j} = \left(\frac{\hat{\mu}_\mp}{\Delta z^j_\mp}\right)\mathcal{A}(\pm P_e^{j\mp})A^j\Bigg|_{\mathrm{f}^\pm_j} \tag{6.77}$$

$$P_e^{j()} = \frac{\hat{\rho}_{()}\, v^j\, \Delta z^j_{()}}{\hat{\mu}_{()}} \tag{6.78}$$

$$a^u_{\mathrm{c}} = a^u_{\mathrm{o}} + \sum_{j=1}^{3}\left(a^u_{\mathrm{f}^+_j} + a^u_{\mathrm{f}^-_j}\right) \tag{6.79}$$

$$\begin{aligned} b^{u_i}_{\mathrm{c}} = {} & S^{u_i}\,\mathcal{V}_{\mathrm{c}} - \sum_{j=1}^{3}\left(A^j_i p\Big|_{\mathrm{f}^+_j} - A^j_i p\Big|_{\mathrm{f}^-_j}\right) + a^u_{\mathrm{o}}\, u_{i,\mathrm{o}} + \\ & -\sum_{j=1}^{3}\left[\left(a^u_{\mathrm{f}^+_j} + Q_{\mathrm{f}^+_j}\right)\Delta u_{i,\mathrm{c}}{}_{\mathrm{f}^+_j} + \left(a^u_{\mathrm{f}^-_j} - Q_{\mathrm{f}^-_j}\right)\Delta u_{i,\mathrm{c}}{}_{\mathrm{f}^-_j}\right] \end{aligned} \tag{6.80}$$

Energy Conservation. The algebraic equation for energy conservation uses the following definitions.

$$\phi = t,\ a^\phi_{\mathrm{c}} = a^t_{\mathrm{c}},\ a^\phi_j = a^t_j,\ s = 0,\ H^j = 0\,. \tag{6.81}$$

Substitution of the above in Eq. (6.58) yields

$$a^t_{\mathrm{c}}\, t_{\mathrm{c}} = \sum_{j=1}^{3}\left(a^t_{\mathrm{f}^+_j}\, t_{\mathrm{f}^+_j} + a^t_{\mathrm{f}^-_j}\, t_{\mathrm{f}^-_j}\right) + b^t_{\mathrm{c}} \tag{6.82}$$

where

$$a^t_{\mathrm{f}^\pm_j} = a^t_{j_\mp}\Big|_{\mathrm{f}^\pm_j} = \left(\frac{\hat{k}_\mp}{\Delta z^j_\mp}\right)\mathcal{A}(\pm P_e^{j\mp})A^j\Bigg|_{\mathrm{f}^\pm_j} \tag{6.83}$$

$$P_e^{j()} = \frac{\hat{c}_{()}\, v^j\, \Delta z^j_{()}}{\hat{k}_{()}} \tag{6.84}$$

$$a^t_{\mathrm{c}} = a^t_{\mathrm{o}} + \sum_{j=1}^{3}\left(a^t_{\mathrm{f}^+_j} + a^t_{\mathrm{f}^-_j}\right) \tag{6.85}$$

$$b_{\mathrm{c}}^{t} = a_{\mathrm{o}}^{t}\, t_{\mathrm{o}} - \sum_{j=1}^{3}\left[\left(a_{\mathrm{f}_j^+}^{t} + Q_{\mathrm{f}_j^+}\right)\Delta t_{\mathrm{c}_{\mathrm{f}_j^+}} + \left(a_{\mathrm{f}_j^-}^{t} - Q_{\mathrm{f}_j^-}\right)\Delta t_{\mathrm{c}_{\mathrm{f}_j^-}}\right] \tag{6.86}$$

The above equations are written in terms of boundary conditions specified at the control-volume faces. These boundary conditions may be either imposed, as in the case of a domain boundary, or calculated as part of the solution, as in the case of field-internal boundaries, as will be shown next.

6.7.1. Boundary Conditions for the Momentum Conservation Equations

For imposed boundary velocity, u_{i,f_j}^{ν}, the face velocity assumes the specified value,

$$u_{i,\mathrm{f}_j} = u_{i,\mathrm{f}_j}^{b},\ i = 1,2,3. \tag{6.87}$$

The equation for the face-node value for "internal" field boundaries of the discretized space domain is calculated from Eq. (6.64) as:

$$u_{i,\mathrm{f}_j} = \frac{\left(G_{j_-}^{u}\ u_{i,\hat{\mathrm{c}}_j^-} + G_{j_+}^{u}\ u_{i,\hat{\mathrm{c}}_j^+}\right)}{\left(G_{j_-}^{u} + G_{j_+}^{u}\right)},\ i = 1,2,3 \tag{6.88}$$

where

$u_{i,\hat{\mathrm{c}}_j^-}$ and $u_{i,\hat{\mathrm{c}}_j^+}$ are the auxiliary-node Cartesian velocities on the negative- and positive directions, respectively, relative to the face, and

$G_{j_-}^{u} = a_{j_-}^{u} + Q^{j}$, and (6.89.a)

$G_{j_+}^{u} = a_{j_+}^{u} - Q^{j}$ (6.89.b)

are the momentum conductances to auxiliary node locations.

For the imposed-normal-velocity boundary condition, the Cartesian face velocity must be "scaled" to yield the imposed value for the normal velocity. If m and m-1 denote the current and previous outer-loop iteration levels, then the Cartesian face velocity for the new iteration level is calculated as

$$u_{i,\mathrm{f}_j}^{m} = u_{i,\mathrm{f}_j}^{m-1} + \left[\left(v^{j,m} - v^{j,m-1}\right)\eta_i^j\right]_{\mathrm{f}_j}, \quad (i,j) = 1,2,3 \tag{6.90}$$

where η_i^j is the j-face-normal unit-vector component in the i-Cartesian direction.

6.7.2. Boundary Conditions for the Energy Equation

For imposed boundary temperature, $t_{\mathrm{f}_j}^{\nu}$, the face temperature assumes the specified value:

$$t_{\mathrm{f}_j} = t_{\mathrm{f}_j}^{b}. \tag{6.91}$$

The boundary condition for the energy equation on internal faces is expressed as:

$$t_{\mathrm{f}_j} = \frac{\left(G_{j_-}^t \; t_{\hat{\mathrm{c}}_j^-} + G_{j_+}^t \; t_{\hat{\mathrm{c}}_j^+} + S_{\mathrm{f}_j}^t\right)}{\left(G_{j_-}^t + G_{j_+}^t\right)} \tag{6.92}$$

where

$t_{\hat{\mathrm{c}}_j^-}$ and $t_{\hat{\mathrm{c}}_j^+}$ are the auxiliary-node Cartesian velocities on the negative- and positive directions, respectively, relative to the face, and directions, respectively, relative to the face,

$S_{\mathrm{f}_j}^{\nu}$ is a surface heat-generation term, and the thermal conductances are calculated as:

$$G_{j_-}^t = a_{j_-}^t + Q^j, \text{ and} \tag{6.93.a}$$

$$G_{j_+}^t = a_{j_+}^t - Q^j \tag{6.93.b}$$

For the convective boundary condition imposed on the negative side of the face, the equation becomes

$$t_{\mathrm{f}_j} = \frac{G_{j_-}^t \; t_{\mathrm{f}_j}^e + G_{j_+}^t \; t_{\hat{\mathrm{c}}_j^+} + S_j^t}{\left(G_{j_-}^t + G_{j_+}^t\right)}, \tag{6.94}$$

and the G's are calculated as:

$$G^t_{j_-} = h^t_{j_-} A^j, \text{ and} \tag{6.95.a}$$

$$G^t_{j_+} = a^t_{j_+}. \tag{6.95.b}$$

For the general convective boundary condition imposed on the positive side of the face, the equation becomes

$$t_{\mathrm{f}_j} = \frac{G^t_{j_-} t_{\hat{\mathrm{c}}_j^-} + G^t_{j_+} t^e_{\mathrm{f}_j} + S^t_j}{\left(G^t_{j_-} + G^t_{j_+}\right)}, \tag{6.96}$$

and the G's are calculated as

$$G^t_{j_-} = a^t_{j_-}, \text{ and} \tag{6.97.a}$$

$$G^t_{j_+} = h^t_{j_+} A^j. \tag{6.97.b}$$

The following definitions apply to the convective boundary conditions above:

$h^t_{j_-}$ and $h^t_{j_+}$ denote the heat transfer coefficients as imposed on the negative and positive sides of the face, respectively, and

$t^e_{\mathrm{f}_j}$ denotes the "environmental" temperature at boundary f_j.

6.7.3. Closure

The algebraic equations for momentum and energy conservation derived above can be solved only if face velocities are known. Furthermore, the momentum equations contain face-pressure values, which are yet to be determined. The method for determining face velocities and pressure values is the subject of the next section.

6.8. Solution Method Requirements

Before initiating the development of the solution procedure, a set of requirements will be laid out:

(1) the pressure field and the face-velocity field must be self-consistent in satisfying mass conservation, and

(2) momentum and energy equations must be solved only after mass conservation is enforced.

A solution procedure with the above requirements should be "robust" in the sense that all conservation laws are satisfied self-consistently throughout the iteration process. Not only the pressure field is self-consistent with mass conservation, but the energy and momentum equations are solved with mass-conserving velocities, which should yield better solutions. This is in contrast with other solution procedures, which solve the momentum equation first based on "guessed" pressure field, and then correct velocities to enforce mass conservation, as in the case of the SIMPLE method, for instance.

Since a co-located grid is being used, the variables in the conservation equations are all calculated at cell nodes. Face velocities, however, need to be obtained for mass conservation. These velocities must be related to the pressure field. In order to obtain face velocities "tied" to a pressure field, the momentum equations at cell nodes are interpolating to face-node locations. This results in a new set of approximated momentum equations at these locations. The result is a dual system of equations: one set with velocities at cell nodes and pressure at face nodes, and another set with velocities at face nodes and pressure at cell nodes. These two sets are solved simultaneously to enforce momentum conservation using the cell-node velocity system, while enforcing mass conservation using the face-node velocity system.

Expressions for face-normal velocities resulting from this new set can be substituted into the algebraic equation for mass conservation to obtain a pressure field consistent with mass conservation first. This pressure field is then used to calculate face velocities. With face velocities and face pressure available, the momentum and energy equations can be solved to enforce momentum and energy conservation. In this manner, all conservation equations are satisfied at the end of the iteration cycle.

6.9. System of Equations

Before engaging in the solution of the equations, it is important to stablish whether a determined system of algebraic equations can be obtained. This is be done by ensuring that there are as many independent equations as there are unknowns. If a determined system of equations can be obtained for one single cell (control volume), then a solution associated with such cell can be found. The same reasoning can be extended to all cells in the domain. To solve all sets as part of the same system, an iterative process can be used.

The proof for the existence of a determined system can be very involved, considering all of the equations involved as part of the solution domain. However, the point can be illustrated by considering a single cell. For an internal cell, the following algebraic equations are available for mass, momentum, and energy:

$$\mathrm{f}\left(\left\{v_{\mathrm{f}_j}\right\}_{j=1,2,\ldots,6}\right)=0 \text{ (mass)}, \tag{6.98.a}$$

$$\mathrm{f}\left(u_{i,\mathrm{c}}, t_{\mathrm{c}}, \left\{p_{\mathrm{f}_j}, v_{\mathrm{f}_j}, u_{i,\mathrm{f}_j}\right\}_{j=1,2,\ldots,6}\right)=0,\ i=1,2,3 \text{ (momentum)}, \tag{6.98.b}$$

$$\mathrm{f}\left(t_{\mathrm{c}}, \left\{v_{\mathrm{f}_j}, t_{\mathrm{f}_j}\right\}_{j=1,2,\ldots,6}\right)=0 \text{ (energy)}, \tag{6.98.c}$$

where the j indices relate to each of the six individual control volume facets. In addition to these equations, a set of equations for interpolating face Cartesian velocities and face temperature is available based on the differencing scheme used to get the coefficients of the algebraic equations:

$$\mathrm{f}\left(v_{\mathrm{f}_j}, u_{i,\mathrm{f}_j}\right)=0,\ i=1,2,3;\ j=1,2,\ldots,6 \text{ (face Cartesian velocities)} \tag{6.99.a}$$

$$\mathrm{f}\left(v_{\mathrm{f}_j}, t_{\mathrm{f}_j}\right)=0,\ j=1,2,\ldots,6 \text{ (face temperatures)} \tag{6.99.b}$$

The above constitutes a system of 29 equations in 40 unknowns, namely,

the face-node normal velocities, v_{f_j}, j = 1,2,...,6 (6 unknowns),

the cell-node velocities, $u_{i,\mathrm{c}}$ (3 unknowns),

the face-node Cartesian velocities, u_{i,f_j}, $i = 1,2,3$, $j = 1,2,\ldots,6$ (18 unknowns),

the face-node pressure, p_{f_j}, $j = 1,2,\ldots,6$ (6 unknowns),

the cell-node temperature, t_{c} (1 unknown), and

the face-node temperature, t_{f_j}, $j = 1,2,\ldots,6$ (6 unknowns).

The following variables are presumed known at neighboring cell nodes:

$$u_{i,\mathrm{c}_j},\ i=1,2,3,\ j=1,2,\ldots,6 \tag{6.100.a}$$

$$t_{\mathrm{c}_j},\ j=1,2,\ldots,6 \tag{6.100.b}$$

The above system cannot be solved as it is, since there are more unknowns than equations available. Therefore, more equations are needed. It is possible to obtain equations for face-normal velocities based on approximated momentum equations by interpolation from adjacent cell neighbors. This results in six additional equations, but it adds one more unknown, being the cell pressure, as shown below:

$$\mathrm{f}\left(v_{\mathrm{f}_j}, p_{\mathrm{c}}, p_{\mathrm{c}_j}, \left\{ u_{i,\mathrm{c}}, u_{i,\mathrm{c}_j} \right\}_{i=1,2,3} \right) = 0,\ j=1,2,\ldots,6. \tag{6.101}$$

The pressure at neighboring cell nodes is presumed known:

$$p_{\mathrm{c}_j},\ j=1,2,\ldots,6 \tag{6.102}$$

At this point, the system is composed of 35 equations in 41 unknowns. The six remaining equations can be obtained from interpolating functions relating face-node pressure and cell-node pressure through each facet:

$$\mathrm{f}\left(p_{\mathrm{f}}, p_{\mathrm{c}}, p_{\mathrm{c}_j} \right) = 0,\ j=1,2,\ldots,6. \tag{6.103}$$

The last six equations complete the set of 41 independent equations in 41 unknowns for an internal cell. Therefore, the system of equations is determined, and it should yield a solution. The variables and equations involved are summarized in Table 6-1 and Table 6-2. Treatment of field-boundary cells is

Table 6-1. Set of Variables in the System of Equations

Variable	*Unknowns*	*Knowns*
v_{f_j}, $j=1,2,\ldots,6$	6	
$u_{i,c}$	3	
t_c	1	
u_{i,f_j}, $i=1,2,3$, $j=1,2,\ldots,6$	18	
t_{f_j}, $j=1,2,\ldots,6$	6	
p_{f_j}, $j=1,2,\ldots,6$	6	
u_{i,c_j}, $i=1,2,3$, $j=1,2,\ldots,6$		18
t_{c_j}, $j=1,2,\ldots,6$		6
p_c	1	
p_{c_j}, $j=1,2,\ldots,6$		6
Total Number of Variables	41	30

Table 6-2. Set of Independent Equations

Equation	*Eq. Number*	*Number of Equations*
Cell Mass Conservation	Eq. (6.98.a)	1
Cell Momentum Conservation	Eq. (6.98.b)	3
Cell Energy Conservation	Eq. (6.98.c)	1
Face-Interpolated Cartesian Velocities	Eq. (6.99.a)	18
Face-Interpolated Temperatures	Eq. (6.99.b)	6
Face-Based Momentum Conservation	Eq. (6.101)	6
Cell-Face Pressure Relations	Eq. (6.103)	6
Total Number of Equations		41

similar, but cell nodes are not available across field boundaries. Instead, the variables are specified or calculated directly at the boundary face-node-locations.

6.10. Iteration Scheme

The above set of equations is highly nonlinear, and care must be exercised in devising the sequence in which calculations are made. An *outer iteration* cycle will be defined as the sequence of steps made, where all of the above equations are used to satisfy all of the requirements stated above. The previous (available) outer loop iteration will be denoted by m-1, while the current iteration will be denoted by m. Intermediate-step solutions will be denoted m*, and they are applied to *inner iterations*.

To satisfy condition (2), mass conservation, Eq. (6.98.a) must be satisfied at the current iteration. Therefore, the following must hold at the end of the current cycle:

$$\mathrm{f}\left(\left\{v_{\mathrm{f}_j}^{m}\right\}_{j=1,2,\ldots,6}\right)=0 \tag{6.104}$$

The algebraic operators in the face-velocity momentum equations, Eq. (6.101), can be "split" into current-iteration level for face velocities and pressure, and previous-iteration level for the Cartesian velocities. In this manner, the face velocities and the pressure field are self-consistent at the end of the cycle, which satisfies condition (1). This yields the following equation:

$$\mathrm{f}\left(v_{\mathrm{f}_j}^{m}, p_{\mathrm{c}}^{m}, p_{\mathrm{c}_j}^{m}, \left\{u_{i,\mathrm{c}}^{m-1}, u_{i,\mathrm{c}_j}^{m-1}\right\}_{i=1,2,3}\right)=0,\ j=1,2,\ldots,6. \tag{6.105}$$

Substitution of this equation into mass conservation Eq. (6.104) yields:

$$\mathrm{f}\left(\left\{p_{\mathrm{c}}^{m}, p_{\mathrm{c}_j}^{m}, \left\{u_{i,\mathrm{c}}^{m-1}, u_{i,\mathrm{c}_j}^{m-1}\right\}_{i=1,2,3}\right\}_{j=1,2,\ldots,6}\right)=0. \tag{6.106}$$

This equation can be solved for the cell-node pressure at the end of the cycle, p_{c}^{m}. The cell-node pressure can be substituted back into the split-operator momentum

equation Eq. (6.105) to solve for the face normal velocities, $v_{f_j}^{m}$. The face pressure can be calculated substituting the cell-node pressure into Eq. (6.103) evaluated at the current iteration level:

$$\mathrm{f}\left(p_{\mathrm{f}}^{m}, p_{\mathrm{c}}^{m}, p_{\mathrm{c}_j}^{m} \right) = 0, \;\; j = 1,2,\ldots,6. \tag{6.107}$$

At this point in the process, the solution has been advanced one cycle for the face velocities and the pressure field. Mass conservation is satisfied with self-consistency between face velocities and the pressure field. The next step is to solve the cell-node momentum and energy equations.

Since temperature appears explicitly in the momentum equations, it is convenient to update the temperature by solving the energy equation first, and then to use the result to update the velocity field by solving the momentum equations. Since the new velocities will affect the temperature field, another outer-loop iteration must be started, and the process repeated until convergence. Solution of the cell-node energy equation, Eq. (6.98.c), must be done simultaneously with face-node temperature equations, Eq. (6.98.b), at the current iteration level:

$$\mathrm{f}\left(t_{\mathrm{c}}^{m}, \left\{ v_{\mathrm{f}_j}^{m}, t_{\mathrm{f}_j}^{m} \right\}_{j=1,2,\ldots,6} \right) = 0 \text{ (cell temperature)} \tag{6.108.a}$$

$$\mathrm{f}\left(v_{\mathrm{f}_j}^{m}, t_{\mathrm{f}_j}^{m} \right) = 0, \;\; j = 1,2,\ldots,6 \text{ (face temperature)} \tag{6.108.b}$$

Solution of the cell-node momentum equation, Eq. (6.98.b), must be done simultaneously with face-node Cartesian-velocity equations, Eq. (6.99.a), at the current iteration level:

$$\mathrm{f}\left(u_{i,\mathrm{c}}^{m}, t_{\mathrm{c}}^{m}, \left\{ p_{\mathrm{f}_j}^{m}, v_{\mathrm{f}_j}^{m}, u_{i,\mathrm{f}_j}^{m} \right\}_{j=1,2,\ldots,6} \right) = 0, \;\; i = 1,2,3 \text{ (cell Cart. vel.)}, \tag{6.109.a}$$

$$\mathrm{f}\left(v_{\mathrm{f}_j}^{m}, u_{i,\mathrm{f}_j}^{m} \right) = 0, \;\; i = 1,2,3; \; j = 1,2,\ldots,6 \text{ (face Cart. vel.)}. \tag{6.109.b}$$

This point marks the end of an iteration cycle. Mass conservation is satisfied, the pressure field is consistent with the mass-conserving face velocities and the previous-step, cell-node Cartesian velocities. Energy conservation is satisfied and

the temperature is consistent with the current face velocities. Momentum conservation is satisfied and the cell-node Cartesian velocities are consistent with the current face velocities. In the next section, the remaining equations are obtained, and the above solution procedure outlined is implemented.

6.11. Pressure-Velocity Coupling Equations

The algebraic equations for momentum and mass conservation derived above are "decoupled". That is, there is no connection yet between the cell-node Cartesian velocities in the algebraic momentum equations and the face-node normal velocities in the algebraic mass conservation equations. The basic approach for "coupling" the set of equations is to "substitute" velocities from the momentum equations into the mass conservation equation to arrive at a pressure equation. Substitution of these velocities cannot be done arbitrarily. The approach followed in the present method is to interpolate momentum equations to face-node locations in order to get expressions for these velocities in terms of cell-node pressure.

6.11.1. Face-Based Momentum Equations and Velocity Vector

Face-based momentum equations are needed in order to interconnect cell-node pressure. The reason for using momentum equations is to obtain face-velocity equations that best model the flow-field physics at such location. Derivation of new momentum equations with a new set of control volumes would be redundant, adding unnecessary complexity. Instead, equations can be obtained by interpolating terms in the existing cell-node momentum equations to face-node locations.

Before proceeding with the interpolation, a slight change must be made to the treatment of the pressure term. It is critical that the volume integral of the pressure derivatives in the momentum equations be left as is. That is, the divergence theorem must not be applied to convert the volume integral of the pressure derivative terms into surface integrals. Failure to interpolate the pressure term as a volume integral will introduce additional pressure nodes that not only are unnecessary, but which could result in an undetermined equation set, and ultimately yielding the well known checkerboard spatial pressure patterns.

The resulting algebraic form of the momentum equation is, then, identical to the previous equation, Eq. (6.76), but with the constant term expressed as

$$b_{\mathrm{c}}^{u_i} = S^{u_i}\,\mathcal{V}_{\mathrm{c}} - \mathcal{V}_{\mathrm{c}}\left(p_{x_i}\right)_{\mathrm{c}} + a_{\mathrm{o}}^{u}\,u_{i,\mathrm{o}} + \\ -\sum_{j=1}^{3}\left[\left(a_{\mathrm{f}_j^+}^{u} + Q_{\mathrm{f}_j^+}\right)\Delta u_{i,\mathrm{c}_{\mathrm{f}_j^+}} + \left(a_{\mathrm{f}_j^-}^{u} - Q_{\mathrm{f}_j^-}\right)\Delta u_{i,\mathrm{c}_{\mathrm{f}_j^-}}\right] \tag{6.110}$$

A vector form of the algebraic momentum equation can be obtained from the individual components appearing in Eq. (6.76) as:

$$\sum_{i=1}^{3} a_{\mathrm{c}}^{u}\,u_{i,\mathrm{c}}\,\vec{\varepsilon}_i = \sum_{i=1}^{3}\left[\sum_{j=1}^{3}\left(a_{\mathrm{f}_j^+}^{u}\,u_{i\,\mathrm{f}_j^+} + a_{\mathrm{f}_j^-}^{u}\,u_{i\,\mathrm{f}_j^-}\right) + b_{\mathrm{c}}^{u_i}\right]\vec{\varepsilon}_i\,, \tag{6.111}$$

which results in the following equation for the cell-node velocity vector:

$$\vec{u}_{\mathrm{c}} = \vec{\hat{u}}_{\mathrm{c}} - G_{\mathrm{c}}^{u}\left(\nabla p\right)_{\mathrm{c}}\,, \tag{6.112}$$

where

$$\vec{u}_{\mathrm{c}} = \sum_{i=1}^{3} u_{\mathrm{i,c}}\,\vec{\varepsilon}_i \tag{6.113}$$

is the velocity vector,

$$\vec{\hat{u}}_{\mathrm{c}} = \sum_{i=1}^{3} \hat{u}_{\mathrm{i,c}}\,\vec{\varepsilon}_i \tag{6.114}$$

is the *pseudo-velocity vector*, that is, a vector containing the three pseudo-velocity components,

$$G_{\mathrm{c}}^{u} = \left(\frac{\mathcal{V}_{\mathrm{c}}}{a_{\mathrm{c}}^{u}}\right) \tag{6.115}$$

is the pressure gradient coefficient, and

$$\left(\nabla p\right)_{\mathrm{c}} = \sum_{i=1}^{3}\left(p_{x_i}\right)_{\mathrm{c}}\,\vec{\varepsilon}_i \tag{6.116}$$

is the pressure gradient at the cell-node location.

The components of the pseudo-velocity vector are expressed as:

$$\hat{u}_{i,\mathrm{c}} = \frac{1}{a^u_{\mathrm{c}}}\left[\sum_{j=1}^{3}\left(a^u_{\mathrm{f}^+_j}\, u_{i\,\mathrm{f}^+_j} + a^u_{\mathrm{f}^-_j}\, u_{i\,\mathrm{f}^-_j}\right) + b^{u_i}_{\mathrm{c}\text{-}p}\right],\ i=1,2,3\,, \tag{6.117}$$

where $b^{u_i}_{\mathrm{c}\text{-}p}$ is a constant term identical to that in the original algebraic equation for momentum conservation (with the surface integral of pressure derivatives), but without the pressure terms:

$$b^{u_i}_{\mathrm{c}\text{-}p} = S^{u_i}\,\mathcal{V}_{\mathrm{c}} + a^u_{\mathrm{o}}\,u_{i,\mathrm{o}} + \\ -\sum_{j=1}^{3}\left[\left(a^u_{\mathrm{f}^+_j} + Q_{\mathrm{f}^+_j}\right)\Delta u_{i,\mathrm{c}_{\mathrm{f}^+_j}} + \left(a^u_{\mathrm{f}^-_j} - Q_{\mathrm{f}^-_j}\right)\Delta u_{i,\mathrm{c}_{\mathrm{f}^-_j}}\right] \tag{6.118}$$

The face-node velocity vector can be expressed in terms of the cell-node pseudo-velocity vector and the pressure gradient by interpolating the cell-node velocity vector from the algebraic momentum equation in adjacent cell nodes to the face node location as:

$$\bar{u}_{\mathrm{f}} = \xi^-_{\mathrm{f}}\bar{u}_{\hat{c}^-} + \xi^+_{\mathrm{f}}\bar{u}_{\hat{c}^+}\,, \tag{6.119}$$

where ξ^- and ξ^+ are weighing fractions for the cell-node values on the negative- and positive sides o the facet. Weighing factors resulting from a linear interpolation scheme based on distances from the face node to auxiliary cell nodes should suffice:

$$\xi^-_{\mathrm{f}} = \frac{\Delta z_+}{\Delta z_{\mathrm{f}}} \tag{6.120.a}$$

$$\xi^+_{\mathrm{f}} = \frac{\Delta z_-}{\Delta z_{\mathrm{f}}} \tag{6.120.b}$$

where

$$\Delta z_{\mathrm{f}} = \Delta z_- + \Delta z_+\,. \tag{6.121}$$

Substitution of Eq. (6.112) in Eq. (6.119) yields:

$$\bar{u}_{\mathrm{f}} = \left(\xi^-_{\mathrm{f}}\bar{\hat{u}}_{\hat{\mathrm{c}}^-} + \xi^+_{\mathrm{f}}\bar{\hat{u}}_{\hat{\mathrm{c}}^+}\right) - \left(\xi^-_{\mathrm{f}}\left(G^u\nabla p\right)_{\hat{\mathrm{c}}^-} + \xi^+_{\mathrm{f}}\left(G^u\nabla p\right)_{\hat{\mathrm{c}}^+}\right). \tag{6.122}$$

The face pseudo-velocity vector is now introduced by interpolating cell-node pseudo-velocities as:

$$\bar{\hat{u}}_{\mathrm{f}} = \xi_{\mathrm{f}}^{-} \bar{\hat{u}}_{\hat{c}^-} + \xi_{\mathrm{f}}^{+} \bar{\hat{u}}_{\hat{c}^+} . \tag{6.123}$$

In order to resolve the pressure at the face-node location, the following approximation is made:

$$G_{\mathrm{f}}^{u} (\nabla p)_{\mathrm{f}} \doteq \left(\xi_{\mathrm{f}}^{-} \left(G^{u} \nabla p \right)_{\hat{\mathrm{c}}^-} + \xi_{\mathrm{f}}^{+} \left(G^{u} \nabla p \right)_{\hat{\mathrm{c}}^+} \right), \tag{6.124}$$

such that

$$G_{\mathrm{f}}^{u} = \xi_{\mathrm{f}}^{-} G_{\hat{\mathrm{c}}^-}^{u} + \xi_{\mathrm{f}}^{+} G_{\hat{\mathrm{c}}^+}^{u} . \tag{6.125}$$

Substitution of Eqs. (6.123) and (6.124) into Eq. (6.122) yields the following expression for the face velocity vector based on the face-node pseudo-velocity vector and the face-node pressure gradient:

$$\bar{u}_{\mathrm{f}} = \bar{\hat{u}}_{\mathrm{f}} - G_{\mathrm{f}}^{u} (\nabla p)_{\mathrm{f}} \tag{6.126}$$

Expressions for the pseudo-velocity vector components and pressure-gradient factors at auxiliary cell nodes are obtained in the same manner used previously to find the dependent variable at these nodes. This is done by adding the cell-node values and increments from the cell node to the cell auxiliary node:

$$\hat{u}_{i\hat{\mathrm{c}}^{\pm}} = \hat{u}_{i\mathrm{c}^{\pm}} + \Delta \hat{u}_{i\mathrm{c}^{\pm}} \tag{6.127}$$

and

$$G_{\hat{\mathrm{c}}^{\pm}}^{u} = G_{\mathrm{c}^{\pm}}^{u} + \Delta G_{\mathrm{c}^{\pm}}^{u} \tag{6.128}$$

where symbols "+" and "-" denote the cell node on the positive (+) side or negative (-) side with respect to a particular face, and the increments from the cell-node to the cell auxiliary node is obtained from a vector scalar product of the position of the auxiliary node relative to the cell node and the gradient of these quantities:

$$\Delta \hat{u}_{i_{\mathrm{c}^{\pm}}} = \Delta \vec{R}\Big|_{\mathrm{c}^{\pm}} \bullet \nabla \hat{u}_i\Big|_{\mathrm{c}^{\pm}}, \quad i = 1,2,3 \tag{6.129}$$

and

$$\Delta G^u_{\hat{\mathrm{c}}^{\pm}} = \Delta \vec{R}\Big|_{\mathrm{c}^{\pm}} \bullet \nabla G^u\Big|_{\mathrm{c}^{\pm}}, \quad i = 1,2,3 \tag{6.130}$$

where the symbols "+" and "-" denote the cell node on the positive (+) side or negative (-) side with respect to a particular face,

$$\nabla \hat{u}_{i_{\mathrm{c}}} = \sum_{i=1}^{3} \left(\hat{u}_{i_{x_i}} \right)_{\mathrm{c}} \vec{\varepsilon}_i , \tag{6.131}$$

and

$$\nabla G^u_c = \sum_{i=1}^{3} \left(G^u_{x_i} \right)_{\mathrm{c}} \vec{\varepsilon}_i . \tag{6.132}$$

Gradient components of the pseudo-velocities and the pressure-gradient factors at cell node locations can be calculated from face values as:

$$\left(\hat{u}_{i_{x_i}} \right)_{\mathrm{c}} = \frac{1}{\mathcal{V}_{\mathrm{c}}} \sum_{j=1}^{3} \left[\hat{u}_{i_{\mathrm{f}_j}} \ \eta_i^j A_{\mathrm{f}}^j \right]_{\mathrm{f}_j^-}^{\mathrm{f}_j^+} \tag{6.133}$$

and

$$\left(G^u_{x_i} \right)_{\mathrm{c}} = \frac{1}{\mathcal{V}_{\mathrm{c}}} \sum_{j=1}^{3} \left[G^u_{\mathrm{f}_j} \ \eta_i^j A_{\mathrm{f}}^j \right]_{\mathrm{f}_j^-}^{\mathrm{f}_j^+} . \tag{6.134}$$

6.11.2. Cell-Facet Normal Velocity

The j-cell-facet normal velocity can be obtained from the face-velocity vector derived above as:

$$v_{\mathrm{f}}^j = \vec{u}_{\mathrm{f}} \bullet \vec{\eta}^j , \tag{6.135}$$

where $\vec{\eta}^j$ is the face-normal unit vector consistent with the j-parametric direction.

Substituting the velocity vector from Eq. (6.126) into Eq. (6.135) yields:

$$v_{\mathrm{f}}^{j} = \bar{\hat{u}}_{\mathrm{f}} \bullet \vec{\eta}^{\,j} - G_{\mathrm{f}}^{u} \left(\nabla p\right)_{\mathrm{f}} \bullet \vec{\eta}^{\,j}, \tag{6.136}$$

which may be rewritten as:

$$v_{\mathrm{f}}^{j} = \hat{v}_{\mathrm{f}}^{j} - G_{\mathrm{f}}^{u} \left(\frac{\delta p}{\delta z^{j}}\right)_{\mathrm{f}}, \tag{6.137}$$

where

$$\hat{v}_{\mathrm{f}}^{j} = \bar{\hat{u}}_{\mathrm{f}} \bullet \vec{\eta}^{\,j} \tag{6.138}$$

is the face-normal pseudo-velocity, which can be expressed in terms of the pseudo-velocity Cartesian components and the face-normal unit vector components as

$$\hat{v}_{\mathrm{f}}^{j} = \sum_{i=1}^{3} \hat{u}_{\mathrm{i,f}}\, \eta_{i}^{j}, \tag{6.139}$$

and

$$\left(\frac{\delta p}{\delta z^{j}}\right)_{\mathrm{f}} = \left(\nabla p\right)_{\mathrm{f}} \bullet \vec{\eta}^{\,j} \tag{6.140}$$

is the pressure derivative in the direction of the face normal in the parametric direction.

The face pressure gradient must be discretized eventually in terms of cell-node values. To achieve that, the face pressure gradient is first expressed in terms of auxiliary-node pressure values by using a difference scheme. Discretization of face pressure gradient can be made based on pressure values at cell nodes on the two sides or on cell nodes and face node pressure for each side separately. Both methods should produce identical results. However, in order to maintain consistency with the discretization of fluxes in the conservation equations, and to preserve the generality in situations when the interface lies between a fluid cell and a solid cell, the latter method was used. Another benefit of using this method is that a general pressure solver can be used, based on face pressure, as will be shown below. Otherwise, the pressure solver would have to involve logic to discriminate

between cell faces interfacing with two fluid cells or one fluid cell and one solid cell. Discretization of the face pressure derivative must provide the same pressure derivative regardless of the face side used. Therefore, the following must hold:

$$\left(\frac{\delta p}{\delta z^j}\right)_{\mathrm{f}_\pm} \doteq \pm \frac{p_{\hat{c}_j^\pm} - p_{\mathrm{f}_j}}{\Delta z_\pm^j}, \tag{6.141.a}$$

$$\left(\frac{\delta p}{\delta z^j}\right)_{\mathrm{f}_-} = \left(\frac{\delta p}{\delta z^j}\right)_{\mathrm{f}_+}, \tag{6.141.b}$$

where pressure values at auxiliary nodes can be expressed in terms of cell-node values and increments from cell nodes to auxiliary nodes as:

$$p_{\hat{c}_j^\pm} = p_{c_j^\pm} + \Delta p_{c_j^\pm} \tag{6.142}$$

Pressure increments are calculated in a similar manner as other scalar increments as

$$\Delta p_{\mathrm{c}_j^\pm} = \Delta \vec{R}\big|_{\mathrm{c}_j^\pm} \bullet \nabla p\big|_{\mathrm{c}_j^\pm} \tag{6.143}$$

where ∇p is the pressure gradient:

$$\nabla p = \sum_{i=1}^{3} p_{x_i} \vec{\varepsilon}_i \,. \tag{6.144}$$

whose components can be calculated based on face values as:

$$p_{x_i} = \frac{1}{\mathcal{V}_\mathrm{c}} \sum_{j=1}^{3} \left[p_{\mathrm{f}_j} \eta_i^j A_\mathrm{f}^j \right]_{\mathrm{f}_j^-}^{\mathrm{f}_j^+} . \tag{6.145}$$

The face-node pressure gradient can be expressed explicitly in terms of cell-node values by substituting Eq. (6.142) into Eq. (6.141) as:

$$\left(\frac{\delta p}{\delta z^j}\right)_{\mathrm{f}_\pm} = \pm \frac{p_{c_j^\pm} - p_\mathrm{f}}{\Delta z_\pm^j} \pm \frac{\Delta p_{c_j^\pm}}{\Delta z_\pm^j} \tag{6.146}$$

Substitution of the above result into Eq. (6.137) yields a final equations for the face normal velocity expressed in terms of face-normal pseudo-velocities and pressure values evaluated at cell nodes and face nodes:

$$v_{\mathrm{f}_\pm}^{j} = \hat{v}_{\mathrm{f}_\pm}^{j} \mp \frac{G_{\mathrm{f}_\pm}^{u}}{\Delta z_{\mathrm{f}_\pm}^{j}} \left(p_{c_j^\pm} - p_{\mathrm{f}} \right), \tag{6.147}$$

where

$$\hat{v}_{\mathrm{f}_\pm}^{j} = \hat{v}_{\mathrm{f}_\pm}^{j} \mp \frac{G_{\mathrm{f}_\pm}^{u}}{\Delta z_{\mathrm{f}_\pm}^{j}} \Delta p_{c_j^\pm} \tag{6.148}$$

are a modified face-normal pseudo-velocities evaluated at cell nodes on the positive (+) or negative (-) sides of the face, and which contain pressure increment terms.

6.11.3. Enforcement of Mass Conservation

The equation for the face-normal velocity derived in the previous section can now be used to find a cell-node pressure field that satisfies mass conservation. The solution is advanced by expressing the face-normal velocities in terms of the previous-iteration pseudo-velocities and the current-iteration pressure. Thus the solution is advanced a full iteration cycle. For this reason, it is important to introduce iteration indices. The previous outer loop iteration will be denoted by m-1, while the current iteration will be denoted by m. The face-normal velocity can be written in terms of pseudo-velocities and other terms evaluated at the previous iteration level, and in terms of pressure evaluated at the current iteration level as follows:

$$v_{\mathrm{f}_\pm}^{j,m} = \hat{v}_{\mathrm{f}_\pm}^{j,m-1} \pm \frac{G_{\mathrm{f}_\pm}^{u,m-1}}{\Delta z_{\mathrm{f}_\pm}^{j}} \left(p_{\mathrm{f}_j}^{m} - p_{c_j^\pm}^{m} \right) \tag{6.149}$$

Before substitution into mass conservation, it is convenient to write the above equations as net volumetric flows across faces by multiplying by the cell-facet area:

$$Q_{\mathrm{f}_\pm}^{j,m} = \hat{\hat{Q}}_{\mathrm{f}_\pm}^{j,m-1} \pm a_{\mathrm{f}_\pm} \left(p_{\mathrm{f}_j}^m - p_{c_j^\pm}^m \right) \tag{6.150}$$

where

$$Q_{\mathrm{f}_\pm}^m = v_{\mathrm{f}_\pm}^{j,m} A_{\mathrm{f}}^j \tag{6.151}$$

are the mass-conserving volumetric flows,

$$\hat{\hat{Q}}_{\mathrm{f}_\pm}^{m-1} = \hat{\hat{v}}_{\mathrm{f}_\pm}^{j,m-1} A_{\mathrm{f}}^j \tag{6.152}$$

are the previous-iteration gross-pseudo-volumetric flows, and

$$a_{\mathrm{f}_\pm}^p = \frac{G_{\mathrm{f}_\pm}^{u,m-1} A_{\mathrm{f}}^j}{\Delta z_{\mathrm{f}_\pm}^j} \tag{6.153}$$

are the j-face negative- and positive-side pressure coefficients, respectively.

Substitution of Eq. (6.150) into mass conservation, Eq. (6.73) at the current iteration step yields:

$$\sum_{j=1}^{3} \left\{ \left[\hat{\hat{Q}}_{\mathrm{f}_-}^{j,m-1} - a_{\mathrm{f}_-}^p \left(p_{\mathrm{f}_j}^m - p_{c_{\mathrm{f}}^-}^m \right) \right]_{\mathrm{f}_j^+} - \left[\hat{\hat{Q}}_{\mathrm{f}_+}^{j,m-1} + a_{\mathrm{f}_+}^p \left(p_{\mathrm{f}_j}^m - p_{c_{\mathrm{f}}^+}^m \right) \right]_{\mathrm{f}_j^-} \right\} = 0 \tag{6.154}$$

A redefinition of pressure variables is needed for pressure, considering that the cell-node pressure on the negative side of the positive-side face and the cell-node pressure on the positive side of the negative-side face are the cell-node pressure itself:

$$p_{c_{\mathrm{f}}^\pm}^m \Big|_{\mathrm{f}_j^\mp} = p_c^m \tag{6.155}$$

A final algebraic equation for the cell-node pressure is obtained after substituting the above definitions into Eq. (6.154) and grouping cell-node pressure terms on the left-hand side of the equation:

$$a_c^p p_c^m = \sum_{j=1}^{3}\left(a_{f_j^+}^p p_{f_j^+}^m + a_{f_j^-}^p p_{f_j^-}^m \right) + b_c^{p,m-1}, \tag{6.156}$$

where

$$a_{f_j^\pm}^p = a_{f_\mp}^p\Big|_{f_j^\pm} \tag{6.157}$$

$$a_c^p = \sum_{j=1}^{3}\left(a_{f_j^+}^p + a_{f_j^-}^p \right), \tag{6.158}$$

$$b_c^{p,m-1} = \sum_{j=1}^{3}\left(\hat{\dot{Q}}_{f_j^+}^{m-1} - \hat{\dot{Q}}_{f_j^-}^{m-1} \right). \tag{6.159}$$

6.11.4. Face-Node Pressure Equation

Once the pressure field at cell-nodes is known, face pressure values become readily available. For faces (between two fluid cells), the face pressure is obtained by equating the discretized pressure gradient from the two face sides in Eq. (6.141):

$$p_{f_j}^m = \frac{p_{\hat{c}_j^+}^m \Delta z_-^j + p_{\hat{c}_j^-}^m \Delta z_+^j}{\left(\Delta z_-^j + \Delta z_+^j\right)}. \tag{6.160}$$

For fluid-boundary faces where the face-normal velocity (or the face volumetric flow) is specified, the face pressure is calculated using Eq. (6.150). For an interface with a fluid cell on the positive (+) or negative (-) side of the face, the face pressure is calculated as:

$$p_{f_{j\pm}}^m = \left[p_{c_j^\pm}^m \right] \pm \left[\frac{\dot{Q}_{f_\pm}^{j,m} - \hat{\dot{Q}}_{f_\pm}^{j,m-1}}{a_{f_\pm}} \right] \tag{6.161}$$

Face velocities are obtained if the face pressure is imposed. This is done using Eq. (6.150) to calculate the volumetric flow rate, and then the velocity using the face area. Pseudo-velocity interpolation is one-sided for fluid boundaries, as in the two cases above when either the face velocity or the face pressure is imposed. Once the face pressure and the face velocities are available, momentum and energy conservation equations can be solved.

6.12. Balance of the Conservation-Quantity Fluxes

Balance of the conservation quantity flow is checked both locally and globally. The local flow balance is checked by calculating the inflow, outflow, storage flow, and generation flow for each fluid cell as:

$$F_{\mathrm{c}}^{\phi,in} = \sum_{\mathrm{f}=all\,faces} F_{\mathrm{c,f}}^{\phi,in}, \tag{6.162}$$

$$F_{\mathrm{c}}^{\phi,out} = \sum_{\mathrm{f}=all\,faces} F_{\mathrm{c,f}}^{\phi,out}, \tag{6.163}$$

$$F_{\mathrm{c}}^{\phi,sto} = C^{\phi}\left(\phi - \phi^{o}\right)\frac{\Delta\mathcal{V}}{\Delta\tau}, \tag{6.164}$$

$$F_{\mathrm{c}}^{\phi,gen} = s_{\mathrm{c}}^{\phi,gen}\Delta\mathcal{V}, \tag{6.165}$$

where C^{ϕ} is the specific capacitance (mass density for the momentum equations, or the product of the mass density and specific heat for the energy equation); ϕ is the transport scalar (u_1,u_2,u_3, or t); ϕ^{o} is the transport scalar at the previous time step level; $\Delta\mathcal{V}$ is the cell volume; and $\Delta\tau$ is the time-step size. Dimensional consistency is implied.

A net cell inflow, $F_{\mathrm{c}}^{\phi,\mathrm{max}}$, is calculated to establish an upper bound for the calculation of errors. It assumes the maximum of the cell's net inflow or net outflow magnitudes. The net inflow is calculated by adding the face inflow, the magnitude of the generation flow, if this flow is positive, and the magnitude of the generation flow, if this flow is negative. The net outflow is calculated by adding the face outflow, the magnitude of the flux generation flow, if this flow is negative, and the magnitude of the generation flow, if this flow is positive. Domain storage flow and flow-balance errors are calculated as

$$\varepsilon_{\mathrm{c}}^{\phi,sto} = \frac{F_{\mathrm{c}}^{\phi,sto}}{F_{\mathrm{c}}^{\phi,\max}}, \text{ and} \tag{6.166}$$

$$\varepsilon_{\mathrm{c}}^{\phi,bal} = \frac{F_{\mathrm{c}}^{\phi,bal}}{F_{\mathrm{c}}^{\phi,\max}}. \tag{6.167}$$

To check the global flow balance, the program adds all of the fluid-domain-boundary momentum inflow and outflow, and all of the momentum storage rates and momentum generation rates from each fluid cell, as follows.

$$F_d^{\phi,in} = \sum_{\mathrm{f}=domain\,faces} F_{d,\mathrm{f}}^{\phi,in}, \tag{6.168}$$

$$F_d^{\phi,out} = \sum_{\mathrm{f}=domain\,faces} F_{d,\mathrm{f}}^{\phi,out}, \tag{6.169}$$

$$F_d^{\phi,sto} = \sum_{\mathrm{c}=domain\,cells} F_{\mathrm{c}}^{\phi,sto}, \tag{6.170}$$

$$F_d^{\phi,gen} = \sum_{\mathrm{c}=domain\,cells} F_{\mathrm{c}}^{\phi,gen}, \tag{6.171}$$

Notice that the solution domain is different for the energy equation and mass and momentum equations. The solution domain for the energy equation includes all sub-domains, while the solution domain for the momentum equation includes only the domain with the fluid phase.

The flow balance is calculated as:

$$F_d^{\phi,bal} = F_d^{\phi,in} - F_d^{\phi,out} - F_d^{\phi,sto} + F_d^{\phi,gen}. \tag{6.172}$$

A net inflow, $F_d^{\phi,\max}$, is calculated to establish an upper bound for the calculation of errors. It assumes the maximum of the net inflow or net outflow magnitudes. The net inflow is calculated by adding the face inflow, the magnitude of the generation flow, if this flux is positive, and the magnitude of the generation flow, if this flow is negative. The net outflow is calculated by adding the face outflow, the magnitude of the generation flow, if this flow is negative, and the magnitude of the generation flow, if this flow is positive. Domain storage flow and flow-balance errors are calculated as:

$$\varepsilon_d^{\phi,sto} = \frac{F_d^{\phi,sto}}{F_d^{\phi,\max}}, \text{ and} \tag{6.173}$$

$$\varepsilon_d^{\phi,bal} = \frac{F_d^{\phi,bal}}{F_d^{\phi,\max}}. \tag{6.174}$$

6.13. Solution Algorithm

A top-level outline of the solution scheme is shown in *Figure 6-5*. Face-node values of the dependent variables are initialize. Some of these are treated as domain-imposed boundary conditions, while others are treated as initial values subject to subsequent updates. Cell-node values of the dependent variables are assumed known as initial conditions. The general solution procedure is best done in a transient loop, in which the equations can be solved in either *true* or *false* transient modes, the difference being whether full flow balance is satisfied at each time step. A transient loop is preferred even if solving steady-state problems, because under-relaxation is achieved using a physics-based scheme, based on the time-derivative discretization and resulting in the storage term in the algebraic equations. In this manner, a steady-state solution can be obtained in false transient mode and under-relaxation controlled by the time step size, while limiting the number of outer loop iterations. Another advantage of this approach is that the time step for solving momentum and energy equations may be set at different values based on the time constant.

For each time step, an outer loop takes care of mass conservation compliance, while inner loops enforce momentum and energy conservation. The outer loop contains a non-iterative procedure for calculating cell- and face-node pressure and face-normal velocities, both consistent with mass conservation. Then, one or more inner loop iterations are allowed for the solution of cell-node and face-node velocities and temperature base on the algebraic conservation equations. Local and global flow balance is checked within inner loops for momentum and energy, while mass conservation checks are done within the outer loop

Equation-variable flowcharts are shown in *Figure 6-6* for the outer loop and in *Figure 6-7* for the inner loops. In these flowcharts, lines and nodes represent equations and the arrows indicate the resulting variable. Only the most important variables are shown. The general solution procedure is as follows:

1. Initialize cell-node and face node velocities, pressure, and temperature.
2. Initialize the coefficients of the momentum equations.
3. Advance the time step level.
4. Calculate the pressure and face-normal velocities.
5. Calculate the cell-node pseudo-velocities.
6. Calculate the face-node pressure coefficients.
7. Calculate the face-node pseudo-velocities.
8. Solve the pressure equation set to obtain cell-node and face-node pressure.
9. Calculate the face velocities.
10. Update the coefficients of the momentum and energy equations.
11. Update the constant term of the energy equation.
12. Solve the energy equation to obtain cell and face temperatures.
13. Update the constant term of the momentum equations.
14. Solve the momentum equations to obtain cell and face cartesian velocities.
15. Repeat from step 4 if the local or global energy or momentum flux errors are larger than a pre-established tolerance.
16. Repeat from step 3 until desired time has been reached (or until steady state).

6.14. Program Checks

Check cases were run to verify that the solution procedure is doing what it was intended to do, from the theoretical standpoint. The following check cases were run:

1. Comparison of solution obtained using a curvilinear grid against that using a rectilinear grid for the same domain:

1.a. One-dimensional conduction in a cube

1.b. Hydrostatic solution in three-dimensional space

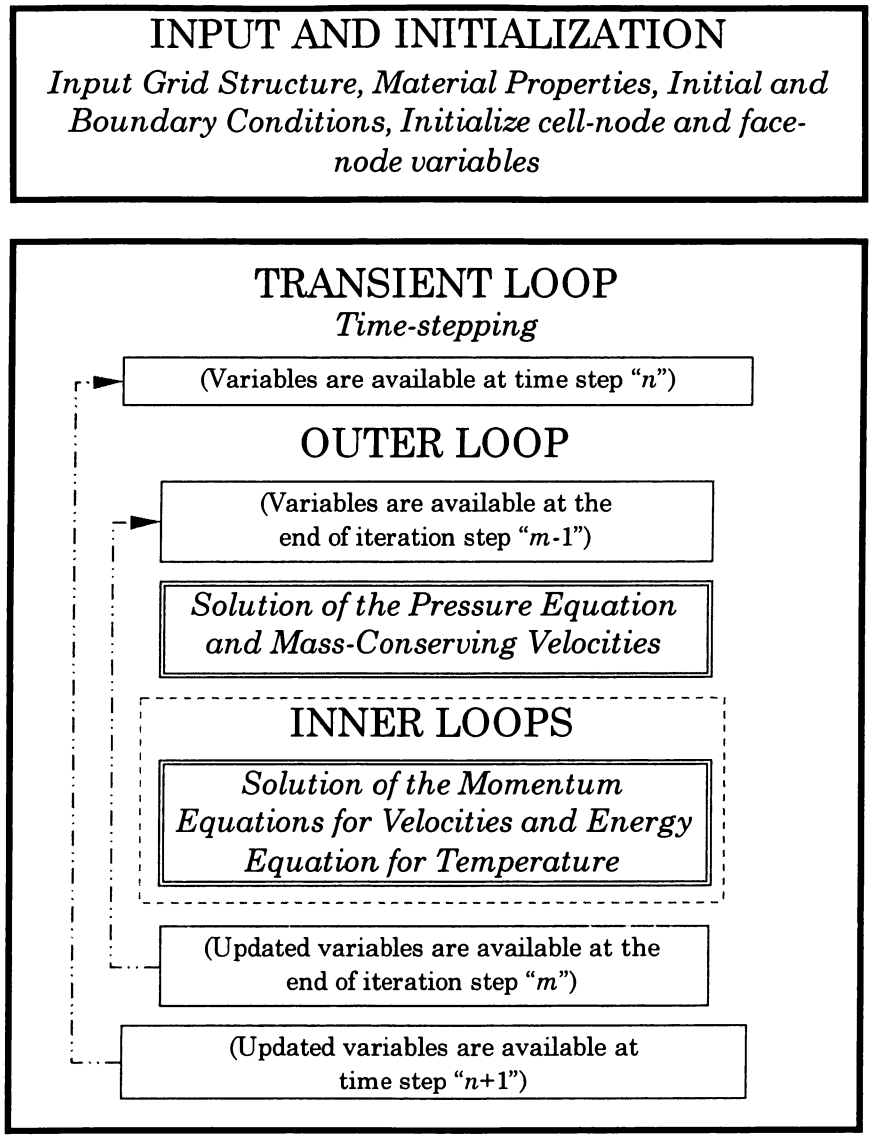

Figure 6-5. Top-Level Solution Scheme

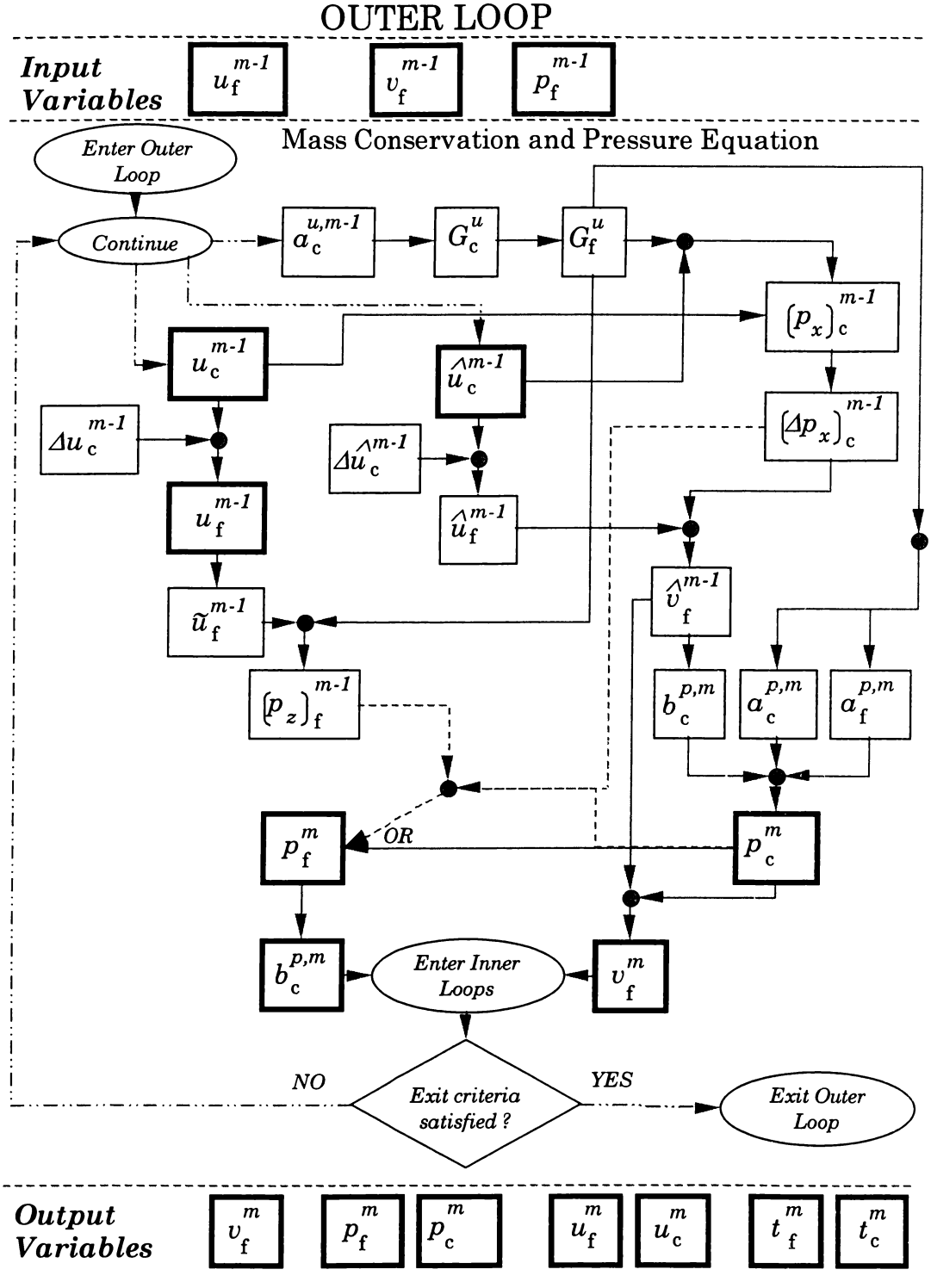

Figure 6-6. Equation-Variable Flowchart for the Outer Loop

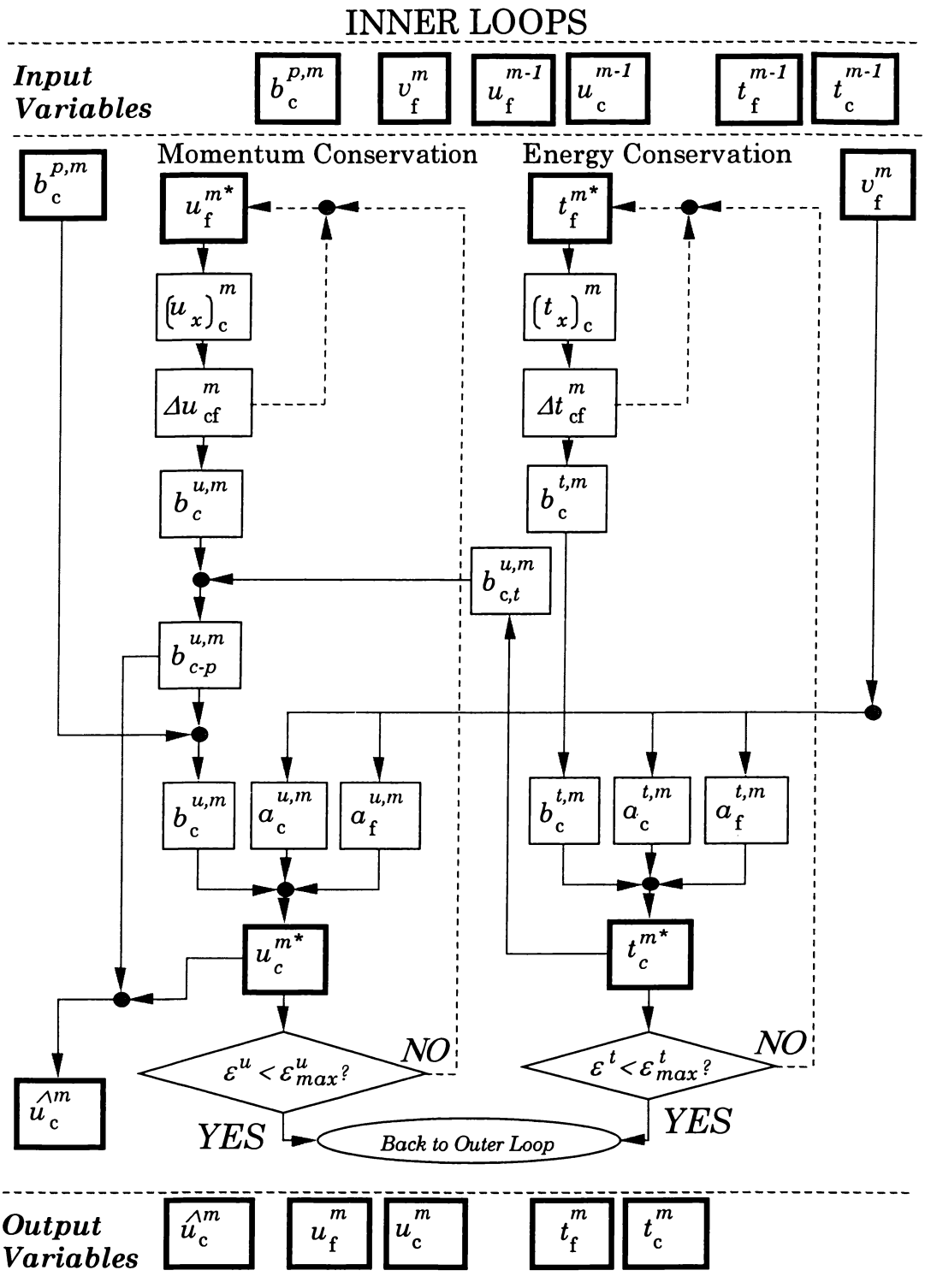

Figure 6-7. Equation-Variable Flowchart for the Inner Loops

1.c. Two-dimensional natural convection in a vertical, differentially heated square enclosure (with grid refinement to test convergence to a grid-independent solution)

2. Boundary condition checks:

2.a. Imposed temperature

2.b. Imposed heat flux

2.c. Imposed mixed convective boundary condition

2.d. Imposed zero face Cartesian velocities (No-slip condition)

2.e. Imposed face-normal velocity (Intended for slip condition or symmetry plane, where Cartesian velocities are not specified.)

3. Natural convection in tilted, rectangular channels (comparison against published data)

All checks above were satisfactory (see APPENDIX D).

7. NUMERICAL MODEL OF THE LIQUID-LENS SYSTEM

7.1. Introduction

This chapter is aimed at benchmarking the numerical model of the liquid-lens system derived in the previous chapter against the experimental data from *Chapter* 3. The banchmarked model is then used to perform a comprehensive thermal analysis of the liquid-lens system.

First, the geometry is buit and volume checks are conducted to ensure that the computational grid reproduced the intended geometry. Then, a hydrostatic case is used to demonstrate that the numerical model produced a "motionless" field in the limit of a uniform temperature field. Finally, inputs to the model are adjusted to optimize the correlation against the experiment.

As will be discussed below, not all of the required thermal boundary conditions and internal temperatures could be determined experimentally. Instead, the code was used to "reverse-engineer" the missing or incomplete boundary conditions, and along with a statistical method, it was used also to identify internal suspect data points. This was achieved by systematically adjusting input boundary conditions, running the program, and checking if the resulting internal temperatures were consistent with experimental data. The procedure was slightly more complex, as the above process had to be repeated for various sets of internal temperature data points, in order to check which set produced the highest correlation coefficient.

7.2. CFD Model Geometry

The physical model used in the numerical calculations includes approximations of the CRT face panel, the enclosure frame, the meniscus frame, and the liquid coolant. The so-called internal temperatures are those measured at the nine thermocouple-grid locations on the CRT face-panel (see *Figure 3-4*). A view of the computational model geometry with all of the dimensions involved is shown in

Figure 7-1. Orthogonal projections are shown in *Figure 7-2.* Since the liquid-lens system is symmetrical about the X_1=0 plane, it is assumed that no fluid flows or energy transfer occur across this plane. Taking this assumption into account and with the main purpose of saving computer memory and CPU time, it was decided to use only one-half of the liquid-lens system in the computational domain. This symmetry-plane assumption is to be tested subsequently, once the model is benchmarked against experimental data. The computational model represents the right half section of the physical domain, for Cartesian coordinates $X_1 \geq 0$ mm. The coordinate plane $X_1 = 0$ mm, becomes a symmetry plane for the computational domain. All of the dimensions describing the model are listed in Table 7-1. The computational model consists of (1) a base plate, (2) a meniscus wall, and (3) the liquid coolant contained between the base plate, the meniscus wall, and a rectangular enclosure shell. Schematic views of the domain showing all of the boundaries are in *Figure 7-3.* These boundaries are listed in Table 7-2. Next is a description of the domains and boundaries in computational model.

Base Plate

The base plate is a simplified model of the CRT face panel. It consists of a parallelepiped, measuring 61.2 mm along X_1, by 97.4 mm along X_2. Its thickness is 7.1 mm (direction X_3). The base plate domain is define as:

$$0 < X_1 < L_1, \; -L_2 < X_2 < L_2, \; -L_3 < X_3 < 0. \tag{7.1}$$

The boundaries of the base plate are defined as follows.

Base Plate Lower Surface:

$$0 < X_1 < L_1, \; X_2 = -L_2, \; -L_3 < X_3 < 0. \tag{7.2}$$

Base Plate Lateral Surface:

$$X_1 = L_1, \; -L_2 < X_2 < L_2, \; -L_3 < X_3 < 0. \tag{7.3}$$

Base Plate Upper Surface:

$$0 < X_1 < L_1, \; X_2 = L_2, \; -L_3 < X_3 < 0. \tag{7.4}$$

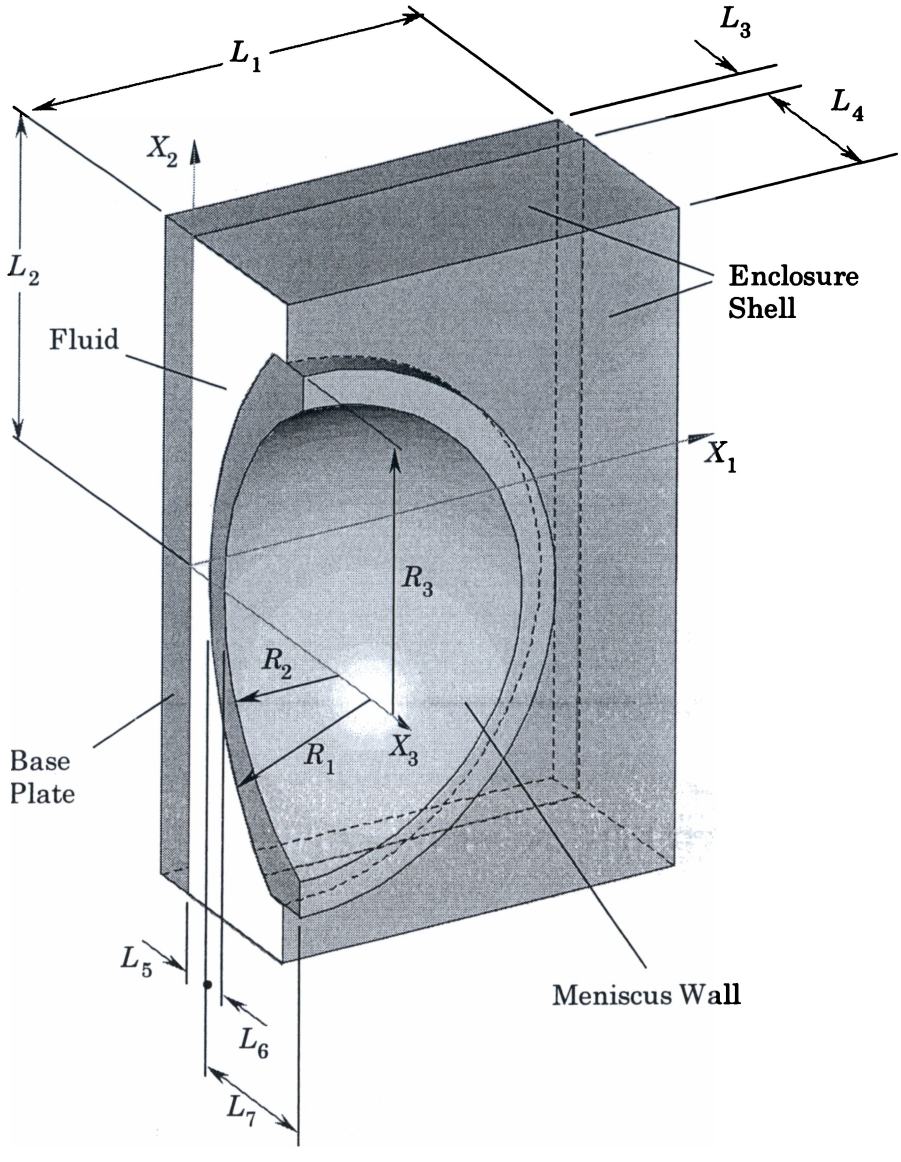

Figure 7-1. Computational Model Geometry

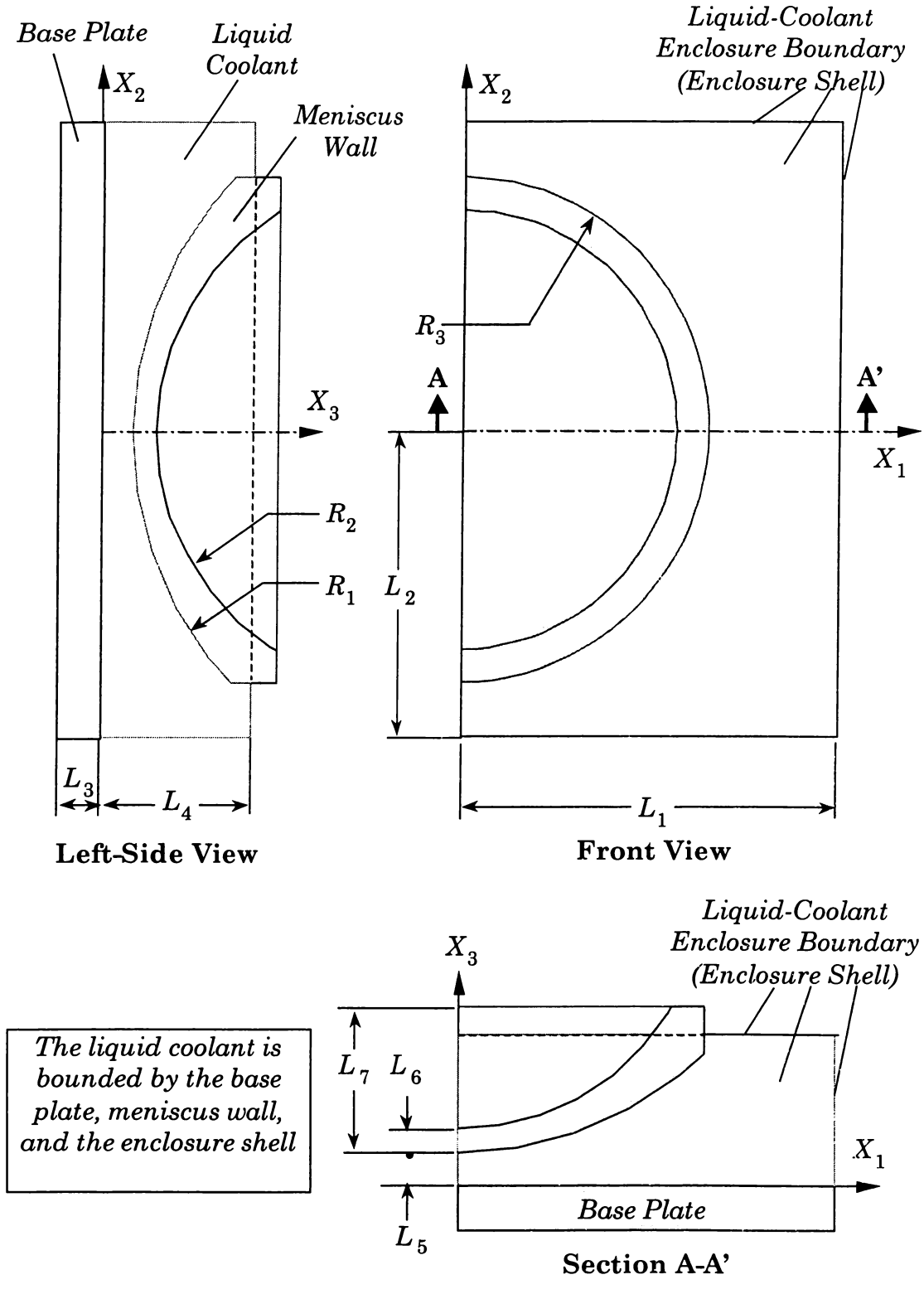

Figure 7-2. Computational Model Dimensions – Orthogonal Projections

Table 7-1. Computational Domain Dimensions

	Description	*Variable*	*Value (mm)*
1	Computational Domain Width	L_1	61.2
2	Computational Domain Half Height	L_2	48.7
3	Base Plate Thickness	L_3	7.1
4	Enclosure Depth	L_4	25.5
5	Meniscus Wall Gap	L_5	5.2
6	Meniscus Wall Centerline Thickness	L_6	4.0
7	Meniscus Wall Overall Depth	L_7	24.8
8	Meniscus Wall Convex Surface Radius	R_1	56.0
9	Meniscus Wall Concave Surface Radius	R_2	39.5
10	Meniscus Wall Outline Cylinder Radius	R_3	40.0

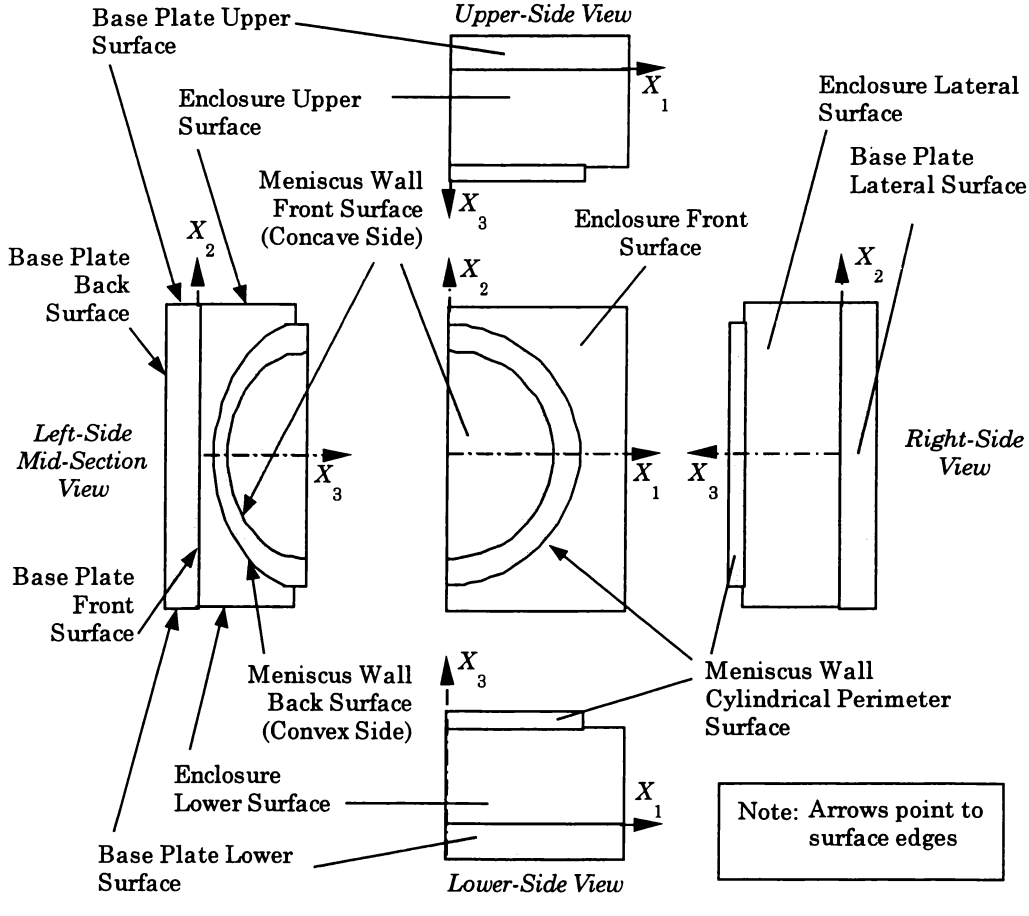

Figure 7-3. Schematic View of the Computational Model Boundaries

Table 7-2. Liquid-Lens System Domain Boundaries

Boundary Number	Description
1	Area within Raster Region on Face Panel Back Surface
2	Area outside Raster Region on Face Panel Back Surface
3	Meniscus Lens Exterior, Center (Concave Side)
4	Face Panel Exterior Lower Surface
5	Face Panel Exterior Lateral Surface
6	Face Panel Exterior Upper Surface
7	Enclosure Frame Exterior Lower Surface
8	Enclosure Frame Exterior Lateral Surface
9	Enclosure Frame Exterior Upper Surface
10	Enclosure Frame Exterior Front Surface
11	Meniscus Lens Cylindrical Perimeter Surface

Base Plate Back Surface:

$$0 < X_1 < L_1,\ -L_2 < X_2 < L_2,\ X_3 = -L_3. \tag{7.5}$$

Base Plate Front Surface:

$$0 < X_1 < L_1,\ -L_2 < X_2 < L_2,\ X_3 = 0. \tag{7.6}$$

Rectangular Enclosure

The rectangular enclosure models the enclosure frame walls. Its dimensions are 61.2 mm along X_1, by 97.4 mm along X_2. Its depth is 25.5 mm (direction X_3). A hole of radios R=R_3 (40.0 mm) on the front surface allows space for the meniscus wall. Equations for the enclosure surfaces are as follows.

Enclosure Lower Surface:

$$0 < X_1 < L_1,\ X_2 = -L_2,\ 0 < X_3 < L_4. \tag{7.7}$$

Enclosure Lateral Surface:

$$X_1 = L_1,\ -L_2 < X_2 < L_2,\ 0 < X_3 < L_4. \tag{7.8}$$

Enclosure Upper Surface:

$$0 < X_1 < L_1,\ X_2 = L_2,\ 0 < X_3 < L_4. \tag{7.9}$$

Enclosure Front Surface:

$$0 < X_1 < L_1,\ -L_2 < X_2 < L_2,\ {X_1}^2 + {X_2}^2 > R_3,\ X_3 = L_4. \tag{7.10}$$

Meniscus Wall

The meniscus wall approximates the meniscus lens. Its geometry is defined by two spheres, a cylinder, and a plane, as follows.

$$\begin{aligned} &{X_1}^2 + {X_2}^2 + \left(X_3 - X_{3,1}\right)^2 < R_1,\ {X_1}^2 + {X_2}^2 + \left(X_3 - X_{3,2}\right)^2 > R_2, \\ &{X_1}^2 + {X_2}^2 < R_3,\ X_3 < X_{3,3}, \end{aligned} \tag{7.11}$$

where $X_{3,1}$, $X_{3,2}$, and $X_{3,3}$ are derived coordinates, defined as:

$$X_{3,1} = R_1 + L_5,\ X_{3,2} = R_2 + L_5 + L_6, \text{ and } X_{3,3} = L_5 + L_7. \tag{7.12}$$

Fluid

The fluid fills the whole space confined by the base plate front surface (X_3 = 0), the enclosure walls, and the meniscus wall interior (convex) surface. The air bubble above the free surface of the liquid in the upper region of the enclosure reported during the experiment was not modeled. The meniscus wall geometry is defined as:

$$\begin{cases} 0 < X_1 < L_1,\ -L_2 < X_2 < L_2,\ 0 < X_3 < L_3, \\ \left[{X_1}^2 + {X_2}^2 + \left(X_3 - X_{3,1}\right)^2 > R_1, \right. \\ \left. {X_1}^2 + {X_2}^2 > R_3 \right] \end{cases} \tag{7.13}$$

7.3. Thermophysical Properties

Thermophysical properties are known with reasonable certainty, as their values were obtained from either published data or experimental measurements conducted as part of this project. Table 7-3 lists all thermophysical properties used. Fluid properties were evaluated at 56 °C, which is the fluid median temperature, based on preliminary computer-model results for the experimental run. Uncertainty values are in parenthesis. Mass density and specific heat for the solid are not relevant for steady-state results, but are needed for consistency during calculations. A detailed description of the calculation of thermal properties is in APPENDIX C.

7.4. Grid-Coordinate Parameterization

The purpose of coordinate parameterization is to establish an order for addressing points in the Cartesian coordinate system within the physical domain. It must be emphasized that the problem is solved within physical space, and not in a transformed domain. The general parameterization functions are:

$$X_i = X_i\left(Y_1, Y_2, Y_3\right),\ i = 1,2,3. \tag{7.14}$$

Table 7-3. Thermophysical Properties Used in the Calculations

	Property	Units	Fluid (56 °C)	Base Plate	Meniscus Wall
1	Mass Density	kg/m^3	1134.5 (±0.2%) [1]	2568 [2]	2568 [2]
2	Specific Heat	J/kg-K	2588 (±0.6%) [1]	837 [2]	837 [2]
3	Thermal Conductivity	W/m-K	0.268 (±0.2%) [1]	0.790 (±5.0%) [1]	0.629 (±5.0%) [1]
4	Kinematic Viscosity	m^2/s	9.61×10^{-6} (±7.3%) [1]	---	---
5	Volume Expansivity	1/K	6.073×10^{-4} (±0.2%) [1]	---	---

[1] Experimentally determined as part of this project

[2] Taken from typical glass plate properties at room temperature.

For convenience, the origin of the curvilinear coordinate system is set at the origin of the Cartesian coordinate system, and Y_1 and Y_2 axes are set parallel, and in the direction of the X_1 and X_2 axes, respectively. For the sake of simplicity, parameterization will be done only for X_3 coordinate, that is, parameterizations for X_1 and X_2 coordinates are given as:

$$X_1 = Y_1 \tag{7.15.a}$$

$$X_2 = Y_2 \tag{7.15.b}$$

Parameterization of X_3 is done depending of the corresponding sub-domain. There are three parameterization sub-domains, delimited by parameterization boundaries, which are designated by "curves" C_0, C_1, and C_2, as shown in *Figure 7-4.*

The parametric coordinate value on these curves is obtained as follows. Parametric Boundary, Curve C_0:

$$Y_{3,C_0} = 0 \tag{7.16}$$

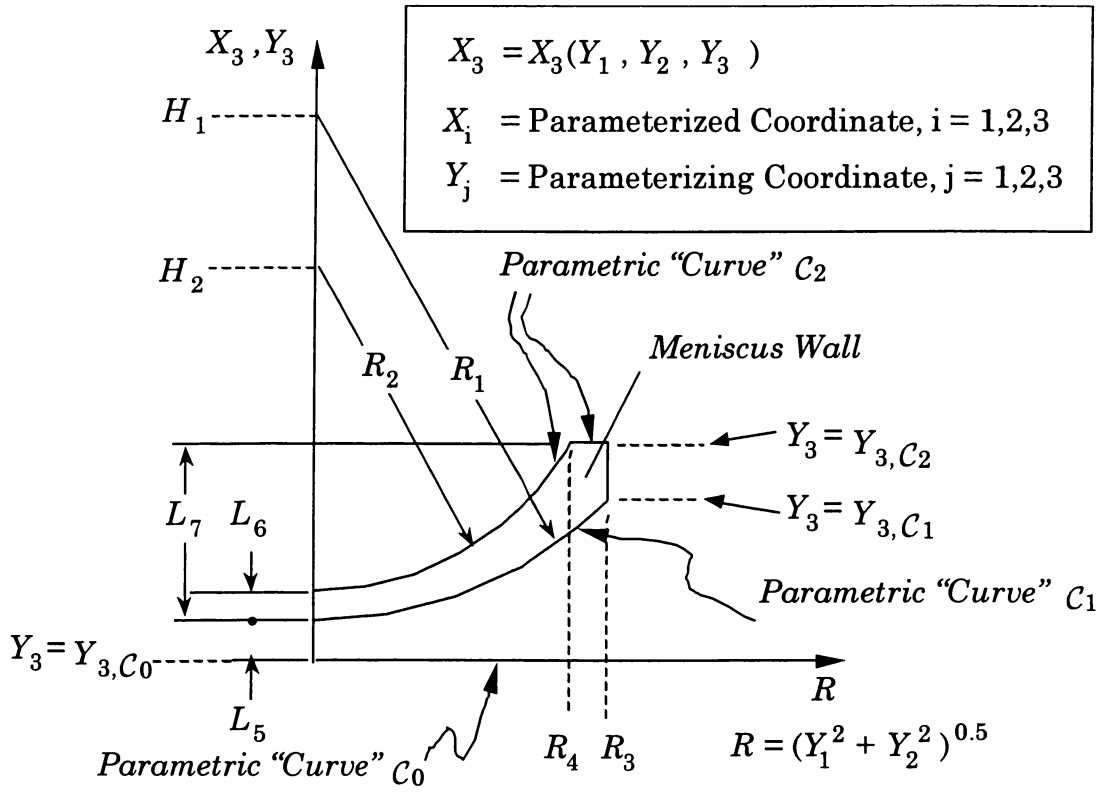

Figure 7-4. Schematic View of the Computational Model Boundaries

Parametric Boundary, Curve C_1:

$$Y_{3,C_1} = H_1 - \left(R_1^2 - R_3^2\right)^{0.5}, \tag{7.17}$$

where

$$H_1 = R_1 + L_4 \tag{7.18}$$

Parametric Boundary, Curve C_2:

$$Y_{3,C_2} = H_2 - \left(R_2^2 - R_4^2\right)^{0.5}, \tag{7.19}$$

where

$$H_2 = R_2 + L_4 + L_5, \tag{7.20}$$

and

$$R_4 = \left(R_2^2 - \left(R_2 - L_7\right)^2\right)^{0.5} \tag{7.21}$$

To obtain X_3 we proceed as follows. First, the radial position, R, is calculated:

$$R = \left(Y_1^2 + Y_2^2\right)^{0.5} \tag{7.22}$$

Then, the X_3 -coordinates are calculated on the parametric curves:

$$X_{3,C_0}(R) = 0 \tag{7.23}$$

$$X_{3,C_1}(R) = H_1 - \left(R_1^2 - R^2\right)^{0.5} \tag{7.24}$$

$$X_{3,C_2}(R) = H_2 - \left(R_2^2 - R^2\right)^{0.5} \tag{7.25}$$

Coordinate X_3 can now be calculated in terms of the above equations as:

$$X_3 = \begin{cases} Y_3, \ Y_3 \le Y_{3,C_0} \\ \dfrac{X_{3,C_0} \cdot \left(Y_{3,C_1} - Y_3\right) + X_{3,C_1} \cdot \left(Y_3 - Y_{3,C_0}\right)}{Y_{3,C_1} - Y_{3,C_0}}, \ Y_{3,C_0} < Y_3 \le Y_{3,C_1} \\ \dfrac{X_{3,C_1} \cdot \left(Y_{3,C_2} - Y_3\right) + X_{3,C_2} \cdot \left(Y_3 - Y_{3,C_1}\right)}{Y_{3,C_2} - Y_{3,C_1}}, \ Y_{3,C_1} < Y_3 \le Y_{3,C_2} \end{cases} \tag{7.26}$$

The above equations were incorporating as part of the program to generate the computational grid.

7.5. Computational Grid

The numerical model requires the Cartesian coordinates (X_1, X_2, and X_3) of the cell vertices (face corners) to proceed with the solution. The cell topology for the present problem was based on hexahedra, so for every cell, 8 vertex locations need to be determined (or 4 vertex locations per cell face). The computational grid is considered generated once the coordinates of these vertices are known for all of the cells in the solution domain. Functions of the Cartesian coordinates (X_1, X_2, and X_3) are already available in terms of the parametric coordinates (Y_1, Y_2, and Y_3). The remaining task is to create a grid within parametric space to determine the values of the parametric coordinates corresponding to cell vertices, and to then feed them into the available functions to calculate their Cartesian coordinates. *Figure 7-5* shows the geometry and domain sub-divisions within parametric space. Face markers are specified along each coordinate to separate sub-domains, including domain boundaries. For the sake of simplicity, a uniform grid was generated within each sub-domain in the parametric space. Therefore, each of the sub-domain intervals is uniformly subdivided into segments representing cells (control volumes) in the physical space domain. The edges of these segments represent face locations. The number of segments is equal to the number of cells assigned, in the respective direction. Table 7-4 shows the total number of cells in each direction, the coordinate limits, and the number of sub-domains per direction. Table 7-5 shows the number of

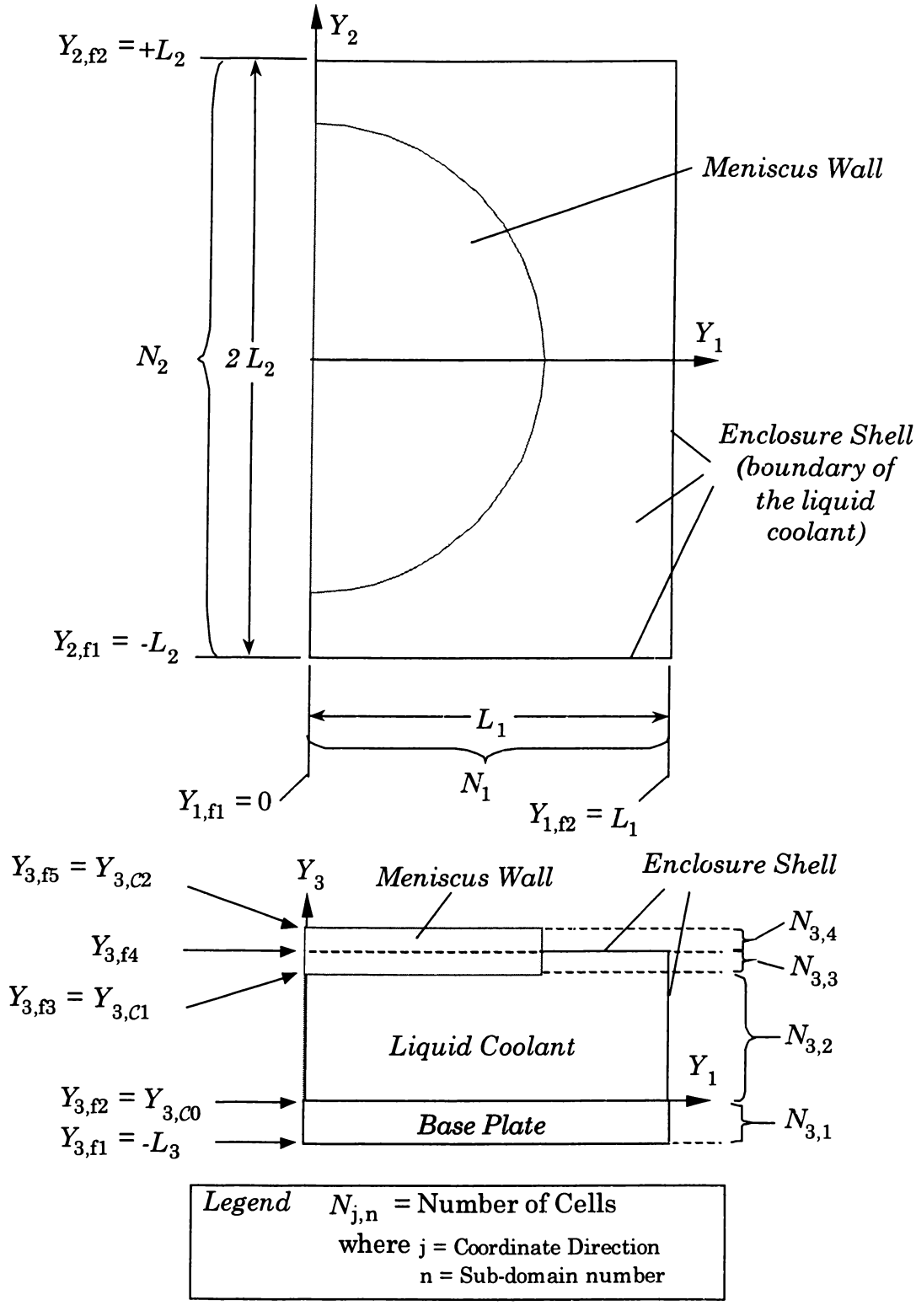

Figure 7-5. Parametric Space Coordinate Markers

Table 7-4. Domain Cell Distribution within Parametric Space

Coordinate Direction, j	Number of Sub-Domains	Number of Cells, N_j	$Y_{j,min}$ (mm)	$Y_{j,max}$ (mm)
1	1	35	0.0	61.2
2	1	54	-48.7	+48.7
3	4	19	-7.1	30.0

Table 7-5. Sub-Domain Cell Distribution within Parametric Space

Coordinate Direction, j	Sub-Domain Number (n)	Number of Cells, $N_{j,n}$	$Y_{j,min}$ (mm)	$Y_{j,max}$ (mm)
3	1	4	-7.1	0.0
3	2	12	0.0	22.0
3	3	1	22.0	25.5
3	4	2	25.5	30.0

cells in each of the sub-domains in direction Y_3, and the extent of each sub-domain. Four sub-domains were created in direction Y_3. *Figure 7-6* shows perspective views of the grid generated with the above information for the base plate, liquid coolant and meniscus wall separately, as an assembly. *Figure 7-7* shows projection views of the grid onto Cartesian coordinate planes.

Volume Check Sum

A comparison between the summation cell volumes for each material in the CFD grid and the exact volume based on the dimensions and coordinate parameterization above is shown in Table 7-6.

The base-plate grid has the exact volume. This was expected, since the cells are not distorted because of domain curvature. The discretized fluid domain has a volume of 0.03% below the exact value. The maximum volume error occurred for the meniscus wall, with a volume of 0.49% above the exact value. The total grid volume was 0.03% above the exact volume. At this point, the geometry of the liquid-lens system has been completely specified, and the computational grid has been generated. The grid models the geometry with good fidelity.

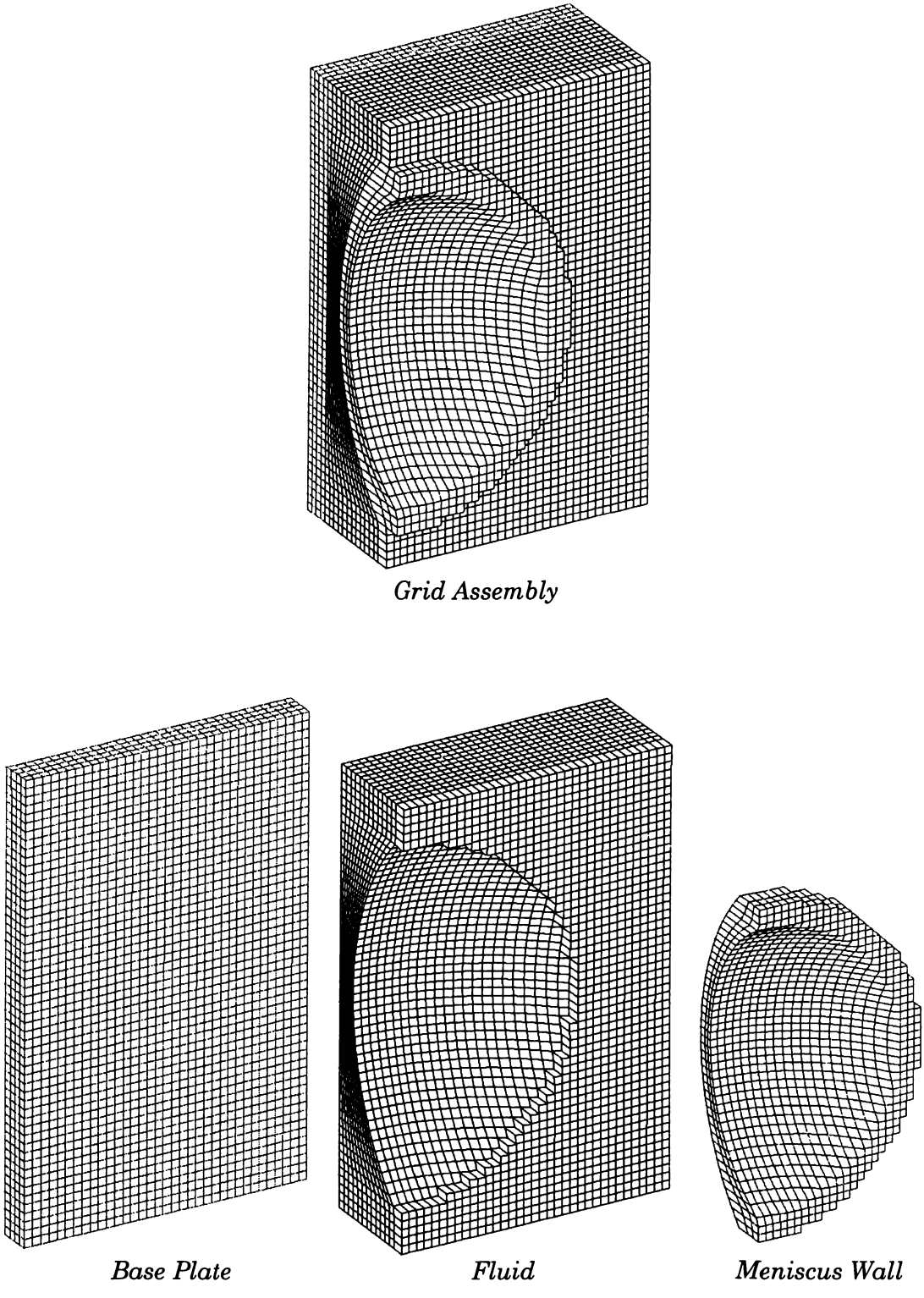

Figure 7-6. Computational Grid Perspective and Exploded Views

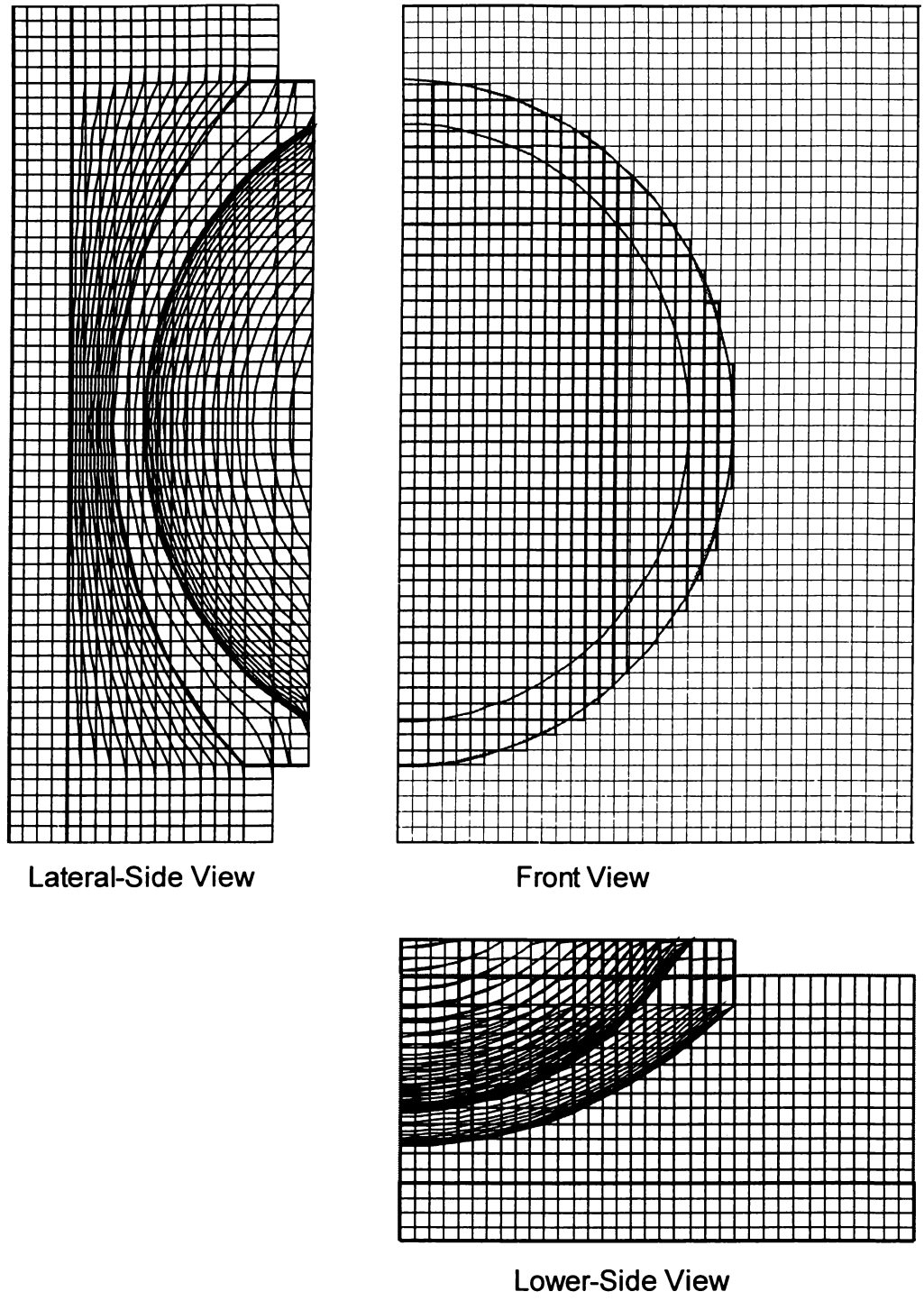

Figure 7-7. Computational Grid Orthogonal Projection Views on Cartesian Planes and Geometry Model Overlays

Table 7-6. Comparison of CFD-Grid and Exact Material Sub-Domain Volumes

	Exact (cm^3)	CFD Cell Summation (cm^3)	Error (%)
Base Plate	42.322	42.322	0.00%
Fluid	120.862	120.824	-0.03%
Meniscus Wall	20.319	20.419	0.49%
Total Volume	183.502	183.565	0.03%

Before proceeding with benchmarking the numerical model with experimentally determined boundary conditions, one more check is needed using the newly generated grid, to ensure that a momentum balance occurs in the limit of a uniform temperature field (hydrostatic limit).

7.6. Hydrostatic Check Run

Based on experience with previous numerical models, distorted grids may result in spurious flows whose order of magnitude were comparable to those of natural convection flows. These spurious flows, although small, may invalidate the natural-convection solution. These flows are believed due to errors in the numerical approximation of momentum fluxes. To ensure that errors of this type do not exist, a case having an isothermal field was used to test the numerical model. The numerical model should produce a hydrostatic pressure field with zero velocities in this limit. Details regarding this run are in APPENDIX D. Results were satisfactory; that is, a zero velocity field with a hydrostatic pressure distribution was obtained. At this point, the program is deemed ready for running actual cases involving conditions in the liquid-lens system.

7.7. Computational Run with Nominal Inputs

A case was run using the best information available for geometry, thermophysical properties, and boundary conditions. This case is referred to as the "nominal" case. Geometry and thermophysical properties are known within

reasonable certainty. They have already been specified as inputs into the existing model. A complete set of boundary conditions, however, is not known with the desired level of certainty, and equipment-specification nominal values were used along with some approximations to arrive at the set of boundary conditions.

7.7.1. Boundary Conditions

Boundary conditions have some uncertainty, since not all of them could be measured directly. Boundary temperature is available at three points along the CRT face-panel perimeter, and at three points on the enclosure-frame exterior surface. The meniscus lens exterior temperature was believed unreliable, and was not used as input to the model. Heat flux data on the CRT face panel back surface is not available. Instead, the power of 14.2 W is available as input to the picture tube. The dimensions of the raster area on the rear side of the face panel, where heat is generated as the waste product of the light emission could not be measured by direct observation. Instead, minimum, nominal specification values for the equipment are available. The task at hand is to use the information available to arrive at a set of boundary conditions that could be used for a nominal run.
Boundary conditions are applied to external boundaries of the base-plate back and side surfaces, the enclosure side and front surfaces, and the meniscus wall exterior cylindrical perimeter and front surfaces – both flat and concave. A description of each of them is presented next.

Base Plate Back Surface

As the electron beam hits a "spot" on the phosphor layer, its energy is absorbed and converted to visible light, X-rays, and internal energy into the material, as shown in *Figure 7-8.* The rise in internal energy results in a temperature rise of the material. The rise in internal energy is itself a manifestation of heat generation occurring at the spot of impact of the electron beam. The temperature rise in the material, in turn gives rise to heat conduction through the face panel glass, and thermal radiation exchange between the phosphor

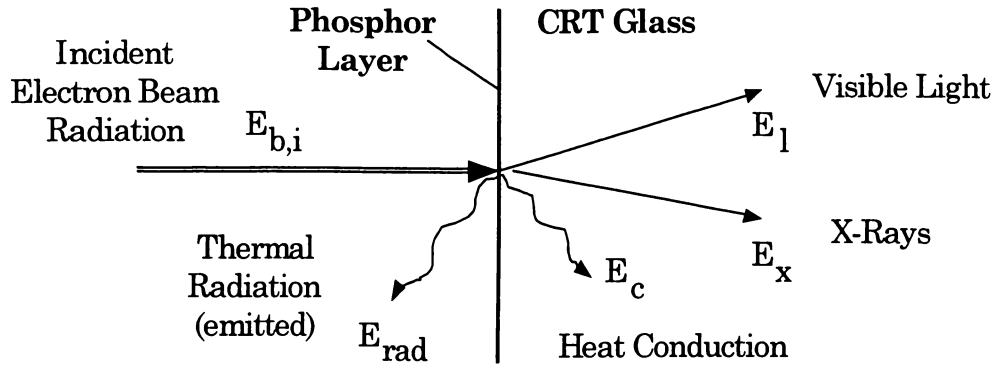

(1) All of the electron beam energy is absorbed at the phosphor layer.	$E_{b,i} = E_{b,a}$
(2) This energy is converted into light, X-rays, and internal energy of the material	$E_{b,a} = E_l + E_x + U$
(3) The internal energy is converted into heat conduction through the glass and thermal radiation emitted to the CRT interior.	$U = E_{rad} + E_c$

Note: U = Internal Energy

$E_{b,a}$ = Electron Beam Absorbed Energy

Figure 7-8. Energy Conversion Model within the Phosphor Layer

layer and the CRT internal glass walls behind the face panel. The fraction of the electron beam energy that is ultimately converted into internal energy, however, is unknown. The heat flux applied to the raster area can be estimated by the use of radiometry and photometry and theory [101]. It is assumed that upon impact, the electron beam releases visible light, X-rays, and thermal energy within the phosphor material (see *Figure 7-9*). Based on calculations using photometry and radiometry theory, and using a combination of tube manufacturer's specifications and tube's voltage and current measurements, the fraction of input power that is carried with visible light from the phosphor screen is approximately 10%. (APPENDIX E, Section E.1 contains these calculations.) If energy carried by X-rays and other forms of non-thermal radiation is neglected, the remaining 90 % of the input power may be assumed converted into internal energy within the phosphor layer, and ultimately dissipated by heat conduction and radiation. As indicated in *Chapter* 3, the electron beam input power was calculated as 14.2 Watts during the experiment. This implies

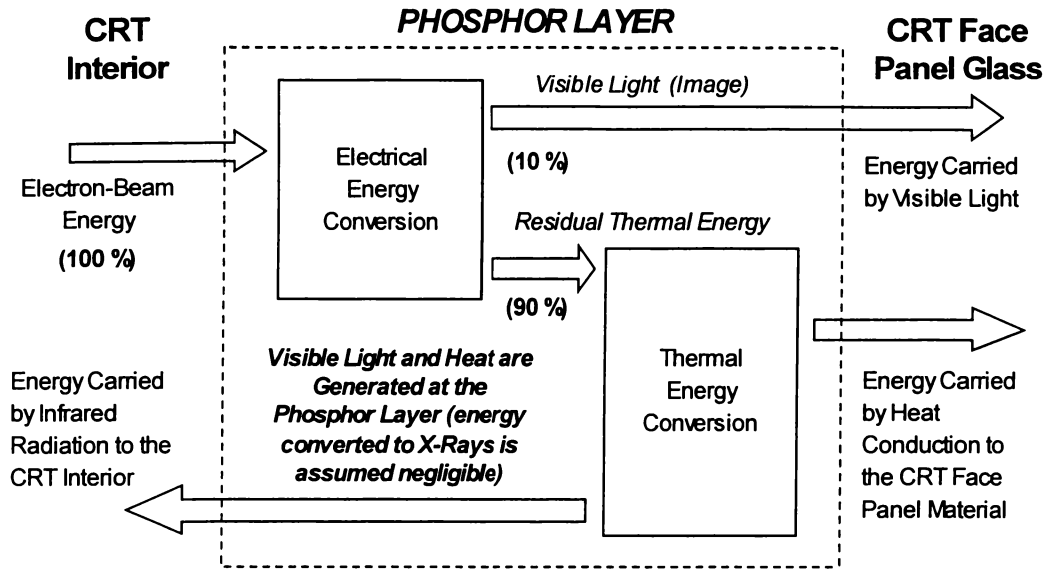

Figure 7-9. Phosphor-Layer Energy Flow Breakdown

that 90% of this power (12.78 Watts) can be assumed converted into thermal energy within at the phosphor layer (within the raster region).

The actual dimensions of the effective raster area in the experiment are also unknown. The manufacturer specifies minimum dimensions for the raster area with the maximum being the physical dimensions of the face panel back surface. This is a source of uncertainty. The size of the raster region can only be assumed, or taken as the minimum dimensions specified by the manufacturer. It is reasonable to assume minimum dimensions of 101.6 mm (full width) by 76.2 mm (full height) to establish a reference case. The resulting heat flux becomes

$$\dot{q}''_o = \frac{0.9 \times 14.2 W}{0.1016 m \times 0.0762 m} = \frac{12.78}{0.00774192} \frac{W}{m^2} = 1650.75 \frac{W}{m^2}. \qquad (7.27)$$

The boundary locations for the area of application of the heat generation rate above may not coincide with cell face edges. Therefore, the heat-generation flux may be applied to partial faces. The program handles this by weighing the heat flux by the partial cell-face area so that the total heat rate is unchanged.

Heat Transfer Through the Face-Panel Glass

Heat throughout the face panel glass may be assumed by conduction only, as the radiation exchange through it was estimated at less than one percent. (See APPENDIX E, Section E.2.)

Heat Transfer from the Face-Panel Back to the Cabinet Environment

Heat transfer occurs between the face panel back surface to the cabinet internal environment by a combination of radiation, conduction, and convection. A model for this process is illustrated in *Figure 7-10.* The process begins by thermal radiation exchange between the face panel back and the picture tube glass interior surface (funnel wall interior). Then, heat conduction takes place through the funnel walls from the interior to the exterior surface. Finally, heat convection and thermal radiation carry the thermal energy to the cabinet interior environment. Model details are included in APPENDIX E. The corresponding effective heat transfer coefficient was calculated to be $h_R = 3.72$ W/m^2-K for the average temperature of 71 °C on the face-panel back. This coefficient accounts for the combined effects of convection, conduction, and radiation. Sensitivity calculations show that the net heat transfer coefficient does not change by more than 4 % if the temperature is changed by 10 °C above or below the reference value of 71 °C, as shown in Table 7-7. The value of 3.72 W/m^2-K was applied uniformly over the base-plate back surface. Small temperature changes should not impact this value significantly.

Boundary Condition within the Raster Region

The boundary condition applied to the raster region is a combination of the uniform heat flux and the above convective-type boundary condition in the form:

$$-k_3 \frac{\partial T}{\partial Z} = \dot{q}_o'' - h_b \left(T - T_a \right), \tag{7.28}$$

where k_3 is the base-plate thermal conductivity, $\dot{q}_o''$ is the heat flux, h_b is the effective heat transfer coefficient calculate above, T_a is the cabinet interior environmental temperature, and Z is the face-local inward-facing spatial coordinate.

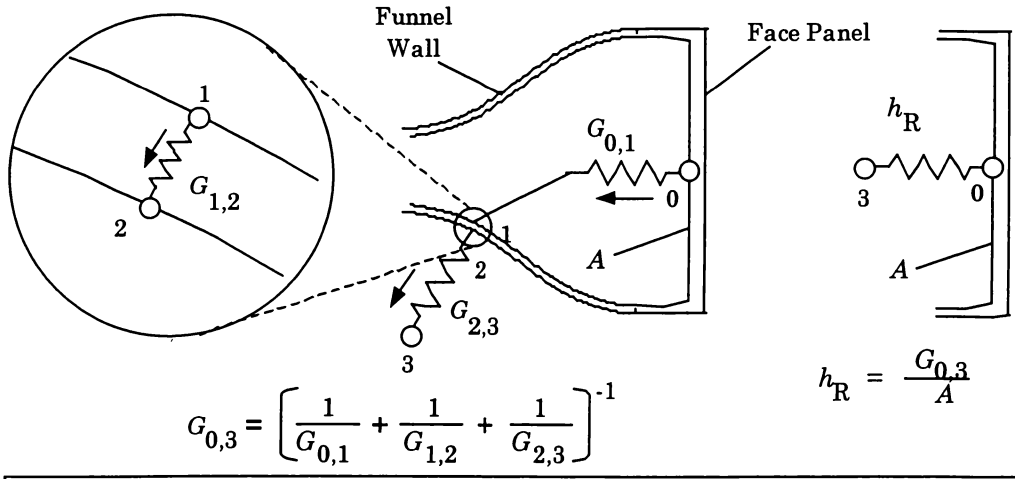

$G_{0,1}$ = Thermal conductance for thermal radiation exchange between the CRT face-panel back and the funnel interior

$G_{1,2}$ = Thermal conductance for conduction through the funnel walls

$G_{2,3}$ = Thermal conductance for convection and thermal radiation between the funnel wall exterior and the cabinet internal environment

h_R = Effective heat transfer coefficient

Figure 7-10. Network Model for Heat Transfer from the Face Panel Back to the Environment

Table 7-7. Sensitivity of the CRT Face-Panel Back-Surface Net Heat Transfer Coefficient to Back-Surface Temperature

	Units	Low	Mid-Value (Reference)	High
CRT Face Panel Back Surface Temperature	°C	61.0	71.0	81.0
h_b	W/m^2-K	3.740	3.872	4.002
$h_b - h_{b,ref}$	W/m^2-K	-0.132	0	0.131
		-3.4%	0	3.4%

Boundary Condition Outside the Raster Region

A convection-type boundary condition was applied to the area outside the raster region on the face panel back as:

$$k_3 \frac{\partial T}{\partial Z} = h_b \left(T - T_a \right), \tag{7.29}$$

where k_3 is the base-plate thermal conductivity, h_b is the effective heat transfer coefficient, T_a is the cabinet-interior environmental temperature, and Z is the face-local inward-facing spatial coordinate.

Base Plate Side Surfaces

A convective-type boundary condition was applied to the base-plate side surfaces. Temperature was not imposed because of two major reasons: (1) only three experimental points were available along the perimeter, and (2) the domain boundaries are too close to the temperature locations that will be used to check the results against. Because of the poor conduction within the glass, there is no assurance that the temperature is maintained within reasonable uniformity along the perimeter. Because of the proximity between the domain boundaries and the "internal" experimental points on the thermocouple grid, imposing the temperature on the boundary may defeat the purpose of using this grid for comparing experimentally and numerically determined temperatures.

Based on the above arguments, it was decided not to impose boundary temperatures on the base-plate side surfaces. Instead, a convective-type boundary condition is imposed with an effective heat-transfer coefficient that accounts for heat conduction through the portion of the glass outside the computational domain, and convection from the CRT face-panel side perimeter to the cabinet interior environment (see *Figure 7-11*). The above model yields the effective heat transfer coefficients shown in Table 7-8.

The boundary conditions for the base-plate side surfaces are stated as follows:

$$k_3 \frac{\partial T}{\partial Z} = h_4 \left(T - T_a \right) \ : \text{boundary \#4 (lower)}, \tag{7.30}$$

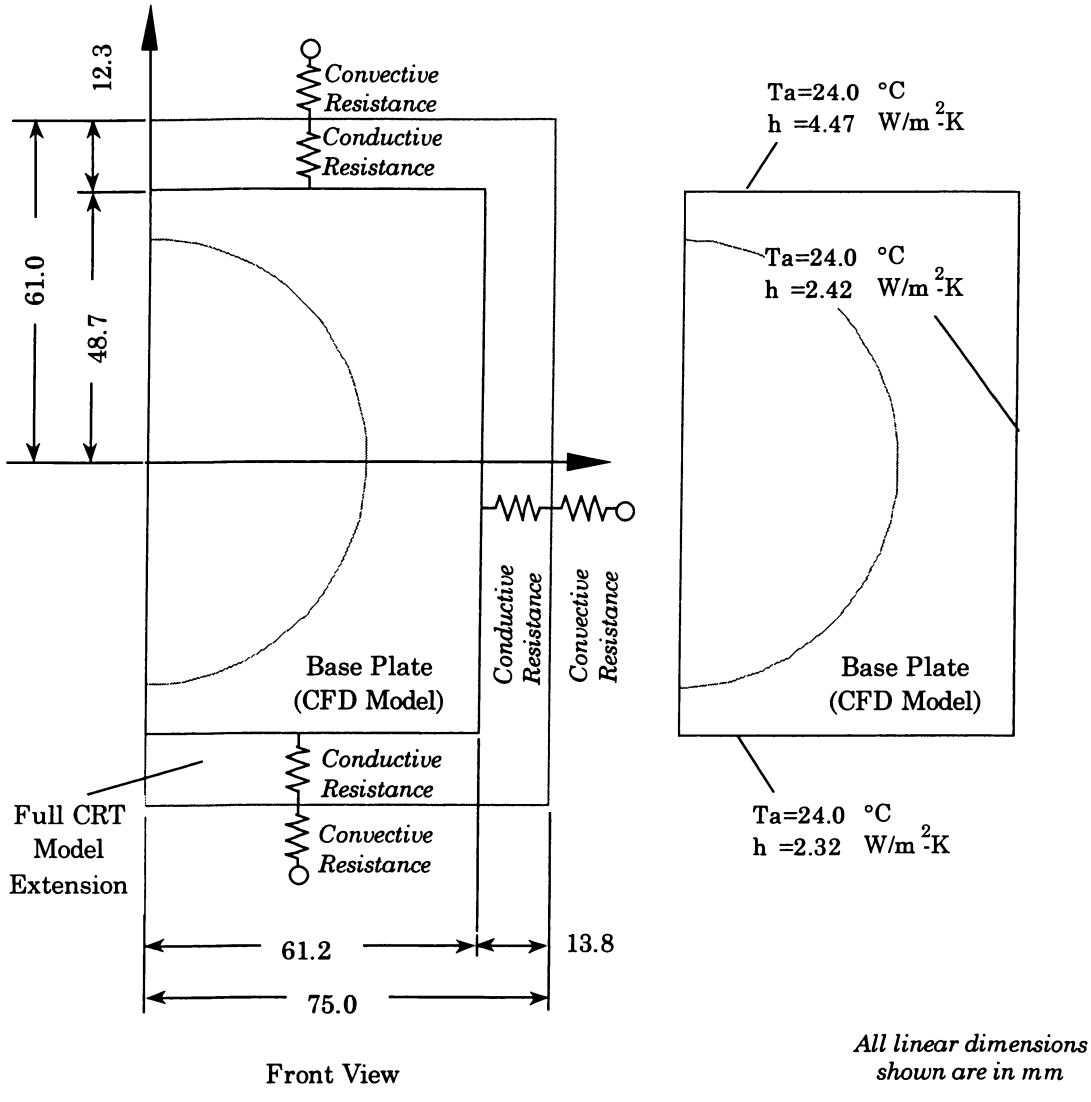

Figure 7-11. Base-Plate Side Boundary Heat Transfer Coefficients

Table 7-8. Base-Plate Side Surface Net Heat Transfer Coefficients

Base Plate Side Surface	Boundary Number	Heat Transfer Coefficient (W/m^2-K)
Upper	6	4.47
Lateral	5	2.42
Lower	4	2.32

$$k_3 \frac{\partial T}{\partial Z} = h_5 \left(T - T_a \right) \quad : \text{boundary \#5 (lateral), and} \tag{7.31}$$

$$k_3 \frac{\partial T}{\partial Z} = h_6 \left(T - T_a \right) \quad : \text{boundary \#6 (upper),} \tag{7.32}$$

where k_3 is the base-plate thermal conductivity, h_4, h_5, and h_6 are the effective heat transfer coefficients for each of the boundaries, as defined above, T_a is the cabinet-interior environmental temperature, and Z is the local inward-facing spatial coordinate on the face.

Enclosure Side Surfaces

Experimental temperatures were measured at the center point of the exterior of the enclosure lower surface, the lateral surface, and the upper surface, and steady-state values are available. For the sake of simplicity, it was assumed that these temperatures are maintained uniform across each of the corresponding surfaces in the numerical model. These temperatures were used as boundary conditions for the enclosure shell lower, lateral, and upper sidewalls as follows:

$$T_4 = 52.0°\text{C} \text{ for the enclosure lower-side surface,} \tag{7.33}$$

$$T_5 = 53.9°\text{C} \text{ for the enclosure lateral-side surface, and} \tag{7.34}$$

$$T_6 = 53.9°\text{C} \text{ for the enclosure upper-side surface.} \tag{7.35}$$

Enclosure Front Surface

The temperature applied to this surface was calculated as the arithmetic mean of the temperatures of the lower, lateral, and upper enclosure side surfaces above for the sake of simplicity:

$$T_{10} = \frac{1}{3}(52.0 + 53.9 + 53.9)°\text{C} = 53.2°\text{C}. \tag{7.36}$$

Meniscus-Wall Cylindrical Perimeter Surface

This surface has a very small heat transfer area, and it was assumed insulated for the sake of simplicity.

Meniscus-Wall Front Surface

A convective-type boundary condition was applied to the meniscus-wall front surface, as:

$$k_2 \frac{\partial T}{\partial Z} = h_3 \left(T - T_a \right), \tag{7.37}$$

where k_2 is the meniscus wall thermal conductivity, h_3 is the linearized heat transfer coefficient including convection and radiation from the meniscus wall exterior to the environment, T_a is the cabinet-interior environmental temperature, and Z is the local inward-facing spatial coordinate on the face. The boundary conditions applied to the CFD domain are summarized in *Figure 7-12* and Table 7-9. The tilt angle was set to 30°, and the hydrostatic reference temperature was 56 °C.

7.7.2. Program Results

The program was run in false-transient mode using the same execution control parameters, namely, the convergence tolerances, iteration limits, under-relaxation factor, and time-step size as used in the hydrostatic run above. Execution time was 2.5 hours for the same convergence parameters and number of iterations, and using the same computer as in the hydrostatic run.

Energy and Momentum Balance

A summary of domain energy and momentum balance, and cell and domain flux errors is shown in Table 7-10. Energy and momentum conservation was satisfied – both locally and globally, as shown by the small "balance" errors.

Comparison of Experimental and Numerical Results

Comparison between experimental and numerical temperatures for each thermocouple grid-point location is shown in Table 7-11. The numerical temperature at grid point j is designated as T_j^N, and experimental temperature at the same point is designated as T_j^E. Typical errors were within approximately 2 °C, except at two points with significant errors. The error on one of these points was

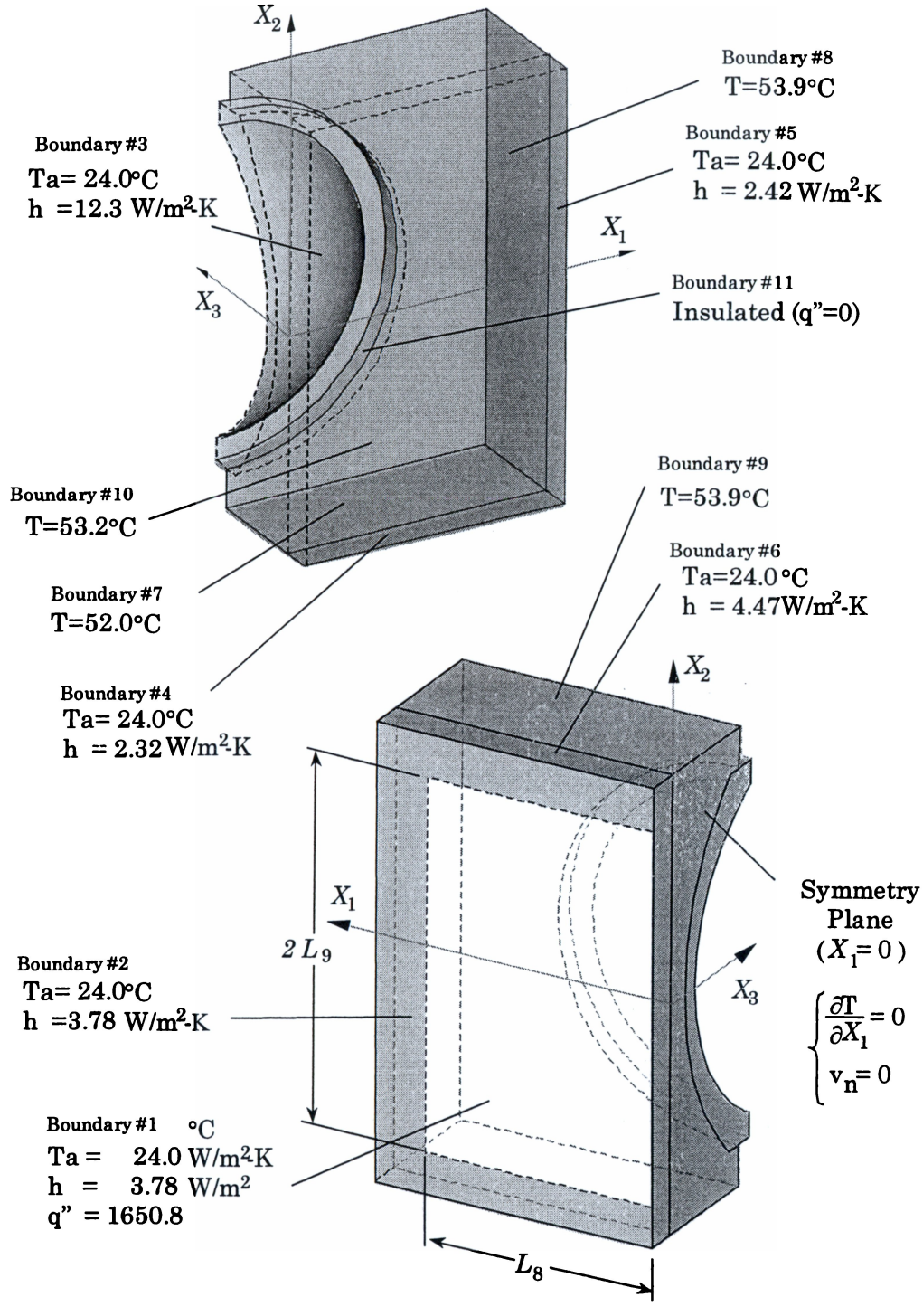

Figure 7-12. Summary of Boundary Conditions

Table 7-9. Boundary Conditions for the Liquid-Lens Nominal Case

No.	Description	Boundary-Condition Type	Value
1	Convective Boundary Condition with Flux Generation within Raster Region Dimensions: $2 \cdot W$ = 101.6 mm H = 76.2 mm	Surface Flux Generation[1]	q'' = 1650.75 W/m²
		Convective[2]	Ta = 24.0 °C, h = 3.8 W/m²-K
2	Area outside Raster Region on Face Panel Back Surface	Convective [2]	Ta = 24.0 °C, h = 3.8 W/m²-K
3	Meniscus Lens Exterior, Center (Concave Side)	Convective [3]	Ta = 24.0 °C, h = 12.3 W/m²-K
4	Face Panel Exterior Lower Surface	Convective [3]	Ta = 24.0 °C, h = 2.32 W/m²-K
5	Face Panel Exterior Lateral Surface	Convective [3]	Ta = 24.0 °C, h = 2.42 W/m²-K
6	Face Panel Exterior Upper Surface	Convective [3]	Ta = 24.0 °C, h = 4.47 W/m²-K
7	Enclosure Frame Exterior Lower Surface	Value[4]	T = 52.00 °C
8	Enclosure Frame Exterior Lateral Surface	Value[4]	T = 53.90 °C
9	Enclosure Frame Exterior Upper Surface	Value[4]	T = 53.90 °C
10	Enclosure Frame Exterior Front Surface	Value[5]	T = 53.20 °C
11	Meniscus Lens Cylindrical Perimeter Surface	Insulated	q'' = 0

(1) Assumes 90% of Input Power Distributed over Raster Region of Nominal Dimensions = 0.9 × 14.2 W /(0.1016 m × 0.0762 m)= 1650.75 W/m²

(2) Radiation to CRT Interior, Conduction through CRT walls, and Convection and Radiation to Environment

(3) Conduction through Part of CRT Glass and Convection to Air

(4) Experimental Surface Temperature

(5) Average of #4, #5, and #6.

Table 7-10. Energy and Momentum Balance – Nominal Case

Dependent Variable	→	T	U_1	U_2	U_3
Variable	*Symbol*				
Cell Storage Error	$\varepsilon_{cell}^{sto} \times 10^9$	0.003	0.067	0.022	0.022
Cell Balance Error	$\varepsilon_{cell}^{bal} \times 10^9$	1.394	0.674	0.298	0.298
Units	→	(W)	(mN)	(mN)	(mN)
Net, Boundary Influx	F^{in}	5.646	0.320	0.473	0.473
Net, Boundary Efflux	F^{out}	5.646	0.320	0.549	0.549
Net, Stored	$F^{sto} \times 10^9$	7.824	-0.022	-0.927	-0.927
Net, Generated	F^{gen}	0.000	0.000	0.076	0.076
Balance	$F^{bal} \times 10^9$	10310.3	0.5	-2.7	-2.7
Domain Storage Error	$\varepsilon^{sto} \times 10^9$	1.386	0.070	1.689	1.689
Domain Balance Error	$\varepsilon^{bal} \times 10^9$	1826.3	1.7	4.9	4.9

Table 7-11. Nominal Case Numerical and Experimental Temperature Comparison at Face Panel Grid Locations

Grid Point	*j*→	*1*	*2*	*3*	*4*	*5*	*6*	*7*	*8*	*9*
X_1	(mm)	0	0	0	25	25	25	50	50	50
X_2	(mm)	-35	0	35	-35	0	35	-35	0	35
T_j^N (numerical)	(C)	57.7	64.4	63.5	57.9	64.2	63.7	55.8	59.8	58.2
T_j^E (experimental)	(C)	57.0	56.8	61.4	56.3	64.9	59.0	54.7	59.9	57.5
$Error = T_j^N - T_j^E$	(C)	0.7	7.6	2.1	1.6	-0.7	4.7	1.1	-0.1	0.7

7.7 °C occurred at grid-point #2, corresponding to the CRT face-panel center-point. The second largest error of 4.8 °C occurred at grid point #6, at coordinates (25,35) mm. Plots of the numerical temperatures along lines parallel to the CRT face-panel minor axis ("vertical axis") are shown in *Figure 7-13*. A discrepancy in the trend for the temperature profile passing through the CRT center point is evident in the figure. To quantify the correlation between the numerical and experimental sets of data, the correlation coefficient must be calculated, as shown next.

Correlation Coefficient

The numerical solution is effectively a "physics-based" curve fit through experimental data. To check the quality of such curve fit, a correlation coefficient [46] can be calculated from experimental and numerical temperatures on the thermocouple grid. If k denotes such set of N_k points, the correlation coefficient, r_k, is calculated as:

$$r_k = \left[1 - \left(\frac{\eta_k}{\sigma_k}\right)^2\right]^{1/2} \quad (\text{if } \eta_k < \sigma_k, \text{ otherwise, } r_k = 0), \tag{7.38}$$

where η_k is the *correlation deviation*, and σ_k is the *standard deviation* associated with the data set k. Notice that if the correlation deviation is greater than the standard deviation, the correlation coefficient would become an imaginary number. This situation may occur when the curve fit used for the data is of very bad quality. In those situations is better to talk in terms of the "square" of the correlation coefficient, r_k^2, which although negative, is still a real number. The standard deviation is calculated as:

$$\sigma_k = \left[\frac{\sum_{j=set\{k\}} \left(T_j^E - \bar{T}_k\right)^2}{(N_k - 1)}\right]^{1/2} \tag{7.39}$$

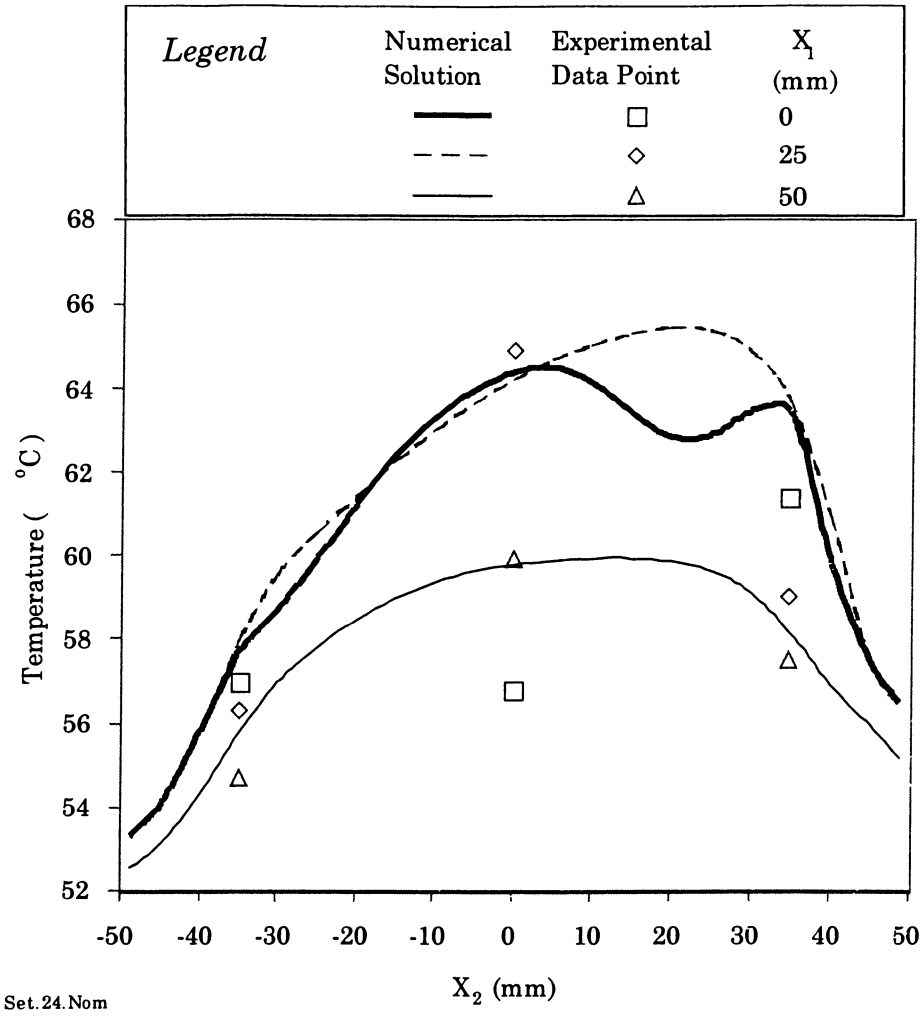

Figure 7-13. Comparison between Numerical and Experimental Temperatures on the CRT Face Panel Grid – Nominal Case

where $\bar{T}_k$ is the experimental-temperature arithmetic mean (average temperature). The average temperature is calculated as:

$$\bar{T}_k = \frac{1}{J_k} \sum_{j=set\{k\}} T_j^E \,. \tag{7.40}$$

The correlation deviation is calculated as:

$$\eta_k = \left(\frac{G_k}{(J_k - 2)} \right)^{1/2} \tag{7.41}$$

where G_k is the *correlation error function*, defined as the sum of the squares of the errors as:

$$G_k = \sum_{j=set\{k\}} \left(T_j^N - T_j^E \right)^2 . \tag{7.42}$$

Results from the above equations are shown in Table 7-12. The curve-fitting deviation is larger than the standard deviation, yielding an imaginary correlation coefficient. In this situation, it is better to state the results in terms of the square of the correlation coefficient, $r_k^2 = -0.339$. The negative value indicates that there is no correlation, and that the numerical solution is a bad curve fit for the experimental data.

The correlation between the experiments and the numerical results could be changed by removing points from the correlation. *Figure 7-14* shows the effect of removing one point at a time from the correlation, and using only the remaining points in the calculations. Removing most of the points results in reductions of the square of the correlation coefficient, except when removing points #2 and #6, which result in an increase; thereby, improving the correlation. This might suggest that these two points are "suspects," but this conclusion should not be made lightly, unless the problem is analyzed in more detail, and the uncertainty in the boundary conditions is removed.

Table 7-12. Nominal-Case Statistics

Minimization Function	G_k (°C^2)	90.065
Number of Points	N_k	9
Average Temperature	$\bar{T}_k$ (°C)	58.6
Standard Deviation	σ_k (°C^2)	3.10
Curve-Fit Deviation	η_k (°C^2)	3.587
Square of the Correlation Coefficient	r_k^2	-0.339
Correlation Coefficient	r_k	---

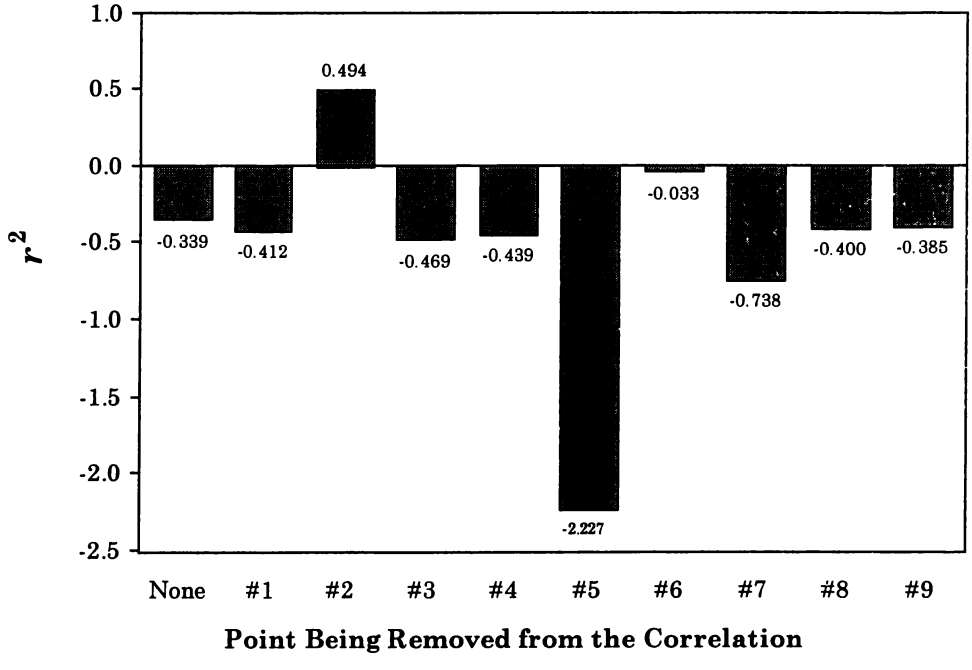

Figure 7-14. Effect of Removing Individual Data Points from the Calculation of the Correlation Coefficient

Discussion

From the above results, it was unclear whether the source of such large discrepancies between the numerical and experimental data can be solely attributed to the set of heat-flux-raster-dimension chosen. There are at least seven potential sources for error, which are not exclusive from each other.

The first explanation involves the validity of the thermocouple measurements. There is the possibility that one or perhaps more thermocouples had a bad connection. Calibration was made prior to the laboratory measurements to ensure that temperatures were measured properly. However, there is always the chance that any physical disturbance, such as relocating equipment, or re-heating could result in the loss of calibration of the instrumentation. There were nine electrical contact points per thermocouple, including the thermocouple junction itself, and any disturbance could potentially change the electrical resistance of these contacts. In addition, the thermocouple junctions were soldered, not welded. Soldered thermocouples are more sensitive to this type of problem. A bad or high-resistance circuit produces "low" temperature readings. From the experimental transient temperature plots, no conclusions could be made regarding the status of the circuitry, as the temperature increase was monotonic from the start, an all of the transient curves follow the same pattern. This does not suggest that the circuitry was working properly, but that the proof of faulty circuitry cannot be established.

The second explanation implicates the physical location of the thermocouple junctions on the face panel. Calculations show that there is a relatively large temperature gradient within the fluid near the face panel surface. The main component of the temperature gradient is in the direction normal to the surface. From computer results, the average magnitude of the temperature gradient in this direction on the face-panel exterior surface is approximately 3.3 °C/mm only at the point of contact with the surface. This value increases to 5.5 °C/mm at the face – panel center. This suggests that any minor gap between the thermocouple and the face-panel surface may lead to significant errors in the temperature readings. This might help explain, at least in part, the 7.6 °C and 4.7 °C errors at grid point #2 (face-panel center) and #6, respectively. These would be reported as "low" readings

by the instrumentation system. There is some likelihood for the presence of low readings, as thermocouples were much easier to remove from the face panel surface than anticipated when dismantling the experimental apparatus.

The third explanation implicates the assumptions made for the development of the mathematical model. The most obvious one has to do with thermal radiation through the fluid. Neglecting radiation through the face panel glass is not as significant as neglecting radiation through the fluid, if there is indeed any. Proximity to the meniscus lens around the face panel center may lead to a reduction in the face panel surface temperature, if radiation were to take place between this surface and the meniscus lens through the fluid. Information about radiative properties of the fluid to pursue this possible source of error was not found.

The fourth explanation implicates the degree of uniformity in the actual rate of heat being generated per unit raster area. Visual observations showed a uniform brightness on the projector monitor screen. Therefore, the electron beam flux had to be uniform, since brightness is directly related to the electron beam flux. Having a uniform electron beam flux implies that the heat flux at the phosphor layer was uniform. Consequently, there is no argument to support that the heat generation rate per unit area (heat flux) wasn't uniform.

The fifth explanation implicates an error in the derivation of the mathematical model, or its implementation into computer code. Several checks have been made to ensure self-consistency within the model, and against published data, and nothing seems to indicate that this is the case.

The sixth explanation concerns the boundary conditions use as program inputs. The temperatures imposed on the enclosure walls are believed to be realistic. The measured temperatures on the lateral and upper sidewalls were nearly identical, and the measured temperature on the lower wall was slightly lower. Small errors in these temperatures should only affect the overall temperature level for the face-panel temperatures – not the trends. Convective-type boundary conditions were applied to the base-plate back surface, the base-plate side surfaces, and the meniscus-wall front surface. The temperature on the base-plate front surface should not be very sensitive to small errors in the heat transfer

coefficient assigned to these surfaces, as long as the order of magnitude is correct. The other boundary conditions are the heat flux applied to the face panel back and the dimensions of the raster region. As mentioned earlier, there is a level of uncertainty associated with these boundary conditions, especially the raster dimensions.

Finally, the seventh explanation the values used for the thermophysical properties for the fluid and solid components. Variation in the fluid viscosity (i.e., Prandtl number) has a large effect on the flow pattern, and could, as well have an effect on the temperature distribution. Variations in the thermal diffusivity also have an effect on the temperature field. However, significant effort was invested into determining approximate values for the thermophysical properties, and it is believed that these values are known with reasonable certainty. Variations within this certainty should not affect the results significantly.

Conclusions

A set of boundary conditions were determined from a combination of direct experimental measurements, the use of heat transfer correlations, and equipment specifications. These boundary conditions were used to numerically solve the conjugate natural convection and conduction heat transfer in the liquid-lens system. A poor correlation between numerical results and the original set of experimental data caused by discrepancies resulting from only two data points. The correlation could have been increased by selectively removing points from the correlation, but without having exhausted all of the possible variations in the boundary conditions with the highest uncertainty, it was preferred to avoid this. The more likely explanation under the assumption that the radiation model is correct (the glass and the fluid are opaque to thermal radiation), is that some of the thermocouples were not in good thermal contact with the face-panel surface.

The next task is to design a method that finds optimum values for the heat flux and raster area dimensions resulting in the minimization of the correlation error function. To identify "suspect" data points, this method will be used for various sets of grid-point combinations used in the correlation.

7.8. Optimization of the Boundary Conditions

The previous case using nominal inputs resulted in no correlation with experimental data; that is, the square of the correlation coefficient was negative. This suggested that either the set of boundary conditions imposed were incorrect, and/or one or more of the thermocouple temperature measurements used to calculate the correlation coefficient was incorrect, or was measuring the temperature correctly, but at the wrong location. Thus, the remaining task is two-fold: finding an optimized set of boundary conditions, and identifying the non-correlating temperature point(s).

7.8.1. Optimization Solution Approach

The boundary condition parameters to be optimized are the heat flux, the raster width, and the raster height. These parameters were selected since they carry the greatest uncertainty. Raster dimensions are only known within a range specified by the manufacturer. Initial values were assumed as "minimum" width and height dimensions. Preliminary estimates for the heat flux were based on these dimensions along with heat-dissipation estimates using radiometry and photometry theory. It is believed that the temperature distribution on the face panel is very sensitive to the above parameters. For the sake of simplicity, the assumption was made that the raster region was centered within the face panel back. Therefore, a symmetric raster area was used for the numerical model, resulting in only two dimensions to adjust (width and height). The criteria for optimization will consist of finding the set of heat-flux and raster dimensions that minimize an optimization function. The optimization function is defined as the correlation error function, G, as defined in Eq. (7.42), which is obtained from numerical results. There are two ways to calculate the optimization function. The first one involves the generation of numerical solutions in sequence, depending of the independent variables requested by the optimization routine. The second involves a pre-calculating the numerical solutions and then using an interpolation function to determine the value of the optimization function.

Optimization by Sequential Numerical Calculations

One way is to specify an initial set of heat flux and raster dimensions, and use an optimization method to find the extrema. This method requires that the CFD program be run sequentially for each set of boundary conditions. In addition, if the solution dependency is highly nonlinear on these guesses, an improper selection of the initial guess may lead to the optimized solution at a local minimum, as depicted in *Figure 7-15*. If this is the case, a new initial guess must be used, and the entire process must be repeated, as the search path may not lie along the previous path.

Optimization by Numerical Solution Pre-Calculation

Another approach is to build a matrix of CFD solutions on the parameter space, as shown in *Figure 7-16*, that can be accessed any number of times by the optimization routine. In this manner, only a set with a finite number of heat flux and raster dimension combinations is needed. The clear advantage of this approach is that the CFD cases required to solve each of the grid points can be run in parallel. If a local minimum were obtained from an improper initial guess, a new guess could be made, and the process be repeated very rapidly, without having to rerun several CFD cases, as required by the previous approach. Thus, the latter approach was chosen because of these advantages.

7.8.2. Process for Identifying Suspect Data Points

In order to identify suspect data points, the optimization process shall allow the systematic removal of data points from the calculation of the optimization function, i.e., the correlation error function, G. The maximum number of points removed shall not exceed 25% of the total number of points. Since there are 9 points total, a maximum of 2 points can be removed. Sets with all the possible combinations of none, one, and two points removed from the calculation will be assembled and each individual combination optimized.

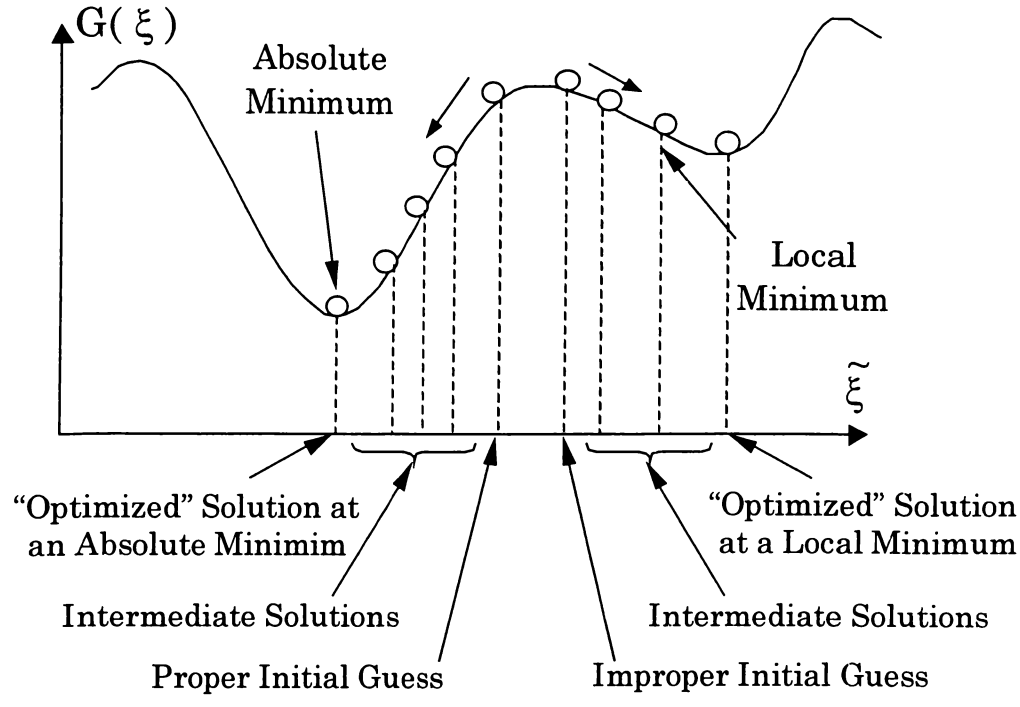

Figure 7-15. Sequential Solution Optimization Search

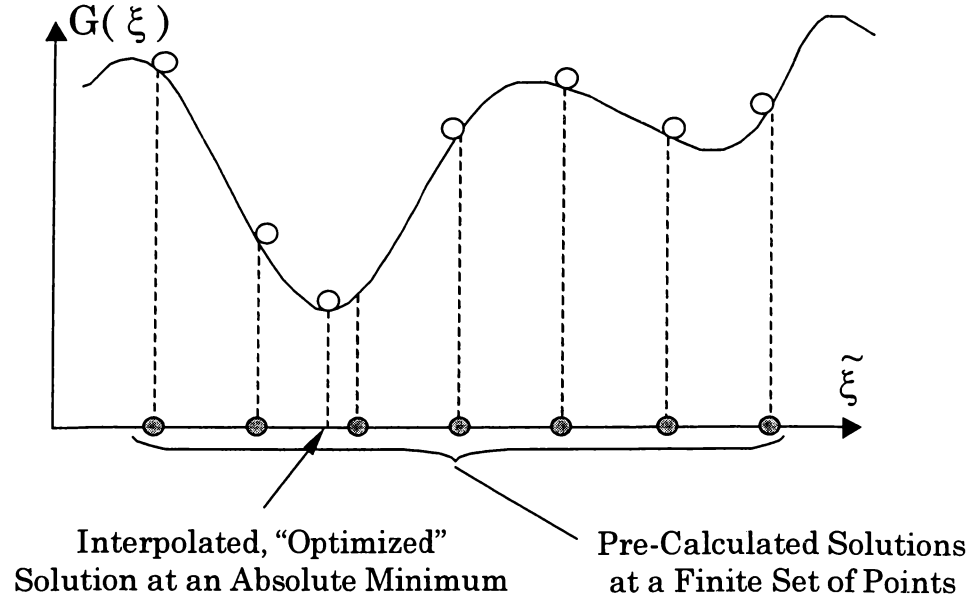

Figure 7-16. Pre-Calculated-Solution Optimization Search

7.8.3. Optimization Methodology

In principle, the larger the number of CFD-run data points, filling the parameter space, the higher the quality of the interpolation function that can be obtained. However, to keep the number of CFD runs to a manageable level, only three values per parameter will be used.

The three-dimensional grid with three parameter coordinates in each direction is shown in *Figure 7-17.* This grid requires 27 CFD runs. A tri-quadratic interpolation function was used to map the parameter space using these points. The middle point is assigned nominal inputs for the boundary conditions. This point also becomes the initial guess. This method should provide adequate solutions if the optimization function is continuous within the parameter space, and if there are no double minima, as the interpolation function does not allow it. It is hoped that the absolute minimum is close enough to the initial guess point. It is possible, however, in the event that a double minimum is suspected, or if more accuracy is required to add more points to the grid and run the CFD cases for the new points. A new interpolation function would, however, be required in this case.

For convenience, ξ_1, ξ_2, and ξ_3 will denote fractions of reference values for heat-flux, raster width, and raster height, as:

$$\xi_1 = \frac{\dot{q}''}{\dot{q}''_{ref}}, \tag{7.43.a}$$

$$\xi_2 = \frac{W}{W_{ref}}, \tag{7.43.b}$$

$$\xi_3 = \frac{H}{H_{ref}}, \tag{7.43.c}$$

where $\dot{q}''_{ref}$ is the reference heat-flux calculated using the measured input power and nominal raster dimensions, W_{ref} is the CRT specification's minimum raster width, and H_{ref} is the CRT specification's minimum raster height. With the reference raster width and height given as:

$$W_{ref} = 101.6\,\text{mm}, \text{ and} \tag{7.44.a}$$

$$H_{ref} = 76.2\,\text{mm} \tag{7.44.b}$$

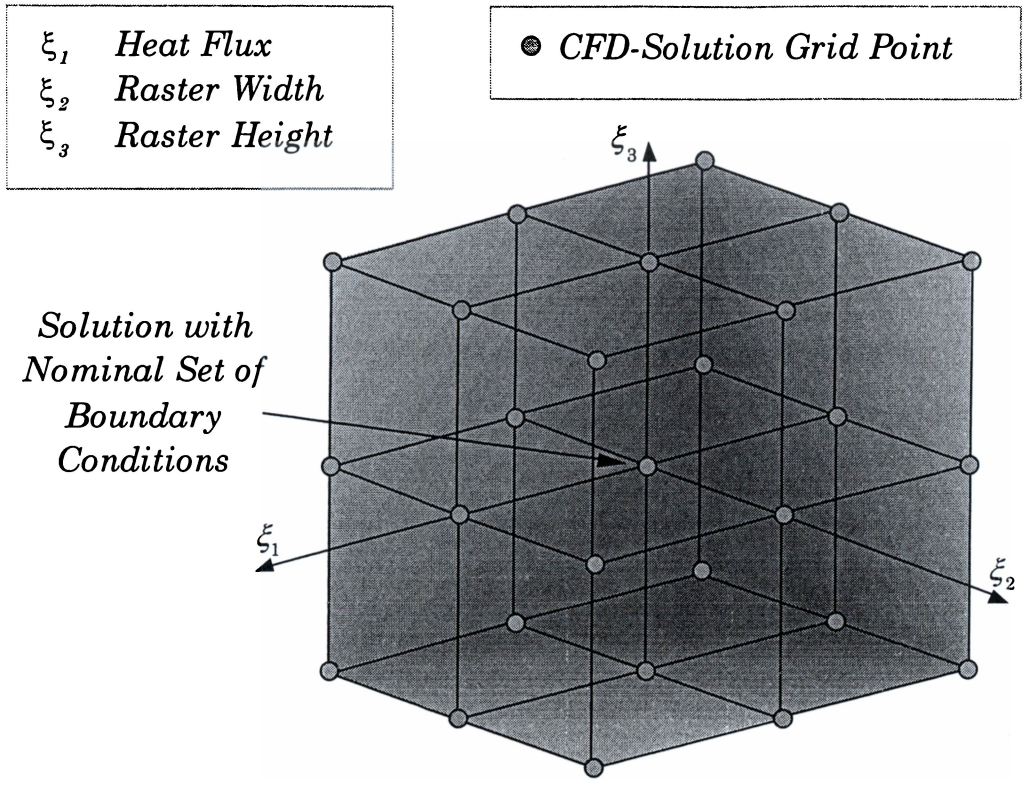

Figure 7-17. Gridded-Solution Optimization Search

the reference heat-flux may be calculated as:

$$\dot{q}''_{ref} = \frac{\dot{Q}_{input}}{W_{ref} \times H_{ref}} = \frac{14.2W}{0.1016m \times 0.0762m} = 1834.2\frac{W}{m^2}. \qquad (7.45)$$

Values for the parameter fractions were selected as shown in Table 7-13.

Pre-Calculation Matrix CFD Runs

The above fractions were used to calculate inputs for the heat flux, raster width, and raster height. Cases were numbered from 1 to 27, with case #1 having all "lows"; that is $\xi_1 = 0.8$, $\xi_2 = 0.9$, and $\xi_3 = 0.9$. Then the fractions for each subsequent case were obtained by increasing first ξ_3, then ξ_2, and finally ξ_1, with case #27 having fractions of $\xi_1 = 1.0$, $\xi_2 = 1.1$, and $\xi_3 = 1.1$. All other program inputs were left identical to those for the nominal case. Program runs were distributed

Table 7-13. Parameter Fractions for the Optimization Grid

		Low	Nominal	High
Heat Flux Density Fraction	ξ_1	0.8	0.9	1.0
Raster Region Width Fraction	ξ_2	0.9	1.0	1.1
Raster Region Height Fraction	ξ_3	0.9	1.0	1.1

among the various computers shown in APPENDIX F for faster execution.

Face-Panel Grid Interpolation

Once CFD runs have been completed for each m-case, m = 1, 2, ..., 27, the temperature values at the CRT face-panel thermocouple-grid locations were interpolated from CFD face-node values on the base-plate front surface.

Intra-Run Interpolation

Before the optimization process can be started, a function capable of interpolating grid-point solutions between runs must be postulated. A tri-quadratic function is used because of its relative simplicity in code implementation. If there are J=9 face-panel grid points, M=27 parameter-space grid points, a polynomial of degree (N-1)=2 can be assembled by adding all of the combinations resulting from the products of the three parameters, ξ_n, n=1,2,3, as

$$T_j\left(\tilde{\xi}\right) = \sum_{m=1}^{M} a_m^j \prod_{n=1}^{N} \xi_n^{i(m,n)}, \quad j = 1,2,\ldots,J \tag{7.46}$$

where j denotes each of the face-panel grid point locations (j=1,2,3,...,J), $\tilde{\xi}$ is the parameter-space vector, a_m^j (j = 1,2,3,...,N; m=1,2,...,M) is the coefficient associated with the mth term of the function (not the CFD run) used to interpolate the temperature at the j-grid-point location, and $i(m,n)$ (m=1,2,...,27; n = 1,2,3) is the exponent of ξ_n in the mth term of the function. The exponent $i(m,n)$ is an integer function with the values specified in Table G-1 (APPENDIX G, Section G.1). As the temperature at each of the face-panel grid points, $T_j\left(\tilde{\xi}\right)$ (j = 1,2,3,...,J), is known from CFD solutions, for all of the M parameter-space grid locations, $\tilde{\xi} = (\xi_1, \xi_2, \xi_3)$, a set of M linearly independent equations is available associated to each of the j-

at a time from correlation calculations. The total number of combinations becomes 46, broken-down as follows.

No points removed:	1	combination
One point removed:	9	combinations
Two points removed:	36	combinations

7.8.6. Optimization Solution Implementation

To solve the optimization problem, an initial sub-grid of the independent variables was created. An initial "search" was made to identify the point resulting in the minimum error function. This was done to ensure that the final optimization did not result in a local minimum. This point was used as the starting point for the final optimization process. The final optimization process was done using the GRG2 optimization program [70]. A computer program was written to read face-panel surface temperatures from computer run output files and call GRG2. The program sorts the information in decreasing value of the correlation coefficient. Results are presented next.

7.8.7. Optimization Program Results

The temperatures interpolated on the face-panel grid are shown in Listing G-2 (APPENDIX G). The coefficients in the tri-quadratic function are included in Listing G-4. Optimized values of the independent variables and the correlation error function, G, are shown in Listing G-5. The correlation coefficient and other statistical data are included in Listing G-6. Listing G-7 contains the optimized grid temperatures, and Listing G-7 contains the grid-temperature errors. To sort the information, each of the combinations was assigned a *configuration-ranking index* based on decreasing value of the correlation coefficient. The configuration-ranking index ranges between 1 and N, where N is the number of combinations for a given set using no point, one point, or two points removed. Thus, three sets of combinations have been ranked. The individual combinations within these sets are arranged such that the configuration-ranking index increases as the correlation coefficient decreases, resulting in the highest correlation coefficient for the

face-panel grid-points. Therefore, nine M-by-M matrices must be inverted to get the coefficients a_m^j. The results are tabulated in Listing G-3 (APPENDIX G, Section G.1).

7.8.4. Optimization Criteria

It was mentioned earlier that bad thermal contact may results in "low" temperature readings. Therefore, experimental readings "above" numerical values should have better quality associated as compared to those readings "below" numerical values. As these points have better quality, the closest the value of the numerical solution approaching from below the data point, the better the quality of the results. Incorporating this into the optimization process requires the quantification of constraints. To simplify the problem, a constraint will be imposed such that the calculated temperature at the point of maximum experimental temperature is equal or greater than the experimental value. The experimental data point with the highest temperature is point #5 with a temperature of 64.9 °C. Therefore, the optimization constraint will be:

$$T_5 \geq T_5^E \left(= T_{\max}^E \right). \tag{7.47}$$

7.8.5. Optimization Process

The process starts by optimizing the boundary conditions having all of the grid points. Then, it proceeds to having one point removed, for instance, grid point #1. Then, optimization of the boundary conditions starts, with the correlation error function, G, calculated using all of the points except point #1. The optimization process should result in optimum values for the independent variables, i.e., the heat flux, and the two raster dimensions. The process is repeated removing point #2, #3, and so on until point #9. Then another set of combinations starts, but removing two points at a time, i.e., points #1, and #2, then #1, and #3, and so on. In total, there are three optimization sets with combinations of none, one, and two points removed

configuration index of one. Results are shown in *Figure 7-18* for the 46 optimized grid-point combinations. A zero correlation coefficient may indicate either zero or an imaginary value. The same order is kept when plotting the correlation error function for each of these sets.

The optimized values for heat flux and raster dimensions, along with a complete set of statistics for the combinations having the highest correlation coefficient among the three sets is provided in Table 7-14. The points removed are also identified. Based on the results, the optimized solution including all of the grid points produces a nominal improvement in the correlation, as r_k^2 increases from -0.339 to -0.247. If one grid point at-a-time is removed from the calculations, the best correlation is obtained without point #2 (face panel center). The resulting value for r_k^2 increases from a negative number to +0.802. This was a significant increase, since the maximum value for this variable is unity. The correlation coefficient becomes $r_k = 0.896$. If two grid-points are removed simultaneously from the calculations, the best correlation is obtained without point #2 and #6 (upper,

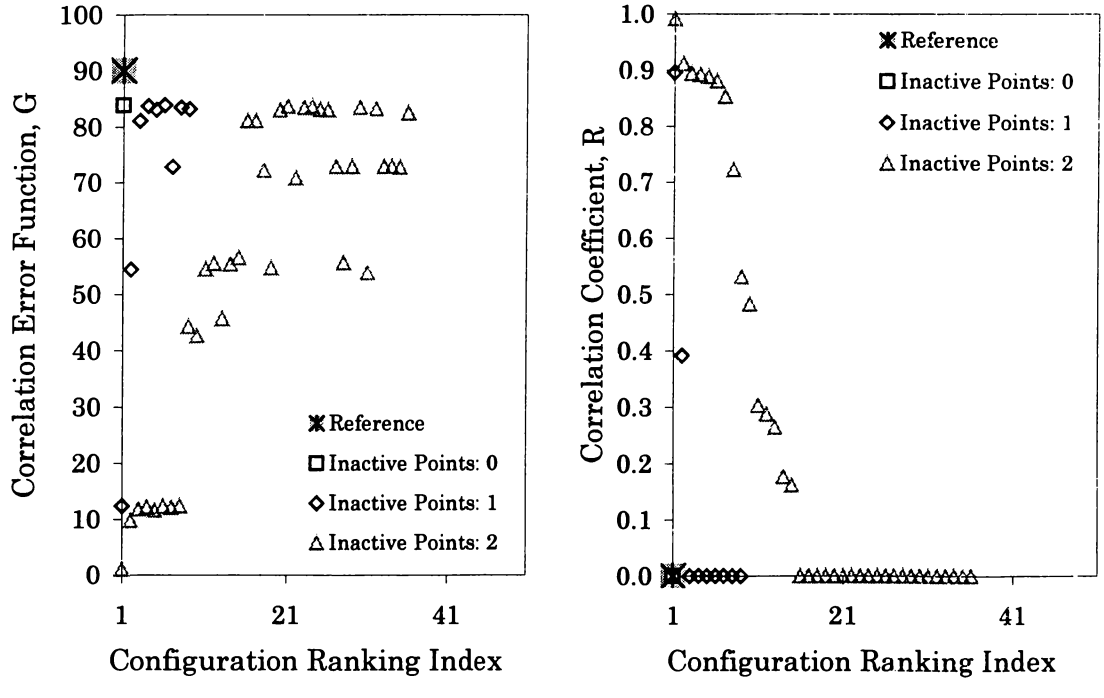

Figure 7-18. Distribution of the Correlation Error Function and the Correlation Coefficient Over the Configuration Space

Table 7-14. Optimization Results' Summary

			Nominal Conditions	Optimization Results		
Number of Points Removed			0	0	1	2
Point Number Removed						
	#1					
	#2				×	×
	#3					
	#4					
	#5					
	#6					×
	#7					
	#8					
	#9					
Heat Flux Density Fraction	ξ_1		0.900	1.033	1.031	1.087
Raster Width Fraction	ξ_2		1.000	0.9852	0.9932	0.9757
Raster Height Fraction	ξ_3		1.000	0.8514	0.8498	0.8831
Correlation Error Function	G_k	(°C²)	90.07	83.88	12.42	1.054
Average Temperature	$\bar{T}_k$	(°C)	58.61	58.61	58.84	58.81
Standard Deviation	σ_k	(°C)	3.100	3.100	3.234	3.492
Correlation Deviation	η_k	(°C)	3.587	3.462	1.439	0.459
Correlation Ratio	r^2		-0.339	-0.247	0.802	0.983
Correlation Coefficient	r		0.000	0.000	0.896	0.991
Heat Flux Density	q	(W/m²)	1650.8	1895.5	1891.1	1993.0
Raster Width	W	(mm)	101.6	100.1	100.9	99.1
Raster Height	H	(mm)	76.2	64.9	64.8	67.3
Power	Q	(W)	12.78	12.31	12.36	13.29
Percent of Input Power		(%)	90.0%	86.7%	87.0%	93.6%

middle grid point). Removal of these points yields increases in the square of the correlation coefficient to 0.983 and in the correlation coefficient to 0.991. Temperature plots are provided for the above combinations in *Figure 7-19*. Points removed from the calculations were also removed from the plots.

7.8.8. Selection of the Reference Case

The purpose for having a reference case established is to have a self-consistent numerical solution that matches experimental results closely enough to serve as a benchmark for subsequent studies. The above results indicated that the correlation with experimental data could be substantially improved if data point #2 (face-panel center grid point) and data point #6 (upper middle grid-point) are removed from the set. Even in the unlikely event that the numerical solution for these two points was mistaken, a valid comparison could still be made for the others. In such scenario, the computer model could still be used for further analysis, as long as temperature results are ignored near these two points. Furthermore, points #2 and #6 did not show experimental maxima; therefore, ignoring them should be of no consequence for the thermal performance results, since thermal performance is evaluated in terms of the maximum temperature, which took place at point #5. Based on the above reasoning, points #2 and #6 will be removed from the validated experimental set.

7.9. Reference Case Final Run

The previous optimized solution was interpolated from a set of CFD solutions. Therefore, fluxes are not directly available, and if they are obtained by interpolation, they may not fully obey conservation laws. In order to get the actual fluxes an additional CFD case was run with the optimized values for heat flux and raster dimensions, as shown in Table 7-15. The temperature profiles are shown in *Figure 7-20* for reference purposes, and the data is tabulated in Table 7-16. The solution is slightly off from the optimized case with two points off, which wasn't surprising, considering that the present solution is the result of a full CFD run. The

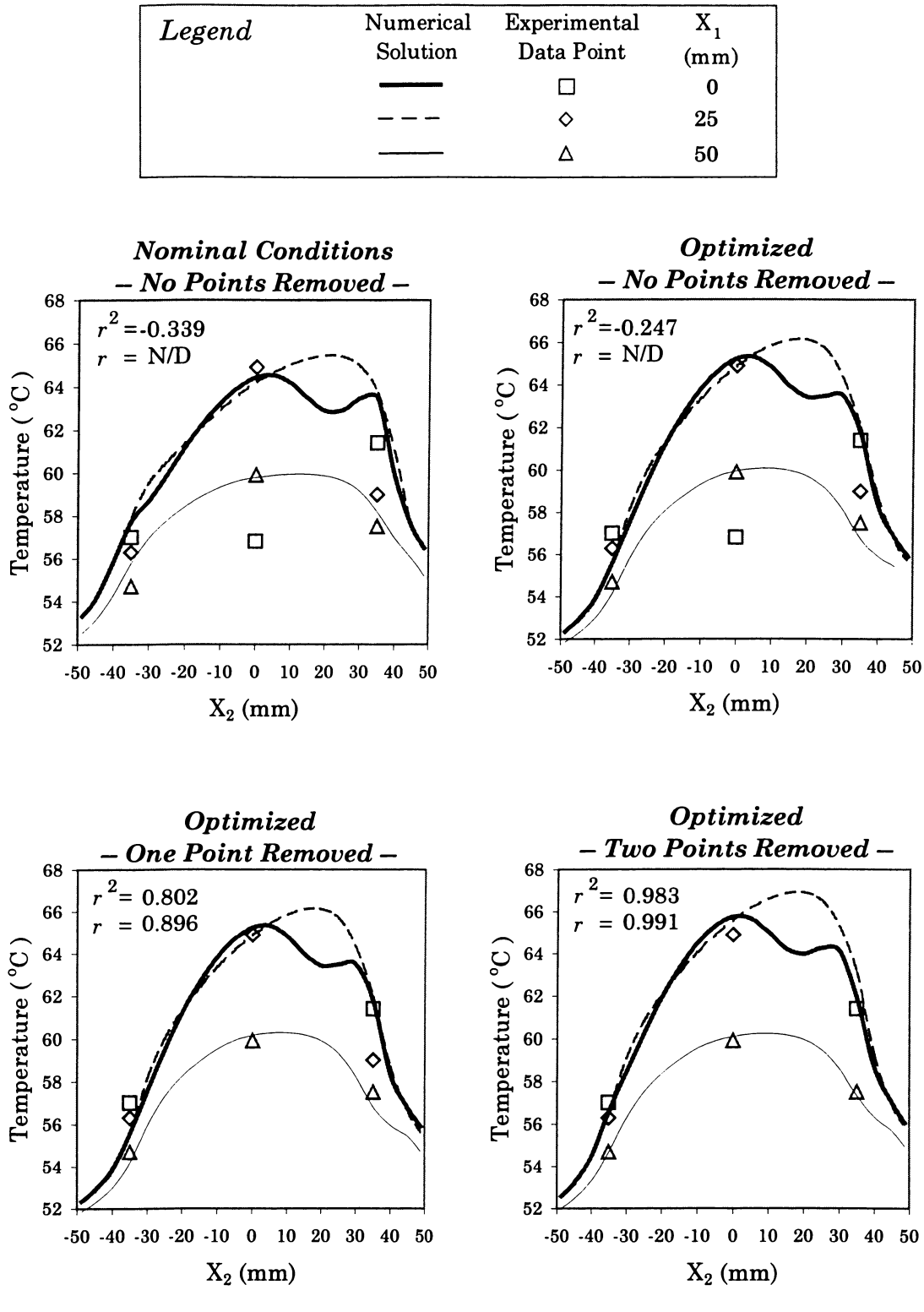

Figure 7-19. Comparison of Optimization Results

Table 7-15. Reference Case Heat Flux and Raster Dimensions

Heat Flux Density	q	(W/m^2)	1993.0
Heated-Region Width	W	(mm)	99.1
Heated-Region Height	H	(mm)	67.3
Power	Q	(W)	13.29
Percent of Input Power		(%)	93.6%
Heated-Region Width Ratio (W/L_1)	σ_1		0.8096
Heated-Region Width Ratio (H/L_2)	σ_2		0.6910

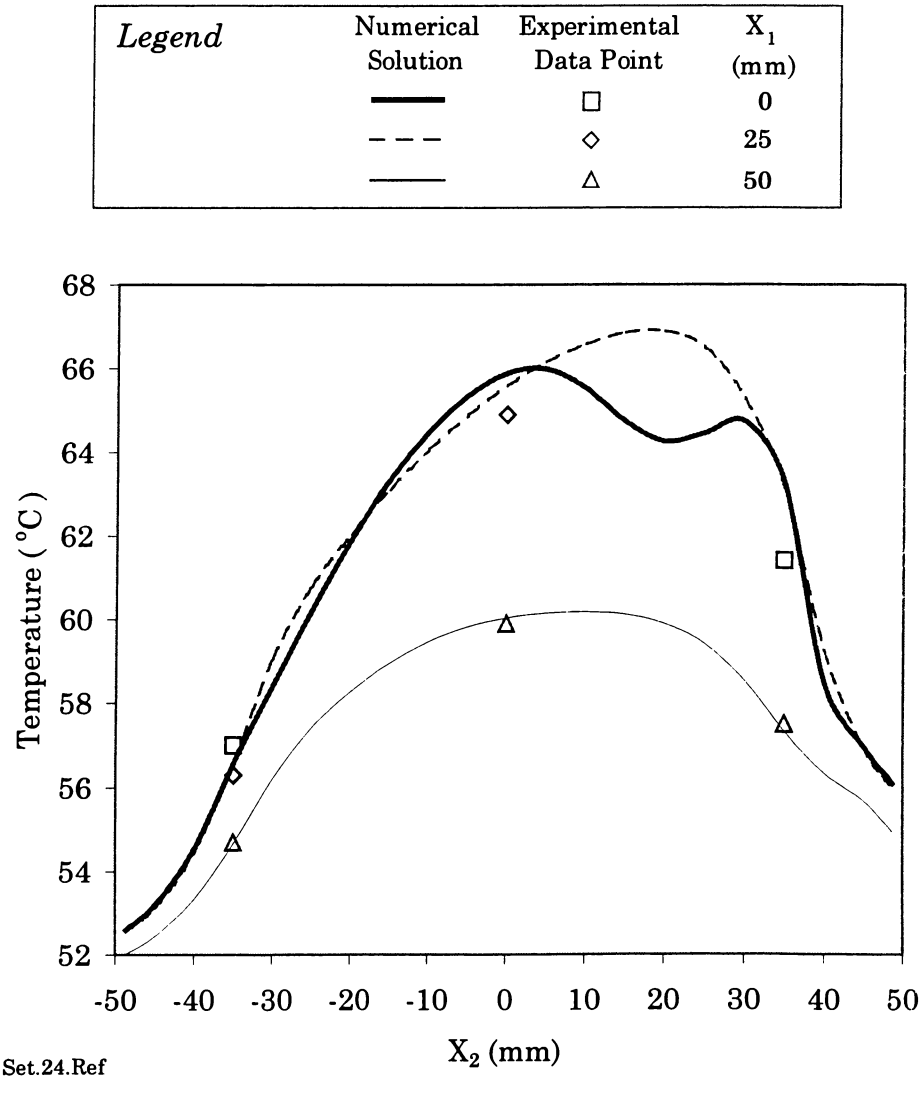

Figure 7-20. Comparison of Numerical and Experimental Temperatures on the CRT Face Panel

Table 7-16. Reference Case Numerical and Experimental Temperature Comparison at CRT Face Panel Grid Locations

Grid Point	*j→*	*1*	*2*	*3*	*4*	*5*	*6*	*7*	*8*	*9*
X_1	(mm)	0	0	0	25	25	25	50	50	50
X_2	(mm)	-35	0	35	-35	0	35	-35	0	35
T_j^N	(C)	56.6	65.9	63.3	56.6	65.6	63.1	54.7	60.0	57.3
T_j^E	(C)	57.0	---	61.4	56.3	64.9	---	54.7	59.9	57.5
$Error = T_j^N - T_j^E$	(C)	-0.4	---	1.9	0.3	0.7	---	0.0	0.1	-0.2

new set of statistic variables is included in Table 7-15. The correlation coefficient dropped from 0.991 to 0.965.

Flux Balance Check

A summary of domain fluxes, and cell and domain flux errors is shown in Table 7-18. Energy conservation was satisfied – both locally and globally, as suggested by the small flux-balance errors.

7.9.2. Liquid-Lens Thermal Performance

The thermal performance of the liquid lens system is compared with the manufacturer's specifications in Table 7-19. The picture tube manufacturer specifies two requirements for thermal performance. They are that (1) the maximum temperature on the face-panel surface does not exceed 90 °C at the center, and (2) that the temperature differential between this point and peripheral points does not exceed 21 °C. The temperature at the face panel center was calculated at 65.9 °C, which is below the maximum allowable value of 90°C. The minimum peripheral-point temperature from the experimental measurements was 50.6 °C. Therefore the edge-to-center point temperature differential becomes 15.3 °C, which is below the maximum allowable differential value of 21 °C. The corresponding mean temperature gradient becomes 0.27 °C/mm, which is below the maximum allowable value of 0.375 °C/mm. The maximum temperature on the base-plate front surface

Table 7-17. Reference Case Statistics

Minimization Function	G_k (°C^2)	4.247
Number of Points	N_k	7
Average Temperature	$\bar{T}_k$ (°C)	58.8
Standard Deviation	σ_k (°C^2)	3.49
Curve-Fit Deviation	η_k (°C^2)	0.922
Square of the Correlation Coefficient	r_k^2	0.930
Correlation Coefficient	r_k	0.965

Table 7-18. Flux Balance – Experimental Reference Case

	Equation →	T	U_1	U_2	U_3
Variable	*Symbol*				
Cell Storage Error	$\varepsilon_{cell}^{sto} \times 10^9$	0.004	0.118	0.029	0.012
Cell Balance Error	$\varepsilon_{cell}^{bal} \times 10^9$	2.781	1.064	0.454	0.064
		(W)	(mN)	(mN)	(mN)
Net Boundary Influx	F^{in}	5.975	0.382	0.519	0.747
Net Boundary Efflux	F^{out}	5.975	0.382	0.650	0.974
Net Storage Flux	$F^{sto} \times 10^9$	11.843	-0.114	-0.340	-0.144
Net Generated Flux	F^{gen}	0.000	0.000	0.131	0.227
Flux Balance	$F^{bal} \times 10^9$	15969.9	-5.4	7.9	0.8
Storage Flux Error	$\varepsilon^{sto} \times 10^9$	1.982	0.298	0.524	0.148
Balance Flux Error	$\varepsilon^{bal} \times 10^9$	2672.8	14.3	12.2	0.9

Table 7-19. Face Panel Thermal Compliance

	Requirement	Numerical Results
Center-Point Temperature (°C)	90	65.9
Center-Point Temperature Differential (°C)	21	15.3
Edge-to-Center-Point Mean Temperature Gradient (°C/mm)	0.375	0.273
Maximum Temperature (°C)	90	67.6

was calculated at 67.6 °C at coordinates (13.5, 18.9) mm. This temperature was higher than the center-point temperature, and should be used instead, for requirement compliance.

7.9.3. Heat Flux Analysis

Table 7-20 summarizes the heat transfer rates and mean temperature on the major domain boundaries. The same results are depicted in *Figure 7-21*. It must be noted that the CFD domain was half the size of the physical domain, which was divided by a symmetry plane perpendicular to the face panel. Therefore, the heat transfer rates reported are half of those in the physical domain.

The net heat-generation rate at the base plate back is 6.647 W. From there, 1.258 W (18.9%) is transferred from the base-plate back to the environment by conduction, convection, and radiation (tube's interior, wall, and surroundings). The total thermal power going forward into the CFD domain from the face panel back becomes 5.389 Watts (81.1 % of the net input). A very small fraction, which amounts to 1.7 % of the total heat, is transferred to the face-panel side surfaces. The remainder (79.3 %) goes forward into the fluid. The heat rates transferred to the enclosure walls are 8.2%, 14.6%, 16.7%, and 24.1% of the total heat, to the lower, lateral, upper, and front walls, respectively. The heat transfer going to the meniscus lens front surface accounts for 15.6% of the total heat. The total thermal power out from the domain is less than 2 mW below the input value, for a percent error of -0.03%.

Table 7-20. Reference Case CFD-Domain Thermal Boundary Fluxes and Mean Temperatures

		Thermal Power (W)	Percent Power (%)		Mean Temperature (°C)	Heat Flux Area (cm^2)
Heat Generation		6.6475	100.0	IN		33.3
Base Plate:						
Back	(B_1, B_2)	1.2585	18.9%	OUT	68.3	59.6
Lower	(B_4)	0.0296	0.4%	OUT	53.7	4.3
Lateral	(B_5)	0.0524	0.8%	OUT	55.6	6.9
Upper	(B_6)	0.0358	0.5%	OUT	57.0	4.3
Front (fluid interface)		5.2694	79.3%	Internal	60.2	59.6
Enclosure:						
Lower	(B_7)	0.5453	8.2%	OUT	51.8	15.6
Lateral	B_8)	0.9717	14.6%	OUT	53.9	24.8
Upper	(B_9)	1.1095	16.7%	OUT	53.9	15.6
Front	(B_{10})	1.6026	24.1%	OUT	53.2	34.4
Meniscus Wall:						
Front	(B_3)	1.0402	15.6%	OUT	50.7	32.4
Energy Balance						
Total Power, IN		6.6475	100.00%	IN		
Total Power, OUT		6.6458	99.97%	OUT		
Percent Difference		-0.0017	-0.03%			

Note: B_i, denotes boundary number "i" on the liquid-lens system's computational model

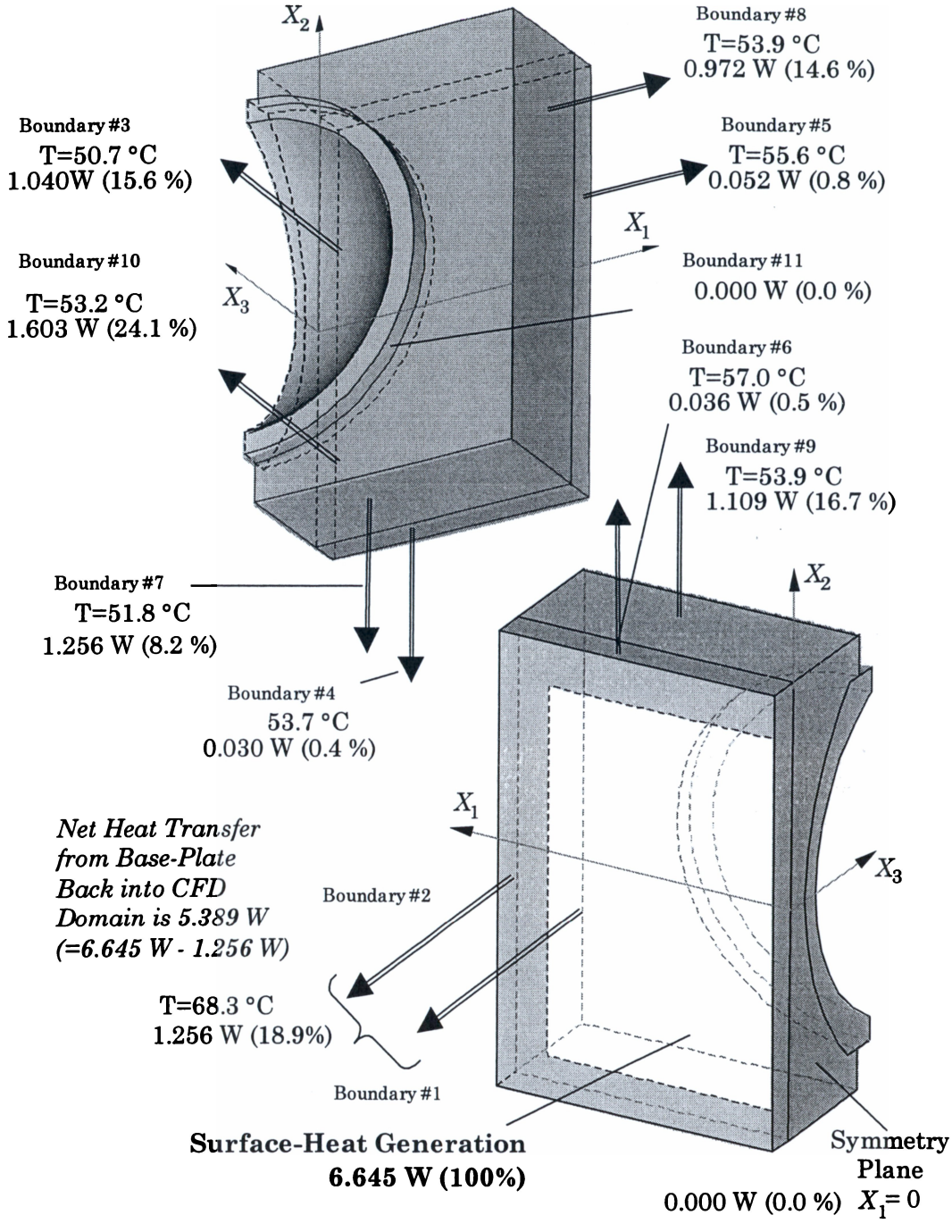

Figure 7-21. Reference Model Boundary Energy Fluxes

7.9.4. Comparison against Predictions Using Heat Transfer Correlations

It is interesting to note that the numerical prediction for the face-panel-front mean temperature was only 0.3 °C below the predicted value using correlations for two-dimensional natural convection in enclosures and a lumped-parameter heat transfer network. The heat-transfer model used in *Chapter* 3, to estimate the mean temperature on the face-panel-front was used again, with the input heat rate changed from 90% to 93.6% of the net input power. This was necessary to reflect the fraction used in the numerical predictions, which corresponds to a net heat rate of 13.29 W. This method resulted in a mean temperature of 60.5 °C, which is close to the one obtained from CFD calculations of 60.2 °C for the base plate front, as shown in Table 7-20.

7.9.5. Full-Enclosure Run

A run using the full enclosure dimensions (without the symmetry-plane assumption) was run. Results showed that the flow was indeed symmetric about the geometric vertical symmetry plane.

7.9.6. Overall Thermal Characterization

The above CFD results were used to determine what fractions of the total heat input were output to the frame and directly to the environment. Table 7-21 shows the fractions of heat transfer going to the mounting frame and to the environment. Heat transfer to the frame accounts for 37 % of the heat transfer dissipated by the enclosure and 24 % of the heat transfer into the system. The experimentally validated model was characterized into a lumped-parameter thermal-network model. This model could be used for sensitivity studies with small variations in the input heat flux, and variations in the thermal conductance to the environment based on the configuration tested. That is, same geometry, properties, and tilt angle. Thermal conductances in the model were derived from heat transfer and temperature data in Table 7-20 and Table 7-21. This model is included in APPENDIX G, Section G.2.

Table 7-21. Heat Dissipation Distribution

					Heat Transfer to Environment		*Heat Transfer to Frame*	
	Flux	*Area*	T_m	ΔT	*Flux*	*Fraction*	*Flux*	*Fraction*
	W	cm^2	°C	°C	W		W	
Base Plate								
Back Surface	2.517	119.2	68.3	44.3	2.517	1.000	0.000	0.000
Lower Surface	0.059	8.69	53.7	29.7	0.059	1.000	0.000	0.000
Lateral Surface	0.105	13.8	55.6	31.6	0.105	1.000	0.000	0.000
Upper Surface	0.072	8.69	57.0	33.0	0.072	1.000	0.000	0.000
Enclosure								
Lower Surface	1.091	31.21	51.8	27.8	0.868	0.796	0.223	0.204
Lateral Surface	1.943	49.67	53.9	29.9	1.485	0.764	0.458	0.236
Upper Surface	2.219	31.21	53.9	29.9	0.933	0.421	1.286	0.579
Front Surface	3.205	68.80	53.2	29.2	2.009	0.627	1.196	0.373
Meniscus Wall	2.080	64.82	50.7	26.7	2.080	1.000	0.000	0.000
Totals:								
Base Plate	2.753	150.43			2.753	100.0%	0.000	0.0%
Enclosure	8.458	180.89			5.295	62.6%	3.163	37.4%
Meniscus Wall	2.080	64.82			2.080	100.0%	0.000	0.0%
System	13.29	396.1			10.128	76.2%	3.163	23.8%

7.9.7. Summary

A mathematical model of the experimental setup was solved and numerical results were obtained. First, a model of the experimental geometry was built into a CFD grid. Material properties were assigned to the CFD model, reflecting a combination of standard table, manufacturer-specification, and measured values. The mathematical model was first tested in the limit of zero-input heat flux with insulated boundaries to check consistency in hydrostatic conditions. Then, nominal boundary conditions were applied, and results were obtained with poor correlation with experimental data. The boundary conditions were optimized, and two suspect internal temperature data points were removed from the experimental set to improve the correlation, which resulted in a correlation coefficient of 0.96, indicating adequate correlation. Momentum and energy balance was checked indicating local and global conservation. Isobars, isotherms, thermal isoflux lines, and thermal isograds were plotted on major domain surfaces.

The maximum temperature at the face-panel center and the maximum temperature differential between face-panel periphery points and center were calculated for reference purposes in order to verify compliance with manufacturer specifications. For a room temperature of 21.7 °C, the calculated values were 65.9 °C and 15.3 °C, respectively, which were below the manufacturer's maximum allowable values of 90 °C and 21 °C, respectively. The maximum temperature on the base plate exterior was calculated at 67.6 °C at coordinates (13.1, 18.6) mm. The maximum temperature-gradient magnitude was used to indicate where fracture of the glass material is more likely to initiate as a result of thermal stresses. The maximum temperature-gradient magnitude was calculated at 2.73 °C/mm at coordinates (7.4, 16.9) mm. The maximum temperature on the base plate back was calculated at 82.5 °C at coordinates (15.8, 12.8) mm, and the maximum temperature-gradient magnitude was calculated at 3.08 °C/mm at coordinates (47.9, 14.4) mm.

8. VISUALIZATION OF NUMERICAL RESULTS

8.1. Introduction

This chapter presents plots for the visualization of various solution fields of the reference (benchmark) solution obtained in *Chapter* 7. The variables used for field visualization are (1) the piezometric pressure, plotted as *isobars*, (2) the velocity field, plotted using *pathlines*, (3) the face-panel temperature field plotted using *isotherms*, (4) the face-panel temperature gradient plotted using lines of constant temperatureogradient magnitude (*isograds*), and (5) energy-flux field, plotted using lines of constant heat-flux magnitude (*thermal isoflux lines*) and with lines tangent to the energy-flux vector field (*heatlines*).

8.2. Isobars

Figure 8-1 shows isobars on coordinate planes. Isobars are nearly horizontal except near the base plate. The maximum and minimum values for static pressure occur on the lower and upper edges of the domain. The maximum piezometric pressure occurs near the point of maximum static pressure, but the minimum value occurs slightly above the base plate center.

8.3. Description of Flow Circulation

Particle pathlines are shown in *Figures 8-2* through *8-7*. The pathlines simulate the trajectories of particles released at selected points in the flow field. The lines are obtained by integration of the velocity vector. The length of the pathline depends on the time specified for integration. The arrowhead at the end of the pathline indicates the direction. *Figure 8-2* shows pathlines starting at grid points 2 mm away from the base plate. The general flow is in the upward direction along the surface except near the upper edge, where the fluid moves downward. The fluid in the upper-right area region moves downward and inward (towards the

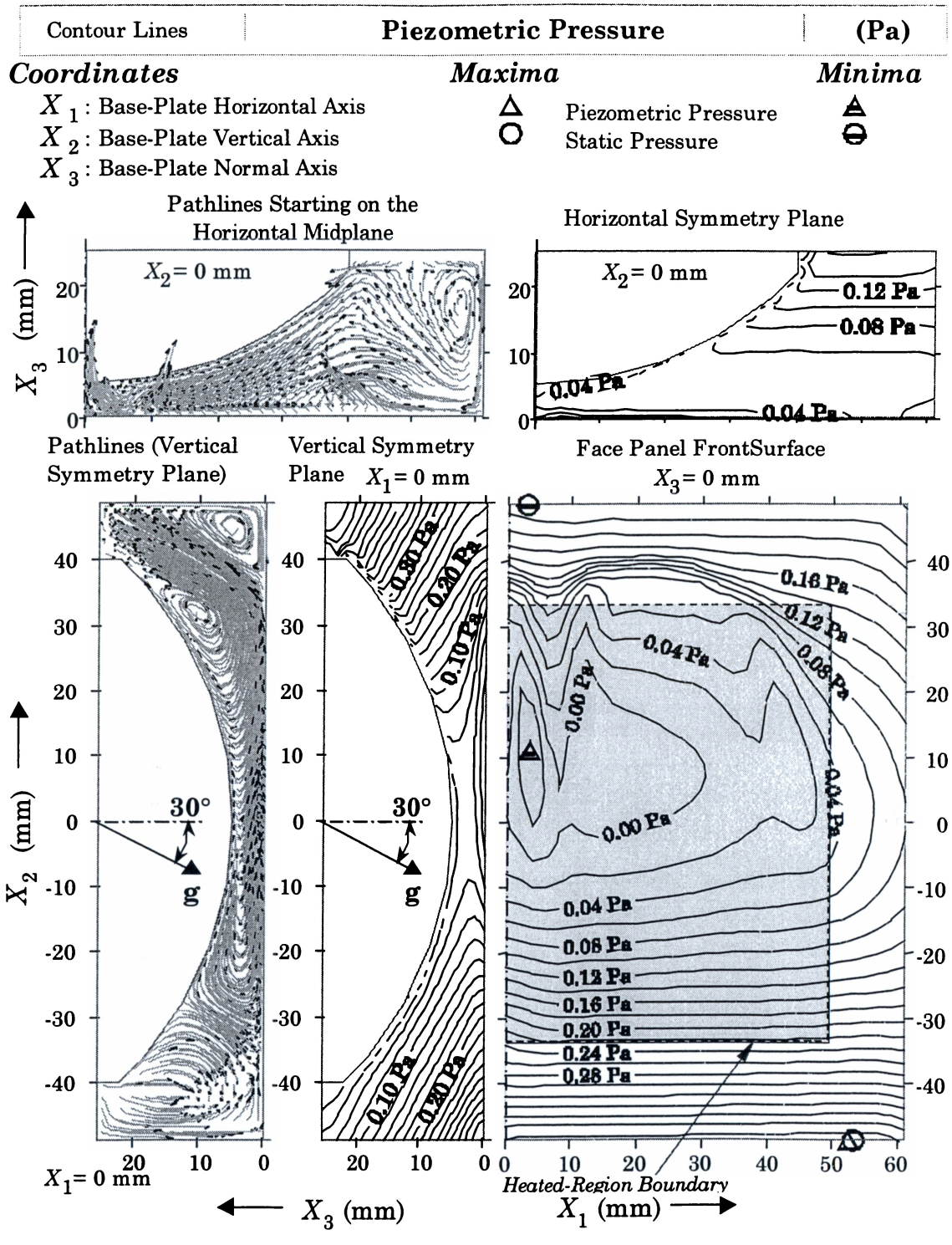

Figure 8-1. Isobars on Coordinate Planes

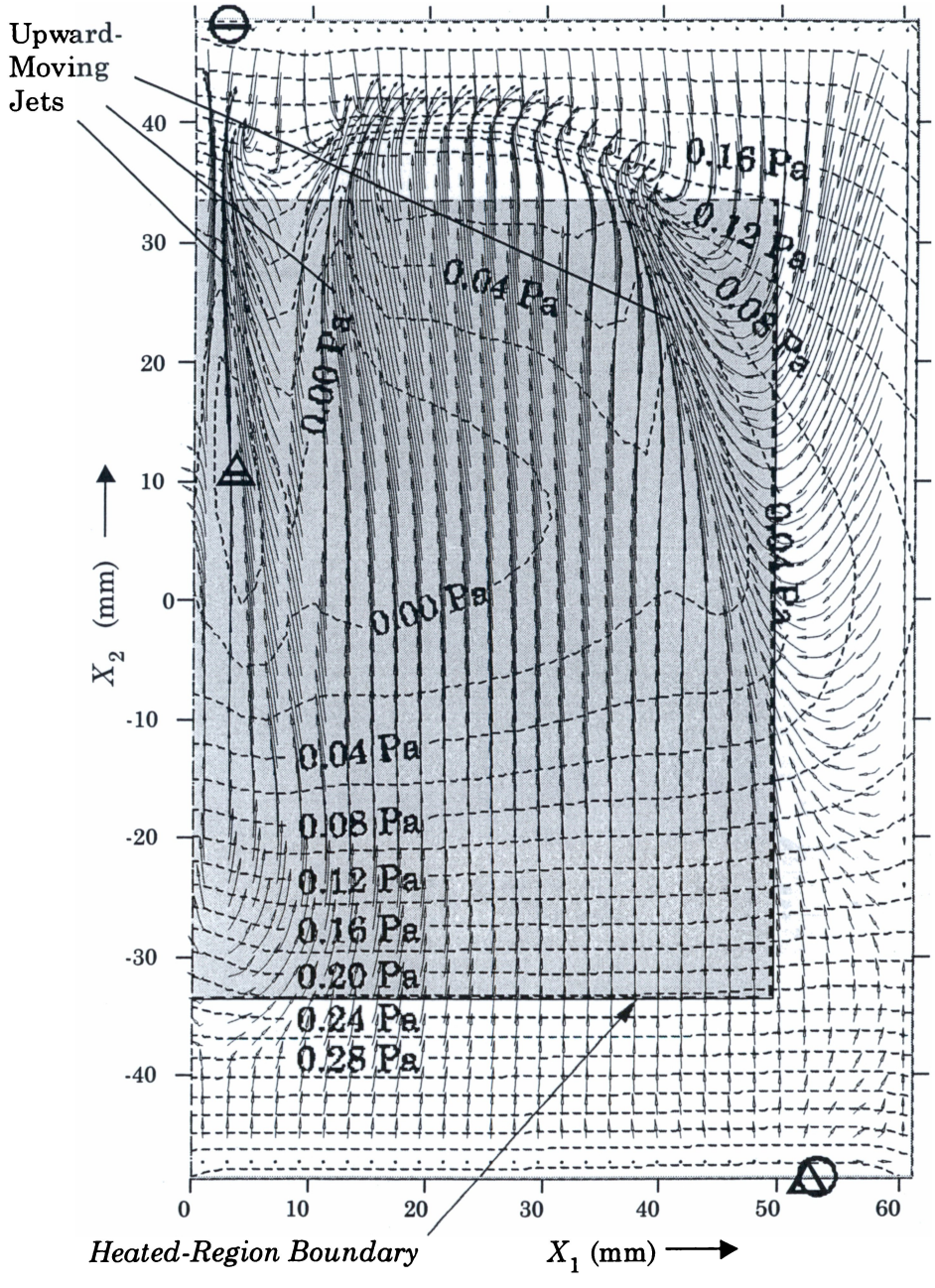

Figure 8-2. Pathlines Starting at Points 2 mm from the Base Plate and Isobar Overlay

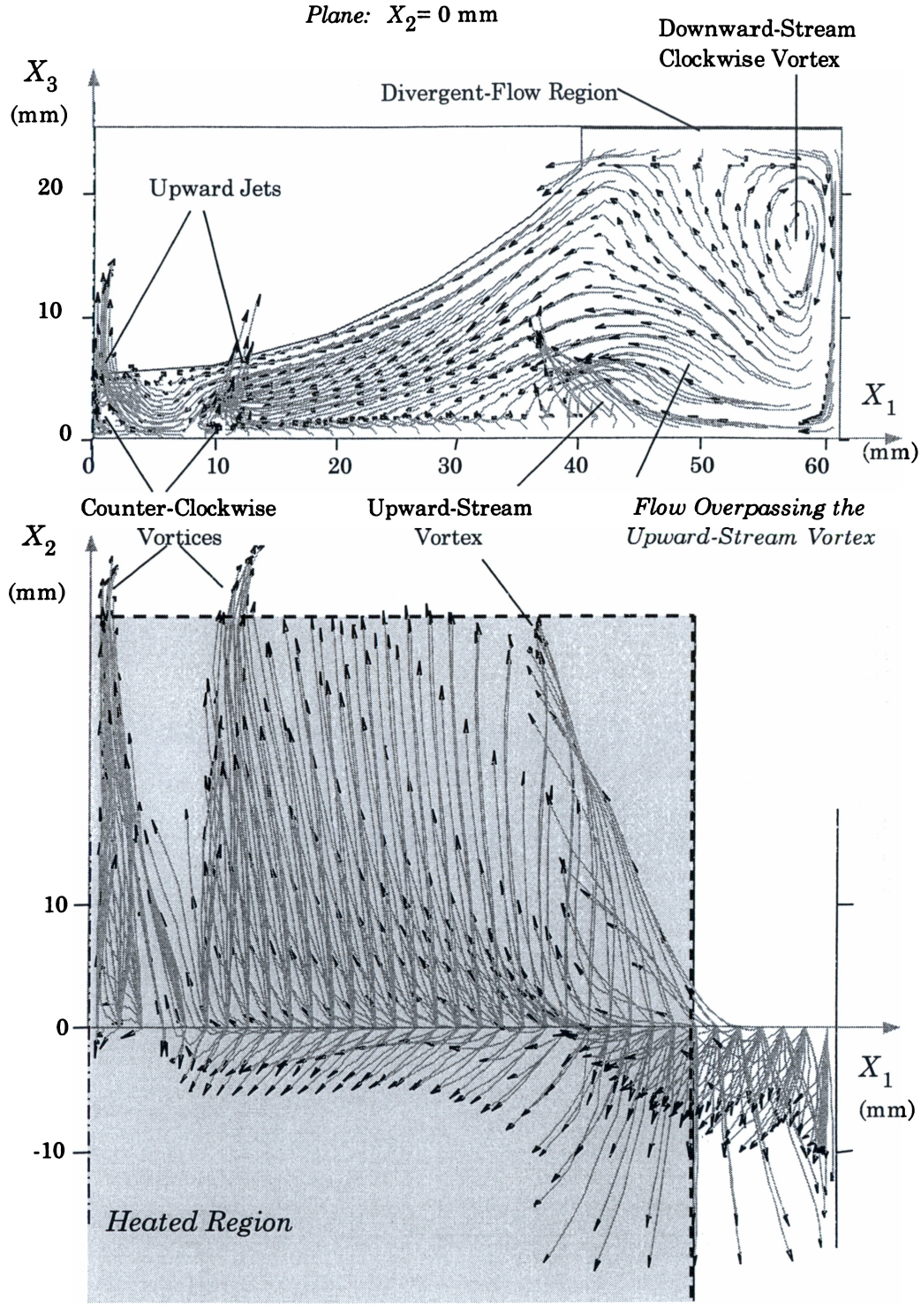

Figure 8-3. Pathlines Starting at Points on the X_2=0 Plane

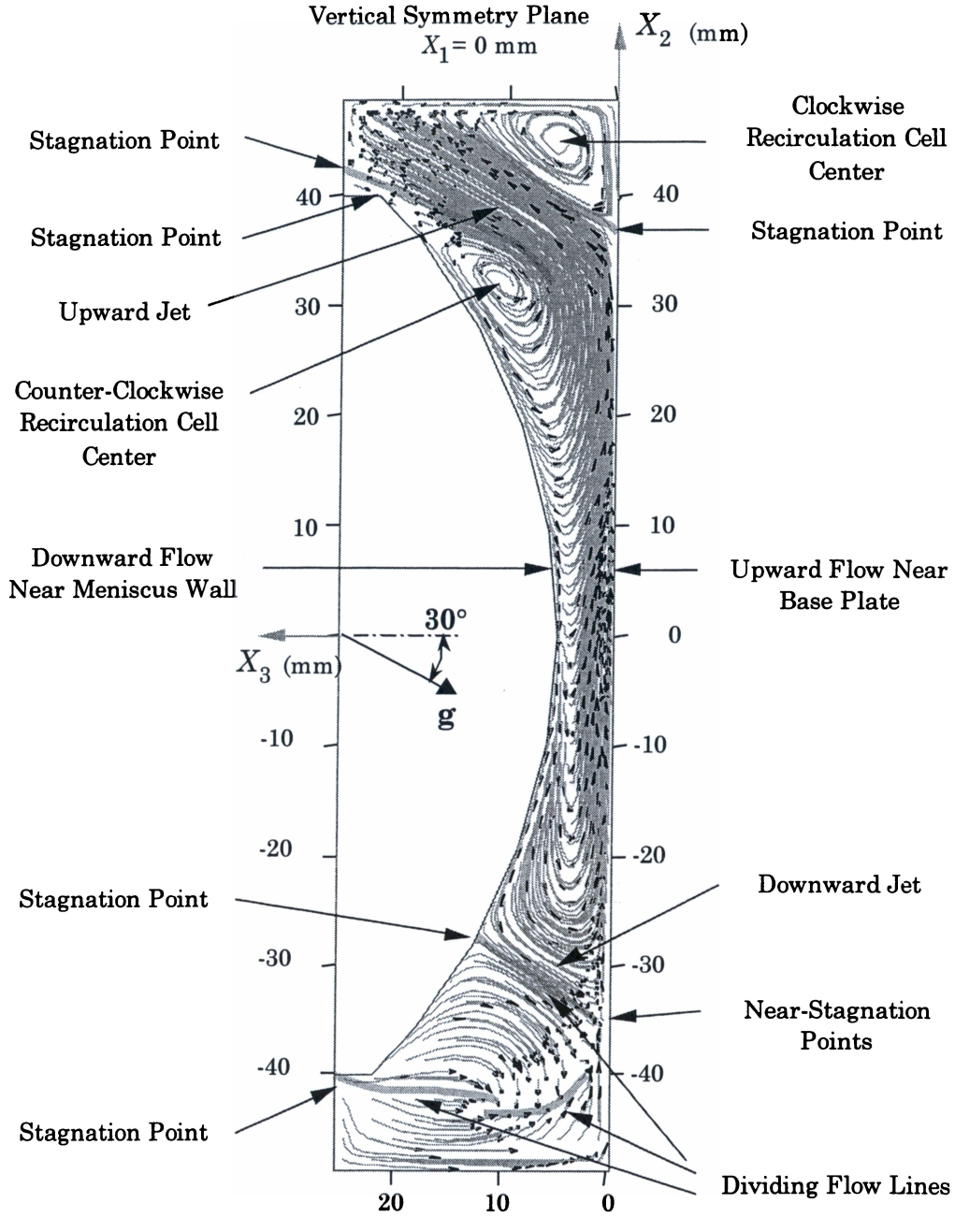

Figure 8-4. Pathlines Starting at Points on the X_1=0 Plane (Symmetry Plane)

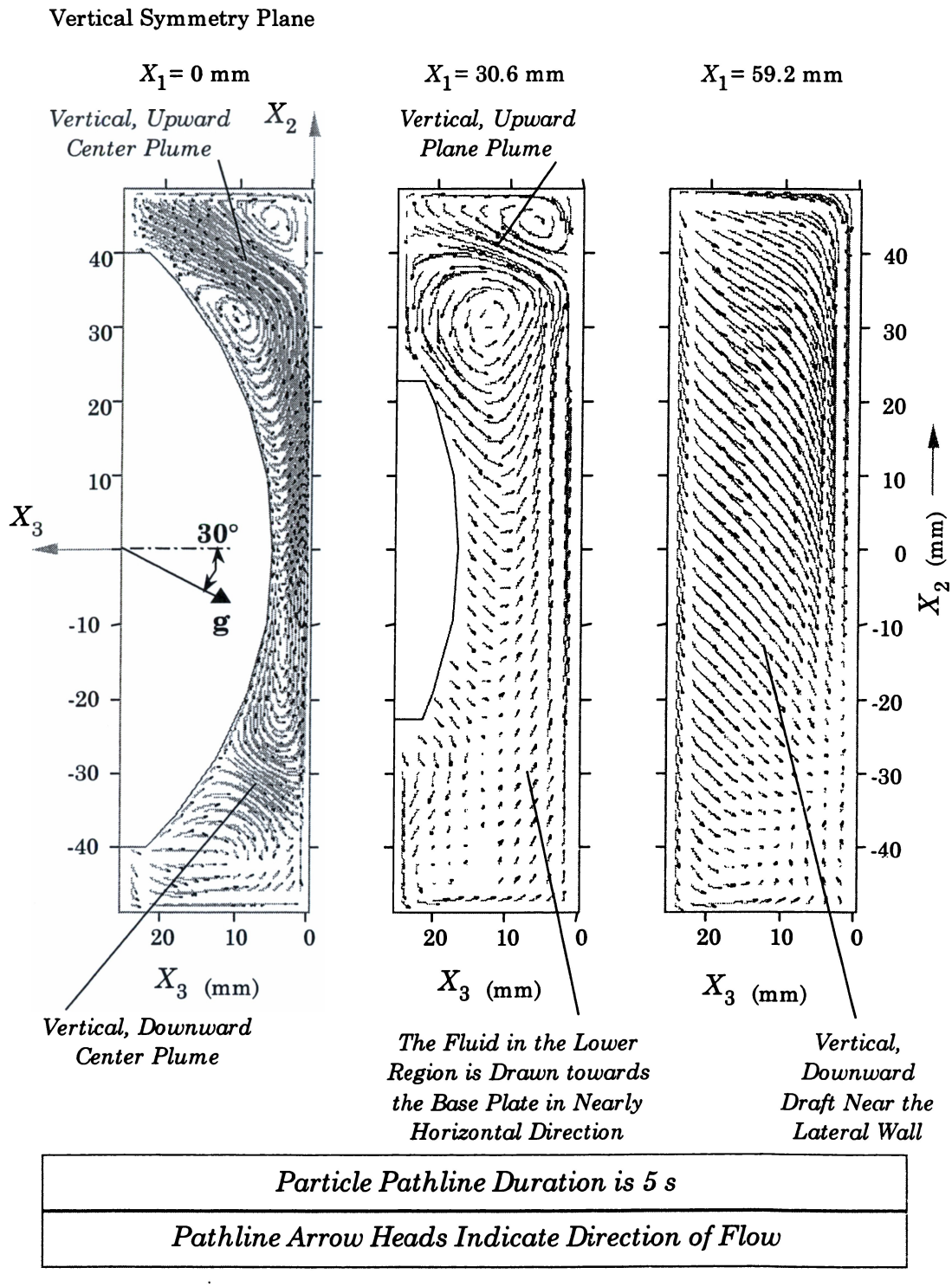

Figure 8-5. Pathlines Starting at Points on Various Vertical Planes (at Constant X_1 Coordinates)

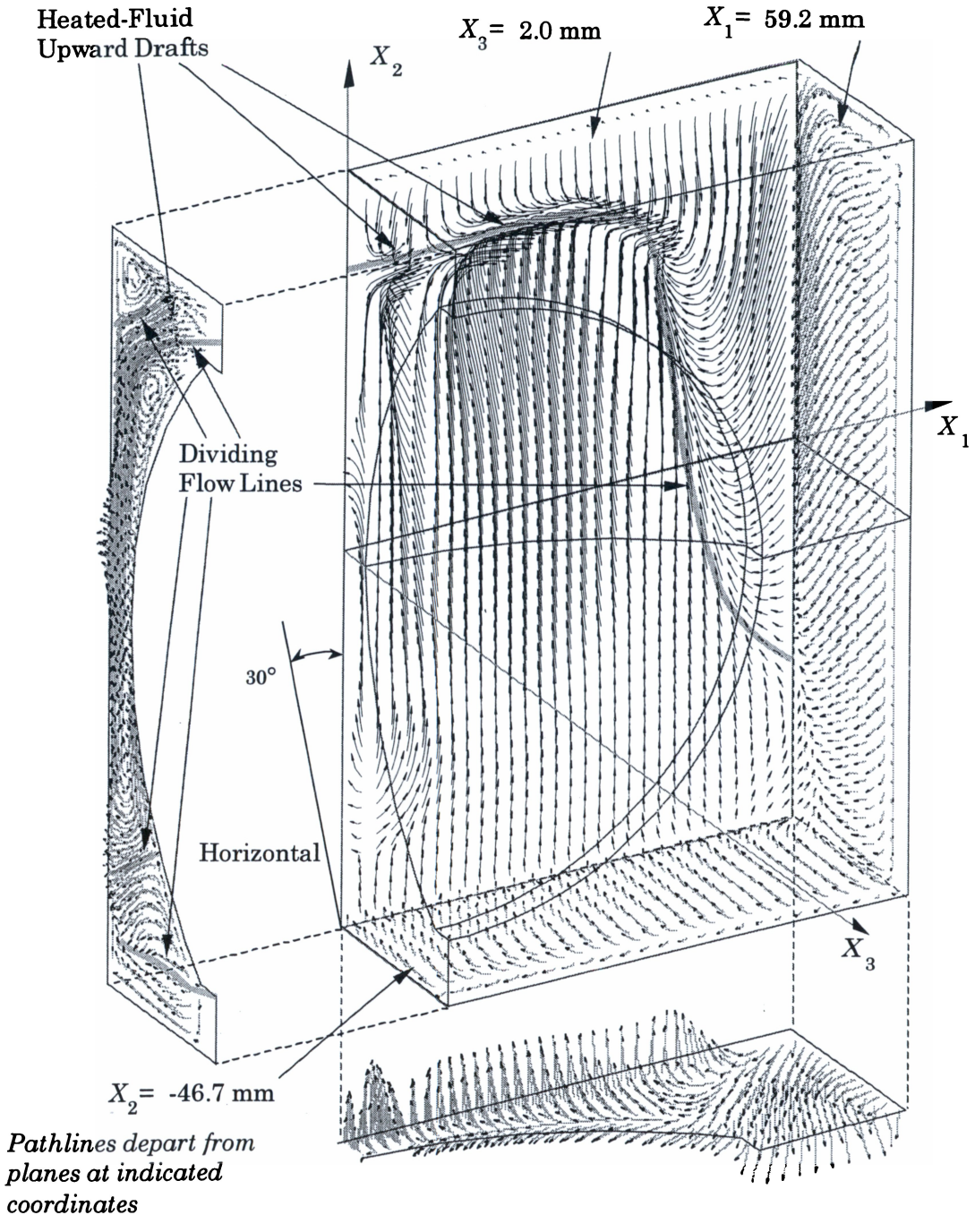

Figure 8-6. Domain Perspective View with Pathlines Departing from Selected Surfaces: Set I – Reference Case

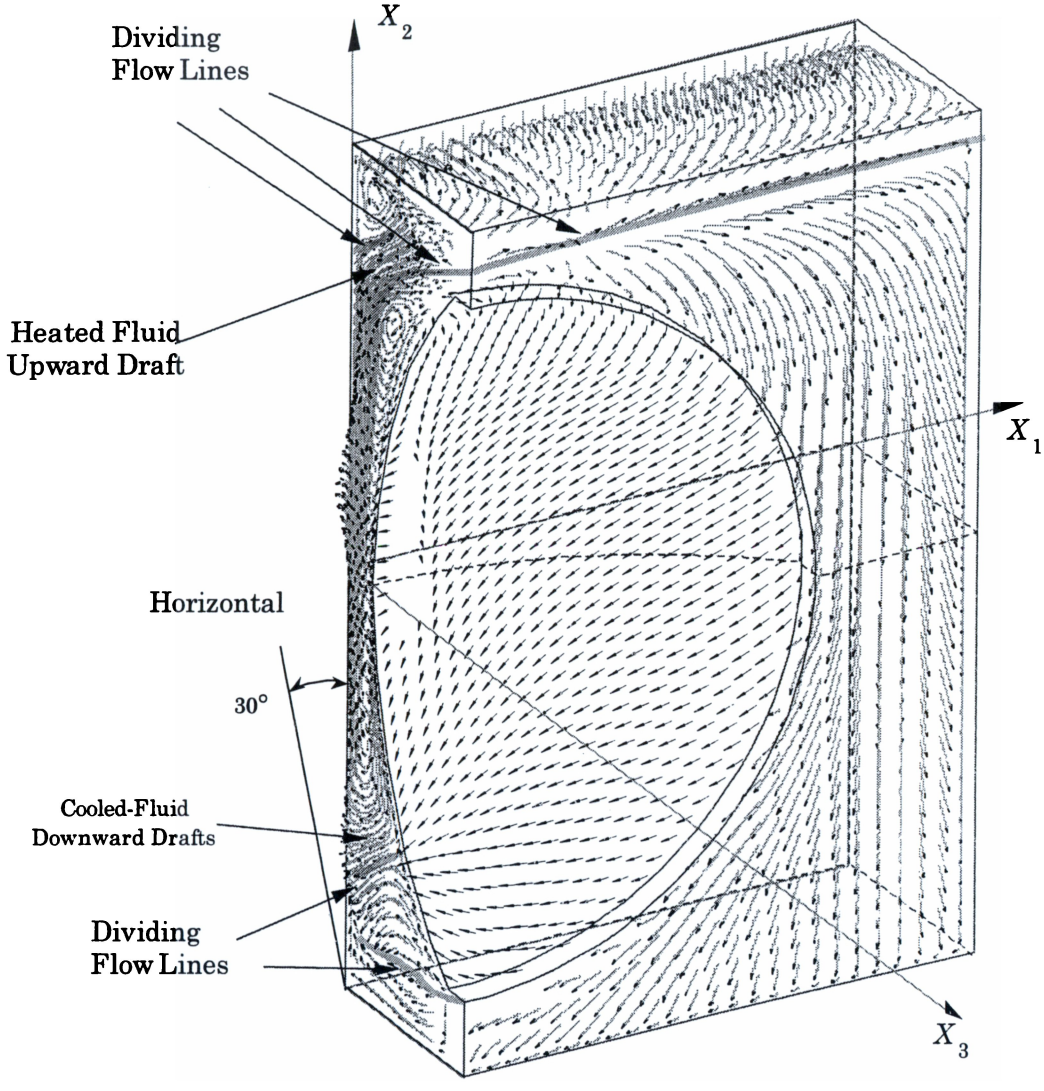

Figure 8-7. Domain Perspective View with Pathlines Departing from Selected Surfaces: Set II – Reference Case

vertical mid plane). Two flow systems are observed. The first system develops near the vertical symmetry plane, in which the flow starts to accelerate as it is heated along the baseplate until it starts to veer toward the symmetry plane in the upper region. The second system is defined by the edges of a plane draft developed between X_1 = 10 and X_1 = 45 mm. The flow near the left edge is drawn to the right as it moves upwards along the baseplate. The flow coming from the region on the right is drawn toward the left into the right edge of the plane draft. The structure of the plane draft created is similar to that formed in a heated horizontal rectangular plate immersed in an isothermal field (see Ref. [35, p. 185]).

Figure 8-3 shows particle pathlines departing from points on coordinate plane X_3-X_1. Particle paths are projected on the X_3-X_1 and the X_1-X_2 planes. Three distinct drafts moving near the base plate in the X_2 direction can be seen. The first draft is close to the vertical symmetry plane. The second draft passes at approximately X_1 = 10 mm. The third draft passes at approximately X_1 = 45 mm, and points inward. The second and third drafts form actually the edges of the plane plume that detaches near the upper wall. Some of the flow in the first draft comes from the region near the meniscus wall from the right, flowing over the second draft. A clockwise roll is seen near the right lateral wall. The roll is formed by a combination of a dynamic force from the divergent flow region pushing the flow to the right, while the flow near the right lateral wall cools and moves downward because of negative buoyancy forces.

Figure 8-4 shows particle pathlines on the vertical symmetry plane. The flow moves upward along the baseplate until it meets the downward flow from the top. A stagnation point forms as a result forcing both flows to detach into a nearly vertical plume. A counterclockwise cell is formed on one side of the plume, and a clockwise cell is formed on the other. The flow in the counterclockwise cell moves downward along the meniscus wall surface until it meets an upward flow from the lower region to form another stagnation point, this time on the lowest most point on the meniscus wall. The flow detaches and forms a downward draft moving in the vertical downward direction. The flow on one side is diverted back upwards along the baseplate to close the loop for the counterclockwise cell. Towards the bottom region

a converging/diverging flow region is formed. Cooled flow returning near the enclosure front surface is directed into the symmetry plane just below the meniscus-wall lower edge. The flow makes a 90° turn and starts to move in the negative X_3-direction. The dotted line in the figure represents near-stagnation points where the flow is divided into both sides of the line. Starting at approximately 10 mm from the baseplate, the flow from both sides moves back towards the line, then it detaches from the symmetry plane. This flow then moves upward along the baseplate to form the roots of the first and second drafts referenced to in the previous paragraph (see also *Figure 8-2*).

Figure 8-5 shows pathline departing from cross-sectional planes at $X_1 = 0$ mm, $X_1 = 30.6$ mm, and $X_1 = 59.2$ mm (2 mm away from the lateral sidewall). The near-vertical plane plume and the two counter-rotating cells in the enclosure upper region prevail for nearly the entire with of the domain. Near the lateral sidewall, however, the flow moves downward, back toward the baseplate and toward the lower sidewall.

Perspective views of the flow field, and pathlines departing from selected planes are shown in *Figure 8-6* and *Figure 8-7*. It must be noted that longitudinal roll pattern exhibited in tilted rectangular channels did not develop.

Flow visualization by complete pathline closure was not sought because complete closure may take several passes near the starting point [82]. In steady-state three-dimensional flow fields, particles travel along a "stream-surface," and should be free to move anywhere on this surface as long as streamlines on the surface are not crossed. The distance it takes for closure depends on this path. Therefore, it is possible for the particle to take infinite time (due to an infinite path distance) to return to the starting point.

8.4. Isotherms

Isotherms are shown on the baseplate back and front surfaces in *Figure 8-8*. Isotherms on the back surface are more concentrated near the perimeter of the heated surface, indicating a steep temperature variation. The maximum temperature on the back surface was calculated at 82.5 °C, at coordinates

Contour Lines	Temperature	(°C)

Dimensions and Boundary Conditions

ψ = 30°	W	H	L_1	L_2	L_3	L_4	L_5	L_6	L_7	R_1	R_2	R_3
(mm)→	99.1	67.3	61.2	48.7	7.1	25.5	5.2	4.0	24.8	56.0	39.5	40.0
q (W/m^2)	Boundary # →		1	2	3	4	5	6	7	8	9	10
1993.0	h ($W/m^2 \cdot K$)→		3.8	3.8	12.3	2.32	2.42	4.47	∞	∞	∞	∞
	T (°C) →		24.0	24.0	24.0	24.0	24.0	24.0	52.0	53.9	53.9	53.2

Coordinates

X_1 : Base-Plate Horizontal Axis

X_2 : Base-Plate Vertical Axis

X_3 : Base-Plate Normal Axis

Maxima

◇ Temperature

□ Energy-Flux Density

▽ Temperature-Gradient Magnitude

△ Piezometric Pressure

○ Static Pressure

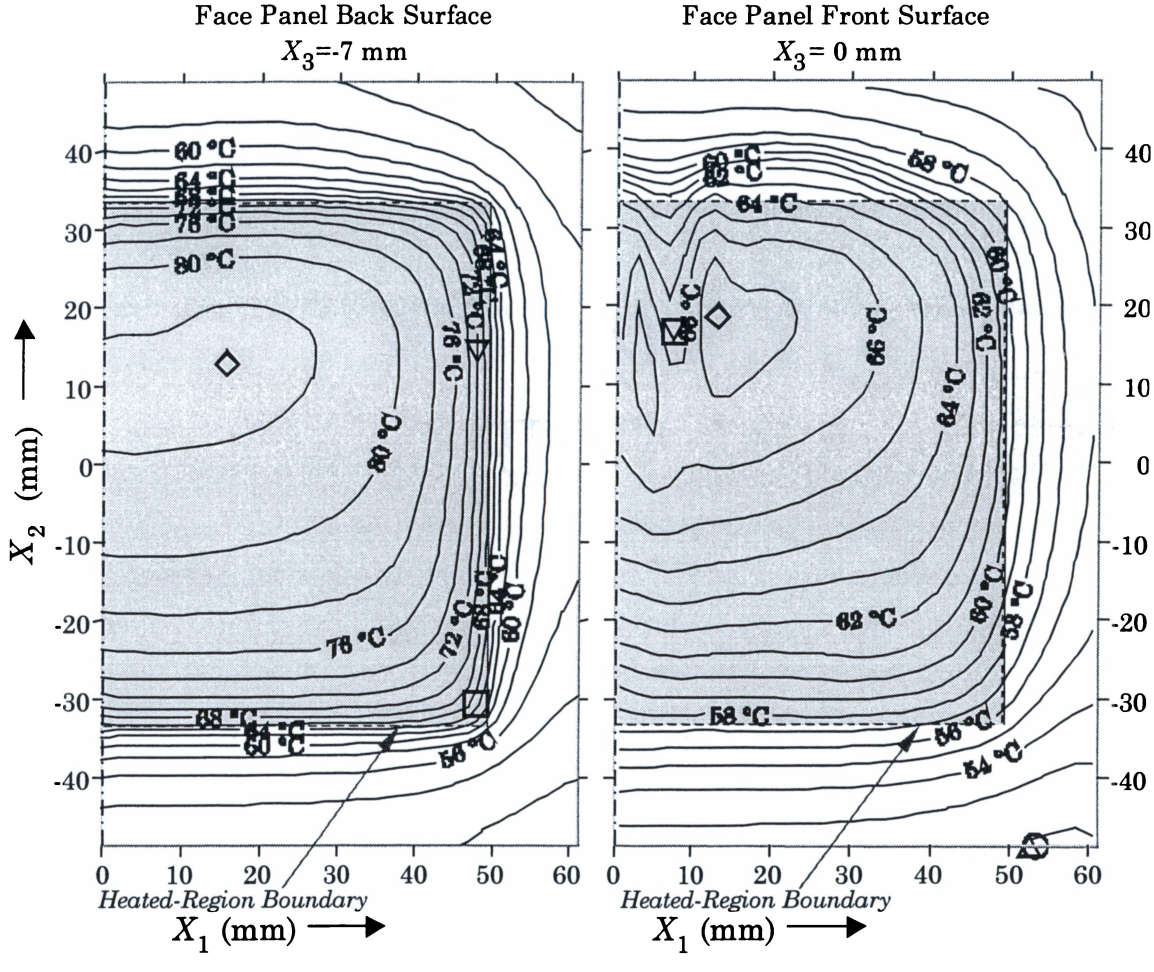

Figure 8-8. Isotherms on the Base Plate Back and Front Surfaces

(15.8, 12.8) mm. Isotherms on the front surface are more evenly spaced. The maximum temperature on the front surface was calculated at 67.6 °C, at coordinates (13.1, 18.6) mm. *Figure 8-9* shows isotherms on the coordinate planes, and *Figure 8-10* shows isotherms on the meniscus lens back and front surfaces.

8.5. Thermal Isoflux Lines

Thermal isoflux lines are defined as lines with constant magnitude of the thermal energy flux (energy flow per unit area). Thermal isoflux lines were plotted on various surfaces across the domain. Thermal isoflux lines on the baseplate back and front surfaces are shown in *Figure 8-11*. Thermal isoflux lines are concentrated near the perimeter of the heated area indicating a large variation. The thermal flux drops from +1800 W/m^2 to –100 W/m^2 in less than 10 mm. The maximum of 2.09 W/m^2 was calculated on the back surface at coordinates (47.2, -30.7) mm. Thermal isoflux lines on the baseplate front surface are more evenly spaced. A maximum heat flux of 2.16 W/m^2 was calculated at coordinates (7.5, 16.7) mm.

Figure 8-12 shows isoflux lines on the lower, lateral, upper, and front domain surfaces, and on the X_2=0 coordinate plane. Thermal isoflux lines on this plane show high fluxes over +2000 W/m^2 in a wide, narrow region near the baseplate and below -3000 W/m^2 in the region near the enclosure upper wall. These high fluxes are due to flux advection with the upward flow near the baseplate and downward flow near the enclosure upper wall. The highest fluxes leaving the domain (of up to 900 W/m^2) are seen on the enclosure upper surface, and in the upper corner region of the enclosure lateral, side surface. Negative values are seen on the enclosure lower surface because the normal flux goes in the negative parametric direction.

8.6. Thermal Isograds

Thermal *isograds* are defined as lines connecting points at constant temperature gradient magnitude. *Figure 8-13* shows thermal isograds on the baseplate back and front surfaces. The trends are similar to isoflux lines, but there is some difference because the thermal isograds take into account heat transfer in all directions. Thermal isograds on the baseplate back surface are concentrated

Coordinates

X_1 : Base-Plate Horizontal Axis
X_2 : Base-Plate Vertical Axis
X_3 : Base-Plate Normal Axis

Maxima

◇ Temperature
□ Energy-Flux Density
▽ Temperature-Gradient Magnitude
△ Piezometric Pressure
⬡ Static Pressure

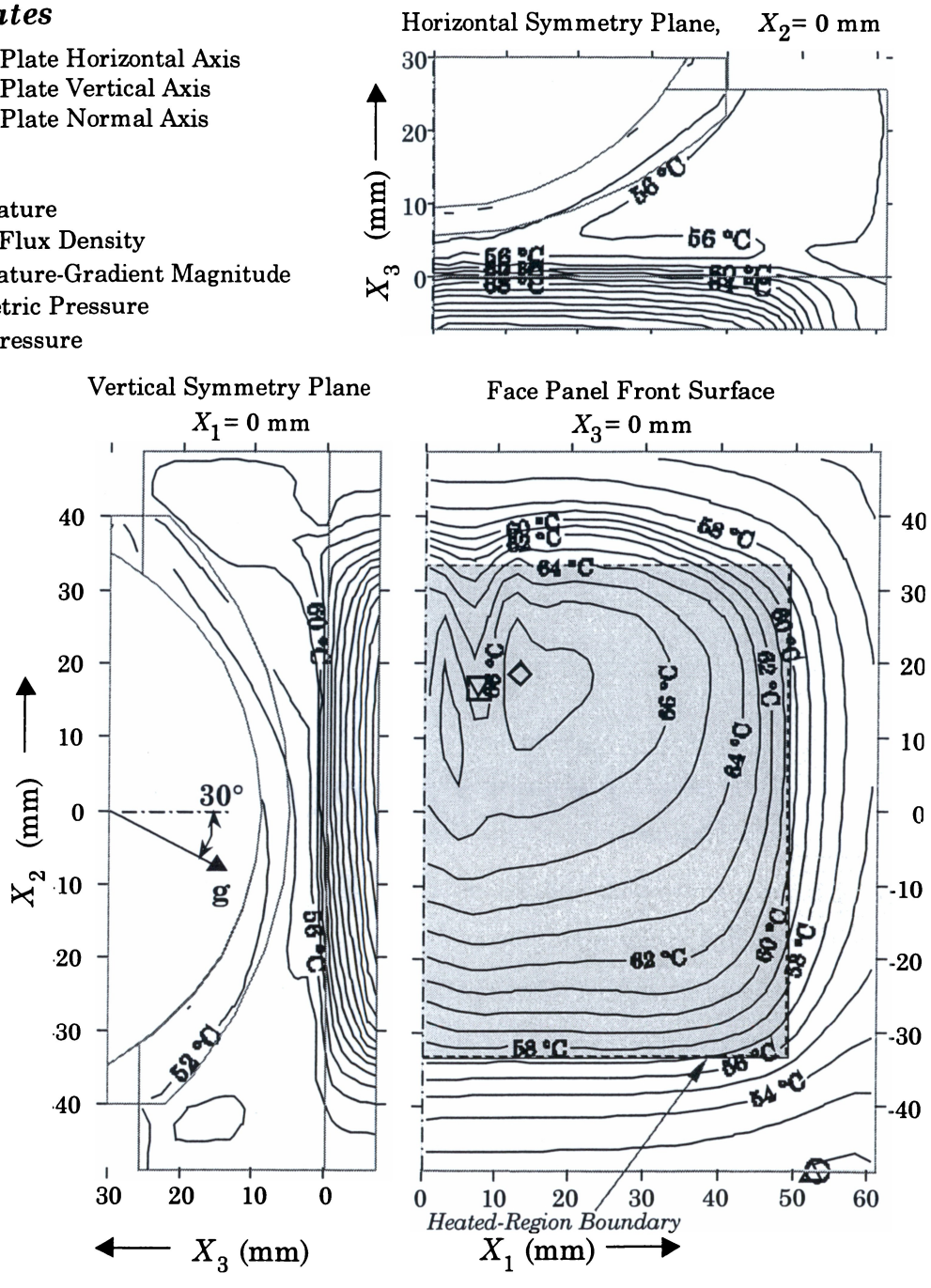

Figure 8-9. Isotherms on Coordinate Planes

Contour Lines	Temperature	(°C)

Dimensions and Boundary Conditions												
ψ = 30°	W	H	L_1	L_2	L_3	L_4	L_5	L_6	L_7	R_1	R_2	R_3
(mm)→	99.1	67.3	61.2	48.7	7.1	25.5	5.2	4.0	24.8	56.0	39.5	40.0
q (W/m^2)	Boundary # →		1	2	3	4	5	6	7	8	9	10
1993.0	h ($W/m^2 \cdot K$)→		3.8	3.8	12.3	2.32	2.42	4.47	∞	∞	∞	∞
	T (°C) →		24.0	24.0	24.0	24.0	24.0	24.0	52.0	53.9	53.9	53.2

Coordinates

X_1 : Base-Plate Horizontal Axis
X_2 : Base-Plate Vertical Axis
X_3 : Base-Plate Normal Axis

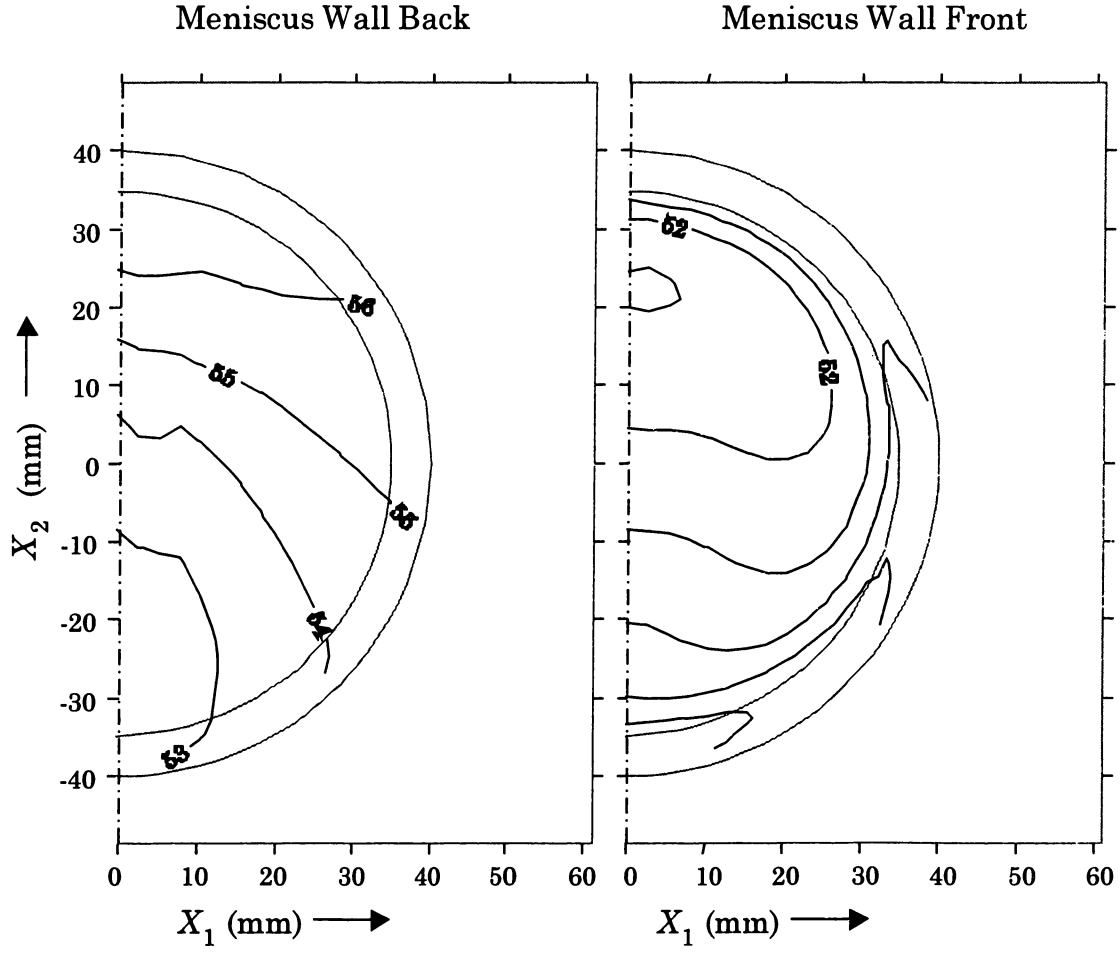

Figure 8-10. Isotherms on the Meniscus Wall

Contour Lines	Energy Flux	(W/m²)

Dimensions and Boundary Conditions

ψ = 30°	W	H	L_1	L_2	L_3	L_4	L_5	L_6	L_7	R_1	R_2	R_3
(mm)→	99.1	67.3	61.2	48.7	7.1	25.5	5.2	4.0	24.8	56.0	39.5	40.0
q (W/m²)	Boundary # →		1	2	3	4	5	6	7	8	9	10
1993.0	h (W/m²·K)→		3.8	3.8	12.3	2.32	2.42	4.47	∞	∞	∞	∞
	T (°C) →		24.0	24.0	24.0	24.0	24.0	24.0	52.0	53.9	53.9	53.2

Coordinates

X_1 : Base-Plate Horizontal Axis

X_2 : Base-Plate Vertical Axis

X_3 : Base-Plate Normal Axis

Maxima

◇ Temperature

□ Energy-Flux Density

▽ Temperature-Gradient Magnitude

△ Piezometric Pressure

○ Static Pressure

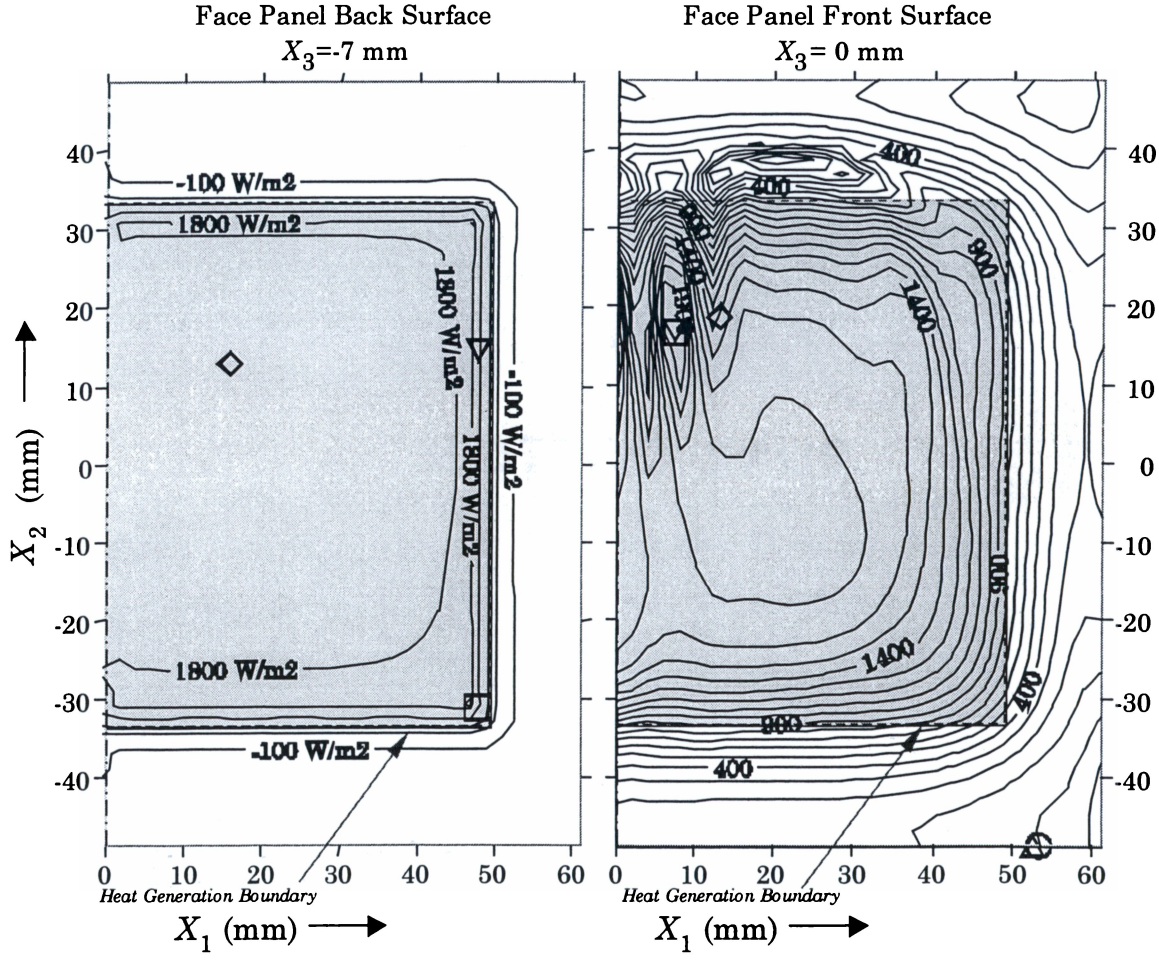

Figure 8-11. Thermal Isoflux Lines on the Base Plate Back and Front Surfaces

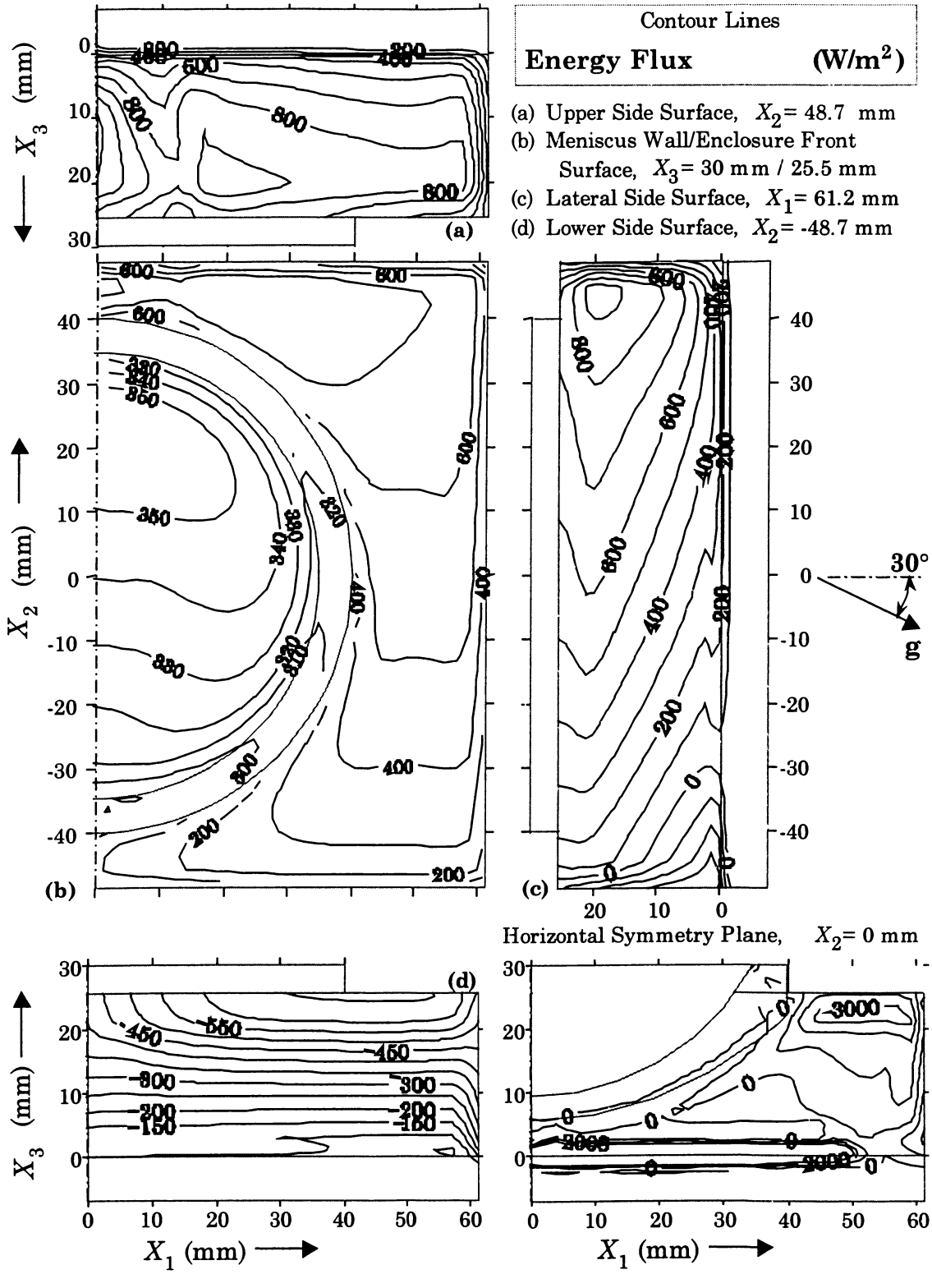

Figure 8-12. Domain-Outward Thermal Isoflux Lines on Cooled Surfaces

Contour Lines	Temperature	(°C)

Coordinates

X_1 : Base-Plate Horizontal Axis

X_2 : Base-Plate Vertical Axis

X_3 : Base-Plate Normal Axis

Maxima

◇ Temperature

□ Energy-Flux Density

▽ Temperature-Gradient Magnitude

△ Piezometric Pressure

○ Static Pressure

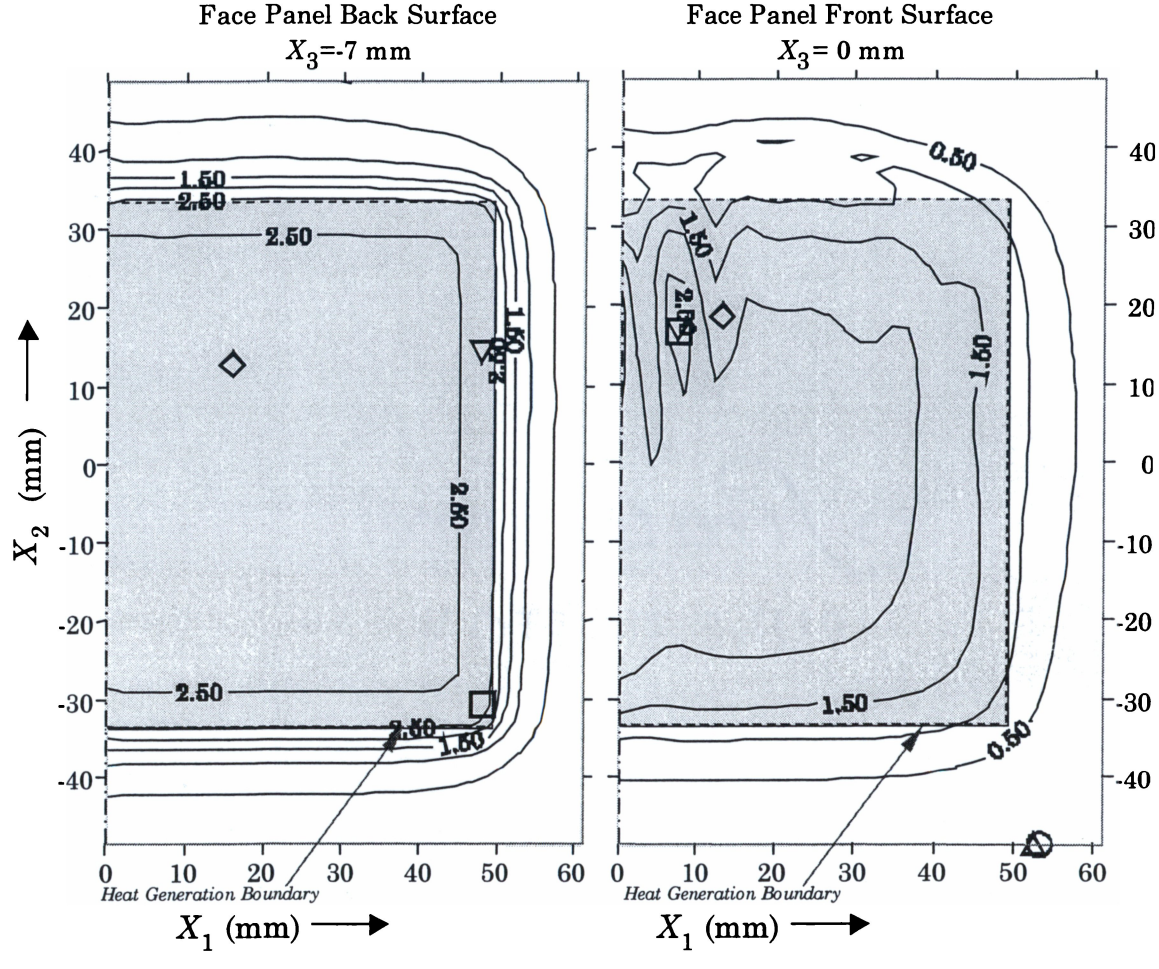

Figure 8-13. Lines of Thermal Isograds on the Base Plate Back and Front Surfaces

near the heated-area perimeter. The maximum of 3.08 °C/mm occurs at coordinates (47.9, 14.4) mm. This is in contrast to the location for maximum normal energy flux at (4.7, -30.7) mm. Thermal isograds on the baseplate front surface are more evenly spaced. The maximum of 2.73 °C/mm occurs at coordinates (7.4, 16.9) mm, resulting in a location very close to that for maximum energy flux at coordinates (7.5, 16.7) mm. This indicates that heat at such location travels almost entirely in the direction normal to the baseplate surface.

8.7. Heatlines

Heatlines [9] are lines tangent to the energy flux vector. Heatlines were obtained by integrating the flux vector from selected starting points. *Figure 8-14* shows heatlines on the vertical symmetry plane. Heatlines depart from the back of the baseplate. The lines cross the baseplate towards the fluid region, except in the upper and lower region, where they are diverted mostly backwards. This provides an indication that a small amount of heat leaves the system through the base plate sides. Fluxline distribution is nearly symmetric within the baseplate. They are orthogonal to the isotherms, as expected for heat conduction. Once in the fluid, the heatlines are distorted due to fluid motion. In the lower half of the domain, most of the heat near the symmetry plane leaves the system through the meniscus wall. In the upper half, the thermal energy is concentrated in the near-vertical plume. Due to flow circulation, heatlines turn back to the baseplate to finally leave the domain through the enclosure upper wall. A perspective view of the domain with thermal heatlines departing from the baseplate back surface is shown in *Figure 8-15*. Heatlines end at domain surfaces. Surface regions with higher concentration of heatlines suggest higher heat flux levels. These regions should be consistent with regions of higher energy flux levels in *Figure 8-12*.

Extrema for temperature, thermal flux, temperature gradient magnitude, piezometric pressure, and static pressure on the baseplate surfaces are summarized in Table 8-1 (maxima) and Table 8-2 (minima).

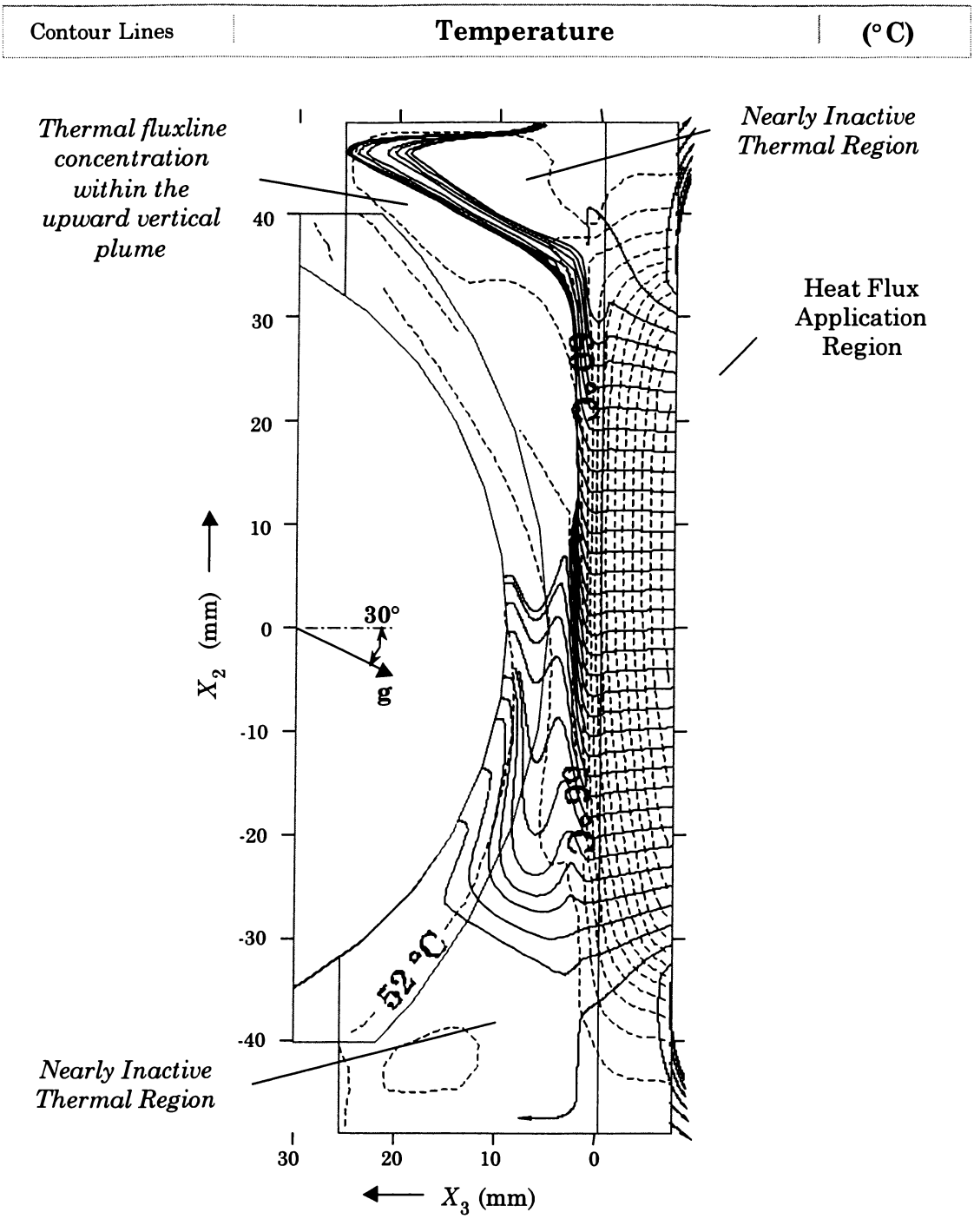

Figure 8-14. Heatlines and Isotherms on the Vertical Symmetry Plane

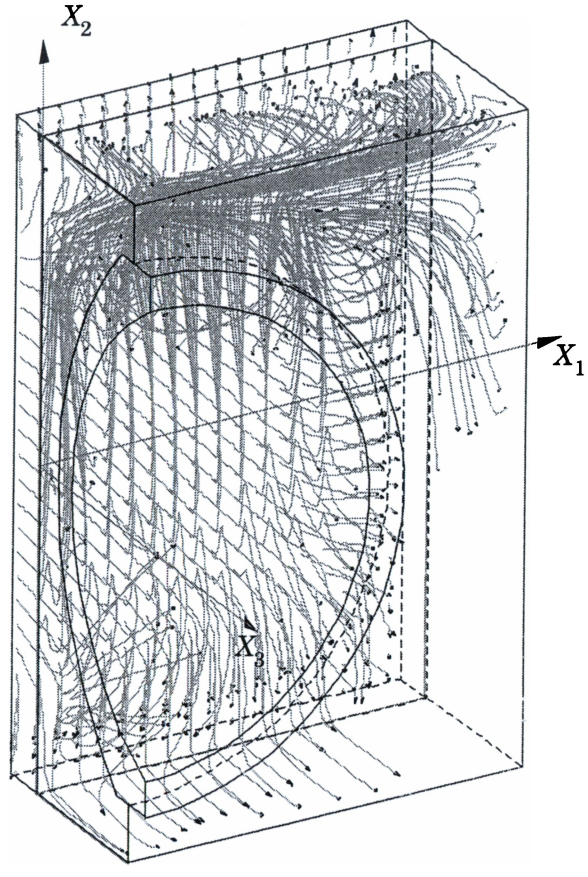

Figure 8-15. Heatlines Departing from the Baseplate Back Surface

Table 8-1. Maximum Values on the Base-Plate Back and Front Surfaces – Reference Case

Variable	*Units*	*Maximum Value*	X_1 (mm)	X_2 (mm)
Base-Plate Back Surface				
Temperature	°C	82.5	15.8	12.8
Energy Flux	W/m²	2.09	47.2	-30.7
Temperature-Gradient Magnitude	°C/mm	3.08	47.9	14.4
Base-Plate Front Surface				
Temperature	°C	67.6	13.1	18.6
Energy Flux	W/m²	2.16	7.5	16.7
Temperature-Gradient Magnitude	°C/mm	2.73	7.4	16.9
Piezometric Pressure	Pa	0.421	52.5	-48.7
Static Pressure	Pa	271.	53.3	-48.7

Table 8-2. Minimum Values on the Base-Plate Back and Front Surfaces – Reference Case

Variable	*Units*	*Minimum Value*	X_1 (mm)	X_2 (mm)
Base-Plate Back Surface				
Temperature	°C	50.9	61.2	-48.7
Energy Flux	W/m²	-0.32	18.4	36.1
Temperature-Gradient Magnitude	°C/mm	0.17	57.7	-48.7
Base-Plate Front Surface				
Temperature	°C	51.7	58.1	-48.7
Energy Flux	W/m²	-0.19	57.4	46.2
Temperature-Gradient Magnitude	°C/mm	0.08	56.9	-48.7
Piezometric Pressure	Pa	-0.042	3.7	10.5
Static Pressure	Pa	-270.	2.5	48.7

9. DIMENSIONLESS PARAMETERS AND SIMPLIFICATION OF BOUNDARY CONDITIONS

9.1. Introduction

This chapter is aimed at determining the minimum number of dimensionless parameters that fully specify the numerical model of the conjugate heat transfer problem in the liquid-lens system. Reference scales for length and velocity are introduced in order to nondimensionalize the problem. In addition, a sensitivity study of boundary conditions will be carried out in order to remove those for which thermal performance sensitivity is negligible, thus reducing the number of parameters. This will be useful in keeping to a minimum the number of parameters to be varied in a subsequent parametric performance study.

9.2. Reference Scales and Dimensionless Variables

The steady-state problem of the liquid-lens system is fully defined in terms of 32 independent variables. These variables are sub-classified as computational-domain dimensions (Table 9-1), thermophysical properties (Table 9-2), environmental properties (Table 9-3), and boundary conditions (Table 9-4). Nondimensionalization of the equations may be achieved by introducing the following dimensionless variables.

$$x_j = \frac{X_j}{X_R}, \quad j = 1,2,3, \tag{9.1.a}$$

$$t = \frac{T - T_R}{\Delta T_R}, \tag{9.1.b}$$

$$\tau = \frac{\tilde{\tau}}{\tilde{\tau}_R}, \tag{9.1.c}$$

$$u_j = \frac{U_j}{U_R}, \quad j = 1,2,3, \tag{9.1.d}$$

$$p = \frac{P}{\rho U_R{}^2}, \tag{9.1.e}$$

Table 9-1. Independent Variables: Computational Domain Dimensions

	Description	*Variable*
1	Computational Domain Width	L_1
2	Computational Domain Half Height	L_2
3	Base Plate Thickness	L_3
4	Enclosure Depth	L_4
5	Meniscus Wall Gap	L_5
6	Meniscus Wall Centerline Thickness	L_6
7	Meniscus Wall Overall Depth	L_7
8	Meniscus Wall Convex Surface Radius	R_1
9	Meniscus Wall Concave Surface Radius	R_2
10	Meniscus Wall Outline Cylinder Radius	R_3

Table 9-2. Independent Variables: Thermophysical Properties

	Description	*Variable*
11	Fluid Mass Density	ρ_o
12	Fluid Specific Heat	$c_{p,o}$
13	Fluid Thermal Conductivity	k_o
14	Fluid Kinematic Viscosity	ν_o
15	Fluid Volume Expansivity	β_o
16	Baseplate Thermal Conductivity	k_1
17	Meniscus Wall Thermal Conductivity	k_2

Table 9-3. Independent Variables: Environmental Properties

	Description	*Variable*
18	Gravitational Acceleration	g
19	Tilt Angle	ψ

Table 9-4. Independent Variables: Boundary Conditions

	Description	*Variable*
20	Heat Flux	$\dot{q}''$
21	Heated Area Half Width	L_8
22	Heated-Area Half Height	L_9
23	Environmental Temperature	Ta
24	Enclosure Lower Surface Temperature	T_7
25	Enclosure Lateral Surface Temperature	T_8
26	Enclosure Upper Surface Temperature	T_9
27	Enclosure Front Surface Temperature	T_{10}
28	Baseplate Back Surface Heat Transfer Coefficient	h_R
29	Baseplate Lower Surface Heat Transfer Coefficient	h_4
30	Baseplate Lateral Surface Heat Transfer Coefficient	h_5
31	Baseplate Upper Surface Heat Transfer Coefficient	h_6
32	Meniscus Wall Front Surface Heat Transfer Coefficient	h_3

where

$$X_R = L = L_4, \tag{9.2.a}$$

$$U_R = \frac{\alpha_o}{X_R}, \tag{9.2.b}$$

$$\tilde{\tau}_R = \frac{X_R}{U_R}, \tag{9.2.c}$$

and α is the fluid thermal diffusivity.

Substitution of the definitions in Eqs. (9.1) and (9.2) into the conservation equations for mass, momentum, and energy yields dimensionless equations written in terms of the Prandtl number:

$$Pr = \frac{\nu_o}{\alpha_o}, \tag{9.3}$$

the modified Rayleigh number:

$$Ra_L^* = \frac{g\,\beta_o\,\dot{q}''\,L^4}{\nu_o\,\alpha_o\,k_o}, \tag{9.4}$$

and the thermal conductivity ratios for the solids:

$$\kappa_1 = \frac{k_1}{k_o} \text{ (face panel conductivity ratio), and} \tag{9.5.a}$$

$$\kappa_2 = \frac{k_2}{k_o} \text{ (meniscus lens conductivity ratio).} \tag{9.5.b}$$

The domain dimensions can be converted to nondimensional form by dividing by the reference length. Temperatures can be nondimensionalized using Eq. (9.1.b) where

$$\Delta T_R = \frac{L}{k_o}\dot{q}'', \text{ and} \tag{9.6.a}$$

$$T_R = T_a \tag{9.6.b}$$

The heat transfer coefficients can be nondimensionalized by introducing the reference scale:

$$h_R = \frac{k_o}{L}. \tag{9.7}$$

The above definitions result in a dimensionless solution as a function of 25 dimensionless parameters and the position vector as:

$$\begin{aligned}\phi = \phi\big(\vec{x}, Ra_L^*, Pr, \psi,\ & l_1, l_2, l_3, l_5, l_6, l_7,\ r_1, r_2, r_3,\ \sigma_1, \sigma_2,\\ & \kappa_1, \kappa_2,\ \hat{h}_B, \hat{h}_3, \hat{h}_4, \hat{h}_5, \hat{h}_6,\ t_7, t_8, t_9, t_{10}\big)\end{aligned} \tag{9.8}$$

where ψ is the tilt angle (measured from the heated-from below orientation),

$$l_i = \frac{L_i}{L} \text{ (dimensionless lengths for } i\text{=1,2,3,5,6,7),} \tag{9.9.a}$$

$$r_i = \frac{R_i}{L} \text{ (dimensionless meniscus-lens radii for } i\text{=1,2,3),} \tag{9.9.b}$$

$$\hat{h}_B = \frac{h_B}{h_R} \text{ (dimensionless convection coefficient on face panel back),} \tag{9.9.c}$$

$$\hat{h}_i = \frac{h_i}{h_R} \text{ (dimensionless convection coefficients on surfaces } i\text{=3,4,5,6),} \tag{9.9.d}$$

$$t_i = \frac{T_i - T_R}{\Delta T_R} \text{ (dimensionless temperatures on surfaces } i\text{=7,8,9,10)} \tag{9.9.e}$$

$$\sigma_1 = \frac{L_8}{L_1} \text{ (ratio of raster area width to enclosure-frame width), and} \qquad (9.9.f)$$

$$\sigma_2 = \frac{L_9}{L_2} \text{ (ratio of raster area height to enclosure-frame height).} \qquad (9.9.g)$$

Notice that the tilt angle above can be considered dimensionless, as it can be expressed in terms of radians (unit length per unit length). To obtain results involving physical variables, 7 additional known constants are needed to complete the set of 32 variables. These constants are:

the reference length scale, L,

the fluid thermal conductivity, k_o,

the fluid density, ρ_o,

the fluid kinematic viscosity, ν_o,

the fluid volume expansivity, β_o,

the gravitational acceleration, g, and

the cabinet-interior environmental temperature, T_a.

9.2.1. Nondimensionalization of the Variables Used in the Benchmark Model

Independent reference scales are shown in Table 9-5. Independent variables for geometry specification are shown in Table 9-6. The independent dimensionless groups are shown in Table 9-7. Finally, the independent boundary conditions are shown in Table 9-8. Derived reference scales are shown in Table 9-9. The total number of independent variables is 32, out of which, 8 were defined in terms of independent reference scales, and 24 were defined in terms of independent groups affecting the dimensionless solution.

Table 9-10 summarizes the numerical results in terms of dimensionless performance parameters and performance indicators. The performance indicators shown are subdivided into heat-transfer-effectiveness indicators, and temperature-level and temperature-gradient-level indicators for the baseplate back and front surfaces. The heat-transfer-effectiveness indicators are the baseplate effective conductivity ratio (k_e/k_1), the meniscus wall Nusselt-number contribution (Nu_1), the

Table 9-5. Independent Reference Scales and Properties

	Scale	*Units*	*Value*
1	Length, $L = L_4$	mm	25.5
2	Thermal Conductivity, k	W/m-K	2.68×10^{-1}
3	Density, ρ	kg/m^3	1134.5
4	Temperature, $T_{ref} = T_a$	°C	24.0
5	Kinematic Viscosity, ν	m^2/s	9.61×10^{-6}
6	Volume Expansivity, β	1/K	6.073×10^{-4}
7	Gravitational Acceleration, g	m/s^2	9.80
8	Tilt Angle (degrees)	ψ	30

Table 9-6. Dimensionless Parameters for Geometry Specification

	Description	*Variable*	*Value*
1	Dimensionless Domain Width	l_1	4.80
2	Dimensionless Domain Height	l_2	3.82
3	Dimensionless Base Plate Thickness	l_3	0.28
4	Dimensionless Meniscus Wall Gap	l_5	0.20
5	Dimensionless Meniscus Wall Centerline Thickness	l_6	0.16
6	Dimensionless Meniscus Wall Overall Depth	l_7	0.97
7	Dimensionless Meniscus Wall Convex Surface Radius	r_1	2.20
8	Dimensionless Meniscus Wall Concave Surface Radius	r_2	1.55
9	Dimensionless Meniscus Wall Outline Cylinder Radius	r_3	1.57

Table 9-7. Property-Related Dimensionless Parameters

	Description	*Variable*	*Value*
10	Prandtl Number	Pr	105.4
11	Rayleigh Number (modified)	Ra^*	2.14×10^7
12	Baseplate Thermal Conductivity Ratio	κ_1	2.951
13	Meniscus-Wall Thermal Conductivity Ratio	κ_2	2.350

Table 9-8. Boundary-Condition Dimensionless Parameters

	Description	*Variable*	*Value*
14	Heated-Region Width Ratio	σ_1	0.8096
15	Heated-Region Height Ratio	σ_2	0.6910
	Dimensionless Heat Flux Density	$q"/q"_{ref}$	1
	Dimensionless Heat Transfer Coefficient		
16	Baseplate Back	$\hat{h}_B$	0.36864
17	Meniscus-Lens Exterior	$\hat{h}_3$	0.952559
18	Baseplate Lower Surface	$\hat{h}_4$	0.220994
19	Baseplate Lateral Surface	$\hat{h}_5$	0.230519
20	Baseplate Upper Surface	$\hat{h}_6$	0.425794
	Dimensionless Temperature		
	Environmental	t_a	0
21	Enclosure Lower Surface	t_7	0.148
22	Enclosure Lateral Surface	t_8	0.158
23	Enclosure Upper Surface	t_9	0.158
24	Enclosure Front Surface	t_{10}	0.154

Table 9-9. Derived Reference Scales

	Scale	*Units*	*Value*
1	Reference Temperature Differential, ΔT	K	1.90×10^2
2	Reference Convection Coefficient, h	W/m²-K	10.50
3	Reference Heat Transfer Rate, Q	W	1.30
4	Reference Heat Flux Density, $q"_{ref}$	W/m²	1992.7

Table 9-10. Dimensionless Results

	Description	*Symbol*	*Value*
1	Baseplate Effective Conductivity Ratio	k_e/k_1	1.0128
2	Meniscus-Wall Nusselt Number Contribution	Nu_1	1.17
3	Enclosure-Frame Nusselt Number Contribution	Nu_2	11.41
4	Net Nusselt Number	Nu	12.58
5	Rayleigh Number based on the baseplate-front-surface mean temperature	Ra_m	8.06×10^5
6	Rayleigh Number Ratio	Ra_m/Ra^*	0.038
	Baseplate Back:		
7	Dimensionless Mean Temperature	$t_{m,b}$	8.19
8	Maximum, Dimensionless Temperature Differential	$(t_{max}\text{-}t_m)_b$	7.25
9	Baseplate Width Fraction for $t_{max,b}$	$\zeta_{1,t,b}$	0.26
10	Baseplate Height Fraction for $t_{max,b}$	$\zeta_{2,t,b}$	0.26
11	Maximum, Dimensionless Temperature Gradient Magnitude	$dt/dx_{max,b}$	0.4143
12	Baseplate Width Fraction for $dt/dx_{max,b}$	$\zeta_{1,g,b}$	0.78
13	Baseplate Height Fraction for $dt/dx_{max,b}$	$\zeta_{2,g,b}$	0.30
	Baseplate Front:		
14	Dimensionless Mean Temperature	$t_{m,f}$	3.77
15	Maximum, Dimensionless Temperature Differential	$(t_{max}\text{-}t_m)_f$	3.81
16	Baseplate Width Fraction for $t_{max,f}$	$\zeta_{1,t,f}$	0.21
17	Baseplate Height Fraction for $t_{max,f}$	$\zeta_{2,t,f}$	0.38
18	Maximum, Dimensionless Temperature Gradient Magnitude	$dt/dx_{max,f}$	0.3671
19	Baseplate Width Fraction for $dt/dx_{max,f}$	$\zeta_{1,g,f}$	0.12
20	Baseplate Height Fraction for $dt/dx_{max,f}$	$\zeta_{2,g,f}$	0.35

enclosure-frame Nusselt number contribution (Nu_2), and the (net) Nusselt number (Nu). The baseplate effective conductivity (k_e) is the hypothetical thermal conductivity that the baseplate would have if it transfers the actual amount of heat flow between the back surface and the front surface, as these surfaces are kept at their corresponding mean temperatures. Its definition is as follows:

$$k_e = \frac{L_3}{\Delta T_{fp}} \frac{\dot{q}_{fp}}{A_{fp}}, \tag{9.10}$$

where L_3 is the baseplate thickness, ΔT_{fp} is the baseplate mean temperature differential between the back surface and the front surface, $\dot{q}_{fp}$ is the net heat flow from the back surface and the front surface, and A_{fp} is the baseplate area exposed to liquid-coolant contact.

The temperature-level indicators for the face-panel back and front surfaces are the dimensionless mean temperature for both of these surfaces ($t_{m,b}$ and $t_{m,f}$) and the maximum dimensionless temperature differentials for both of these surfaces ($(t_{max}\text{-}t_m)_b$ and $(t_{max}\text{-}t_m)_f$). The location for temperature maximum is indicated in terms of dimensionless coordinates as the baseplate width and height fractions ($(\zeta_{1,t,b}, \zeta_{2,t,b})$ and $(\zeta_{1,t,f}, \zeta_{2,t,f})$), defined as:

$$\zeta_{1,t,b} = \left(\frac{X_1}{L_1}\right)_{t,b} \tag{9.11.a}$$

$$\zeta_{2,t,b} = \left(\frac{X_2}{L_2}\right)_{t,b} \tag{9.11.b}$$

for the back surface and

$$\zeta_{1,t,f} = \left(\frac{X_1}{L_1}\right)_{t,f} \tag{9.12.a}$$

$$\zeta_{2,t,f} = \left(\frac{X_2}{L_2}\right)_{t,f} \tag{9.12.b}$$

for the front surface.

The temperature-gradient indicators for the face-panel back and front surfaces are the maximum dimensionless temperature-gradient magnitude for both of these surfaces ($dt/dx_{max,b}$ and $dt/dx_{max,f}$). Their location is indicated in terms of dimensionless coordinates as the baseplate width and height fractions (($\zeta_{1,g,b}$, $\zeta_{2,g,b}$) and ($\zeta_{1,g,f}$, $\zeta_{2,g,f}$)), defined as:

$$\zeta_{1,g,b} = \left(\frac{X_1}{L_1}\right)_{g,b} \tag{9.13.a}$$

$$\zeta_{2,g,b} = \left(\frac{X_2}{L_2}\right)_{g,b} \tag{9.13.b}$$

for the back surface and

$$\zeta_{1,g,f} = \left(\frac{X_1}{L_1}\right)_{g,f} \tag{9.14.a}$$

$$\zeta_{2,g,f} = \left(\frac{X_2}{L_2}\right)_{g,f} \tag{9.14.b}$$

for the front surface.

The baseplate effective-conductivity ratio being very close to unity suggests that conduction within the baseplate is essentially one-dimensional. This is in agreement with Kaminski and Prakash [56], who concluded that one-dimensional conduction prevailed for Grashof numbers below 10^5. The Grashof number for the present case is $Gr = 7647$.

The Nusselt number of 12.58, which is based on the baseplate front surface mean temperature, is higher than that corresponding to two-dimensional natural convection in differentially heated enclosures. This is in part due to heat being transferred to the enclosure's upper, lateral, and lower side walls, in addition to that transferred to the front wall.

It was shown above that a dimensionless solution could be specified in terms of 25 dimensionless parameters (Ra^*, Pr, ψ, l_1, l_2, l_3, l_5, l_6, l_7, r_1, r_2, r_3, σ_1, σ_2, κ_1, κ_2, $\hat{h}_B$, $\hat{h}_3$, $\hat{h}_4$, $\hat{h}_5$, $\hat{h}_6$ t_7, t_8, t_9, t_{10}). Before proceeding with the parametric study, it will be beneficial, for the sake of simplicity in the analysis, to try to reduce the

number of independent parameters. Reduction in the number of geometry-related parameters is hard to justify. However, as will be seen, some of the boundary conditions can be simplified with only negligible effects on the solution. By doing so, the set of independent parameters is more manageable, and the subsequent analyses become easier to conduct. This is the subject of the next section.

9.3. Simplification of Boundary Conditions

This section is aimed at simplifying the boundary conditions in order to have a more manageable problem. In particular it is of interest to examine the effect of insulating the face panel side surfaces, having an isothermal enclosure and meniscus lens exterior, and removing the convective-type boundary condition on the face panel back surface.

(1) Effect of Insulating Face Panel Side Surfaces. As shown by the reference-case numerical results, heat transfer to the face panel sides represents 1.7 % of the total heat generation applied to the heated area on the face panel back. Therefore, heat transfer to these surfaces is relatively small, and insulating these surfaces should not affect the results significantly. The changes in input variables are as follows:

$$h_4 = 0 \text{ W/m}^2\text{-K} \tag{9.15.a}$$

$$h_5 = 0 \text{ W/m}^2\text{-K} \tag{9.15.b}$$

$$h_6 = 0 \text{ W/m}^2\text{-K} \tag{9.15.c}$$

(2) Effect of Having an Isothermal Enclosure Frame. This case checks the effect of assuming an isothermal enclosure frame. The temperatures applied to the enclosure frame for the reference case run were 52,0 °C on the lower wall, 53.9 °C on the lateral sidewall and upper wall, and 53.2 °C on the front wall. The temperature applied to the walls of the isothermal enclosure frame was arbitrarily set to the temperature the front wall (53.2 °C). The changes in input variables are as follows:

$$T_7 = 53.2 \text{ °C} \tag{9.15.d}$$

$$T_8 = 53.2 \text{ °C} \tag{9.15.e}$$

$$T_9 = 53.2 \text{ °C} \tag{9.15.f}$$

(3) Effect of Having an Isothermal Meniscus lens Exterior. This case checks the effect of forcing the exterior surface of the meniscus lens to be at the same temperature as the enclosure front surface. The input changes are:

$$h_3 = \infty \text{ W/m}^2\text{-K} \quad (9.15.g)$$

$$T_3 = 53.2 \text{ °C} \quad (9.15.h)$$

(4) Effect of Insulating the Face Panel Back Surface. This case checks the effect of insulating the face panel back surface while keeping the net heat transfer into the face panel constant. This is achieved by reducing the heat-generation flux to compensate for heat that now will not be transferred by radiation from the face panel back surface. The new heat flux was taken equal to the forward heat flux into the face panel material from the reference case. The input changes are:

$$h_1 = 0 \text{ W/m}^2\text{-K} \quad (9.15.i)$$

$$q'' = 1616.1 \text{ W/m}^2 \quad (9.15.j)$$

The resulting modified Rayleigh number becomes $Ra^* = 1.73 \times 10^7$ (laminar flow).

(5) Combined Effects. This case combines all of the above changes.

(6) Effect of Applying Heat Generation to the Entire Face Panel Back. This case checks the effect of applying the heat flux to the entire face panel back surface. The input changes are all of the above changes in addition to the following:

$$\sigma_{1,\max} = L_8/L_1 = 1 \ (L_8 = 61.2 \text{ mm}) \quad (9.15.k)$$

$$\sigma_{2,\max} = L_9/L_2 = 1 \ (L_9 = 48.7 \text{ mm}) \quad (9.15.l)$$

Results from the above cases are summarized in Table 9-11, and will be described next.

9.3.1. Case 1 – Effect of Insulating Face Panel Side Surfaces

Insulating the face panel sides results in a slight increase in the mean temperature, and consequently in a slight reduction in the Nusselt number. The dimensionless temperature gradient within the face panel is reduced from 0,4143 to

Table 9-11. Performance Summary for Variations from the Reference Configuration

Case →	#0	#1	#2	#3	#4	#5	#6
	Reference	Insulated Face Panel Sides	Isothermal Enclosure	Isothermal Meniscus Lens	Insulated Face Panel Back, Same Net Flux In	Combination (#1 to #4)	#5/w Heat Generation on Entire Face Panel Back
Inputs							
Ra^*	2.14×10^7	2.14×10^7	2.14×10^7	2.14×10^7	1.73×10^7	1.73×10^7	1.73×10^7
Pr	105.4	105.4	105.4	105.4	105.4	105.4	105.4
κ_1	2.951	2.951	2.951	2.951	2.951	2.951	2.951
κ_2	2.350	2.350	2.350	2.350	2.350	2.350	2.350
σ_1	0.8096	0.8096	0.8096	0.8096	0.8096	0.8096	1.0000
σ_2	0.6910	0.6910	0.6910	0.6910	0.6910	0.6910	1.0000
Outputs							
k_e/k_1	1.0128	1.0000	1.0128	1.0129	1.0135	0.9996	0.9998
Nu_1	1.17	1.14	1.15	0.74	1.19	0.69	0.70
Nu_2	11.41	11.09	11.29	11.53	11.19	11.06	11.54
Nu	12.58	12.23	12.44	12.26	12.38	11.75	12.24
Ra_m	8.06×10^5	8.28×10^5	8.15×10^5	8.26×10^5	7.83×10^5	8.26×10^5	1.42×10^6
Ra_m/Ra^*	0.038	0.039	0.038	0.039	0.045	0.048	0.082
Face-panel back							
$t_{m,b}$	8.19	8.34	8.23	8.28	9.73	10.04	17.60
$(t_{max}\text{-}t_m)_b$	7.25	7.14	7.23	7.30	7.88	7.63	1.80
ζ_1	0.26	0.26	0.25	0.25	0.26	0.29	0.46
ζ_2	0.26	0.26	0.26	0.25	0.27	0.24	0.49
$dt/dx_{max,b}$	0.4143	0.4127	0.4153	0.4146	0.4460	0.4459	0.3418
ζ_1	0.78	0.78	0.78	0.78	0.78	0.78	0.50
ζ_2	0.30	0.30	0.27	0.28	0.31	0.25	0.84
Face-panel front							
$t_{m,f}$	3.77	3.88	3.81	3.86	4.52	4.76	8.17
$(t_{max}\text{-}t_m)_f$	3.81	3.75	3.76	3.83	4.22	4.16	2.59
ζ_1	0.21	0.22	0.07	0.20	0.22	0.22	0.42
ζ_2	0.38	0.39	0.24	0.36	0.40	0.35	0.61
$dt/dx_{max,f}$	0.3671	0.3663	0.4966	0.3760	0.4077	0.4270	0.4451
ζ_1	0.12	0.12	0.00	0.12	0.12	0.13	0.18
ζ_2	0.35	0.35	0.41	0.36	0.35	0.29	0.05

0.4127. The face panel effective conductivity ratio is also reduced from 1.0128 to 1.0000. Changes in the coordinates of the maximum dimensionless temperature and maximum dimensionless temperature gradient magnitude are negligible. The Rayleigh number (based on the face panel-front mean temperature) increases slightly from 8.06×10^5 to 8.28×10^5.

9.3.2. Case 2 – Effect of Having an Isothermal Enclosure Frame

Using an isothermal-enclosure boundary condition results in a slight increase in the dimensionless mean temperature from 3.77 to 3.81. The Nusselt number is slightly reduced from 12.58 to 12.44. The maximum magnitude of the dimensionless temperature gradient within the face panel, which occurs on the back, shows a negligible increase from 0.4143 to 0.4153 (0.2% increase). The coordinates of the location of maximum temperature and temperature gradient on the face panel back show negligible changes. The Rayleigh number (based on the face panel-front mean temperature) increases slightly from 8.06×10^5 to 8.15×10^5.

9.3.3. Case 3 – Effect of Having an Isothermal Meniscus lens Exterior

Forcing the meniscus lens exterior to be isothermal at the same temperature as the enclosure front surface results in a negligible increase in the dimensionless mean temperature (1% increase). The Nusselt number shows a slight reduction of 2.5% (from 12.58 to 12.26). The maximum magnitude of the dimensionless temperature gradient within the face panel (on the back) shows a negligible increase of 0.7%. The face panel effective conductivity ratio is unchanged. The coordinates for the location of the maximum dimensionless temperature and maximum dimensionless temperature gradient magnitude experience negligible changes. The Rayleigh number (based on the face panel-front mean temperature) increases slightly from 8.06×10^5 to 8.26×10^5.

9.3.4. Case 4 – Effect of Insulating the Face Panel Back Surface

Insulating the face panel back while keeping the net heat flux input to the face panel constant results in an increase in the dimensionless mean temperature from 8.19 to 9.73. The Nusselt number is reduced from 12.58 to 12.38 (1.6% drop). The maximum magnitude of the dimensionless temperature gradient within the face panel is slightly increased from 0.4143 to 0.4460 (7.6% increase). The face panel effective conductivity ratio shows a negligible increase from 1.0128 to 1.0135. The coordinates for the location of maximum dimensionless temperature and maximum dimensionless temperature gradient magnitude show negligible changes. The Rayleigh number (based on the face panel-front mean temperature) drops from 8.06×10^5 to 7.83×10^5.

9.3.5. Case 5 – Combined Effects

Combining all of the above changes results in an increase of the dimensionless mean temperature of 22.6% on the face-panel back and 26.3% on the face panel front. The Nusselt number drops by 6.6 %. The face-panel effective conductivity ratio drops slightly by 1.3 %. Negligible changes occur to the coordinates for the location of maximum dimensionless temperature and maximum dimensionless temperature gradient magnitude on the face panel back. The Rayleigh number (based on the face-panel-front mean temperature) increases from 8.06×10^5 to 8.26×10^5.

9.3.6. Case 6 – Effect of Applying Heat Generation to the Entire Face Panel Back

Applying the heat generation flux to the entire face panel back (Case #6) while keeping all other inputs as in the previous case (Case #5) results in an increase in the face panel dimensionless mean temperature. The dimensionless mean temperature increases in approximately the same ratio as the heat generation area. The Nusselt number increases slightly. The dimensionless temperature gradient drops on the face panel back, but increases on the face panel front. The

Rayleigh number (based on the face panel-front mean temperature) increases from 8.26×10^5 to 1.42×10^6.

9.4. Selection of Simplified Boundary Conditions to be Used in the Performance Study

By using the set of boundary-condition parameters in Case 5 above, seven independent variables are removed from the problem specification. This leaves the nine dimensionless geometry parameters, three dimensionless parameters involving thermophysical properties (Pr, κ_1, and κ_2) two parameters involving boundary conditions (κ_1 and κ_2), the modified Rayleigh number (Ra^*), and the tilt angle (ψ). In this manner, the problem can be specified in terms of 16 parameters, instead of 25.

The following chapter will examine the effect of varying these parameters on the thermal performance.

10.A PERFORMANCE STUDY OF THE LIQUID-LENS SYSTEM

10.1. Introduction

During the design process, it may be of interest to the designer of a liquid-lens system to anticipate thermal performance trends when trading various materials or to anticipate what may occur if enclosure dimensions are adjusted or if the meniscus lens geometry are changed. In addition, it may be of interest to anticipate trends in thermal performance resulting from uncertainty in the raster area size, and due to the orientation of the system. This chapter studies these effects by varying thermophysical properties, heat flux, raster area dimensions, tilt angle, enclosure-frame dimensions, and meniscus lens geometry.

10.2. Variation in Thermophysical Properties and Boundary Conditions

This section is aimed at providing the thermal designer or system integrator with the effects on thermal performance resulting from variation in boundary conditions and the thermophysical properties of the materials involved, namely, the liquid coolant, the CRT face panel, and the meniscus lens. The dimensionless parameters containing such information are the modified Rayleigh number and the Prandtl number for the liquid coolant, and the conductivity ratios for the CRT face panel and the meniscus lens. The ratio of raster dimensions to base plate dimensions will be kept as in the reference case (*Chapter* 7).

10.2.1. Variation in the Prandtl Number

Figure 10-1 contains plots showing the effect of the variation in the Prandtl number from 10^{-1} to 10^{3} on the thermal performance indicators for the reference heated-region dimensions. In general, the Nusselt number increases very slightly and the effective-conductivity ratio stays nearly constant and close to unity as the Prandtl number increases.

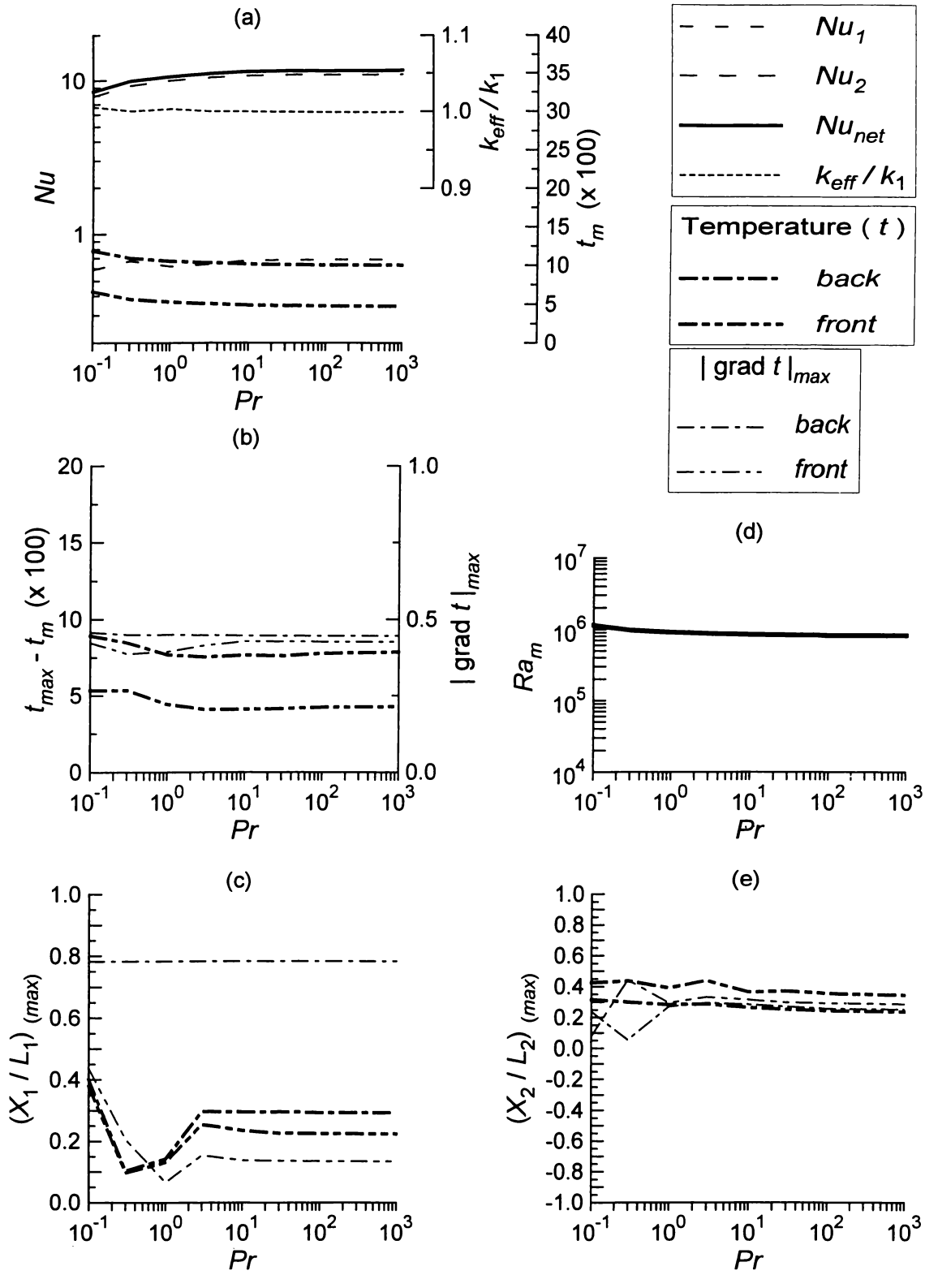

Figure 10-1. Effect of Variation in the Prandtl Number with Heat Generation Applied to the Reference Area

The dimensionless mean temperature on the face-panel back and front surfaces drops with increasing *Pr*, but at a very small rate. As *Pr* becomes large (*Pr* >10) the dimensionless mean temperature becomes insensitive to the Prandtl number. The Rayleigh number based on the face-panel-front mean temperature (Ra_m) experiences approximately the same behavior as the mean temperature.

The maximum dimensionless temperature for both face panel back and front surfaces decreases slightly from *Pr* = 0.1 to 2, but thereafter it remains nearly constant. The point of maximum temperature stays in the upper region of the face panel between $\zeta_2 \cong 0.2$ and 0.4 (*Figure 10-1e*). The horizontal coordinate for the maximum temperature experiences a steep drop, from $\zeta_1 \cong 0.4$ to 0.1 as *Pr* increases from 0.1 to 3. This is followed by an increase to $\zeta_1 \cong 0.3$ on the back surface and $\zeta_1 \cong$ 0.25 on the front surface as *Pr* increases further. As *Pr* becomes large, these values approach $\zeta_1 \cong 0.3$ and 0.22, respectively (*Figure 10-1c*). The dimensionless temperature gradient on the face-panel back and front surfaces remains nearly constant at around 0.4 for the above range of Prandtl number.

The most significant result from the above calculations is that the variation of the Prandtl number within the range of $10 < Pr < 1000$ has no effect on dimensionless temperatures and temperature gradients, while maintaining other dimensionless parameters constant. Additionally, for constant heat flux and thermal conductivity, the definition of the reference temperature implies that temperature and temperature gradients on the face panel should not be affected under the above assumptions.

10.2.2. Effect of Variation in the Modified Rayleigh Number

The modified Rayleigh number involves a mix of boundary-condition and thermophysical-property information, namely, the gravitational acceleration, the fluid's volume expansivity, viscosity, thermal diffusivity, the heat flux applied to the raster area, and a characteristic length scale. *Figure 10-2* contains plots showing the effect of increasing the modified Rayleigh number (Ra^*) from 1.73×10^6 to 8.67×10^7 on the thermal performance parameters for the reference heated-region dimensions.

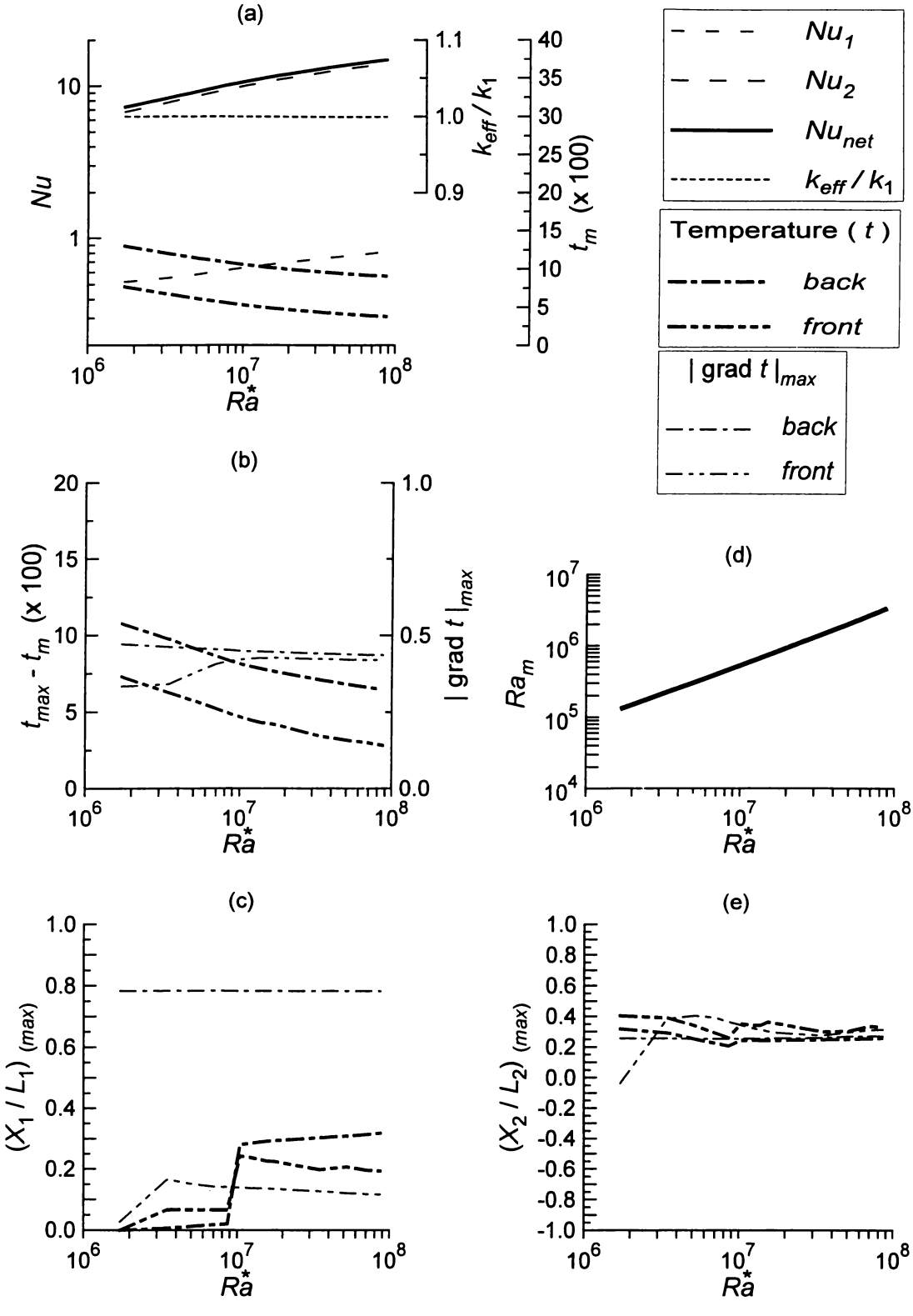

Figure 10-2. Effect of Variation in the Modified Rayleigh Number with Heat Generation Applied to the Reference Area

According to calculations, the Nusselt number increases, while the face-panel effective conductivity ratio stays nearly constant and close to unity as the modified Rayleigh number increases. The dimensionless mean temperature on the face panel back and front surfaces drops with increasing Ra^*. The Rayleigh number based on the face panel-front mean-temperature (Ra_m) increases with increasing Ra^*.

The maximum dimensionless temperature decreases monotonically for both face panel back and front surfaces. In the case where the heated region has reference dimensions, the location for maximum temperature stays in the upper region of the face panel at $\zeta_2 \cong 0.3$ (*Figure 10-2e*), and close to the symmetry plane for $Ra^* < 9 \times 10^6$. As the Ra^* is increased past 10^7 the point of maximum temperature moves away from the symmetry plane to $\zeta_1 \cong 0.3$ for the face panel back surface and $\zeta_1 \cong 0.2$ for the face panel front surface (*Figure 10-2c*).

The temperature gradient on the face panel back remains nearly constant for the range of Rayleigh number. The temperature gradient on the face panel front surface increases with Rayleigh number when the heat-generation region has reference dimensions, but it drops as the Rayleigh number increases when heat generation is applied to the entire face panel back. The location of maximum temperature gradient on the face panel back surface remains at $\zeta_1 \cong 0.79$ and $\zeta_2 \cong 0.25$. On the front surface, both coordinate locations increase as Ra^* increases up to 4×10^6. The coordinate locations remain at a nearly constant level past this value of Ra^* at $\zeta_1 \cong 0.1$ to 0.15 and $\zeta_2 \cong 0.3$ to 0.4.

10.2.3. Effects of Variations in the Face-Panel Conductivity Ratio

Figure 10-3 contains plots showing the effect of varying the face panel conductivity ratio from 0.4 to 40 on the thermal performance indicators for the reference heated-region dimensions. In general, the Nusselt number remains nearly constant for the above range in conductivity ratio. The face panel effective-conductivity ratio stays nearly constant at unity for dimensionless face panel conductivity (κ_1) below 20, but it increases with κ_1 above such value.

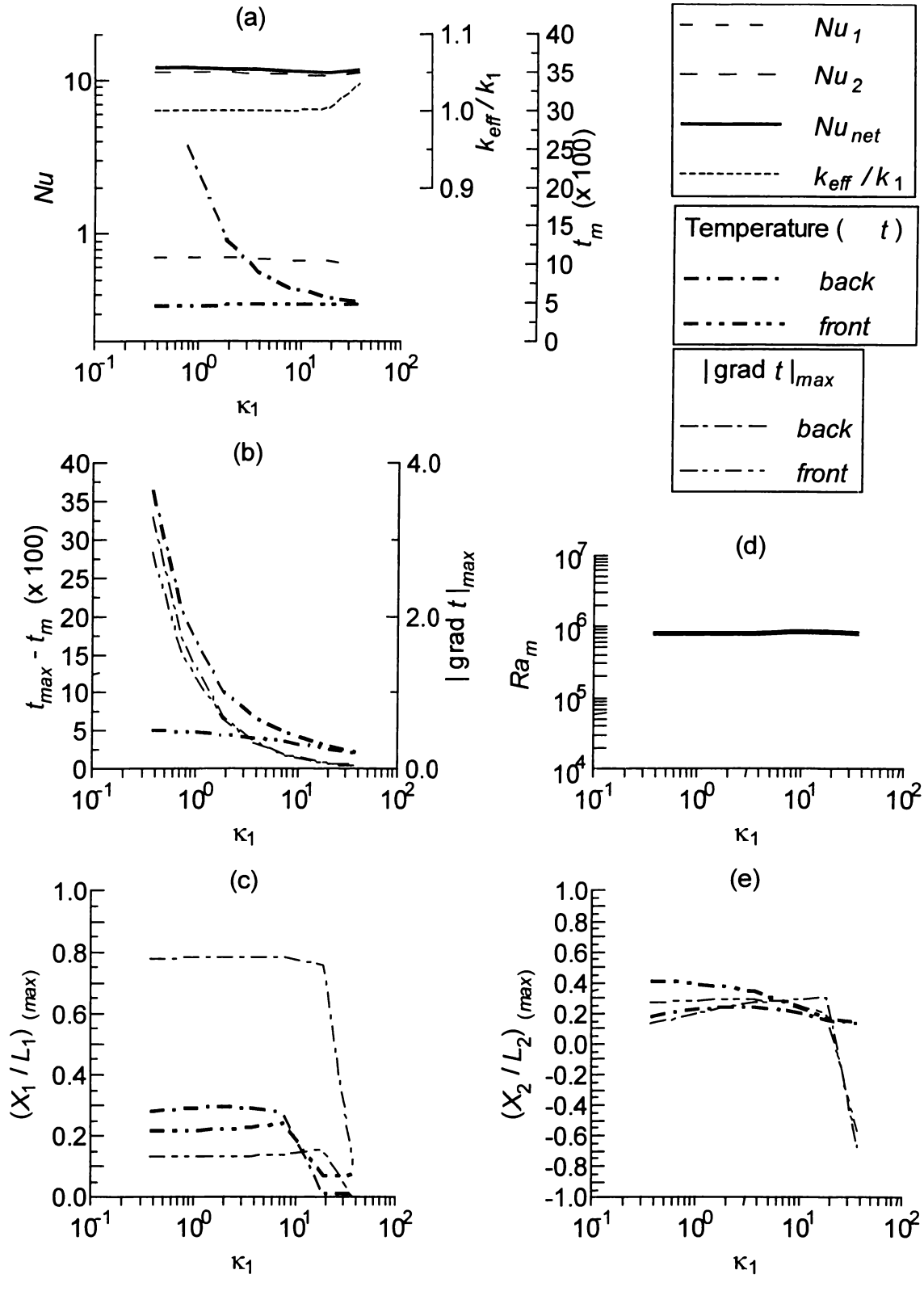

Figure 10-3. Effect of Variation in the Face panel Conductivity ratio with Heat Generation Applied to the Reference Area

As the conductivity ratio becomes large, the dimensionless mean temperature on the face panel back and front surfaces approach the value of 500 for heated-region reference dimensions. This means that the face panel becomes isothermal at this value. As the face panel conductivity ratio decreases, the mean temperature on the front surface stays approximately the same, but the mean temperature on the back side increases to infinity as the conductivity ratio approaches zero. The Rayleigh number based on the face panel-front mean-temperature remains nearly constant at $Ra_m \cong 9 \times 10^5$.

The maximum dimensionless temperature and dimensionless temperature gradient for the face panel back approach infinity as the face panel conductivity ratio approaches zero. The maximum dimensionless temperature and dimensionless temperature gradient for the face panel back and front approach zero as the face panel conductivity ratio approaches infinity (isothermal limit). The location for maximum temperature stays at $\zeta_1 = 0.2$ to 0.3 and ζ_2 between 0.2 and 0.4 for the face panel conductivity ratio below 8.

Based on the results above, selection of the face panel material with a smaller thermal conductivity leads to an increase in temperature at the back of the face panel. This would lead to deterioration of the phosphor layer. In addition, temperature gradients would rise resulting in higher thermal stresses. Selection of this material, however, is under the control of the manufacturer of the picture tube, and not the thermal designer or integrator of the liquid-lens system.

10.2.4. Effects of Variations in the Meniscus Lens Conductivity Ratio

Figure 10-4 contains plots showing the effect of varying the meniscus lens conductivity ratio from 0.4 to 40 on the thermal performance indicators for the reference heated-region width and height fractions. In general, the Nusselt number increases very slightly as the meniscus lens conductivity ratio (κ_2) increases, but theoretically, it should approach a finite value as κ_2 approaches infinity (isothermal meniscus lens). The increase is due to the contribution from the increase in heat transfer though the meniscus lens. The contribution to the Nusselt number from heat transfer to the enclosure stays nearly constant. The face-panel effective

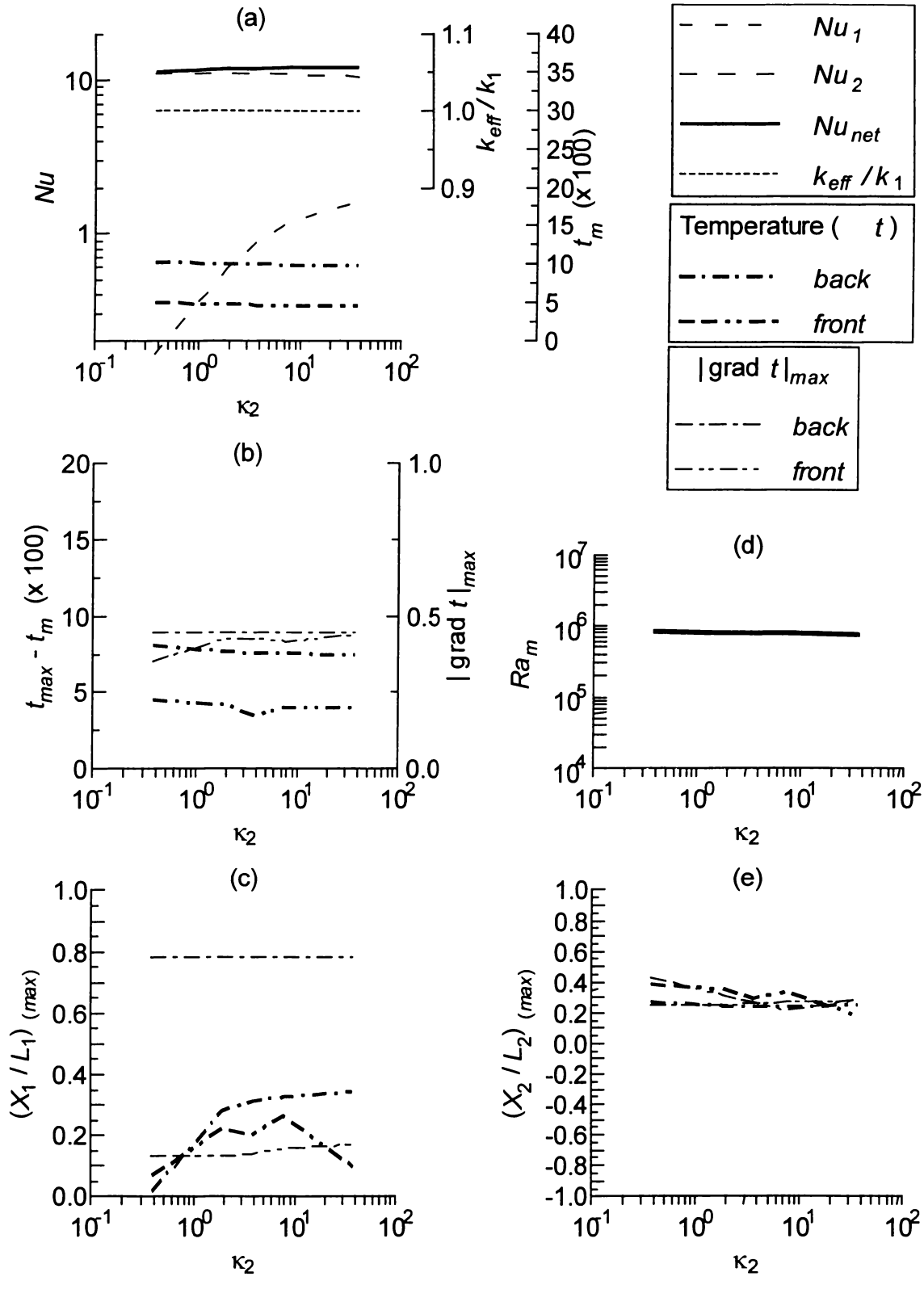

Figure 10-4. Effect of Variation in the Meniscus lens Conductivity Ratio with Heat Generation Applied to the Reference Area

conductivity ratio stays nearly constant at unity for the entire range of meniscus-wall conductivity ratio, κ_2. The mean temperature and the Rayleigh number based on the face panel-front mean-temperature drop very slightly, and again should approach a finite value as κ_2 becomes large.

The maximum dimensionless temperature and dimensionless temperature gradient for the face panel back and front are little affected by variations in κ_2 within the range considered.

Based on the results above, variation in the meniscus-lens thermal conductivity has a negligible effect on thermal performance, that is, face-panel temperature and temperature gradient.

10.2.5. Discussion

Based on the above results, the dimensionless temperature drops with increasing modified Rayleigh number, and remains unaffected by changes in the Prandtl number in the range of $10 < Pr < 1000$, and for changes in the thermal conductivity of the meniscus lens. In order to determine the effects of varying thermophysical properties on physical temperature, the definition of the reference temperature must be accounted for. It is assumed that design dimensions are fixed. The reference temperature was previously defined as (see Eq. (9.6)):

$$\Delta T_o = \frac{L}{k_o}\dot{q}'', \tag{10.1}$$

where L is the reference length scale, k_o is the thermal conductivity, and $\dot{q}''$ is the heat flux. Since this definition involves the thermal conductivity, it is convenient to rewrite the modified Rayleigh number in Eq. (9.4) terms of this property as:

$$Ra_L^* = \frac{c_o\, g\, \beta_o\, \dot{q}''\, L^4}{\nu_o\, k_o^{\,2}}, \tag{10.2}$$

and the Prandtl number in Eq. (9.3) as:

$$Pr = \frac{\nu_o\, c_o}{k_o}, \tag{10.3}$$

where c_o is the thermal capacity per unit volume (product of density and specific heat), β_o is the liquid volume expansivity, ν_o is the kinematic viscosity, g is the gravitational acceleration. The temperature can be calculated using Eq. (9.1.a), in terms of the dimensionless temperature (t), the reference temperature differential (ΔT_o), and the reference temperature (T_o) as:

$$T = t \cdot \Delta T_o + T_o . \tag{10.4}$$

The temperature gradient can be calculated by multiplying the dimensionless temperature gradient by the reference scale for temperature gradient. The reference scale for temperature gradient is obtained from Eq. (10.1) as:

$$\left(\frac{\mathrm{d}T}{\mathrm{d}X}\right)_o = \frac{\dot{q}''}{k_o} . \tag{10.5}$$

Thermal Conductivity Variations

From Eq. (10.1), it may be shown that for a fixed heat flux, the reference temperature can be reduced by increasing the liquid-coolant thermal conductivity (assuming a fixed reference length scale). Increasing the thermal conductivity results in reductions of the modified Rayleigh number, and based on the results in the preceding sections, this is accompanied by increases in the dimensionless temperature. However, these increases are offset by the increase in the reference temperature from definition in Eq. (10.1), resulting in reductions in the face-panel temperature levels. A similar argument can be made for the temperature gradient using Eq. (10.5).

Thermal Capacity per Unit Volume

The modified Rayleigh number in Eq. (10.2) has the thermal capacity per unit volume (c_o) in the numerator, and so does the Prandtl number definition in Eq. (10.3). Therefore, increasing the thermal capacity per unit volume results in increases of both the modified Rayleigh number and the Prandtl number. Based on the above results, increases in Prandtl number alone does not result in changes in

thermal performance. However, increases in the modified Rayleigh number results in reductions in the dimensionless temperature levels within the face panel. For fixed values of the heat flux and the liquid coolant thermal conductivity, the reference temperature remains fixed, and therefore, based on Eq. (10.4), the temperature levels within the face panels should drop. A similar argument can be made for the temperature gradient using Eq. (10.5).

Volume Expansivity

The modified Rayleigh number in Eq. (10.2) has the volume expansivity (β_o) in the numerator. Therefore, increasing the volume expansivity results in increases in the modified Rayleigh number. From the above results, increases in the modified Rayleigh number results in dimensionless temperature reductions. For constant heat flux and thermal conductivity, the reference temperature remains fixed, and therefore, based on Eq. (10.4), the temperature of the face panel should drop. A similar argument can be made for the temperature gradient using Eq. (10.5).

Kinematic Viscosity

The modified Rayleigh number in Eq. (10.2) has the kinematic viscosity (ν_o) in the denominator, while the Prandtl number definition in Eq. (10.3) has the kinematic viscosity in the numerator. Therefore, drops in the kinematic viscosity results in increases of the modified Rayleigh number and reductions in the Prandtl number. It was shown that the variation of the Prandtl number within the range of $10 < Pr < 1000$ has no effect on thermal performance. Therefore, variations in the kinematic viscosity resulting in only variations in the Prandtl number within this range has no bearing on thermal performance. However, the kinematic viscosity affects also the modified Rayleigh number, and based on the results above, increases in the modified Rayleigh number results in drops in the dimensionless temperature. For constant heat flux and thermal conductivity, the reference temperature remains fixed, and therefore, based on Eq. (10.4), the temperature of the face panel should

drop. A similar argument can be made for the temperature gradient using Eq. (10.5).

10.2.6. Conclusion

This section dealt with examining the effects of varying thermophysical properties on thermal performance. For a constant heat flux, the liquid-lens thermal performance can be improved by selecting a liquid coolant with a larger volume expansivity, a larger thermal capacity per unit volume (product of density and specific heat), smaller kinematic viscosity, or larger thermal conductivity. No significant effects are predicted by changes in the thermal conductivity of the meniscus lens. Increasing the thermal conductivity of the face-panel material yields lower phosphor screen temperatures, and lower temperature gradients within the face panel, but the selection of this material and its properties is under the control of the picture tube manufacturer.

10.3. Uncertainty in the Raster Region Dimensions

This section is aimed at providing the designer or integrator of projection monitors with information as to how the thermal performance can be affected by variation of the raster region width and height. These parameters are specified in terms of minimum dimensions, but their precise values cannot be determined with certainty. In the next sub-sections, the heated-region (raster region) width and height will be varied throughout the full range of possible values. It is understood that realistic values for these dimensions expected during actual operation should be in the range from approximately 70% to 100% of the width and height of the face panel back.

10.3.1. Effects of the Heated-Region Width Uncertainty

Figure 10-5 contains plots showing the effect of varying the heated-region width fraction (σ_1) on the thermal performance indicators, using the heated-region reference height fraction ($\sigma_{2,ref}$). The Nusselt number first increases rapidly as the

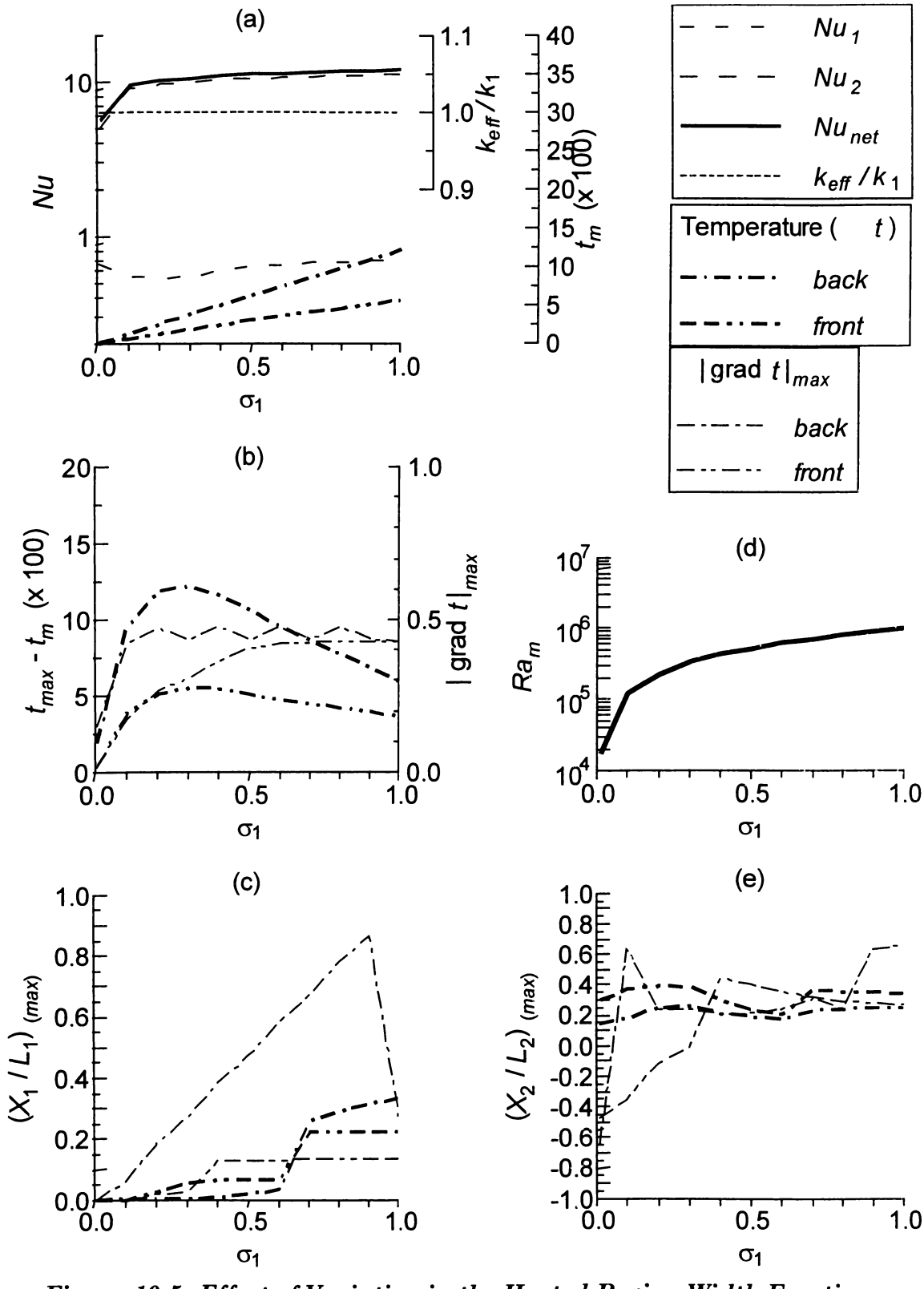

Figure 10-5. Effect of Variation in the Heated-Region Width Fraction at the Reference Height Fraction

width fraction departs from zero, but it then increases more slowly and remains nearly constant for width fractions above $\sigma_1 = 0.6$. The face-panel effective-conductivity ratio stays nearly constant at unity for the entire width fraction range. The mean temperature for both face-panel surfaces increases in a near-linear dependency with the width fraction. The Rayleigh number based on the face panel-front mean-temperature increases in the same fashion.

The maximum dimensionless temperature differential increases rapidly as the heated-region width fraction departs from zero until a maximum is reached at $\sigma_1 = 0.2$. Its value then drops almost linearly until a finite value is reached at width fraction of unity. The location for maximum temperature stays close to the symmetry plane for width fractions below 0.6. Past this width fraction, the location for maximum temperature moves off the symmetry plane in the neighborhood of 0.2 to 0.3 for the heated-region reference-height fraction and 0.4 for a heated-region height fraction of unity.

The maximum dimensionless temperature gradient also experiences steep increases as the width fraction is increased from zero, and then it remains at a nearly constant level in the neighborhood of 0.45 as the width fraction is increased past 0.5.

10.3.2. Effects of the Heated-Region Height Uncertainty

Figure 10-6 contains plots showing the effect of varying the heated-region height fraction (σ_2) on the thermal performance indicators, using the heated-region reference width fraction ($\sigma_{1,ref}$). The Nusselt number behaves similarly to the case when the heated-region width was varied. It increases from a finite value at zero height fraction to a maximum value for a height fraction of unity. The Nusselt number first increases rapidly as the height fraction departs from zero, but it then increases more slowly and remains nearly constant for height fractions above 0.6.

The face-panel effective-conductivity ratio stays nearly constant at unity for the entire range of height fraction. The mean temperature for both face-panel surfaces increases in a near-linear dependency with the height fraction. The Rayleigh number based on the face panel-front mean-temperature increases in the

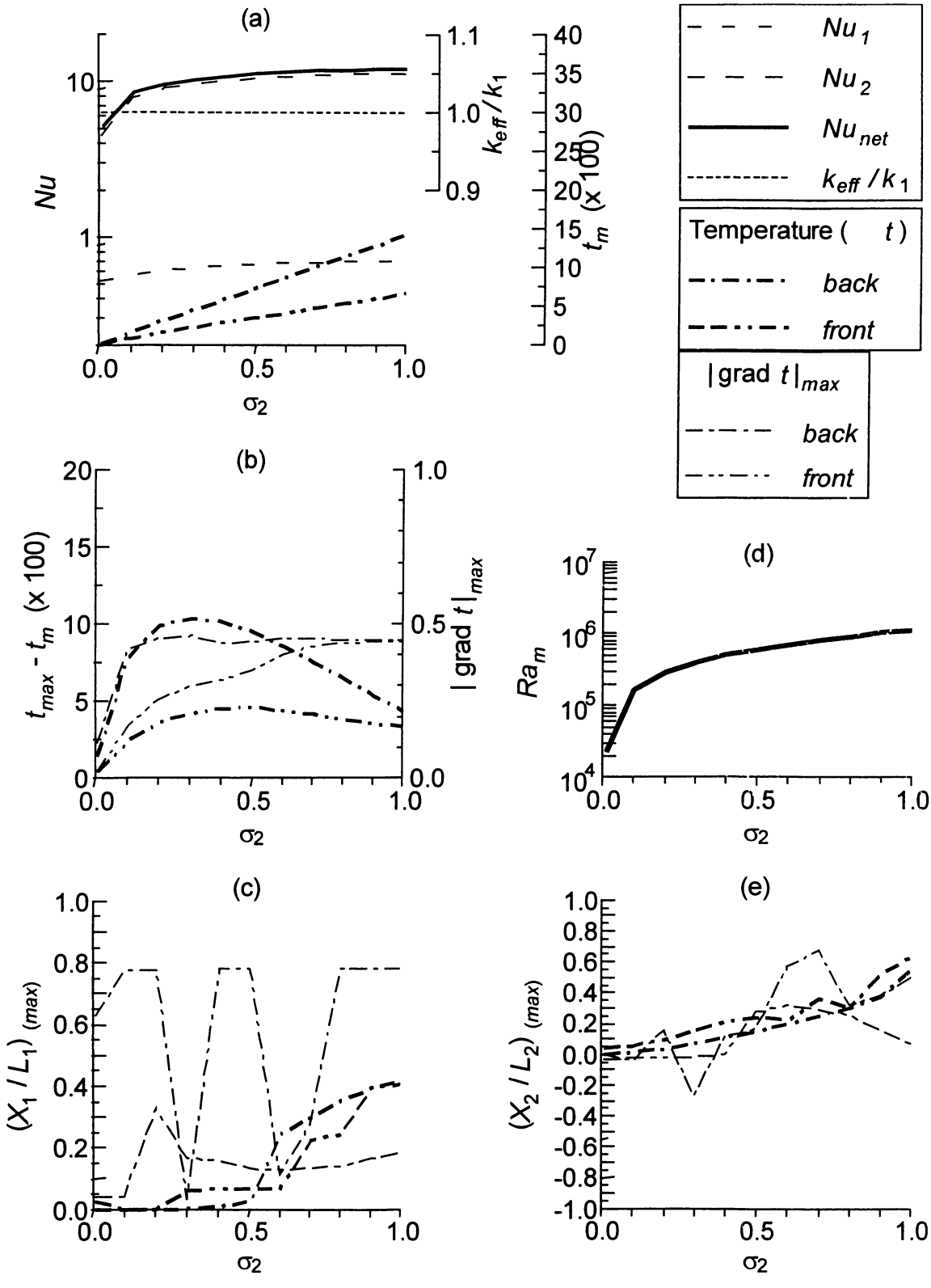

Figure 10-6. Effect of Variation in the Heated-Region Height Fraction at the Reference Width Fraction

same manner. The maximum dimensionless temperature differential increases rapidly as the heated-region height fraction departs from zero until a maximum is reached. Its value then drops almost linearly until a finite value is reached at a height fraction of unity. The location for maximum temperature stays close to the symmetry plane for height fractions below 0.3. Past this height fraction, the location for maximum temperature moves off the symmetry plane and approaches the value of approximately 0.4 as σ_2 approaches unity. The vertical position for maximum temperature starts at $\zeta_2 = 0$ for $\sigma_2 = 0$, and then increases progressively as σ_2 increases. For $\sigma_2 = 1$, the vertical location for maximum temperature is in the neighborhood of $\zeta_2 = 0.6$.

The maximum dimensionless temperature gradient increases more rapidly on the face panel back surface as compared to the front surface as σ_2 increases. It then stays in the neighborhood of 0.45 as the height-fraction approaches unity.

10.3.3. Summary

This section studied the effect of the uncertainty in the raster area width and height. Increases in the raster area width and height while maintaining constant heat flux results in increases in the face panel mean temperatures on the back and front surfaces. The maximum magnitude of the temperature gradient, however, remains unaffected. It is then concluded that uncertainty in the raster area width and height does not affect the temperature-differential requirement in the tube's specification. Notice that if the input power to the picture tube is kept constant, the heat flux applied to the raster area decreases, resulting in smaller temperature maximums. In this case, uncertainty in the raster dimensions is beneficial as input power specifications are for raster-area minimum dimensions.

10.4. Variation in the Tilt Angle

This section is aimed at studying the effect of the tilt angle of the liquid-lens system on thermal performance. For the sake of completeness, all angles were considered regardless of whether they are practical for the purposes of integration

within a projection monitor. *Figure 10-7* contains plots showing the effect of varying the tilt angle (ψ) from 0° (face panel facing up or heated-from-below orientation) to 180° (face panel facing down or heated-from-above orientation) on the thermal performance indicators for the reference heated-region width and height fractions. The Nusselt number has a minimum at the heated-from-above orientation. This result is consistent with that obtained from differentially heated rectangular enclosures. However, unlike results for differentially heated rectangular enclosures, the Nusselt number does not have a maximum in the heated-from-below orientation. In this orientation, the Nusselt number has a local minimum of $Nu = 12.07$ when heat is applied to the entire face panel back surface, and $Nu = 11.01$ when heat is applied to the heated-region reference width and height fractions. The absolute maximum of $Nu = 12.34$ occurs at $\psi = 18.7°$ when heat is applied to the entire face panel back surface, and $Nu = 11.99$ occurs at $\psi = 7.6°$ when heat is applied to the heated-region reference width and height fractions. Past these angles, the Nusselt number drops at first slowly as the tilt angle increases to up to approximately 150°. The Nusselt number then experiences a steeper decrease as the tilt angle is further increased until it reaches a minimum at $\psi = 180°$. The minimum Nusselt number is $Nu = 4.44$ at $\psi = 180°$. The face panel effective-conductivity ratio stays nearly constant at unity for the entire range of tilt angles. The mean temperature and the Rayleigh number based on the face panel-front mean-temperature experience effects similar to the Nusselt number, but with
opposite signs in the first derivative. That is, as the tilt angle is increased from zero, a small drop occurs in these variables, followed by a monotonic increase.

The maximum dimensionless temperature differential for the face panel back remains nearly constant for tilt angles between 0° and 130° (*Figure 10-7b*). Their values increase as the tilt angle is increased above 130°. The maximum-temperature location stays near or at the symmetry plane for tilt angles above 40° and between $\zeta_2 = 0.2$ and 0.4 for tilt angles between 20° and 170°. At $\psi = 180°$, the maximum temperature occurs at the face panel center of symmetry. The maximum dimensionless temperature gradient on the face-panel back surface remains nearly

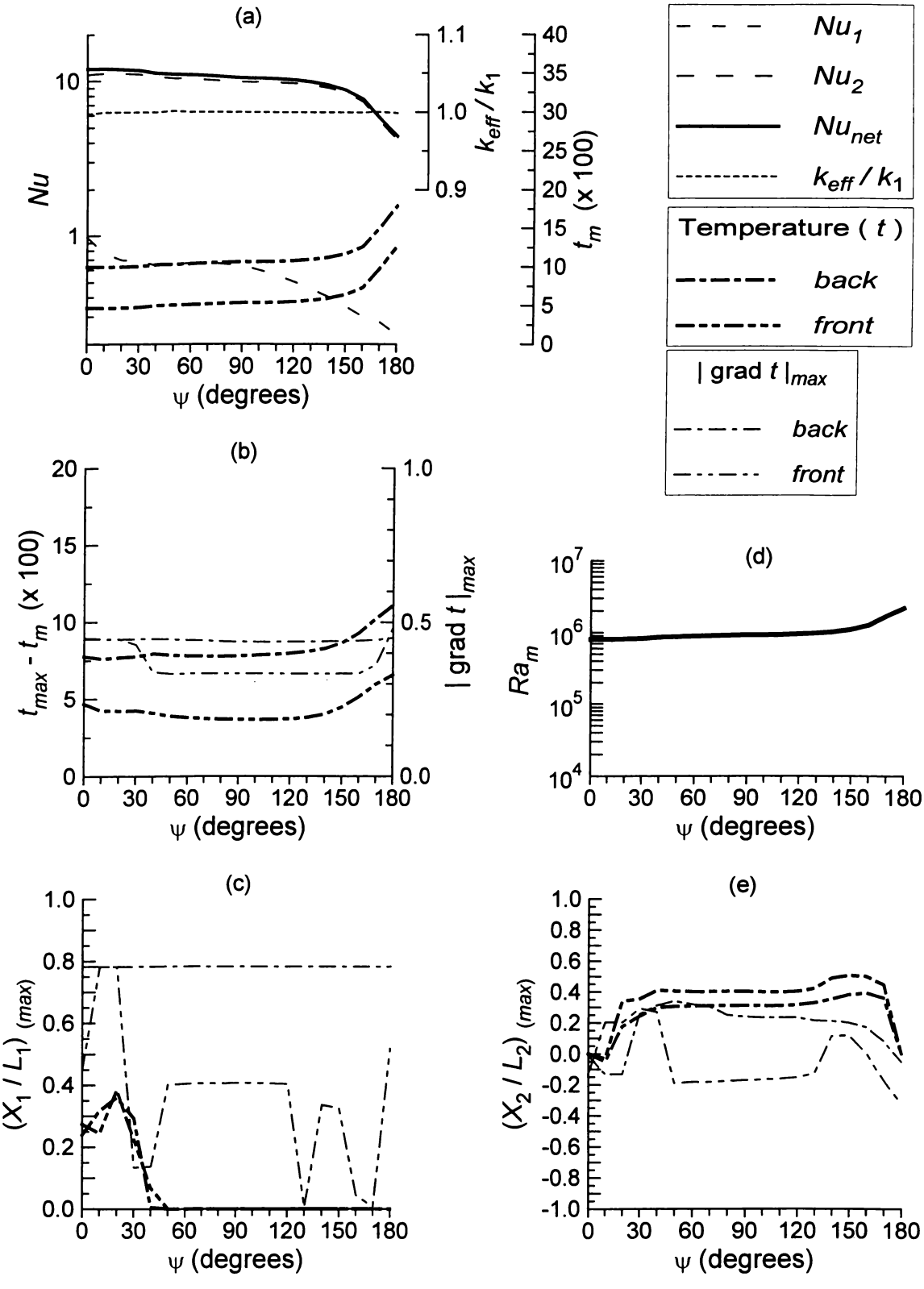

Figure 10-7. Effect of Variation in the Tilt Angle with Heat Generation Applied to the Reference Area

constant at 0.44 for all tilt angles. On the face-panel front surface, it drops from 0.44 to approximately 0.33 for tilt angles between 40° and 160°.

In summary, thermal performance was evaluated for the range of tilt angles from the heated-from-below (face-panel up) orientation to the heated-from-above orientation (face-panel down). Thermal performance was found best when the face panel points downward (tilt angle zero); that is, temperature and temperature gradients are minimum. As the system is tilted away from such orientation, thermal performance begins to degrade, but not significantly until the tilt angle reaches approximately 130°. For tilt angles between 130° and 180° (heated-from above) the face panel temperature experiences severe increases. Liquid-lens orientations in this range of tilt angles should be avoided.

10.5. The Effects of Varying Geometry on Thermal Performance

The sections ahead examine the effects of varying the dimensions of the enclosure frame and shape of the meniscus lens on thermal performance. It is assumed that the dimensions of the base plate are fixed, and that the position of the focusing lens (in front of the liquid-lens system) is fixed. The enclosure frame width and height were increased up to 20%. The increase is applied only to the enclosure frame – not to the base plate. This increase will result in additional liquid-coolant volume while maintaining the same face-panel area. For enclosure depth variations, it is assumed that the distance from the base plate to the enclosure frame front wall, can be adjusted as long as no interference is made with the optical path or with the design space of the focusing lens.

10.5.1. Effect of Variation in the Enclosure Frame Width

This section examines the effect of varying the enclosure width. Two cases were run with 10% and 20% increases in width. All other inputs were kept the same as in the reference case (*Chapter* 7). Table 10-1 shows the thermal performance results. An increase of 20% in enclosure width produces a drop of only 0.4 °C in the baseplate-back-surface maximum temperature. The mean temperature on the

Table 10-1. Effect of Enclosure Frame Width Variations on Thermal Performance

Parameter / Location	*Units*	*Reference Case*	*10% Width Increase*	*20% Width Increase*
Enclosure Half Width, L_1 =	mm	61.2	67.1	73.4
Base-Plate Back Surface				
Temperature				
Mean	°C	68.7	68.7	68.6
Maximum	°C	82.5	82.3	82.1
$X_{1(max)}$	mm	15.8	16.1	16.0
$X_{2(max)}$	mm	12.8	12.9	13.0
Temperature-Gradient Magnitude				
Mean	°C/mm	1.69	1.69	1.69
Maximum	°C/mm	3.08	3.07	3.15
$X_{1(max)}$	mm	47.9	47.9	47.6
$X_{2(max)}$	mm	14.4	16.3	31.0
Base-Plate Front Surface				
Temperature				
Mean	°C	60.4	60.3	60.2
Maximum	°C	67.6	67.3	67.1
$X_{1(max)}$	mm	13.1	13.3	13.4
$X_{2(max)}$	mm	18.6	19.0	19.2
Temperature-Gradient Magnitude				
Mean	°C/mm	1.26	1.26	1.26
Maximum	°C/mm	2.73	2.72	2.71
$X_{1(max)}$	mm	7.4	7.4	7.4
$X_{2(max)}$	mm	16.9	17.2	17.8

baseplate back drops by only 0.1 °C. The maximum temperature gradient magnitude on the baseplate back increases from 3.08 to 3.15 °C/mm, and the mean temperature gradient magnitude on the baseplate back remains virtually unchanged. It may be concluded that no significant benefit is achieved by increasing the enclosure width by as much as 20 %.

10.5.2. Effect of Variation in the Enclosure Height

This section examines the effect of varying the enclosure height. Two cases were run with 10% and 20% increase in height. All other inputs were kept the same as in the reference case (*Chapter* 7). Table 10-2 shows the thermal performance results. An increase of 20% in enclosure height produces a drop of only 0.4 °C in the baseplate-back-surface maximum temperature. The mean temperature on the baseplate back drops by only 0.1 °C. The maximum temperature gradient magnitude on the baseplate back increases from 3.08 to 3.15 °C/mm. The mean temperature gradient magnitude on the baseplate back remains virtually unchanged. It may be concluded that no significant benefit is achieved by increasing the enclosure height by as much as 20 %.

10.5.3. Effect of Variation in the Enclosure Depth

This section examines the effect of varying the enclosure depth. Variation in the enclosure depth was subject to realistic design constraints. The reference enclosure depth was 25.5 mm. *Figure 10-8* depicts these constraints. The minimum enclosure depth must be such that it does not interfere with the light coming from the phosphor screen into the meniscus lens. To ensure this, the enclosure depth must not be less than 22 mm, which is the distance between the baseplate exterior and the edge of the convex surface facing the baseplate. The maximum enclosure depth must not be much larger than the distance between the baseplate exterior and the outer-most surface of the meniscus lens. For convenience that distance will be chosen as the maximum depth, that distance being 30 mm. Two cases were run

Table 10-2. Effect of Enclosure Height Variations on Thermal Performance

Parameter/Location	*Units*	*Reference Case*	*10% Height Increase*	*20% Height Increase*
Enclosure Half Height, L_2 =	mm	48.7	53.6	58.4
Base-Plate Back Surface				
Temperature				
Mean	°C	68.7	67.6	66.7
Maximum	°C	82.5	82.4	82.4
$X_{1(max)}$	mm	15.8	16.0	16.2
$X_{2(max)}$	mm	12.8	12.8	12.7
Temperature-Gradient Magnitude				
Mean	°C/mm	1.69	1.57	1.44
Maximum	°C/mm	3.08	3.08	3.08
$X_{1(max)}$	mm	47.9	47.9	47.9
$X_{2(max)}$	mm	14.4	14.4	14.4
Base-Plate Front Surface				
Temperature				
Mean	°C	60.4	59.8	59.4
Maximum	°C	67.6	67.5	67.5
$X_{1(max)}$	mm	13.1	13.4	13.7
$X_{2(max)}$	mm	18.6	19.1	19.6
Temperature-Gradient Magnitude				
Mean	°C/mm	1.26	1.35	1.41
Maximum	°C/mm	2.73	4.35	4.42
$X_{1(max)}$	mm	7.4	42.0	2.7
$X_{2(max)}$	mm	16.9	-53.3	-58.4

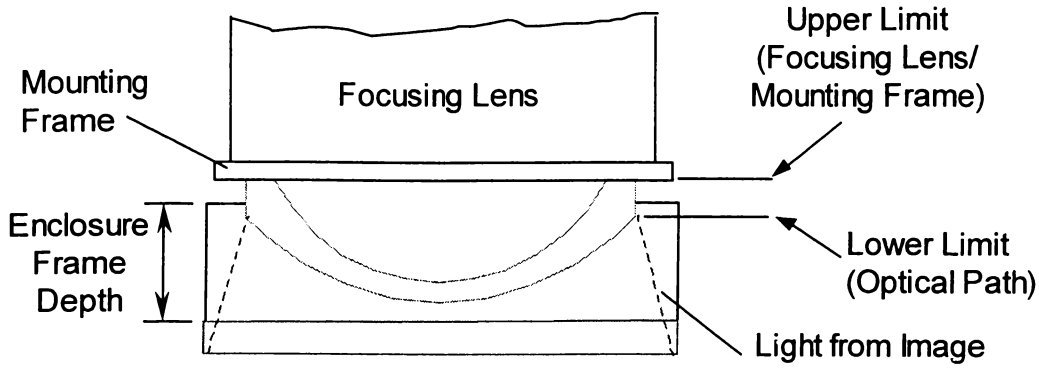

Figure 10-8. Variations Limits for the Dimensions of the Enclosure-Frame Depth

representing these two extremes. The first case uses an enclosure depth of 22 mm, and the second run used an enclosure depth of 30 mm.

Table 10-3 shows the thermal performance results. Reducing the enclosure depth from 25.5 mm to 22 mm produces a negligible increase in the baseplate back maximum and mean temperature of only 0.1 °C. Increasing the enclosure depth to 30 mm produces a small drop in the baseplate back maximum of only 0.4 C, and a small drop in the mean temperature of only 0.2 °C. The maximum and mean values of the temperature gradient magnitude on the baseplate back surface are virtually unchanged. It may be concluded that no significant benefit is achieved by increasing the enclosure depth within realistic design allowances.

10.5.4. Effect of Replacing the Meniscus Wall with a Circular Plate

The situation may present in which the thermal designed is faced with the possibility that the shape of the meniscus lens is altered for any particular reason. It is, therefore, of interest to determine the effects of changes in the meniscus lens on thermal performance. For the sake of simplicity, an extreme case will be considered for analysis. This is the case where the meniscus lens is replaced with a circular plate.

Figure 10-9 shows the geometry, domain dimensions, and the computational grid. Table 10-4 compares results for selected variables against the reference case.

The maximum temperature and maximum temperature gradient magnitude on the baseplate back stayed at nearly the same levels. Their location also remained nearly unchanged. On the baseplate front surface, on the other hand, there was a small drop in the maximum temperature of 0.6 °C, and drop in maximum temperature gradient magnitude from 2.73 °C/mm to 2.22 °C/mm. The location for maximum temperature moved towards the symmetry plane, and the location for maximum temperature gradient moved towards the coordinate origin (CRT center).

Based on the above results, the presence of the meniscus wall yields a slight reduction in the baseplate mean temperature, but a slight increase in the maximum temperature. These changes are not significant. The maximum temperature gradient on the baseplate back surface experiences a slight drop, as the meniscus wall is in place. This is not the case on the baseplate front surface, where the maximum temperature gradient experiences a significant increase. If the maximum overall temperature gradient in the baseplate is used as the design parameter for material structural failure, then the presence of the meniscus wall does not produce an adverse effect on thermal stresses. Based on the above observations, it is then concluded that changes in the shape of the meniscus lens does not significantly influence the liquid-lens thermal performance. The implications are twofold: (1) the performace of the thermal design can be calculated with a simplified geometry, such as the one of the circular plate, and (2) given a working thermal design, the meniscus lens shape/model can be changed without concern about the system thermal performance.

10.6. Summary

This chapter examined the effects of changing thermophysical properties, tilt andgle, enclosure frame dimensions, and meniscus lens geometry on thermal performance. When selecting the optical liquid, it was determined that thermal performance improves with higher thermal conductivity, density, specific heat, and volume expansivity, or lower kinematic viscosity. Thermal performance is virtually insensitive to the thermal conductivity of the meniscus lens. Uncertainty in the raster area width and height are beneficial to thermal performance. For tilt angle

Table 10-3. Effect of Enclosure Depth Variations on the Thermal Performance Parameters

Parameter/Location	*Units*	*Reference Case*	*Minimum Depth*	*Maximum Depth*
Enclosure Depth, L_3 =	mm	25.5	22.0	30.0
Base-Plate Back Surface				
Temperature				
Mean	°C	68.7	68.8	68.5
Maximum	°C	82.5	82.6	82.1
$X_{1(max)}$	mm	15.8	16.4	15.9
$X_{2(max)}$	mm	12.8	12.5	13.0
Temperature-Gradient Magnitude				
Mean	°C/mm	1.69	1.69	1.69
Maximum	°C/mm	3.08	3.08	3.08
$X_{1(max)}$	mm	47.9	47.9	47.9
$X_{2(max)}$	mm	14.4	14.7	15.3
Base-Plate Front Surface				
Temperature				
Mean	°C	60.4	60.4	60.1
Maximum	°C	67.6	67.6	66.1
$X_{1(max)}$	mm	13.1	12.8	6.8
$X_{2(max)}$	mm	18.6	17.3	9.2
Temperature-Gradient Magnitude				
Mean	°C/mm	1.26	1.26	1.26
Maximum	°C/mm	2.73	2.80	3.65
$X_{1(max)}$	mm	7.4	7.3	7.4
$X_{2(max)}$	mm	16.9	16.2	19.8

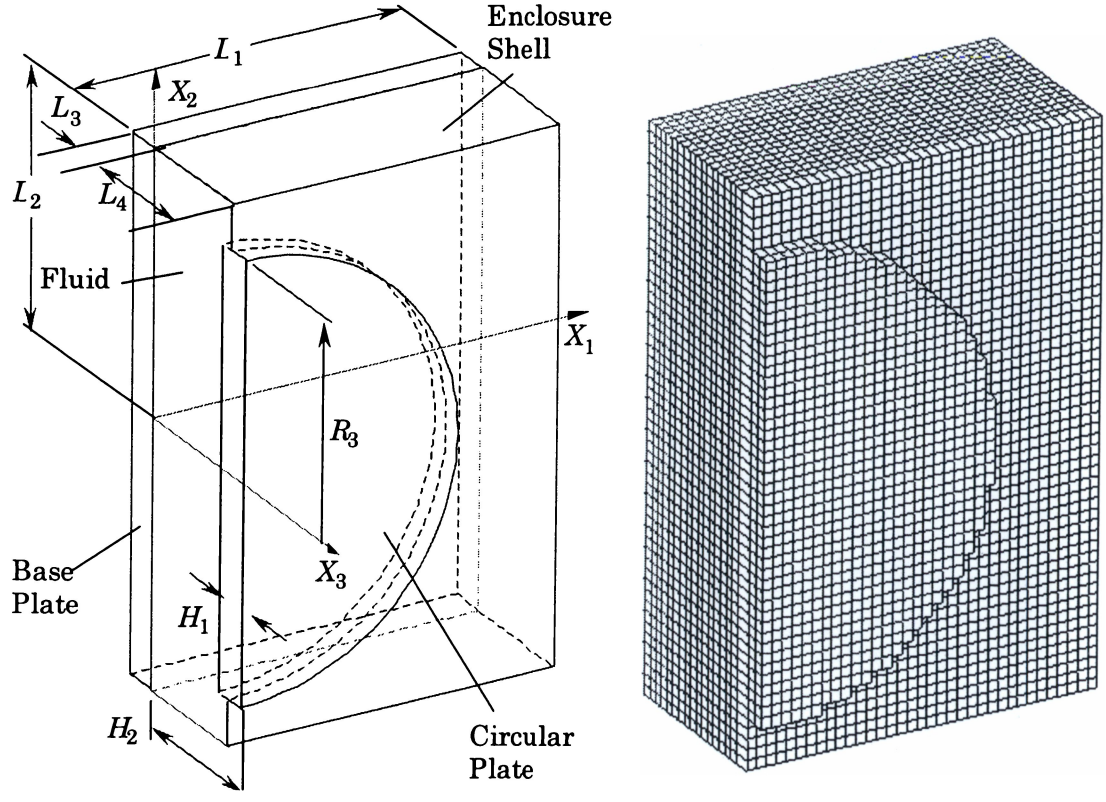

(a) Geometry Model (b) Computational Grid

Figure 10-9. Computational Model Geometry

Table 10-4. Maxima on the Base-Plate Back and Front Surfaces

Parameter	*Units*	*Maximum Value*	X_1 (mm)	X_2 (mm)
Base-Plate Back Surface				
Reference Case Temperature	°C	82.5	15.8	12.8
Present Case Temperature		82.5	0.9	13.4
Energy Flux				
Reference Case	W/m^2	2.09	47.2	-30.7
Present Case		2.09	48.1	-31.6
Temperature-Gradient Magnitude				
Reference Case	°C/mm	3.08	47.9	14.4
Present Case		3.09	47.9	13.6
Base-Plate Front Surface				
Reference Case Temperature	°C	67.6	13.1	18.6
Present Case Temperature		67.0	0.9	18.9
Energy Flux				
Reference Case	W/m^2	2.16	7.5	16.7
Present Case		1.75	2.9	-1.2
Temperature-Gradient Magnitude				
Reference Case	°C/mm	2.73	7.4	16.9
Present Case		2.22	2.9	-1.6

variations, the effects on thermal performance for angles between 0° (face up) and 130° are negligible. Tilt angles above 130° result in sharp increases in face panel temperature and temperature gradients. These angles should be avoided. Changes in enclosure frame dimensions and in the geometry and position of the meniscus lens present negligible effects on thermal performance.

11. ALTERNATIVE COOLING METHODS

11.1. Introduction

In *Chapter* 7 it was shown that thermal resistance calculations based on mean-temperature differentials resulted in the thermal resistance between the face-panel front surface and the liquid-lens enclosure to be approximately one quarter of the thermal resistance between the enclosure and the cabinet interior environment. This suggests that more benefits could be derived from enhancing the heat transfer between the liquid-lens system exterior and the cabinet interior environment than is enhancing the heat transfer within the liquid lens. The effects of enhancing natural convection within the liquid lens by adding heat transfer area to the enclosure frame interior are limited, as the face-panel front area -- a major heat transfer path controlling the overall thermal resistance -- is fixed. An alternative to natural convection inside the liquid lens is forced convection. This chapter is aimed at examining the effects of using forced convection inside the liquid lens, and proposing alternatives for enhancing the heat transfer outside the liquid lens to the cabinet interior.

11.2. Enhancement of Internal Heat Transfer

This section examines the effect of using forced convection to transfer heat from the face panel into a recirculating liquid. It is assumed that cold liquid is fed through the enclosure lower wall, and the heated liquid is withdrawn through the enclosure upper wall. This can be implemented by the use of reservoirs replacing these walls and the use of a fine screen to ensure flow uniformity, as shown in *Figure 11-1*. The liquid is fed at the reference temperature of the wall itself, that is, 52 °C. The normal velocity on these surfaces is assumed uniformly distributed. Velocities of 5 and 10 mm/s were used to compare against reference results. The net volumetric flow rates were 15.6 and 31.2 ml/s, respectively.

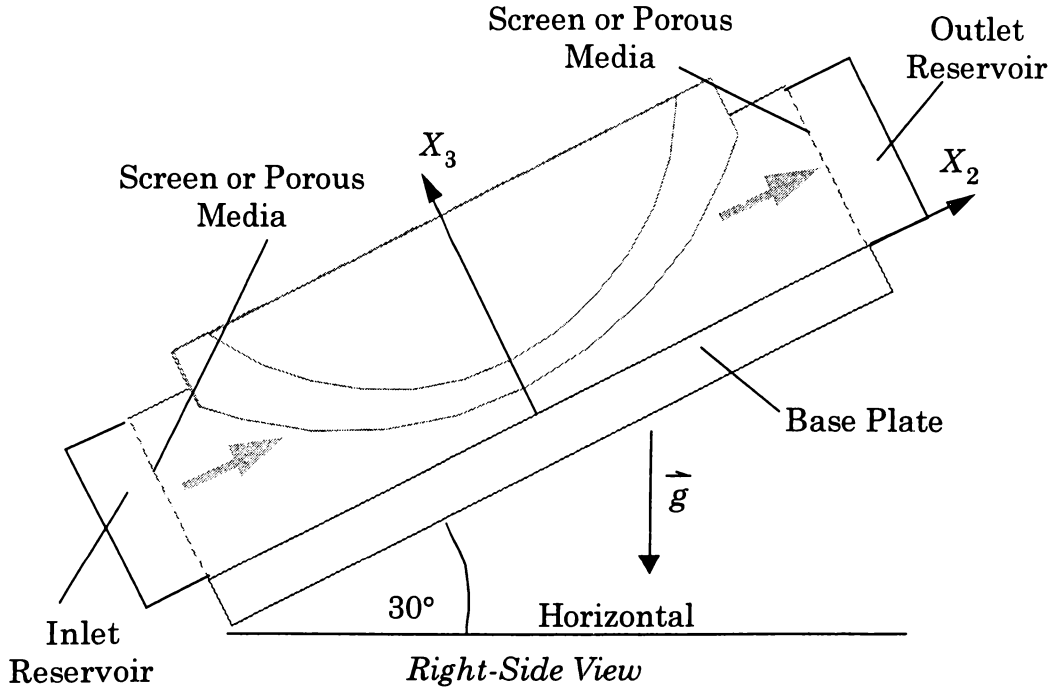

Figure 11-1. Internal Forced-Convection Concept

Table 11-1 shows the thermal performance results. Forced convection lowers the maximum temperature significantly. The maximum temperature on the baseplate back surface is reduced from 82.5 °C to 76.4 °C with a flow of 31.2 ml/s. The temperature gradient magnitude is also reduced. Notice that in the case of forced convection, the overall system temperature is highly dependent on the inlet fluid temperature. Therefore, it is anticipated that for the same flow rate, lowering the inlet liquid temperature by certain amount should result in approximately equal reduction in the maximum baseplate temperature. It may be concluded that forced convection by flow recirculation with external cooling lowers the temperature significantly without adverse impact on the temperature gradients.

It has been shown above, that the thermal design of the liquid-lens system meets the picture tube manufacturer's thermal requirements for a wide range in environmental temperature. There are situations, however, that may demand additional cooling capability. For instance, if a more powerful electron gun is used, additional heat would be generated at the phosphor screen, resulting in increases of

Table 11-1. Effect of Forced Convection on Thermal Performance

Parameter / Location	*Units*	*Reference Case*	*Velocity*	
Flow Normal Velocity, V =	mm/s	0	5	10
Net Volumetric Flow Rate	ml/s	0	15.6	31.2
Base-Plate Back Surface				
Temperature				
Mean	°C	68.7	65.5	64.7
Maximum	°C	82.5	77.7	76.4
$X_{1(max)}$	mm	15.8	6.9	11.5
$X_{2(max)}$	mm	12.8	14.8	17.7
Temperature-Gradient Magnitude				
Mean	°C/mm	1.69	1.66	1.65
Maximum	°C/mm	3.08	3.04	3.02
$X_{1(max)}$	mm	47.9	47.9	47.8
$X_{2(max)}$	mm	14.4	13.6	13.5
Base-Plate Front Surface				
Temperature				
Mean	°C	60.4	57.0	56.2
Maximum	°C	67.6	62.2	61.1
$X_{1(max)}$	mm	13.1	14.0	17.8
$X_{2(max)}$	mm	18.6	20.3	23.5
Temperature-Gradient Magnitude				
Mean	°C/mm	1.26	1.25	1.24
Maximum	°C/mm	2.73	2.41	2.47
$X_{1(max)}$	mm	7.4	0.0	0.0
$X_{2(max)}$	mm	16.9	-4.6	-2.5

the screen temperature and the face-panel glass temperature gradients, potentially reaching or surpassing their respective maximum allowable value. The temperature of the phosphor screen can also be increased if the face panel is made thicker. This is the case of an improved picture tube model (Hitachi 180AMB22), which uses a face panel measuring 10.3 mm in thickness, instead of the 7 mm, as used in the picture tube evaluated.

Improvement of the liquid-lens thermal design itself is not expected to enhance thermal performance too significantly. It seems clear that natural convection itself within the liquid lens cannot be significantly improved, as the mayor thermal resistance being that between the face panel and the mean liquid temperature depends on the face panel area, which happens to be a fixed parameter. This thermal resistance accounts for approximately two thirds of the temperature differential between the face panel and the enclosure walls. Therefore no matter how natural convection is improved, the temperature differential between the face panel and the enclosure walls should not drop much below two thirds of the original reference value. Forced convection within the liquid lens, however, may reduce the face panel temperature significantly without having a major impact or significantly negative effect on the face-panel temperature gradients.

Forced convection within the liquid lens can be achieved either by liquid recirculation, or by a stirring mechanism inside the liquid lens away from the light path from the raster area and the meniscus lens optical bounds (see *Figure 11-2*). Having the stirring mechanism, at the most can bring the face panel temperature down as close as possible to that of the enclosure walls. In the limit of an infinite convection coefficient (very intense stirring) the face panel mean temperature can be brought down by 7°C for the system evaluated under "specification" operating conditions. If active cooling using liquid recirculation, the face panel temperature can be brought down by a much larger amount.

11.3. Enhancement of External Heat Transfer

Thermal resistance external to the liquid-lens system was shown to account for approximately 80% of the total resistance in the path of heat transfer between the face panel and the cabinet environment. This suggests that significant reductions in the face panel temperature can be achieved by improving external cooling. This can be achieved by various means, for instance, the use of added external area to the enclosure walls, i.e. using fins, and/or using fans to take advantage of forced air convection (see *Figure 11-3*). Alternatives may involve the use of the use of thermoelectric cooling devices [36] and heat pipes [109]. Thermoelectric coolers are semiconductor devices that operate under the principle of thermocouples, but in "reverse." That is, they receive electric power as input and induce heat transfer flow from a cold region to a hot region. These devices can be attached to the enclosure frame to enhance heat transfer across its wall to the environment in the cabinet interior. Heat pipes are sealed vessels containing a refrigerant that flows back and forth between two ends at different temperatures. The refrigerant is condensed at the cold end (condenser) and flows to the hot end (evaporator) in the form of liquid. In the evaporator, the refrigerant absorbs the heat and is converted into vapor. The vapor then travels back to the condenser to be converted back into liquid. The evaporator end of a heat pipe can be attached to the exterior of the enclosure frame to transfer the heat to a remote heat sink.

(a) Internal Stirring Device

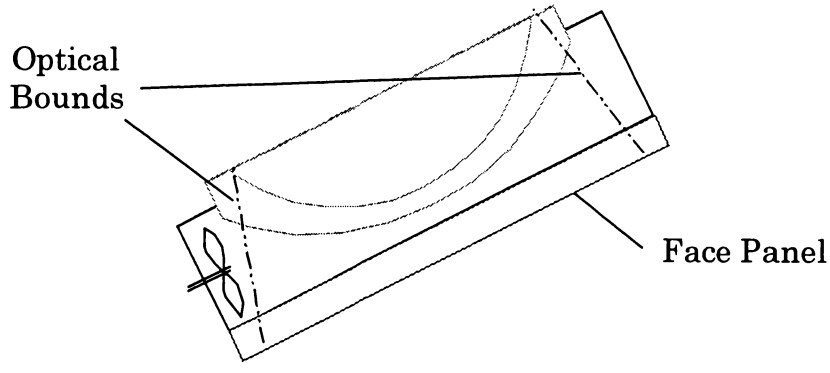

(b) Recirculating Liquid Loop

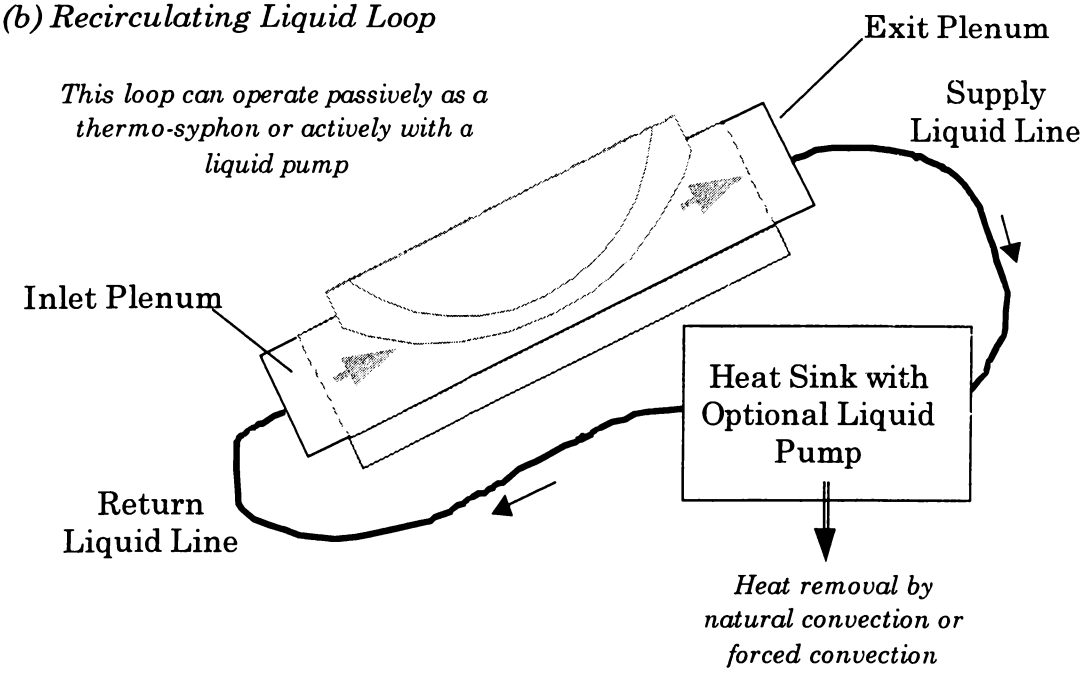

Figure 11-2. Improved Cooling by Enhancements of Internal Heat Transfer

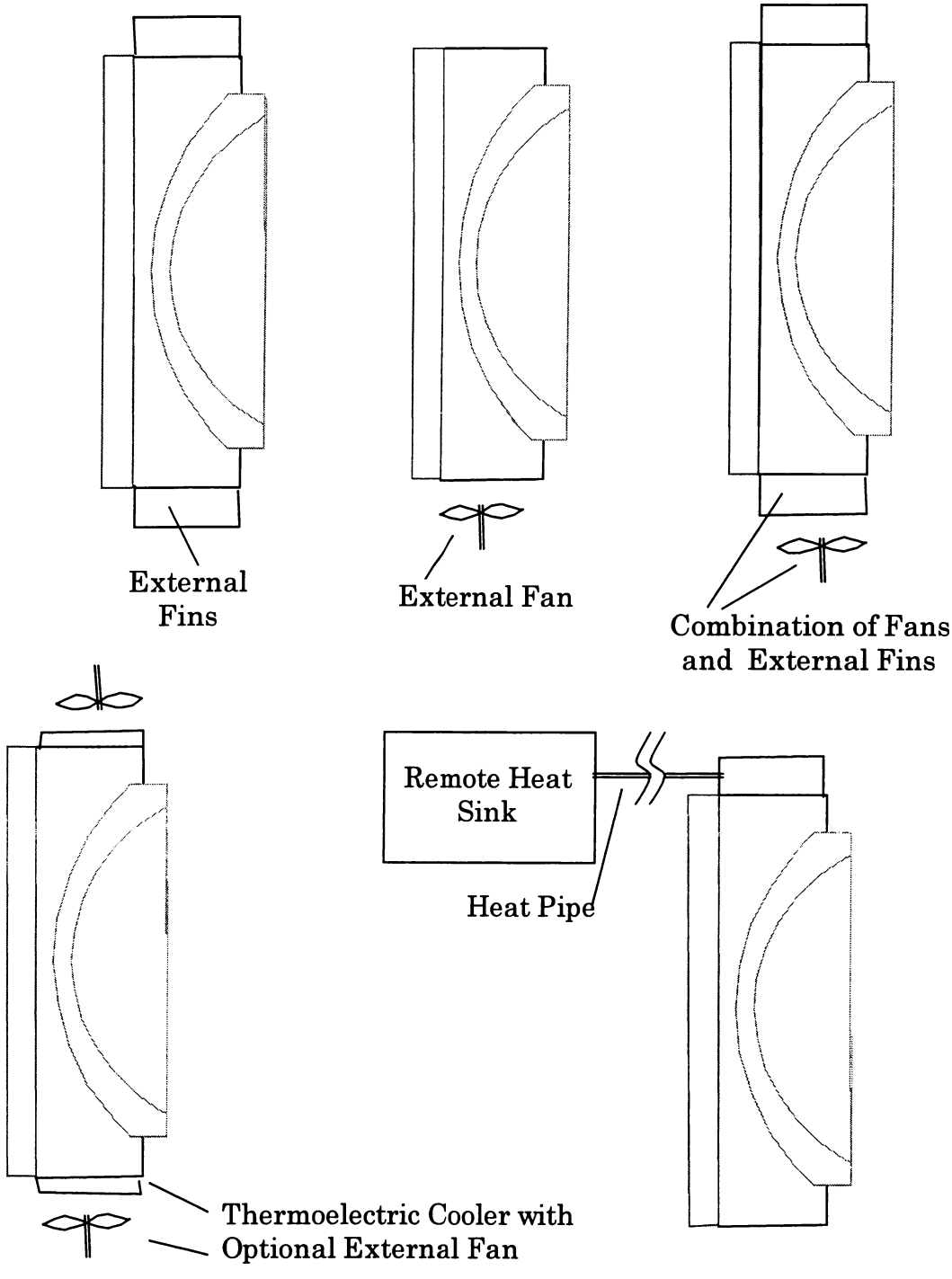

Figure 11-3. Improved Cooling by Enhancing External Heat Transfer

12. CONCLUSIONS AND RECOMMENDATIONS

12.1. Summary

The thermal design of a liquid-lens system used to cool picture tubes in projection television receivers was evaluated using an experimentally benchmarked numerical model. The evaluation was made based on specifications for these tubes indicating a maximum allowable temperature at the face-panel center and a maximum allowable temperature differential between the center and perimeter points. For the present evaluation, these values were 90°C for the maximum temperature and 21°C for the maximum allowable temperature differential, as required by the tube manufacturer.

A numerical model was developed to simulate the conjugate heat transfer and fluid flow processes within the liquid-lens system. A primitive-variable, non-staggered grid, finite-volume solution procedure was used. The equations were written in conservative form to enforce local and global conservation of mass, momentum, and energy. A non-staggered grid was used with the dependent variables at cell-node locations, and boundary conditions imposed and evaluated at face-node locations. The concept of finite volumes was strictly used such that cells were treated as independent control volumes, with boundary conditions applied to face nodes. A robust method for solving the implicitly derived set of algebraic mass-momentum-energy equations was developed using a forward four-way prediction scheme for cell-node pressure, face-node pressure, face-node velocities, and Cartesian cell-node velocities, in that order. Mass conservation is enforced from the start of the iteration process by calculating the pressure first. Next, mass-conserving face velocities are calculated followed by Cartesian cell-node velocities and other scalars such as temperature, without the need for velocity correction. One or more iterations can be made within each time step, and the steady-state solution may be obtained in true or false transient modes. The numerical model reproduces a hydrostatic field free from spurious momentum sources in the limiting case of an isothermal field.

Laboratory temperature measurements were made to gather face-panel temperature and heat flux data using a 46-inch Magnavox commercial projection monitor to benchmark the numerical model. An input power of 14.2 Watts resulted in steady-state face panel temperatures ranging between 50 °C and 65 °C for a room air temperature of 21.7°C. Good correlation was obtained as the correlation coefficient based on the face-panel temperatures was calculated at 0.965. Results suggested that approximately 6% of the electrical input power is converted into visible light and the remaining 94% into heat.

The thermal performance of the liquid-lens system satisfied all of the design constraints on temperature and temperature gradients. Thus, the original design was judged satisfactory. The temperature at the face panel center was calculated at 65.9 °C, which is well below the manufacturer's requirements of 90 °C. In addition, the maximum temperature differential between this point and periphery points was 15.3 °C, also below the manufacturer's requirements of 21 °C. These results provide adequate performance margins such that the power input to the tube or the maximum allowable room air temperature in the design specification could be increased. Specifically, assuming that changes to the heat transfer coefficients are negligible, the room air temperature could be increased to approximately 36 °C, without exceeding the maximum allowable face-panel temperature.

Most of the heat (79%) is transferred to the face-panel front by conduction. A smaller fraction (19%) is transferred from the face panel back to the tube interior by radiation. The remainder (2%) is conducted to the face panel sidewalls. The thermal resistance from the liquid-lens enclosure to the cabinet interior environment is approximately four times larger than the thermal resistance due to natural convection within the liquid coolant. This suggests that improvements in heat transfer can have more impact if made outside the liquid lens, from the enclosure to the interior environment of the TV cabinet.

12.2. Effects of Design Changes on Thermal Performance

Thermal performance is nearly insensitive to changes in the shape of the meniscus lens or the dimensions of the liquid-lens enclosure frame. Thus,

modifications to the enclosure frame and design and positioning changes of the meniscus lens can be made without concern for significant changes in the maximum face-panel temperature or temperature differentials.

12.3. Effects of Orientation Changes on Thermal Performance

Thermal performance is nearly insensitive to variations in the tilt angle of the liquid-lens system between 0° (face panel pointing upward) and 130°. For tilt angles greater than 130°, temperature levels within the face panel experience a sharp rise, with a maximum at the tilt angle of 180° (face panel pointing downward). Angles between 130° and 180° should be avoided under present operating conditions and thermal performance requirements.

12.4. Effects of Variation in Material Properties on Thermal Performance

Variations in the thermal conductivity of the meniscus lens did not result in significant thermal performance changes. It was shown that improvements in thermal performance could be obtained by increases in thermal conductivity, mass density, specific heat, and volume expansivity and reductions in kinematic viscosity.

12.5. Effects of the Uncertainty Raster Area Dimensions on Thermal Performance

Since the picture tube manufacturer specifies *minimum* raster area dimensions and a nominal input power, uncertainty in these dimensions implies that the area could only increase, which would result in smaller heat fluxes. Since smaller heat fluxes yield lower levels in the temperature gradient, and better performance, uncertainty in these dimensions should not present negative effects on performance.

12.6. Recommendations for Thermal Design Improvements

The major thermal resistance for the heat flowing to the fluid is that of the interface between the face panel and the liquid coolant. The heat transfer area for such thermal resistance, that is, the face panel area, is fixed for a given picture tube. This suggests that limited improvement can be achieved using natural convection alone within the liquid lens. Alternatively, thermal performance can be improved by the use of internal forced convection and/or enhancement of the heat transfer from the exterior surfaces of the liquid lens assembly to the air in the interior of the TV cabinet. In this context, internal forced convection refers to forced convection of the liquid coolant inside the liquid-lens system, while external forced convection refers to that of the air outside the system (within the cabinet). Internal forced convection may be achieved by the use of a circulating loop using the liquid coolant as the heat transfer media to an external cooler. Improvement of external heat transfer may be achieved with the use of external fans and/or fins added to the enclosure exterior.

Alternative means for improving external heat transfer could involve thermoelectric devices or heat pipes attached to the enclosure-frame walls. Thermoelectric devices are attractive because they do not produce noise, but may be costly and only transfer heat through small distances. Heat pipes are attractive because unlike thermoelectric devices, they can transfer the heat to a remote heat sink, however they may generate noise due the refrigerant flow along the pipes. Added noise and electromagnetic interference are factors to be considered as part of these design solutions, in addition to the added cost.

LIST OF REFERENCES

[1] Anderson, D. A., Tannehill, J. C., and Pletcher, R. H., Computational Fluid Mechanics and Heat Transfer, *Hemisphere Publishing Corporation,* U.S.A. (1984)

[2] Applied Mathematics and Computation, ed. by J. F. Thompson, *North-Holland* (1982) Vols. 10-11

[3] Arnold, J. N., Catton, I., and Edwards, D. K. , "Experimental Investigation of Natural Convection in Inclined Rectangular Regions of Different Aspect Ratios," *Journal of Heat Transfer* (February 1976) pp. 67-71

[4] Arnold, J. N., Edwards, D. K., and Wu, P. S., "Effect of Cell Size on Natural Convection in High L/D Tilted Rectangular Cells Heated and Cooled on Opposite Faces," ASME Publication No. 78-WA/HT-5 (Aug. 1975) pp. 1-5

[5] Ayyaswamy, P. and Catton , I. , "The Boundary-Layer Regime for Natural Convection in a Differentially Heated, Tilted Rectangular Cavity," *Journal of Heat Transfer* (November 1973) pp. 543-545

[6] Baker, A. J., Finite Element Computational Fluid Mechanics, *Hemisphere Publishing Corporation,* U.S.A. (1983)

[7] Baker, H. D., Ryder, E. A., and Baker, N. H., Temperature Measurement in Engineering, *Omega Press* (1975) Vols. 1 and 2

[8] Baliga, B. R. and Patankar, S. V., "A New Finite-Element Formulation for Convection-Diffusion Problems," *Numerical Heat Transfer* (1980) Vol. 3, pp. 393-409

[9] Bejan, A., Convection Heat Transfer, *John Wiley & Sons,* New York (1995)

[10] Bontoux, P., Smutek, C., Roux, B., and Lacroix, J. M., "Three-dimensional Buoyancy-driven Flows in Cylindrical Cavities with Differentially Heated Endwalls. Part 1. Horizontal Cylinders," *J. Fluid Mech.* (1986) Vol. 169, pp. 211-227

[11] Braaten, M. E. and Shyy, W., "Study of Pressure Correction Methods with Multigrid for Viscous Flow Calculations in Nonorthogonal Curvilinear Coordinates," *Numerical Heat Transfer* (1987) Vol. 11, pp. 417-442

[12] Caretto, L. S., Curr, R. M., and Spalding, D. B., Two Numerical Methods for Three-Dimensional Boundary Layers," *Computer Methods in Applied Mechanics and Engineering* (1972) Vol. 1, pp. 39-57

[13] Caretto, L. S., Gosman, A. D., Patankar, S. V., and Spalding, D. B., Two Calculation Procedures for Steady, Three-Dimensional Flows with Recirculation," *Proc. 3rd Int. Conf. Num. Methods Fluid Dyn., Paris* (1972) pp. 60-68

[14] Churchill, V., Brown, J. W., and Verhey, R. F., Complex Variables and Applications, 3rd Ed., *McGraw-Hill, Inc.* (1974)

[15] Customer's Acceptance Specifications: Projection Tube 180AXB22(R), 180AXB22(G), 180AXB22(B), Hitachi Electron Tube Division, Hitachi, Ltd., September 20, 1986

[16] Bishop, E. H., Mack, L. R., and Scanlan, J. A., "Heat Transfer by Natural Convection between Concentric Spheres," *Int. J. Heat Mass Transfer* (1966) Vol. 9, pp. 649-662

[17] Catton, I., "Natural Convection in Enclosures," Proceedings of the Sixth International Heat Transfer Conference, Toronto, Canada (Aug. 7-11, 1978) Vol. 6, pp. 13-31

[18] Catton, I., Ayyaswamy, P. S., and Clever, R. M., "Natural Convection Flow in a Finite, Rectangular Slot Arbitrarily Oriented with Respect to the Gravity Vector," *Int. J. Heat Mass Transfer* (1974) Vol. 17, pp. 173-184

[19] Chao, P., Ozoe, H., and Churchill S. W., "The Effect of a Non-Uniform Surface Temperature on Laminar Natural Convection in a Rectangular Enclosure," *Chem. Eng. Commun.* (1981) Vol. 9, pp. 245-254

[20] Churchill, S. W., "Free Convection in Layers and Enclosures," *Heat Exchanger Design Handbook, Hemisphere Publishing Corporation* (1983) Section 2.5.8., pp. 1-25

[21] Cocking, W. T. , Television Receiving Equipment, *Philosophical Library, Inc.*, New York (1957)

[22] Coulter, J. P. and Gouceri, I. G., "Laminar and Turbulent Natural Convection within Irregularly Shaped Enclosures," *Numerical Heat Transfer* (1987) Vol. 12, pp. 211-227

[23] Davis, G. De Vahl, "Finite Difference Methods For Natural and Mixed Convection in Enclosures," Proceedings of the Eighth International Heat Transfer Conference, San Francisco, California, U.S.A. (1986) pp. 101-109

[24] Davis, G. de Vahl, "Natural Convection of Air in a Square Cavity: A Benchmark Numerical Solution," *Int. J. Num. Methods in Fluids* (1983) Vol. 3, pp. 249-264

[25] Dhake, A. M. , Television Engineering, *McGraw-Hill Book Company* (1980)

[26] Dickinson, W. A. , "Monochrome Picture Report - A Status Report," *IEEE Transactions on Broadcasting and Television Receivers* (Nov. 1967) Vol. BTR-13, pp. 44-48

[27] Doormaal, J. P. van and Raithby, G. D., "Enhancements of the SIMPLE Method for Predicting Incompressible Fluid Flows," *Numerical Heat Transfer* (1984) Vol. 7, pp. 147-163

[28] Eiseman, P. R., "Grid Generation for Fluid Mechanics Computations," *Ann. Rev. Fluid Mech.* (1985) Vol. 17, pp. 487-522

[29] Farouk, B. and Gouceri, S. I., "Laminar and Turbulent Natural Convection in the Annulus Between Horizontal Concentric Cylinders," *Journal of Heat Transfer* (November 1982) Vol. 104, pp. 631-636

[30] Faghri, M., Sparrow, E. M. and Prata, A. T., "Finite-Difference Solutions of Convection-Diffusion Problems in Irregular Domains, Using a

Nonorthogonal Coordinate Transformation," *Numerical Heat Transfer* (1984) Vol. 7, pp. 183-209

[31] Ferziger, J. H. and Peric, M., Computational Methods for Fluid Dynamics, *Springer* (1996)

[32] Fusegi, T. and Farouk, B., "Predictions of Fluid and Heat Transfer Problems by the Vorticity-Velocity Formulation of the Navier-Stokes Equations," *J. Comp. Phys.* (1986) Vol. 65, pp. 227-243

[33] Ganzarolli, M. M., and Milanez, L. F., "Natural Convection in Rectangular Enclosures Heated from Below and Symmetrically Cooled from the Sides," *Int. J. Heat Mass Transfer* (1995) Vol. 38, No. 6, pp. 1063-1073

[34] Garabedian, P. R., Partial Differential Equations, 2nd Ed., *Chelsa Publishing Company*, New York, N.Y. (1986)

[35] Gebhart, B., Jaluria, Y., Mahajan, R. L., and Sammakia, B., Buoyancy-Induced Flows and Transport, Textbook Edition, *Hemisphere Publishing Corporation* (1988)

[36] Goldsmid, H. J., Thermoelectric Refrigeration, *Plenum Press, New York* (1964)

[37] Greenwood, D. T., Principles of Dynamics, *Prentice-Hall, Inc.* (1965)

[38] Hadjisophocleous, G. V., Sousa, A. C. M. and Venart, J. E. S., "Prediction of Transient Natural Convection in Enclosures of Arbitrary Geometry Using A Nonorthogonal Numerical Model," *Numerical Heat Transfer* (1988) Vol. 13, pp. 373-392

[39] Han, T., Humphrey, J. A. C., and Launder, B. E., "A Comparison of Hybrid and Quadratic-Upstream Differencing in High Reynolds Number Elliptic Flows," *Computer Methods in Applied Mechanics and Engineering, North-Holland Publishing Company* (1981) Vol. 29, pp. 81-95

[40] Harlow, F.H. and Welch, J.E., "Numerical Calculation of Time-Dependent Viscous Incompressible Flow of Fluid with Free Surface," *Phys. Fluids* (1965) Vol. 8, pp. 2182-2189

[41] Hart, J. E., "Stability of the Flow in a Differentially Heated Inclined Box," *J. Fluid Mech.* (1971) Vol. 47, Part 3, pp. 547-579

[42] "High-contrast Monitor Offered," *IEEE Spectrum* (Feb. 1986) p. 24

[43] Hirt, C. W., Amsden, A. A., and Cook, J. L., "An Arbitrary Lagrangian-Eulerian Computing Method for All Flow Speeds," *J. Comp. Phys.* (1974) Vol. 14, pp. 227-253

[44] Hollands, K. G. T., and Konicek, L., "Experimental Study of the Stability of Differentially Heated Inclined Air Layers," *Int. J. Heat Mass Transfer* (1973) Vol. 16, pp. 1467-1476

[45] Hollands, K. G. T., Unny, T. E., Raithby, G. D., and Konicek, L., "Free Convective Heat Transfer Across Inclined Air Layers," *Journal of Heat Transfer* (May 1976) pp. 189-193

[46] Holman, J. P., Experimental Methods for Engineers, *McGraw-Hill Book Company* (1989)

[47] Huang, P. G., Launder, B. E., and Leschziner, M. A., "Discretization of Nonlinear Convection Processes: A Broad-Range Comparison of Four Schemes," *Computer Methods in Applied Mechanics and Engineering* (1985) Vol. 48, pp. 1-24

[48] Incropera, F. P. and DeWitt, D. P., Fundamentals of Heat and Mass Transfer, 2nd Ed., *John Wiley & Sons* (1981)

[49] Ioffe, A. F., "Semiconductor Thermoelements and Thermo-Electric Cooling," *Infosearch, Ltd., London* (1957)

[50] Issa, R. I., "Solution of Implicitly Discretized Fluid Flow Equations by Operator-Splitting," Imperial College, University of London (1982)

[51] Issa, R. I., "Solution of Implicitly Discretized Fluid Flow Equations by Operator Splitting," *J. Comp. Phys.* (1986) Vol. 62, pp. 40-65

[52] Jaluria, Y. and Torrance, K.E., Computational Heat Transfer, *Hemisphere Publishing Corporation* U.S.A. (1986)

[53] Jang, D. S. Jetli, R., and Acharya, S., "Comparison of the PISO, SIMPLER, and SIMPLEC Algorithms for the Treatment of the Pressure-Velocity Coupling in steady Flow Problems," *Numerical Heat Transfer* (1986) Vol. 10, pp. 209-228

[54] Kakac, S., Aung, W., and Viskanta, R., Natural Convection: Fundamentals and Applications, *Hemisphere Publishing Corporation* (1985)

[55] Kakac, S., Shah, R. K., and Aung, W., Handbook of Single-Phase Convective Heat Transfer, *John Wiley & Sons* (1987)

[56] Kaminski, D. A., and Prakash, C., "Conjugate Natural Convection in a Square Enclosure: Effect of Conduction in One Vertical Wall," *Int. J. Heat Mass Transfer* (1986) Vol. 29, No. 12, pp. 1979-1988

[57] Kamotani, Y., Wang, L. W., and Ostrach, S., "Experiments on Natural Convection Heat Transfer in Low Aspect Ratio Enclosures," AIAA 16th. Thermophysics Conference (Jun. 1981) pp. 1-6.

[58] Karki, K. C. and Patankar, S. V., "Calculation Procedure for Viscous Incompressible Flows in Complex Geometries," *Numerical Heat Transfer* (1988) Vol. 14, pp. 295-307

[59] Karyakin, Y. E., "Transient Natural Convection in Prismatic Enclosures of Arbitrary Cross-Section," *Int. J. Heat Mass Transfer* (1989) Vol. 32, No. 6, pp. 1095-1103

[60] Karyakin, Y. E., Sokovishin, Y. A., and Martyneko, O. G., "Transient Natural Convection in Triangular Enclosures," *Int. J. Heat Mass Transfer* (1988) Vol. 31, No. 9, pp. 1759-1766

[61] Kaviani, M., "Effect of a Protuberance on Thermal Convection in a Square Cavity," *Journal of Heat Transfer* (Nov. 1984) Vol. 106, pp. 830-834

[62] Kays, W. M. and Crawford, M. E., Convective Heat and Mass Transfer, 2nd Ed., *McGraw-Hill Book Company* (1980)

[63] Kim, D. M. and Viskanta, R., "Effect of Wall Conduction on Natural Convection Heat Transfer in a Square Enclosure," *Journal of Heat Transfer* (Feb. 1985) Vol. 107, pp. 139-146

[64] Kimura, S. and Bejan, A., "Experimental Study of Natural Convection in a Horizontal Cylinder with Different End Temperatures," *Int. J. Heat Mass Transfer* (1980) Vol. 23, pp. 1117-1126

[65] Krane, R. J. and Jesse, J., "Some Detailed Field Measurements for a Natural Convection Flow in a Vertical Square Enclosure," ASME-JSME Thermal Engineering Joint Conference (1983) Vol. 1, pp. 323-329

[66] Kreith, F., Principles of Heat Transfer, 3rd Ed., *Harper and Row Publishers* (1973)

[67] Kuehn, T. H. and Goldstein, R. J., "An Experimental and Theoretical Study of Natural Convection in the Annulus between Horizontal Concentric Cylinders," *J. Fluid Mech.* (1976) Vol. 74, pp. 695-719

[68] Lam, S. W., Gani, R., and Symons, J. G., "Experimental and Numerical Studies of Natural Convection in Trapezoidal Cavities," *Journal of Heat Transfer* (May 1989) Vol. 111, pp. 372-377

[69] Larson, D. W. and Viskanta, R., "Transient Combined Laminar Free Convection and Radiation in a Rectangular Enclosure," *J. Fluid Mech.* (1976) Vol. 78, Part 1, pp. 65-85

[70] Lasdon, L. S. and Waren, A. D., GRG2 (Generalized Reduced-Gradient Computer Program), *The University of Texas at Austin* (1986), http://www.optimalmethods.com

[71] Latimer, B. R. and Pollard, A., "Comparison of Pressure-Velocity Coupling Solution Algorithms," *Numerical Heat Transfer* (1985) Vol. 8, pp. 635-652

[72] Lee, J. H. and Lee, S. R., "Natural Convection in Irregular Enclosures Using a Non-orthogonal Algebraic Coordinate Transformation," Proceedings of the Heat Transfer Korea-U.S.A. Seminar (Oct. 16-22, 1986) pp. 495-507

[73] Lee, J. J., Liu, K. V., Yang, K. T., and Kelleher, M. D., "Laminar Natural Convection in a Rectangular Enclosure Due to a Heated Protrusion on One Vertical Wall--Part II: Numerical Simulation," Proceedings of the 1987 ASME-JSME Thermal Engineering Joint Conference (1987) Vol. 2, pp.179-185

[74] Leonard, B. P., "A Stable and Accurate Convective Modelling Procedure Based on Quadratic Upstream Interpolation," *Computer Methods in Applied Mechanics and Engineering* (1979) Vol. 19, pp. 59-98

[75] Leonard, B. P., "A Survey of Finite Differences of Opinions on Numerical Muddling of the Incomprehensible Defective Confusion Equation," Finite Element Methods in Convection Dominated Flows, Applied Mechanics Division, ASME Winter Annual Meeting, New York (Dec. 1979) pp. 1-17

[76] Le Peutrec, Y. and Lauriat, G., "Effects of the Heat Transfer at the Side Walls on Natural Convection in Cavities," *Journal of Heat Transfer* (May 1990) Vol. 112, pp. 370-378

[77] Leschhziner, M. A., "Practical Evaluation of Three Finite Difference Schemes for the Computation of Steady-State Recirculating Flows," *Computer Methods in Applied Mechanics and Engineering* (1980) Vol. 23, pp. 293-312

[78] Liang, S. F. and Acrivos, A., "Stability of Buoyancy-Driven Convection in a Tilted Slot," *Int. J. Heat Mass Transfer* (May 1970) Vol. 13, pp. 449-458

[79] Linthorst, S. J. M., Schinkel, W. M. M., and Hoogendoorn, C. J., "Flow Structure with Natural Convection in Air-Filled Enclosures," *Journal of Heat Transfer* (Aug. 1981) Vol. 103, pp. 535-539

[80] Liu, K. V., Yang, K. T., and Kelleher, M. D., "Three-Dimensional Natural Convection Cooling of an Array of Heated Protrusions in an Enclosure Filled with a Dielectric," Proceedings of the International Symposium on Cooling Technology for Electronic Equipment, Honolulu, Hawaii (Mar. 17-21, 1987) pp. 486-497

[81] Lytel, A. , TV Picture Projection and Enlargement, *John F. Rider Publisher, Inc.,* New York (1949)

[82] Mallinson, G. D. and de Vahl Davis, G., "Three-dimensional Natural Convection in a Box: A Numerical Study," *J. Fluid Mech.* (1977) Vol. 83, Part 1, pp. 1-31

[83] Martyneko, O. G., Sokovishin, Y. A., and Karyakin, Y. Y., "Free Convection at a Vertical Surface and in Regions of Arbitrary Configuration," *Heat Transfer-Soviet Research* (1990) Vol. 22, No. 3, pp. 311-351

[84] Maruyama, K. , Customer's Acceptance Specifications, Projection Tube Type 180AXB22, *Hitachi Electron Tube Division, Hitachi, Ltd.* (Sep. 20, 1986)

[85] Mason, C., Saabas, H. J., and Baliga, B. R., "Co-Located Equal-Order Control-Volume Finite Element Method for Two-Dimensional Axisymmetric Incompressible Fluid Flow," *Int. J. Num. Methods in Fluids* (1994) Vol. 18, pp. 1-26

[86] Material Safety Data Sheet, "Developmental Heat Transfer Fluid," Product Code 11137.01, Dec. 12, 1986, *Dow Chemical, Midland, MI 48674* (1986)

[87] Merzkirch, W., Flow Visualization, *Academic Press, Inc.*, New York (1974)

[88] Morrison, G. L. and Tran, V. Q., "Laminar Flow in Vertical Free Convective Cavities," *Int. J. Heat Mass Transfer* (1978) Vol. 21, pp. 203-213

[89] North American Philips Consumer Electronics Corporation, Strawberry Plains, Tennessee (1987) *Personal Communication*

[90] North American Philips Consumer Electronics Corporation, Strawberry Plains, Tennessee (1987) *Personally Handed Document:* Memo From: A. Kojima, *Hitachi America, Ltd., Electron tube Division, 300 N. Martingale Road, Suite 600, Schaumburg, IL 60173* To: S. H. Baker, *Section Leader, Projection TV Engineering, NAPCEC, March 20, 1987*

[91] November, M., and Nansteel, M. W., "Natural Convection in Rectangular Enclosures Heated from Below and Cooled along One Side," *Int. J. Heat Mass Transfer* (1987) Vol. 30, No. 11, pp. 2433-2440

[92] Ozoe, H., Sayama, H., and Churchill, S. W., "Natural Convection in an Inclined Square Channel," *Int. J. Heat Mass Transfer* (1974) Vol. 17, pp. 401-406

[93] Ozoe, H., Sayama, H., and Churchill, S. W., "Natural Convection in an Inclined Rectangular Channel at Various Aspect Ratios and Angles--Experimental Measurements," *Int. J. Heat Mass Transfer* (1975) Vol. 18, pp. 1425-1431

[94] Ozoe, H., Sayama, H., and Churchill, S. W., "Natural Convection Patterns in an Long Inclined Rectangular Box Heated from Below – Part I. Three-Directional Photography," *Int. J. Heat Mass Transfer* (1977) Vol. 20, pp. 123-129

[95] Ozoe, H., Sayama, H., and Churchill, S. W., "Natural Convection Patterns in an Long Inclined Rectangular Box Heated from Below – Part II. Three-Dimensional Numerical Results," *Int. J. Heat Mass Transfer* (1977) Vol. 20, pp. 123-129

[96] Ozoe, H., Yamamoto, K., Sayama, H., and Churchill S. W., "Natural Circulation in an Inclined Rectangular Channel Heated on One Side and Cooled on the Opposite," *Int. J. Heat Mass Transfer* (1974) Vol. 17, pp. 1209-1217

[97] Ozoe, H., Yamamoto, K., Churchill S. W., and Sayama, H., "Three-Dimensional, Numerical Analysis of a Laminar Natural Convection in a Confined Fluid Heated from Below," *Journal of Heat Transfer* (May 1976) pp. 202-207

[98] Oshima, Y., "Experimental Studies of Free Convection in a Rectangular Cavity," *Journal of the Physical Society of Japan* (Mar. 1971) Vol. 30, No. 3, pp. 872-882

[99] Ostrach, S., "Natural Convection Heat Transfer in Cavities and Cells," Proceedings of the Sixth International Heat Transfer Conference, Toronto, Canada (Aug. 7-11, 1978) pp. 365-379

[100] Ozisik, M. N., Basic Heat Transfer, *McGraw-Hill Book Company* (1977)

[101] Palmer, J. M., Radiometry and Photometry FAQ, Version 1.01, Optical Sciences Center University of Arizona, Tucson, AZ; 85721 (Jun. 10, 1999) pp.1-14, jpalmer@azstarnet.com, www.optics.arizona.edu/Palmer/.

[102] Patankar, S. V., "A Numerical Method for Conduction in Composite Materials, Flow in Irregular Geometries and Conjugate Heat Transfer," Proceedings of the Sixth International Heat Transfer Conference, Toronto, Canada (1978) Vol. 3, pp. 297-302

[103] Patankar, S.V., Numerical Heat Transfer and Fluid Flow, *McGraw-Hill Book Company* (1980)

[104] Patankar, S.V. and Spalding, D. B., "A Calculation Procedure for Heat, Mass and Momentum Transfer in Three-Dimensional Parabolic Flows," *Int. J. Heat Mass Transfer* (1972) Vol. 15, pp. 1787-1806

[105] Peric , M., "A Finite Volume Method for the Prediction of Three-Dimensional Fluid Flow in Complex Ducts," Ph.D. Thesis, Imperial College, University of London (1985)

[106] Pollock, D. D., The Theory and Properties of Thermocouple Elements, ASTM STP 492, *Omega Press* (1971)

[107] Powe, R. E. and Warrington, Jr., R. O., "Natural Convection Heat Transfer Between Bodies and Their Spherical Enclosure," *Journal of Heat Transfer* (1994) Vol. 37, pp. 1605-1617

[108] Powell, R. L., Hall, W. J., Hyink, Jr., C. H., Sparks, L. L., Burns, G. W., Scroeger, M. G., and Plumb, H. H., Thermocouple Reference Tables Based on the IPTS-68, NBS MN-125, *Omega Press* (1975)

[109] Reay, D. A. (Ed.), Advances in Heat Pipe Technology: Proceedings of the Ivth International Heat Pipe Conference, London, 7-10 September, 1981, *Pergamon Press*, New York (1982)

[110] Raithby, G. D., Galpin, P. F., and Van Doormaal, J. P., "Prediction of Heat and Fluid Flow in Complex Geometries Using General Orthogonal Coordinates," *Numerical Heat Transfer* (1986) Vol. 9, pp. 125-142

[111] Raithby, G. D. and Schneider, G. E., "Numerical Solutions of Problems in Incompressible Fluid Flow: Treatment of Velocity-Pressure Coupling," *Numerical Heat Transfer* (1979) Vol. 2, pp. 417-440

[112] Raithby, G. D. and Schneider, G. E., "Erratum," *Numerical Heat Transfer* (1980) Vol. 3, p. 513

[113] Raithby, G. D., Hollands, K. G. T., and Unny, T. E., "Analysis of Heat Transfer by Natural Convection Across Vertical Fluid Layers," *Journal of Heat Transfer* (May 1977) Vol. 99, pp. 287-293

[114] Relative Spectral Power Distribution Plots for the 180AXB22, Green, Red, and Blue Type Tubes, North American Philips Consumer Electronics Corporation (1987) *Personal Communication*

[115] Schneider, G. E. and Raw, M. J., "Control Volume Finite-Element Method for Heat Transfer and Fluid Flow Using Colocated Variables – 1. Computational Procedure," *Numerical Heat Transfer* (1987) Vol. 11, pp. 363-390

[116] Sherbiny, S. M. El-, Hollands, K. G. T., and Raithby, G. D., "Effect of Thermal Boundary Conditions on Natural Convection in Vertical and Inclined Air Layers," *Journal of Heat Transfer* (Aug. 1982) Vol. 104, pp. 515-520

[117] Shih, T. M., Tan, C. H., and Hwang, B. C., "Effects of Grid Staggering on Numerical Schemes," *Int. J. Num. Methods in Fluids* (1989) Vol. 9, pp. 193-212

[118] Shiina, Y., Fujimura, K., Kunugi, T., and Akino, A. , "Natural Convection in a Hemispherical Enclosure Heated from Below," *Int. J. Heat Mass Transfer* (1994) Vol. 37, No. 11, pp. 1605-1617

[119] Shiralkar, G. S. and Tien, C. L., "A Numerical Study of Laminar Natural Convection in Shallow Cavities," *Journal of Heat Transfer* (May 1981) Vol. 107, pp. 226-231

[120] Shyy, W., Tong, S. S., and Correa, S. M., "Numerical Recirculation Flow Calculation Using a Body-Fitted Coordinate System," *Numerical Heat Transfer* (1985) Vol. 8, pp. 99-113

[121] Siegel, R. and Howell, J. R., Thermal Radiation Heat Transfer, 2nd Edition, *Hemisphere Publishing Corporation/McGraw-Hill Book Company* (1981)

[122] Spradley, L. W. and Churchill, S. W., "Pressure- and Buoyancy-Driven Thermal Convection in Rectangular Enclosure," *J. Fluid Mech.* (1975) Vol. 70, Part 4, pp. 705-720

[123] Stork, K. and Muller, U., "Convection in Boxes: Experiments," *J. Fluid Mech.* (1972) Vol. 54, Part 4, pp. 599-611

[124] Strada, M. and Heinrich, J. C., "Heat Transfer Rates in Natural Convection at High Rayleigh Numbers in Rectangular Enclosures: A Numerical Study," *Numerical Heat Transfer* (1982) Vol. 5, pp. 81-93

[125] Symons, J. G. and Peck, M. K., "Natural Convection Heat Transfer Through Inclined Longitudinal Slots," *Journal of Heat Transfer* (November 1984) Vol. 106, pp. 824-829

[126] Thompson, J. F., "Grid Generation Techniques in Computational Fluid Dynamics," *AIAA Journal* (Nov. 1984) Vol. 22, No. 11, pp. 1505-1523

[127] Thompson, J. F., Warsi, Z. U. A., and Mastin, C. W., Numerical Grid Generation--Foundations and Applications, *Elsevier Science Publishing Co., Inc.* (1985)

[128] Tutty, O. R., "On Vector Potential-Vorticity Methods for Incompressible Flow Problems," *J. Comp. Phys.* (1986) Vol. 64, pp. 368-379

[129] Unny, T. E., "Thermal Instability in Differentially Heated Inclined Fluid Layers," *Journal of Applied Mechanics* (March 1972) pp. 41-46

[130] Vemuri, V. and Karplus, W. J., Digital Computer Treatment of Partial Differential Equations, *Prentice-Hall, Inc.* (1981)

[131] Vest, C. M. and Arpaci, V. S., "Stability of Natural Convection in a Vertical Slot," *J. Fluid Mech.* (1969) Vol. 36, Part 1, pp. 1-15

[132] Waddell, S., "Summary of PTV Optical Coupling System Development," *North American Philips Consumer Electronics Corporation, Strawberry Planes, Tennessee* (June 23, 1986)

[133] White, F. M., Viscous Fluid Flow, *McGraw-Hill, Inc.* (1974)

[134] Wijngaart, R. F. van der, "Composite-Grid Techniques and Adaptive Mesh Refinements in Computational Fluid Dynamics," Ph.D. Thesis, Stanford University (1990)

[135] Wirtz, R. A., Righi, J., and Zirilli, F., "Measurements of Natural Convection Across Tilted Rectangular Enclosures of Aspect Ratio 0.1 and 0.2," *Journal of Heat Transfer* (Aug. 1982) Vol. 104, pp. 521-526

[136] Wong A. K. and Reizes, J. A., "An Effective Vorticity-Vector Potential Formulation for the Numerical Solution of Three-Dimensional Duct Flow Problems," *J. Comp. Phys.* (1984) Vol. 55, pp. 98-114

[137] Wong A. K. and Reizes, J. A., "The Vector Potential in the Numerical Solution of Three-Dimensional Fluid Dynamic Problems in Multiply Connected Regions," *J. Comp. Phys.* (1986) Vol. 62, pp. 124-142

[138] Wong, H. H. and Raithby, G. D., "Improved Finite-Difference Methods Based on a Critical Evaluation of the Approximating Errors," *Numerical Heat Transfer* (1979) Vol. 2, pp. 139-163

[139] Wraith, G. D., Hollands, K. G. T., and Unny, T. E., "Free Convection Heat Transfer Across Fluid Layers of Large Aspect Ratios," ASME Publication No. 76-HT-37 (1976) pp. 1-9

[140] Wylen, G. J. van and Sonntag, R. E., Fundamentals of Classical Thermodynamics, 2nd Ed., *John Wiley and Sons, Inc.* (1973)

[141] Yang, H. Q., Yang, K. T., and Lloyd, J. R., "Flow Transition in Laminar Buoyant Flow in a Three-Dimensional Tilted Rectangular Enclosure," Proceedings of the Eighth International Heat Transfer Conference, San Francisco, California, U.S.A. (1986) pp. 1495-1500

[142] Yang, K. T., "Transitions and Bifurcations in Laminar Buoyant Flows in Confined Enclosures," *Journal of Heat Transfer* (November 1988) Vol. 110, pp. 1191-1204

[143] Zimmerman, E. and Acharya, S., "Free Convection Heat Transfer in a Partially Divided Vertical Enclosure With Conducting End Walls," *Int. J. Heat Mass Transfer* (1987) Vol. 30, No. 2, pp. 319-331

[144] Zworykin, V. K. and Morton, G. A. , Television: The Electronics of Image Transmission, *John Wiley and Sons, Inc.,* New York (1940)

APPENDIX

APPENDIX A. EXPERIMENTAL APPARATUS

A.1. Equipment Description

A production model of a 46-inch Magnavox color projection monitor containing three monochrome picture tubes was used for data collection. Model dimensions and layout of the projection assemblies with the picture tubes is shown in *Figure A-1.* A breakdown of the major components of the projection monitor used for laboratory measurements is shown in Table A-1. The model width was 42.5 inches, the height 49 inches, and the depth 26 inches. The viewing screen diagonal measured was 46 inches. On the inside, the model had three monochrome projection units (Red, Green, and Blue projectors), a 28-inch-by-18-inch rectangular mirror, in addition to all the electronics to process and output the video signal to the projectors.

A.1.1. Monochrome Projectors

The monochrome projectors are self-contained assemblies for image reproduction and projection. They are mounted on metallic frames towards the bottom of the unit, with the optical axis tilted 60 degrees above the horizontal, facing the back mirror. The green projector sits at the center, the red and blue projectors are to the left and right hand sides of the green projector, and are tilted inward (in the direction of the back mirror).

Each monochrome projector consists of a projection picture tube (CRT), an enclosure frame with an expansion chamber, a meniscus lens, a focusing lens, and supporting assembly hardware. A list of projector components is shown in Table A-2. The projection picture tubes in these projectors are models 180AXB22(R), 180AXB22(G), and 180AXB22(B), manufactured by Hitachi's Electron Tube Division, Hitachi, Ltd. The green tube was selected for instrumentation and data gathering for two major reasons. First, as the green tube has a symmetric enclosure frame, the mathematical model should also be simpler to implement. Second, being in between the red and blue tube, the green tube was presumed to be in the "hottest" location, making it a good candidate for getting the worst operating condition.

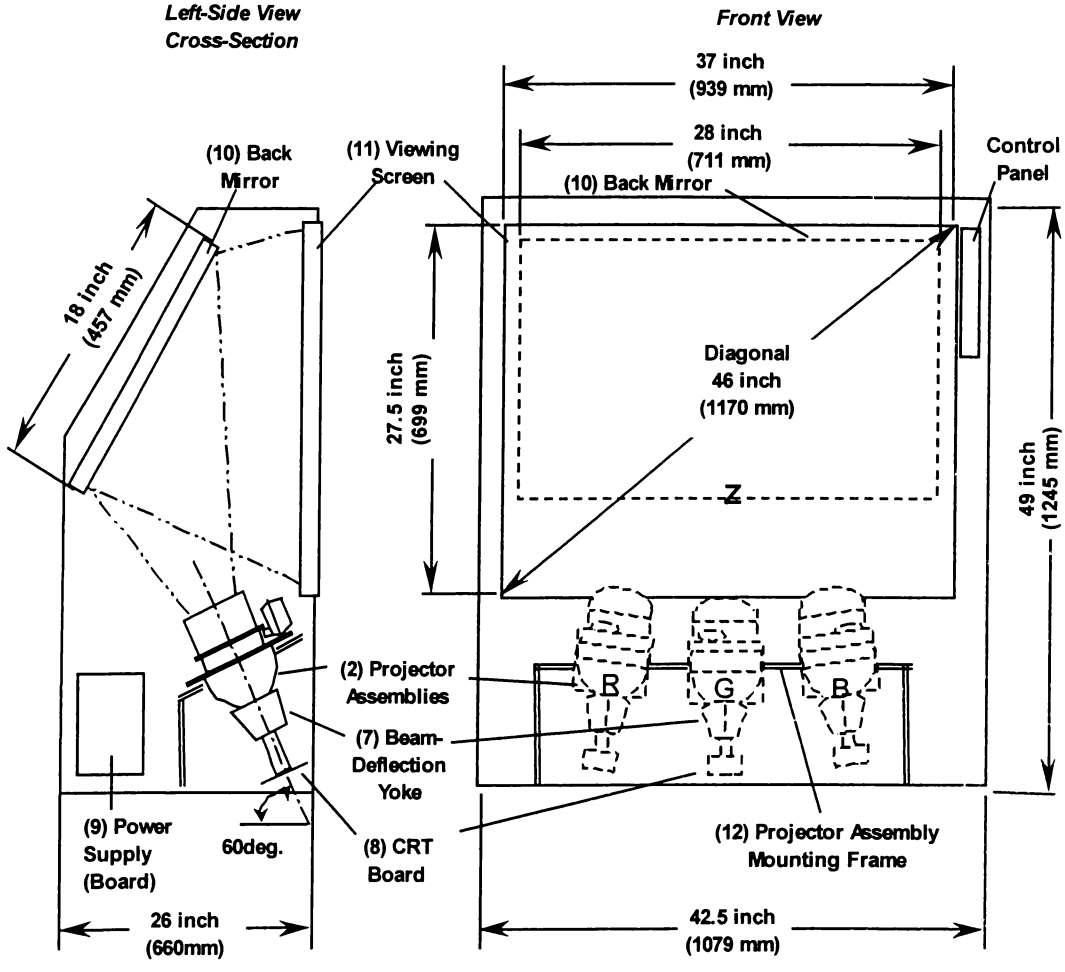

Figure A-1. Schematic of the 46-inch Color Projection Television Receiver Used for Laboratory Measurements

Picture tube mechanical data is listed in Table A-3, and performance ratings data is listed in Table A-4. These data were extracted from the manufacturer specification sheet for the picture tube HITACHI 180AXB22(G).

Figure A-2 shows the major dimensions of the picture tube. A plot of the relative spectral power distribution for the light from the green CRT 180AXB22(G) is shown in *Figure A-3*, and Table A-5 contains the numerical data. Major dimensions for the enclosure frame, the meniscus lens, and the focusing lens assembly are shown in *Figure A-4*, *Figure A-5*, and *Figure A-6*, respectively.

Table A-1. Components of the Projection Monitor

No.	Item ID	Item	Description
1	1	Cabinet/Frame	Dimensions: 42.5 x 49 x 26 inches
2	2	Projector Assemblies (Projectors)	Overall Assembly Length: 394 mm
3	2.1	Red-Image Projection CRT	180AXB22 (R)
4	2.2	Green-Image Projection CRT	180AXB22(G)
5	2.3	Blue- Image Projection CRT	180AXB22(B)
6	3	Electrical Interface	
7	3.1	Beam-Deflection Yoke	Mounts to the neck of CRT
8	3.2	CRT Board	Connects to Projection CRT end plug (PTV300-EIA232D)
9	3.3	Power Supply Board for CRT	POWER SUPPLY EIA 2220
10	4	Rectangular Back Mirror	28 x 18 in (back reflective coating)
11	5	Viewing Screen	Width 939 mm x Height 699 mm
12	6	Projector Mounting Frame	Support the Projectors in place
13	7	Miscellaneous	Controls, I/O Connectors, and Electric/Electronic Components

Table A-2. Projection Assembly Parts

No.	Item ID	Item Designation	Description/Model	Qty.
1	1	Projection CRT	Hitachi Model 180AXB22(G), NAP P/N 330275-6	1
2	2	Enclosure Frame	NAP P/N 734919-1	1
3	3	Meniscus Lens	NAP P/N 645826-1	1
4	4	Focus-Lens Assembly	Delta 18-0C, Rev. B, S/N 091587	1
5	5	Expansion Chamber		1
6	6	Liquid Coolant	Dow Chemical XUS 11137.01 Developmental Heat Transfer Fluid	1
7	7	Seals		1
8	7.1	d-Ring	Seals the gap between the Projection CRT and the Enclosure Frame	1
9	7.2	O-Ring	Seals the gap between the Enclosure Frame and the Meniscus Lens	1
10	8	Assembly Hardware	All necessary hardware to assemble the parts above	1
11	8.1	CRT Bracket	Holds the Projection CRT against the Enclosure Frame	1
12	8.2	CRT Fasteners	Hold the CRT Bracket in place	4
13	8.3	CRT Springs	Are placed against the CRT Studs	4
14	8.4	CRT Spacers	Serve as "stops" for the CRT Fasteners	4
15	8.5	CRT Studs	Mount against the Enclosure Frame	4
16	8.6	CRT Stud Fasteners		4
17	8.7	Mating Flange	NAP P/N 734988-1. Secures the Meniscus Lens in place and serves as the mounting platform for the Focus-Lens Assembly	1
18	8.8	Mating Flange Fasteners	Hold the Mating Flange in Place	4
19	8.9	Mating Flange Spacers	Serve as "stops" for the Assembly Flange Fasteners	4
20	8.10	Mating Flange Nuts	Hold the Mating Flange in Place	4
21	8.11	Focusing-Lens Assembly Fasteners	Hold the Focusing-Lens Assembly in Place	4

Table A-3. Picture Tube Mechanical Data

Overall Length	268 ± 7.0 mm
Minimum Useful Screen Dimensions (Projected)	
Diagonal	127.0 mm
Horizontal Axis	101.6 mm
Vertical Axis	76.2 mm
Area	
Base Designation	B10-277
Bulb Contact Designation	Recessed Small Cavity Cap (JEDEC No. J1-21)
Bulb:	
Funnel	EIAJ No. L0F03
Face Panel	EIAJ No. H9001
Pad	Integrated
Weight	1.4 kg
Face Panel:	
Thickness	7.0 ± 0.3 mm
Inner Radius	Flat
Outer Radius	Flat
Minimum Flat Area of Outer Surface:	
Diagonal	168.1 mm
Horizontal Axis	144.9 mm
Vertical Axis	117.5 mm

Table A-4. Picture Tube Performance Ratings

Minimum Useful Screen Dimensions:	
Diagonal	127.0 mm
Horizontal Axis	101.6 mm
Vertical Axis	76.2 mm
Anode voltage	32,000 V max
	25,000 V min.
Anode current	500μA max.
Input Power (Long-term average)	1.7 mW/mm^2
Raster Size (Diagonal)	5.0 inch max.
	3.5 inch min.
Temperature of Face Panel (center)	90 °C max.
Temperature Differential between Center and Peripheral Points	21 °C max
Radiance (@ anode voltage of 28000 V and current of 200 μA)	4800 cd/m^2

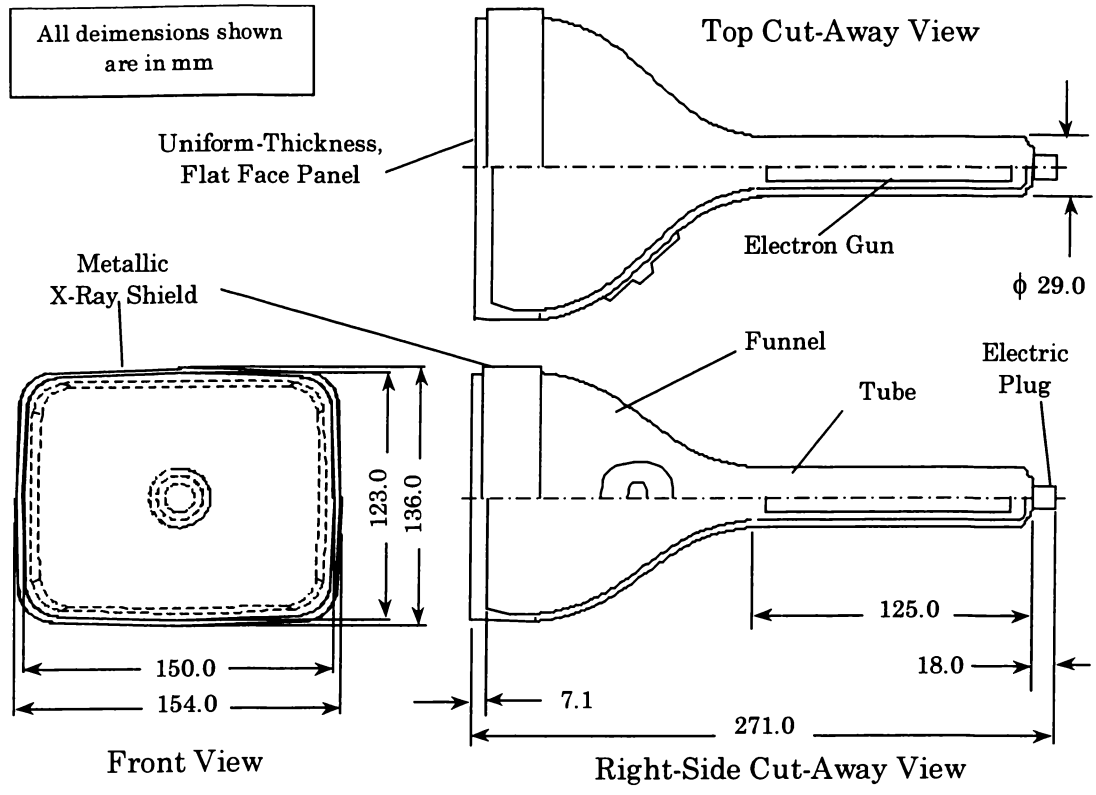

Figure A-2. Projection Picture Tube Dimensions

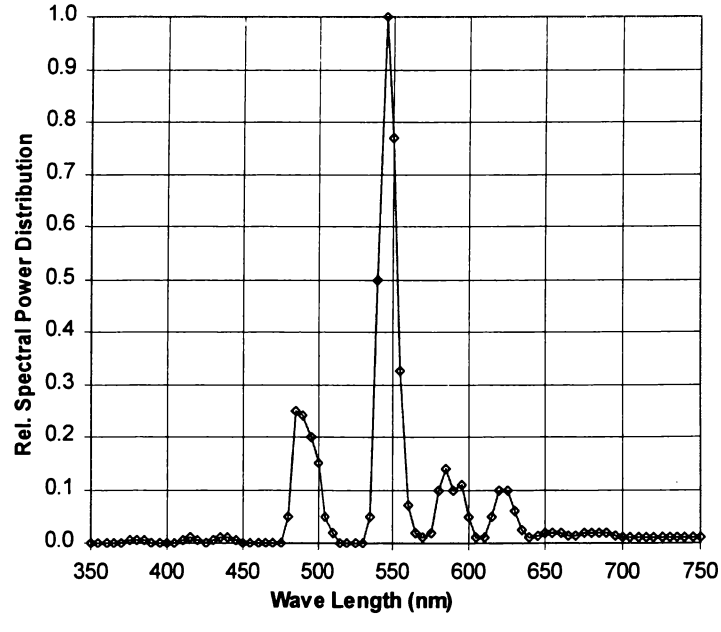

Figure A-3. Relative Spectral Power Distribution for the Green CRT

Table A-5. Relative Spectral Power Distribution Data for the Green CRT

λ (nm)	R_λ	λ (nm)	R_λ	λ (nm)	R_λ
350	0.000	485	0.250	620	0.100
355	0.000	490	0.240	625	0.100
360	0.000	495	0.200	630	0.060
365	0.000	500	0.150	635	0.025
370	0.000	505	0.050	640	0.010
375	0.005	510	0.020	645	0.015
380	0.005	515	0.000	650	0.020
385	0.005	520	0.000	655	0.020
390	0.000	525	0.000	660	0.020
395	0.000	530	0.000	665	0.015
400	0.000	535	0.050	670	0.015
405	0.000	540	0.500	675	0.020
410	0.005	545	1.000	680	0.020
415	0.010	550	0.770	685	0.020
420	0.005	555	0.325	690	0.020
425	0.000	560	0.070	695	0.015
430	0.005	565	0.020	700	0.010
435	0.010	570	0.010	705	0.010
440	0.010	575	0.020	710	0.010
445	0.005	580	0.100	715	0.010
450	0.000	585	0.140	720	0.010
455	0.000	590	0.100	725	0.010
460	0.000	595	0.110	730	0.010
465	0.000	600	0.050	735	0.010
470	0.000	605	0.010	740	0.010
475	0.000	610	0.010	745	0.010
480	0.050	615	0.050	750	0.010

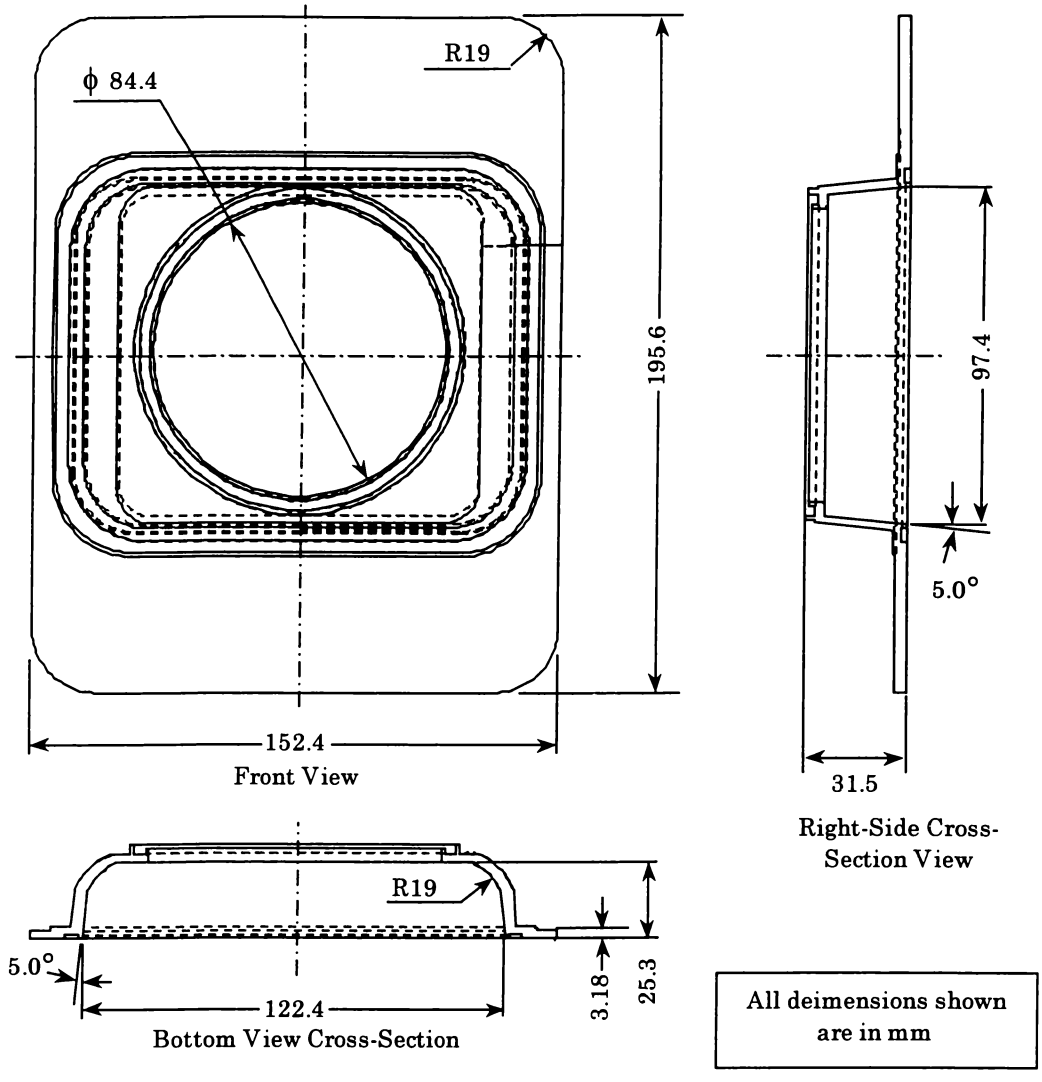

Figure A-4. Enclosure Frame Dimensions

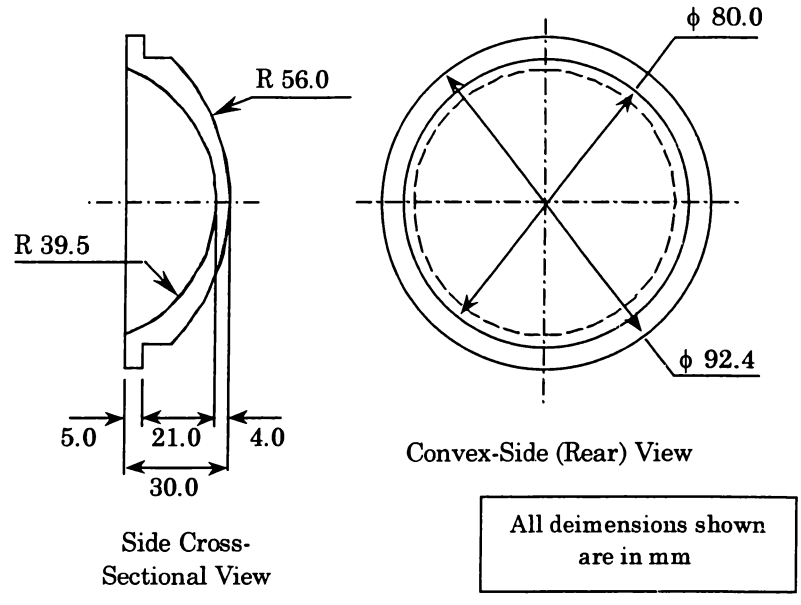

Figure A-5. Meniscus Lens Dimensions

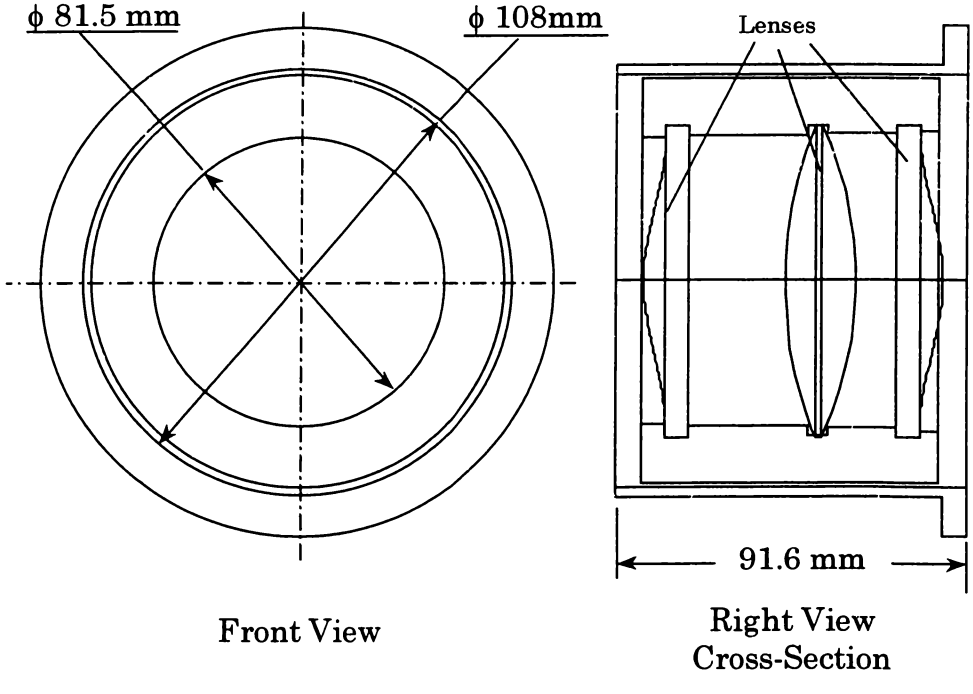

Figure A-6. Focusing Lens Dimensions

A.1.2. Liquid Coolant Characteristics

The liquid coolant was manufactured by Dow Chemical, Midland, MI 48674 The liquid coolant is identified as follows. Product Name: XUS 11137.01 Developmental Heat Transfer Fluid, Effective Date: 12/09/86, Product Code: 11137.01

Ingredients

Ethylene Glycol[1]	CAS# 000107-21-1	69%
Glycerin[1]	CAS# 000056-81-5	30%
Proprietary Ingredients[1]	1%	

Physical Data

Boiling Point[1]	>387 °F (197 °C)
Vapor Pressure[1]	< 1.0 mmHg @ 20 °C
Vapor Density[1]	2.43 (Air = 1)
Solubility in Water[1]	Miscible
Specific Gravity[1]	1.1591 @ 25/25 °C
Appearance[1]	Colorless Liquid
Odor[1]	Practically Odorless
Specific Heat[2]	0.58 BTU/lb-°F
Index of Refraction[1]	1.4432 @ 25 °C

[1] Material Safety Data Sheet, Product Code 11137.01 (1986) *Dow Chemical.*
[2] NAPCEC Personal Communication (1987)

A.2. Instrumentation Procedure

Table A-6 lists all of the instrumentation and data acquisition equipment. The rear and front panels, and the screen of the model were removed to access the parts to be instrumented. The focusing lens (Delta 18-0C, Rev. B, S/N 091587) was removed first from the assembly, by removing four screws from the mounting plate that secures the meniscus lens. An air bubble was noticed at the to of the enclosure frame with the free-surface level intersecting the point on the meniscus lens on the edge of the convex surface. The green-tube projection assembly was removed from

Table A-6. Data Acquisition and Instrumentation Items

No.	Category #	Item	Description/Model
1	1.0	Temperature Measurement	
2	1.1	Thermocouple Wire	OMEGA Copper-Constantan Thermocouple, Wire Diameter: 0.05 mm
3	1.2	Insulated Container	Custom Made
4	1.3	Thermometer #1	
5	1.4	Thermometer #2	
6	2.0	Voltage Measurement	
7	2.1	Digital Multi-meter	Micronta No. 22-196U
8	3.0	Data Processing	
9	3.1	Data Acquisition and Control Unit	Hewlett-Packard Model HP3497A
10	3.2	Computer	Hewlett-Packard Model HP9826
11	3.3	Printer	Hewlett-Packard Model HP2671G
12	4.0	Video Signal Generation	
13	4.1	Video Camera	
14	4.2	Video Cable	

the mounting location. The expansion chamber was loosened and removed, then the liquid coolant (Dow Chemical XUS 11137.01 Developmental Heat Transfer Fluid) was drained and stored in an airtight container. A liquid coolant volume of approximately 224 ml was measured. The meniscus lens securing plate was removed by removing four screws from the coupler frame. Then, the meniscus lens (P/N 645826-1) was removed along with the O-Ring. Next, the enclosure frame (coupler) (P/N 734919-1) was detached from the picture tube (Model 180AXB22(G), P/N 330275-6) by removing four spring-loaded screws at the back of the face panel. The rubber ring that serves as a seal between the coupler and the CRT face panel glass was removed from the face panel glass.

The exterior of the face panel was marked with horizontal and vertical centerlines along the major and minor axes of the panel, respectively. Then two lines were marked at 35 mm above and below the horizontal line (major axis), and two lines were marked at 25 and 50 mm to the right-hand-side of the vertical centerline (minor axis). The line intersections form a 3x3 rectangular grid of nine points. Small groves of no greater than 0.5 mm in depth were carved along these lines to pass the thermocouple wire. Thermocouple wire was routed along these groves and the junctions were glued with epoxy to the CRT face panel glass at these designated locations. Two additional thermocouples were attached along the vertical centerline at 56 mm off the center, and one additional thermocouple junction was attached along the horizontal centerline at 69 mm off the CRT center, to the right-hand side. A schematic of the wire routing is shown in *Figure A-7.* In total, 12 thermocouple junctions were mounted on the CRT face panel: nine thermocouple junctions were mounted at grid locations and three at points near the CRT face panel perimeter. The rubber seal was attached to the coupler, and the coupler was mounted back to the face panel. The four spring-loaded screws were tightened. A sealant was added to the perimeter of the face panel to prevent liquid coolant leakage along the groves carved and the thermocouple wires.

Thermocouples were attached to the enclosure frame and the meniscus lens. Three thermocouple junctions were attached to the coupler exterior: one at the center of the upper surface, one at the center of the lateral surface, and one at the

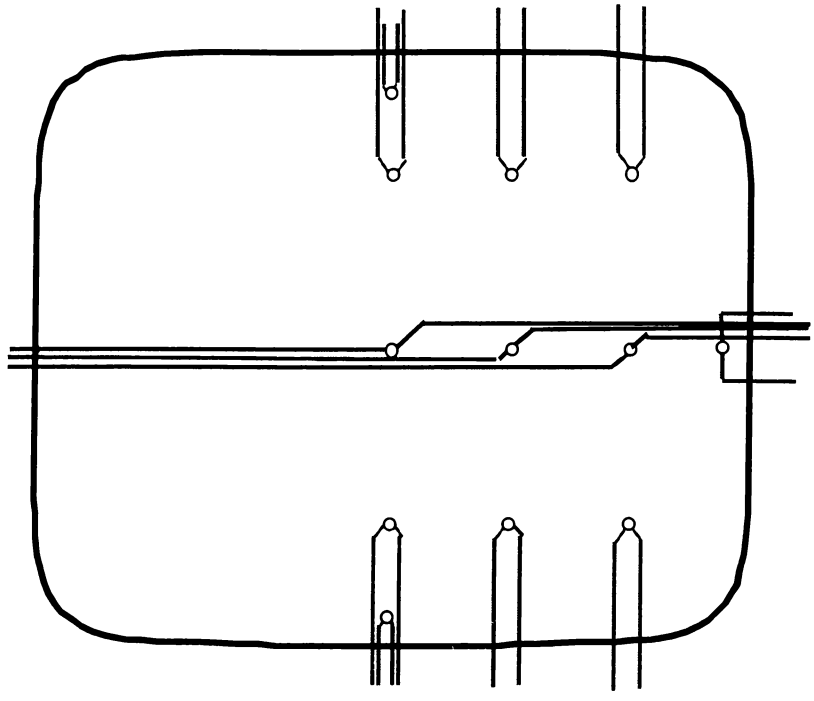

Figure A-7. Schematic of the CRT Face Panel Thermocouple Wire Routing

center of the lower surface. Two thermocouple junctions were attached to the meniscus lens -- one to the inner (convex) surface, and one to the outer (concave) surface. The meniscus lens O-Ring was placed in position on the coupler slot, then the meniscus lens was carefully positioned to prevent damage to the thermocouple wire from the inner surface junction. This wire had to be passed between the meniscus lens glass flange and the O-Ring. The meniscus lens securing plate was then positioned on top of the meniscus lens and then secured with four screws to the coupler frame. A thermocouple junction was attached to the center of the innermost lens of the focusing lens mechanism. The focusing lens was mounted back to the projection assembly with four screws attached to the meniscus lens securing plate. The unit was reassembled and it was filled with the same amount of fluid removed originally.

The instrumented projection tube assembly was mounted back into position in the projection TV unit. To measure the input electrical power to the electron

beam, the beam electrical current and the anode voltage are required. To measure the beam electrical current, a voltmeter was used to read the voltage across resistor R10 on the circuit board that connects to the CRT. Resistor R10 has a resistance of 954 Ω, and has one of its terminals connected to pin #8. This pin connects directly to the CRT cathode. The anode voltage was taken from the anode electrode on the CRT funnel side and measured with respect the ground voltage at the cathode terminal (pin #8). Another reason is that the green tube is in between the red and blue tube, which was presumed to be the worst location for heat transfer reasons.

APPENDIX B. DATA COLLECTION

B.1. Preparation

Once instrumented, the projector assembly was mounted into position on the 46-inch projection monitor. The thermocouple wires were routed and connected to the data acquisition system. A thermocouple junction (Channel #0) was attached to the bulb of a mercury thermometer and submerged into an insulated container for an ice/water bath. Another mercury glass thermometer was used to measure the room air temperature. A video camera was used to generate a "white-screen" image on the projection monitor screen. The experimental apparatus was shielded from air currents.

Before the data acquisition session, all instruments were checked and preset to avoid delays when engaging in data recording. The voltmeter was checked and voltage reading checks taken. The video camera was set to output a white screen signal, and the projection monitor was turned on and checked to ensure an adequate level of brightness. The data acquisition system was checked. All systems were turned off, and left overnight for the temperatures to stabilize for approximately 12 hours, before the data acquisition session.

B.2. Procedure

The data acquisition system was turned on and checked. Ice and water were added to the insulated container. The thermometer and attached thermocouple were submerged and positioned near the middle of the ice/water volume. The container was closed with lid was placed with a hole in the middle for passing the thermometer and thermocouple lead. The ice/water temperature was checked using the glass bulb thermometer until a temperature of 0.0 °C was reached. Temperature readings from the data acquisition unit were checked against the ice point in the ice/water bath. The digital voltmeter was turned on and voltage measurements were tested. The video camera was turned on and the video signal checked to ensure

a "white screen" image. The room air temperature was recorded. Finally, the projection monitor was turned on and data recording was initiated simultaneously. The time of day was recorded for such event. The anode and cathode resistor voltage were measured and recorded. The room air temperature and the ice/water temperature were monitored regularly. Voltage readings from the anode and cathode resistor were monitored regularly. The system was left on and data recording continued for 8.5 hours. At the end of data recording, voltage readings from the anode terminal and cathode resistor were taken, and the resistance of resistor R10 was measured. Temperature and voltage measurements are presented next.

B.3. Experimental Measurements

Data collection was done every 600 seconds. In each data collection event, 10 samples spaced at 0.05 seconds were collected per each channel. The average of the 10 samples was recorded for each data collection event. After 30600 seconds of data collection, the temperatures were rising at a rate of 0.2 to 0.3 °C/h, and it was decided to terminate the experiment (see Table B-1). The room temperature was measured then at 21.7 °C and the ice/water bath temperature at 0.0 °C. A compilation of the data acquisition recordings for the 20 channels is shown in Table B-2 (channels 0–9) and Table B-3 (channels 10-19). Questionable data points were flagged with a minus (-) sign. The data in row for data collection event #13

Table B-1. Rate of Change in the Mean Temperature at the End of the Experiment

Channel #	*℃/h*	*Channel #*	*℃/h*
0	0.00	10	0.14
1	0.17	11	0.24
2	open	12	0.21
3	open	13	0.33
4	0.22	14	0.17
5	0.21	15	0.25
6	0.21	16	0.25
7	0.26	17	0.30
8	0.22	18	0.34
9	open	19	-0.54

Table B-2. Thermocouple Temperatures: Channels #00 - #09

#	t_o(s)	t_f(s)	Channel# 0	1	2	3	4	5	6	7	8	9
1	0.00	16.33	0.00	20.65	19.91	21.03	20.68	20.56	20.44	20.60	20.55	20.65
2	600.00	616.35	0.00	21.21	22.24	21.12	24.13	23.53	22.54	22.35	23.35	23.58
3	1200.00	1216.32	0.00	21.17	28.57	21.31	28.26	27.59	26.28	25.21	27.32	27.51
4	1800.00	1816.34	0.00	21.17	30.57	21.39	31.65	31.11	29.66	29.16	30.73	30.87
5	2400.00	2416.31	0.00	21.66	34.93	21.47	34.62	34.09	32.64	31.68	33.74	33.82
6	3000.00	3016.33	0.00	21.69	37.50	21.55	37.12	36.80	35.24	34.41	36.38	36.39
7	3600.00	3616.34	0.00	21.83	38.96	21.58	39.15	39.19	37.51	37.13	38.73	38.65
8	4200.00	4216.34	0.00	22.07	41.14	21.64	41.16	41.22	39.50	39.00	40.76	40.61
9	4800.00	4816.32	0.00	21.50	43.54	21.64	42.76	42.93	41.19	40.42	42.51	42.30
10	5400.00	5416.33	0.00	21.39	44.79	22.26	44.10	44.42	42.61	42.09	43.95	43.74
11	6000.00	6016.34	0.00	21.78	45.95	22.69	45.39	45.69	43.86	43.36	45.20	44.97
12	6600.00	6616.32	0.00	22.55	48.11	22.34	46.87	46.76	44.95	43.78	46.34	46.05
13	7200.00	7200.00	-99.99	-99.99	-99.99	-99.99	-99.99	-99.99	-99.99	-99.99	-99.99	-99.99
14	7800.00	7816.33	0.00	22.94	49.73	22.44	48.52	48.61	46.72	45.83	48.09	47.83
15	8400.00	8416.35	0.00	22.68	50.45	22.45	49.11	49.36	47.43	46.50	48.85	48.56
16	9000.00	9016.32	0.00	23.20	51.72	22.47	49.55	49.93	48.02	46.53	49.49	49.16
17	9600.00	9616.34	0.00	23.03	51.09	22.67	50.32	50.54	48.58	48.00	49.97	49.70
18	10200.00	10216.31	0.00	23.09	51.97	22.89	50.95	51.01	49.03	48.20	50.46	50.16
19	10800.00	10816.33	0.00	23.53	52.77	21.86	51.10	51.38	49.42	48.28	50.88	-23.71
20	11400.00	11416.35	0.00	23.42	52.93	-21.09	51.49	51.76	49.77	48.67	51.22	-22.77
21	12000.00	12016.32	0.00	23.20	53.07	-20.72	51.10	52.08	50.06	49.27	51.50	-20.76
22	12600.00	12616.34	0.00	22.86	53.48	22.57	51.51	52.32	50.31	49.18	51.77	-20.51
23	13200.00	13216.32	0.00	23.44	53.82	22.20	52.50	52.56	50.52	49.43	51.99	-20.83
24	13800.00	13816.33	0.00	23.01	53.58	23.29	51.93	52.77	50.71	50.04	52.15	-20.22
25	14400.00	14416.35	0.00	23.19	53.82	22.20	52.40	52.89	50.85	50.05	52.30	-20.33
26	15000.00	15016.32	0.00	23.22	53.98	-20.43	53.08	53.05	50.96	50.37	52.42	-20.33
27	15600.00	15616.34	0.00	23.14	54.79	-20.39	52.94	53.12	51.07	49.75	52.58	-19.68
28	16200.00	16216.31	0.00	23.49	54.90	-20.43	53.26	53.23	51.20	49.87	52.69	-19.78
29	16800.00	16816.33	0.00	23.82	54.45	-20.34	53.22	53.36	51.29	50.60	52.74	-19.74
30	17400.00	17416.35	0.00	23.00	54.43	-20.31	53.30	53.45	51.34	50.69	52.82	-19.73
31	18000.00	18016.32	0.00	23.35	54.90	-20.22	53.54	53.46	51.37	50.49	52.85	52.55
32	18600.00	18616.33	0.00	23.13	55.39	-20.35	53.57	53.43	51.41	50.08	52.92	52.61
33	19200.00	19216.35	0.00	23.87	55.16	-20.33	53.57	53.52	51.46	50.51	52.93	52.66
34	19800.00	19816.33	0.00	23.45	55.07	-20.35	53.63	53.58	51.50	50.59	53.00	-20.46
35	20400.00	20416.35	0.00	23.74	54.81	-20.35	53.65	53.65	51.56	50.83	53.03	-20.47
36	21000.00	21016.34	0.00	23.27	55.83	-20.43	53.70	53.64	51.62	50.20	53.13	-20.46
37	21600.00	21616.32	0.00	23.47	-19.37	-20.27	53.85	53.73	51.69	50.61	53.17	-20.71
38	22200.00	22216.33	0.00	23.44	-19.04	-20.16	53.48	53.80	51.73	51.00	53.19	-20.20
39	22800.00	22816.35	0.00	23.93	-18.81	-19.56	53.44	53.91	51.72	51.07	53.19	-19.88
40	23400.00	23416.32	0.00	23.78	-18.85	-19.59	53.82	53.87	51.73	51.13	53.21	-19.88
41	24000.00	24016.34	0.00	23.77	-18.80	-19.59	53.78	53.87	51.80	51.17	53.25	-19.88
42	24600.00	24616.32	0.00	23.51	-19.21	-19.66	53.99	53.81	51.77	50.22	53.31	-19.90
43	25200.00	25216.33	0.00	24.23	-19.03	-19.63	53.95	53.87	51.84	50.96	53.30	-19.91
44	25800.00	25816.31	0.00	23.90	-18.93	-19.63	52.92	53.92	51.86	51.22	53.32	-19.93
45	26400.00	26416.32	0.00	23.85	-18.95	-19.65	53.88	53.92	51.89	51.16	53.35	-19.99
46	27000.00	27016.34	0.00	24.16	-18.93	-19.66	53.65	53.97	51.92	51.27	53.38	-19.99
47	27600.00	27616.32	0.00	23.70	-19.19	-19.72	54.14	53.97	51.93	50.78	53.44	-20.03
48	28200.00	28216.33	0.00	24.23	-19.00	-19.71	54.03	54.04	52.00	51.32	53.45	-20.07
49	28800.00	28816.31	0.00	24.13	-19.01	-19.72	54.23	54.06	52.00	51.37	53.48	-20.09
50	29400.00	29416.33	0.00	24.09	-19.36	-19.80	54.22	54.00	52.01	50.44	53.54	-20.12
51	30000.00	30016.34	0.00	23.94	-19.06	-19.77	54.15	54.09	52.02	51.31	53.52	-20.16
52	30600.00	30616.32	0.00	24.02	-19.12	-19.79	54.13	54.10	52.04	51.28	53.54	-20.21

Table B-3. Thermocouple Temperatures: Channels #10 - #19

--	--------	Channel#	10	11	12	13	14	15	16	17	18	19
--	--------	--------	-----	-----	-----	-----	-----	-----	-----	-----	-----	-----
#	t_0(s)	t_f(s)										
--	--------	--------	-----	-----	-----	-----	-----	-----	-----	-----	-----	-----
1	0.00	16.33	20.30	21.04	20.79	21.37	21.17	21.71	20.82	21.33	21.25	18.70
2	600.00	616.35	24.87	27.32	26.95	29.30	34.48	30.26	26.13	31.97	31.56	19.55
3	1200.00	1216.32	29.07	30.56	31.49	32.42	39.52	32.99	30.59	34.99	35.77	23.68
4	1800.00	1816.34	31.90	34.59	34.57	37.30	42.07	36.36	34.23	38.01	39.47	20.90
5	2400.00	2416.31	35.30	37.37	38.01	39.59	45.70	38.63	37.43	40.40	41.85	21.39
6	3000.00	3016.33	37.93	40.17	40.60	42.53	48.15	40.97	40.19	42.92	44.52	22.02
7	3600.00	3616.34	40.03	42.64	42.33	45.67	49.91	43.14	42.15	45.11	47.36	23.13
8	4200.00	4216.34	42.00	44.67	44.55	47.78	51.95	44.91	44.42	47.13	49.18	23.40
9	4800.00	4816.32	44.05	46.26	46.63	48.76	54.20	46.29	46.45	48.46	50.67	23.11
10	5400.00	5416.33	45.31	47.87	47.84	50.91	55.28	47.86	47.84	50.07	52.47	23.28
11	6000.00	6016.34	46.54	49.16	49.03	52.33	56.51	49.03	49.12	51.31	53.49	23.77
12	6600.00	6616.32	48.37	49.76	50.00	52.01	58.16	49.62	49.97	51.69	54.15	24.34
13	7200.00	7200.00	99.99	-99.99	-99.99	-99.99	-99.99	-99.99	-99.99	-99.99	-99.99	-99.99
14	7800.00	7816.33	49.72	51.92	52.14	54.79	59.75	51.73	52 19	53.95	56.00	24.81
15	8400.00	8416.35	50.81	52.29	52.41	54.73	60.62	52.02	52.54	54.06	56.64	25.39
16	9000.00	9016.32	51.60	52.97	53.54	54.97	61.67	52.74	53.59	54.86	57.29	25.54
17	9600.00	9616.34	51.56	53.69	53.47	56.91	61.43	53.39	53.77	55.55	57.85	26.53
18	10200.00	10216.31	52.30	53.96	53.95	56.64	62.12	53.64	54.18	55.75	58.13	27.02
19	10800.00	10816.33	52.94	54.24	54.53	56.43	62.78	53.98	54.74	56.01	58.72	25.60
20	11400.00	11416.35	53.37	54.63	54.87	56.87	63.18	54.38	55.11	56.38	59.13	26.51
21	12000.00	12016.32	53.14	55.15	54.96	58.35	63.00	54.90	55.34	57.12	59.43	26.59
22	12600.00	12616.34	53.69	55.22	55.28	57.75	63.54	54.94	55.55	56.95	59.57	26.95
23	13200.00	13216.32	54.05	55.41	55.60	57.77	63.91	55.17	55.85	57.20	59.87	26.69
24	13800.00	13816.33	53.76	55.84	55.64	59.07	63.65	55.53	56.03	57.72	60.10	26.64
25	14400.00	14416.35	53.90	55.92	55.76	59.07	63.82	55.65	56.18	57.83	60.18	26.32
26	15000.00	15016.32	53.88	56.12	55.92	59.36	63.99	55.78	56.28	57.85	60.37	26.36
27	15600.00	15616.34	54.58	55.93	56.16	58.40	64.45	55.76	56.44	57.82	60.37	27.23
28	16200.00	16216.31	54.93	56.05	56.49	58.11	64.90	55.96	56.81	57.97	60.56	26.32
29	16800.00	16816.33	54.17	56.60	56.45	60.03	64.24	56.28	56.79	58.54	60.82	26.85
30	17400.00	17416.35	54.22	56.65	56.54	60.04	64.38	56.42	57.04	58.69	60.83	27.01
31	18000.00	18016.32	54.28	56.64	56.67	59.90	64.52	56.45	57.10	58.71	60.95	26.72
32	18600.00	18616.33	55.05	56.23	56.61	58.45	65.02	56.13	56.95	58.17	61.10	26.83
33	19200.00	19216.35	54.38	56.76	56.71	60.10	64.55	56.49	57.08	58.80	60.92	27.15
34	19800.00	19816.33	54.98	56.44	56.52	59.00	64.94	56.24	56.93	58.24	60.99	27.10
35	20400.00	20416.35	54.45	56.86	56.73	60.27	64.57	56.59	57.14	58.84	61.08	27.82
36	21000.00	21016.34	54.93	56.76	57.13	59.36	65.15	56.66	57.48	58.86	61.45	-25.63
37	21600.00	21616.32	55.21	56.57	56.73	59.15	65.09	56.40	57.08	58.50	61.14	-25.66
38	22200.00	22216.33	54.89	56.82	56.68	59.97	64.82	56.53	57.13	58.66	61.33	-25.84
39	22800.00	22816.35	54.60	57.00	56.92	60.33	64.77	56.78	57.46	59.13	61.48	-24.96
40	23400.00	23416.32	54.55	56.99	56.80	60.47	64.61	56.72	57.25	59.05	61.52	-25.03
41	24000.00	24016.34	54.58	57.00	56.82	60.49	64.70	56.77	57.38	59.15	61.55	-24.99
42	24600.00	24616.32	55.36	56.78	57.23	59.04	65.44	56.77	57.63	59.02	61.78	-25.01
43	25200.00	25216.33	54.81	57.09	57.07	60.26	64.97	56.89	57.60	59.24	61.67	-25.05
44	25800.00	25816.31	54.65	57.09	56.89	60.53	64.78	56.80	57.36	59.16	61.65	-25.13
45	26400.00	26416.32	54.75	57.17	57.02	60.57	64.90	56.94	57.57	59.33	61.72	-25.19
46	27000.00	27016.34	54.75	57.17	57.02	60.57	64.90	56.94	57.57	59.33	61.72	-25.19
47	27600.00	27616.32	55.25	56.83	56.88	59.74	65.10	56.71	57.30	58.91	61.69	-25.24
48	28200.00	28216.33	54.81	57.24	57.07	60.67	64.91	56.96	57.52	59.30	61.66	-25.26
49	28800.00	28816.31	54.87	57.27	57.18	60.57	65.07	57.04	57.72	59.46	61.89	-25.25
50	29400.00	29416.33	55.67	56.86	57.26	59.05	65.65	56.80	57.62	58.88	61.85	-25.35
51	30000.00	30016.34	54.97	57.33	57.31	60.59	65.18	57.15	57.84	59.50	61.90	-25.33
52	30600.00	30616.32	55.04	57.30	57.37	60.35	65.35	57.14	57.92	59.46	62.06	-25.33
--	--------	--------	-----	-----	-----	-----	-----	-----	-----	-----	-----	-----

(7200 seconds of elapsed time) was lost during the process, and was flagged as "-99.99".

B.4. Steady-State Limit

The objective is to use curve-fitting functions to standardize the data, to check proximity to steady state to be able to extrapolate to steady-state conditions for subsequent analyses. Curve-fitting functions that use a standard exponential function of time of the form

$$T(t) = A + Be^{Ct}, \tag{B.1}$$

where A, B, and C are constants, were used to pass a least-square fit through experimental data, and provided curves with poor correlation coefficients. The plots of these curves did not follow the experimental data throughout the whole extent of the elapsed time of data collection. Part of the reason for the failure, is that such type of functions is equivalent to those obtained by using a lumped-parameter method [48], which assumes a constant thermal capacitance and a constant thermal conductance to dissipate the heat. Before starting to postulate other functions, a closer look must be given to the physics involved, as it is always best to base curve-fitting equation on a physics-based model rather than an arbitrary function. The above exponential function models a linear system with dissipation and restoring force, but not impedance. The equivalent to such system is a linear mass-spring-damper system with negligible mass. Thus, one way to improve the curve-fitting function is to add the mass, or impedance component to the model. The differential equation modeling the displacement *x(t)* in a linear mass-spring-damper system of mass, m, spring constant, k, and damping coefficient, c, subject to an initial displacement and speed can be expressed as [37, p.97]:

$$\ddot{x} + 2\zeta\omega_n\dot{x} + \omega_n^2 x = 0, \tag{B.2}$$

$$x(0) = x_o, \tag{B.3}$$

$$\dot{x}(0) = \dot{x}_o, \tag{B.4}$$

where ζ is the *damping ratio*, expressed as:

$$\zeta = \frac{c}{2\sqrt{km}} \tag{B.5}$$

and ω_n is the *undamped natural frequency* expressed as:

$$\omega_n = \sqrt{\frac{k}{m}}\,. \tag{B.6}$$

The differential equation above has three solution forms, depending on the value of ζ, namely, *over-damped* motion for $\zeta>1$, *critically damped* motion for $\zeta=1$, and *under-damped* motion for $\zeta<1$. Over-damped motion ($\zeta>1$) will not be considered. The solution for critically damped motion is given as:

$$x(t) = e^{-\omega_n t}[x_o + (\dot{x}_o + \omega_n x_o)t] \quad (\zeta=1), \tag{B.7}$$

and the solution for under-damped motion is given as

$$x(t) = e^{-\zeta\omega_n t}[A\cos(\omega_d t) + B\sin(\omega_d t)] \quad (\zeta<1), \tag{B.8}$$

where A and B are given as

$$A = x_o\,, \tag{B.9}$$

$$B = \frac{\dot{x}_o + \zeta\omega_n x_o}{\omega_d}\,, \tag{B.10}$$

and ω_d is the *damped natural frequency* defined in terms of the undamped natural frequency and the damping ratio as:

$$\omega_d = \omega_n\sqrt{1-\zeta^2} \quad (\zeta<1)\,. \tag{B.11}$$

These solutions can be now used if *x(t)* is redefined as the temperature of the thermal system, and ζ and ω_n are redefined in terms of thermal parameters. These parameters, as well as the initial conditions, become curve-fitting unknowns, which are calculated from experimental data. A coordinate transformation must be used, to resolve the sign of the function and to account for the unknown value of the temperature at steady state. Let the coordinate transformation be stated as:

$$y(t) = y_\infty - x(t) \tag{B.12}$$

where y_∞ is the temperature at steady state (infinite time). Substituting Eq. (B.12) into Eqs. (B.3) and (B.4) yield expressions for the transformation of the initial conditions:

$$x_o = y_\infty - y_o, \tag{B.13}$$

$$\dot{x}_o = -\dot{y}_o, \tag{B.14}$$

where

$$y(0) = y_o, \tag{B.15}$$

$$\dot{y}(0) = \dot{y}_o, \tag{B.16}$$

Substituting Eq. (B.12) in Eqs. (B.7) and (B.8), and using Eqs. (B.13) and (B.14) yields:

$$y(t) = y_\infty - e^{-\omega_n t}[(y_\infty - y_o) + (-\dot{y}_o + \omega_n(y_\infty - y_o))t] \tag{B.17}$$

and

$$y(t) = y_\infty - e^{-\zeta\omega_n t}[A\cos(\omega_d t) + B\sin(\omega_d t)], \tag{B.18}$$

where

$$A = (y_\infty - y_o) \tag{B.19}$$

and

$$B = \frac{-\dot{y}_o + \zeta\omega_n(y_\infty - y_o)}{\omega_d}. \tag{B.20}$$

The curve fitting criteria will be that of least squares, which attempts to minimize the sum of the squares of the differences between the curve-fitting function, y_j, and the experimental temperature, y_j^E, at each data point, j:

$$G_k = \sum_{j=set\{k\}} \left(y_j - y_j^E\right)^2, \tag{B.21}$$

where

$$y_j = y(t_j), \quad j = set\{k\} \tag{B.22}$$

where $set\{k\}$ denotes the set of admissible data points for channel "k".

Critically Damped Motion. The solution for a critically damped motion is:

$$T(t) = Z_3 - (Z_1 \cdot (1 + Z_4 t) - Z_2 \cdot \Delta T) \cdot \exp(-Z_4 t), \tag{B.23}$$

Under-Damped Motion. The solution for under-damped motion is given as:

$$T(t) = Z_3 - \exp(-Z_5 \cdot Z_4 \cdot t) \cdot \left[A \cos(\omega_d t) + B \sin(\omega_d t) \right], \tag{B.24}$$

where

$$\begin{aligned} \omega_d &= Z_4 \sqrt{1 - Z_5^2} \\ A &= Z_1 \\ B &= \left(-Z_2 + Z_5 Z_4 Z_1 \right) / \omega_d \end{aligned} \quad , \tag{B.25}$$

where the Z's are defined in Table B-4, and the frequencies and amplitudes are defined in Table B-5. Results are shown for the temperature in channels 0 through 9 in Table B-6, and channels 10 through 19 in Table B-7. The type of damping mode chosen is indicated in the tables by "CD" and "UD" for critically damped and under-damped motions, respectively.

Table B-4. Optimization-Variable Definitions

		Critically Damped	*Under-Damped*
Z_1	°C	ΔT_∞	ΔT_∞
Z_2	°C/s	$\Delta T/dt$	$\Delta T/dt$
Z_3	°C	T_∞	T_∞
Z_4	rad/s	ω_n	ω_n
Z_5	1		ζ

Table B-5. Calculation of Constants in the Curve-Fitting Equation (Equation of Motion)

		Critically Damped	*Under-Damped*
ω_n	rad/s	$\omega_n = \sqrt{\frac{k}{m}}$	$\omega_n = \sqrt{\frac{k}{m}}$
ω_d	rad/s		$\omega_d = \omega_n \sqrt{1 - \zeta^2}$ $(\zeta < 1)$
A	°C		Z_1
B	°C		$(-Z_2 + Z_5 * Z_4 * Z_1) / \omega_d$

B.5. Uncertainty Analysis

Temperature overall uncertainty from the thermocouple and data acquisition system used was 0.5 °C. The uncertainty for power is calculated using the generalized equation [46] as:

$$w_F = \left[\sum_{i=1}^{N} \left(\frac{\partial F}{\partial \phi_i} w_i \right)^2 \right]^{1/2} \tag{B.26}$$

where F is the function of N variables, $F = F(\phi_1, \phi_2, \phi_3, \ldots, \phi_N)$ whose uncertainty is being calculated, ϕ_i is the measured variable with known uncertainty, w_i. Power uncertainty comes from uncertainty in the anode voltage, the cathode resistor voltage, and its resistance. Table B-8 shows measured values of these parameters.

The input power is calculated as :

$$P = V_a * I = V_a * V_r / R = \phi_1 * \phi_2 / \phi_3 = F \tag{B.27}$$

where

V_a is the anode voltage,

V_r is the cathode resistor voltage, and

R is the cathode resistor resistance.

Substituting Eq. (B.27) into Eq. (B.26) and using the values in Table B-8 for the above variables yields an input power uncertainty of 0.67 Watts.

B.6. Lumped-Parameter Model

Results from a preliminary thermal network lumped-parameter model for the liquid-lens system used to assess experimental results is shown in *Figure B-1.* The enclosure Nusselt number was calculated following the procedure presented in Ref. [48] (Section 9.7.1, Eqs. (9.37), (9.38), and (9.43) of the reference), based on a critical angle of $\psi_c = 59°$ (off the heated-from below orientation), and assuming two-dimensional natural convection in inclined differentially heated rectangular enclosures. The convection coefficient for heat transfer between the two isothermal walls was calculated from the above Nusselt number. Then the convection

Table B-6. Summary of Curve-Fitting Results – Channels 0 thru 9

Channel:		0	1	2	3	4	5	6	7	8	9
Location:			AMBIENT	C-ELEMENT INTERIOR	C-ELEMENT EXTERIOR	COUPLER TOP WALL	COUPLER SIDE WALL	COUPLER BOTTOM WALL	CRT (0,-56)	CRT (69,0)	CRT (0,56)
Damping Mode:			CD	UD	CD	UD	UD	UD	UD	UD	UD
Variable	Units										
N	points		51	35	22	51	51	51	51	51	20
Z_1	°C		2.83	35.52	1.64	33.60	33.91	32.12	30.77	32.99	32.41
$Z_2 \times 10^4$	°C/s		1.07	75.59	1.06	76.78	74.01	63.51	65.69	59.58	67.37
Z_3	°C		23.9	54.8	22.6	53.9	53.9	51.8	50.4	53.5	52.7
$Z_4 \times 10^4$	rad/s		2.07	3.31	3.97	2.26	3.01	3.25	1.68	3.33	3.33
Z_5	1			0.9999		0.9999	0.9999	0.9999	0.9599	0.9999	0.9999
A	°C			35.52		33.60	33.91	32.12	30.77	32.99	32.41
B	°C			897		-26	661	891	-34	1067	861
$\omega_d \times 10^6$	rad/s			4.68		3.20	4.26	4.60	47.09	4.71	4.71
T_o	°C		21.07	19.31	20.99	20.34	20.02	19.69	19.60	20.55	20.25
T_f	°C		23.87	54.82	22.63	53.91	53.91	51.80	50.58	53.53	52.65
ΔT_f	°C		2.80	35.51	1.64	33.57	33.90	32.11	30.98	32.98	32.40
T_∞	°C		23.9	54.8	22.6	53.9	53.9	51.8	50.4	53.5	52.7
ΔT_∞	°C		2.83	35.52	1.64	33.60	33.91	32.12	30.77	32.99	32.41
$\Delta T/\Delta T_\infty$	1		0.989	1.000	1.000	0.999	1.000	1.000	1.007	1.000	1.000
$1-\Delta T/\Delta T_\infty$	1		-0.011	0.000	0.000	-0.001	0.000	0.000	0.007	0.000	0.000
G	$°C^2$		4.5	9.8	2.0	7.6	1.3	2.3	14.3	1.5	0.7
T_m	°C		23.1	47.7	22.0	48.9	49.0	47.1	46.3	48.5	41.6
σ	°C		0.945	9.923	0.619	8.235	8.396	8.077	7.930	8.287	9.888
η	°C		0.303	0.546	0.315	0.393	0.164	0.217	0.541	0.175	0.201
R^2	1		0.897	0.997	0.741	0.998	1.000	0.999	0.995	1.000	1.000

Table B-7. Summary of Curve-Fitting Results – Channels 10 thru 19

Channel:		10	11	12	13	14	15	16	17	18	19
Location:		CRT (50,-35)	CRT (25,-35)	CRT (0,-35)	CRT (50,0)	CRT (25,0)	CRT (0,0)	CRT (50,35)	CRT (25,35)	CRT (0,35)	LENS ARRAY INTERIOR
Damping Mode:		UD	UD	UD	UD	UD	UD	UD	UD	UD	CD
Variable	Units										
N	points	51	51	51	51	51	51	51	51	51	34
Z_1	°C	34.17	35.09	35.24	37.25	42.38	33.34	36.24	36.07	38.71	7.96
$Z_2 \times 10^4$	°C/s	74.44	87.20	88.04	94.15	127.74	81.69	87.91	95.09	105.95	11.27
Z_3	°C	54.7	56.3	57.0	59.9	64.9	56.8	57.5	59.0	61.4	27.5
$Z_4 \times 10^4$	rad/s	3.40	3.33	2.48	2.53	3.01	2.44	2.42	2.63	2.73	2.11
Z_5		0.9999	0.9999	0.9999	0.9998	0.9998	0.9998	0.9999	0.9998	0.9999	
A	°C	34.2	35.1	35.2	37.3	42.4	33.3	36.2	36.1	38.7	
B	°C	869	629	-18	0	0	-9	-6	-2	-11	
$\omega_d \times 10^6$	rad/s	4.81	4.71	3.51	5.05	6.03	4.87	3.42	5.27	3.86	
T_o	°C	20.50	21.24	21.75	22.69	22.50	23.45	21.25	22.89	22.69	19.51
T_f	°C	54.67	56.33	56.97	59.93	64.87	56.77	57.46	58.95	61.39	27.43
ΔT_f	°C	34.17	35.09	35.23	37.24	42.38	33.32	36.22	36.06	38.70	7.92
T_∞	°C	54.7	56.3	57.0	59.9	64.9	56.8	57.5	59.0	61.4	27.5
ΔT_∞	°C	34.17	35.09	35.24	37.25	42.38	33.34	36.24	36.07	38.71	7.96
$\Delta T/\Delta T_\infty$	1	1.000	1.000	1.000	1.000	1.000	0.999	0.999	1.000	1.000	0.995
$1-\Delta T/\Delta T_\infty$	1	0.000	0.000	0.000	0.000	0.000	-0.001	-0.001	0.000	0.000	-0.005
G	°C^2	5.7	3.0	3.3	24.2	68.3	13.0	7.7	34.2	29.9	15.3
T_m	°C	50.1	52.1	52.1	54.9	60.0	52.1	52.4	54.2	56.5	25.0
σ	°C	8.477	8.480	8.453	8.870	9.180	7.913	8.749	8.211	8.780	2.379
η	°C	0.342	0.246	0.259	0.703	1.181	0.515	0.395	0.836	0.782	0.692
R^2	1	0.998	0.999	0.999	0.994	0.983	0.996	0.998	0.990	0.992	0.915

Table B-8. Power-Measurement Related Values and Uncertainty

i	Variable		Units	ϕ_i	W_i
1	Anode Voltage , V_a	ϕ_1	V	27800	550
2	Resistor R10 Voltage, V_r	ϕ_2	V	0.487	0.005
3	Resistor R10 Resistance , R	ϕ_3	ohm	954	40
	Power ($P = V_a * I = V_a * V_r / R = \phi_1 * \phi_2 / \phi_3$)	P	W	14.2	0.67

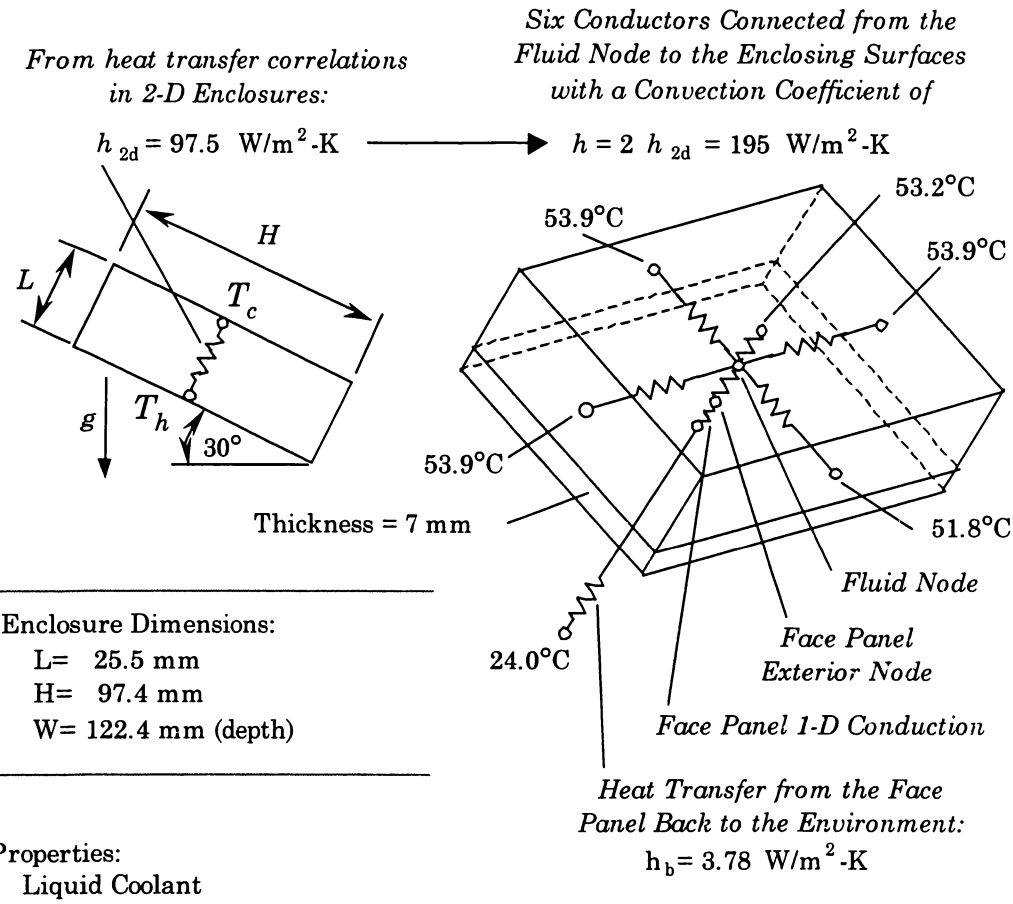

Enclosure Dimensions:
- L= 25.5 mm
- H= 97.4 mm
- W= 122.4 mm (depth)

Properties:

Liquid Coolant		
Density	1134.5	kg/m³
Specific Heat	2588	kJ/kg-K
Thermal Conductivity	0.268	W/m-K
Kinematic Viscosity	9.61×10^{-6}	m²/s
Volume Expansivity	6.07×10^{-4}	1/K
Face Panel		
Thermal Conductivity	0.790	W/m-K

Predicted Face-Panel Exterior Mean Temperature: 60.3 °C
(for an input heat rate of 90% x 14.2 W = 12.78 W)

Figure B-1. Lumped-Parameter Model Used to Predict the Face-Panel Exterior Mean Temperature

coefficient from the enclosure node to the mean fluid node was assumed as twice that value to reflect two identical thermal resistance paths in series. Then it was assumed that the convection heat transfer coefficient was the same for all walls in the three-dimensional enclosure to calculate the thermal conductances and heat transfer rates.

APPENDIX C. THERMOPHYSICAL PROPERTIES

C.1. Fluid Thermophysical Properties

From preliminary CFD and experimental data analyses, it was determined that the fluid temperature ranged between 53 and 59 °C. Therefore, estimates for fluid properties in this range are needed. From all of the relevant fluid thermophysical properties, only specific gravity and specific heat were available, both at 25 °C. Therefore, some properties needed to be measured and some were taken from tables and adjusted. Additionally, it was necessary to verify whether the fluid was Newtonian or Non-Newtonian, so the dynamic viscosity was measured as a function of rate of strain. Next, laboratory measurements of mass density, kinematic viscosity, and dynamic viscosity are presented.

C.1.1. Reference Fluid Thermophysical Properties

The fluid reference data for specific gravity and specific heat are as follows.

Fluid Specific Gravity [86]	1.1591 @ 25/25 °C
Fluid Specific Heat [89]	0.58 BTU/lb-°F

Reference properties for the major components in the fluid mixture are in Table C-1 for ethylene glycol, and Table C-2 for glycerin.

Table C-1. Reference Properties for Ethylene Glycol

T	T	ρ	c_p	$\mu \times 10^2$	$\nu \times 10^6$	$k \times 10^3$	$\alpha \times 10^7$	Pr	$\beta \times 10^6$
C	K	kg/m^3	kJ/kg-K	Pa-s	m^2/s	W/m-K	m^2/s	1	1/K
26.85	300	1111	2.415	1.570	14.10	252.	0.939	151	0.65
36.85	310	1104	2.460	1.070	9.65	255.	0.939	103	0.65
46.85	320	1096	2.505	0.757	6.91	258.	0.940	73	0.65
56.85	330	1090	2.549	0.561	5.15	260.	0.936	55	0.65

Reference: Incropera, F. P., Fundamentals of Heat and Mass Transfer, 2nd Ed., *John Wiley & Sons* (1981)

Table C-2. Reference Properties for Glycerin

T	T	ρ	c_p	$\mu \times 10^2$	$\nu \times 10^6$	$k \times 10^3$	$\alpha \times 10^7$	Pr	$\beta \times 10^6$	
C	K	kg/m^3	kJ/kg-K	Pa-s	m^2/s	W/m-K	m^2/s	1	1/K	
26.85	300	1260	2.427	79.9	634.	286.	0.935	6780	0.48	(1)
36.85	310	1254	2.490	35.2	281.	286.	0.916	3060	0.49	(1)
46.85	320	1247	2.564	21.0	168.	287.	0.897	1870	0.50	(1)
56.85	330	1240	2.630	16.0	120.	287.	0.880	1363.6	0.51	(2)

(1) Reference: Incropera, F. P., Fundamentals of Heat and Mass Transfer, 2nd Ed., *John Wiley & Sons* (1981)

(2) Extrapolated

Thermophysical properties for the mixture will be calculated based on laboratory measurements and the use of the above reference data.

C.1.2. Measurement of Fluid Mass Density

The fluid mass density was verified by conducting mass and volume measurements. According to laboratory measurements, the mass density at 80 °F (26.7 °C) is 1151.1 kg/m^3. The temperature-adjusted mass density from manufacturer's specifications was calculated at 1154.5 kg/m^3 at the same temperature. The percent difference based on manufacturer's data is –0.3 %.

Equipment

Fisher Scientific Triple-Beam Balance, Capacity: 2610 g, U.S Pat. 2,729,439

Graduated Cylinder

Thermometer

Measurements

Empty Mass (m_1):	129.6 g
Gross Mass (m_2):	244.0 g
Net Mass ($m = m_2$-m_1):	114.4 g
Fluid Volume (V):	99.4 ml
Mass Density ($\rho = m/V$):	1151. kg/m^3 at 80 °F (26.7 °C)
Reference Value(1):	1.1591 @ 25/25 °C
Reference Value Adjusted for Temperature:	1154.5 kg/m^3 at 300 K (26.8 °C)
Percent Difference from Ref. Value:	-0.3 %

(1) Dow Chemical, "Developmental Heat Transfer Fluid" Data Sheet, and adjusted for temperature.

C.1.3. Calculation of Mass Density, Specific Heat, and Volume Expansivity

For the calculation of mass-or volume-dependent properties, such as mass density, specific heat, and volume expansivity, a fluid mixing model was used. It was assumed a mixture of 70% ethylene glycol and 30% glycerin. Values were calculated at the desired temperatures, and then adjusted for consistency with the reference data at 25 °C. Ratios applied to calculation of mass density and specific heat are shown in Table C-3.

Mixing Model. Let the ethylene glycol be designated as Component 1, and the glycerin be designated as Component 2. Let the volume fractions for the two components be defined as:

$$\xi_1 = \frac{\mathcal{V}_1}{\mathcal{V}} = 0.7$$
$$\xi_2 = \frac{\mathcal{V}_2}{\mathcal{V}} = 0.3 \qquad \text{(C.1)}$$

Let ρ_1 and ρ_2 denote mass densities for component 1 and component 2, respectively. The mass density for the mixture is calculated as:

$$\rho = \frac{m}{\mathcal{V}} = \frac{m_1 + m_2}{\mathcal{V}} = \frac{\rho_1 \mathcal{V}_1 + \rho_2 \mathcal{V}_2}{\mathcal{V}} = \xi_1 \rho_1 + \xi_2 \rho_2 . \qquad \text{(C.2)}$$

Let c_{p1} and c_{p2} denote specific heats for component 1 and component 2, respectively.

Table C-3. Correction Ratios for Density and Specific Heat

	Mass Density	Specific Heat
	ρ	c_p
	kg/m3	kJ/kg-K
Calculated at 25 C	1155.7	2.428
Reference at 25 C	1156.5	2.412
	ρ / ρ_{ref}	$c_p / c_{p,ref}$
Ratio	0.99935	1.006533

The specific heat for the mixture is calculated as:

$$c_p = \frac{C_p}{m} = \frac{C_{p1} + C_{p2}}{m} = \frac{\mathcal{V}_1 \rho_1 c_{p1} + \mathcal{V}_2 \rho_2 c_{p2}}{\rho \mathcal{V}} = \frac{\xi_1 \rho_1 c_{p1} + \xi_2 \rho_2 c_{p2}}{\xi_1 \rho_1 + \xi_2 \rho_2}. \quad \text{(C.3)}$$

Let β_1 and β_2 denote volume expansivities for component 1 and component 2, respectively. The volume expansivity for the mixture is calculated as

$$\beta = \frac{1}{v}\left(\frac{\partial v}{\partial T}\right)_p = \frac{1}{\mathcal{V}}\left(\frac{\partial \mathcal{V}}{\partial T}\right)_p = -\frac{1}{\mathcal{V}}\left(\frac{\partial\left(\mathcal{V}_1 + \mathcal{V}_2\right)}{\partial T}\right)_p = \xi_1 \beta_1 + \xi_2 \beta_2. \quad \text{(C.4)}$$

The models above were used to calculate mixture properties at the reference temperatures. The results from property calculation are shown in Table C-4.

The above results were curve-fitted and adjusted to reflect available data using the rations in Table C-3. The following equations resulted for density, specific heat, and volume expansivity:

$$\rho(T) = \left(8.49447 \times 10^{-4}\, T^2 - 7.82236 \times 10^{-1}\, T + 1.17561 \times 10^{3}\right) \frac{\text{kg}}{\text{m}^3} \pm 0.18\% \quad \text{(C.5.a)}$$

$$c_p(T) = \left(7.98288 \times 10^{-7}\, T^2 + 5.21157 \times 10^{-3}\, T + 2.29387\right) \frac{\text{kJ}}{\text{kg-K}} \pm 0.60\% \quad \text{(C.5.b)}$$

$$\beta(T) = \left(2.99805 \times 10^{-4}\, T + 5.90561 \times 10^{-1}\right) \text{K}^{-1} \pm 0.15\% \quad \text{(C.5.c)}$$

C.1.4. Calculation of Thermal Conductivity

Thermal conductivity was not readily available. Thus, a conduction model had to be used for the mixture. Two models representing extreme situations were used to

Table C-4. Fluid Properties Resulting from the Mixture Model

T	T	ρ	c_p	$\beta \times 10^3$
C	K	kg/m^3	kJ/kg-K	1/K
26.85	300	1156.0	2.419	0.599
36.85	310	1148.8	2.470	0.602
46.85	320	1141.5	2.524	0.605
56.85	330	1134.7	2.576	0.608
Error		0.2%	0.6%	0.2%

provide bounds for the value, as shown in *Figure C-1.* A parallel conduction model (Model 1) assumed that the fluid is separated into the two components and then placed side-by-side along slabs of equal lengths. A series conduction model (Model 2) assumed that fluid is separated into the two components and then placed side-by-side, along slabs of equal cross-sectional areas.

Let ξ_1 and ξ_2 denote the fluid volume fractions for the two components:

$$\xi_1 = \frac{\mathcal{V}_1}{\mathcal{V}} = \frac{A_1 L_1}{A_1 L_1 + A_2 L_2} \tag{C.6.a}$$

$$\xi_2 = \frac{\mathcal{V}_2}{\mathcal{V}} = \frac{A_2 L_2}{A_1 L_1 + A_2 L_2} \tag{C.6.b}$$

The parallel conduction model (Model 1) yields the following equation for the thermal conductivity:

$$k_p = k_1 \xi_1 + k_2 \xi_2 . \tag{C.7}$$

The series conduction model (Model 2) yields the following equation for the thermal conductivity:

$$k_s = \left(\frac{\xi_1}{k_1} + \frac{\xi_2}{k_1} \right)^{-1} \tag{C.8}$$

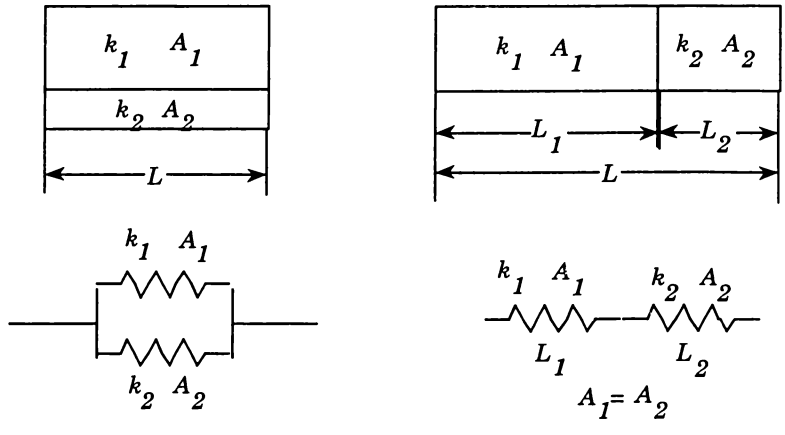

Conduction in Parallel (Model 1) *Conduction in Series (Model 2)*

Figure C-1. Conduction Models

The models above were used to calculate the thermal conductivity at the reference temperatures. A mean thermal conductivity is defined as:

$$k = \frac{1}{2}\left(k_p + k_s\right). \tag{C.9}$$

The maximum error from the mean is calculated as:

$$k_{err} = \frac{1}{2}\left|k_p - k_s\right|. \tag{C.10}$$

The above equations are used to calculate the thermal conductivity values at the reference temperatures. The results are Table C-5. Notice that the thermal conductivity obtained using the two models are very close to each other – the maximum percent difference being 0.35%. Since the thermal conductivity will be specified as the mean value of the two models, the maximum percent error becomes 0.17%. This is the maximum error based on the models, and not the uncertainty. Results from the above model were curve-fitted into the following equation:

$$k(T) = \left(-2.12744\times10^{-4}\,T^3 + 2.48786\times10^{-2}\,T^2 + \right.$$
$$\left. -7.14468\times10^{-1}\,T + \ 2.67126\times10^{2}\right)\times10^{-3}\,\frac{\text{W}}{\text{m-K}} \pm 0.17\% \tag{C.11}$$

C.1.5. Measurement of Fluid Kinematic Viscosity

The kinematic viscosity of the liquid coolant (Dow Chemical XUS 11137.01) was measured using the Fisher/Tag Saybolt viscosimeter shown in *Figure C-2*, according to standard ASTM D-88. Table C-6 lists the equipment used. In total, 28

Table C-5. Conduction Model Results at the Reference Temperatures

T	T	$k_p \times 10^3$	$k_s \times 10^3$	$k \times 10^3$	$k_{err} \times 10^3$	$\%k_{err}$
C	K	W/m-K	W/m-K	W/m-K	W/m-K	%
26.85	300	262.2	261.3	261.8	0.4	0.17%
36.85	310	264.3	263.6	263.9	0.4	0.14%
46.85	320	266.7	266.1	266.4	0.3	0.12%
56.85	330	268.1	267.6	267.8	0.3	0.10%

$k = 0.5 \times (k_p + k_s)$; $k_{err} = 0.5 \times |k_p - k_s|$

measurement samples were taken for a temperature range from 77 to 144 °F. Table C-7 shows the viscosity experimental measurements. A plot of viscosity vs. temperature is shown in *Figure C-3.* The kinematic viscosity was curve-fitted using an exponential least square fit, resulting in the following equation for kinematic viscosity in m^2/s as a function of temperature in °C:

$$\nu(T) = 9.637 \times 10^{-5} \exp\left(-4.130 \times 10^{-2} T\right) \frac{m^2}{s} \pm 7.3\% \qquad (C.12)$$

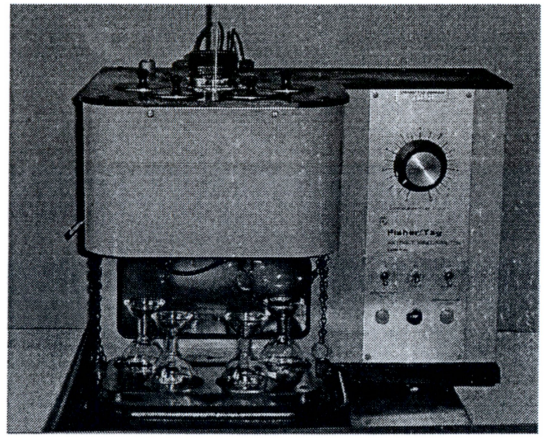

Figure C-2. Fisher/Tag Saybolt Viscosimeter Used for Kinematic Viscosity Measurements

Table C-6. Equipment for Kinematic Viscosity Measurements

Item	*Description*
Viscosimeter	Fisher/Tag Saybolt Viscosimeter
Measurement Standard	ASTM D-88
Flasks	60-ml
Bulb Thermometers	ASTM-rated for the temperature range
Stop Watch	MEDANA; Resolution: 0.01 seconds from 0 to 30 minutes, and 1 second after 30 minutes

Table C-7. Kinematic Viscosity Laboratory Data

Sample #	T	T	Saybolt Seconds	ν	ν
	(°F)	(°C)	(s)	(cs)	(m^2/s)
1	77	25.0	173	36.0	3.60E-05
2	78	25.6	173	36.0	3.60E-05
3	79	26.1	161	32.0	3.20E-05
4	80	26.7	151	31.9	3.19E-05
5	81	27.2	147	31.5	3.15E-05
6	95	35.0	110	22.5	2.25E-05
7	100	37.8	97.3	20.0	2.00E-05
8	104	40.0	88.8	17.9	1.79E-05
21	117	47.2	73.9	14.0	1.40E-05
20	118	47.8	71.0	13.1	1.31E-05
19	119	48.3	70.2	12.9	1.29E-05
18	120	48.9	67.7	12.4	1.24E-05
17	121	49.4	66.8	12.0	1.20E-05
9	122	50.0	67.0	12.0	1.20E-05
16	122.4	50.2	65.5	11.5	1.15E-05
15	123.4	50.8	64.2	11.3	1.13E-05
14	125	51.7	62.9	10.9	1.09E-05
13	126	52.2	62.9	10.9	1.09E-05
12	128.4	53.6	61.6	10.7	1.07E-05
28	129	53.9	62.4	10.8	1.08E-05
10	130	54.4	61.5	10.4	1.04E-05
27	131.8	55.4	58.7	9.8	9.75E-06
11	132	55.6	59.2	9.9	9.90E-06
26	134	56.7	57.7	9.5	9.50E-06
25	136.8	58.2	55.3	8.8	8.80E-06
24	139	59.4	54.3	8.5	8.45E-06
23	141	60.6	53.0	8.2	8.20E-06
22	144	62.2	52.0	7.8	7.80E-06

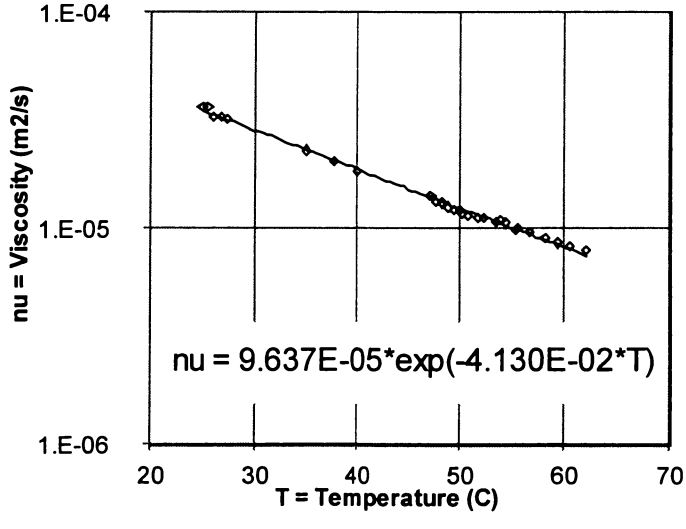

Figure C-3. Kinematic Viscosity Temperature Dependency

C.1.6. Measurement of Fluid Dynamic Viscosity

The kinematic viscosity of the liquid coolant (Dow Chemical XUS 11137.01) was measured using the Fisher MacMichael viscosimeter shown *Figure C-4* for sample temperatures of 27.1, 38.3, and 49.2 °C. The rate of strain was varied from just above unity to 6 s^{-1}. The equipment used is listed in Table C-8. Table C-9 shows the results for dynamic viscosity, compares the corresponding values of kinematic viscosity against the kinematic viscosity measured previously with the Fisher-Tag viscosimeter. The dynamic viscosity is plotted against rate of strain in *Figure C-5*. As the dynamic viscosity does not change significantly with rate of fluid strain, it is concluded that the fluid is Newtonian.

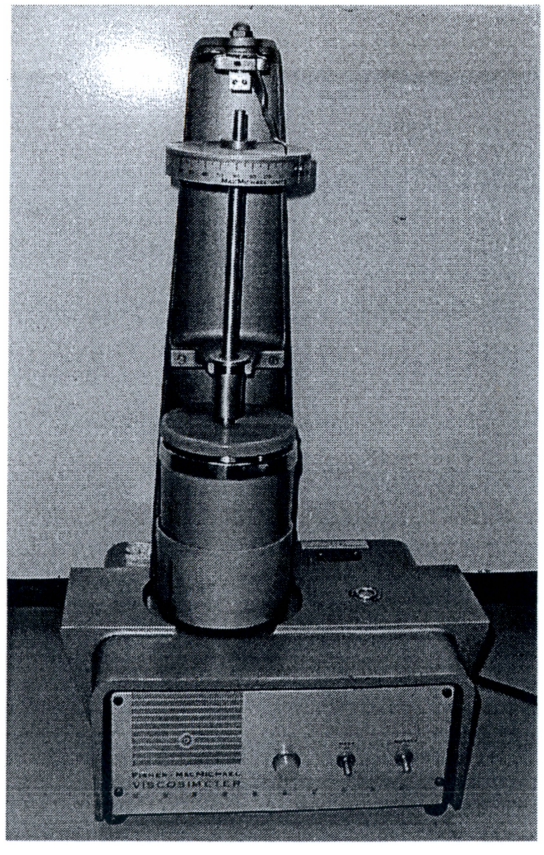

Figure C-4. Fisher MacMichael Viscosimeter Used for Dynamic Viscosity Measurements

Table C-8. Equipment for Thermal Conductivity Measurements

Item	*Description*
Viscosimeter	Fisher MacMichael Viscosimeter
Torsion Wire	B & S Gauge 30
Sample Cup	Radius, R2 = 1.5 cm
Plunger	Radius, R1 = 1 cm Immersion Depth, H = 4.0 cm
Bulb Thermometers	ASTM-rated for the temperature range
Stop Watch	MEDANA; Resolution: 0.01 seconds from 0 to 30 minutes, and 1 second after 30 minutes

Table C-9. Dynamic Viscosity Laboratory Data and Comparison with Kinematic Viscosity Measurements

T (°F) →	80.8	101.0	120.5	80.8	101.0	120.5
T (°C) →	27.1	38.3	49.2	27.1	38.3	49.2
Density (kg/m³) →				1155.0	1147.8	1140.6
Rate of Strain (1/s)	Dynamic Viscosity (Pa-s)			Kinematic Viscosity (m²/s)		
1.263	3.82E-02	2.21E-02	1.47E-02	3.31E-05	1.92E-05	1.29E-05
1.767	3.78E-02	2.18E-02	1.49E-02	3.27E-05	1.90E-05	1.31E-05
2.178	3.78E-02	2.21E-02	1.52E-02	3.28E-05	1.92E-05	1.33E-05
2.644	3.63E-02	2.18E-02	1.48E-02	3.14E-05	1.90E-05	1.30E-05
3.277	3.66E-02	2.26E-02	1.50E-02	3.17E-05	1.97E-05	1.32E-05
3.840	3.63E-02	2.29E-02	1.51E-02	3.14E-05	2.00E-05	1.33E-05
4.344	3.58E-02	2.28E-02	1.50E-02	3.10E-05	1.99E-05	1.32E-05
4.839	3.52E-02	2.27E-02	1.51E-02	3.05E-05	1.98E-05	1.32E-05
5.222	3.55E-02	2.29E-02	1.51E-02	3.07E-05	1.99E-05	1.33E-05
5.647	3.51E-02	2.27E-02	1.50E-02	3.04E-05	1.98E-05	1.31E-05
6.021	3.52E-02	2.25E-02	1.53E-02	3.04E-05	1.96E-05	1.34E-05
Average →	3.63E-02	2.24E-02	1.50E-02	3.15E-05	1.96E-05	1.32E-05
Kinematic Viscosity Saybolt Viscosimeter →				3.15E-05	1.98E-05	1.26E-05
Error →				0.0%	-1.2%	4.1%

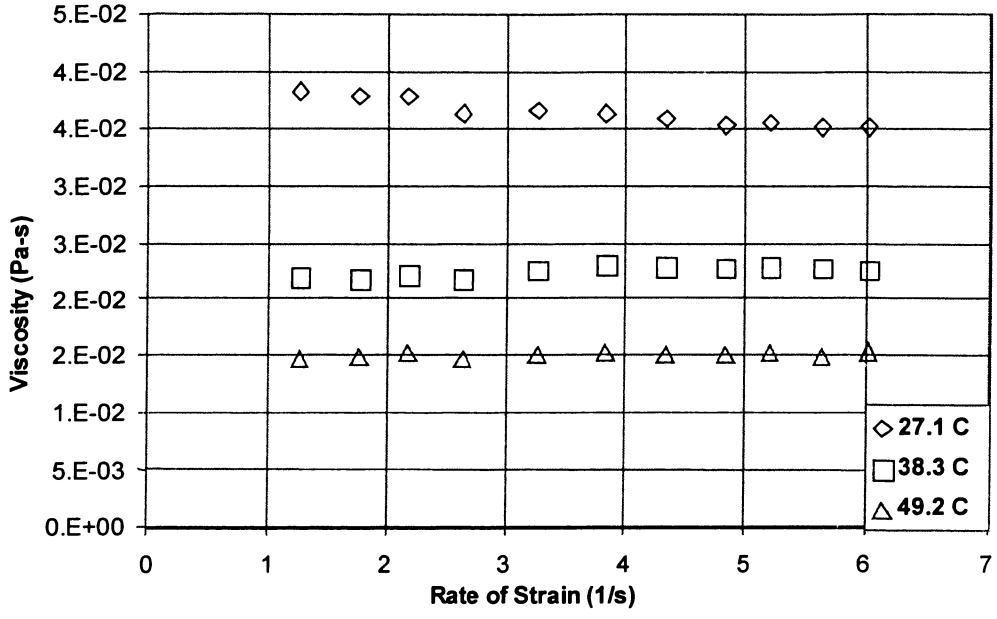

Figure C-5. Dynamic Viscosity and Fluid Strain Rate

C.1.7. Summary of Fluid Properties

The equations obtained above for the fluid properties are summarized in Table C-10. Fluid properties were calculated using the equations in Table C-10 for domain-temperature upper bound, lower bound, and median value of 59, 53, and 56 °C, respectively. The results are shown in Table C-11. Values for the dynamic viscosity, thermal diffusivity, and Prandtl number were derived from primary properties obtained from the equations.

C.2. Solid Thermophysical Properties

Thermal conductivity of the CRT face panel and the meniscus lens was measured using the Lafayette Instrument Company[1] Thermal Comparator model TC-1000. The instrument is shown in *Figure C-6.* The equipment used is listed inTable C-12. A calibration curve was obtained for ebonite, corning glass #7740, and

[1] Lafayette Instrument Company, P.O. Box Sagamore Parkway, North Lafayette, Indiana 47902

Table C-10. Fluid Property Functions

Property	*Units*	*Equation*	*Error* (%)
Mass Density ρ	$\frac{kg}{m^3}$	$\left(8.49447\times10^{-4}T^2 - 7.82236\times10^{-1}T + 1.17561\times10^{3}\right)$	0.18
Specific Heat c_p	$\frac{kJ}{kg\text{-}K}$	$\left(7.98288\times10^{-7}T^2 + 5.21157\times10^{-3}T + 2.29387\right)$	0.60
Kinematic Viscosity ν	$\frac{m^2}{s}$	$\left(9.637\times10^{-5}\exp\left(-4.130\times10^{-2}T\right)\right)$	7.3
Thermal Conductivity $k \times 10^3$	$\frac{W}{m\text{-}K}$	$\left(-2.12744\times10^{-4}T^3 + 2.48786\times10^{-2}T^2 + -7.14468\times10^{-1}T + 2.67126\times10^{2}\right)$	.17
Volume Expansivity $\beta \times 10^3$	K^{-1}	$\left(2.99805\times10^{-4}T + 5.90561\times10^{-1}\right)$	0.15

Table C-11. Fluid Properties Used for Interpolation

T	T	ρ	c_p	$\mu \times 10^2$	$\nu \times 10^6$	$k \times 10^3$	$\alpha \times 10^7$	Pr	$\beta \times 10^3$
C	K	kg/m^3	kJ/kg-K	Pa-s	m^2/s	W/m-K	m^2/s	1	1/K
59	332.15	1132.4	2.603	0.954	8.43	268.1	0.9095	9.3	0.6082
56	329.15	1134.5	2.588	1.082	9.54	267.7	0.9118	10.5	0.6073
53	326.15	1136.5	2.573	1.227	10.80	267.3	0.9141	11.8	0.6065
Error		±0.2%	±0.6%		±7.3%	±0.2%			±0.2%



Figure C-6. Thermal Conductivity Measurement Instrument

Table C-12. Equipment for Thermal Conductivity Measurements

Thermal Comparator	Lafayette Instrument Company's Thermal Comparator Model TC-1000
Reference Samples	Ebonite (k = 0.18 W/m-K) Corning Glass #7740 (k = 1.15 W/m-K) Quartz (k = 1.4 W/m-K)
Stop Watch	MEDANA; Resolution: 0.01 seconds from 0 to 30 minutes and 1 second after 30 minutes

quartz, of known, reference thermal conductivity.

Subject Material:

(1) CRT Face Panel
(2) Meniscus Lens

Calibration Curve

Transient EMF readings were taken for the reference samples of known conductivity, ebonite, glass #7740, and quartz, in various trials. The average of all trials for each sample is shown in Table C-13. The calibration's steady-state EMF and the reference conductivity values are shown in Table C-14. The calibration plot

relating EMF with thermal conductivity is shown in *Figure C-7.* The calibration function relating EMF and thermal conductivity is given as:

$$k(E) = C_1 \, e^{C_2 E}, \tag{C.13}$$

where E ≡ EMF,

C_1 = 0.0936419 (W/m-K), and

C_2 = 0.0136616 (1/μV).

The transient measurements of EMF vs. elapsed time are listed for the reference samples and test materials (meniscus lens and face panel glass) in Table C-15, and plotted in *Figure C-8.* The thermal conductivity of the meniscus lens and face panel glass was obtained by applying C.13. These values are shown along with the uncertainty in Table C-16.

Table C-13. EMF Transient Values for Ebonite, Glass 7740, and Quartz

Elapsed Time	*Ebonite (EMF)*	*Glass 7740 (EMF)*	*Quartz (EMF)*
minutes	μV	μV	μV
0	100.0	227.5	238.0
1	74.0	217.0	224.0
2	70.8	209.7	225.0
4	65.0	203.5	219.3
6	61.0	199.7	214.5
8	58.3	196.8	211.0
10	56.0	193.7	208.5
12	54.5	191.8	206.5
14	52.8	190.2	204.5
16	51.8	188.2	203.5
18	51.0	187.0	202.5
20	50.3	186.2	201.5
22	49.5	185.2	200.8
24	49.0	184.8	200.5
26	48.5	184.7	200.5
28	48.0	184.0	196.5
30	48.0	183.8	196.5
32	47.8	183.5	
34	47.8	183.5	

Table C-14. Steady-State EMF Calibration Values for Ebonite, Glass 7740, and Quartz

Material:		*Ebonite*	*Glass 7740*	*Quartz*
Reference Conductivity	W/m-C	0.18	1.15	1.4
Calibration EMF	μV	47.83	183.6	200.6

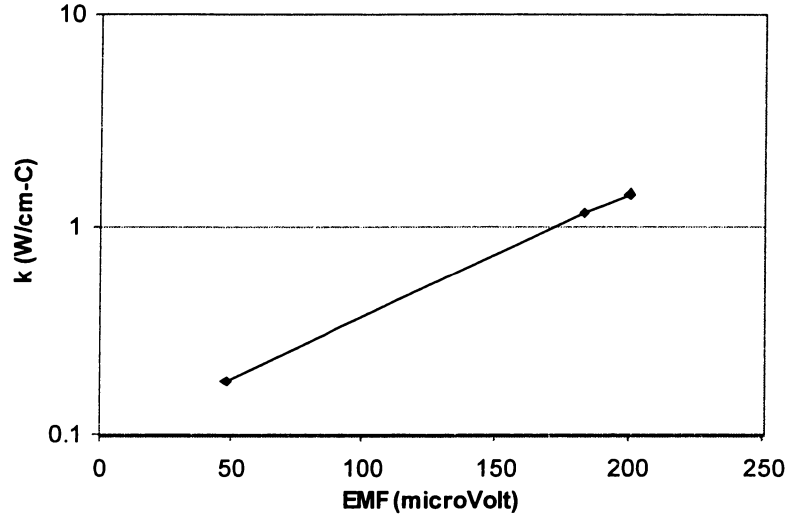

Figure C-7. Thermal Conductivity Calibration Curve

Table C-15. EMF Transient Values for the CRT Face Panel Glass and the Meniscus Lens Glass

Elapsed Time	*CRT Face-Panel Glass EMF*	*Meniscus-Lens Glass EMF*	*Elapsed Time*	*CRT Face-Panel Glass EMF*	*Meniscus-Lens Glass EMF*
minutes	μV	μV	minutes	μV	μV
0	212	175	18	162	142
1	199	164	20	161	141
2	194	159	22	159	141
4	185	152	24	159	141
6	179	149	26	158	141
8	174	147	28	158	141
10	170	145	30	158	141
12	167	144	32	157	
14	165	143	34	157	
16	163	143			

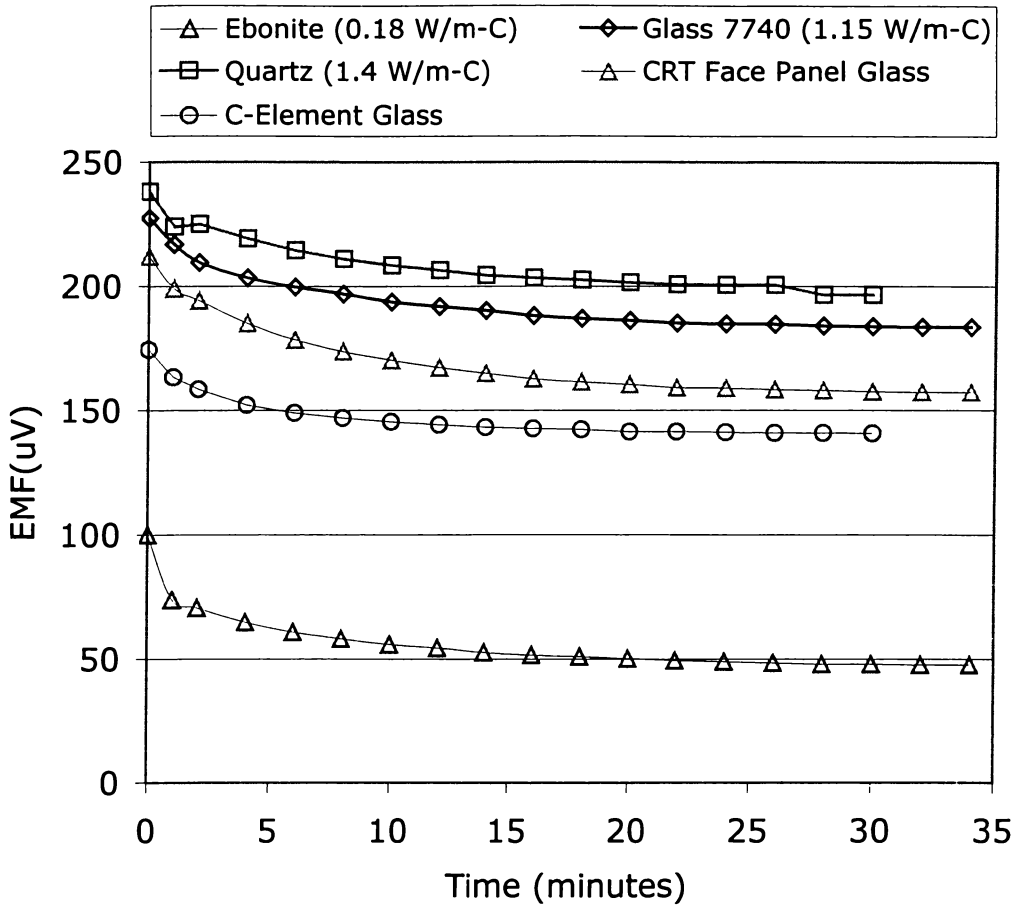

Figure C-8. EMF Transient Values for all Materials

Table C-16. Experimentally Determined Thermal Conductivity Values for the CRT Face-Panel Glass and the Meniscus-Lens Glass

Parameter	Units	CRT Face-Panel Glass	Meniscus-Lens Glass
EMF	μV	157	141
k	W/m-C	0.803	0.641
Uncertainty	W/m-C	±0.040	±0.032
Uncertainty	%	±5%	±5%

APPENDIX D. NUMERICAL MODEL BENCHMARK CASES

D.1. Heat Conduction in a Cubical Domain

One-dimensional conduction in a cubical domain of solid material was used to check the solution of the energy equation for conduction in rectilinear and curvilinear grids. *Figure D-1* shows the domain and computational grid. The domain was divided by a horizontal plane passing through $X_2 = 0.5$ (mid plane) into a lower and an upper region with solids of different thermal conductivity. Values for the dimensionless thermal conductivity of k=0.5 and k=2 were assigned to the lower and upper region, respectively. Two sets of boundary conditions were used. The first set had imposed temperatures on the lower and upper horizontal surfaces and imposed zero flux density (insulated) on all other surfaces. The second set had imposed heat flux density on the lower surface, imposed temperature on the upper surface, and imposed zero flux density (insulated) on all other surfaces. If a dimensionless temperature of one is imposed on the lower surface and zero on the upper surface, the heat flux becomes 0.8 and the mid-plane temperature becomes 0.2. The first set of boundary conditions was used first on a rectilinear grid. Then a curvilinear grid was used with parameterization of X_2-coordinate, then X_2-coordinate, then X_3-coordinate, and finally parameterization in of all coordinates simultaneously. This process was repeated with the second set of boundary conditions the same grids.

The program was run until energy balance was satisfied within a convergence tolerance of τ = 1.E-5. The energy balance error was defined as the absolute value of the cell's dimensionless energy flux balance divided by the cell's dimensionless volume. Table D-1 shows the result for the first set of boundary condition (imposed temperature on lower and upper walls and insulated everywhere else). The theoretical solution was obtained in all cases except for the case having coordinate parameterization in all directions with a heat flux error of 0.017% (from theoretical). All cases satisfied energy balance self-consistently to no less than six significant digits.

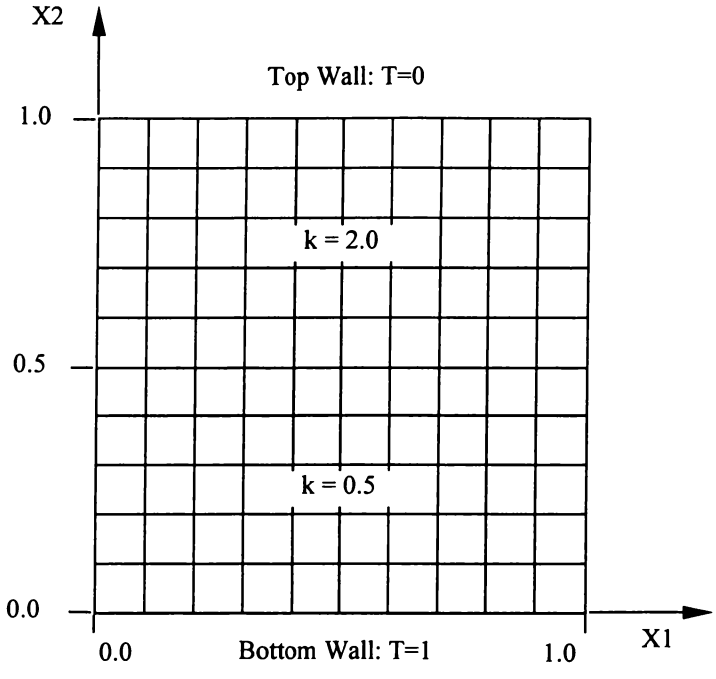

Left wall, Right Wall, Front Wall, Back Wall: Insulated

Figure D-1. **Exterior-Surface-Grid for *Conduction in a Cube***

Table D-1. Heat transfer in Differentially Heated Cubical Domain with Isothermal Lower and Upper Surfaces

	Solution/Grid	(Imposed) Temperature at $X_2 = 0$	(Imposed) Temperature at $X_2 = 1$	(Calculated) Temperature at $X_2 = 0.5$	(Calculated) Heat Flux Through Plane at $X_2 = 0$	(Calculated) Heat Flux Through Plane at $X_2 = 1$
1	Theoretical	1	0	0.200000	0.800000	0.800000
2	Rectilinear	1	0	0.200000	0.800000	0.800000
3	Curvilinear (F24: dir. 1)	1	0	0.200000	0.800000	0.800000
4	Curvilinear (F24: dir. 2)	1	0	0.200000	0.800000	0.800000
5	Curvilinear (F24: dir. 3)	1	0	0.200000	0.800000	0.800000
6	Curvilinear (F24: dir. 1,2,3)	1	0	0.200000	0.800135	0.800135

Table D-2 shows the result for the second set of boundary condition (imposed heat flux density on the lower wall, imposed temperature on the upper wall, and insulated everywhere else). Again, the theoretical solution was obtained in all cases except for the case having coordinate parameterization in all directions with a mean temperature error of -0.013% (from theoretical) on the lower surface. All cases satisfied energy balance self-consistently to no less than six significant digits.

Running the program with parameterization of any single coordinate at a time yields the theoretical solution to an accuracy of six significant digits as tested. (Obtaining more significant digits was not pursued, but it is possible up to the computer truncation error limited by the REAL*8 instruction by reducing the convergence tolerance.) Running the program with parameterization of all coordinates simultaneously may produce a small deviation from the theoretical solution. However, in all cases, heat balance was satisfied self-consistently to six significant digits. Energy balance was satisfied globally (whole domain), as well as locally (each cell).

Table D-2. Solutions for Imposed Heat Flux and Isothermal Walls

	Solution/Grid	(Calculated) Temperature at $X_2 = 0$	(Imposed) Temperature at $X_2 = 1$	(Calculated) Temperature at $X_2 = 0.5$	(Imposed) Heat Flux Through Plane at $X_2 = 0$	(Calculated) Heat Flux Through Plane at $X_2 = 1$
1	Theoretical	1.00000	0	0.200000	0.8	0.800000
2	Rectilinear	1.00000	0	0.200000	0.8	0.800000
3	Curvilinear (F24: dir. 1)	1.00000	0	0.200000	0.8	0.800000
4	Curvilinear (F24: dir. 2)	1.00000	0	0.200000	0.8	0.800000
5	Curvilinear (F24: dir. 3)	1.00000	0	0.200000	0.8	0.800000
6	Curvilinear (F24: dir. 1,2,3)	0.999869 (mean)	0	0.200000	0.8	0.800000

D.2. Convection Boundary Condition

A case was used to verify that the program processes correctly the convection boundary condition. The grid consisted of a single cubical cell, as shown in *Figure D-2*. The imposed-convection node temperature at $X^1 = 0$ was $T^c_{f1} = 1$. The imposed face node temperature at $X^1 = 1$ was $T_{f1} = 0$. The imposed energy flux density on all other faces was

$F_{f2} = 0$ at $X^2 = 0$,

$F_{f2} = 0$ at $X^2 = 1$,

$F_{f3} = 0$ at $X^3 = 0$, and

$F_{f3} = 0$ at $X^3 = 1$.

The cell-face conductance was set to G=2 from the cell node to all face nodes. The convection conductance was set to G=1 from the convection node to the convection face node. *Figure D-3* shows the equivalent resistor network.

The program calculates the cell-node temperature to be $Tc = 0.25$, as expected from the network solution, and the face temperatures at:

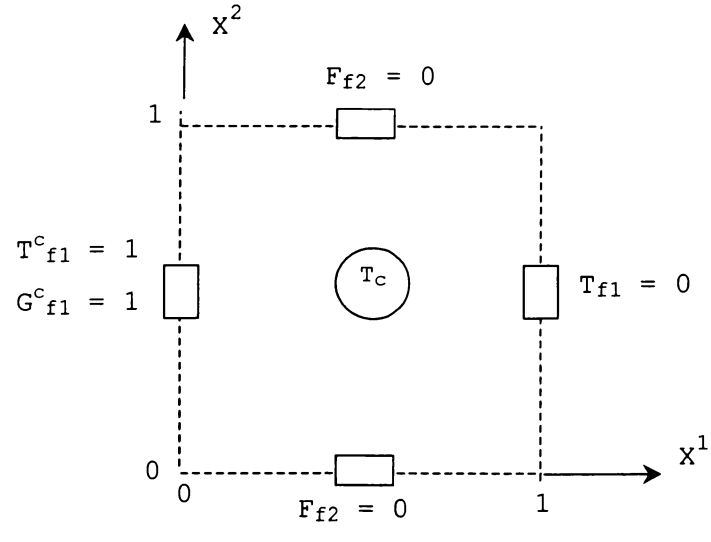

Figure D-2. Domain and Boundary Conditions for Checking the Solution with Convection Boundary Condition

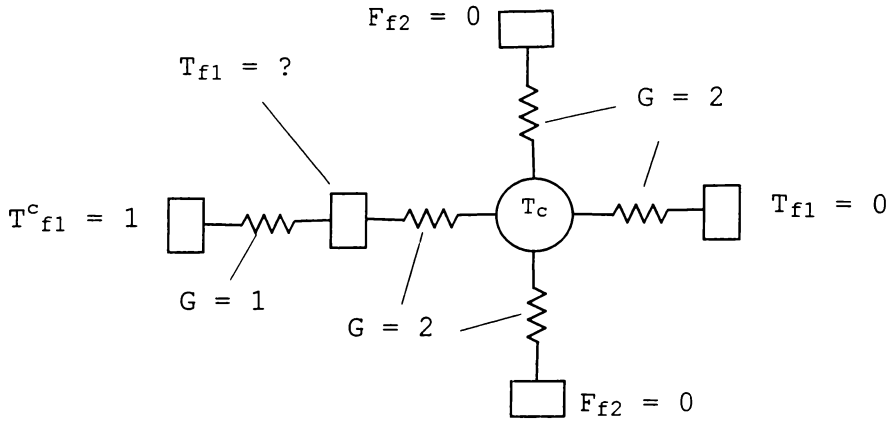

Figure D-3. Equivalent Resistor Network

$T_{f1} = 0.50$ at $X^1 = 0$,
$T_{f2} = 0.25$ at $X^2 = 0$,
$T_{f2} = 0.25$ at $X^2 = 1$,
$T_{f3} = 0.25$ at $X^3 = 0$, and
$T_{f3} = 0.25$ at $X^3 = 1$.

D.3. Self-Consistency between Curvilinear and Rectilinear Grids

Cases were run to compare solutions using rectilinear and curvilinear grids on the same physical domain. The case was that of natural convection heat transfer in a differentially heated vertical cubical enclosure. The left vertical wall was heated and the right wall was cooled. Both walls were isothermal. The top and bottom walls were insulated. Symmetry boundary conditions were applied to the front and back walls: insulated and normal velocity set to zero. The computational grid is shown in *Figure D-4*. Runs were made first on a rectilinear grid having 10 cells in the horizontal (left-to-right) and vertical directions, and 1 in the front-to-back direction. Then the number of cells was increased to 20, then 40, and finally 60 in each direction. Runs were repeated using a curvilinear grid inside the domain. In these cases, the parameterization was made for the vertical coordinate using a normalized sine function. The variables compared were heated wall minimum,

maximum, and mean Nusselt numbers and their respective locations on the left vertical wall, the vertical mid-plane maximum horizontal velocity, the horizontal mid-plane maximum vertical velocity, and the vertical mid-plane mean Nusselt number. Solution results from both the rectilinear and the curvilinear grid approach the benchmark solution with grid refinement, as shown in *Figure D-5* for centerline maximum velocities, and *Figure D-6* for the Nusselt number. The curvilinear grid produces larger deviations from the benchmark solution. The numerical solutions satisfy energy balance locally and globally. An excerpt of the program code with the coordinate parameterization function used to obtain the results for the curvilinear grid above is included in Listing D-1.

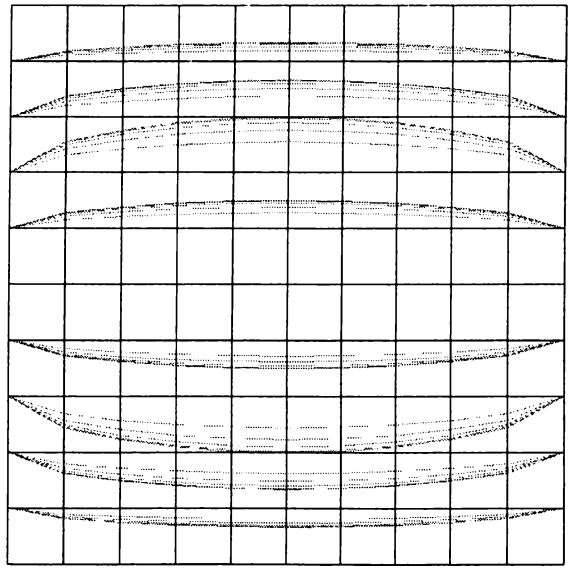

Figure D-4. Natural Convection Square Domain Enclosure with Superimposed 10x10 Rectilinear and Curvilinear Grids

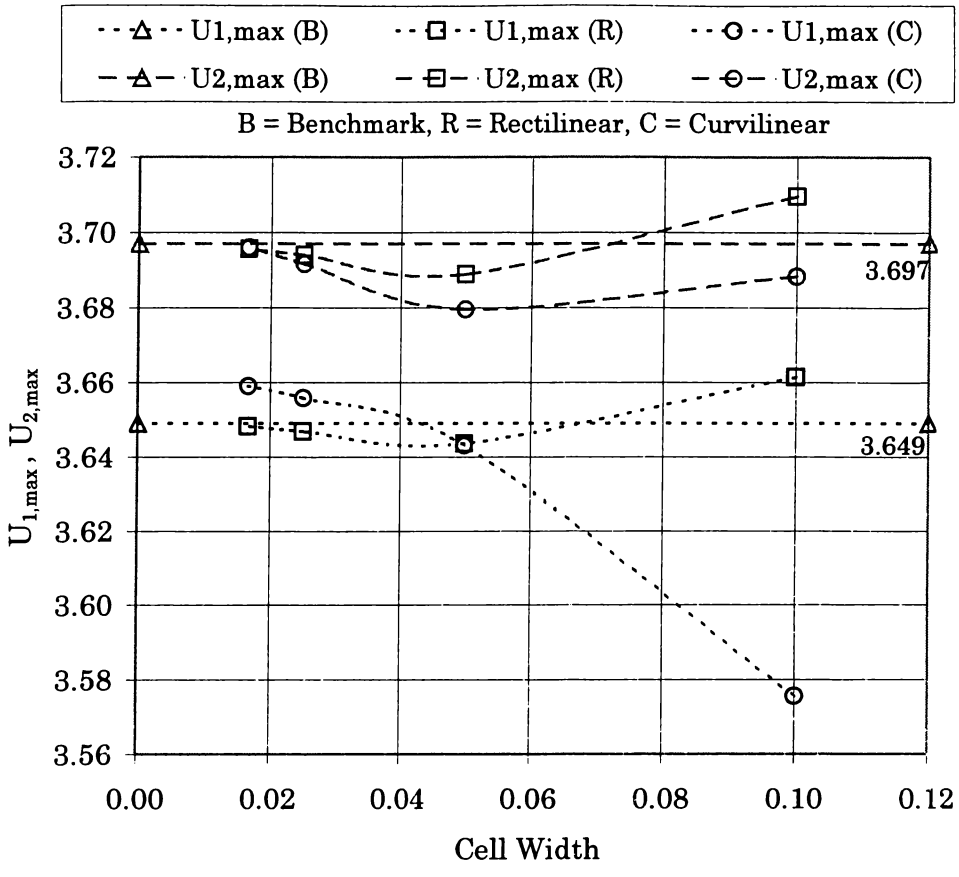

Figure D-5. Comparison of the Horizontal and Vertical Centerline Maximum Velocities for Solutions using Rectilinear and Curvilinear Grids

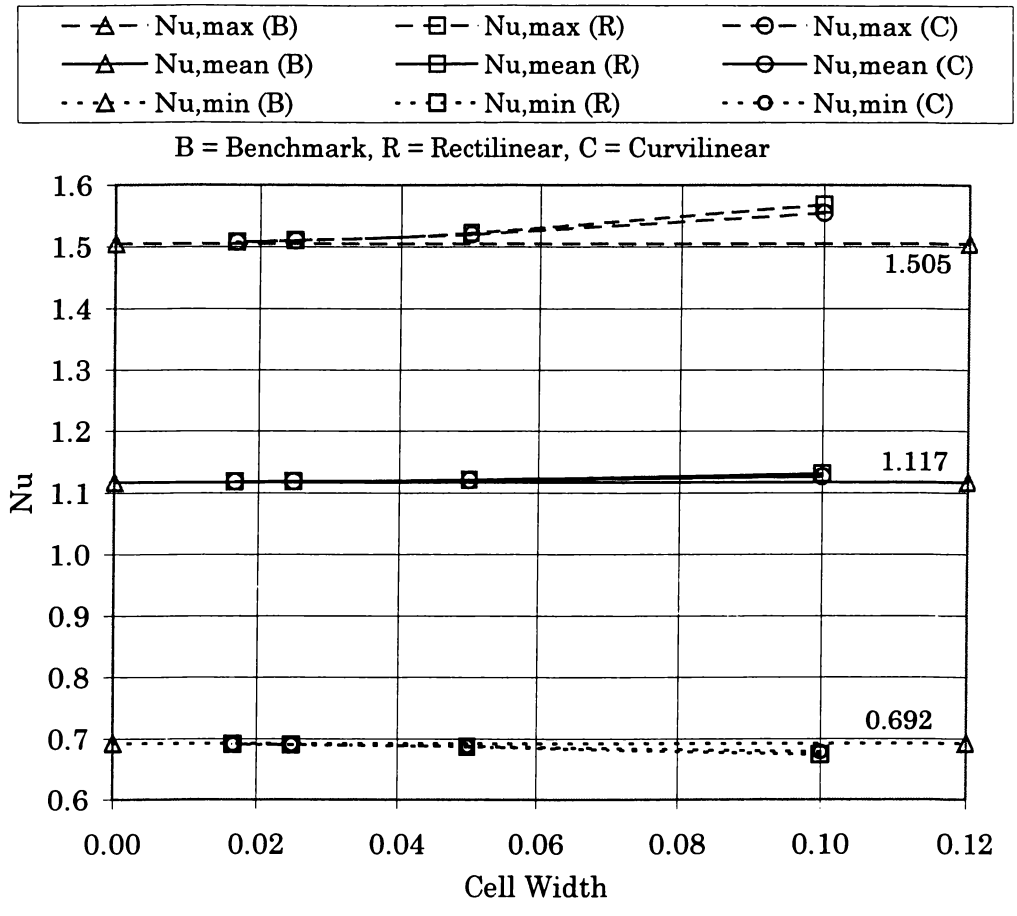

Figure D-6. Comparison of the Nusselt Number at the Heated-Wall from Rectilinear and Curvilinear Grid Solutions

Listing D-1. Parameterization Function for the Curvilinear Grid Used to Check Self-Consistency with the Rectilinear Grid Solution

```
! Parameterization #24
! J. A. Lamas, Jan 29, 2001
! 3-d sine wave transformation for Xi
! Symmetric about Yimid
! as a function of Y1,Y2,Y3
! Independent coordinate parameterization range
         Yi_mid = .5 ! mid symmetry plane
         Yi_min =  0.
         Yi_max = +1.
         Yj_min =  0.
         Yj_max = +1.
         Yk_min =  0.
         Yk_max = +1.
! Dependent coordinate parameterization range
         X_max = +1.0
         X_mid =  0.5
         X_min =  0.0
!  Determine the weighing function
         If ((Yj_min.lt.Yj).and.(Yj.lt.Yj_max) .and.
     &       (Yk_min.lt.Yk).and.(Yk.lt.Yk_max)) Then
           ! Apply sine function
           A = sqrt(
     &      sin(PI*(Yj-Yj_min)/(Yj_max-Yj_min))
     &     *sin(PI*(Yk-Yk_min)/(Yk_max-Yk_min)))
         Else      ! Constant
           A = 0.
         End If
         If (Yi.gt.Yi_mid) Then ! Parameterizing-function limits
          Xc_cntr=  0.8
          Xc_edge=  0.7
          X_c = Xc_cntr*A+ Xc_edge*(1.- A)
          Yic = Xc_edge ! mapping limiting curve location
          If (Yi_max.le.Yi) Then
            FX_ = Yi ! linear mapping
          Else If (Yic.lt.Yi .and. Yi.lt.Yi_max) Then
            FX_ = ((Yi-Yic)*X_max + (Yi_max-Yi)*X_c )/(Yi_max-Yic)
          ElseIf (Yi .eq. Yic) Then
            FX_ = X_c
          ElseIf (Yi_mid.lt.Yi .and. Yi .lt. Yic) Then
            FX_ = ((Yi-Yi_mid)*X_c + (Yic-Yi)*X_mid)/(Yic-Yi_mid)
          End If
         Else If (Yi.lt.Yi_mid) Then
          Xc_cntr=  0.2
          Xc_edge=  0.3
          X_c = Xc_cntr*A+ Xc_edge*(1.- A)
          Yic = Xc_edge ! mapping limiting curve location
          If (Yic.lt.Yi .and. Yi.lt.Yi_mid) Then
            FX_ = ((Yi-Yic)*X_mid + (Yi_mid-Yi)*X_c )/(Yi_mid-Yic)
          ElseIf (Yi .eq. Yic) Then
            FX_ = X_c
          ElseIf (Yi_min.lt.Yi .and. Yi .lt. Yic) Then
            FX_ = ((Yi-Yi_min)*X_c + (Yic-Yi)*X_min)/(Yic-Yi_min)
          ElseIf (Yi .le. Yi_min) Then
            FX_ = Yi ! linear mapping
          End If
         Else If (Yi.eq.Yi_mid) Then
            FX_ = Yi ! linear mapping
       End If
```

D.4. Calculation Checks on Natural Convection in Tilted Rectangular Enclosures

This case involves natural convection flow in a tilted differentially heated enclosure with a long third dimension [93], as shown in the *Figure D-7.* A two-dimensional domain was used to model the natural convection flow in enclosures of aspect ratios 3 and 4. The aspect ratio, A_R, is defined as the ratio of the heated/cooled wall dimension to the insulated wall dimension. The heated and cooled walls are parallel to each other, and are kept isothermal. The other two walls are insulated. The enclosure was tilted from 0° to 180° in 10° intervals. The tilt angle, ψ, is zero in the heated-from-below orientation. It must be pointed-out that according to experiments, fluid cells are longitudinal for tilt angles below 30°. As the model is 2-dimensional, cell rotation is forced to be transversal; therefore, good agreement is not expected with experimental data for this range of tilt angles. Three sets of Rayleigh and Prandtl numbers were used as shown in Table D-3. *Figure D-9* shows plots of the Nusselt number as a function of the tilt angle for the above runs.

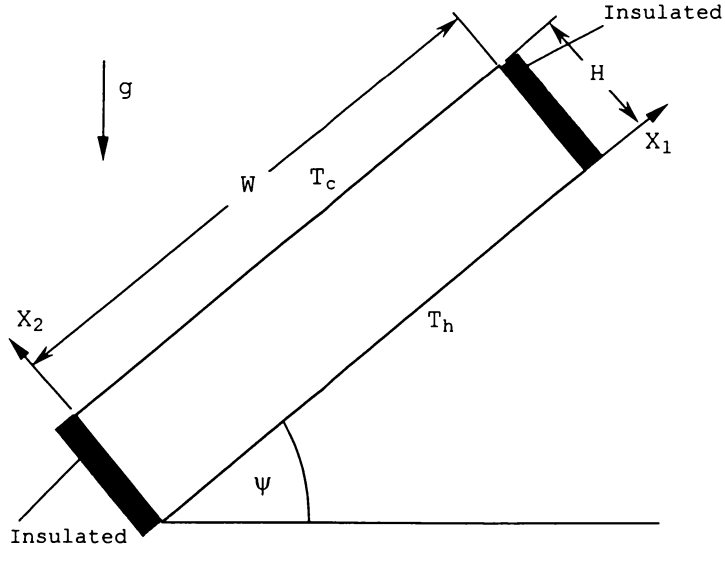

Figure D-7. Geometry and Boundary Conditions for the Case of Natural Convection in Tilted Rectangular enclosures

Table D-3. Rayleigh Number, Prandtl Number, and Aspect Ratio for Cases of Natural Convection in Tilted Enclosure

	Aspect Ratio 3		Aspect Ratio 4	
Set	Ra	Pr	Ra	Pr
1	4600	4270	3050	4300
2	20000	3880	6200	4200
3			16800	3900

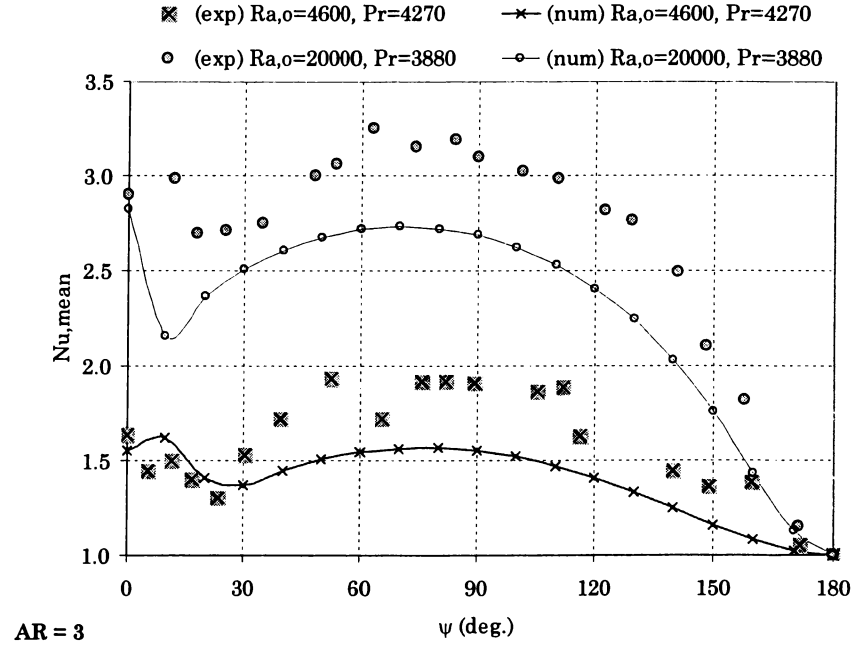

Figure D-8. Comparison between Present Numerical Results and Experimental Data in the Literature for Natural Convection in a Tilted Differentially Heated Rectangular enclosure of Aspect Ratio 3 and for Various Rayleigh and Prandtl Number Sets

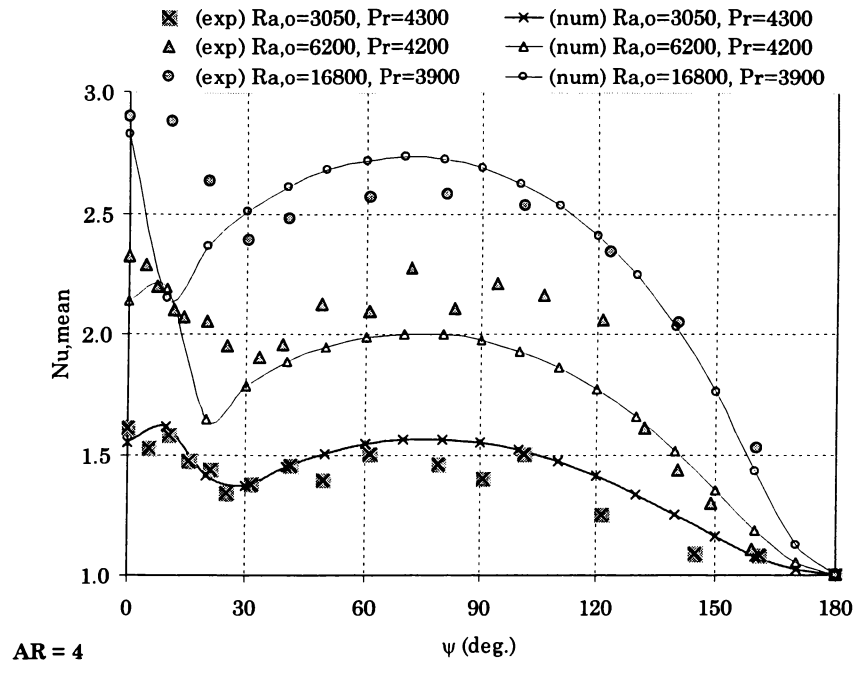

Figure D-9. Comparison between Present Numerical Results and Experimental Data in the Literature for Natural Convection in a Tilted Differentially Heated Rectangular enclosure of Aspect Ratio 4, and for Various Rayleigh and Prandtl Number Sets

D.5. Hydrostatic Check Run

This case is intended to validate the solution in the limiting case of a uniform temperature field with the temperature different from the Boussinesq reference temperature. The result should be a hydrostatic field with zero velocities.

D.5.1. Boundary and Operating Conditions

The domain orientation angle and boundary conditions are shown in *Figure D-10.* The domain was oriented to resemble the experimental hardware, tilted such that the major-base-plate axis was horizontal and the minor-base-plate axis made a 30°-angle with the horizontal, with the back surface facing downward. That is, the X_1-axis was horizontal and the X_2-axis was pointing 30° above the horizontal. All of the domain boundaries were insulated, and an initial temperature of 66°C was imposed on the entire computational domain.

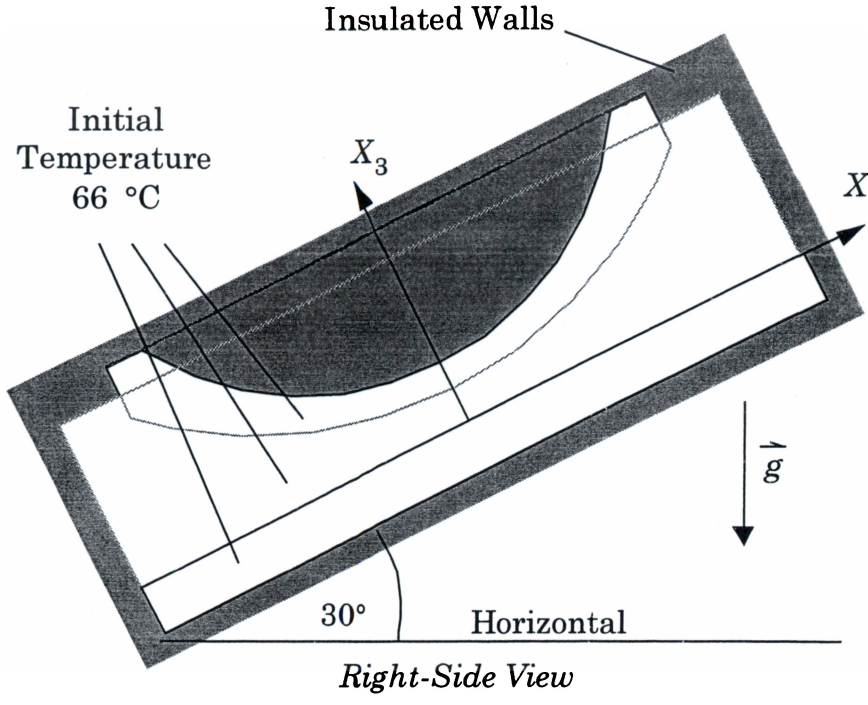

Figure D-10. Computational Model Orientation, Initial, and Boundary Conditions

Hydrostatic Solution Validation Criteria

The program will be considered validated for this limiting case, if it reproduces the hydrostatic field with a null velocity field and a hydrostatic pressure distribution. Since the numerical model will produce an approximation to the exact solution, a tolerance will be specified to judge the results. The numerical solution will be deemed acceptable if the maximum absolute value of the calculated velocity is less than 0.1% of a characteristic velocity, and the difference between the exact and calculated pressure gradient is within 0.1%. The characteristic velocity and exact pressure gradient are calculated next.

NATURAL CONVECTION VELOCITY UPPER BOUND

Any residual currents should have velocity magnitudes well below those from a characteristic natural-convection velocity. A value for the characteristic

natural-convection upper-bound velocity may be calculated by using the piezometric pressure head and Bernoulli's equation as

$$V_{max} = \sqrt{2\left(g\,\beta_o\,\Delta T_o\right)h} \tag{D.1}$$

where h is the characteristic head, calculated as the net elevation change between the lower most and upper-most fluid boundaries. A value for h can be obtained in terms of the previously defined dimensions as

$$h = 2L_2\sin(30°) + L_4\cos(30°) = 70.8\,mm. \tag{D.2}$$

The characteristic velocity is calculated as

$$\begin{aligned} V_{max} &= \sqrt{2\left(9.8\text{m/s}^2 \times 6.073\times10^{-4}\text{K}^{-1} \times 10\text{K}\right)\times\left(0.0708\text{m}\right)} \\ &= 9.18\,\frac{cm}{s} \end{aligned} \tag{D.3}$$

This would be the hypothetical exit velocity from an orifice at the top of a container immersed in a fluid at the reference temperature of 56 °C, and with the fluid in its interior set at 66 °C. A schematic of the concept is shown in *Figure D-11.* The magnitude of the maximum velocity resulting from the program solution should be well below this number, since the above estimate is made for an inviscid flow.

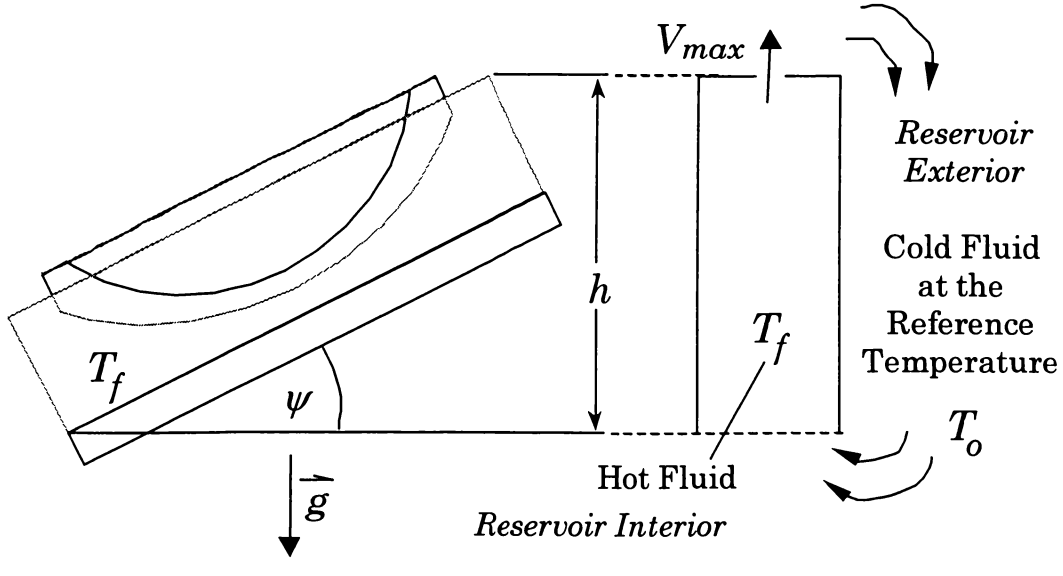

Figure D-11. Natural-Convection Upper-Bound-Velocity Scaling Model

HYDROSTATIC PRESSURE GRADIENT

Since the program uses the piezometric pressure for all calculations, a piezometric pressure gradient will be calculated for comparison against the numerical solution. The piezometric pressure has been defined as the difference between the static within the solution domain and the hydrostatic pressure in a reference field (see Eq. (5.34)). The exact solution for the piezometric pressure gradient is given as:

$$\nabla P = -\rho_o \, \vec{g} \, \beta_o \, \Delta T_o \,, \tag{D.4}$$

or for each individual coordinate direction,

$$\frac{\partial P}{\partial X_i} = -\rho_o \, g_i \, \beta_o \, \Delta T_o \,, \; i = 1,2,3 \,, \tag{D.5}$$

where

$$\begin{cases} \rho_o = 1134.5 \, \mathrm{kg/m^3} \\ \beta_o = 6.073 \times 10^{-4} \, \mathrm{K^{-1}} \\ \Delta T_o = 10.0 \, \mathrm{K} \end{cases} \tag{D.6}$$

and g_i are the components of the gravitational acceleration in X_i directions (i=1,2,3). If the domain is oriented in the same manner as during the experiments, that is, with the X_1-axis horizontal, and the X_2-axis pointing 30° above the horizontal, the following gravitational acceleration components are obtained:

$$\begin{cases} g_1 = 0 \, \mathrm{m/s^2} \\ g_2 = -4.9 \, \mathrm{m/s^2} \\ g_3 = -8.48707 \, \mathrm{m/s^2} \end{cases} \tag{D.7}$$

The values for the hydrostatic pressure gradient, and the static pressure gradient are provided for closure, and calculated as follows:

$$\frac{\partial P_{hs,o}}{\partial X_i} = -\rho_o \, g_i \;, \; i = 1,2,3 \,, \tag{D.8}$$

$$\frac{\partial P_s}{\partial X_i} = \frac{\partial P}{\partial X_i} + \frac{\partial P_{hs,o}}{\partial X_i} \quad , \quad i = 1,2,3 , \tag{D.9}$$

where $P_{hs,o}$ is the hydrostatic pressure at the reference field, and P_s is the static pressure in the solution field. The results for the above pressure gradient components are shown in Table D-4.

D.5.2. Program Run

The program was run in false-transient mode until steady state. That is, accurate convergence was not sought at each time step. All of the equations were solved, that is, mass, momentum, and energy. The energy equation was solved to ensure that there were no residual flux sources or sinks, and to make sure that the solution was stable in the limit of insulated boundaries with no internal heat generation.

Exit tolerances and limits on the number of iterations are shown in Table D-5. The pressure equation was solved using a successive over-relaxation (SOR) method. The SOR method uses a weighting factor between the "old" and the "new" solution to calculate the pressure: $P = (1-\omega)\, P^o + \omega\, P^n$, where ω is the over-relaxation factor, P^o is the "old" pressure solution, and P^n is the "new" pressure solution. A relaxation factor of ω=0.9 was used to solve the pressure equation. The time-step size was 0.1 s for the momentum equations and 1000 s for the energy

Table D-4. Exact Solution for the Hydrostatic Check Case

	i→	1	2	3
g_i	(m/s²)	0	-4.9	-8.48705
$\frac{\partial P}{\partial X_i}$	(Pa/m)	0	33.7601	58.4742
$\frac{\partial P_{hs,o}}{\partial X_i}$	(Pa/m)	0	-5559.0500	-9628.5570
$\frac{\partial P_s}{\partial X_i}$	(Pa/m)	0	-5525.2899	-9570.0828

equation. These were chosen differently for convenience, without invalidating the steady-state solution. The time step for the energy equation was chosen larger to accelerate convergence. This choice of time-step for the energy equation cuts the execution time to approximately one tenth, as compared to using the same time-step size for solving the momentum equations. The program was run on a Pentium IV Personal Computer with a clock speed of 1.5 GHz, and with 512 MB of RAM (Computer #3, see APPENDIX F.). The program ran using approximately 180 MB of RAM. Execution was complete in approximately 2.2 hours for 5000 time steps. Program results are shown in Table D-5.

Body Force and Momentum Generation

To verify consistency in the net amount of momentum generation rate, the exact value of the Boussinesq body force will be checked against program results. Table D-6 shows the parameters used in the calculation of the body force.

The mass of 0.137 kg is calculated from the exact volume and the fluid density. The components of the gravitational force (weight) acting in each coordinate direction is calculated as:

$$F^{u_i} = m\, g_i \,,\; i = 1,2,3\,. \tag{D.10}$$

Table D-5. Iteration Control: Exit Tolerances and Limits on the Number of Iterations

	Exit Tolerance	Maximum Number of Iterations
Transient Loop	10^{-4}	5000
Outer Loop	10^{-4}	1
Inner Loop:		
Temperature Solver	10^{-5}	1
Velocity Solvers	10^{-5}	1
Pressure Solver	10^{-7}	10

Table D-6. Inputs Used in the Calculation of the Net Body Force

Input Description	*Variable*	*Value*	*Units*
Fluid Volume (Cell Summation)	$\mathcal{V}$	120.862	cm^3
Fluid Mass Density	ρ	1134.5	kg/m^3
Fluid Mass (Cell Summation)	m	0.137	kg
Gravitational Acceleration	g	9.8	m/s^2
Tilt Angle	ψ	30.0	degrees
Volume Expansivity	β	6.073×10^{-4}	1/K
Fluid Temperature	T	56.0	°C
Boussinesq Reference Temperature	T_o	66.0	°C
Boussinesq Temperature Differential	ΔT_o	10.0	°C

The component of the force contribution due to buoyancy effects (Boussinesq body force), $F_B^{u_i}$, is calculated as:

$$F_B^{u_i} = -F^{u_i}\,\beta_o\,\Delta T_o,\ i = 1,2,3. \tag{D.11}$$

The body-force results from the above calculations are summarized in Table D-7.

D.5.3. Program Results

Energy and Momentum Balance

A summary of the quantities describing global energy and momentum balance is shown in Table D-8. A small storage error is an indication of steady state, while a small balance error is an indication of flux balance. Conservation equations for momentum and energy were satisfied, both locally and globally, as indicated by the small domain errors. The net rate of momentum generated within the solution domain, as reported by the program, is consistent with the theoretical (exact) value of the Boussinesq body-force calculated previously, as evidenced by the -0.03% error (last line in the table).

Table D-7. Calculation of the Net Body-Force in Each Coordinate Direction

			Cartesian Direction, i		
			1	2	3
Variable	*Symbol*	*Units*			
Gravitational Acceleration Component	g_i	(m/s²)	0.0	-4.9	-8.487049
Gravitational Force (Weight) Component	F^{u_i}	(mN)	0.0	-671.9	-1163.7
Boussinesq Body Force Component	$F_B^{u_i}$	(mN)	**0.000**	**4.080**	**7.067**

Maximum Velocity

The maximum cell-node velocity magnitude was reported by the program at 0.5×10^{-13} cm/s (at coordinates X_1= 23.6 mm, X_2= 29.8 mm, and X_3= 17.6 mm). The error is 5.4×10^{-13} %, based on the upper bound of 9.18 cm/s calculated above.

Pressure Gradient

The maximum and minimum values of the pressure gradient at cell nodes were extracted from the solution. The results are shown for the three directions in Table D-9. The pressure calculated by the program and the exact value match to at least six significant figures. This yields an error no greater than 1.5×10^{-4} %.

Isobars and Pressure Distribution

Isobars of the piezometric pressure, hydrostatic pressure, and static pressure are shown in *Figure D-12.* All isobars are horizontal, as expected. Plots of variations of the piezometric pressure and the hydrostatic pressure on the base-plate surface, along the X_2-coordinate are in *Figure D-13.* The static pressure wasn't shown as it virtually overlaps the hydrostatic reference pressure. As the X_2-coordinate increases, the hydrostatic pressure decreases, while the piezometric pressure increases. Both vary linearly, as expected for a hydrostatic field.

Table D-8. Hydrostatic Problem: Flux Balance and Body-Force

Dependent Variable, $\phi \rightarrow$		t	u_1	u_2	u_3
Variable	*Symbol*				
Cell Storage Error	$\varepsilon_c^{\phi,sto} \times 10^{12}$	---	0.080	0.005	0.000
Cell Balance Error	$\varepsilon_c^{\phi,bal} \times 10^{12}$	---	0.280	0.033	0.001
		(W)	(mN)	(mN)	(mN)
Net, Boundary Influx	$F_d^{\phi,in}$	0.000	2.601	1.159	2.515
Net, Boundary Efflux	$F_d^{\phi,out}$	0.000	2.601	5.238	9.580
Net, Stored	$F_d^{\phi,sto} \times 10^{15}$	0.004	0.019	5.201	-0.050
Net, Generated	$F_d^{\phi,gen}$	0.000	**0.000**	**4.079**	**7.065**
Flux Balance	$F_d^{\phi,bal} \times 10^{15}$	0.000	-3.4	-207.3	978.1
Domain Storage Error	$\varepsilon_d^{\phi,sto} \times 10^{15}$	---	0.007	0.993	0.005
Domain Balance Error	$\varepsilon_d^{\phi,bal} \times 10^{15}$	---	1.3	39.6	102.1
Boussinesq Body Force (BBF) Exact Value ($BBF_i = - m g_i \beta \Delta T_o$)	BBF_i	(mN)	**0.000**	**4.080**	**7.067**
Boussinesq Body Force Error (BBFE) ($BBFE_i = F_d^{u_i,gen}/BBF_i - 1$)	$BBFE_i$	(%)	0.00%	-0.03%	-0.03%

Table D-9. Pressure Comparison against the Exact Solution

Coordinate Direction	i→	1	2	3
Exact Solution $\frac{\partial P}{\partial X_i}$ (Pa/m)		0	33.7601	58.4742
Numerical Result $\frac{\partial P}{\partial X_i}$ (Pa/m)	max.	0.154357×10^{-10}	33.7601	58.4742
	min.	$-.996600 \times 10^{-11}$	33.7601	58.4742

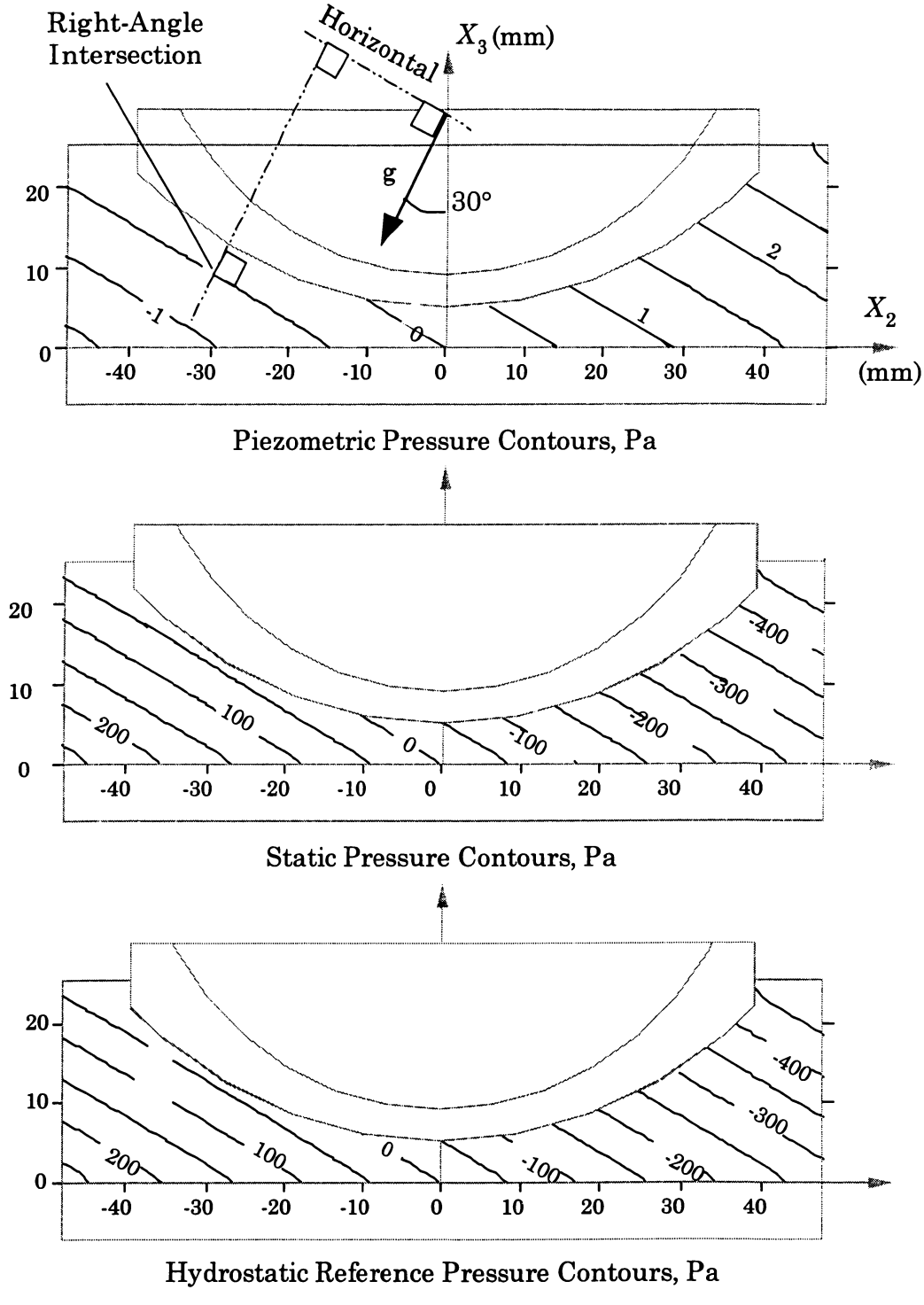

Figure D-12. Isobars on the Vertical Symmetry Plane

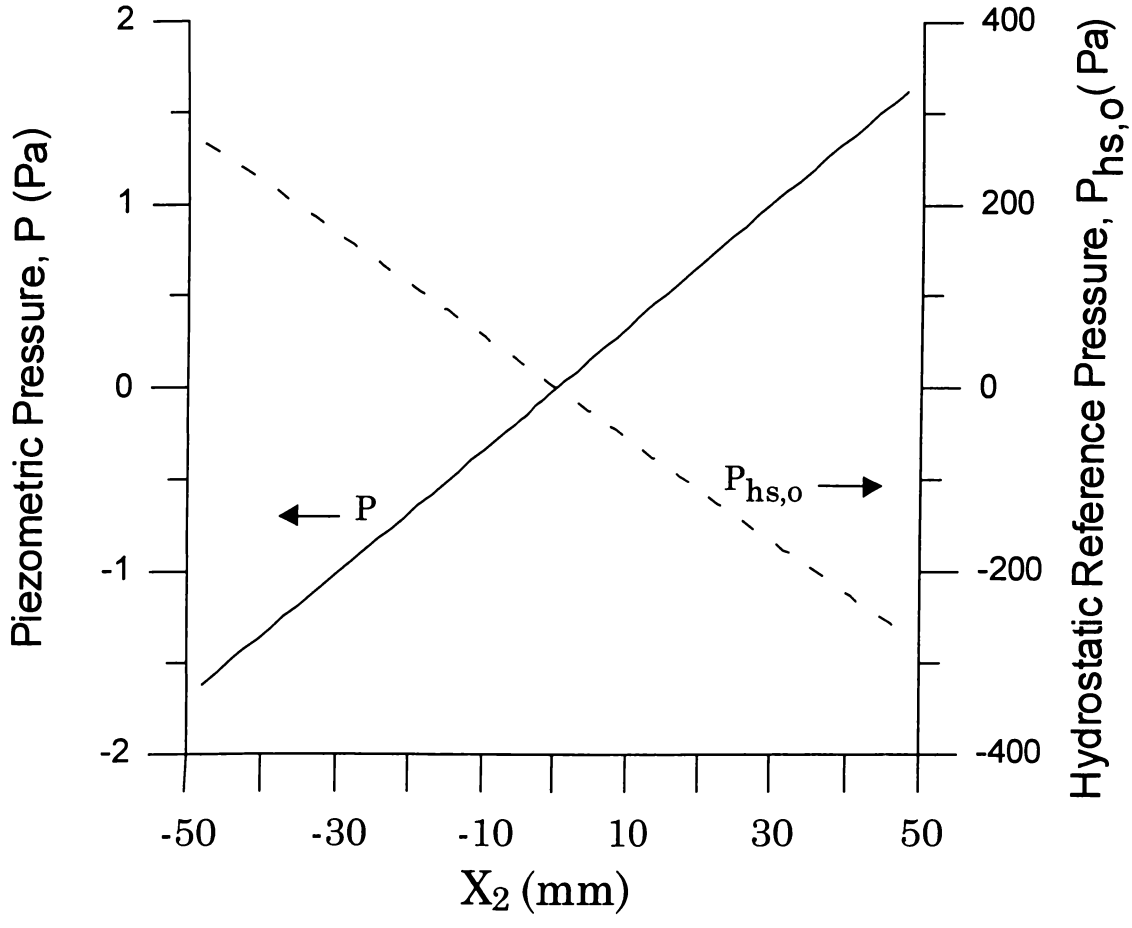

Figure D-13. Pressure Profiles along the Base Plate Slope

D.5.4. Summary of Results for the Hydrostatic Check Case

The results calculated by the code for the hydrostatic check case reproduce the exact results with a very high degree of accuracy. This is necessary to ensure that residual flows from flux imbalance resulting from the distorted, non-orthogonal grid would not affect the natural convection flows. The above results have increased the level of confidence for the cases of interest in this investigation, by reassuring that the program is self-consistent in the hydrostatic limit. Since all of the geometry and thermophysical properties have already been specified, it only remains to specify the thermal boundary conditions for the benchmarking case.

APPENDIX E. APPROXIMATION OF EXPERIMENTAL BOUNDARY CONDITIONS AS INPUTS TO THE NUMERICAL MODEL

E.1. CRT Face Panel Light Conversion Efficiency

The validation of the mathematical model requires the heat generation rate distribution on the phosphor screen. A direct measurement of this parameter could not be made. Instead, the total input power to the electron beam was available. The following calculations are made to estimate the fraction of the electron beam power that is converted into light. Once this is done, the rate of heat generation becomes available if one assumes that the power fraction converted into X-rays is negligible. The calculations are based on the Hitachi Projection Tube 180AXB22(G) Customer's Acceptance Specifications [15].

Data was available from N.A.P. for the radiance of the green picture tube[1] along with spectral power distribution plot. Data for radiance indicated 4800 cd/m^2 at an anode current of 200 μA. The anode voltage was assumed 28 kV, and the raster area was assumed to have dimensions of 102 mm (width) by 76 mm (height), as required by the tube manufacturer (Hitachi) for testing. The luminous flux could be calculated as the product of the radiance and the raster area:

$$P_v = L_v \times A_{RASTER} = 233.8 \text{ lm}, \qquad (E.1)$$

where

P_v is the luminous flux,

L_v is the radiance (4800 cd/m^2), and

A_{RASTER} is the raster surface area = 0.007752 m^2.

Since the present experiment used a different anode current, a scaling of the radiance was necessary. This was done by using data available for the radiance as a function of the peak cathode current. The tables below show radiance as a function

[1] NAPCEC, Personally handed information (1987)

of peak cathode current from tube specifications, and the scaled radiance for average anode current.

Peak Cathode Current	*Radiance*		*Average Current*	*Radiance*
(μA)	(ft-L)		(μA)	(ft-L)
0.2	1550		0.2	1401
0.5	5200		0.5	4700
1	10000		1	9039

Resulting curve fit for the radiance as a function of the average anode current:

$$L_v = -2899.9\, I_k^2 + 13027\, I_k - 1088.4, \qquad \text{(E.2)}$$

where I_k is the anode current in mA and L_v is the radiance in ft-L.

Substituting the experimentally determined anode current of 510 mA in the above equation results in an estimated radiance, L_v of

$$L_v = 4801 \text{ ft-L } (= 4801 \times 3.426 \text{ cd/m}^2 = 16449 \text{ cd/m}^2). \qquad \text{(E.3)}$$

Now, the luminous intensity can be obtained:

$$I_v = L_v\, A_R = 16449 * 0.007752 \text{ cd} = 127.51 \text{ cd}. \qquad \text{(E.4)}$$

The luminous flux can be obtained from the luminous intensity as

$$P_v = 2\pi\, I_v = 2\pi\, 127.51 \text{ lm} = 801.2 \text{ lm}. \qquad \text{(E.5)}$$

At this stage, the luminous flux is known as 801.2 lm, but a connection must be made to power. To calculate the power emitted as light, the definition of the candela (cd) is applied, which states that one Watt of radiant flux from a light source at a wavelength of 555 nm produces 683 lumens of luminous flux (lm). If P is the total power in the light emitted, and all of the light was emitted at 555 nm, then the luminous flux would be calculated as

$$P_v = (683 \text{ lm/W}) P. \qquad \text{(E.6)}$$

However, not all of the light is emitted at 555 nm. Light emitted at wavelengths other than 555 nm produces a smaller amount of lumens per Watt. This amount is dictated by the product of spectral power of the light emitted, P_λ, by the spectral

luminous efficiency for photopic vision, $V(\lambda)$. To cover the whole range of wavelengths, this product is integrated over the visible range.

$$P_v=(683\ \text{lm/W}) \int_{350}^{750} P_\lambda \times V(\lambda)\ d\lambda\ , \tag{E.7}$$

where P_λ is the spectral power in W/nm, and $V(\lambda)$ is the spectral luminous efficiency for photopic vision:

$$V(\lambda) = \exp(-285.4(\lambda-0.559)^2). \tag{E.8}$$

The relative spectral power, R_λ, is available as a distribution function in the form of a plot. *Figure E-1* shows the data and the spectral luminous efficiency. We may express the spectral power in terms of the peak spectral power and the relative spectral power as follows:

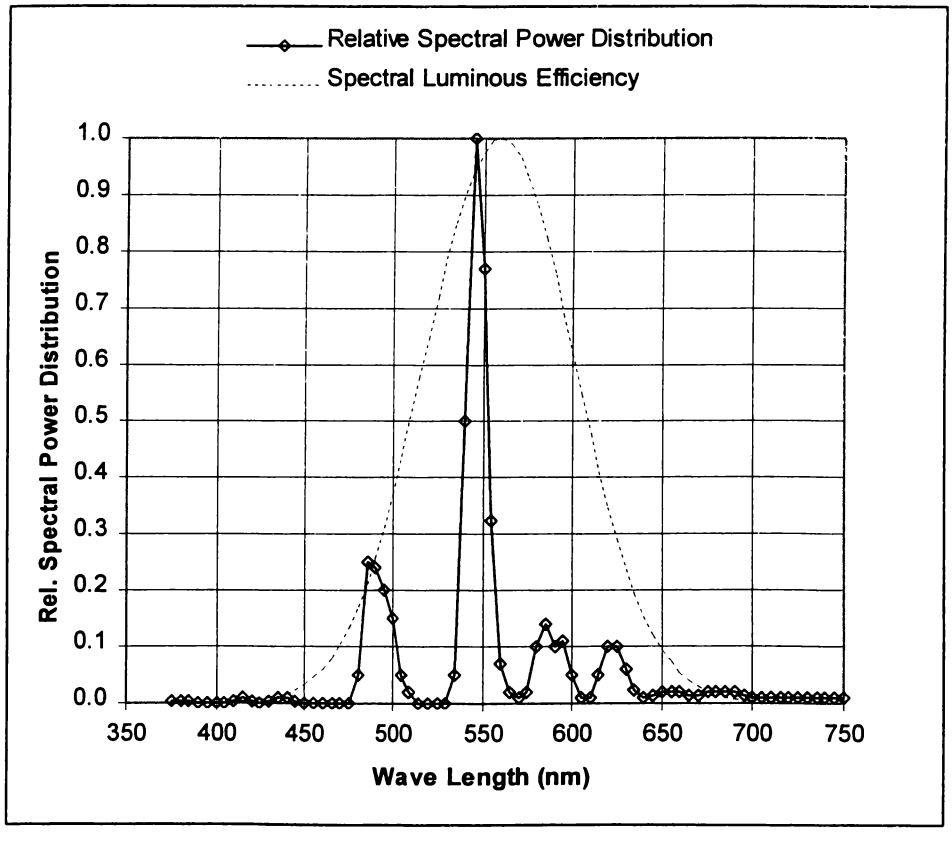

Figure E-1. Spectral Power Distribution

$$P_\lambda = R_\lambda \times P_{max} \tag{E.9}$$

substituting in Eq. (E.7) yields

$$P_v = P_{max}\ (683\ \text{lm/W}) \int_{350}^{750} R_\lambda \times V(\lambda)\ \mathrm{d}\lambda\ , \tag{E.10}$$

and solving for P_{max} yields

$$P_{max} = \frac{Pv}{(683\ \text{lm/W}) \int_{350}^{750} R_\lambda \times V(\lambda)\ \mathrm{d}\lambda}\ . \tag{E.11}$$

Integrating the above equation with P_v = 233.8 lm, results in the value of P_{max} = 0.06869 W/nm. Once P_{max} is known, the power can be found by integration:

$$P = P_{max} \int_{350}^{750} R_\lambda\ \mathrm{d}\lambda = 1.42\ \text{W} \tag{E.12}$$

The light conversion efficiency can be calculated as the ratio of visible-light power to input power to the electron gun. With the input power from the present experimental measurements calculated at 14.2 Watts (Appendix B), the light conversion efficiency can be calculated as

$$\eta = \frac{P}{P_{input}} = \frac{1.42}{14.2} = 10\% \tag{E.13}$$

E.2. Radiation Heat Transfer through the CRT Face Panel Glass

Heat radiation through the glass is a complex problem, as it involves a participating media. To estimate the order of magnitude of heat transfer through the glass, some simplifications can be made. It will be assumed that only the back surface of the face panel emits radiation heat. Internal layers only allow transmission, and do not emit radiative heat. To obtain an upper bound on the forward radiation component, the emissive power at the back surface will be used.

This is the same as saying that no radiation travels in the opposite direction. A schematic of the model is shown below.

The blackbody spectral emissive power is given by the following equation [48]

$$E_{\lambda,b}(\lambda,T)=\frac{C_1}{\lambda^5\left[\exp\left(\frac{C_2}{\lambda\cdot T}\right)-1\right]} \tag{E.14}$$

where $C_1 = 3.742 \times 10^8$ W· μm^4/m^2 and $C_2 = 1.439 \times 10^4$ μm·K. To obtain the net heat radiation forward, the above equation is substituted in the following equation,

$$\dot{q}''_{rad} = \int_{\lambda=0}^{\lambda=\infty} E_{\lambda,b}(\lambda,T)\cdot\tau_\lambda \, d\lambda, \tag{E.15}$$

where τ_λ is the glass transmittance.

The spectral transmittance for a fused-quartz plate of 6 mm in thickness drops from approximately 0.9 at $\lambda \approx 3$ μm to zero at $\lambda \approx 5$ μm, and remains zero thereafter [48]. This information may be used, as the thickness is similar to the one in the present problem. The figure below shows the black-body emissive power for a temperature of 344 K and an approximation for the spectral transmittance above.

Integrating Eq. (E.15) yields a net heat flux density of 8.5 W/m^2, which is only 0.5 % of the nominal flux of 1650 W/m^2. It may be concluded that radiation through the glass is small enough that it may be neglected. Table E-1 shows the numerical values used in the above calculations.

Table E-1. Black-body Emissive Power and Glass Transmittance Used to Estimate Heat Radiation through the Face-Panel Glass

λ	$E_{\lambda,b}$(344K)	τ_λ	Cumulative Flux
μm	W/m^2-μm		W/m^2
1.5	3.87E-05	0.9	0
1.6	1.60E-04	0.9	8.93E-06
1.7	5.49E-04	0.9	4.08E-05
1.8	1.62E-03	0.9	1.38E-04
2.0	9.75E-03	0.9	1.16E-03
2.2	4.05E-02	0.9	5.68E-03
2.4	1.28E-01	0.9	2.08E-02
2.6	3.27E-01	0.9	6.17E-02
2.8	7.12E-01	0.9	1.55E-01
3.0	1.36E+00	0.9	3.42E-01
3.2	2.36E+00	0.85	6.68E-01
3.4	3.76E+00	0.8	1.17E+00
3.6	5.59E+00	0.75	1.90E+00
3.8	7.87E+00	0.7	2.87E+00
4.0	1.06E+01	0.6	4.07E+00
4.2	1.36E+01	0.5	5.40E+00
4.4	1.69E+01	0.3	6.62E+00
4.6	2.05E+01	0.2	7.56E+00
4.8	2.42E+01	0.1	8.23E+00
5.0	2.80E+01	0	8.49E+00
5.2	3.17E+01	0	8.49E+00
5.4	3.54E+01	0	8.49E+00
5.6	3.89E+01	0	8.49E+00
5.8	4.22E+01	0	8.49E+00
6.0	4.53E+01	0	8.49E+00
6.2	4.82E+01	0	8.49E+00
6.4	5.08E+01	0	8.49E+00
6.6	5.31E+01	0	8.49E+00
6.8	5.51E+01	0	8.49E+00
7.0	5.68E+01	0	8.49E+00
7.2	5.83E+01	0	8.49E+00
7.4	5.95E+01	0	8.49E+00
7.6	6.05E+01	0	8.49E+00
7.8	6.12E+01	0	8.49E+00
8.0	6.17E+01	0	8.49E+00

E.3. Effective Heat Transfer Coefficient for the CRT Face Panel Back

A conductor network model for heat transfer from the CRT face panel back to the environment is shown in *Figure E-2.* An excerpt of the worksheet used to calculate the thermal conductance values and the effective heat transfer coefficient based on this model is shown in

Listing E-1.

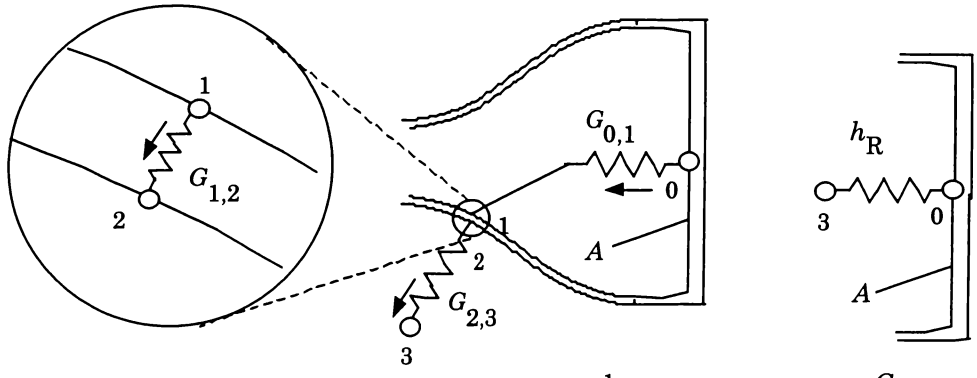

$$G_{0,3} = \left[\frac{1}{G_{0,1}} + \frac{1}{G_{1,2}} + \frac{1}{G_{2,3}} \right]^{-1} \qquad h_R = \frac{G_{0,3}}{A}$$

Figure E-2. Network Model for Heat Transfer from the Face Panel Back to the Environment

Listing E-1. Calculations of the Linearized Heat Transfer Coefficient for Heat Transfer from the Face Panel Back to the Environment

Col	2	3	4	5	6	7
Row						
4	CRT face panel front surface width	Wf	0.15	0.15	0.15	m
5	CRT face panel front surface height	Hf	0.122	0.122	0.122	m
6	Interior					
7	CRT face panel back surface width	Wb	0.142	0.142	0.142	m
8	CRT face panel back surface height	Hb	0.114	0.114	0.114	m
9	Distance from CRT face panel back surface to neck	L	0.14	0.14	0.14	m
11	Temperature on CRT face panel back surface	T_0	61.0	71.0	81.0	C
12	Temperature on CRT interior surface	T_1	43.3	49.3	55.8	C
13	Temperature on CRT exterior surface	T_2	43.0	48.9	55.3	C
14	Environmental temperature	T_3	24.0	24.0	24.0	C
15	Stefan-Boltzmann constant	Sigma	5.67E-08	5.67E-08	5.67E-08	W/m2-K4
16	Emissivity of CRT face panel back surface	Emiss_1	1	1	1	
17	View factor from CRT face panel back surface	F_01	1	1	1	
18	Area of CRT face panel back surface	A_0	0.016188	0.016188	0.016188	m2
19	CRT wall thermal conductivity	k	0.79	0.79	0.79	W/m-K
20	CRT Wall Thickness	Lw	0.004	0.004	0.004	m
21	CRT wall conduction area	A_12	0.03936	0.03936	0.03936	m2
22	Convection coefficient -- CRT ext. surface to environment	h_23	3	3	3	W/m2-K
23	Surface emissivity of CRT exterior surface	Emiss_2	1	1	1	
24	View factor from CRT exterior surface	F_23	1	1	1	
25	Area of CRT exterior surface	A_2	0.03936	0.03936	0.03936	m2
26	Thermal Conductance from CRT face panel back surface to int. surface	G_01	0.126279	0.135915	0.14626	W/C
27	Thermal Conductance from CRT int. surface to ext. surface	G_12	7.773531	7.773531	7.773531	W/C
28	Thermal Conductance from CRT ext. surface to environment	G_23	0.118079	0.118079	0.118079	W/C
29	Heat rate from CRT face panel back surface to int. surface	q_01	2.240179	2.945766	3.692982	W
30	Heat rate from CRT int. surface to ext. surface	q_12	2.240179	2.945766	3.692982	W
31	Heat rate from CRT ext. surface to environment	q_23	2.240179	2.945766	3.692982	W
32		G_03	0.060545	0.062676	0.064789	W/C
33		Aref	0.016188	0.016188	0.016188	m2
34	**Effective Heat Transfer Coefficient**	**h_eff**	3.740	**3.872**	4.002	**W/m2-K**
36	Gross, input		14.2	14.2	14.2	W
37	Light Conversion efficiency		0.1	0.1	0.1	
38	Net, input (as heat transfer)		12.8	12.8	12.8	W
39	heat transfer to back		2.2	2.9	3.7	W
40	heat transfer to front		10.5	9.8	9.1	W
41	heat transfer to front % of Net input		82.5%	77.0%	71.1%	

The linearized radiation heat transfer coefficient is obtained as follows. Let the heat flux density due to radiation be written as

$$\dot{q}'' = F\varepsilon\sigma(T_h^4 - T_c^4) = F\varepsilon\sigma(T_h^2 + T_c^2)\times(T_h + T_c)\times(T_h - T_c)\,. \tag{E.16}$$

This equation can be rewritten as

$$\dot{q}'' = h\times(T_h - T_c)\,, \tag{E.17}$$

where h is the linearized heat transfer coefficient, calculated as

$$h = F\varepsilon\sigma(T_h^2 + T_c^2)\times(T_h + T_c)\,. \tag{E.18}$$

Listing E-2. Program Code for the Calculation of the Net Heat Transfer Coefficient from the Face Panel Back to the Environment

```
Note: The format for the input function "Cells", below, is Cells(irow,icol), where irow
          is the row number and icol is the column number in the calculation worksheet.
Sub Button_SolveCRTBack()
  Application.ScreenUpdating = False

   T_0 = Cells(11, 4) + 273 'K
   T_3 = Cells(14, 4) + 273 'K
   Sigma = Cells(15, 4) 'W/m2-K4
   Eps_1 = Cells(16, 4)
   F_01 = Cells(17, 4)
   A_0 = Cells(18, 4)
   k = Cells(19, 4)
   Lw = Cells(20, 4)
   A_12 = Cells(21, 4)
   h_23 = Cells(22, 4)
   Eps_2 = Cells(23, 4)
   F_23 = Cells(24, 4)
   A_2 = Cells(25, 4)
   Call SolveCRTBack(T_0, T_3, Sigma, Eps_1, F_01, A_0, k, Lw, A_12, _
  h_23, Eps_2, F_23, A_2, T_1, T_2, G_01, G_12, G_23, q_01, q_12, q_23)
   Cells(12, 4) = T_1 - 273 'C
   Cells(13, 4) = T_2 - 273 'C
   Cells(26, 4) = G_01 'W/C
   Cells(27, 4) = G_12 'W/C
   Cells(28, 4) = G_23 'W/C
   Cells(29, 4) = q_01 'W
   Cells(30, 4) = q_12 'W
   Cells(31, 4) = q_23 'W
  Application.StatusBar = "Ready"
  Application.ScreenUpdating = True

  End Sub
  Sub SolveCRTBack(T_0, T_3, Sigma, Eps_1, F_01, A_0, k, Lw, A_12, _
  h_23, Eps_2, F_23, A_2, T_1, T_2, G_01, G_12, G_23, q_01, q_12, q_23)
  T_1 = 2 / 3 * (T_0 - T_3) + T_3
  T_2 = 1 / 3 * (T_0 - T_3) + T_3
  i = 0
  imax = 100000
  Tol = 0.00000001
Label_1:
   i = i + 1
   If (i < imax) Then
    G_01 = F_01 * Sigma * Eps_1 * (T_0 ^ 2 + T_1 ^ 2) * (T_0 + T_1) * A_0
    G_12 = k / Lw * A_12
    Gc_23 = h_23 * A_2
    Gr_23 = F_02 * Sigma * Eps_2 * (T_2 ^ 2 + T_3 ^ 2) * (T_2 + T_3) * A_2
    G_23 = Gc_23 + Gr_23

    T_1 = (T_0 * G_01 + T_2 * G_12) / (G_01 + G_12)
    T_2 = (T_1 * G_12 + T_3 * G_23) / (G_12 + G_23)
    q_01 = G_01 * (T_0 - T_1)
    q_12 = G_12 * (T_1 - T_2)
    q_23 = G_23 * (T_2 - T_3)
    If (Abs(q_23 / q_01 - 1) > Tol) Then GoTo Label_1
   End If
  End Sub
```

E.4. Base Plate Side Boundary Conditions

Enclosure Side Wall			Lower	Lateral	Upper
Boundary No.			4	5	6
Air Heat Transfer					
Gravitational Acceleration	g	m/s2	9.8	9.8	9.8
Volume Expansivity	beta	1/C	0.002463	0.00246305	0.002463
Surface Temperature	Ts	C	52	52	52
		K	325	325	325
Air Temperature	Ta	C	22	22	22
		K	295	295	295
Film Temperature	Tavg	C	133	133	133
		K	406	406	406
Kinematic Viscosity	nu	m2/s	1.60E-05	1.60E-05	1.60E-05
Thermal Diffusivity	alpha	m2/s	2.30E-05	2.30E-05	2.30E-05
Thermal Conductivity	k	W/m-K	2.63E-02	2.63E-02	2.63E-02
Prandtl Number	Pr		6.96E-01	6.96E-01	6.96E-01
Characteristic Length	L	m	0.15	0.122	0.15
Rayleigh Number	Ra		6.64E+06	3.57E+06	6.64E+06
Nusselt Number	NuL		13.70647	11.7388893	2.74E+01
Heat Transfer Coefficient	h_conv	W/m2-K	2.40E+00	2.53E+00	4.81E+00
Face Panel Heat transfer					
Conduction Length	Lc	m	0.0123	0.0138	0.0123
Thermal Conductivity	k	W/m-K	7.90E-01	7.90E-01	7.90E-01
Heat Transfer Coefficient	h_cod	W/m2-K	6.42E+01	5.72E+01	6.42E+01
Net Heat Transfer Coefficient	h_net	W/m2-K	2.32	2.42	4.47

E.5. Effective Heat Transfer Coefficient for the Meniscus-Wall Front Surface

The equation below was used to obtain the Nusselt number for free convection heat transfer on a vertical plate [48]. Calculation results are shown in Table E-2.

$$\overline{Nu}_L = 0.68 + \frac{0.670\mathrm{Ra}^{1/4}}{\left[1+\left(\frac{0.492}{\mathrm{Pr}}\right)^{9/16}\right]^{4/9}}. \qquad \text{(E.19)}$$

Table E-2. Calculations of the Linearized Heat Transfer Coefficient for Heat Transfer from the Face Panel Back to the Environment

Acceleration of Gravity	g	9.8	m/s2
Volume Expansivity	beta	0.002463	1/C
Surface Temperature	Ts	52	C
		325	K
Air Temperature	Ta	22	C
		295	K
Average (Film) Temperature	Tavg	133	C
		406	K
Characteristic Length	L	0.08	m
Kinematic Viscosity (air)	nu	1.60E-05	m2/s
Thermal Diffusivity (air)	alpha	2.30E-05	m2/s
Thermal Conductivity (air)	k	2.63E-02	W/m-C
Rayleigh Number	Ra	1.01E+06	
Prandtl Number	Pr	6.96E-01	
Nusselt Number (based on L)	NuL	16.93487	
Convection Coefficient	h_conv	5.57E+00	W/m2-C
Stefan-Boltzmann Constant	sigma	5.67E-08	W/m2-K4
Emissivity	emmis	1	
Linearized Radiation Coefficient	h_rad	6.77E+00	W/m2-C

Net Heat Transfer Coefficient	h_net	1.23E+01	W/m2-C

APPENDIX F. COMPUTER SETUP

All computer runs in this dissertation were made using the computers shown below.

Computer #	1	2	3	4
Motherboard Brand/Model	SuperMicro P6DLS	SuperMicro P6DLS	Abit TH7-RAID	Abit VP6
CPU	Pentium II	Pentium II	Pentium 4	Pentium III
Quantity	2	2	1	2
Clock Speed	233 MHz	333 MHz	1.5 GHz	933 MHz
Bus Speed	66 MHz	66 MHz	400 MHz	133 MHz
RAM	512 MB SDRAM	512 MB SDRAM	512 MB PC800 RDRAM	512 MB PC133 SDRAM

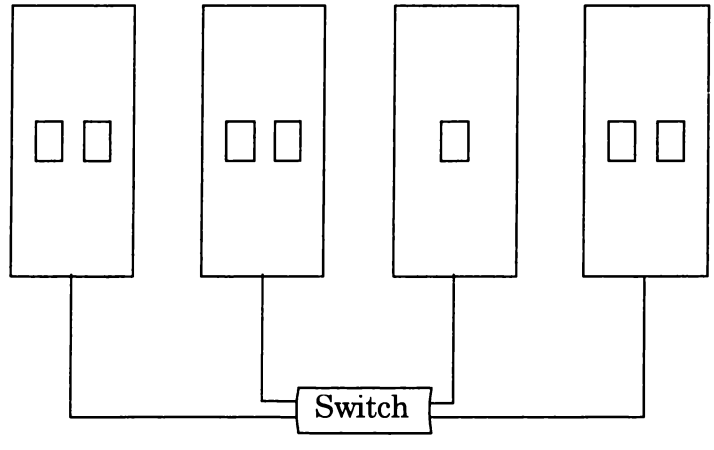

APPENDIX G. CALCULATIONS FOR THE NUMERICAL MODEL OF THE EXPERIMENTAL RUN

G.1. Optimization of Boundary Conditions

Table G-1 contains the matrix of exponent values used for the interpolation of face-panel grid-point temperatures with the parametric coordinates as independent variables. The exponent, i, is a function of the run index, m, and the parameter index, n: $i = i(m,n)$, m =1,2,...,M, and n =1,2,3, where M is the number of CFD runs forming the matrix. Listing G-1 shows the input data for the boundary condition optimization program. Listing G-2 shows the temperatures obtained from each of the 27 CFD runs at the 9 experimental grid points. Listing G-3 shows the interpolation coefficients used to interpolate between CFD run data points for each experimental location. Listing G-4 shows the optimization program results for all of the combinations (all points used, one inactive point, and two inactive points) with configurations sorted in order of decreasing correlation coefficient. Listing G-5 shows statistical parameters (mean, standard deviation, and curve-fitting deviation) in order of decreasing correlation coefficient. Listing G-6 shows the optimized temperatures at experimental grid points, and Listing G-7 shows the temperature differentials (deviations) from experimental values for all of the configurations in order of decreasing correlation coefficient.

Table G-1. Exponent of the Parametric Variables in the Cross-Run Interpolation Function

n→ m	1	2	3	n→ m	1	2	3	n→ m	1	2	3
1	0	0	0	10	0	0	1	19	0	0	2
2	1	0	0	11	1	0	1	20	1	0	2
3	2	0	0	12	2	0	1	21	2	0	2
4	0	1	0	13	0	1	1	22	0	1	2
5	1	1	0	14	1	1	1	23	1	1	2
6	2	1	0	15	2	1	1	24	2	1	2
7	0	2	0	16	0	2	1	25	0	2	2
8	1	2	0	17	1	2	1	26	1	2	2
9	2	2	0	18	2	2	1	27	2	2	2

Listing G-1. Optimization Program Input Data File

```
Run Map Data
------------------------------------------------------------
J:\Cfd\Runs\Liquid-Lens       : Run Set Directory
CFDpst_Base-Plate_front.dat   : Data File Name
3 37 : I1min, I1max
3 56 : I2min, I2max
1834.2 0.80 0.90 1.00 : Var1_ref, f1, f2, f3
101.60 0.90 1.00 1.10 : Var2_ref, f1, f2, f3
76.200 0.90 1.00 1.10 : Var3_ref, f1, f2, f3
------------------------------------------------------------
i  X1_a       X2_a       T_exp
1    0.0E-3  -35.0E-3  57.0
2    0.0E-3    0.0E-3  56.8
3    0.0E-3   35.0E-3  61.4
4   25.0E-3  -35.0E-3  56.3
5   25.0E-3    0.0E-3  64.9
6   25.0E-3   35.0E-3  59.0
7   50.0E-3  -35.0E-3  54.7
8   50.0E-3    0.0E-3  59.9
9   50.0E-3   35.0E-3  57.5
------------------------------------------------------------
27 : Runs
No Run.No. IV1 IV2 IV3
-- ------- --- --- ---
01 Set.24.01  1   1   1
02 Set.24.02  1   1   2
03 Set.24.03  1   1   3
04 Set.24.04  1   2   1
05 Set.24.05  1   2   2
06 Set.24.06  1   2   3
07 Set.24.07  1   3   1
08 Set.24.08  1   3   2
09 Set.24.09  1   3   3
10 Set.24.10  2   1   1
11 Set.24.11  2   1   2
12 Set.24.12  2   1   3
13 Set.24.13  2   2   1
14 Set.24.Nom 2   2   2
15 Set.24.15  2   2   3
16 Set.24.16  2   3   1
17 Set.24.17  2   3   2
18 Set.24.18  2   3   3
19 Set.24.19  3   1   1
20 Set.24.20  3   1   2
```

```
21 Set.24.21  3   1   3
22 Set.24.22  3   2   1
23 Set.24.23  3   2   2
24 Set.24.24  3   2   3
25 Set.24.25  3   3   1
26 Set.24.26  3   3   2
27 Set.24.27  3   3   3
-------------------------------------------------------------
----------
X1_grid:
13 points
----------
J1 X1
-- -------
1    0.0E-3
2    5.0E-3
3   10.0E-3
4   15.0E-3
5   20.0E-3
6   25.0E-3
7   30.0E-3
8   35.0E-3
9   40.0E-3
10  45.0E-3
11  50.0E-3
12  55.0E-3
13  61.2E-3
----------
X2_grid:
21 points
----------
J2 X2
-- -------
1  -48.7E-3
2  -45.0E-3
3  -40.0E-3
4  -35.0E-3
5  -30.0E-3
6  -25.0E-3
7  -20.0E-3
8  -15.0E-3
9  -10.0E-3
10 -05.0E-3
11  00.0E-3
12 +05.0E-3
13 +10.0E-3
14 +15.0E-3
15 +20.0E-3
16 +25.0E-3
17 +30.0E-3
18 +35.0E-3
19 +40.0E-3
20 +45.0E-3
21 +48.7E-3
```

Listing G-2. Face-Panel-Grid Interpolated CFD Temperatures

No	IV1	IV2	IV3	T(1)	T(2)	T(3)	T(4)	T(5)	T(6)	T(7)	T(8)	T(9)
1	1	1	1	55.169	62.889	61.154	55.395	62.275	60.739	53.192	56.478	55.420
2	1	1	2	56.704	63.152	61.524	57.044	62.644	62.207	53.851	56.652	56.036
3	1	1	3	58.019	63.256	62.214	58.431	62.990	63.081	54.460	56.837	56.624
4	1	2	1	55.406	63.299	59.047	55.577	62.649	60.963	54.208	58.864	56.483
5	1	2	2	56.982	63.441	60.448	57.261	63.060	62.561	55.318	59.062	57.572
6	1	2	3	58.309	63.589	62.130	58.677	63.431	63.697	56.257	59.234	58.539

7	1	3	1	55.621	63.359	58.919	55.722	62.962	61.168	55.133	61.160	57.502
8	1	3	2	57.220	63.719	60.502	57.431	63.405	62.869	56.629	61.422	59.048
9	1	3	3	58.565	63.907	62.277	58.872	63.808	64.158	57.872	61.623	60.430
10	2	1	1	55.713	63.939	61.853	55.872	63.345	61.648	53.437	56.952	55.799
11	2	1	2	57.450	64.105	62.945	57.700	63.763	63.309	54.164	57.162	56.492
12	2	1	3	58.908	64.327	63.542	59.226	64.134	64.529	54.825	57.368	57.148
13	2	2	1	55.965	64.270	62.093	56.071	63.767	61.946	54.558	59.574	56.972
14	2	2	2	57.724	64.438	63.465	57.934	64.216	63.707	55.779	59.790	58.184
15	2	2	3	59.203	64.668	63.029	59.497	64.632	65.135	56.808	59.989	59.261
16	2	3	1	56.183	64.545	62.222	56.231	64.115	62.164	55.582	62.119	58.104
17	2	3	2	57.964	64.759	61.245	58.125	64.607	63.960	57.236	62.395	59.810
18	2	3	3	59.456	65.006	63.193	59.713	65.053	65.523	58.599	62.611	61.335
19	3	1	1	56.260	64.828	62.660	56.345	64.404	62.515	53.681	57.428	56.176
20	3	1	2	58.167	65.099	64.136	58.344	64.863	64.381	54.467	57.664	56.944
21	3	1	3	59.758	65.387	64.785	60.006	65.276	65.909	55.177	57.890	57.668
22	3	2	1	56.510	65.181	62.889	56.560	64.863	62.839	54.905	60.276	57.462
23	3	2	2	58.434	65.454	64.625	58.597	65.358	64.760	56.233	60.515	58.796
24	3	2	3	60.046	65.741	65.612	60.300	65.816	66.364	57.345	60.736	59.977
25	3	3	1	56.706	65.530	62.873	56.733	65.249	63.068	56.025	63.062	58.701
26	3	3	2	58.660	65.804	61.942	58.807	65.787	64.970	57.832	63.356	60.570
27	3	3	3	60.288	66.102	64.062	60.541	66.276	66.752	59.314	63.592	62.234

Listing G-3. Tri-Quadratic Function Coefficient Matrix for Inter-Run

j→ m	1	2	3	4	5	6	7	8	9
1	4.26E+03	-3.39E+04	-7.74E+05	1.97E+03	5.79E+03	6.50E+03	1.73E+03	3.79E+03	7.46E+02
2	-8.84E+03	7.05E+04	1.71E+06	-4.14E+03	-1.24E+04	-1.74E+04	-3.36E+03	-8.08E+03	-1.23E+03
3	4.56E+03	-3.65E+04	-9.28E+05	2.19E+03	6.61E+03	1.13E+04	1.85E+03	4.24E+03	7.29E+02
4	-8.11E+03	6.73E+04	1.60E+06	-3.82E+03	-1.13E+04	-1.33E+04	-3.31E+03	-7.40E+03	-1.32E+03
5	1.70E+04	-1.39E+05	-3.53E+06	8.20E+03	2.44E+04	3.55E+04	6.69E+03	1.60E+04	2.36E+03
6	-8.77E+03	7.19E+04	1.91E+06	-4.36E+03	-1.30E+04	-2.31E+04	-3.66E+03	-8.42E+03	-1.39E+03
7	3.89E+03	-3.35E+04	-8.18E+05	1.89E+03	5.53E+03	6.56E+03	1.63E+03	3.64E+03	6.12E+02
8	-8.14E+03	6.92E+04	1.80E+06	-4.07E+03	-1.20E+04	-1.76E+04	-3.34E+03	-7.89E+03	-1.13E+03
9	4.20E+03	-3.57E+04	-9.77E+05	2.16E+03	6.37E+03	1.15E+04	1.81E+03	4.16E+03	6.51E+02
10	-8.50E+03	6.53E+04	1.62E+06	-3.88E+03	-1.15E+04	-1.40E+04	-3.38E+03	-7.56E+03	-1.54E+03
11	1.79E+04	-1.35E+05	-3.58E+06	8.40E+03	2.48E+04	3.76E+04	6.81E+03	1.62E+04	2.77E+03
12	-9.24E+03	7.00E+04	1.94E+06	-4.44E+03	-1.32E+04	-2.44E+04	-3.75E+03	-8.50E+03	-1.62E+03
13	1.64E+04	-1.29E+05	-3.34E+06	7.74E+03	2.26E+04	2.87E+04	6.69E+03	1.50E+04	2.93E+03
14	-3.44E+04	2.67E+05	7.37E+06	-1.66E+04	-4.88E+04	-7.66E+04	-1.36E+04	-3.22E+04	-5.35E+03
15	1.78E+04	-1.38E+05	-4.00E+06	8.85E+03	2.60E+04	4.96E+04	7.43E+03	1.69E+04	3.10E+03
16	-7.89E+03	6.41E+04	1.71E+06	-3.84E+03	-1.11E+04	-1.42E+04	-3.30E+03	-7.37E+03	-1.38E+03
17	1.65E+04	-1.33E+05	-3.76E+06	8.26E+03	2.39E+04	3.80E+04	6.78E+03	1.59E+04	2.56E+03
18	-8.56E+03	6.85E+04	2.04E+06	-4.39E+03	-1.27E+04	-2.47E+04	-3.67E+03	-8.37E+03	-1.46E+03
19	4.26E+03	-3.12E+04	-8.39E+05	1.95E+03	5.72E+03	7.69E+03	1.69E+03	3.77E+03	8.30E+02
20	-8.96E+03	6.48E+04	1.85E+06	-4.21E+03	-1.24E+04	-2.06E+04	-3.44E+03	-8.06E+03	-1.53E+03
21	4.65E+03	-3.35E+04	-1.01E+06	2.23E+03	6.58E+03	1.32E+04	1.89E+03	4.22E+03	8.74E+02
22	-8.24E+03	6.17E+04	1.73E+06	-3.89E+03	-1.12E+04	-1.58E+04	-3.35E+03	-7.48E+03	-1.60E+03
23	1.73E+04	-1.28E+05	-3.81E+06	8.37E+03	2.43E+04	4.19E+04	6.87E+03	1.60E+04	2.97E+03
24	-8.98E+03	6.60E+04	2.07E+06	-4.45E+03	-1.29E+04	-2.69E+04	-3.74E+03	-8.42E+03	-1.68E+03
25	3.97E+03	-3.06E+04	-8.81E+05	1.93E+03	5.50E+03	7.86E+03	1.65E+03	3.69E+03	7.58E+02
26	-8.33E+03	6.34E+04	1.94E+06	-4.16E+03	-1.19E+04	-2.08E+04	-3.42E+03	-7.93E+03	-1.42E+03
27	4.32E+03	-3.27E+04	-1.05E+06	2.21E+03	6.33E+03	1.34E+04	1.85E+03	4.17E+03	7.98E+02

Listing G-4. Program Validation Optimization Analysis: Face Panel Active Points and Optimization Parameter Sorted in Order of Decreasing Correlation Coefficient

Legend
I = Configuration Ranking Index (in order of decreasing correlation coefficient); Cnfg = Configuration Number
Xf(1) = Heat Flux Fraction of Nominal Value (Optimization-Final)
Xf(2) = Raster Area Width Fraction of Nominal Value (Optimization-Final)
Xf(3) = Raster Area Height Fraction of Nominal Value (Optimization-Final)
Gf = Optimization Function (Optimization-Final)

Face Panel Point#

Inactive Points: 0

I	Cnfg	1	2	3	4	5	6	7	8	9	Xf(1)	Xf(2)	Xf(3)	Gf
1	1	1	1	1	1	1	1	1	1	1	0.1033E+01	0.9852E+00	0.8514E+00	0.8388E+02

Inactive Points: 1

I	Cnfg	1	2	3	4	5	6	7	8	9	Xf(1)	Xf(2)	Xf(3)	Gf
1	3	1	0	1	1	1	1	1	1	1	0.1031E+01	0.9932E+00	0.8498E+00	0.1242E+02
2	9	1	1	1	1	1	1	1	0	1	0.1200E+01	0.7200E+00	0.8529E+00	0.5444E+02
3	2	0	1	1	1	1	1	1	1	1	0.1051E+01	0.9784E+00	0.8241E+00	0.8112E+02
4	4	1	1	0	1	1	1	1	1	1	0.1030E+01	0.9878E+00	0.8561E+00	0.8375E+02
5	5	1	1	1	0	1	1	1	1	1	0.1042E+01	0.9832E+00	0.8368E+00	0.8308E+02
6	6	1	1	1	1	0	1	1	1	1	0.1033E+01	0.9852E+00	0.8515E+00	0.8388E+02
7	7	1	1	1	1	1	0	1	1	1	0.1016E+01	0.9834E+00	0.8868E+00	0.7287E+02
8	8	1	1	1	1	1	1	0	1	1	0.1039E+01	0.9784E+00	0.8459E+00	0.8349E+02
9	10	1	1	1	1	1	1	1	1	0	0.1041E+01	0.9757E+00	0.8448E+00	0.8321E+02

Inactive Points: 2

I	Cnfg	1	2	3	4	5	6	7	8	9	Xf(1)	Xf(2)	Xf(3)	Gf
1	22	1	0	1	1	1	0	1	1	1	0.1087E+01	0.9757E+00	0.8831E+00	0.1054E+01
2	11	0	0	1	1	1	1	1	1	1	0.1040E+01	0.9962E+00	0.8300E+00	0.9732E+01
3	25	1	0	1	1	1	1	1	1	0	0.1035E+01	0.9875E+00	0.8457E+00	0.1186E+02
4	24	1	0	1	1	1	1	1	0	1	0.1025E+01	0.1012E+01	0.8476E+00	0.1221E+02
5	20	1	0	1	0	1	1	1	1	1	0.1036E+01	0.9952E+00	0.8380E+00	0.1161E+02
6	19	1	0	0	1	1	1	1	1	1	0.1028E+01	0.9958E+00	0.8536E+00	0.1228E+02
7	23	1	0	1	1	1	1	0	1	1	0.1034E+01	0.9892E+00	0.8463E+00	0.1212E+02
8	21	1	0	1	1	0	1	1	1	1	0.1031E+01	0.9932E+00	0.8499E+00	0.1242E+02
9	46	1	1	1	1	1	1	1	0	0	0.1200E+01	0.7200E+00	0.8530E+00	0.4426E+02
10	13	0	1	1	0	1	1	1	1	1	0.1200E+01	0.8975E+00	0.7201E+00	0.4265E+02
11	18	0	1	1	1	1	1	1	1	0	0.1200E+01	0.8974E+00	0.7212E+00	0.5447E+02
12	17	0	1	1	1	1	1	1	0	1	0.1200E+01	0.8965E+00	0.7302E+00	0.5551E+02
13	44	1	1	1	1	1	1	0	0	1	0.1200E+01	0.7200E+00	0.8529E+00	0.4570E+02
14	36	1	1	1	0	1	1	1	1	0	0.1200E+01	0.8975E+00	0.7200E+00	0.5540E+02
15	35	1	1	1	0	1	1	1	0	1	0.1200E+01	0.8967E+00	0.7266E+00	0.5658E+02
16	12	0	1	0	1	1	1	1	1	1	0.1051E+01	0.9779E+00	0.8235E+00	0.8112E+02
17	14	0	1	1	1	0	1	1	1	1	0.1051E+01	0.9784E+00	0.8241E+00	0.8112E+02
18	15	0	1	1	1	1	0	1	1	1	0.1021E+01	0.9841E+00	0.8758E+00	0.7220E+02
19	16	0	1	1	1	1	1	0	1	1	0.1200E+01	0.8975E+00	0.7213E+00	0.5472E+02
20	26	1	1	0	0	1	1	1	1	1	0.1041E+01	0.9839E+00	0.8380E+00	0.8307E+02
21	27	1	1	0	1	0	1	1	1	1	0.1030E+01	0.9878E+00	0.8561E+00	0.8375E+02
22	28	1	1	0	1	1	0	1	1	1	0.1002E+01	0.9829E+00	0.9183E+00	0.7080E+02
23	29	1	1	0	1	1	1	0	1	1	0.1037E+01	0.9802E+00	0.8492E+00	0.8345E+02
24	30	1	1	0	1	1	1	1	0	1	0.1020E+01	0.1011E+01	0.8564E+00	0.8365E+02
25	31	1	1	0	1	1	1	1	1	0	0.1039E+01	0.9770E+00	0.8473E+00	0.8317E+02
26	32	1	1	1	0	0	1	1	1	1	0.1042E+01	0.9831E+00	0.8367E+00	0.8307E+02
27	33	1	1	1	0	1	0	1	1	1	0.1016E+01	0.9834E+00	0.8870E+00	0.7287E+02
28	34	1	1	1	0	1	1	0	1	1	0.1200E+01	0.8975E+00	0.7200E+00	0.5564E+02
29	37	1	1	1	1	0	0	1	1	1	0.1016E+01	0.9834E+00	0.8868E+00	0.7287E+02
30	38	1	1	1	1	0	1	0	1	1	0.1039E+01	0.9784E+00	0.8459E+00	0.8350E+02
31	39	1	1	1	1	0	1	1	0	1	0.1200E+01	0.7200E+00	0.8529E+00	0.5384E+02
32	40	1	1	1	1	0	1	1	1	0	0.1041E+01	0.9757E+00	0.8447E+00	0.8321E+02
33	41	1	1	1	1	1	0	0	1	1	0.1017E+01	0.9821E+00	0.8858E+00	0.7285E+02
34	42	1	1	1	1	1	0	1	0	1	0.1017E+01	0.9822E+00	0.8869E+00	0.7287E+02
35	43	1	1	1	1	1	0	1	1	0	0.1019E+01	0.9795E+00	0.8842E+00	0.7273E+02
36	45	1	1	1	1	1	1	0	1	0	0.1056E+01	0.9567E+00	0.8310E+00	0.8249E+02

Listing G-5. Program Validation Optimization Analysis: Statistical Parameters Sorted in Order of Decreasing Correlation Coefficient

Legend
I = Configuration Ranking Index (in order of decreasing correlation coefficient); Cnfg = Configuration Number
Mean = Mean Exper. Temperature; Sigma = Standard Deviation;
Eta = Curve-Fitting Deviation; R = Correlation Coefficient

Face Panel Point#

Inactive Points: 0

I	Cnfg	1	2	3	4	5	6	7	8	9	Mean	Sigma_y	Sigma_yx	Corr. Coeff
1	1	1	1	1	1	1	1	1	1	1	0.5861E+02	0.3100E+01	0.3462E+01	0.0000E+00

Inactive Points: 1

I	Cnfg	1	2	3	4	5	6	7	8	9	Mean	Sigma_y	Sigma_yx	Corr. Coeff
1	3	1	0	1	1	1	1	1	1	1	0.5884E+02	0.3234E+01	0.1439E+01	0.8956E+00
2	9	1	1	1	1	1	1	1	0	1	0.5845E+02	0.3274E+01	0.3012E+01	0.3917E+00
3	2	0	1	1	1	1	1	1	1	1	0.5881E+02	0.3251E+01	0.3677E+01	0.0000E+00
4	4	1	1	0	1	1	1	1	1	1	0.5826E+02	0.3120E+01	0.3736E+01	0.0000E+00
5	5	1	1	1	0	1	1	1	1	1	0.5890E+02	0.3182E+01	0.3721E+01	0.0000E+00
6	6	1	1	1	1	0	1	1	1	1	0.5782E+02	0.2151E+01	0.3739E+01	0.0000E+00
7	7	1	1	1	1	1	0	1	1	1	0.5856E+02	0.3311E+01	0.3485E+01	0.0000E+00
8	8	1	1	1	1	1	1	0	1	1	0.5910E+02	0.2920E+01	0.3730E+01	0.0000E+00
9	10	1	1	1	1	1	1	1	1	0	0.5875E+02	0.3284E+01	0.3724E+01	0.0000E+00

Inactive Points: 2

I	Cnfg	1	2	3	4	5	6	7	8	9	Mean	Sigma_y	Sigma_yx	Corr. Coeff
1	22	1	0	1	1	1	0	1	1	1	0.5881E+02	0.3492E+01	0.4592E+00	0.9913E+00
2	11	0	0	1	1	1	1	1	1	1	0.5910E+02	0.3400E+01	0.1395E+01	0.9119E+00
3	25	1	0	1	1	1	1	1	1	0	0.5903E+02	0.3444E+01	0.1540E+01	0.8944E+00
4	24	1	0	1	1	1	1	1	0	1	0.5869E+02	0.3462E+01	0.1563E+01	0.8923E+00
5	20	1	0	1	0	1	1	1	1	1	0.5920E+02	0.3313E+01	0.1524E+01	0.8879E+00
6	19	1	0	0	1	1	1	1	1	1	0.5847E+02	0.3309E+01	0.1567E+01	0.8807E+00
7	23	1	0	1	1	1	1	0	1	1	0.5943E+02	0.2990E+01	0.1557E+01	0.8538E+00
8	21	1	0	1	1	0	1	1	1	1	0.5797E+02	0.2280E+01	0.1576E+01	0.7226E+00
9	46	1	1	1	1	1	1	1	0	0	0.5859E+02	0.3512E+01	0.2975E+01	0.5312E+00
10	13	0	1	1	0	1	1	1	1	1	0.5917E+02	0.3336E+01	0.2921E+01	0.4830E+00
11	18	0	1	1	1	1	1	1	1	0	0.5900E+02	0.3464E+01	0.3301E+01	0.3035E+00
12	17	0	1	1	1	1	1	1	0	1	0.5866E+02	0.3479E+01	0.3332E+01	0.2877E+00
13	44	1	1	1	1	1	1	0	0	1	0.5899E+02	0.3134E+01	0.3023E+01	0.2642E+00
14	36	1	1	1	0	1	1	1	1	0	0.5910E+02	0.3382E+01	0.3329E+01	0.1775E+00
15	35	1	1	1	0	1	1	1	0	1	0.5876E+02	0.3409E+01	0.3364E+01	0.1623E+00
16	12	0	1	0	1	1	1	1	1	1	0.5844E+02	0.3325E+01	0.4028E+01	0.0000E+00
17	14	0	1	1	1	0	1	1	1	1	0.5794E+02	0.2296E+01	0.4028E+01	0.0000E+00
18	15	0	1	1	1	1	0	1	1	1	0.5879E+02	0.3510E+01	0.3800E+01	0.0000E+00
19	16	0	1	1	1	1	1	0	1	1	0.5940E+02	0.3018E+01	0.3308E+01	0.0000E+00
20	26	1	1	0	0	1	1	1	1	1	0.5854E+02	0.3259E+01	0.4076E+01	0.0000E+00
21	27	1	1	0	1	0	1	1	1	1	0.5731E+02	0.1722E+01	0.4093E+01	0.0000E+00
22	28	1	1	0	1	1	0	1	1	1	0.5816E+02	0.3355E+01	0.3763E+01	0.0000E+00
23	29	1	1	0	1	1	1	0	1	1	0.5877E+02	0.2990E+01	0.4085E+01	0.0000E+00
24	30	1	1	0	1	1	1	1	0	1	0.5803E+02	0.3293E+01	0.4090E+01	0.0000E+00
25	31	1	1	0	1	1	1	1	1	0	0.5837E+02	0.3353E+01	0.4078E+01	0.0000E+00
26	32	1	1	1	0	0	1	1	1	1	0.5804E+02	0.2226E+01	0.4076E+01	0.0000E+00
27	33	1	1	1	0	1	0	1	1	1	0.5889E+02	0.3437E+01	0.3818E+01	0.0000E+00
28	34	1	1	1	0	1	1	0	1	1	0.5950E+02	0.2907E+01	0.3336E+01	0.0000E+00
29	37	1	1	1	1	0	0	1	1	1	0.5766E+02	0.2266E+01	0.3818E+01	0.0000E+00
30	38	1	1	1	1	0	1	0	1	1	0.5827E+02	0.1881E+01	0.4086E+01	0.0000E+00
31	39	1	1	1	1	0	1	1	0	1	0.5753E+02	0.2140E+01	0.3282E+01	0.0000E+00
32	40	1	1	1	1	0	1	1	1	0	0.5787E+02	0.2319E+01	0.4079E+01	0.0000E+00
33	41	1	1	1	1	1	0	0	1	1	0.5911E+02	0.3154E+01	0.3817E+01	0.0000E+00
34	42	1	1	1	1	1	0	1	0	1	0.5837E+02	0.3528E+01	0.3818E+01	0.0000E+00
35	43	1	1	1	1	1	0	1	1	0	0.5871E+02	0.3546E+01	0.3814E+01	0.0000E+00
36	45	1	1	1	1	1	1	0	1	0	0.5933E+02	0.3076E+01	0.4062E+01	0.0000E+00

Listing G-6. Program Validation Optimization Analysis: Numerical Temperatures at Face Panel Grid Points for Each Configuration, Sorted in Order of Decreasing Correlation Coefficient

Legend
I = Configuration Index (in order of decreasing correlation coefficient)
Cnfg = Configuration Number; T(1) = Temperature for Channel #12
T(2) = Temperature for Channel #15; T(3) = Temperature for Channel #18
T(4) = Temperature for Channel #11; T(5) = Temperature for Channel #14
T(6) = Temperature for Channel #17; T(7) = Temperature for Channel #10
T(8) = Temperature for Channel #13; T(9) = Temperature for Channel #16

Inactive Points: 0

I	Cnfg	T(1)	T(2)	T(3)	T(4)	T(5)	T(6)	T(7)	T(8)	T(9)
1	1	55.989	63.510	60.028	56.177	62.971	61.641	54.677	59.203	56.969

Inactive Points: 1

I	Cnfg	T(1)	T(2)	T(3)	T(4)	T(5)	T(6)	T(7)	T(8)	T(9)
1	3	55.663	64.122	61.410	55.747	63.568	61.548	54.628	60.224	57.043
2	9	58.475	57.717	61.326	58.893	62.109	58.224	54.750	56.321	56.591
3	4	54.680	57.363	44.231	54.740	61.585	59.438	54.987	62.067	57.194
4	7	56.882	63.405	60.369	57.161	63.003	62.456	55.166	58.883	57.411
5	10	55.915	63.475	60.058	56.107	62.917	61.563	54.523	58.936	56.806
6	2	55.657	63.567	59.887	55.808	62.982	61.319	54.523	59.453	56.840
7	5	55.942	63.519	60.015	56.124	62.975	61.596	54.655	59.239	56.951
8	6	55.987	63.354	59.740	56.202	62.800	61.588	54.522	58.733	56.781
9	8	55.987	63.508	60.030	56.175	62.970	61.638	54.671	59.192	56.962

Inactive Points: 2

I	Cnfg	T(1)	T(2)	T(3)	T(4)	T(5)	T(6)	T(7)	T(8)	T(9)
1	22	56.384	64.115	61.892	56.525	63.680	62.269	55.105	60.056	57.494
2	11	55.242	64.221	61.394	55.286	63.599	61.172	54.314	60.339	56.762
3	24	55.529	63.986	61.465	55.567	63.506	61.309	55.023	61.711	57.483
4	25	55.572	64.158	61.437	55.650	63.587	61.481	54.502	60.086	56.922
5	20	55.458	64.180	61.424	55.521	63.593	61.368	54.479	60.296	56.911
6	19	55.664	64.143	61.461	55.747	63.590	61.560	54.623	60.224	57.041
7	30	54.950	57.040	46.919	54.714	62.715	59.760	55.372	64.796	57.822
8	23	55.645	64.129	61.419	55.727	63.572	61.535	54.606	60.204	57.022
9	42	58.627	57.203	61.377	59.007	62.205	57.864	54.829	56.370	56.663
10	21	55.680	63.949	60.972	55.783	63.392	61.491	54.647	60.082	57.033
11	12	54.537	57.244	37.154	54.589	61.558	59.159	54.761	61.861	56.942
12	26	54.577	57.250	37.876	54.613	61.638	59.227	54.815	62.032	57.010
13	28	54.736	57.427	47.660	54.803	61.581	59.555	55.082	62.133	57.300
14	31	54.644	57.347	42.338	54.702	61.580	59.365	54.928	62.010	57.127
15	13	53.684	58.414	61.225	53.364	62.753	58.378	53.588	64.247	56.127
16	29	54.709	57.367	45.962	54.772	61.580	59.496	55.037	62.102	57.249
17	33	56.695	61.984	61.459	57.209	61.539	61.153	55.706	58.727	57.799
18	46	54.978	61.675	61.364	55.353	61.049	60.163	52.988	55.710	55.036
19	43	56.849	63.407	60.385	57.125	63.000	62.428	55.125	58.851	57.370
20	17	54.295	61.028	61.480	54.564	60.811	59.269	52.741	55.707	54.798
21	41	56.732	62.036	61.444	57.234	61.584	61.258	55.915	59.051	58.047
22	27	54.628	57.456	45.913	54.736	61.380	59.373	54.933	61.694	57.112
23	15	56.761	63.439	60.385	57.024	63.020	62.362	55.103	58.942	57.357
24	35	54.740	61.585	61.274	55.061	61.091	59.908	52.915	55.784	54.986
25	18	55.565	63.513	59.907	55.724	62.899	61.220	54.315	59.034	56.618
26	14	55.662	63.384	59.617	55.846	62.778	61.270	54.333	58.813	56.609
27	16	55.629	63.561	59.897	55.780	62.968	61.291	54.473	59.370	56.788
28	32	55.945	63.361	59.729	56.156	62.801	61.550	54.502	58.753	56.763
29	34	55.932	63.518	60.017	56.114	62.971	61.586	54.642	59.222	56.937
30	36	55.838	63.487	60.034	56.022	62.917	61.489	54.482	58.971	56.770
31	37	56.659	61.946	61.351	57.182	61.501	61.078	55.536	58.475	57.602
32	38	55.951	63.335	59.749	56.168	62.773	61.550	54.454	58.620	56.709
33	39	55.874	61.738	60.698	56.465	60.863	60.605	53.229	55.386	55.180
34	40	55.812	63.175	59.740	56.049	62.579	61.375	54.121	57.967	56.349
35	44	55.186	61.885	61.246	55.570	61.212	60.418	53.075	55.780	55.134
36	45	55.877	63.459	60.070	56.070	62.893	61.523	54.454	58.823	56.734

Listing G-7. Program Validation Optimization Analysis: Temperature Deviation with Respect to Experimental Values at Face Panel Grid Points for Each Configuration, Sorted in Order of Decreasing Correlation Coefficient

Legend
I = Configuration Index (in order of decreasing correlation coefficient)
Cnfg = Configuration Number; Err(1)=(Tnum - Texp) for Channel #12
Err(2)= (Tnum - Texp) for Channel #15; Err(3)= (Tnum - Texp) for Channel #18
Err(4)= (Tnum - Texp) for Channel #11; Err(5)= (Tnum - Texp) for Channel #14
Err(6)= (Tnum - Texp) for Channel #17; Err(7)= (Tnum - Texp) for Channel #10
Err(8)= (Tnum - Texp) for Channel #13; Err(9)= (Tnum - Texp) for Channel #16

Inactive Points: 0

I	Cnfg	Err(1)	Err(2)	Err(3)	Err(4)	Err(5)	Err(6)	Err(7)	Err(8)	Err(9)
1	1	-1.420	8.449	0.317	-0.748	0.000	2.990	-0.558	0.055	-0.746

Inactive Points: 1

I	Cnfg	Err(1)	Err(2)	Err(3)	Err(4)	Err(5)	Err(6)	Err(7)	Err(8)	Err(9)
1	3	-1.450	8.456	0.336	-0.782	0.000	2.961	-0.516	0.265	-0.700
2	9	-1.125	3.687	-0.315	-0.658	0.770	4.420	-2.956	-7.465	-3.190
3	2	-2.003	8.429	-0.062	-1.381	0.000	2.430	-0.980	-0.106	-1.134
4	4	-1.323	8.450	0.422	-0.643	0.001	3.081	-0.474	0.119	-0.667
5	5	-1.727	8.446	0.072	-1.081	0.000	2.697	-0.773	0.012	-0.942
6	6	-1.419	8.449	0.318	-0.747	0.000	2.991	-0.557	0.056	-0.745
7	7	-0.720	8.426	1.109	0.010	0.001	3.648	-0.118	-0.016	-0.347
8	8	-1.536	8.442	0.194	-0.875	0.000	2.879	-0.685	-0.120	-0.868
9	10	-1.561	8.439	0.170	-0.902	0.000	2.856	-0.721	-0.190	-0.903

Inactive Points: 2

I	Cnfg	Err(1)	Err(2)	Err(3)	Err(4)	Err(5)	Err(6)	Err(7)	Err(8)	Err(9)
1	22	-0.462	8.941	0.491	0.222	0.691	4.081	-0.044	0.199	-0.178
2	11	-1.869	8.460	0.072	-1.235	0.000	2.567	-0.780	0.361	-0.936
3	25	-1.539	8.452	0.226	-0.878	0.000	2.877	-0.618	0.121	-0.798
4	24	-1.492	8.473	0.492	-0.827	0.000	2.926	-0.407	0.743	-0.581
5	20	-1.697	8.461	0.161	-1.048	0.001	2.729	-0.669	0.327	-0.836
6	19	-1.373	8.457	0.426	-0.698	0.001	3.034	-0.443	0.331	-0.631
7	23	-1.525	8.454	0.247	-0.863	0.000	2.890	-0.596	0.165	-0.777
8	21	-1.448	8.457	0.338	-0.780	0.000	2.963	-0.515	0.266	-0.699
9	46	-1.123	3.695	-0.216	-0.656	0.770	4.420	-2.957	-7.465	-3.191
10	13	-4.275	5.178	-0.344	-4.166	0.784	0.244	-2.299	-2.058	-2.352
11	18	-4.242	5.210	-0.345	-4.129	0.789	0.280	-2.287	-2.057	-2.340
12	17	-3.985	5.442	-0.512	-3.843	0.826	0.557	-2.193	-2.062	-2.249
13	44	-1.124	3.690	-0.280	-0.657	0.770	4.420	-2.956	-7.465	-3.191
14	36	-4.277	5.174	-0.358	-4.168	0.784	0.242	-2.300	-2.059	-2.353
15	35	-4.089	5.341	-0.526	-3.959	0.811	0.446	-2.231	-2.065	-2.286
16	12	-2.017	8.427	-0.067	-1.397	0.000	2.416	-0.992	-0.118	-1.145
17	14	-2.003	8.429	-0.062	-1.381	0.000	2.430	-0.980	-0.106	-1.134
18	15	-0.932	8.436	0.842	-0.221	0.000	3.449	-0.249	0.010	-0.467
19	16	-4.241	5.213	-0.331	-4.127	0.789	0.280	-2.287	-2.056	-2.340
20	26	-1.702	8.447	0.091	-1.054	0.000	2.721	-0.751	0.031	-0.922
21	27	-1.323	8.450	0.421	-0.644	0.000	3.081	-0.474	0.119	-0.667
22	28	-0.145	8.386	1.885	0.631	0.000	4.181	0.249	-0.052	-0.010
23	29	-1.468	8.445	0.256	-0.801	0.000	2.944	-0.628	-0.075	-0.815
24	30	-1.310	8.466	0.640	-0.631	0.000	3.092	-0.276	0.733	-0.462
25	31	-1.507	8.441	0.215	-0.843	0.000	2.907	-0.677	-0.157	-0.862
26	32	-1.729	8.445	0.071	-1.084	0.000	2.695	-0.774	0.011	-0.944
27	33	-0.717	8.425	1.113	0.013	0.000	3.651	-0.116	-0.016	-0.345
28	34	-4.277	5.175	-0.347	-4.168	0.783	0.242	-2.300	-2.058	-2.353
29	37	-0.720	8.425	1.109	0.009	0.000	3.648	-0.118	-0.016	-0.347
30	38	-1.535	8.442	0.195	-0.874	0.000	2.880	-0.685	-0.121	-0.868
31	39	-1.125	3.687	-0.319	-0.659	0.770	4.420	-2.956	-7.465	-3.190
32	40	-1.561	8.439	0.170	-0.902	0.000	2.855	-0.721	-0.190	-0.903
33	41	-0.739	8.426	1.080	-0.011	0.000	3.630	-0.144	-0.050	-0.372
34	42	-0.718	8.425	1.108	0.011	0.000	3.650	-0.129	-0.048	-0.359
35	43	-0.771	8.427	1.032	-0.045	0.000	3.602	-0.189	-0.116	-0.417
36	45	-1.860	8.393	0.033	-1.228	0.000	2.567	-1.035	-0.693	-1.205

G.2. Experimental Reference Case

G.2.1. Thermal Network Model

The lumped-parameter thermal network used to characterize the heat transfer process throughout the liquid-lens system is shown in *Figure G-1*. Nodes are represented by hollow circles, and identified by numbers in bold. The Q's represent the heat transfer rates, and the G's represent the thermal conductances. The sub-indices in Q and G denote the resistor number (identifier). Listing G-8 shows node data and Listing G-9 shows resistor data. The thermal network is shown with numerical values for nodal temperatures, and resistor's heat flow and thermal conductance in *Figure G-2*.

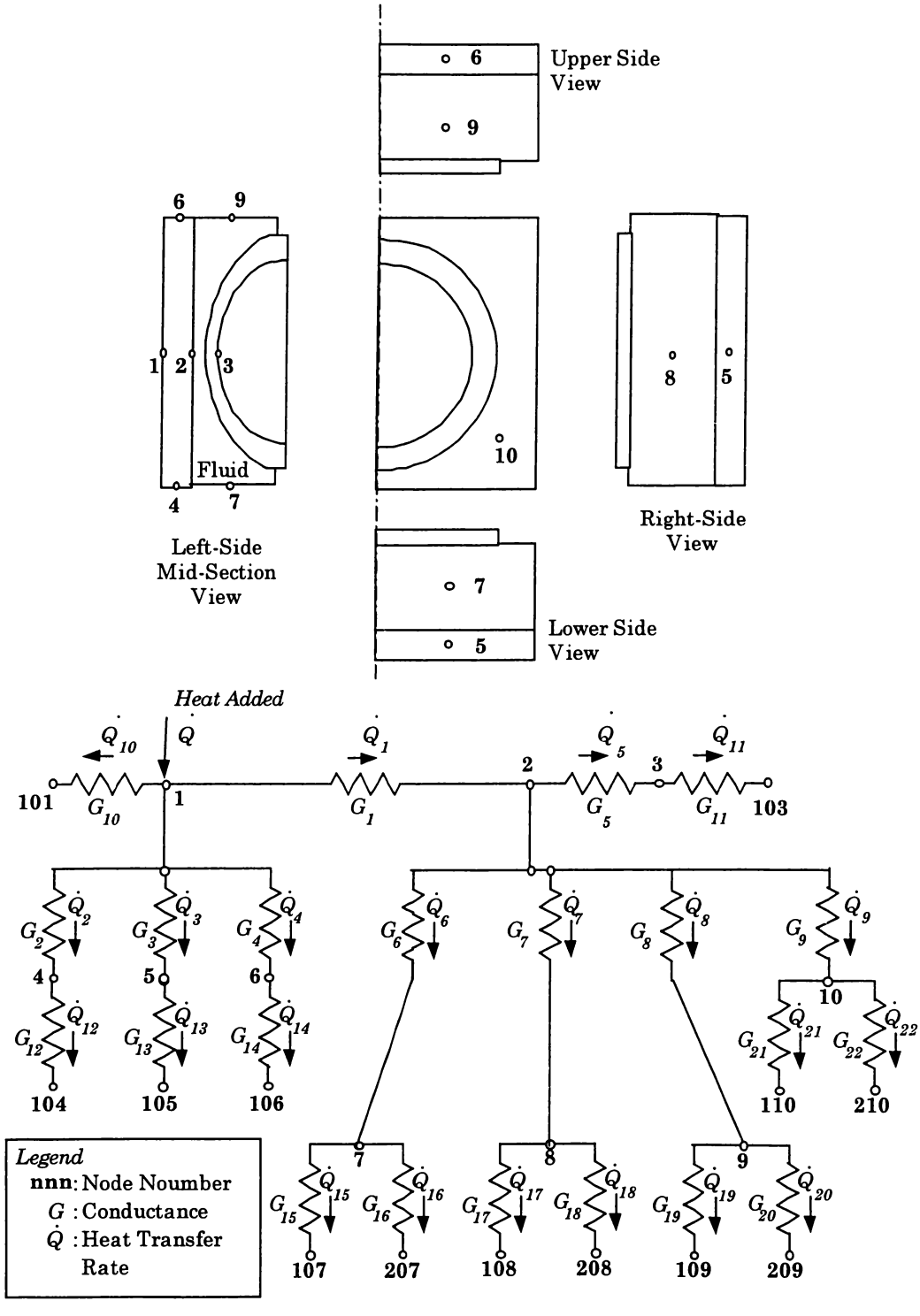

Figure G-1. Network Model for Lumped-System Analysis

Listing G-8. Thermal Network Model for the Experimental Reference Case: Node Parameters

Node ID		*Node Temperature*	*Heat Generation Rate*
i		T(i) (°C)	Q_{gen}(i) (W)
1	Base Plate Back	68.3	13.295
2	Base Plate Front	60.2	0.000
3	Meniscus Lens Front	50.7	0.000
4	Base Plate Lower Surface	53.7	0.000
5	Base Plate Lateral Surface	55.6	0.000
6	Base Plate Upper Surface	57.0	0.000
7	Enclosure Lower Surface	51.8	0.000
8	Enclosure Lateral Surface	53.9	0.000
9	Enclosure Upper Surface	53.9	0.000
10	Enclosure Front Surface	53.2	0.000
101	Environmental Node for the Base Plate Back	24.0	0.000
Natural-Convection Environmental Air Nodes:			
103	Meniscus Lens	24.0	0.000
104	Base Plate Lower Surface	24.0	0.000
105	Base Plate Lateral Surface	24.0	0.000
106	Base Plate Upper Surface	24.0	0.000
107	Enclosure Lower Surface	24.0	0.000
108	Enclosure Lateral Surface	24.0	0.000
109	Enclosure Upper Surface	24.0	0.000
110	Enclosure Front Surface	24.0	0.000
Thermal Radiation Environmental Nodes:			
207	Enclosure Lower Surface	24.0	0.000
208	Enclosure Lateral Surface	24.0	0.000
209	Enclosure Upper Surface	24.0	0.000
210	Enclosure Front Surface	24.0	0.000

Listing G-9. Thermal Network Model for the Experimental Reference Case: Conductor Parameters

(1)	(2)	(3)	(4)	(5)	(6)	(7)	(8)
n	*i*	*j*	*T(i)* (°C)	*T(j)* (°C)	*Q(i,j)* (W)	*ΔT(i,j)* (°C)	*G(i,j)* (W/C)
1	1	2	68.3	60.2	10.539	-8.0	1.3119
2	1	4	68.3	53.7	0.059	-14.6	0.0041
3	1	5	68.3	55.6	0.105	-12.7	0.0082
4	1	6	68.3	57.0	0.072	-11.3	0.0063
5	2	3	60.2	50.7	2.080	-9.6	0.2172
6	2	7	60.2	51.8	1.091	-8.4	0.1293
7	2	8	60.2	53.9	1.943	-6.3	0.3067
8	2	9	60.2	53.9	2.219	-6.3	0.3502
9	2	10	60.2	53.2	3.205	-7.0	0.4555
10	1	101	68.3	24.0	2.517	-44.3	0.0569
11	3	103	50.7	24.0	2.080	-26.7	0.0780
12	4	104	53.7	24.0	0.059	-29.7	0.0020
13	5	105	55.6	24.0	0.105	-31.6	0.0033
14	6	106	57.0	24.0	0.072	-33.0	0.0022
15	7	107	51.8	24.0	0.868	-27.8	0.0312
16	7	207	51.8	24.0	0.223	-27.8	0.0080
17	8	108	53.9	24.0	1.485	-29.9	0.0497
18	8	208	53.9	24.0	0.458	-29.9	0.0153
19	9	109	53.9	24.0	0.933	-29.9	0.0312
20	9	209	53.9	24.0	1.286	-29.9	0.0430
21	10	110	53.2	24.0	2.009	-29.2	0.0688
22	10	210	53.2	24.0	1.196	-29.2	0.0410

(1) *n* = Conductor Index
(2) *i* = "From" Node
(3) *j* = "To" Node
(4) *T(i)* = Temperature at Node *i*
(5) *T(j)* = Temperature at Node *j*
(6) Heat Transfer Rate from Node *i* to Node *j*
(7) Temperature Change from Node *i* to Node *j*
(8) Thermal Conductance along Conductor *n*

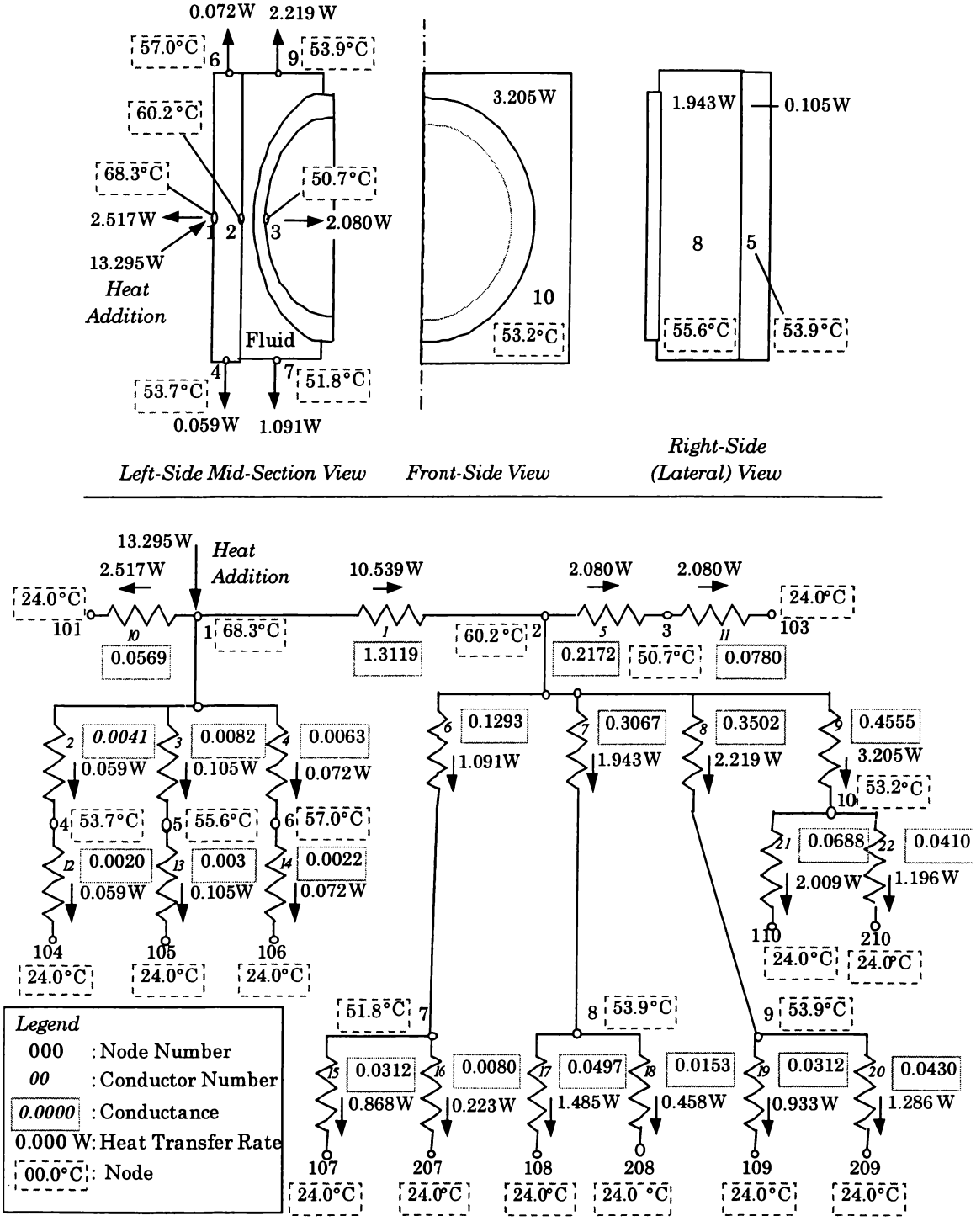

Figure G-2. Network Model for the Experimental Reference Case

APPENDIX H. MATHEMATICAL BACKGROUND

H.1. Material Time Derivative Operator

The material time-derivative operator is a kinematic operator that transforms the total time derivative of a property relative to an observer moving with the particle to one that is at an independent location. If ϕ is a physical property, the total time derivative can be decomposed into local and advective time derivatives as shown below.

$$\frac{\mathrm{D}\phi}{\mathrm{D}t} = \frac{\partial \phi}{\partial t} + \vec{U} \bullet \nabla \phi , \tag{H.1}$$

where

$\frac{\partial \phi}{\partial t}$ is the local time derivative,

$\vec{U}$ is the velocity vector in the field,

and $\nabla \phi$ is the gradient of the property.

All of the above evaluated at the local point, relative to the independent observer.

H.2. Vector Operations

H.2.1. Gradient of a scalar function

Given a scalar field as a function of position, $\phi = \phi(\vec{X})$, the gradient of ϕ is denoted as $\mathrm{grad}(\phi)$ or, alternatively, $\nabla \phi$. If $\vec{X} = (X_1, X_2, X_3)$ is the Cartesian coordinate position vector, with $\vec{\varepsilon}_i$, i=1,2,3, the unit coordinate vectors, the gradient of ϕ is expressed as

$$\nabla \phi = \sum_{i=1}^{3} \vec{\varepsilon}_i \frac{\partial \phi}{\partial X_i} \tag{H.2}$$

H.2.2. Scalar (Dot) Product of Two Vectors

Given two vector fields, $\vec{A} = (A_1, A_2, A_3)$ and $\vec{B} = (B_1, B_2, B_3)$, the scalar product of $\vec{A}$ and $\vec{B}$ is denoted as $\vec{A} \bullet \vec{B}$. If $\vec{A}$ and $\vec{B}$ are defined in terms of Cartesian directions,

$$\vec{A} = \sum_{i=1}^{3} A_i \vec{\varepsilon}_i, \text{ and} \tag{H.3}$$

$$\vec{B} = \sum_{i=1}^{3} B_i \vec{\varepsilon}_i \tag{H.4}$$

where $\vec{\varepsilon}_i$, i=1,2,3, are the unit coordinate vectors, the scalar product of $\vec{A}$ and $\vec{B}$ is expressed as

$$\vec{A} \bullet \vec{B} = \sum_{i=1}^{3} A_i B_i \tag{H.5}$$

H.3. Matrix Operations

H.3.1. Unit Matrix

The unit matrix is defined as

$$\mathbb{I} = \begin{bmatrix} 1 & 0 & 0 \\ 0 & 1 & 0 \\ 0 & 0 & 1 \end{bmatrix} \tag{H.6}$$

H.3.2. Transpose Operator.

Given a matrix $\mathbb{A}$,

$$\mathbb{A} = \begin{bmatrix} A_{1,1} & A_{1,2} & A_{1,3} \\ A_{2,1} & A_{2,2} & A_{2,3} \\ A_{3,1} & A_{3,2} & A_{3,3} \end{bmatrix} \tag{H.7}$$

the transpose of $\mathbb{A}$ is denoted as $(\mathbb{A})^{\mathrm{T}}$ and defined as

$$\left(\mathbb{A}\right)^{\mathrm{T}} = \begin{bmatrix} A_{1,1} & A_{2,1} & A_{3,1} \\ A_{1,2} & A_{2,2} & A_{3,2} \\ A_{1,3} & A_{2,3} & A_{3,3} \end{bmatrix} \tag{H.8}$$

H.3.3. Velocity Vector Gradient

$$\nabla \vec{U} = \begin{bmatrix} \frac{\partial U_1}{\partial X_1} & \frac{\partial U_1}{\partial X_2} & \frac{\partial U_1}{\partial X_3} \\ \frac{\partial U_2}{\partial X_1} & \frac{\partial U_2}{\partial X_2} & \frac{\partial U_2}{\partial X_3} \\ \frac{\partial U_3}{\partial X_1} & \frac{\partial U_3}{\partial X_2} & \frac{\partial U_3}{\partial X_3} \end{bmatrix} \tag{H.9}$$

H.3.4. Transposed Velocity Vector Gradient

$$\left(\nabla \vec{U}\right)^{\mathrm{T}} = \begin{bmatrix} \frac{\partial U_1}{\partial X_1} & \frac{\partial U_2}{\partial X_1} & \frac{\partial U_3}{\partial X_1} \\ \frac{\partial U_1}{\partial X_2} & \frac{\partial U_2}{\partial X_2} & \frac{\partial U_3}{\partial X_2} \\ \frac{\partial U_1}{\partial X_3} & \frac{\partial U_2}{\partial X_3} & \frac{\partial U_3}{\partial X_3} \end{bmatrix} \tag{H.10}$$

H.3.5. Divergence of the Velocity Vector Gradient

$$\nabla \bullet \left(\nabla \vec{U}\right) = \nabla \bullet \begin{bmatrix} \frac{\partial U_1}{\partial X_1} & \frac{\partial U_1}{\partial X_2} & \frac{\partial U_1}{\partial X_3} \\ \frac{\partial U_2}{\partial X_1} & \frac{\partial U_2}{\partial X_2} & \frac{\partial U_2}{\partial X_3} \\ \frac{\partial U_3}{\partial X_1} & \frac{\partial U_3}{\partial X_2} & \frac{\partial U_3}{\partial X_3} \end{bmatrix} = \begin{bmatrix} \frac{\partial^2 U_1}{\partial {X_1}^2} & \frac{\partial^2 U_1}{\partial {X_2}^2} & \frac{\partial^2 U_1}{\partial {X_3}^2} \\ \frac{\partial^2 U_2}{\partial {X_1}^2} & \frac{\partial^2 U_2}{\partial {X_2}^2} & \frac{\partial^2 U_2}{\partial {X_3}^2} \\ \frac{\partial^2 U_3}{\partial {X_1}^2} & \frac{\partial^2 U_3}{\partial {X_2}^2} & \frac{\partial^2 U_3}{\partial {X_3}^2} \end{bmatrix}$$

$$\therefore \nabla \bullet \left(\nabla \vec{U}\right) = \left(\nabla \bullet \nabla\right)\vec{U} = \nabla^2 \vec{U} \tag{H.11}$$

H.3.6. Divergence of the Transposed Velocity Vector Gradient

$$\nabla\bullet\left(\nabla\vec{U}\right)^{\mathrm{T}} = \nabla\bullet\begin{bmatrix} \frac{\partial U_1}{\partial X_1} & \frac{\partial U_2}{\partial X_1} & \frac{\partial U_3}{\partial X_1} \\ \frac{\partial U_1}{\partial X_2} & \frac{\partial U_2}{\partial X_2} & \frac{\partial U_3}{\partial X_2} \\ \frac{\partial U_1}{\partial X_3} & \frac{\partial U_2}{\partial X_3} & \frac{\partial U_3}{\partial X_3} \end{bmatrix} = \begin{bmatrix} \frac{\partial}{\partial X_1} \\ \frac{\partial}{\partial X_2} \\ \frac{\partial}{\partial X_3} \end{bmatrix} \nabla\bullet\vec{U}$$

$$\therefore \nabla\bullet\left(\nabla\vec{U}\right)^{\mathrm{T}} = \nabla^{\mathrm{T}}\left(\nabla\bullet\vec{U}\right) \qquad \text{(H.12)}$$

APPENDIX I. Preliminary Numerical Models

I.1. Preliminary Cartesian Model

A CFD program was written first in Cartesian coordinates to test the various features that the final program should posses. Among these were the choice for the flux-discretization interpolation scheme, and the treatment of internal fluid-solid boundaries. The program was developed initially using a staggered grid arrangement with Cartesian velocity nodes on the faces of the mass-conservation control volumes. The mass-conservation control volume was used also for energy conservation. Thus, conservation of mass fluxes ensured conservation of advected energy fluxes. Pressure and temperature were co-located at the central nodes of these control volumes. The SIMPLER algorithm was used to solve the pressure-velocity-coupling problem, which at the time was believed adequate, despite of its inconsistency in the treatment of pressure. The initial flux-discretization scheme was the Patankar's power-law [103] differencing scheme (PLDS), because the simplicity of its implementation. This code was used as a benchmark for testing further improvements. One of the improvements dealt with a better choice for the flux-discretization interpolation schemes.

I.2. Preliminary Advection-Diffusion Interpolation Schemes

It was desired that the interpolation scheme be simple enough to implement into the numerical solution, and that it provided bounded solutions, that is, stable solutions, while providing reasonable levels of false diffusion. After reviewing the flux-discretization interpolation schemes above, it was concluded that QUDS was a good candidate. QUDS was presumed more accurate, but required six more three-dimensional coefficient arrays, and required more effort as part of the implementation. From reviews of the literature, QUDS seemed to be the most appropriate, because it is known to reduce the amount of false diffusion as compared to PLDS or other exponential-type schemes. QUDS was implemented for testing

into the preliminary Cartesian CFD program. However, successful computer runs required a very fine grid, otherwise the solution was unstable, that is, it resulted in computer-overflow. Troubleshooting the problem revealed that the cause was having grid Peclet numbers well in excess of the critical value of two.

Tests were conducted to compare against the solution using PDLS with similar grids. Results indicated that PLDS produced solutions were very close to those obtained using QUDS, with QUDS requiring additional computation time. Subsequent tests were conducted using hybrid versions of QUDS and PDLS, with added computational effort. It was then decided, in order to keep the interpolation scheme as simple as possible to drop QUDS.

Additional tests were conducted to check a new version of the exponential scheme. This version used the exact solution to the one-dimensional advection/diffusion problem for magnitudes of the grid-Peclet number between $P_{e\min}$ and $P_{e\max}$; a linear interpolation for $P_e < P_{e\min}$; and asymptotic values when the magnitude of the grid-Peclet number is greater that $P_{e\max}$. The values for $P_{e\min}$ and $P_{e\max}$ were selected as:

$$\begin{aligned} P_{e\min} &= 1\times10^{-4}, \text{and} \\ P_{e\max} &= 40. \end{aligned} \tag{I.1}$$

These values were selected to provide good resolution of the exponential function, while avoiding singularities and numerical overflows in the limits of $Pe = 0$ and infinity. Results were satisfactory, as solutions were compared against the exact solution (EDS) and PDSL, showing a virtual overlap between the solutions for a wide range of Peclet numbers – both positive and negative. Execution time for the new interpolation scheme was shorter than with PDLS. This scheme was adopted instead of PDLS for the final calculations.

The Cartesian CFD program was tested successfully using standard cases of internal natural-convection flows in rectangular boxes. Heat transfer across solid-fluid boundaries was validated, as well as local and global energy balance. The next step was to extend the capabilities of this model to solve problems with non-

conforming boundaries. That is, boundaries not lying along Cartesian coordinate surfaces. The most logical step was to use coordinate transformation to write the partial differential equations in terms of curvilinear coordinates, and integrate the equations in the transformed domain, while using the previous grid structure to solve the equations.

I.3. Preliminary Advection-Diffusion Interpolation Schemes

A boundary-conforming grid system was used, along with curvilinear coordinate to transform the system of equations from Cartesian space into the transformed domain. The first step in constructing the model involves the selection of the grid topology.

Selection of the Grid Topology

Figure I-1 shows four grid topologies that were considered as potential candidates. These were (a) a cylindrical-coordinate-based non-orthogonal grid, (b) a cylindrical-coordinate-based orthogonal grid, (c) a Cartesian-coordinate-based non- orthogonal grid, (d) a Cartesian-coordinate-based orthogonal grid. The Cartesian coordinates are denoted as x_1, x_2, and x_3 and the curvilinear coordinates are denoted as y^1, y^2, and y^3.

Selection of the type of grid was based on the complexity in the transformed equations, and in generating the grid. Complexity in the transformed equations is dictated mainly by the orientation of coordinate surfaces with respect to the Cartesian system, and the angle of intersection between curvilinear coordinate lines and coordinate surfaces. A Cartesian grid is the simplest to implement, as coordinate surfaces have only one projection component on Cartesian coordinate planes, and the coordinate lines are always orthogonal to coordinate surfaces. Table I-1 contains the components of the face-normal unit vectors in each Cartesian direction, and the Jacobian of the discretized space. Values for these parameters are shown for the Cartesian grid as reference. This table provides an indication of the number of "outer" partial derivatives of the advection-diffusion terms in the

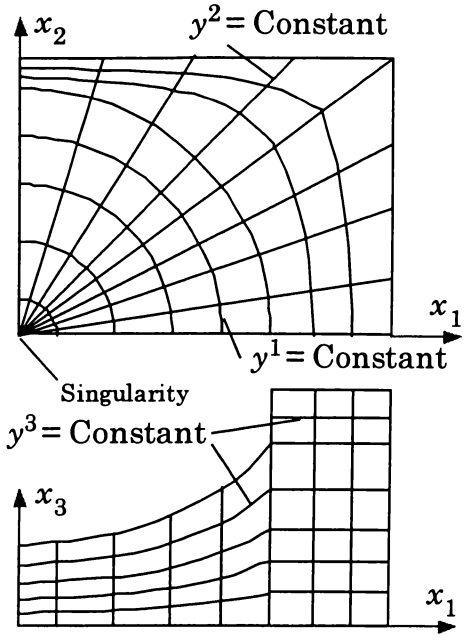

A. Cylindrical-Coordinate-Based Non-Orthogonal Grid

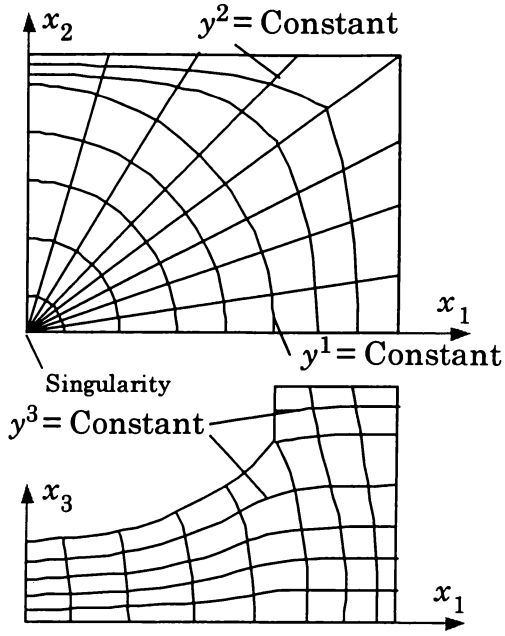

B. Cylindrical-Coordinate-Based Orthogonal Grid

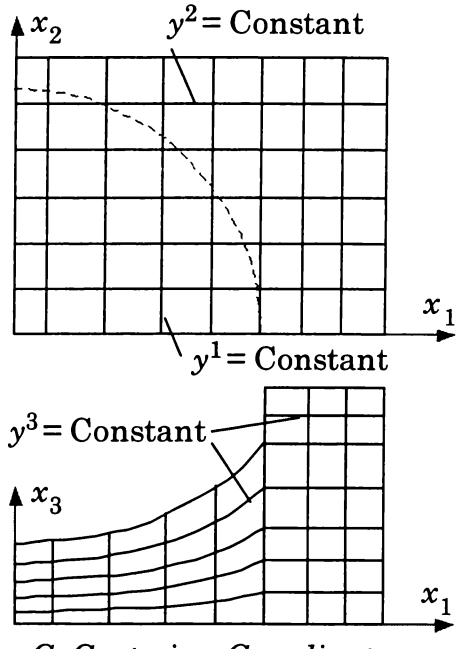

C. Cartesian-Coordinate-Based Non-Orthogonal Grid

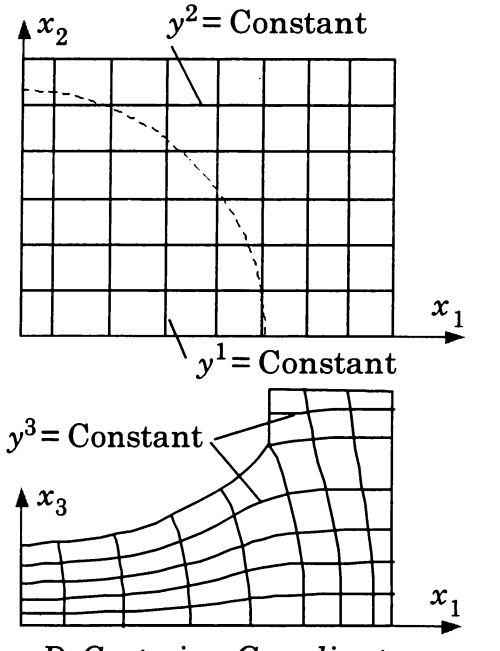

D. Cartesian-Coordinate-Based Orthogonal Grid

Figure I-1. Options for Grid Coordinate Parameterization

Table I-1. Surface/Volume-Discretization Metrics for Various Grid Options

Option→	Cartesian Grid	Grid "A"	Grid "B"	Grid "C"	Grid "D"
η_1^1	1	$f(y^1,y^2)$	$f(y^1,y^2,y^3)$	1	$f(y^1,y^2,y^3)$
η_2^1	0	$f(y^1,y^2)$	$f(y^1,y^2,y^3)$	0	$f(y^1,y^2,y^3)$
η_3^1	0	0	$f(y^1,y^2,y^3)$	0	$f(y^1,y^2,y^3)$
η_1^2	0	$f(y^1,y^2)$	$f(y^1,y^2,y^3)$	0	$f(y^1,y^2,y^3)$
η_2^2	1	$f(y^1,y^2)$	$f(y^1,y^2,y^3)$	1	$f(y^1,y^2,y^3)$
η_3^2	0	0	$f(y^1,y^2,y^3)$	0	$f(y^1,y^2,y^3)$
η_1^3	0	$f(y^1,y^2,y^3)$	$f(y^1,y^2,y^3)$	$f(y^1,y^2,y^3)$	$f(y^1,y^2,y^3)$
η_2^3	0	$f(y^1,y^2,y^3)$	$f(y^1,y^2,y^3)$	$f(y^1,y^2,y^3)$	$f(y^1,y^2,y^3)$
η_3^3	1	$f(y^1,y^2,y^3)$	$f(y^1,y^2,y^3)$	$f(y^1,y^2,y^3)$	$f(y^1,y^2,y^3)$
Jacobian	1	$f(y^1,y^2,y^3)$	$f(y^1,y^2,y^3)$	$f(y^1,y^2,y^3)$	$f(y^1,y^2,y^3)$

transformed equations. The options with orthogonal grids involve nine outer-derivative terms. Option "C" with coordinate parameterization in direction x_3 involves only five outer derivatives. For all options, the Jacobian of the transformation is a function of position.

Another important feature relevant to flux discretization is the orthogonality of local coordinates and the face area. Table I-2 summarizes the local-coordinate orthogonality for the options considered. The orthogonal grids in Options "B" and "D" are locally orthogonal. That is, the face fluxes should not contain cross-derivatives. Option "A" involves flux cross-derivatives on y^3-constant faces, and Option "C" involves flux cross-derivatives in all faces.

Orthogonal grids require the least amount of effort in discretizing the flux terms, but the generation of the grid itself may require the solution of elliptic systems. On the other hand, using non-orthogonal grids, as in Option "C," requires the least amount of effort in the grid generation, but the flux discretization requires the greatest amount of effort. Option "C" was selected because of the simplicity in

Table I-2. Flux-Discretization Node-Cluster Coordinate Orthogonality for Various Grid Options

Option→	Cartesian Grid	Grid "A"	Grid "B"	Grid "C"	Grid "D"
y^1	Yes	Yes	Yes	No	Yes
y^2	Yes	Yes	Yes	No	Yes
y^3	Yes	No	Yes	No	Yes

"Yes" indicates that the lines joining the face node and adjacent cell nodes are normal to the face surface.
"No" indicates otherwise.

generating the grid using algebraic grid generation. This, in turn,requires the derivation of a solver capable of handling non-orthogonal grids, which are significantly more complex than orthogonal-grid solvers. The major advantage of this approach is the flexibility of being able to use other types of grids if the algebraically generated grid proves to be deficient.

Integration and Discretization

Integration and discretization of the scalar equations for temperature and the three velocities was carried-out in the transformed domain. The process was relatively simple, once the derivation for a generalized advection/diffusion equation is applied to these equations, and the concept of cyclical indices is used. The general advection/diffusion equation has the following integrated form.

$$c\left(\phi-\phi^{o}\right)\frac{\overline{J}\Delta\Omega}{\Delta\tau}+$$
$$+\sum_{j=1}^{3}\left(c\,\overline{v^{j}}\phi-\gamma\sum_{i=1}^{3}\overline{J_{i}^{j}}\frac{1}{J}\sum_{k=1}^{3}\left(\overline{\hat{J}_{i}^{k}}\phi_{y^{k}}\right)+\sum_{i=1}^{3}\overline{J_{i}^{j}}h_{i}\right)\Bigg|_{y_{-}^{j}}^{y_{+}^{j}}\Delta\sigma^{j}=s\overline{J}\Delta\Omega, \tag{I.2}$$

where:

c is the capacity density,

ϕ is the generic dependent variable,

$\overline{v^{j}}$ is the transformed velocity,

γ is the diffusivity,

J_i^j is the area equivalence factor for face fluxes,

$\hat{J}_i^k$ is the area equivalence factor for diffusion cross derivatives,

h_i is a generic face flux,

$\Delta\sigma^j$ is the transformed area element,

s is the volumetric flux source,

$\overline{J}$ is the Jacobian of the transformation, and

$\Delta\Omega$ is the transformed volume element.

The most critical issue was to discretize the transformation metric parameters consistently with physical space. The Jacobian of the transformation, $\overline{J}$, maps the volume from one domain to the other, and is defined as the transformed-space-to-physical-space volume ratio and given by:

$$\overline{J} = \frac{\Delta\Omega}{\Delta\mathcal{V}}. \tag{I.3}$$

The area equivalence factor is defined as the ratio of the face-area Cartesian component to transformed area and given by:

$$\overline{J_i^l} = \frac{\overline{\eta_i^l}\,\Delta A^l}{\Delta\sigma^l},\ (i,l) = 1,2,3. \tag{I.4}$$

The transformed velocities are defined in terms of summation involving Cartesian velocities and area equivalence factors,

$$\overline{v^j} = \sum_{i=1}^{3}\left(\overline{J_i^j}u_i\right), j = 1,2,3. \tag{I.5}$$

Details of the derivations are in APPENDIX J.

Flux discretization was done in the same manner as with the Cartesian program to treat advection and diffusion fluxes in each of the coordinate directions. Face fluxes resulting from cross-derivatives were treated explicitly.

Programming of the calculation procedure for solving these variables as scalar quantities was relatively simple, as each cell node had only six associated neighboring nodes in the algebraic equations, and the procedure for one scalar was

identical as the others. The challenge was to devise a coupling scheme for the pressure-velocity solution.

Grid/Variable Arrangement

The original intention was to reuse the Cartesian model based on the SIMPLER algorithm and perform some modifications to treat the transformed equations as if they were solved in Cartesian space. However, this proved difficult because of the extent of the modifications required. The best option was to develop a program from the ground-up to treat curvilinear grids. The best candidates available for grid arrangement were the co-located grid, the staggered grid, and the dual grid arrangement. Because the idea was to apply the notion of the staggered-grid arrangement in SIMPLER to the new solver, the co-located arrangement was ignored. The staggered arrangement required a cumbersome treatment of the pressure-velocity coupling if the face was not orthogonal to any of the Cartesian coordinate directions, and was also rejected. The dual-grid arrangement could be used along with the SIMPLE procedure to produce face-normal velocities (or equivalent contra-variant velocities in transformed space). The dual grid was used despite the knowledge that no published research showed its applicability to three-dimensional problems. However, extension from two-dimensions to three-dimensions seemed obvious at the time. The pressure-velocity node cluster is shown in *Figure I-2*. Pressure and temperature were evaluated at the "main" control-volume nodes, whereas the velocities were evaluated at "dual" control-volume nodes located at the cell's vertices. This arrangement resulted in two sets of control volumes and two sets of geometrical parameters, one associated with the main grid structure, and the other associated with the dual grid structure.

Solution Method for the Pressure-Velocity System

Each of the velocity equations had associated eight pressure nodes. Since the SIMPLER procedure was used, the velocities written in terms of pseudo-velocities and the pressure terms needed to be substituted into mass conservation equation.

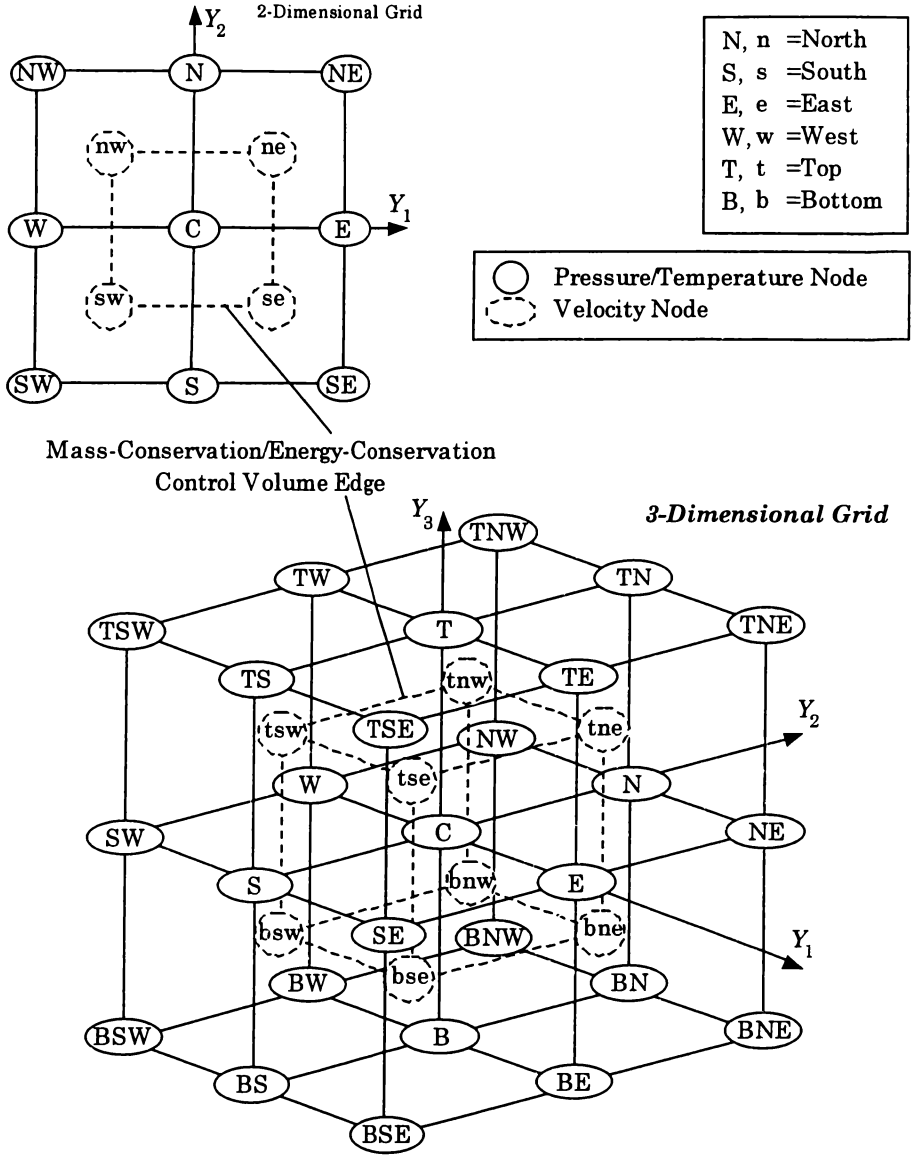

Figure I-2. Pressure Node Cluster for the Dual Grid Arrangement

The mass conservation equation operates on the main cells. Therefore averages of the four velocity nodes per face had to be substituted per main-cell face, and there were six faces. The result was a pressure equation with 27 pressure nodes. The pressure corrector was calculated based on these nodes to correct the velocity field, and the pressure was updated based on the corrected velocities.

The resulting program was tested, but severe problems existed due to the manner in which the pressure was calculated. The system of pressure equations had more unknowns than equations, yielding an undetermined system, which allowed seemingly independent node pressure systems to coexist and produce a checkerboard-like pressure field, resulting in a correct velocity field. This, however would not be a major problem, as the average pressure on the velocity control volumes was the physical pressure. The more serious and challenging problem was keeping the program from diverging. Two-dimensional cases did not show problems as severe as three-dimensional cases. Several benchmark problems were solved successfully for natural convection in enclosures. Two-dimensional solutions were compared against the benchmark numerical solution (De Vahl Davis [24]), the experimental measurements of natural convection flow in a vertical, square cavity (Krane *and* Jesse [65]), and the experimental measurements of natural convection flow in the annulus between two differentially heated horizontal, concentric cylinders (Kuehn *and* Goldstein [67]). All of these numerical solutions compared well with experimental data.

Three-dimensional problems required, in most cases, extremely small time-step intervals and large under-relaxation were required to prevent the solution from diverging. This was unacceptable for program execution time. Problems similar to the one encountered, i.e. the checkerboard pressure patterns, have been reported in the past by Shih, Tan, and Hwang [117] and van der Wijngaart [134]. Wijngaart proposed a method to "filter" the calculated pressure field and produce an "oscillation-free" pressure field.

The above solution would have been sufficient if it had not been for self-consistency in the limit of a uniform temperature field. In such a field, the correct

solution is a hydrostatic pressure field with a null velocity field. The program produced the exact solution in one-, two-, or three-dimensional problems using Cartesian and orthogonal grids, but not when the grid was non-orthogonal. A model for the geometry of interest was set-up and, spurious flow currents prevailed at steady state. The magnitude of the velocities were small (a few millimeters per second), but comparable to those in natural convection at similar boundary temperatures.

Attempts to correct the problem were unsuccessful, and the approach was abandoned. The next attempt used a technique similar to that presented by Peric [105]. A coordinate transformation procedure very similar to that of Peric was used with a co-located grid arrangement. The major difference was in the treatment of the pressure. Peric treats momentum fluxes due to pressure as volume integrals, but this approach would not enforce global momentum conservation. The approach taken used area integrals, instead, resulting in face values. The SIMPLER procedure was no longer used as the pressure-velocity-coupling algorithm. Instead, an approach similar to the operator-splitting procedure (Issa [51]) was used, in which the velocities are written explicitly along the iteration coordinate instead of time, and a one prediction/correction pass is made. In this manner, several outer-loop iterations within a single time step are allowed, in contrast to Issa's procedure, which proceeds to the next time level following the correction steps. This was done by repeating the prediction step for the velocities using the momentum equation following a correction. This procedure proved to be more robust than SIMPLER, producing converged solutions without having to continually adjust convergence parameters. (More detail about the solution procedure will be shown in subsequent sections.)

Unfortunately, the approach adopted above, namely, the coordinate transformation part, did not produce satisfactory solutions to the hydrostatic problem. The source of the problem was not believed existed in the method for discretizing the scalar conservation equations for temperature and velocity, or in the prediction-correction concept, but in the method for interpolating parameters

involved when assembling the pressure equation. Problems with the individual scalar equations were ruled-out because tests of these equations indicated full compliance with conservation laws when mass-conserving velocities were imposed on control-volume faces. As the pressure equation is assembled and solved in curvilinear space, there is the chance that some error prevailed for the calculation of "distances" resulting in inconsistencies between the Cartesian space and the curvilinear space. The discretization of distances used for interpolating variables related to the pressure equation, i.e., cell-to-face pseudo-velocity, and cell-to-face pressure interpolation, is crucial for the reproduction of a hydrostatic field. The discretization of such distances must be consistent with physical space. No errors are allowed. Any minor approximation could lead to an imbalance resulting in the spurious currents mentioned above, which in natural convection are unacceptable because of the order of magnitude of the velocities in these flows.

At this point, it was decided to abandon any effort to transform the equations and instead, to solve the problem directly in physical space using a Cartesian coordinate system and Cartesian unit vectors as base vectors.

I.4. Summary

This chapter focused on the assumptions used for the mathematical model and the preliminary efforts in the numerical approximation. The problem was decomposed into the thermal and fluid flow phenomena within the liquid-lens system and heat transfer outside the liquid-lens system to the surroundings. The numerical model was intended to handle the process within the liquid-lens system, and the process outside the system was model through boundary conditions applied to the liquid-lens system. Assumptions for the mathematical model were listed.

A discussion was presented regarding a preliminary Cartesian model and the selection of the solution advancing procedure and the interpolation scheme. It was concluded that the exponential differencing scheme was more stable than the quadratic-differencing scheme, and that it would be selected for further calculations.

Four options for grid-coordinate parameterization were presented, and the Cartesian-coordinate-based non-orthogonal grid system was selected for grid discretization. The integrated form of the transformed advection-diffusion general equation was presented. Grid/variable arrangement was discussed, and the dual-grid arrangement was selected for implementation of the SIMPLER algorithm. Problems encountered in trying to calculate the pressure field were mentioned, resulting in spurious currents, and it was concluded that a direct integration within physical space was preferable.

APPENDIX J. COORDINATE TRANSFORMATION

J.1. Base Vectors

Figure J-1 shows the Cartesian and curvilinear coordinates, as well as the covariant and contravariant base vectors. The covariant base vector is tangent to curvilinear coordinate lines, while the contravariant base vector is orthogonal to curvilinear surfaces. These are defined as [127]

$$\vec{a}_i \equiv \frac{\partial \vec{x}}{\partial y^i} \left(= \vec{x}_{,y^i} \right), \; i = 1,2,3 \text{ (covariant base vector), and} \tag{J.1}$$

$$\vec{a}^i \equiv \nabla y^i, \; i = 1,2,3 \text{ (contravariant base vector),} \tag{J.2}$$

where $\vec{x}$ is the position vector, and y^i is the curvilinear coordinate, i = 1,2,3.

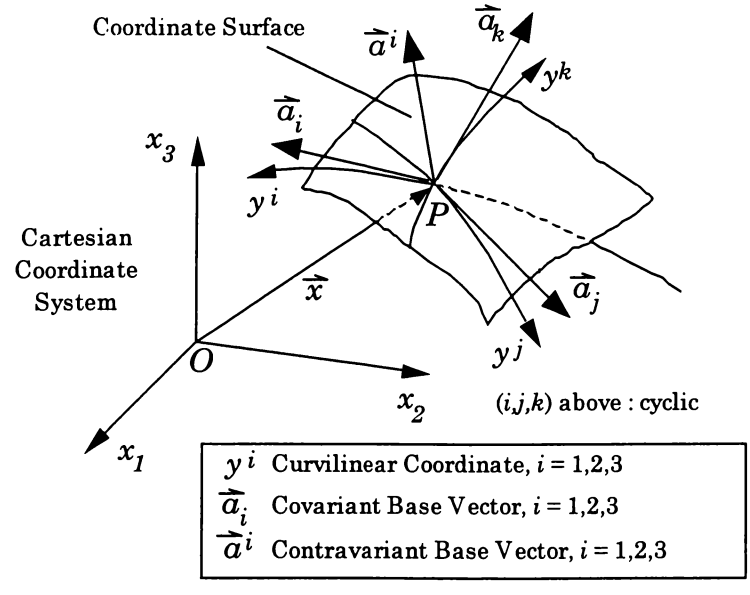

Figure J-1. Schematic of Curvilinear Coordinates and Base Vectors in Cartesian Space

J.2. Length, Area, and Volume Elements

Arc length, area, and volume elements can be expressed in terms of curvilinear parameters as

$$\delta\xi^i = \left|\vec{a}_i\right| \delta y^i \,, \; i = 1,2,3 \,, \tag{J.3}$$

$$\delta A^i = \left|\vec{a}_j \otimes \vec{a}_k\right| \delta\sigma^i \,, \; i = 1,2,3; \; (i,j,k)\text{cyclic}, \text{ and} \tag{J.4}$$

$$\delta V = J\delta\Omega \,, \tag{J.5}$$

where δy^i is the transformed-domain displacement element in the y^i coordinate direction, $\delta\sigma^i$ is the transformed-domain surface element in the i-contravariant direction, defined as

$$\delta\sigma^l = \delta y^m \delta y^n, \; l = 1,2,3; \; (l,m,n)\,\text{cyclic} \,, \tag{J.6}$$

and $\delta\Omega$ is the transformed-domain volume element, defined as

$$\delta\Omega = \delta y^i \delta y^j \delta y^k \,, \; (i,j,k)\,\text{cyclic} \,. \tag{J.7}$$

The factor appearing in the volume element equation is the Jacobian of the transformation, which may be expressed in terms of covariant base vectors products as [127]

$$J \equiv \vec{a}_i \bullet \vec{a}_j \otimes \vec{a}_k \,, \; (i,j,k)\,\text{cyclic} \,. \tag{J.8}$$

The Jacobian of the transformation is essentially a Cartesian-to-transformed space volume ratio.

J.3. Area Element Relationships

The surface area element in the Cartesian domain can be expressed in terms of curvilinear base vectors and coordinate displacements as

$$\vec{\eta}^l \delta A^l = \vec{a}_m \otimes \vec{a}_n \, \delta y^m \delta y^n, \; l = 1,2,3; \; (l,m,n)\,\text{cyclic} \,, \tag{J.9}$$

where

$\vec{\eta}^l$ is the surface normal unit vector in contravariant direction l, l = 1,2,3,

δA^l is the surface element area associated with $\vec{\eta}^l$, l = 1,2,3,

$\vec{a}_l$ is the covariant base vector in direction l, l = 1,2,3, and

δy^l is the curvilinear displacement in direction l, l = 1,2,3.

But it may be shown [127] that

$$\vec{a}_m \otimes \vec{a}_n = J\vec{a}^l,\ l=1,2,3;\ (l,m,n)\ \text{cyclic}, \tag{J.10}$$

where $\vec{a}^l$ is the contravariant base vector in direction l, l = 1,2,3, and J is the Jacobian of the transformation. Substituting Eq. (J.10) in Eq. (J.9) yields

$$\vec{\eta}^l \delta A^l = J\vec{a}^l\, \delta y^m \delta y^n,\ l=1,2,3;\ (l,m,n)\ \text{cyclic}. \tag{J.11}$$

Applying a scalar product with $\vec{\varepsilon}_i$ on both sides of the equation yields

$$\vec{\varepsilon}_i \bullet \vec{\eta}^l \delta A^l = \vec{\varepsilon}_i \bullet J\vec{a}^l\, \delta y^m \delta y^n,\ i,l=1,2,3;\ (l,m,n)\ \text{cyclic}, \tag{J.12}$$

which may be conveniently expressed as

$$\eta_i^l\, \delta A^l = J\, a^l{}_i\ \delta y^m \delta y^n,\ i,l=1,2,3;\ (l,m,n)\ \text{cyclic}. \tag{J.13}$$

where

$$\begin{cases} \eta_i^l \equiv \vec{\eta}^l \bullet \vec{\varepsilon}_i,\ i,l=1,2,3;\ (l,m,n)\ \text{cyclic, and} & \text{(a)} \\ a^l{}_i \equiv \vec{a}^l \bullet \vec{\varepsilon}_i,\ i,l=1,2,3;\ (l,m,n)\ \text{cyclic}. & \text{(b)} \end{cases} \tag{J.14}$$

Substituting this definition into Eq. (J.12) yields a fundamental relationship between Cartesian-space and curvilinear-space area elements in terms of unit-normal, and contravariant projections on Cartesian unit vectors as

$$\eta_i^l\, \delta A^l = J\, a^l{}_i\, \delta\sigma^l,\ i,l=1,2,3. \tag{J.15}$$

For convenience, the above equation is rewritten as

$$\eta_i^l\, \delta A^l = J_i^l\, \delta\sigma^l,\ i,l=1,2,3. \tag{J.16}$$

where J_i^l is the *l-i area equivalence factor*, which is projection of the l-contravariant base vector along the i-direction Cartesian coordinate, the defined as

$$J_i^l = J\, y^l_{x_i}\ \left(= J\, a^l{}_i\right),\ (i,l)=1,2,3. \tag{J.17}$$

The factor J_i^l above, when multiplied by the transformed area element associated, produces an area projection equivalent to that of the physical area element projected on the plane normal to the Cartesian coordinate direction i. This holds for l = 1,2,3, and i =1,2,3.

J.4. Transformation of the General Advection/Diffusion Equation

The transformation of conservation partial-differential equations can be generalized by writing these equations in the general advection/diffusion form for ϕ as the dependent variable, (x_1, x_2, x_3) as the Cartesian coordinates, and τ as time:

$$\begin{cases} (c\phi)_\tau + \sum_{i=1}^{3} (f_i)_{x_i} = s & (a) \\ f_i = c\, u_i \phi - \gamma \phi_{x_i} + h_i \,, \; i = 1,2,3. & (b) \end{cases} \tag{J.18}$$

If (y^1, y^2, y^3) are the curvilinear coordinates, such that points in the transformed domain map to unique points in the Cartesian domain, the following equality holds

$$\phi(x_1, x_2, x_3) = \phi(y^1, y^2, y^3). \tag{J.19}$$

Applying chain rule yields the following equation for the transformation of the partial derivative of ϕ with respect to any of the Cartesian coordinates.

$$\phi_{x_i} = \sum_{j=1}^{3} \left(\phi_{y^j} \; y^j_{x_i} \right), i = 1,2,3. \tag{J.20}$$

For convenience, the above equation will be rewritten as

$$\phi_{x_i} = \frac{1}{J} \sum_{j=1}^{3} \left(J_i^j \, \phi_{y^j} \right), i = 1,2,3, \tag{J.21}$$

where J_i^j is as defined in Eq. (J.17).

Equation (J.21) is written in non-conservative form. Application of this form to transform the outer partial derivative will not ensure global flux conservation. To

ensure global flux conservation the operator for the transformation of partial derivatives must be expressed in conservative form. It may be shown that the above equation can be rewritten in conservative form as

$$\phi_{x_i} = \frac{1}{J}\sum_{j=1}^{3}\left(J_i^j \phi\right)_{y^j}, i = 1,2,3 \text{ (conservative)}. \tag{J.22}$$

The above operator is now applied to the outer partial derivative, which results in the following equation

$$(c\phi)_\tau + \frac{1}{J}\sum_{i=1}^{3}\sum_{j=1}^{3}\left(J_i^j\left(c\, u_i \phi - \gamma \phi_{x_i} + h_i\right)\right)_{y^j} = s. \tag{J.23}$$

Rearranging terms,

$$(c\phi)_\tau + \frac{1}{J}\sum_{j=1}^{3}\left(c\sum_{i=1}^{3}\left(J_i^j u_i\right)\phi - \gamma\sum_{i=1}^{3}J_i^j\phi_{x_i} + \sum_{i=1}^{3}J_i^j h_i\right)_{y^j} = s \tag{J.24}$$

or

$$(c\phi)_\tau + \frac{1}{J}\sum_{j=1}^{3}\left(c\, v^j\phi - \gamma\sum_{i=1}^{3}J_i^j\phi_{x_i} + \sum_{i=1}^{3}J_i^j h_i\right)_{y^j} = s \tag{J.25}$$

where v^j is the "transformed" velocity, expressed as

$$v^j = \sum_{i=1}^{3}\left(J_i^j u_i\right), j = 1,2,3. \tag{J.26}$$

There is no restriction for the inner derivative of the dependent variable in the general A/D equation, since this term represents the diffusion model for the conservation equation. However, it is convenient to write the transformed derivatives for this term in non-conservative form. The result follows.

$$(c\phi)_\tau + \frac{1}{J}\sum_{j=1}^{3}\left(c\, v^j\phi - \gamma\sum_{i=1}^{3}J_i^j\frac{1}{J}\sum_{k=1}^{3}\left(\hat{J}_i^k\phi_{y^k}\right) + \sum_{i=1}^{3}J_i^j h_i\right)_{y^j} = s \tag{J.27}$$

Notice that a distinction was made between the area equivalence factors from the conservative operator applied to the outer derivative, J_i^j, and the one from the non-conservative operator applied to the inner derivative, $\hat{J}_i^k$. This is done because the discretization scheme for the two does not necessarily have to be the same. Before integration, it is convenient to multiply both sides of the equation by the Jacobian to obtain the following equation

$$J(c\phi)_\tau + \sum_{j=1}^{3}\left(c\, v^j\phi - \gamma \sum_{i=1}^{3} J_i^j \frac{1}{J} \sum_{k=1}^{3}\left(\hat{J}_i^k \phi_{y^k}\right) + \sum_{i=1}^{3} J_i^j h_i \right)_{y^j} = Js \tag{J.28}$$

Integration of the above equation in the transformed space yields

$$\begin{aligned} &\int_{\delta\tau}\int_{\delta\Omega} J(c\phi)_\tau\, \delta\Omega\,\delta\tau + \\ &+ \int_{\delta\tau}\int_{\delta\Omega} \sum_{j=1}^{3}\left(c\, v^j\phi - \gamma \sum_{i=1}^{3} J_i^j \frac{1}{J} \sum_{k=1}^{3}\left(\hat{J}_i^k \phi_{y_k}\right) + \sum_{i=1}^{3} J_i^j h_i \right)_{y_j} \delta\Omega\,\delta\tau = \\ &= \int_{\delta\tau}\int_{\delta\Omega} Js\,\delta\Omega\,\delta\tau \end{aligned} \tag{J.29}$$

A fully implicit time discretization scheme yields the following integrated form of the conservation equation, assuming that the variables within the integrals are representative means over the integration surface elements. For the sake of simplicity, the bars representing the mean will be applied to the transformed velocity, the Jacobian, and area equivalence factors, $\overline{J}$, J_i^l, $\hat{J}_i^k$, as shown below.

$$\begin{aligned} &c\left(\phi - \phi^o\right)\frac{\overline{J}\Delta\Omega}{\Delta\tau} + \\ &+ \sum_{j=1}^{3}\left(c\, \overline{v^j}\phi - \gamma \sum_{i=1}^{3} \overline{J_i^j} \frac{1}{J} \sum_{k=1}^{3}\left(\overline{\hat{J}_i^k \phi_{y^k}}\right) + \sum_{i=1}^{3} \overline{J_i^j} h_i \right)\Bigg|_{y_-^j}^{y_+^j} \Delta\sigma^j = s\overline{J}\Delta\Omega \end{aligned} \tag{J.30}$$

where y_-^j and y_+^j are the integration limits along curvilinear coordinate in I-direction.

The value of $\overline{J}$ and J_i^j in the above equation cannot be approximated arbitrarily. They must be calculated consistently with the discretization of space in

the physical domain resulting from the coordinate transformation. If $\overline{J}$ is discretized incorrectly, volumes in the transformed space may not map to volumes in the Cartesian space. If the factors J_i^j are not discretized properly, control-volume face areas may not map correctly between Cartesian and transformed spaces. In addition, the transformed velocities may be improperly evaluated, as this variable is used in their calculation. The result is improper accounting of volumes, surfaces, and mass flux, which in turn, may result in overall flux imbalance, even if the flux discretization scheme works as intended.

To properly account for volume and surface areas, the Jacobian, $\overline{J}$, must be calculated based on the integrated version of the equation used in its definition in Eq. (J.5). Integrating this equation yields

$$\int_{\delta\Omega} \delta\mathcal{V} = \int_{\delta\Omega} J\delta\Omega, \tag{J.31}$$

or

$$\Delta\mathcal{V} = \overline{J}\Delta\Omega, \tag{J.32}$$

which results in the following equation for the Jacobian

$$\overline{J} = \frac{\Delta\Omega}{\Delta\mathcal{V}}. \tag{J.33}$$

In the same manner, to properly account for surface areas, the area equivalence ratio, J_i^j, must be calculated based on the integrated version of the equation used in its definition in Eq. (J.16). Integrating this equation yields

$$\int_{\delta\sigma^l} \eta_i^l \delta A^l = \int_{\delta\sigma^l} J_i^l \delta\sigma^l, \ (i,l) = 1,2,3, \tag{J.34}$$

or

$$\overline{\eta_i^l}\,\Delta A^l = \overline{J_i^l}\,\Delta\sigma^l, \ (i,l) = 1,2,3. \tag{J.35}$$

In the above equation, η_i^l and J_i^l are representative means over the surface integral area. The area equivalence factors may be obtained, once the Cartesian face area and face unit normal vectors are known, using the following equation

$$\overline{J_i^l} = \frac{\overline{\eta_i^l}\,\Delta A^l}{\Delta \sigma^l},\ (i,l) = 1,2,3, \tag{J.36}$$

where the representative mean of the unit-normal vector projection, η_i^l, is calculated based on the representative mean of the unit-normal vector of the control-volume face area as

$$\overline{\eta_i^l} = \overline{\vec{\eta}^l} \bullet \vec{\varepsilon}_i,\ (i,l) = 1,2,3. \tag{J.37}$$

The transformed velocities can be calculated using the above results as

$$\overline{v^j} = \sum_{i=1}^{3}\left(\overline{J_i^j u_i}\right), j = 1,2,3. \tag{J.38}$$

Closure

If the above transformation parameters are calculated correctly, and the results substituted into the integrated advection/diffusion equation obtained above, the Cartesian version of this equation should be recovered, as if it were integrated within Cartesian space. This is done by first substituting back the transformed velocity, Eq. (J.38) into the integrated conservation equation, Eq. (J.30) to obtain the following equation.

$$\begin{aligned} & c\left(\phi - \phi^o\right)\frac{\overline{J}\Delta\Omega}{\Delta\tau} + \\ & + \sum_{j=1}^{3}\left(c\sum_{i=1}^{3}\left(\overline{J_i^j u_i}\right)\phi - \gamma\sum_{i=1}^{3}\overline{J_i^j}\frac{1}{J}\sum_{k=1}^{3}\left(\overline{\hat{J}_i^k \phi_{y^k}}\right) + \sum_{i=1}^{3}\overline{J_i^j h_i}\right)\Bigg|_{y_-^j}^{y_+^j}\Delta\sigma^j = s\overline{J}\Delta\Omega \end{aligned} \tag{J.39}$$

Then, substitution of Eqs. (J.33) and (J.36), yields the following finite-volume equation as if integrated in Cartesian space.

$$c\left(\phi-\phi^{o}\right)\frac{\Delta\mathcal{V}}{\Delta\tau}+$$

$$+\sum_{j=1}^{3}\left(c\sum_{i=1}^{3}\left(\overline{\eta_i^j u_i}\right)\phi-\gamma\sum_{i=1}^{3}\overline{\eta_i^j}\frac{1}{J}\sum_{k=1}^{3}\left(\overline{\hat{J}_i^k\phi_{y^k}}\right)+\sum_{i=1}^{3}\overline{\eta_i^j}h_i\right)\Bigg|_{y_-^j}^{y_+^j}\Delta A^j=s\Delta\mathcal{V} \tag{J.40}$$

where the integration limits, y_-^j and y_+^j, denote opposite boundary locations along a curvilinear coordinate. This equation can be further reorganized as

$$c\left(\phi-\phi^{o}\right)\frac{\Delta\mathcal{V}}{\Delta\tau}+\sum_{j=1}^{3}\left(\sum_{i=1}^{3}\left(cu_i\phi-\gamma\frac{1}{J}\sum_{k=1}^{3}\left(\overline{\hat{J}_i^k\phi_{y^k}}\right)+h_i\right)\overline{\eta_i^j}\right)\Bigg|_{y_-^j}^{y_+^j}\Delta A^j=s\Delta\mathcal{V}, \tag{J.41}$$

which may be rewritten in terms of the flux density as

$$c\left(\phi-\phi^{o}\right)\frac{\Delta\mathcal{V}}{\Delta\tau}+\sum_{j=1}^{3}\left(\sum_{i=1}^{3}f_i^{\phi}\overline{\eta_i^j}\right)\Bigg|_{y_-^j}^{y_+^j}\Delta A^j=s\Delta\mathcal{V}, \tag{J.42}$$

where f_i^{ϕ} is the discretized flux density of ϕ in Cartesian direction i:

$$f_i^{\phi}=\left(cu_i\phi-\gamma\frac{1}{J}\sum_{k=1}^{3}\left(\overline{\hat{J}_i^k\phi_{y^k}}\right)+h_i\right),\ i=1,2,3. \tag{J.43}$$

Both Eqs. (J.30) and (J.40) are equivalent and should yield the same results when implemented into computer code.

VITA

Jose A. Lamas was born in Havana, Cuba on November 27, 1957. He and his family moved to Caracas, Venezuela in 1961, following the Cuban revolution. There, he attended elementary and high schools at "Colegio Claret." He completed his Bachelor of Science degree in Mechanical Engineering at the "Universidad Simon Bolivar," Caracas, in May of 1981. He then pursued his master's program at the University of Tennessee, Knoxville and received his Master of Science degree in Mechanical Engineering in August of 1985. He started his doctoral studies the following spring at the same school. Having his coursework completed, he engaged in a full time position with General Dynamics in Sterling Heights, Michigan in April of 1992. In August of 1996, he relocated to Woodbridge, Virginia with the same company. He returned to Knoxville in July of 2000 to complete his doctoral degree, and received the Doctor of Philosophy degree with major in Mechanical Engineering in May of 2002.

3238 2553 39
07•24•02 MRB